Advances in Clinical and Experimental Medicine

MONTHLY ISSN 1899-5276 (PRINT) ISSN 2451-2680 (ONLINE) advances.umw.edu.pl

2026, Vol. 35, No. 7 (July)

Impact Factor (IF) – 2.5
Ministry of Science and Higher Education – 70 pts
Index Copernicus (ICV) – 161.00 pts

Wroclaw Medical University

Advances
in Clinical and Experimental
Medicine

Advances
in Clinical and Experimental Medicine

ISSN 1899-5276 (PRINT) ISSN 2451-2680 (ONLINE) advances.umw.edu.pl

MONTHLY 2026
Vol. 35, No. 7
(July)

Advances in Clinical and Experimental Medicine (*Adv Clin Exp Med*) publishes high-quality original articles, research-in-progress, research letters and systematic reviews and meta-analyses of recognized scientists that deal with all clinical and experimental medicine.

Editorial Office
ul. Marcinkowskiego 2–6
50-368 Wrocław, Poland
Tel.: +48 71 784 12 05
E-mail: acem.journal@umw.edu.pl

Publisher
Wroclaw Medical University
Wybrzeże L. Pasteura 1
50-367 Wrocław, Poland

Online edition is the original version of the journal

Editor-in-Chief
Prof. Donata Kurpas

Deputy Editor
Prof. Robert Śmigiel

Managing Editor
Marek Misiak, MA

Statistical Editors
Wojciech Bombała, MSc
Łucja Janek, MSc
Assoc. Prof. Andrzej Paweł Karpiński
Anna Kopszak, MSc
Dr. Krzysztof Kujawa
Prof. Łukasz Łaczmański
Jakub Wronowicz, MSc
Maciej Wuczyński, MSc

Manuscript editing
Marek Misiak, MA
Paulina Piątkowska, MA

Scientific Committee
Prof. Sabine Bährer-Kohler
Prof. Sandra Maria Barbalho
Prof. Antonio Cano
Prof. Chong Chen
Prof. Breno Diniz
Prof. Erwan Donal
Prof. Chris Fox
Prof. Yuko Hakamata
Prof. Carol Holland
Prof. Markku Kurkinen
Prof. Christopher S. Lee
Prof. Christos Lionis
Prof. Leszek Lisowski
Prof. Raimundo Mateos
Prof. Zbigniew W. Raś
Prof. Dorota Religa
Prof. Jerzy W. Rozenblit
Prof. Silvina Santana
Prof. Sajee Sattayut
Prof. Barbara Schneider
Prof. James Sharman
Prof. Jamil Shibli
Prof. Luca Testarelli
Prof. Michał J. Toborek
Prof. László Vécsei
Prof. Cristiana Vitale
Prof. Ming Yi
Prof. Hao Zhang

Section Editors

Basic Sciences
Prof. Iwona Bil-Lula
Prof. Dorota Danuta Diakowska
Prof. Bartosz Kempisty
Dr. Wiesława Kranc
Dr. Anna Lebedeva
Dr. Piotr Chmielewski
Dr. Phuc Van Pham
Dr. Sławomir Woźniak

Biochemistry
Assoc. Prof. Mateusz Labudda
Dr. Anna Leśków

Clinical Anatomy, Legal Medicine, Innovative Technologies
Prof. Rafael Boscolo-Berto

Dentistry
Prof. Marzena Dominiak
Prof. Tomasz Gedrange
Prof. Jamil Shibli
Prof. Luca Testarelli

Laser Dentistry
Prof. Kinga Grzech-Leśniak

Dermatology
Prof. Jacek Szepietowski
Assoc. Prof. Marek Konop

Emergency Medicine, Innovative Technologies
Dr. Jarosław Janc
Prof. Jacek Smereka

Evidence-Based Healthcare
Assoc. Prof. Aleksandra Królikowska
Dr. Robert Prill

Gynecology and Obstetrics
Assoc. Prof. Tomasz Fuchs
Dr. Jakub Staniczek

Histology and Embryology
Dr. Mateusz Olbromski

Internal Medicine

Angiology
Dr. Angelika Chachaj

Cardiology
Dr. Daniel Morris
Assoc. Prof. Joanna Popiołek-Kalisz
Prof. Pierre François Sabouret
Assoc. Prof. Magdalena Karolina Wawrzyńska

Endocrinology
Prof. Marek Bolanowski
Assoc. Prof. Agnieszka Zubkiewicz-Kucharska

Gastroenterology
Assoc. Prof. Wojciech Błoński
Dr. Anna Kofla-Dłubacz
Assoc. Prof. Katarzyna Neubauer

Hematology
Prof. Andrzej Deptała
Prof. Dariusz Wołowiec

Nephrology and Transplantology
Prof. Mirosław Banasik
Prof. Krzysztof Letachowicz
Assoc. Prof. Tomasz Gołębiowski

Rheumatology
Assoc. Prof. Agata Sebastian
Dr. Sylwia Szafraniec-Buryło

Lifestyle Medicine, Nutrition and Health Promotion
Assoc. Prof. Michał Czapla
Prof. Raúl Juárez-Vela
Dr. Anthony Dissen
Prof. Antonio Martínez-Sabater

Microbiology
Prof. Emil Paluch
Assoc. Prof. Adam Junka

Molecular Biology
Dr. Monika Bielecka
Prof. Dorota Danuta Diakowska
Dr. Phuc Van Pham

Neurology
Assoc. Prof. Magdalena Koszewicz
Dr. Nasrollah Moradikor
Assoc. Prof. Anna Pokryszko-Dragan
Dr. Masaru Tanaka

Neuroscience
Dr. Simone Battaglia
Dr. Francesco Di Gregorio
Dr. Nasrollah Moradikor

Omics, Bioinformatics and Genetics
Assoc. Prof. Izabela Łaczmańska
Prof. Łukasz Łaczmański
Prof. Mariusz Fleszar
Assoc. Prof. Paweł Andrzej Karpiński

Oncology
Prof. Andrzej Deptała
Prof. Adam Maciejczyk
Prof. Hao Zhang

Gynecological Oncology
Dr. Marcin Jędryka

Ophthalmology
Dr. Małgorzata Gajdzis
Prof. Marta Misiuk-Hojło

Orthopedics
Prof. Paweł Reichert

Otolaryngology
Prof. Tomasz Zatoński

Pediatrics

Pediatrics, Metabolic Pediatrics, Clinical Genetics, Neonatology, Rare Disorders
Dr. Anna Kofla-Dłubacz
Prof. Robert Śmigiel

Pediatric Nephrology
Prof. Katarzyna Kiliś-Pstrusińska

Pediatric Oncology and Hematology
Assoc. Prof. Marek Ussowicz

Pharmaceutical Sciences
Assoc. Prof. Marta Kepinska
Prof. Adam Matkowski

Pharmacoeconomics
Dr. Sylwia Szafraniec-Buryło

Psychiatry
Dr. Melike Küçükkarapınar
Prof. Jerzy Leszek
Assoc. Prof. Bartłomiej Stańczykiewicz

Public Health
Prof. Monika Sawhney
Prof. Izabella Uchmanowicz

Pulmonology
Prof. Anna Brzecka

Qualitative Studies, Quality of Care
Prof. Ludmiła Marcinowicz
Assoc. Prof. Anna Rozensztrauch

Radiology
Prof. Paweł Gać

Rehabilitation
Assoc. Prof. Aleksandra Królikowska
Dr. Robert Prill

Surgery
Assoc. Prof. Mariusz Chabowski

Telemedicine, Geriatrics, Multimorbidity
Assoc. Prof. Maria Magdalena Bujnowska-Fedak
Prof. Ferdinando Petrazzuoli

Editorial Policy

Advances in Clinical and Experimental Medicine (Adv Clin Exp Med) is an independent multidisciplinary forum for exchange of scientific and clinical information, publishing original research and news encompassing all aspects of medicine, including molecular biology, biochemistry, genetics, biotechnology and other areas. During the review process, the Editorial Board conforms to the "Uniform Requirements for Manuscripts Submitted to Biomedical Journals: Writing and Editing for Biomedical Publication" approved by the International Committee of Medical Journal Editors (www.ICMJE.org). The journal publishes (in English only) original papers and reviews. Short works considered original, novel and significant are given priority. Experimental studies must include a statement that the experimental protocol and informed consent procedure were in compliance with the Helsinki Convention and were approved by an ethics committee.

For all subscription-related queries please contact our Editorial Office: acem.journal@umw.edu.pl
For more information visit the journal's website: advances.umw.edu.pl

Pursuant to the ordinance of the Rector of Wroclaw Medical University No. 37/XVI R/2024, from March 1, 2024, authors are required to pay a fee for each manuscript accepted for publication in the journal Advances in Clinical and Experimental Medicine. The fee amounts to 1600 EUR for all types of papers.

Indexed in: MEDLINE, Science Citation Index Expanded, Journal Citation Reports/Science Edition, Scopus, EMBASE/Excerpta Medica, Ulrich's™ International Periodicals Directory, Index Copernicus

Typographic design: Piotr Gil, Monika Kolęda
DTP: Wydawnictwo UMW
Cover: Monika Kolęda
Printing and binding: Agencja Wydawnicza "ARGI" s.c.

Advances
in Clinical and Experimental Medicine

MONTHLY 2026, Vol. 35, No. 7 (July)

ISSN 1899-5276 (PRINT)
ISSN 2451-2680 (ONLINE)
advances.umw.edu.pl

Contents

Editorials

Ophthalmology

1127 Jakub Kozimor, Małgorzata Gajdzis, Radosław Kaczmarek
Advancing evidence-based glaucoma care: Methodological, therapeutic, and structural changes in the 6th edition of the European Glaucoma Society guidelines in the context of the Polish Ophthalmological Society Recommendations

Original papers

Cardiology

1133 Konrad Stępień, Grzegorz Horosin, Natalia Kachnic, Alicia del Carmen Yika, Aleksandra Karcińska, Piotr Walczak, Karol Nowak, Mateusz Podolec, Jadwiga Nessler, Jarosław Zalewski
Statin therapy improves long-term survival in patients with myocardial infarction and non-obstructive coronary arteries (MINOCA)

Cardiology

1143 Pei Shi, Xiaojuan Meng
Nonalcoholic fatty liver disease and cardiovascular risk in patients with unstable angina: A 3-year prospective follow-up study

Pediatric nephrology

1153 Ewelina Jarosz-Wójcik, Mateusz A. Zajączkowski, Dorota Drożdż, Palina Warmachowska, Mikołaj Brzeźniak, Aleksandra M. Molek, Oliwia Andrasz, Olga Szczerbak, Monika Miklaszewska
Impact of the COVID-19 pandemic on pediatric hemolytic uremic syndrome: Epidemiology, complications, and outcomes

Microbiology

1163 Dominika Giżycka, Paweł Sacha, Piotr Majewski, Karolina Maternia-Dudzik, Marta Musz-Kawecka, Anna Żaczek, Jan Kochanowicz, Elżbieta A. Tryniszewska
Antibiotic resistance and molecular characteristics of OXA-48-producing *Klebsiella pneumoniae* isolates from northeastern Poland

Immunology; hematology; molecular biology; oncology

1169 Junyi Li, Huoyan Zhu, Chaoqiong Ye, Shengnan Xu, Zhihua Wu, Yuping Deng
Single-cell RNA sequencing reveals immunological heterogeneity of the tumor microenvironment in acute myeloid leukemia

Basic sciences; microbiology

1187 Lili Ma, Lin Lu, Xiaohui Liu, Lei Wang, Yan Liu, Yaqi Wang, Yankun Liu, Jinghua Zhang, Yufeng Li
Nanog promotes proliferation, migration, and invasion of gastric cancer cells via regulation of the KDM5B/H3K4me3 epigenetic axis

Cardiac surgery; heart and cardiovascular system; molecular biology

1199 Shushu Yu, Mingliang Wang, Yun Xie, Bo Wang, Yawei Xu
Let-7e-5p promotes cardiac hypertrophy by targeting *LBH* and regulating the IGF–PI3K–AKT signaling pathway

Basic sciences; orthopedics

1215 Guihao Zheng, Yulong Ouyang, Shuilin Chen, Bei Hu, Shuai Xu, Guicai Sun
Identification and validation of novel diagnostic biomarkers across multiple tissues in osteoarthritis

Metabolic pediatrics, clinical genetics, rare disorders
1235 Lifeng Zhang, Xiangjing Chen, Xin Zhang, Ya Yan, Renzhong Wang
Family and dietary risk factors associated with childhood sleep disorders: Evidence from a cross-sectional study in China

Dental surgery; maxillofacial surgery
1247 Sebastian Dominiak, Aleksandra Kowalczyk, Paweł Kubasiewicz-Ross, Marzena Dominiak, Alicja Baranowska, Cyprian Olchowy, Michał Ciszyński
Effect of low-level laser therapy on healing after sinus floor augmentation using allograft and xenograft bone materials

Oral pathology; endocrinology; metabolic pediatrics
1259 Natalia Torlińska-Walkowiak, Katarzyna Anna Majewska, Anna Sowińska, Andrzej Kędzia, Justyna Opydo-Szymaczek
Correlation between dental, bone, and chronological age in children with growth hormone deficiency

Dental surgery; periodontology
1269 Nanxi Tao, Renata Samulak, Łukasz Wilczyński, Maciej Mularczyk, Mariusz Suwała, Joanna Hetmańska-Kołacz, Monika Machoy-Rakoczy
Optical coherence tomography and biometric ultrasound for gingival phenotype and epithelial thickness assessment: A cross-sectional pilot study

Reviews

Neurology
1281 Justyna A. Pigońska, Marta Banach , Paweł S. Walkowiak, Aneta Zygulska
Oxaliplatin-induced peripheral neuropathy in cancer treatment: Mechanisms, risk factors, and management strategies

Gastroenterology and hepatology
1297 Eyad Gadour, Bogdan Miutescu, Mohammed Saad AlQahtani, Deiana Vuletici, Ghassan Elsayed, Ielmina Domilescu, Antonio Facciorusso
Diagnostic challenges in progressive familial intrahepatic cholestasis type 3 (PFIC3) misdiagnosed as Wilson's disease: A systematic review

Metabolic pediatrics, clinical genetics, neonatology, rare disorders
1307 Joanna Chrzanowska, Aleksandra Oparska, Agata Wróblewska, Krzysztof Ciucias, Maria Luboińska-Cebula, Robert S. Śmigiel, Beata Wikiera
Complex mosaic form of trisomy chromosome 18 and monosomy chromosome X in a girl with esophageal atresia and mild developmental delay: Diagnostic and therapeutic challenge and a review of literature

Advancing evidence-based glaucoma care: Methodological, therapeutic, and structural changes in the 6th edition of the European Glaucoma Society guidelines in the context of the Polish Ophthalmological Society Recommendations

Jakub Kozimor[A–F], Małgorzata Gajdzis[A,C–F], Radosław Kaczmarek[A,E,F]

Department and Clinic of Ophthalmology, Medical University Hospital, Wrocław, Poland

A – research concept and design; B – collection and/or assembly of data; C – data analysis and interpretation;
D – writing the article; E – critical revision of the article; F – final approval of the article

Advances in Clinical and Experimental Medicine, ISSN 1899–5276 (print), ISSN 2451–2680 (online) *Adv Clin Exp Med*. 2026;35(7):1127–1131

Address for correspondence
Jakub Kozimor
E-mail: jakub.kozimor@gmail.com

Funding sources
None declared

Conflict of interest
None declared

Received on February 26, 2026
Reviewed on March 13, 2026
Accepted on May 14, 2026

Published online on July 3, 2026

Abstract

This article presents selected recommendations included in the 6th Edition of European Glaucoma Society (EGS) guidelines and highlights key differences compared to the previous (5th) and the latest revisions of Polish Ophthalmology Society (PTO) guidelines. The current edition is primarily an update to the earlier guidelines, incorporating the context of new technologies, the results of recent scientific research, and responses to important clinical questions – including those informed by input from the Experts by Experience (EbE-EGS) patient panel. These guidelines constitute a comprehensive, coherent, and evidence-based set of information and recommendations, useful both for making complex therapeutic decisions and in everyday clinical practice.

Key words: glaucoma, intraocular pressure, practice guidelines as topic, evidence-based medicine, patient participation

Cite as
Kozimor J, Gajdzis M, Kaczmarek R. Advancing evidence-based glaucoma care: Methodological, therapeutic, and structural changes in the 6th edition of the European Glaucoma Society guidelines in the context of the Polish Ophthalmological Society Recommendations. *Adv Clin Exp Med*. 2026;35(7):1127–1131. doi:10.17219/acem/221825

DOI
10.17219/acem/221825

Copyright
Copyright by Author(s)
This is an article distributed under the terms of the Creative Commons Attribution 3.0 Unported (CC BY 3.0) (https://creativecommons.org/licenses/by/3.0/)

Highlights

- The 6th edition of the European Glaucoma Society (EGS) guidelines introduces updated evidence-based recommendations integrating new ophthalmic technologies and recent glaucoma research findings.
- The revised glaucoma management guidelines emphasize patient-centered care by incorporating clinical questions and perspectives from the Experts by Experience (EbE-EGS) patient panel.
- A comparative analysis of the EGS and Polish Ophthalmological Society (PTO) guidelines highlights key updates in glaucoma diagnosis, treatment strategies, and everyday clinical decision-making.

Introduction

On September 9, 2025, the 6th edition of the European Glaucoma Society (EGS) Guidelines was published in the *British Journal of Ophthalmology*. The authors stated their mission as follows: "The aim of care for patients with glaucoma or at risk of developing it is to promote well-being and quality of life (QoL) within a sustainable healthcare system."[1] Published regularly for nearly 30 years, the European Glaucoma Society Guidelines have served as an important source of knowledge for clinicians involved in glaucoma care since their inception. The current 6th edition updates and expands upon the 5th edition in response to the rapid growth of scientific evidence and technological advances. It places particular emphasis on evidence synthesis, patient-centered care, and the incorporation of new clinical questions, especially in areas such as artificial intelligence (AI), cost-effectiveness analyses, strategies to improve adherence to recommendations, and pediatric glaucoma.

Evidence was collected in 2024 through systematic reviews addressing diagnostics, prognosis, and treatment, in collaboration with the US Cochrane Eyes and Vision Group. Rigorous methodological criteria based on the GRADE system were again applied to address key clinical questions. These questions were developed on the basis of surveys conducted among EGS members and the EGS Experts by Experience (EbE EGS) patient panel. The inclusion of patient perspectives in the development of clinical questions reflects the principles of patient-centered medicine, and patient feedback became an integral component of the methodological framework. In addition to answers to the key clinical questions, the recommendations and guidance included in the publication were also based on expert consensus.[1,2]

Key clinical questions and evidence-based recommendations

The core of the guidelines consists of a series of key clinical questions addressing a broad spectrum of diagnostic and therapeutic issues. This edition expands the discussion of risk factors, treatment selection, surgical options, strategies to improve adherence, and the role of emerging technologies.

Among the recognized risk factors, the following were identified as significant: elevated intraocular pressure (IOP), pseudoexfoliation syndrome, advanced age, non-White ethnicity, family history, myopia, unstable blood pressure, and cardiovascular comorbidity. The evidence regarding certain systemic diseases as risk factors, including hypertension, Alzheimer's disease, migraine, and Raynaud's syndrome, was considered inconclusive.[1]

According to the recommendations, treatment of primary open-angle glaucoma should begin with monotherapy, most commonly a prostaglandin analog, which remains the most effective pharmacological option, or with selective laser trabeculoplasty (SLT), which has been shown to be at least as effective as pharmacological treatment in patients with mild-to-moderate disease. The choice of therapy should take into account patient comorbidities, treatment costs, the ability to self-administer eye drops, and individual patient preferences.[1]

Regarding surgical management, trabeculectomy remains the gold standard for the treatment of open-angle glaucoma, although minimally invasive glaucoma surgery (MIGS) procedures may reduce the pharmacological burden in the earlier stages of the disease. In advanced glaucoma, trabeculectomy is preferred because MIGS procedures are generally insufficient to achieve the target IOP.

The Guidelines also address the choice of surgical procedure in patients with coexisting cataract. Phacoemulsification alone is usually insufficient to adequately control IOP, although it may result in a modest reduction in IOP, particularly in pseudoexfoliative glaucoma. Combined procedures should be considered when the target IOP cannot be achieved with cataract surgery alone. If a filtering bleb procedure is planned, cataract surgery is recommended as the first step, when clinically appropriate, followed by glaucoma surgery, as simultaneous phacoemulsification has been shown to compromise bleb function.[1]

To improve adherence, it is advised to simplify treatment regimens, enhance education, ensure effective communication, and provide regular reminders of recommendations.[1] Attention was also drawn to the lack of strong

evidence supporting the efficacy of acupuncture, cannabinoids, or alternative therapies. Research is ongoing regarding the potential neuroprotective effects of citicoline and nicotinamide.[1] The optimal frequency of follow-up examinations was not explicitly defined. For ocular hypertension (OHT), intervals shorter than 1 year were generally considered not cost-effective. Increased frequency of examinations may be justified in patients with additional risk factors, failure to achieve target IOP, or evidence of progression.[1]

Despite promising results in screening, diagnosis, and predicting progression, the use of AI models is not yet recommended for routine clinical use due to limited evidence, generalization issues, and concerns about personal data protection.[1] Questions from the previous edition were reiterated and enriched by feedback from the patient panel. A questionnaire facilitating patient interviews at both the diagnosis and follow-up stages was also suggested.

An important section of the guidelines is the "Choosing Wisely" component. It indicates interventions to avoid due to insufficient evidence, promoting effective resource utilization and evidence-based practice. Noteworthy recommendations include refraining from routine laser iridotomies in eyes with suspected angle closure without additional risk factors, not modifying IOP measurements using algorithms that rely on central corneal thickness, and avoiding the diagnosis of glaucoma based solely on optical coherence tomography (OCT) findings.[1]

Diagnostics, classification, and terminology

In the current edition, greater emphasis is placed on integrating new technologies in diagnostics rather than on innovations in fundamental issues. Although the changes in classification are minor, they reflect trends observed in current scientific research related to secondary glaucoma and pediatric ophthalmology. Pediatric glaucoma is divided into primary congenital glaucoma, juvenile open-angle glaucoma, and secondary glaucoma, with specific underlying causes.[1]

Open-angle glaucoma is categorized into primary open-angle glaucoma and secondary glaucoma, including glaucoma caused by eye diseases (with specification of the underlying cause), trauma, iatrogenic factors, and systemic diseases.[1] Angle-closure glaucoma is divided into primary and secondary types. Primary angle-closure glaucoma is further classified according to the timing of onset into acute and chronic forms. For secondary glaucoma, the classification has been expanded based on the underlying causes.[1] The importance of performing gonioscopy is once again emphasized due to its impact on prognosis and the effectiveness of therapeutic methods.[1,2]

Treatment

In this edition of the guidelines, recommendations were expanded to include issues related to patients' lifestyles and QoL as well as the likelihood of adherence to therapeutic regimens. The authors recognize patients' behavioral aspects and their actual adherence to recommendations as key determinants of therapeutic outcomes. Among the methods proposed to improve cooperation, the importance of simplifying the regimen for instilling eye drops and suggesting technological support through reminder systems and alarms is emphasized. An intriguing development in enhancing treatment efficacy involves emerging methods of sustained drug delivery, including prostaglandin-releasing implants, drug-eluting contact lenses, and subconjunctival implants. However, these methods are currently not available in Europe.

Therapeutic strategies prioritize preserving visual function and QoL by lowering IOP to a predetermined target level. The guidelines define the target pressure as the upper limit of IOP that allows halting or sufficiently slowing the progression of visual field loss in order to maintain QoL for the expected duration of the patient's life. The target is determined by the severity of neuropathy, baseline IOP, rate of progression, and risk factors.[1]

In the general principles of therapeutic interventions developed by the EGS, strong emphasis is placed on individualization to achieve the target IOP, which requires regular re-evaluation.

The recommendations for pharmacological therapy uphold prostaglandin analogs as first-line treatment due to their efficacy and safety profiles. The escalation ladder includes switching to an alternative monotherapy and subsequently to combination therapy if the target IOP is not achieved. The use of preservative-free formulations may improve tolerance.[1,2]

Selective laser trabeculoplasty is an effective alternative to pharmacological treatment for many patients with primary open-angle glaucoma (POAG) and OHT Laser iridotomy remains an important treatment for angle closure. Peripheral thermal iridoplasty is indicated as a supportive treatment for plateau iris in patients with angle closure who have undergone iridotomy, although its effectiveness in lowering IOP is limited.[1]

Regarding surgical interventions, the central role of trabeculectomy is again emphasized as the procedure that provides the greatest reduction in IOP, particularly in cases of advanced disease. Minimally invasive glaucoma surgery is appropriate in selected cases of early and moderate glaucoma to reduce the pharmacological burden. Cycloablative procedures are reserved for cases in which filtration surgery has a low likelihood of success, for the acute management of malignant glaucoma due to aqueous misdirection, and for treatment-resistant cases.[1] The guidelines also address treatment during pregnancy, dietary supplementation, and neuroprotection.

Patient feedback and impact on diagnostics

Feedback from patients in the EbE panel informed revisions to recommendations on diagnostic tests. Examinations conducted during the initial visit should include visual acuity assessment, gonioscopy, tonometry, central corneal thickness measurement, visual field assessment, and optic nerve head evaluation. Optical coherence tomography has been recognized as useful but insufficient as a standalone diagnostic tool. Patients emphasized the importance of understanding the purpose and sequence of tests, the concept of target IOP, and the reasons for measuring corneal thickness. Gonioscopy remains an essential examination and, according to the authors, cannot be replaced solely by imaging techniques.

PTO vs EGS recommendations comparison

A clear distinction between the 6th edition of the EGS guidelines and the Polish Ophthalmological Society (PTO) guidelines lies in the degree of emphasis placed on methodological rigor and patient participation. The EGS document relies extensively on systematic reviews, evidence synthesis, and structured input from the EbE patient panel. In contrast, the PTO guidelines, while clinically practical and aligned with most EGS principles, maintain a more expert opinion-based approach, focusing on applicability within the national healthcare system and providing more operational detail on diagnostic sequencing, treatment organization, and follow-up logistics.[1,3]

Specific divergence emerges in therapeutic recommendations, particularly regarding laser therapy, pharmacological choices, and the sequencing of surgical interventions. The EGS strongly elevates SLT to a first-line option equivalent to prostaglandin analogs for POAG and OHT, emphasizing its efficacy and cost-effectiveness across mild and moderate stages of the disease. In contrast, the PTO guidelines still present topical monotherapy, especially prostaglandin analogs, as the standard starting point, reserving SLT mainly for inadequate response, intolerance, or anticipated adherence issues.[1,3]

Differences are also visible in the approach to medication sequencing. The EGS explicitly promotes switching within monotherapy classes before escalating to fixed combinations and highlights the importance of minimizing preservatives, whereas the Polish guidelines more readily move to combination therapy and strongly emphasize the use of preservative-free preparations for ocular surface protection, even earlier in the treatment course.[1,3]

In cataract-related decision-making, the EGS states that phacoemulsification alone is insufficient for meaningful IOP control, except for modest reductions in pseudoexfoliative glaucoma, and recommends performing cataract surgery before trabeculectomy when both procedures are indicated, as combined procedures compromise bleb survival. The PTO guidelines, while acknowledging these principles, provide more detailed procedural pathways, reflecting a more step-by-step, sequential approach.[1,4]

Moreover, the EGS consistently positions trabeculectomy as the gold standard for achieving a low target IOP in advanced glaucoma, with MIGS primarily recommended to reduce medication burden in early or moderate disease. By contrast, the Polish surgical guidelines provide broader indications for seton implants and describe a larger role for cyclodestructive procedures in selected cases, including those with a poor visual prognosis or a low probability of success with filtration surgery.[1,4]

Together, these differences reflect the complementary roles of international evidence-based frameworks and national practice-oriented recommendations.

Conclusions

The EGS guidelines are a comprehensive and exhaustive source of scientific knowledge on glaucoma. By integrating systematic reviews, expert opinions, and patient perspectives, this publication serves not only as a compendium for researchers but also as a practical framework for clinicians. By considering the psychosocial dimensions of care and patient interests, it offers recommendations that facilitate clinical decision-making in real-world settings.

The transition from the 5th to the 6th edition of the EGS guidelines represents a necessary update and further development of strategies for understanding the disease and improving communication in the care of patients with glaucoma. In contrast to previous editions, the methodology used to develop recommendations was updated to incorporate patient consultations; the evidence base was expanded; and issues related to new technologies (including AI models) and adherence were further addressed. Compared with the PTO guidelines, the EGS guidelines present a more general, evidence-based perspective, whereas the PTO guidelines adopt a more procedural, practice-oriented approach.

The new edition of the guidelines is a richer and more practical resource that does not abandon the clinical foundations established in the previous edition.

Use of AI and AI-assisted technologies

Not applicable.

ORCID iDs

Radosław Kaczmarek https://orcid.org/0000-0001-9920-4406
Małgorzata Gajdzis https://orcid.org/0009-0005-6633-3902
Jakub Kozimor https://orcid.org/0009-0000-9706-311X

References

1. Pazos M, Traverso CE, Viswanathan A, et al. European Glaucoma Society: Terminology and guidelines for glaucoma, 6th Edition. *Br J Ophthalmol*. 2025;109(Suppl 1):1–212. doi:10.1136/bjophthalmol-2025-egsguidelines
2. European Glaucoma Society. European Glaucoma Society Terminology and Guidelines for Glaucoma, 5th Edition. *Br J Ophthalmol*. 2021;105(Suppl 1):1–169. doi:10.1136/bjophthalmol-2021-egsguidelines
3. Szaflik JP, Dobrowolski D, Grabska-Liberek I, et al. Wytyczne diagnostyki i leczenia jaskry (aktualizacja 2022). Warsaw, Poland: Polskie Towarzystwo Okulistyczne; 2022. https://pto.com.pl/wp-content/uploads/2022/05/Wytyczne-diagnostyki-i-leczenia-jaskry-aktualizacja-2022.pdf
4. Wierzbowska J, Grabska-Liberek I, Majszyk-Ionescu J, Skowyra A, Zaleska-Żmijewska A. Leczenie chirurgiczne jaskry. Warsaw, Poland: Polskie Towarzystwo Okulistyczne; 2017. https://pto.com.pl/wp-content/uploads/2017/08/Leczenie-chirurgiczne-jaskry.pdf

Statin therapy improves long-term survival in patients with myocardial infarction and non-obstructive coronary arteries (MINOCA)

Konrad Stępień[1,2,A–F], Grzegorz Horosin[3,B–D,F], Natalia Kachnic[3,B–D,F], Alicia del Carmen Yika[3,B–D,F], Aleksandra Karcińska[3,B–D,F], Piotr Walczak[3,B–D,F], Karol Nowak[1,2,B–F], Mateusz Podolec[1,4,B–F], Jadwiga Nessler[1,5,A–F], Jarosław Zalewski[1,5,A–F]

[1] Department of Coronary Artery Disease and Heart Failure, St. John Paul II Hospital, Cracow, Poland
[2] Department of Thromboembolic Disorders, Institute of Cardiology, Jagiellonian University Medical College, Cracow, Poland
[3] Student Research Group at Department of Coronary Artery Disease and Heart Failure, Jagiellonian University Medical College, Cracow, Poland
[4] Center for Innovative Medical Education, Jagiellonian University Medical College, Cracow, Poland
[5] Department of Coronary Artery Disease and Heart Failure, Jagiellonian University Medical College, Cracow, Poland

A – research concept and design; B – collection and/or assembly of data; C – data analysis and interpretation;
D – writing the article; E – critical revision of the article; F – final approval of the article

Advances in Clinical and Experimental Medicine, ISSN 1899–5276 (print), ISSN 2451–2680 (online) *Adv Clin Exp Med*. 2026;35(7):1133–1141

Address for correspondence
Konrad Stępień
E-mail: konste@interia.eu

Funding sources
This work was supported by the science fund of the St. John Paul II Hospital, Cracow, Poland (grant No. FN/17/2025 to K.S.).

Conflict of interest
None declared

Received on March 7, 2025
Reviewed on June 15, 2025
Accepted on October 2, 2025

Published online on April 27, 2026

Cite as
Stępień K, Horosin G, Kachnic N, et al. Statin therapy improves long-term survival in patients with myocardial infarction and non-obstructive coronary arteries (MINOCA). *Adv Clin Exp Med*. 2026;35(7):1133–1141. doi:10.17219/acem/211628

DOI
10.17219/acem/211628

Copyright
Copyright by Author(s)
This is an article distributed under the terms of the Creative Commons Attribution 3.0 Unported (CC BY 3.0) (https://creativecommons.org/licenses/by/3.0/)

Abstract

Background. Current guidelines suggest that statins may be beneficial in patients with myocardial infarction (MI) with non-obstructive coronary arteries (MINOCA). However, the available data are ambiguous.

Objectives. We sought to investigate the effect of statin therapy on long-term mortality among MINOCA patients.

Materials and methods. Between 2012 and 2019, coronary angiography was performed in 1,011 patients hospitalized with a diagnosis of MI. Patients with lesions narrowing coronary arteries by less than 50% were classified as MINOCA. Baseline clinical characteristics, laboratory and echocardiographic parameters, statin type prescribed at discharge, as well as long-term all-cause mortality were collected in the MINOCA group.

Results. MINOCA was diagnosed in 77 (7.6%) patients, while statins were prescribed in 57 (74%) of them at discharge. Subjects treated with statins had a higher prevalence of hypertension (94.7 vs 70%, p = 0.008) and dyslipidemia (77.2 vs 45%, p = 0.008), had a higher body mass index (BMI; p = 0.028), and were less likely to suffer from active cancer (17.5 vs 55.0%, p = 0.001). In multivariable logistic regression, active cancer independently reduced (odds ratio (OR) = 0.143, 95% confidence interval (95% CI): 0.027–0.748), whereas higher baseline low-density lipoorotein cholesterol (LDL-C) (OR = 3.216, 95% CI: 1.192–8.686) independently increased the likelihood of statin prescription at discharge. In the median follow-up of 69.2 [interquartile range (IQR): 37.8–79.9] months, all-cause mortality was significantly higher in MINOCA patients not treated with statins (p = 0.025).

Conclusions. Roughly 75% of MINOCA patients were treated with statins at discharge. This decision was independently influenced by clinical characteristics and lipid profile. Statin prescription was associated with lower long-term all-cause mortality.

Key words: statin therapy, myocardial infarction with non-obstructive coronary arteries (MINOCA), long-term mortality, secondary prevention, survival analysis

Highlights

- Statin therapy significantly reduced long-term all-cause mortality in patients with myocardial infarction with non-obstructive coronary arteries (MINOCA).
- About 3/4 of MINOCA patients were prescribed statins at discharge, a decision influenced by lipid profile and comorbid conditions.
- Higher LDL-C levels increased and active cancer reduced the likelihood of statin prescription among MINOCA patients.
- Long-term follow-up confirmed a survival benefit of statins, supporting their use in secondary prevention for MINOCA.

Background

The European Society of Cardiology (ESC) has proposed specific criteria for diagnosing myocardial infarction (MI) in patients with non-obstructive coronary arteries (MINOCA), which include an episode of acute MI with no lesions ≥50% in major epicardial arteries and the exclusion of other identifiable specific causes for the acute presentation.[1–3] It is thought to be present in 5–7% of individuals with acute coronary syndrome and 3–15% of patients with acute MI.[4] Atherosclerotic plaque disruption, supply-demand mismatch, coronary microvascular dysfunction, coronary thromboembolism, epicardial coronary vasospasm, and spontaneous coronary artery dissection are some of the possible causes of MINOCA, although the precise pathophysiology of the condition is still unclear.[5–9] Even though the underlying mechanism is most likely complex, 8–25% of individuals still have an unknown reason for MINOCA.[3,6] Additionally, compared with obstructive acute MI, MINOCA patients are more likely to be younger, non-white women with a lower burden of classic cardiovascular risk factors.[6,8,10]

Given the absence of obstructive atherosclerosis, MINOCA patients are often misleadingly classified as "less severe" and as having a better prognosis than those with classic acute MI.[5,6,8] Although some studies indeed suggest favorable outcomes in MINOCA compared with acute MI,[4] others have shown a similar or even worse prognosis of MINOCA.[11–13] Patients with MINOCA still lack comprehensive guidelines regarding the best medical therapy because of the disease's complicated origin, lack of data, and frequently unclear underlying diagnosis.[5,6,8] Previous studies have documented that the use of classical secondary prevention in MINOCA was lower compared with acute MI.[6,14] Several studies have shown beneficial effects of statin use in the MINOCA population. Statin-treated patients had a substantially decreased incidence of major adverse cardiac events (MACEs) throughout a mean follow-up of 4.1 years, according to an observational analysis of MINOCA patients from the SWEDEHEART registry.[7] However, a prospective trial with an average follow-up of 19 months revealed that while statin therapy was linked to considerably longer survival in a Kaplan–Meier analysis, there was no correlation between statin use and MACE or death in a Cox regression analysis.[7] Five observational studies, including those described above, were recently meta-analyzed, with follow-up ranging from 1.3 years to 7.5 years.[5] However, a precise explanation of this improved survival, as well as the determinants of statin initiation in MINOCA patients, remains insufficiently elucidated.

Objectives

The aim of our study was to identify independent predictors of statin use and their effect on long-term mortality of MINOCA patients enrolled in the real-life acute MI registry.

Materials and methods

Between 2012 and 2019, coronary angiography was performed in a total of 1,011 patients hospitalized in the Department of Coronary Artery Disease and Heart Failure of the St. John Paul II Specialist Hospital (Cracow, Poland) with a diagnosis of MI (Fig. 1). MINOCA was defined in accordance with current guidelines using classic MI criteria without epicardial artery stenosis ≥50%.[1–3] According to ESC guidelines,[15] patients with acute coronary syndrome were categorized as either non-ST-segment elevation MI (NSTEMI) or ST-segment elevation MI (STEMI). The included patients were divided into statin and non-statin MINOCA groups based on whether they were taking statins at the time of discharge (Fig. 1). Then, long-term all-cause mortality was assessed in all patients (Fig. 1). The long-term follow-up data were collected using the Polish National Death Registry.

The study design was approved by the Jagiellonian University Medical College Ethics Committee (approval No. 1072.6120.59.2018). The Declaration of Helsinki was followed when conducting the study. Every person who was enrolled in the study gave informed consent.

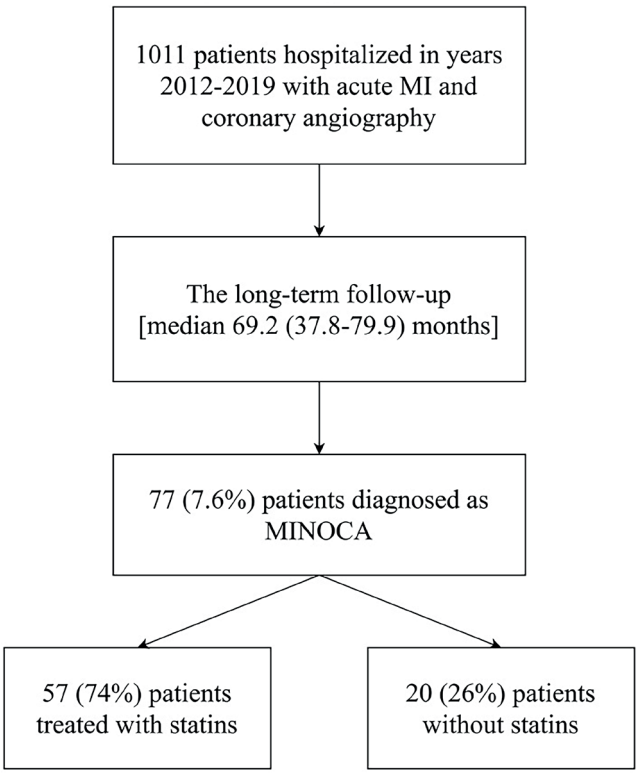

Fig. 1. Study flowchart

MINOCA – myocardial infarction with non-obstructive coronary arteries.

Study population

Data were collected on patients' demographic, laboratory, and echocardiographic results. Previous medical history, cardiovascular risk factors, and medications at discharge were analyzed. Dyslipidemia was diagnosed as plasma lipoprotein concentration above the therapeutic target for low-density lipoprotein cholesterol (LDL-C) >1.8 mmol/L (>70 mg/dL).[16] Hypertension was defined according to the ESC guidelines as repeated office systolic blood pressure (SBP) values ≥140 mm Hg and/or diastolic blood pressure (DBP) ≥90 mm Hg.[17] Diabetes mellitus was determined by fasting plasma glucose values ≥7.0 mmol/L (126 mg/dL) on 2 separate days, 2-h post-load plasma glucose ≥11.1 mmol/L (200 mg/dL), HbA1c ≥6.5%, or random blood glucose ≥11.1 mmol/L (200 mg/dL) in the presence of signs and symptoms.[18] Cancer diagnosed within the last 6 months, requiring treatment with antimitotic drugs at that time, recurring, metastatic, regionally progressed, or inoperable, was classified as active disease. All patients were assessed with the Killip classification on admission.

Laboratory tests performed on admission or within the first 24 h of hospitalization were assessed. Serum total cholesterol, LDL-C, high-density lipoprotein cholesterol (HDL-C), and triglycerides were measured using a Cobas 6000™ biochemical analyzer (Roche Diagnostics GmbH, Mannheim, Germany).

Angiography and echocardiography

Each of the coronary angiograms was analyzed offline. Unaware of the clinical information, an interventional cardiologist evaluated each artery in 2 contralateral projections. Quantitative coronary angiography (QCA Quantcor; Siemens, Munich, Germany) was used for a thorough assessment of borderline lesions between 40% and 70%. Epicardial artery lesions resulting in <50% coronary lumen stenosis were considered angiographically insignificant.[1–3] All patients with insignificant stenosis were categorized into 2 groups: 1) those with normal coronary arteries or minimal intracoronary irregularities defined by stenosis <30%, or 2) those with mild to moderate lesions characterized by ≥30% and <50% lumen narrowing.

Between the 2nd and 4th day of hospitalization, a qualified medical professional performed 2-dimensional transthoracic echocardiography. Using a Vivid S5 ultrasound system (GE Healthcare, Solingen, Germany) equipped with a multifrequency harmonic transducer (3Sc-RS, 1.3–4 MHz), the examination was conducted while the patient was at rest in the left decubitus position. Every measurement was performed in line with the guidelines provided by the European Association of Echocardiography (EAE)[19] and the American Society of Echocardiography (ASE). To characterize distinct cardiac components and facilitate their functional evaluation, standard data were gathered.[20]

Statistical analyses

Continuous variables were first assessed for normal distribution using the Lilliefors test and expressed as mean ± standard deviation (SD) for normal distribution, and median (Q1–Q3) for non-normal distribution, whereas categorical variables were expressed as number (percentage). Continuous variables were compared using Student's t-test with Levene's test for variance homogeneity or the Mann–Whitney U test if the distribution was normal or non-normal, respectively. Categorical variables were analyzed using the χ^2 test or Fisher's exact test. Fisher's exact test was performed if any of the expected counts were less than or equal to 5. All parameters based on theoretical knowledge associated with statin treatment were included in the multivariable logistic regression model. In the logistic regression model, the assumption of linearity of all continuous predictors was checked with the Box–Tidwell test, the assumption of lack of multicollinearity with the variance inflation factor (VIF), and the assumption of no influential outliers based on Cook's distance. Kaplan–Meier curves for all-cause mortality in the studied groups were constructed and compared using the Gehan–Breslow–Wilcoxon test. Statistical significance was defined as a 2-sided p-value less than 0.05. All statistical analyses were conducted using Statistica v. 13.3 (StatSoft Poland, Cracow, Poland) or IBM SPSS v. 29.0 (IBM Corp., Armonk, USA).

Results

Baseline characteristics

Of 1,011 consecutive acute MI patients, 77 (7.6%) were diagnosed with MINOCA. Of these, 57 (74%) were treated with statins and 20 (26%) without statins at discharge (Fig. 1). Women constituted the majority in both groups – 50.9% in the statin MINOCA group and 55% in the non-statin group (Table 1). MINOCA patients treated with statins had a higher body mass index (BMI; 26.8 [interquartile range (IQR): 24.2–32.0] kg/m^2 vs 23.6 [21.8–29.3] kg/m^2, p = 0.028), with a more frequent diagnosis of hypertension (94.7 vs 70%, p = 0.008) and dyslipidemia (77.2% vs 45%, p = 0.008), as well as a lower prevalence of active cancer (17.5% vs 55%, p = 0.001) (Table 1).

Table 1. Baseline clinical characteristics

Variable		Statin MINOCA (n = 57)	Non-statin MINOCA (n = 20)	p-value
Female gender		29 (50.9)	11 (55.0)	0.751
Age [years]		72 (66–78)	73 (54–79)	0.680
BMI [kg/m^2]		26.8 (24.2–32)	23.6 (21.8–29.3)	**0.028**
Diabetes mellitus		17 (29.8)	4 (20.0)	0.562
Hypertension		54 (94.7)	14 (70.0)	**0.008**
Dyslipidemia		44 (77.2)	9 (45.0)	**0.008**
Pre-ESRD or ESRD		3 (5.3)	0 (0.0)	0.564
Active smoking		6 (10.5)	1 (5.0)	0.669
Anemia		15 (26.3)	6 (30.0)	0.750
Thrombocytopenia		3 (5.3)	2 (10.0)	0.600
Prior myocardial infarction		11 (19.3)	3 (15.0)	1.000
Prior stroke		5 (8.8)	3 (15.0)	0.421
Heart failure		18 (31.6)	10 (50.0)	0.141
Active cancer		10 (17.5)	11 (55.0)	**0.001**
Killip class III/IV on admission		2 (3.5)	4 (20.0)	**0.037**
Clinical presentation	NSTEMI	49 (86.0)	16 (80.0)	0.498
	STEMI	8 (14.0)	4 (20.0)	–
Epicardial lesions	<30% stenosis	37 (64.9)	15 (75.0)	0.580
	30–50% stenosis	20 (35.1)	5 (25.0)	–
Treatment on discharge	aspirin	31 (54.3)	12 (60.0)	0.664
	P2Y12 inhibitor	29 (50.9)	6 (30.0)	0.107
Proton pump inhibitor		39 (68.4)	11 (55.0)	0.279
ACEI/ARB		50 (87.7)	15 (75.0)	0.280
β-blocker		47 (82.5)	15 (75.0)	0.518

Data are shown as number (percentage) for qualitative variables or median (Q1–Q3) for quantitative variables. Normal distribution was checked using the Lilliefors test. The characteristics of statistical tests used for the assessment of baseline clinical data are shown in Supplementary Tables 1 and 4. Values in bold are statistically significant. BMI – body mass index; ACEI – angiotensin-converting enzyme inhibitor; ARB – angiotensin receptor blocker; ESRD – end-stage renal disease; MINOCA – myocardial infarction with non-obstructive coronary arteries; NSTEMI – non-ST-segment elevation myocardial infarction; STEMI – ST-segment elevation myocardial infarction.

Subjects in both groups did not differ in clinical presentation (NSTEMI vs STEMI), but patients in the statin MINOCA group less frequently showed Killip class III/IV on admission (3.5% vs 20%, p = 0.037) (Table 1). The severity of nonsignificant atherosclerotic lesions was similar in both groups (Table 1). The use of the most important drug classes in both compared groups was similar (Table 1).

The analysis of laboratory parameters assessed on admission did not show significant divergence between the 2 analyzed populations, except for LDL-C, which was higher in MINOCA patients treated with statins compared to those without statins by 25.9% (2.7 [1.7–3.4] mmol/L vs 2 [1.5–2.6] mmol/L, p = 0.047) (Table 2).

In subjects receiving statin therapy, a tendency toward higher values of left ventricular ejection fraction (LVEF) (55% [45–60%] vs 47% [30–55%], p = 0.055) was observed, with no differences in other echocardiographic parameters (Table 3).

Statins regimen

As shown in Table 4, the most prescribed statin at discharge was atorvastatin (59.6%), with the most frequent doses of 20 mg (52.9%) and 40 mg (41.2%). The 2nd most common statin was simvastatin (21.1%), with 20 mg as the most common dose (75%). The least frequently prescribed statin, in only 19.3% of patients, was rosuvastatin. Notably, ezetimibe was not administered to any of the patients in the analyzed population (Table 4).

Independent predictors of statin use

The assumptions regarding linearity between predictors, lack of multicollinearity between explanatory variables, and absence of influential outliers were met for the model used to determine independent predictors of statin use. The multivariable logistic regression analysis revealed that active cancer (odds ratio (OR) = 0.143, 95% confidence interval (95% CI): 0.027–0.748) independently reduced, whereas higher baseline LDL-C (OR = 3.216, 95% CI: 1.192–8.686) independently increased the likelihood of statin prescription at discharge (Table 5).

Long-term mortality

In the median follow-up period of 69.2 [37.8–79.9] months, all-cause mortality was significantly higher in MINOCA patients who did not receive statin therapy (n = 13, 65%) compared with the others (n = 16, 28.1%) (p = 0.025) (Fig. 2).

Discussion

The current study demonstrated that 75% of patients with MINOCA received statins at discharge. The decision to introduce statins was made based on clinical

Table 2. Baseline laboratory characteristics

Variable	Statin MINOCA (n = 57)	Non-statin MINOCA (n = 20)	p-value
Troponin [ng/mL]	0.140 (0.036–0.350)	0.098 (0.045–0.411)	0.807
Troponin peak [ng/mL]	0.190 (0.077–0.590)	0.108 (0.046–0.530)	0.550
Creatine kinase [IU/L]	134 (92–295)	129 (80–212)	0.321
Creatine kinase peak [IU/L]	156 (99–408)	136 (88–250)	0.169
Creatine kinase MB isoenzyme [IU/L]	20 (15–29)	20 (13–29)	0.693
Creatine kinase MB isoenzyme peak [IU/L]	24 (16–36)	22 (15–30)	0.332
Hemoglobin [g/dL]	13.7 (12.1–14.4)	13.7 (11–14.8)	0.881
Hematocrit [%]	41 (36–43)	40 (33–43)	0.990
White blood cells [$\times 10^3$/µL]	8.9 ±3	8.9 ±3.8	0.967#
Platelet count [$\times 10^3$/µL]	222 ±70	225 ±100	0.883#
Sodium [mmol/L]	141 (138–143)	139 (136–144)	0.338
Potassium [mmol/L]	4.1 (3.8–4.4)	4.1 (3.9–4.4)	0.838
Creatinine [µmol/L]	90 (76–113)	77 (58–114)	0.167
Glomerular filtration rate [mL/min]	62 (50–81)	63 (40–94)	0.582
Glucose [mmol/L]	6.1 (5.6–7.6)	6.7 (5.6–8.7)	0.659
Total cholesterol [mmol/L]	4.3 ±1.2	3.8 ±0.8	0.075#
LDL-C [mmol/L]	2.6 ±1.2	2 ±0.8	0.047#
HDL-C [mmol/L]	1.2 (1–1.6)	1.2 (0.9–1.6)	0.778
Triglycerides [mmol/L]	1.2 ±0.5	1.1 ±0.6	0.235#

Data are shown as number (percentage) for qualitative variables, as mean ± standard deviation (SD) for normal distribution, and as median (Q1–Q3) for non-normal distribution of quantitative variables. # normal distribution was checked with Lilliefors test. The characteristics of statistical tests used for the assessment of baseline laboratory data are shown in Supplementary Tables 2 and 4. Values in bold are statistically significant. HDL-C – high-density lipoprotein cholesterol; LDL-C – low-density lipoprotein cholesterol; MINOCA – myocardial infarction with non-obstructive coronary arteries.

Table 3. Echocardiographic parameters

Variable	Statin MINOCA (n = 57)	Non-statin MINOCA (n = 20)	p-value
LV ejection fraction [%]	55 (45–60)	47 (30–55)	0.055
End-diastolic LV diameter [mm]	48 (45–51)	50 (40–55)	0.832
End-systolic LV diameter [mm]	30 (25–34)	36 (25–48)	0.119
Left atrium [mm]	40 ±6	38 ±9	0.274#
Left atrium area [cm^2]	22 ±6	23 ±6	0.487#
E/A ratio	0.8 (0.6–0.9)	0.8 (0.6–1.0)	0.775
Right ventricular systolic pressure [mm Hg]	33 (26–43)	33 (28–50)	0.453
TAPSE [mm]	23 ±5	22 ±6	0.629#
Ascending aorta diameter [mm]	36 ±5	34 ±6	0.354#
Aortic valve peak gradient [mm Hg]	8 (6–11)	8 (6–9)	0.752

Data are shown as number (percentage) for qualitative variables, as mean ± standard deviation (SD) for normal distribution, and as median (Q1–Q3) for non-normal distribution of quantitative variables. # normal distribution was checked with Lilliefors test. The characteristics of statistical tests used for the assessment of echocardiographic parameters are show in Supplementary Tables 3 and 4. LV – left ventricle; MINOCA – myocardial infarction with non-obstructive coronary arteries; TAPSE – tricuspid annular plane systolic excursion.

characteristics. Moreover, a large proportion of patients were not receiving the currently recommended high doses of statins, and none of the patients was receiving lipid-lowering combination therapy. Given the demonstrated positive association with long-term survival, our data may support the routine use of statins also in the MINOCA population.

As has been mentioned above, there is evidence on the positive impact of statins on survival and outcomes in MINOCA patients. In the largest synthesis of 5 observational studies, Masson et al. showed that statins were administered to 81.7% of patients with MINOCA, which led to a significant decrease in mortality and MACEs.[5] The results of this investigation are consistent with both the better prognosis and the prevalence of statin use.[5] However, there has not been any prior analysis of statin types, dosages, or predictors of their use.[5] Randomized clinical studies assessing the role of statins in the MINOCA

Table 4. The applied lipid-lowering therapy

Variable		Statin MINOCA (n = 57)	
Simvastatin	10 mg	1 (8.3)	12 (21.1)
	20 mg	9 (75.0)	
	40 mg	2 (16.7)	
	80 mg	0 (0.0)	
Atorvastatin	10 mg	1 (2.9)	34 (59.6)
	20 mg	18 (52.9)	
	30 mg	0 (0.0)	
	40 mg	14 (41.2)	
	60 mg	0 (0.0)	
	80 mg	1 (2.9)	
Rosuvastatin	5 mg	0 (0.0)	11 (19.3)
	10 mg	5 (45.5)	
	15 mg	0 (0.0)	
	20 mg	4 (36.4)	
	30 mg	2 (18.2)	
	40 mg	0 (0.0)	
Ezetimibe	–	0 (0.0)	–

Data are shown as number (percentage). MINOCA – myocardial infarction with non-obstructive coronary arteries.

Table 5. The independent predictors of statin use

Independent variables	Multivariable model		
	p-value	OR	95% CI for OR
Age (per 1 year)	0.201	1.044	0.977–1.116
Gender (male vs female)	0.095	0.238	0.044–1.281
Hypertension (yes vs no)	0.127	4.946	0.635–38.556
LDL-C (per 1 mmol/L)	**0.021**	3.217	1.192–8.686
Active cancer (yes vs no)	**0.021**	0.143	0.027–0.748
Constant	**0.069**	0.12	–

95% CI – 95% confidence interval; LDL-C – low-density lipoprotein cholesterol; OR – odds ratio. Negelkerke $R^2 = 0.448$, Hosmer–Lemenshow p = 0.07. The full characteristics of multivariable logistic regression for determination of independent predictors of statin use and the results of checking the assumptions of the model are shown in Supplementary Table 4. Values in bold are statistically significant.

population have not yet been reported. Additionally, none of the research has discussed the individualized therapy that is now advised based on the etiology of MINOCA. It is known that statins can improve exercise duration and time to ST-segment depression in patients with syndrome X and are favorable in vasospastic angina by increasing endothelial-dependent vasodilation.[21,22] However, some studies suggest that the use of statins may not be appropriate for clinical conditions not directly related to cholesterol accumulation. Retrospective data from the Mayo Clinic group suggest a slightly increased incidence of spontaneous coronary artery dissection recurrence in patients using statins.[23]

The direct mechanism explaining the positive prognostic effect of statins in MINOCA remains unknown. Statins work primarily by inhibiting HMG-CoA reductase, an enzyme that regulates the process of cholesterol biosynthesis in the liver.[24] However, the numerous pleiotropic benefits of statins, regardless of LDL-C levels, are even more substantial in the case of MINOCA, given its mostly non-atherosclerotic origin, which is characterized by the absence of major lesions in the coronary arteries.[25]

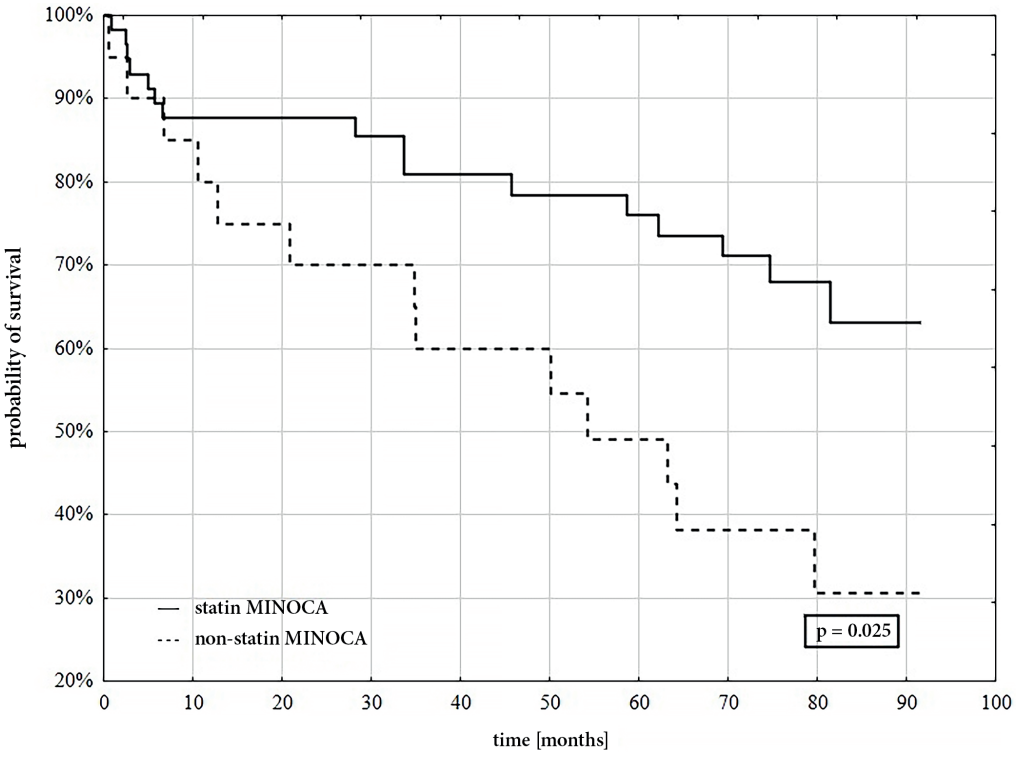

Fig. 2. Long-term all-cause mortality in the studied groups. Kaplan–Meier curves for all-cause mortality in the studied groups were constructed and compared using the Gehan–Breslow–Wilcoxon test ($\chi^2 = 5.072$, degrees of freedom (df) = 1)

MINOCA – myocardial infarction with non-obstructive coronary arteries.

By increasing nitric oxide (NO) generation, statins may affect endothelial function through a variety of pleiotropic mechanisms.[26,27] Reduction of systemic and vascular inflammation is another pathway in the general population that is not dependent on LDL-C levels. Ridker et al. demonstrated that among a healthy population without high lipid levels but with elevated high-sensitivity C-reactive protein (CRP) levels, rosuvastatin, compared to placebo, significantly lowered the incidence of MACE as well as all-cause mortality.[28] Furthermore, the MIRACL study found that individuals with acute coronary syndrome experienced a greater reduction in inflammation while taking high doses of atorvastatin.[29] Additionally, it has been shown that statins have antithrombotic properties. According to reports, they promote protein C activation and reduce thrombin production while improving fibrin coagulation properties.[25] The JUPITER study found that using 20 mg of rosuvastatin significantly decreased the incidence of venous thromboembolism in healthy individuals over a median follow-up of nearly 2 years.[30] As we recently showed, individuals with stable coronary heart disease and venous thromboembolism had lower levels of coagulation factors while taking high doses of statins.[31,32] Considering the emerging reports on hypercoagulable states in MINOCA, the antithrombotic effect of statins may be crucial and could be a potential explanation for the observed mortality reduction.[9]

It has been shown that statins are less commonly prescribed in MINOCA compared with acute MI patients with obstructive coronary artery disease (CAD).[8] However, it has not been determined why, since according to current guidelines, statins should be prescribed in all patients with acute MI.[3] Our findings indicate that the lack of active cancer and higher LDL-C levels were the 2 independent determinants associated with the prescription of statins at discharge. The reasons for not prescribing statins in patients with cancer may be multifactorial and include a lack of potential benefits from treatment and worsening of health status due to neoplastic disease progression. Moreover, the absence of visible stenosis in the arteries could indicate less frequent prescription in this group than in MI patients with obstructed coronary arteries. In the study by Ishii et al., the only clinically relevant factor that influenced statin prescription in patients with coronary vasospastic angina was the presence of dyslipidemia.[33] Our real-life results indicate that the decision to include statins in MINOCA is based on clinical characteristics and is not as strictly followed as in the case of classical acute MI. However, these results require verification in further studies.

Limitations of the study

It is important to note several limitations. First, we were able to obtain only data concerning all-cause mortality in the long-term observation without separation of cardiovascular and non-cardiovascular mortality, so a detailed analysis was not possible. Second, our study did not analyze adherence to the treatment regimen after hospitalization in patients with MINOCA, which may have affected the results. Moreover, it could also be speculated that the observed associations do not necessarily indicate a direct prognostic impact of statin use and should preferably be verified in further randomized studies. The current study relied on data from our center and comprised a relatively small number of patients. Finally, we refrained from using advanced imaging techniques, especially magnetic resonance imaging (MRI) and intracoronary imaging (ICI), as the diagnostic significance of these procedures was still uncertain at the time of patient enrollment in the registry.[34] More research should be conducted to determine the relationship between statin administration and the exact MINOCA etiology.

Conclusions

This real-life study found that statins are administered in 3 out of 4 MINOCA patients after diagnosis. This decision was independently determined by clinical characteristics and lipid profile, but not by the MINOCA diagnosis itself. Moreover, a large proportion of MINOCA patients do not receive the currently recommended high doses of statins. As has been shown, in-hospital statin initiation was associated with lower all-cause mortality in the long-term observation. Further randomized controlled studies are required to determine the direct prognostic impact of statins and their appropriate doses in the MINOCA population.

Supplementary data

The supplementary materials are available at https://doi.org/10.5281/zenodo.17600120. The package contains the following files:

Supplementary Table 1. The characteristics of statistical tests used for the assessment of baseline clinical data.

Supplementary Table 2. The characteristics of statistical tests used for the assessment of baseline laboratory data.

Supplementary Table 3. The characteristics of statistical tests used for the assessment of echocardiographic parameters.

Supplementary Table 4. The characteristics of statistical tests used for the assessment of the normality assumption (Lilliefors test) and the homogeneity of variances assumption (Levene's test).

Data Availability Statement

The datasets supporting the findings of the current study are openly available in Zenodo at https://doi.org/10.5281/zenodo.17598275.

Consent for publication of personal information

Not applicable

Use of AI and AI-assisted technology

Not applicable

ORCID iDs

Konrad Stępień https://orcid.org/0000-0002-5779-8434
Aleksandra Karcińska https://orcid.org/0009-0001-7155-7741
Jadwiga Nessler https://orcid.org/0000-0002-5076-5816
Jarosław Zalewski https://orcid.org/0000-0002-4374-3694

References

1. Agewall S, Beltrame JF, Reynolds HR, et al. ESC working group position paper on myocardial infarction with non-obstructive coronary arteries. *Eur Heart J*. 2016;38(3):143–153. doi:10.1093/eurheartj/ehw149
2. Thygesen K, Alpert JS, Jaffe AS, et al. Fourth Universal Definition of Myocardial Infarction (2018). *Circulation*. 2018;138(20):e618–e651. doi:10.1161/CIR.0000000000000617
3. Byrne RA, Rossello X, Coughlan JJ, et al. 2023 ESC Guidelines for the management of acute coronary syndromes. *Eur Heart J*. 2023;44(38):3720–3826. doi:10.1093/eurheartj/ehad191
4. Pasupathy S, Air T, Dreyer RP, Tavella R, Beltrame JF. Systematic review of patients presenting with suspected myocardial infarction and nonobstructive coronary arteries. *Circulation*. 2015;131(10):861–870. doi:10.1161/CIRCULATIONAHA.114.011201
5. Masson W, Lobo M, Barbagelata L, Lavalle-Cobo A, Molinero G. Prognostic value of statin therapy in patients with myocardial infarction with nonobstructive coronary arteries (MINOCA): A meta-analysis. *Acta Cardiol*. 2022;77(6):480–487. doi:10.1080/00015385.2021.1955480
6. Gasior P, Desperak A, Gierlotka M, et al. Clinical characteristics, treatments, and outcomes of patients with myocardial infarction with non-obstructive coronary arteries (MINOCA): Results from a Multicenter National Registry. *J Clin Med*. 2020;9(9):2779. doi:10.3390/jcm9092779
7. Lindahl B, Baron T, Erlinge D, et al. Medical therapy for secondary prevention and long-term outcome in patients with myocardial infarction with nonobstructive coronary artery disease. *Circulation*. 2017;135(16):1481–1489. doi:10.1161/CIRCULATIONAHA.116.026336
8. Paolisso P, Bergamaschi L, Saturi G, et al. Secondary prevention medical therapy and outcomes in patients with myocardial infarction with non-obstructive coronary artery disease. *Front Pharmacol*. 2020;10:1606. doi:10.3389/fphar.2019.01606
9. Stepień K, Nowak K, Wypasek E, Zalewski J, Undas A. High prevalence of inherited thrombophilia and antiphospholipid syndrome in myocardial infarction with non-obstructive coronary arteries: Comparison with cryptogenic stroke. *Int J Cardiol*. 2019;290:1–6. doi:10.1016/j.ijcard.2019.05.037
10. Stepień K, Nowak K, Szlosarczyk B, Nessler J, Zalewski J. Clinical characteristics and long-term outcomes of MINOCA accompanied by active cancer: A retrospective insight into a Cardio-Oncology Center Registry. *Front Cardiovasc Med*. 2022;9:785246. doi:10.3389/fcvm.2022.785246
11. Kang WY, Jeong MH, Ahn YK, et al. Are patients with angiographically near-normal coronary arteries who present as acute myocardial infarction actually safe? *Int J Cardiol*. 2011;146(2):207–212. doi:10.1016/j.ijcard.2009.07.001
12. Planer D, Mehran R, Ohman EM, et al. Prognosis of patients with non-ST-segment-elevation myocardial infarction and nonobstructive coronary artery disease: Propensity-matched analysis from the acute catheterization and urgent intervention triage strategy trial. *Circ Cardiovasc Interv*. 2014;7(3):285–293. doi:10.1161/CIRCINTERVENTIONS.113.000606
13. Stępień K, Nowak K, Nessler J, Zalewski J. Worse long-term prognosis in myocardial infarction occurring at weekends or public holidays with insight into myocardial infarction with nonobstructive coronary arteries. *Pol Arch Intern Med*. 2020;130(11):942–952. doi:10.20452/pamw.15615
14. Schmitz K, Groth N, Mullvain R, Renier C, Oluleye O, Benziger C. Prevalence, clinical factors, and outcomes associated with myocardial infarction with nonobstructive coronary artery. *Crit Pathw Cardiol*. 2021;20(2):108–113. doi:10.1097/HPC.0000000000000249
15. Stepień K, Nowak K, Skorek P, et al. Baseline indicators of coronary artery disease burden in patients with non-ST-segment elevation acute coronary syndrome. *Minerva Cardioangiol*. 2019;67(3):181–190. doi:10.23736/S0026-4725.19.04838-2
16. Mach F, Baigent C, Catapano AL, et al. 2019 ESC/EAS Guidelines for the management of dyslipidaemias: Lipid modification to reduce cardiovascular risk. *Eur Heart J*. 2020;41(1):111–188. doi:10.1093/eurheartj/ehz455
17. Mancia G, Kreutz R, Brunström M, et al. 2023 ESH Guidelines for the management of arterial hypertension The Task Force for the management of arterial hypertension of the European Society of Hypertension: Endorsed by the International Society of Hypertension (ISH) and the European Renal Association (ERA). *J Hypertens*. 2023;41(12):1874–2071. doi:10.1097/HJH.0000000000003480
18. Marx N, Federici M, Schütt K, et al. 2023 ESC Guidelines for the management of cardiovascular disease in patients with diabetes. *Eur Heart J*. 2023;44(39):4043–4140. doi:10.1093/eurheartj/ehad192
19. Lang RM, Badano LP, Mor-Avi V, et al. Recommendations for Cardiac Chamber Quantification by Echocardiography in Adults: An update from the American Society of Echocardiography and the European Association of Cardiovascular Imaging. *J Am Soc Echocardiogr*. 2015;28(1):1–39.e14. doi:10.1016/j.echo.2014.10.003
20. Siniarski A, Stępień K, Golińska-Grzybała K, et al. Thrombin generation, fibrin clot permeation and lysis in patients with severe mitral regurgitation undergoing transcatheter edge-to-edge mitral valve repair: Mitral Fibrin Study. *Pol Arch Intern Med*. 2024;134(7–8):16755. doi:10.20452/pamw.16755
21. Kayikcioglu M, Payzin S, Yavuzgil O, Kultursay H, Can LH, Soydan I. Benefits of statin treatment in cardiac syndrome-X1. *Eur Heart J*. 2003;24(22):1999–2005. doi:10.1016/s0195-668x(03)00478-0
22. Tani S, Nagao K, Anazawa T, et al. Treatment of coronary spastic angina with a statin in addition to a calcium channel blocker: A pilot study. *J Cardiovasc Pharmacol*. 2008;52(1):28–34. doi:10.1097/FJC.0b013e31817d4507
23. Tweet MS, Hayes SN, Pitta SR, et al. Clinical features, management, and prognosis of spontaneous coronary artery dissection. *Circulation*. 2012;126(5):579–588. doi:10.1161/CIRCULATIONAHA.112.105718
24. Istvan ES, Deisenhofer J. Structural mechanism for statin inhibition of HMG-CoA reductase. *Science*. 2001;292(5519):1160–1164. doi:10.1126/science.1059344
25. Undas A. Statins in prevention of thromboembolic events: From seminal studies to recent advances. *Pol Arch Intern Med*. 2022;132(2):16208. doi:10.20452/pamw.16208
26. Oesterle A, Laufs U, Liao JK. Pleiotropic effects of statins on the cardiovascular system. *Circ Res*. 2017;120(1):229–243. doi:10.1161/CIRCRESAHA.116.308537
27. Laufs U, La Fata V, Plutzky J, Liao JK. Upregulation of endothelial nitric oxide synthase by HMG CoA reductase inhibitors. *Circulation*. 1998;97(12):1129–1135. doi:10.1161/01.CIR.97.12.1129
28. Ridker PM, Danielson E, Fonseca FAH, et al. Rosuvastatin to prevent vascular events in men and women with elevated C-reactive protein. *N Engl J Med*. 2008;359(21):2195–2207. doi:10.1056/NEJMoa0807646
29. Kinlay S, Schwartz GG, Olsson AG, et al. High-dose atorvastatin enhances the decline in inflammatory markers in patients with acute coronary syndromes in the MIRACL study. *Circulation*. 2003;108(13):1560–1566. doi:10.1161/01.CIR.0000091404.09558.AF
30. Glynn RJ, Danielson E, Fonseca FAH, et al. A randomized trial of rosuvastatin in the prevention of venous thromboembolism. *N Engl J Med*. 2009;360(18):1851–1861. doi:10.1056/NEJMoa0900241
31. Stępień K, Siudut J, Konieczyńska M, Nowak K, Zalewski J, Undas A. Effect of high-dose statin therapy on coagulation factors: Lowering of factor XI as a modifier of fibrin clot properties in coronary artery disease. *Vascul Pharmacol*. 2023;149:107153. doi:10.1016/j.vph.2023.107153

32. Stępień K, Żółciński M, Ząbczyk M, Zalewski J, Undas A. Effect of three-day atorvastatin administration on coagulation factors in patients with prior venous thromboembolism and healthy subjects: A preliminary study. *J Cardiovasc Pharmacol*. 2024;83(3):289–296. doi:10.1097/FJC.0000000000001529
33. Ishii M, Kaikita K, Sato K, et al. Impact of statin therapy on clinical outcome in patients with coronary spasm. *J Am Heart Assoc*. 2016;5(5):e003426. doi:10.1161/JAHA.116.003426
34. Gerbaud E, Arabucki F, Nivet H, et al. OCT and CMR for the diagnosis of patients presenting with MINOCA and suspected epicardial causes. *JACC Cardiovasc Imaging*. 2020;13(12):2619–2631. doi:10.1016/j.jcmg.2020.05.045

Nonalcoholic fatty liver disease and cardiovascular risk in patients with unstable angina: A 3-year prospective follow-up study

Pei Shi[1,B–D,F], Xiaojuan Meng[2,A,E,F]

[1] Department of Geriatrics, Xi'an Third Hospital, China
[2] Department of Cardiac Function, Xi'an Third Hospital, China

A – research concept and design; B – collection and/or assembly of data; C – data analysis and interpretation;
D – writing the article; E – critical revision of the article; F – final approval of the article

Advances in Clinical and Experimental Medicine, ISSN 1899–5276 (print), ISSN 2451–2680 (online) *Adv Clin Exp Med*. 2026;35(7):1143–1151

Address for correspondence
Xiaojuan Meng
E-mail: XiaojuanMeng202409@163.com

Funding sources
None declared

Conflict of interest
None declared

Received on April 7, 2025
Reviewed on July 8, 2025
Accepted on October 15, 2025

Published online on July 3, 2026

Abstract

Background. Nonalcoholic fatty liver disease (NAFLD) is increasingly recognized as a multisystem disorder with potential cardiovascular consequences. Its role in patients with unstable angina (UA), a high-risk manifestation of coronary artery disease (CAD), remains underexplored.

Objectives. To evaluate the impact of NAFLD on long-term cardiovascular outcomes in patients with UA.

Materials and methods. This prospective cohort study enrolled 150 patients diagnosed with UA, who were categorized into NAFLD and non-NAFLD groups based on imaging and clinical criteria. Baseline metabolic and liver function parameters were recorded. Patients were followed for 3 years to document major adverse cardiovascular events (MACE). Kaplan–Meier analysis was used to assess event-free survival, and multivariate logistic regression was performed to identify independent predictors of MACE.

Results. Patients with NAFLD exhibited worse metabolic and liver function profiles than those without NAFLD. During the 3-year follow-up period, the incidence of MACE was significantly higher in the NAFLD group. Kaplan–Meier analysis revealed shorter MACE-free survival time among patients with NAFLD ($p < 0.05$). However, in multivariate logistic regression analysis, diabetes mellitus, but not NAFLD, remained an independent predictor of MACE after adjustment for potential confounding factors.

Conclusions. Nonalcoholic fatty liver disease is associated with metabolic dysfunction and an increased risk of cardiovascular events in patients with UA. Although it is not an independent predictor of MACE, its presence may indicate a higher long-term cardiovascular risk and should be considered in clinical risk stratification.

Key words: nonalcoholic fatty liver disease, unstable angina, cardiovascular diseases, Kaplan–Meier analysis, logistic regression

Cite as
Shi P, Meng X. Nonalcoholic fatty liver disease and cardiovascular risk in patients with unstable angina: A 3-year prospective follow-up study. *Adv Clin Exp Med*. 2026;35(7):1143–1151. doi:10.17219/acem/212807

DOI
10.17219/acem/212807

Copyright
Copyright by Author(s)
This is an article distributed under the terms of the Creative Commons Attribution 3.0 Unported (CC BY 3.0) (https://creativecommons.org/licenses/by/3.0/)

Highlights

- Nonalcoholic fatty liver disease (NAFLD) was associated with worse metabolic and liver profiles in patients with unstable angina, indicating higher cardiovascular vulnerability.
- Patients with NAFLD experienced a significantly higher incidence of major adverse cardiovascular events (MACE) and shorter event-free survival over 3 years.
- Multivariate analysis identified diabetes mellitus, rather than NAFLD alone, as an independent predictor of long-term MACE in unstable angina.
- NAFLD may serve as a useful clinical marker for enhanced cardiovascular risk stratification and management in patients with unstable angina.

Background

Unstable angina (UA) is a manifestation of acute coronary syndrome (ACS) and is often considered a precursor to myocardial infarction, representing a critical cardiovascular emergency. It is characterized by new-onset, worsening, or rest angina without an obvious cause.[1] Epidemiological data indicate that UA is one of the most common cardiovascular events among older adults, with its incidence increasing with age. The condition is particularly prevalent in individuals with known coronary artery disease (CAD), who are at higher risk of progressing to myocardial infarction or sudden cardiac death.[2,3] The clinical significance of UA lies not only in its symptomatic presentation but also in its associated complications and unfavorable long-term prognosis.[4] Research indicates that individuals with UA face an elevated risk of myocardial infarction or cardiac death within a short period, particularly when timely treatment is not administered.[5,6] Long-term outcomes in these patients are influenced by several factors, including the severity of coronary artery stenosis, coexisting conditions such as diabetes mellitus and hypertension, and the timeliness and effectiveness of medical interventions.[7] Therefore, UA is considered a cardiovascular emergency requiring prompt diagnosis and treatment to reduce mortality and improve prognosis.

Nonalcoholic fatty liver disease (NAFLD), a chronic liver condition associated with metabolic syndrome, is characterized by fat accumulation in the liver in the absence of significant alcohol consumption. Its prevalence is increasing globally, particularly among adults with obesity or type 2 diabetes (T2D). Nonalcoholic fatty liver disease encompasses a broad pathological spectrum, ranging from simple steatosis to nonalcoholic steatohepatitis, which may progress to fibrosis or cirrhosis.[8–10] Increasing evidence highlights its strong association with systemic metabolic disorders and cardiovascular diseases. Studies suggest that NAFLD increases the risk of major adverse cardiovascular events (MACE) and is associated with poorer outcomes in patients with pre-existing cardiovascular conditions.[11,12]

Mechanistically, NAFLD may contribute to atherosclerosis and cardiovascular injury through insulin resistance, endothelial dysfunction, chronic inflammation, and oxidative stress.[13,14] Clinical studies have further identified NAFLD as an independent risk factor for both malignant arrhythmias in patients with ACS and increased CAD severity, as evidenced by its association with higher Gensini scores and an increased risk of coronary heart disease.[15,16] These findings underscore the systemic cardiovascular impact of NAFLD. However, evidence regarding the prognostic value of NAFLD specifically in patients with UA remains scarce, and prospective studies with long-term follow-up in this population are particularly limited. This highlights the need to clarify whether NAFLD independently influences cardiovascular outcomes in this high-risk subgroup.

Objectives

Despite growing evidence linking NAFLD to cardiovascular diseases, studies specifically examining its impact on the long-term prognosis of patients with UA remain limited. This study aimed to investigate the influence of NAFLD on the 3-year incidence of MACE and cardiovascular outcomes in patients with UA using a prospective cohort design. Findings from this research may provide valuable insights into clinical risk stratification and the long-term management of patients with UA, particularly those with coexisting NAFLD.

Materials and methods

Study population

This was a single-center prospective cohort study that enrolled all eligible patients with UA treated at Xi'an Third Hospital (China) between January 2020 and December 2021. A total of 150 patients aged >18 years were included and divided into 2 groups based on the presence of NAFLD: the non-NAFLD group and the NAFLD group. The diagnostic criteria for UA were as follows[17]: 1) typical anginal chest pain; 2) ischemic changes on electrocardiography

(ECG), including new or transient ST-segment depression ≥0.1 mV or T-wave inversion ≥0.2 mV; and 3) normal cardiac biomarker levels, including cardiac troponin T (TnT), cardiac troponin I (TnI), and creatine kinase-MB isoenzyme (CK-MB).

Exclusion criteria included: 1) other cardiovascular conditions, such as stable angina, myocardial bridging, coronary artery anomalies, cardiomyopathy, valvular or congenital heart disease, or heart failure; 2) a history of percutaneous coronary intervention (PCI) or coronary artery bypass grafting (CABG); 3) recent use (within 1 month) of steroids, anti-inflammatory agents, antibiotics, non-steroidal anti-inflammatory drugs (NSAIDs), or immunosuppressants; 4) chronic liver diseases, including hepatitis B, hepatitis C, autoimmune liver disease, or drug-induced liver injury; and 5) severe infections, renal dysfunction, malignancies, or other significant comorbidities.

Nonalcoholic fatty liver disease was diagnosed based on the following criteria: 1) absence of significant alcohol consumption, defined as an average ethanol intake of <210 g/week for men and <140 g/week for women, maintained consistently over the preceding 6 months; 2) exclusion of other specific liver diseases, such as viral hepatitis; and 3) characteristic findings on abdominal B-mode ultrasonography, including increased hepatic echogenicity compared with the spleen and kidney, uniform enhancement of the near field with posterior attenuation, indistinct intrahepatic vascular architecture, and mild-to-moderate hepatomegaly with rounded borders. All patients provided written informed consent. The present study was conducted in accordance with the Declaration of Helsinki and was approved by the Ethics Committee of Xi'an Third Hospital (approval No. XATH-20200041).

The required sample size was calculated using a cohort study formula, with parameters based on preliminary estimates of NAFLD prevalence among patients with UA. Using a 95% confidence level (Z = 1.96), an estimated NAFLD proportion (p = 0.28), and a margin of error (d = 0.072), the sample size was calculated as follows:

$$n = Z^2 \times p \times (1 - p)/d^2 = 1.96^2 \times 0.28 \times (1 - 0.28)/0.072^2 \approx 150.$$

Thus, a sample size of 150 was considered adequate to detect significant differences in cardiovascular outcomes between the groups.

Data collection

Demographic, epidemiological, and clinical data were collected, including age, sex, body mass index (BMI), smoking status, alcohol consumption history, and comorbidities such as hypertension and diabetes mellitus. Blood tests were performed using an automated biochemical analyzer (Hitachi 7600; Hitachi Corporation, Tokyo, Japan) to assess the following parameters: lipid metabolism markers, including total cholesterol (TC), triglycerides (TG), high-density lipoprotein cholesterol (HDL-C), and low-density lipoprotein cholesterol (LDL-C); liver function markers, including alanine aminotransferase (ALT) and aspartate aminotransferase (AST); cardiac biomarkers, including N-terminal pro-B-type natriuretic peptide (NT-proBNP), CK-MB activity, and TnI; and inflammatory markers, including C-reactive protein (CRP) and procalcitonin (PCT), as previously described.[18,19]

Follow-up and observation indicators

All patients were followed for 3 years after discharge. For patients who died during follow-up, the time and cause of death were recorded. MACE were defined as the occurrence of any of the following events during follow-up: sudden cardiac death, heart failure, cardiogenic shock, recurrent myocardial infarction, or arrhythmias associated with hemodynamic instability. MACE-free survival time was documented for each patient.

Statistical analyses

Statistical analyses were performed using IBM SPSS v. 25.0 (IBM Corp., Armonk, USA). Data normality was assessed separately in each group. The Shapiro–Wilk test was used for the NAFLD group (n = 48), whereas the Kolmogorov–Smirnov test was applied to the non-NAFLD group (n = 102), in accordance with standard recommendations based on sample size (Supplementary Table 1).

Continuous variables were expressed as mean ± standard deviation (SD) for normally distributed data or as median (range, interquartile range (IQR)) for non-normally distributed data. Comparisons between groups were conducted using Student's t-test or the Mann–Whitney U test, as appropriate. For variables that were normally distributed in both groups, equality of variances was assessed using Levene's test; if variances were unequal, Welch's t-test was applied instead of the standard Student's t-test.

Categorical variables were compared using Pearson's χ^2 test of independence, as all cross-tabulations had a minimum expected cell count greater than 5. Survival analysis was performed using the Kaplan–Meier method, and differences in survival distributions were assessed with the log-rank test. Multivariate logistic regression analyses were conducted to identify independent predictors of MACE.

The assumptions of logistic regression were assessed as follows: linearity of continuous variables with the logit of the outcome was tested using the Box–Tidwell procedure; multicollinearity was evaluated using variance inflation factors (VIFs); and potential outliers or influential observations were examined using Cook's distance and studentized residuals obtained from the SPSS regression diagnostics output. Model fit was assessed using the Hosmer–Lemeshow goodness-of-fit test and Nagelkerke's R^2.

A two-sided $p < 0.05$ was considered statistically significant. This study involved several hypothesis tests. No formal adjustment for multiple comparisons was performed, as all comparisons were conducted using standard statistical methods (Student's t-test, Mann–Whitney U test, and χ^2 test).

Results

Comparison of demographic characteristics, liver function, and lipid metabolism indicators between the NAFLD and non-NAFLD groups

As shown in Table 1, there were no significant differences between the NAFLD and non-NAFLD groups in terms of age, sex distribution, smoking status, alcohol consumption history, or the prevalence of hypertension and diabetes mellitus. However, the NAFLD group had a significantly higher BMI ($p < 0.001$), accompanied by an unfavorable lipid profile, including elevated TG levels ($p < 0.001$) and decreased HDL-C levels ($p < 0.001$), whereas no significant differences were observed in TC or LDL-C levels. Additionally, liver function markers were significantly impaired in the NAFLD group, as evidenced by higher ALT and AST levels (both $p < 0.001$). Median MACE-free survival time was also significantly shorter in the NAFLD group than in the non-NAFLD group ($p = 0.006$). The original results of Levene's test are presented in Supplementary Table 2.

Comparison of cardiac biomarkers and inflammatory factor levels between the NAFLD and non-NAFLD groups

Cardiac biomarker and inflammatory marker levels were further compared between the 2 groups. As shown in Fig. 1, the NAFLD group had significantly higher levels of NT-proBNP, TnI, and PCT (all $p < 0.001$). No significant differences were observed in CK-MB or CRP levels. These findings suggest that patients with NAFLD may have more pronounced myocardial injury and systemic inflammation.

Comparison of MACE incidence between the NAFLD and non-NAFLD groups

To further evaluate long-term outcomes, the incidence of MACE was compared between the 2 groups. During the 3-year follow-up period, a total of 29 patients (19.33%) developed MACE. The NAFLD group exhibited a significantly higher incidence of MACE than the non-NAFLD group ($p = 0.003$; Table 2). Post hoc power analysis ($\alpha = 0.05$, two-sided), based on the observed MACE incidence rates (31.3% vs 13.7%) and sample sizes (48 vs 102), yielded a statistical power of 95.6%. Although the NAFLD group showed numerically higher rates of sudden cardiac death, myocardial infarction, and heart failure, none of these differences reached statistical significance. These findings suggest a potential association between NAFLD and an increased overall cardiovascular risk in patients with UA.

Table 1. Basic characteristics of all patients

Variable	NAFLD group (n = 48)	Non-NAFLD group (n = 102)	t/Z/χ^2	p-value
Age [years]*	61 (48–71, 12)	61 (51–71, 11.5)	Z (n = 48 vs 102) = 0.157	0.875
Male sex, n (%)#	21 (43.75)	43 (42.16)	χ^2 (1) = 0.052	0.820
BMI&	26.93 ±2.58	24.50 ±2.41	t (148) = 5.638	<0.001
Smoking status, n (%)#	19 (39.58)	38 (37.25)	χ^2 (1) = 0.115	0.735
Alcohol consumption history, n (%)#	11 (22.92)	23 (22.55)	χ^2 (1) = 0.004	0.950
Hypertension, n (%)#	27 (56.25)	53 (51.96)	χ^2 (1) = 0.371	0.543
Diabetes, n (%)#	12 (25.00)	17 (16.67)	χ^2 (1) = 2.103	0.147
TC (mmol/L)&	4.61 ±0.45	4.53 ±0.46	t (148) = 0.903	0.368
TG (mmol/L)&	2.12 ±0.43	1.45 ±0.28	t (65.507) = 9.741	<0.001
LDL-C (mmol/L)&	2.74 ±0.43	2.75 ±0.43	t (148) = –0.235	0.815
HDL-C (mmol/L)*	0.93 (0.59–1.20, 0.34)	1.14 (0.82–1.48, 0.29)	Z (n = 48 vs 102) = –5.686	<0.001
ALT (U/L)*	57.51 (28.65–73.21, 20.54)	24.14 (11.32–35.14, 13.43)	Z (n = 48 vs 102) = –9.407	<0.001
AST (U/L)*	44.76 (20.68–67.73, 25.79)	29.18 (12.81–39.01, 11.81)	Z (n = 48 vs 102) = –6.708	<0.001
MACE disease-free survival [days]*	1095 (159–1095, 349.5)	1095 (293–1095, 802)	Z (n = 48 vs 102) = –2.750	0.006

*Non-normally distributed continuous variables, expressed as median (range, interquartile range (IQR)) and analyzed using the Mann–Whitney U test, including age, HDL-C, ALT, AST, and median DFS. #Categorical variables (column percentages) were compared using Pearson's χ^2 test of independence, as all expected cell counts were ≥5 and all analyses were performed using non-rounded values in the SPSS Crosstabs procedure. These variables included sex, smoking status, alcohol consumption history, hypertension, and diabetes mellitus. &Normally distributed continuous variables, expressed as mean ± standard deviation (SD) and analyzed using Student's t-test, including BMI, TC, TG, and LDL-C. BMI – body mass index; TC – total cholesterol; TG – triglycerides; LDL-C – low-density lipoprotein cholesterol; HDL-C – high-density lipoprotein cholesterol; ALT – alanine aminotransferase; AST – aspartate aminotransferase; DFS – disease-free survival.

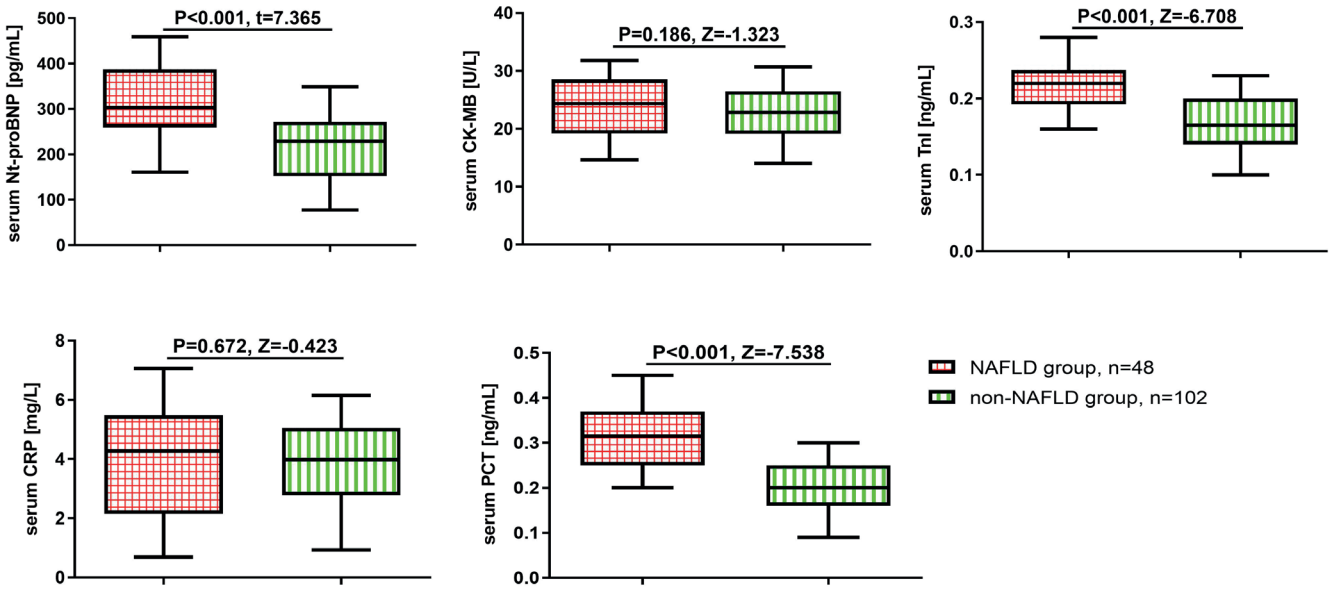

Fig. 1. Cardiac biomarker and inflammatory marker levels in the nonalcoholic fatty liver disease (NAFLD) and non-NAFLD groups. Data are presented as box plots, with whiskers indicating the minimum and maximum values. N-terminal pro-B-type natriuretic peptide (NT-proBNP) followed a normal distribution and was compared using Student's t-test, whereas all other variables were non-normally distributed and analyzed using the Mann–Whitney U test

CK-MB – creatine kinase-MB isoenzyme; TnI – cardiac troponin I; CRP – C-reactive protein; PCT – procalcitonin.

Table 2. MACE incidence between the NAFLD and non-NAFLD groups

Variable	NAFLD group (n = 48)	Non-NAFLD group (n = 102)	χ^2	p-value
Sudden cardiac death, n (%)[#]	4 (8.33)	3 (2.94)	χ^2 (1) = 2.732	0.098
Myocardial infarction, n (%)[#]	5 (10.42)	6 (5.88)	χ^2 (1) = 1.377	0.241
Heart failure, n (%)[#]	4 (8.33)	4 (3.92)	χ^2 (1) = 1.691	0.193
MACE, n (%)[#]	15 (31.25)	14 (13.73)	χ^2 (1) = 8.804	0.003

[#] Categorical variables (column percentages) were compared using Pearson's χ^2 test of independence, as all expected cell counts were ≥5, including sudden cardiac death (minimum expected count = 5.64), myocardial infarction (minimum expected count = 8.15), heart failure (minimum expected count = 6.13), and MACE (minimum expected count = 22.49). All analyses were performed using non-rounded values in the SPSS Crosstabs procedure. MACE – major adverse cardiovascular events; NAFLD – nonalcoholic fatty liver disease.

Kaplan–Meier analysis of MACE-free survival in the NAFLD and non-NAFLD groups

To further assess the prognostic impact of NAFLD, Kaplan–Meier analysis was performed to compare MACE-free survival between the 2 groups. As shown in Fig. 2, the NAFLD group had significantly shorter MACE-free survival than the non-NAFLD group (p = 0.006), indicating a higher cumulative incidence of cardiovascular events over time.

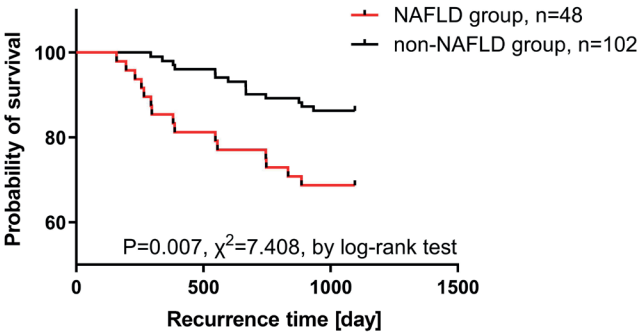

Fig. 2. Kaplan–Meier analysis of major adverse cardiovascular event (MACE)-free survival in the nonalcoholic fatty liver disease (NAFLD) and non-NAFLD groups

Multivariate logistic regression analysis of risk factors for MACE

To identify independent risk factors for MACE, a multivariate binary logistic regression analysis was performed, including all clinically relevant variables. Given their highly skewed distributions and unstable estimates in the initial model, TnI and PCT were transformed into binary variables using the median as the cutoff value to improve interpretability and model stability. The model demonstrated acceptable goodness of fit, as indicated by a non-significant Hosmer–Lemeshow test (p = 0.254) and a Nagelkerke R^2 value of 0.357. Multicollinearity was assessed using variance inflation factors (VIFs), which showed that all variables had VIF values <5, except for NAFLD (VIF = 7.046). Given its clinical importance and

Table 3. Logistic regression analysis of risk factors for MACE occurrence within 3 years in UA patients

Variables	OR	95% CI	p-value
Age	1.086	0.996–1.185	0.062
Male	0.660	0.224–1.943	0.451
BMI	0.918	0.747–1.128	0.416
Smoking	0.687	0.237–1.992	0.490
Drinking	0.552	0.193–1.579	0.268
Hypertension	1.260	0.420–3.781	0.680
Diabetes mellitus	10.269	3.148–33.495	<0.001
TC	2.753	0.790–9.594	0.112
TG	1.718	0.398–7.406	0.468
LDL-C	1.167	0.345–3.948	0.804
HDL-C	1.915	0.103–35.514	0.663
ALT	0.980	0.931–1.031	0.432
AST	1.003	0.960–1.049	0.880
NT-proBNP	0.995	0.988–1.002	0.150
CK-MB	1.002	0.887–1.132	0.971
TnI (group)	1.600	0.456–5.607	0.463
CRP	1.003	0.735–1.369	0.983
PCT (group)	1.430	0.430–4.752	0.559
NAFLD	0.172	0.014–2.054	0.164

BMI – body mass index; TC – total cholesterol; TG – triglycerides; LDL-C – low-density lipoprotein cholesterol; HDL-C – high-density lipoprotein cholesterol; ALT – alanine aminotransferase; AST – aspartate aminotransferase; NT-proBNP – N-terminal pro-B-type natriuretic peptide; CK-MB – creatine kinase-MB isoenzyme; TnI – cardiac troponin I; CRP – C-reactive protein; PCT – procalcitonin; NAFLD – nonalcoholic fatty liver disease; OR – odds ratio; 95% CI – 95% confidence interval.

predefined role as the primary exposure variable, NAFLD was retained in the model despite its elevated VIF (Supplementary Table 3). However, we acknowledge that its inclusion introduces potential multicollinearity and therefore represents a methodological compromise that may have affected its statistical significance. Residual diagnostics revealed no studentized residuals exceeding ±3.0, and all Cook's distance values were below 1.0, indicating the absence of influential outliers. Leverage values were within acceptable limits, supporting the robustness of the regression model (Supplementary Table 4). Linearity between continuous predictors and the logit of the outcome was assessed using the Box–Tidwell test. All interaction terms were non-significant ($p > 0.05$), except for AST ($p = 0.019$), which showed a mild deviation from linearity. However, given the overall model stability and clinical relevance, AST was retained in the final model (Supplementary Table 5). As shown in Table 3, diabetes mellitus was independently associated with an increased risk of MACE (odds ratio (OR) = 10.269, 95% confidence interval (95% CI): 3.148–33.495, $p < 0.001$). No other variables, including NAFLD, age, lipid parameters, liver enzymes, cardiac biomarkers, or inflammatory markers, reached statistical significance in the multivariate model.

Discussion

Unstable angina is a clinical concern not only because of its acute symptomatic burden but also due to its high instability and potential to progress to myocardial infarction or sudden cardiac death.[20] In this prospective cohort study, we found that patients with coexisting NAFLD had a significantly higher incidence of MACE during the 3-year follow-up period compared with those without NAFLD.

MACE occurrence in patients with UA is influenced by various factors. Alongside established cardiovascular risk factors such as hypertension, diabetes mellitus, hyperlipidemia, smoking, and family history, key determinants of prognosis include the severity of coronary artery lesions, cardiac function, inflammatory marker levels, and the timeliness and effectiveness of therapeutic interventions. Studies have identified several predictors of MACE in patients with UA. For instance, 1 study found a higher incidence of MACE in men than in women (4.1% vs 2.6%, $p < 0.05$), despite similar in-hospital cardiac mortality rates.[21] Another study identified advanced age, diabetes mellitus, reduced left ventricular ejection fraction (LVEF), elevated high-sensitivity C-reactive protein (hs-CRP), and high SYNTAX scores as independent predictors of MACE within 2 years after discharge.[22] Additionally, unstable plaques and elevated $CD4^+/CD8^+$ ratios have been associated with increased plaque instability.[23] Emerging serum markers, such as NLRP3 and growth differentiation factor 15 (GDF-15), have also been associated with prognosis in patients with UA.[24,25]

In our study, the overall 3-year incidence of MACE was 19.3%, which is comparable to long-term MACE rates reported in population-based cohorts with NAFLD. For instance, an Australian cohort study reported an 18.8% incidence of 5-point MACE over a mean follow-up period of approx. 18 years.[26] Given that our study focused on a hospitalized UA population with an inherently higher baseline risk, the observed event rate is clinically plausible.

Furthermore, patients with NAFLD had a significantly higher incidence of MACE during follow-up; however, NAFLD was not identified as an independent predictor after adjustment for confounding factors. This finding suggests that the adverse cardiovascular outcomes observed in patients with UA and NAFLD may be mediated by coexisting metabolic abnormalities, particularly diabetes mellitus, which showed the strongest independent association in our model. In addition, multicollinearity between NAFLD and metabolic parameters such as BMI and triglyceride levels may have attenuated the independent statistical contribution of NAFLD in the multivariate analysis.

Although age did not reach statistical significance in the multivariate model ($p = 0.062$), the observed trend suggests a potential association that may warrant further investigation in larger cohorts. Among the analyzed variables, diabetes mellitus showed the strongest independent

association with MACE, indicating that metabolic dysfunction may be the primary driver of poor prognosis in this subgroup. This finding is consistent with studies in other disease populations, in which cardiovascular risk factors have been shown to independently affect disease phenotype and prognosis, such as in patients with polycythemia vera and essential thrombocythemia.[27]

Compared with previous studies that identified various inflammatory and structural indicators as predictors of MACE, our findings highlight the need to clarify whether NAFLD acts as a mediator, amplifier, or merely a marker of metabolic risk in predicting cardiovascular outcomes in patients with UA.

Nonalcoholic fatty liver disease is an established independent risk factor for cardiovascular diseases and is linked to metabolic disorders and chronic inflammation. It increases the risk of hypertension, coronary heart disease, cardiomyopathy, and arrhythmias, thereby contributing to higher cardiovascular morbidity and mortality.[28] A cohort study involving more than 210,000 participants confirmed NAFLD as a predictor of all-cause mortality and adverse cardiovascular outcomes, highlighting the value of incorporating NAFLD into cardiovascular risk assessment.[29] Additionally, NAFLD has been associated with an increased incidence of myocardial infarction, irrespective of other risk factors.[30] A meta-analysis further revealed that female patients with NAFLD face significantly higher rates of coronary events and mortality.[31]

The pathophysiological mechanisms underlying NAFLD are closely related to insulin resistance, which leads to dysfunction of adipokines produced by adipose tissue, particularly adiponectin. Furthermore, increased formation of reactive oxygen species (ROS) promotes the oxidation of free fatty acids, while triglyceride accumulation enhances de novo lipogenesis, resulting in a pro-inflammatory state and increased oxidative stress. These mechanisms may contribute to the formation and progression of atherosclerotic plaques, potentially increasing cardiovascular risk in patients with NAFLD.[12]

Although NAFLD is widely recognized as an independent cardiovascular risk factor in the general population, its role as an independent predictor of MACE in patients with UA was not confirmed in our cohort after adjustment for confounding factors. Nonetheless, the prospective design of our study and the 3-year follow-up period strengthen the evidence for an association between NAFLD and adverse cardiovascular outcomes in patients with UA, even if NAFLD was not independently predictive in the multivariate analysis.

Limitations of the study

While this study provides valuable insights into the impact of NAFLD on patients with UA, several limitations should be acknowledged. First, this was a single-center study with a relatively limited sample size, which may affect the generalizability of the findings. Although potential confounding factors were considered, influences such as lifestyle and genetic background may not have been fully accounted for. In addition, the 3-year follow-up period may be insufficient to capture the full long-term effects of NAFLD in patients with UA. Furthermore, due to the relatively low number of MACE events and the inclusion of multiple clinically relevant variables, the multivariate model may have been affected by limited statistical power and potential overfitting. Nevertheless, the modeling approach was retained to preserve a comprehensive assessment of cardiovascular risk. In addition, CK-MB was measured as enzymatic activity rather than mass concentration, which may be more susceptible to false-positive results due to skeletal muscle injury or macro-CK interference and should therefore be considered a potential source of diagnostic imprecision. Finally, because multiple hypotheses were tested, there is a potential risk of type I error, and the results should therefore be interpreted with caution.

Conclusions

In patients with UA, coexisting NAFLD was associated with a higher incidence of major adverse cardiovascular events during a 3-year follow-up period, although it was not identified as an independent predictor after adjustment for confounding factors. These findings suggest that NAFLD may serve as a marker of increased cardiovascular risk and highlight the importance of comprehensive metabolic assessment and long-term follow-up in this population.

Supplementary data

The supplementary materials are available at: https://doi.org/10.5281/zenodo.17370159. The package contains the following files:

Supplementary Table 1. Results of normality tests.

Supplementary Table 2. Original Student's t-test results for Table 1 of the main text, including Levene's test results.

Supplementary Table 3. VIF results for the logistic regression analysis presented in Table 3.

Supplementary Table 4. Residual and influence diagnostics for the logistic regression model presented in Table 3, including studentized residuals, Cook's distance, leverage values, and Mahalanobis distance.

Supplementary Table 5. Box–Tidwell test results for assessing the linearity of continuous variables in the logistic regression model (Table 3).

Supplementary Table 6. χ^2 test results for sex (Table 1).

Supplementary Table 7. χ^2 test results for smoking status (Table 1).

Supplementary Table 8. χ^2 test results for alcohol consumption history (Table 1).

Supplementary Table 9. χ^2 test results for hypertension (Table 1).

Supplementary Table 10. χ^2 test results for diabetes mellitus (Table 1).

Supplementary Table 11. χ^2 test results for sudden cardiac death (Table 2).

Supplementary Table 12. χ^2 test results for myocardial infarction (Table 2).

Supplementary Table 13. χ^2 test results for heart failure (Table 2).

Supplementary Table 14. χ^2 test results for MACE (Table 2).

Data Availability Statement

The datasets supporting the findings of the present study are openly available in Zenodo at https://doi.org/10.5281/zenodo.17370189.

Use of AI and AI-assisted technologies

This manuscript underwent language editing using GPT-4o, a large language model developed by OpenAI, to improve clarity and readability. All scientific content, data interpretation, and conclusions were generated by the authors.

Consent for publication of personal information

Not applicable.

ORCID iDs

Pei Shi https://orcid.org/0009-0007-5659-8151
Xiaojuan Meng https://orcid.org/0009-0006-9959-8162

References

1. Koivunen M, Tynkkynen J, Oksala N, Eskola M, Hernesniemi J. Incidence of sudden cardiac arrest and sudden cardiac death after unstable angina pectoris and myocardial infarction. *Am Heart J*. 2023; 257:9–19. doi:10.1016/j.ahj.2022.11.009
2. Timmis A, Kazakiewicz D, Townsend N, Huculeci R, Aboyans V, Vardas P. Global epidemiology of acute coronary syndromes. *Nat Rev Cardiol*. 2023;20(11):778–788. doi:10.1038/s41569-023-00884-0
3. Tegn N, Eek C, Abdelnoor M, et al. Patients aged 80 years or older with non-ST-elevation myocardial infarction or unstable angina pectoris randomised to an invasive versus conservative strategy: Angiographic and procedural results from the After Eighty study. *Open Heart*. 2020;7(2):e001256. doi:10.1136/openhrt-2020-001256
4. Kristensen AMD, Pareek M, Kragholm KH, Sehested TSG, Olsen MH, Prescott EB. Unstable angina as a component of primary composite endpoints in clinical cardiovascular trials: Pros and cons. *Cardiology*. 2022;147(3):235–247. doi:10.1159/000524948
5. Fladseth K, Wilsgaard T, Lindekleiv H, et al. Outcomes after coronary angiography for unstable angina compared to stable angina, myocardial infarction and an asymptomatic general population. *IJC Heart Vasc*. 2022;42:101099. doi:10.1016/j.ijcha.2022.101099
6. Chacko L, P. Howard J, Rajkumar C, et al. Effects of percutaneous coronary intervention on death and myocardial infarction stratified by stable and unstable coronary artery disease: A meta-analysis of randomized controlled trials. *Circ Cardiovasc Qual Outcomes*. 2020; 13(2):e006363. doi:10.1161/CIRCOUTCOMES.119.006363
7. Piątek Ł, Janion-Sadowska A, Piątek K, et al. Long-term clinical outcomes in patients with unstable angina undergoing percutaneous coronary interventions in a contemporary registry data from Poland. *Coron Artery Dis*. 2020;31(3):215–221. doi:10.1097/MCA.0000000000000812
8. Pouwels S, Sakran N, Graham Y, et al. Non-alcoholic fatty liver disease (NAFLD): A review of pathophysiology, clinical management and effects of weight loss. *BMC Endocr Disord*. 2022;22(1):63. doi:10.1186/s12902-022-00980-1
9. Maurice J, Manousou P. Non-alcoholic fatty liver disease. *Clin Med (Lond)*. 2018;18(3):245–250. doi:10.7861/clinmedicine.18-3-245
10. Papatheodoridi M, Cholongitas E. Diagnosis of non-alcoholic fatty liver disease (NAFLD): Current concepts. *Curr Pharm Des*. 2019;24(38): 4574–4586. doi:10.2174/1381612825666190117102111
11. Simon TG, Roelstraete B, Hagström H, Sundström J, Ludvigsson JF. Non-alcoholic fatty liver disease and incident major adverse cardiovascular events: Results from a nationwide histology cohort. *Gut*. 2022;71(9):1867–1875. doi:10.1136/gutjnl-2021-325724
12. Galiero R, Caturano A, Vetrano E, et al. Pathophysiological mechanisms and clinical evidence of relationship between nonalcoholic fatty liver disease (NAFLD) and cardiovascular disease. *Rev Cardiovasc Med*. 2021;22(3):755. doi:10.31083/j.rcm2203082
13. Niederseer D, Wernly B, Aigner E, Stickel F, Datz C. NAFLD and cardiovascular diseases: Epidemiological, mechanistic and therapeutic considerations. *J Clin Med*. 2021;10(3):467. doi:10.3390/jcm10030467
14. Li M, Cui M, Li G, et al. The pathophysiological associations between obesity, NAFLD, and atherosclerotic cardiovascular diseases. *Horm Metab Res*. 2024;56(10):683–696. doi:10.1055/a-2266-1503
15. Chen X, Zhao X, Wu H, et al. Association of nonalcoholic fatty liver disease with ventricular tachycardia and sinus arrest in patients with non-ST-segment elevation myocardial infarction. *Int Heart J*. 2022; 63(5):814–820. doi:10.1536/ihj.22-113
16. Zhao J, Fan H, Wang T, et al. TyG index is positively associated with risk of CHD and coronary atherosclerosis severity among NAFLD patients. *Cardiovasc Diabetol*. 2022;21(1):123. doi:10.1186/s12933-022-01548-y
17. Anderson JL, Adams CD, Antman EM, et al. 2012 ACCF/AHA focused update incorporated into the ACCF/AHA 2007 guidelines for the management of patients with unstable angina/non-ST-elevation myocardial infarction: A report of the American College of Cardiology Foundation/American Heart Association Task Force on Practice Guidelines. *J Am Coll Cardiol*. 2013;61(23):e179–347. doi:10.1016/j.jacc.2013.01.014
18. Wang J, Huang D, Zhang T, et al. Nrf2, gp91phox and IL-17 are associated with severity and clinical outcomes of patients with subclinical hypothyroidism: A comparative study. *Scand J Clin Lab Invest*. 2024;84(5):297–304. doi:10.1080/00365513.2024.2377966
19. Huang R, Zhang L, Deng L, Fang J. Diagnostic and prediction value of synthetic magnetic resonance imaging in acute ischemic stroke patients. *Adv Clin Exp Med*. 2024;34(2):179–186. doi:10.17219/acem/185496
20. Braunwald E. Unstable angina and non-ST elevation myocardial infarction. *Am J Respir Crit Care Med*. 2012;185(9):924–932. doi:10.1164/rccm.201109-1745CI
21. Xu M, Li HW, Chen H, Guo CY. Sex and age differences in patients with unstable angina pectoris: A single-center retrospective study. *Am J Med Sci*. 2020;360(3):268–278. doi:10.1016/j.amjms.2020.05.020
22. Xu M, Chen H, Li HW. The association between SYNTAX score and long-term outcomes in patients with unstable angina pectoris: A single-centre retrospective study. *BMC Cardiovasc Disord*. 2022;22(1):155. doi:10.1186/s12872-022-02604-x
23. Chai D, Kong X, Lu S, Zhang J. $CD4^+/CD8^+$ ratio positively correlates with coronary plaque instability in unstable angina pectoris patients but fails to predict major adverse cardiovascular events. *Ther Adv Chronic Dis*. 2020;11:2040622320922020. doi:10.1177/2040622320922020
24. Pan S, Wang Y, Zhang Y, et al. The relationship between the serum NLRP3 and adiponectin levels and coronary lesions in patients with unstable angina with type 2 diabetes. *Clin Interv Aging*. 2024;19: 1301–1308. doi:10.2147/CIA.S467291
25. Raygan F, Etminan A, Mohammadi H, Akbari H, Nikoueinejad H. Serum levels of growth differentiation factor-15 as an inflammatory marker in patients with unstable angina pectoris. *J Tehran Univ Heart Cent*. 2021;16(1):15–19. doi:10.18502/jthc.v16i1.6595

26. Vaz K, Kemp W, Majeed A, et al. NAFLD and MAFLD independently increase the risk of major adverse cardiovascular events (MACE): A 20-year longitudinal follow-up study from regional Australia. *Hepatol Int*. 2024;18(4):1135–1143. doi:10.1007/s12072-024-10706-1
27. Sobieralski P, Bieniaszewska M, Bołkun Ł, et al. Polycythemia vera and essential thrombocythemia of intermediate-age: A real-life, multicenter analysis of first-line treatment approach. *Adv Clin Exp Med*. 2024;34(1):25–32. doi:10.17219/acem/182857
28. Kasper P, Martin A, Lang S, et al. NAFLD and cardiovascular diseases: A clinical review. *Clin Res Cardiol*. 2021;110(7):921–937. doi:10.1007/s00392-020-01709-7
29. Ma W, Wu W, Wen W, et al. Association of NAFLD with cardiovascular disease and all-cause mortality: A large-scale prospective cohort study based on UK Biobank. *Ther Adv Chronic Dis*. 2022;13:20406223221122478. doi:10.1177/20406223221122478
30. Sinn DH, Kang D, Chang Y, et al. Non-alcoholic fatty liver disease and the incidence of myocardial infarction: A cohort study. *J Gastroenterol Hepatol*. 2020;35(5):833–839. doi:10.1111/jgh.14856
31. Khalid YS, Dasu NR, Suga H, et al. Increased cardiovascular events and mortality in females with NAFLD: A meta-analysis. *Am J Cardiovasc Dis*. 2020;10(3):258–271. PMID:32923108. PMCID:PMC7486530.

Impact of the COVID-19 pandemic on pediatric hemolytic uremic syndrome: Epidemiology, complications, and outcomes

Ewelina Jarosz-Wójcik[1,3,B–D], Mateusz A. Zajączkowski[2,B,C], Dorota Drożdż[1,3,E,F], Palina Warmachowska[2,B], Mikołaj Brzeźniak[2,B], Aleksandra M. Molek[2,B], Oliwia Andrasz[2,B], Olga Szczerbak[2,B], Monika Miklaszewska[1,3,A–E]

[1] Department of Pediatric Nephrology and Hypertension, Jagiellonian University Medical College, Cracow, Poland
[2] Student Research Group at Department of Pediatric Nephrology and Hypertension, Jagiellonian University Medical College, Cracow, Poland
[3] Department of Pediatric Nephrology and Hypertension, University Children's Hospital of Cracow, Poland

A – research concept and design; B – collection and/or assembly of data; C – data analysis and interpretation; D – writing the article; E – critical revision of the article; F – final approval of the article

Advances in Clinical and Experimental Medicine, ISSN 1899–5276 (print), ISSN 2451–2680 (online) *Adv Clin Exp Med*. 2026;35(7):1153–1162

Address for correspondence
Monika Miklaszewska
E-mail: monika.miklaszewska@uj.edu.pl

Funding sources
None declared

Conflict of interest
None declared

Received on September 7, 2025
Reviewed on November 10, 2025
Accepted on December 2, 2025

Published online on June 5, 2026

Abstract

Background. Hemolytic-uremic syndrome (HUS) is a thrombotic microangiopathy that is most commonly caused by infection with Shiga toxin-producing *Escherichia coli* (STEC-HUS). Atypical HUS (aHUS) is associated with inappropriate activation of the alternative complement pathway caused by infections, including SARS-CoV-2, malignancies, medications, or other triggering factors in genetically predisposed individuals.

Objectives. Assessment of the impact of the COVID-19 pandemic on epidemiology, course, complications, and outcome of HUS in children in a single tertiary nephrological center in Poland.

Materials and methods. It is a retrospective study, in which a total number of 74 pediatric patients with HUS were analyzed, including 16 cases in 5-year period before the outbreak of the COVID-19 pandemic (HUS-5) and 58 cases in 5-year period after the outbreak of the pandemic (HUS+5).

Results. A more than 3.6-fold increase in HUS cases and a 7-fold higher incidence of STEC-HUS were reported in the HUS+5 population. Strokes and persistent neurological complications were observed only in this group. 91.9% of patients presented with abnormal renal ultrasound (USG) findings at admission, and these findings improved significantly more frequently in the HUS-5 (68.75% vs 25.9%, $p = 0.002$) group. Mortality did not differ significantly between the 2 analyzed groups and was 6.8% for the entire population.

Conclusions. The COVID-19 pandemic has had a significant impact on the incidence of HUS in the pediatric population. SARS-CoV-2 infection most markedly increases the risk of neurological complications but does not affect overall mortality.

Key words: hemolytic-uremic syndrome, COVID-19, child, Shiga toxin-producing *Escherichia coli*, neurologic complications

Cite as
Jarosz-Wójcik E, Zajączkowski MA, Drożdż D, et al. Impact of the COVID-19 pandemic on pediatric hemolytic uremic syndrome: Epidemiology, complications, and outcomes. *Adv Clin Exp Med*. 2026;35(7):1153–1162. doi:10.17219/acem/214976

DOI
10.17219/acem/214976

Copyright
Copyright by Author(s)
This is an article distributed under the terms of the Creative Commons Attribution 3.0 Unported (CC BY 3.0) (https://creativecommons.org/licenses/by/3.0/)

Highlights

- Pediatric hemolytic uremic syndrome (HUS) incidence increased 3.6-fold following the COVID-19 outbreak, including a 7-fold rise in STEC-HUS.
- In pediatric HUS, COVID-19 was associated with neurological complications, including stroke and persistent deficits.
- Mortality in pediatric HUS remained stable despite increased disease severity after COVID-19.

Background

Hemolytic uremic syndrome (HUS) is one of the conditions associated with thrombotic microangiopathy (TMA) and constitutes a life-threatening, rare disease characterized by microangiopathic hemolytic anemia, thrombocytopenia, and acute kidney injury (AKI).

Depending on the triggering factors, HUS can be generally classified as hereditary or acquired.[1] Additionally, HUS may be classified as follows: infection-associated HUS (including causes such as Shiga toxin-producing *Escherichia coli* (STEC), *Streptococcus pneumoniae*, influenza A, H1N1, HIV, norovirus, Epstein–Barr virus (EBV), parvovirus B19, and COVID-19), HUS secondary to pregnancy, bone marrow or solid organ transplantation, systemic malignancies, radio- or chemotherapy, autoimmune conditions (such as systemic lupus erythematosus (SLE), antiphospholipid antibody syndrome, and scleroderma), some drugs (quinine, calcineurin inhibitors, and a few chemotherapeutic agents), malignant hypertension (HT), cobalamin C disorder, and finally atypical HUS (aHUS) due to alternative complement pathway dysregulation (complement-mediated HUS; CM-HUS) and mutations in the diacylglycerol kinase epsilon (*DGKE*) gene.[2–5]

Shiga toxin-producing *Escherichia coli* HUS (STEC-HUS), also traditionally called typical HUS, constitutes 90–95% of pediatric HUS cases, while aHUS accounts for 5–10%. The incidence of HUS among individuals infected with STEC ranges from 5% to 15%, predominantly affecting children younger than 5 years.[5,6]

Genetic variants in complement regulatory proteins (CRPs, including *CFH*, *CFI*, *MCP*, *CFB*, and *C3*) or autoantibodies to factor H (FH) account for 50–60% of all aHUS cases, with approx. 30–50% having no known identifiable mutation.[4,7] While genetic mutations can predispose a person toward developing aHUS, the disease usually requires a trigger event to manifest clinically. Recent studies have suggested that viral infections, including COVID-19, may trigger aHUS in genetically susceptible individuals as severe acute respiratory syndrome coronavirus 2 (SARS-CoV-2) may cause widespread microvascular damage, including TMA, driven by inflammation, cytokine storm, and dysregulated complement system activation.[8–12]

Epidemiologically, HUS is a rare disease in children, and the incidence varies considerably depending on the data source and geographical region, but collectively for STEC-HUS and aHUS, it is estimated at an average of 6.3–14.2/million age-related population/year, while the incidence of CM-HUS in children is relatively constant at 0.25–2/million age-related population/year.[5,13–15]

According to the literature, renal involvement in COVID-19 is reported to be 10–15%.[16] In a meta-analysis by Gu et al., patients with COVID-19 had a 1.5-fold higher risk of AKI and a more than twofold higher risk of death when AKI occurred, with statistically significant results despite moderate heterogeneity.[17] However, in a series of patients with COVID-19 who were biopsied because of AKI or proteinuria, glomerular TMA was a relatively rare finding compared to acute tubular necrosis or collapsing glomerulopathy.[18] On the other hand, numerous reports have linked COVID-19 infection in the pediatric population with new episodes or relapses of HUS.[9,19–21] Therefore, due to the severity and potentially fatal complications of this condition, this study addresses this issue in more detail.

Objectives

There are limited original papers or reports on the effect of SARS-CoV-2 infection on the occurrence of HUS in children. The aim of this project was to assess the impact of the COVID-19 pandemic on the epidemiology, clinical course, complications, and outcomes of HUS in pediatric patients hospitalized in our tertiary pediatric nephrology center.

Materials and methods

The study is a single-center, retrospective chart review of patients who were newly diagnosed with HUS, and were hospitalized at the Department of Pediatric Nephrology and Hypertension University Children's Hospital of Cracow (Poland), a tertiary reference center, during a 10-year period (from January 1, 2015, to December 31, 2024).

The study population was divided into 2 groups: a subpopulation with HUS before the outbreak of the COVID-19 pandemic, covering the period from January 1, 2015, to December 31, 2019 (HUS-5; 16 patients), and a subpopulation

after the outbreak of the pandemic, covering the period from January 1, 2020, to December 31, 2024 (HUS+5; 58 patients).

The ethics committee of Jagiellonian University Medical College, Cracow, Poland, approved the study (approval No. 118.0043.1.429.2024), and informed consent was waived due to its retrospective nature. The study involved a detailed analysis of data from the medical histories and outpatient documentation of each patient included in the study.

STEC-HUS (typical HUS) was diagnosed when genetic material from enteropathogenic *Escherichia coli* (EPEC), enterohemorrhagic *Escherichia coli* (EHEC), or STEC (STEC 1 or 2) was identified in the patient's stool or anal swab using multiplex polymerase chain reaction (PCR) assay (The QIAstat-Dx® Gastrointestinal Panel; Qiagen, Hilden, Germany).[22] Atypical HUS was diagnosed when stool testing was negative for these pathogens and ADAMTS13 activity exceeded 10%. This group also included 2 patients with *Streptococcus pneumoniae* infection who developed HUS (Strep-HUS).

Contact with SARS-CoV-2 was defined as the presence of positive immunoglobulin M or G (IgM or IgG) antibodies against SARS-CoV-2, or a positive antigen or PCR test for SARS-CoV-2 performed upon admission. None of the children had been vaccinated against COVID-19.

Semi-quantitative renal ultrasonography (USG) assessment was performed by evaluating the results of examinations performed on admission and at hospital discharge. The following parameters were assessed: kidney size (normal/enlarged: 0/1 point), parenchymal echogenicity (normal/increased: 0/1 point), and corticomedullary differentiation (normal/reduced/none: 0/1/2 points). The range of possible points was 0–4. After summing up the points, the renal USG findings were categorized as follows: normal (0 points), minor damage (1–2 points), and major damage (3–4 points).

Hypertension was diagnosed according to the European Society of Hypertension (ESH) guidelines for children and adolescents as an average of at least 3 blood pressure measurements greater than or equal to the 95th percentile for age, sex, and height in children aged 0–15 years of age, or ≥140/90 mm Hg for adolescents aged 16 years or older, using an appropriately sized cuff and a validated sphygmomanometer.[23]

Estimated glomerular filtration rate (eGFR) was calculated using the Schwartz formula.[24] When defining the outcome, the basic factors were the eGFR value as well as the presence and severity of proteinuria. The occurrence of HT and the renal USG findings were supplementary factors to the overall assessment. Hence, the outcome of a patient was classified as either:

1) complete recovery, defined as: eGFR > 90 mL/min/1.73 m^2 and the absence of proteinuria, the absence of HT, and normal or close to normal renal USG (0–1 points);

2) a) superior partial recovery, defined as: eGFR ≥ 45 mL/min and absence or presence of non-nephrotic range proteinuria (<50 mg/kg/day). Abnormalities including HT and/or abnormal renal USG (2–4 points) may or may not be present; b) inferior partial recovery, defined as: eGFR ≤ 44 mL/min, and/or presence of nephrotic range proteinuria (≥50 mg/kg/day), the presence of non-nephrotic range proteinuria or absence of proteinuria. Abnormalities including HT and/or abnormal renal USG (2–4 points) may or may not be present.

For points 2a and 2b – the final qualification of a child to an outcome group depended on which factor (eGFR or proteinuria) the result was more severe.

3) death.

Statistical analyses

Normality of distribution of variables was assessed using the Shapiro–Wilk test. As most samples deviated from normality, results are reported as medians and interquartile ranges (IQR). Non-normally distributed variables were compared using the nonparametric Wilcoxon rank-sum test (Mann–Whitney U test) with a significance level set at 0.05 (pW). For Gaussian-distributed variables, Student's t-test (tS) was applied; in cases of heteroscedasticity, Welch's t-test was used. In cases of significant heterogeneity of variances in Levene's or Brown–Forsythe test ($p < 0.05$), Welch's t-test was applied. Categorical paired data were analyzed using McNemar's test. The significance of the difference between 2 distributions was assessed using a one-sided Fisher's exact test. The threshold value of $p = 0.05$ was adopted when assessing statistical significance. Statistica v. 10 PL package (StatSoft Poland, Cracow, Poland) was used for the analysis.

Results

In this study, we analyzed data from 74 pediatric patients hospitalized for HUS in our center, including 16 cases before the pandemic (HUS-5) and 58 cases after the outbreak of the pandemic (HUS+5). No patient was excluded from the study. In both subgroups, there were boys and girls with almost equal frequency, and the median age was 55.5 months in HUS-5 and 29.3 months in HUS+5.

A more than 3.6-fold increase in the number of HUS cases in the pediatric population was observed after the outbreak of the COVID-19 pandemic compared with the corresponding period before the pandemic (HUS-5 population: 3.2 vs HUS+5 population: 11.6 cases per year).

Interestingly, in the HUS-5 group, the proportion of aHUS was 2.1 times higher than in the post-pandemic period (62.5% vs 29.3%, $p = 0.017$), with an overall rate of 36.5% during the 10-year observation period. In both subgroups, the mortality rate was comparable and amounted to 6.8% for the entire population. Nineteen patients (32.8%) in the HUS+5 group had confirmed contact with COVID-19 (active – 2, past – 17). The other analyzed

Table 1. Clinical characteristics of the study population and comparison of subgroups (HUS-5 vs HUS+5)

Number of cases (% vs number of patients)	HUS-5 (n = 16)	HUS+5 (n = 58)	pF	All patients (n = 74)
Number of patients (% vs 74)	21.6%	78.4%	N/A	74 (100%)
Sex (females) (% vs 16/58)	8 (50.0%)	28 (48.3%)	0.563	36 (48.7%)
aHUS cases (% vs 16/58)	10 (62.5%)	17 (29.3%)	0.017	27 (36.5%)
STEC HUS	6 (37.5%)	41 (70.7%)	CT	47 (63.5%)
ICU stay	4 (25.0%)	20 (34.5%)	0.346	24 (32.4%)
Circulatory failure	0 (0.0%)	7 (12.0%)	0.167	7 (9.5%)
Respiratory failure	3 (18.75%)	18 (31%)	0.263	21 (28.4%)
Oxygen therapy	2 (12.5%)	15 (25.9%)	0.229	17 (23.0%)
SIMV/intubation	3 (18.75%)	13 (22.4%)	0.526	16 (21.6%)
Death	1 (6.3%)	4 (6.9%)	0.706	5 (6.8%)
Age (vs number of patients)	**HUS-5 (n = 16)**	**HUS+5 (n = 58)**	**pF**	**All patients (n = 74)**
≤1 year (≤12 months)	3 (18.8%)	6 (10.3%)	0.300	9 (12.2%)
1–5 years (13–59 months)	4 (25.0%)	33 (56.9%)	0.023	37 (50.0%)
5–10 years (60–119 months)	5 (31.2%)	11 (19.0%)	0.232	16 (21.6%)
≥10 years (≥120 months)	4 (25.0%)	8 (13.8%)	0.236	12 (16.2%)
Onset season	**HUS-5 (n = 16)**	**HUS+5 (n = 58)**	**pF**	**All patients (n = 74)**
Warm season (April–September)	8 (50.0%)	40 (69.0%)	0.134	48 (64.9%)
Cold season (October–March)	8 (50.0%)	18 (31.0%)	0.134	26 (35.1%)
Variables (median, IQR)*	**Median (IQR)**	**Median (IQR)**	**pW**	**Median (IQR)**
Age [months]	55.5 (88.8)	29.3 (56.0)	0.130	36.5 (62.2)
Body mass [kg]	20.4 (20.7)	13.8 (11.2)	0.100	15.5 (15.0)
Body mass [percentiles]	32.4 (63.0)	49 (53.0)	0.881	51.5 (53.0)
Height [cm]	114.5 (48.3)	94.8 (39.5)	0.172	100 (42.0)
Height [percentiles]	52 (66.0)	71.5 (43.0)	0.148	68 (46.0)
Hospitalization [days]	24 (30.0)	16 (20.0)	0.210	19 (25.0)
ICU stay [days] (only population of ICU patients)	30.5 (23.0)	18 (24.0)	0.543	23.5 (25.0)
ICU [% days] (only population of ICU patients)	81.5 (43.0)	28.2 (34.5)	0.369	45.3 (46.0)

Data are presented as absolute numbers and percentages, with p-values from the one-sided Fisher's exact test (pF). *medians with interquartile ranges (IQR) and corresponding p-values from the Wilcoxon rank-sum test (pW). aHUS – atypical hemolytic uremic syndrome; STEC-HUS – Shiga toxin–producing *Escherichia coli*-associated HUS; ICU – intensive care unit; SIMV – synchronized intermittent mandatory ventilation; computed tomography (CT) – data analyzed within the same contingency table as in the previous row. N/A – not applicable.

parameters, including age, body weight, height, length of stay in the intensive care unit (ICU), circulatory or respiratory failure, and the need for oxygen therapy or intubation, did not differ significantly between the groups.

In the aHUS population, 18 of 27 patients (66.7%) received eculizumab; since 2018, when the drug became available in our country, the proportion was 18 of 20 (90%).

During the summer months (April–September), the incidence of HUS was 1.85 times higher than in the winter months (October–March). Moreover, in the HUS+5 group, there was a significantly higher proportion of children aged 1–5 years compared to the HUS-5 period (Table 1).

Among the analyzed symptoms, diarrhea occurred 1.4 times more frequently in patients in the HUS+5 group compared with the HUS-5 group (81% vs 56.3%, p = 0.046), and its duration, calculated for the entire study population, was also longer in this group (4 days vs 1.5 days, p = 0.03). This is likely due to the fact that this group had a significantly higher proportion of typical HUS cases than in the HUS-5 group (72.4% vs 37.5%). In addition, in this group, the number of schistocytes was 2.3 times higher compared with the HUS-5 group (44.5/μL vs 19/μL, p = 0.03). The remaining symptoms, complications, need for interventions, and their duration did not differ significantly between the studied groups. The most common complaints, besides diarrhea, were abdominal pain (78.4% of the entire study population), nausea and vomiting (75.7%), and oligo/anuria (68.9%). The frequency of HT was approx. 60.8% at admission (similar in both HUS-5 and HUS+5 groups) and 41.9% at discharge (Table 2).

Neurological symptoms occurred in approx. 36.5% of patients, with similar rates in both groups. The severity of these symptoms also did not differ significantly. In the HUS-5 group, no strokes were recorded and no neurological deficits were observed at discharge. In contrast, in the HUS+5 group, strokes (both ischemic and hemorrhagic) occurred in 7 patients (12%). Additionally, at discharge, persistent neurological deficits were observed in 14.8% of patients, the majority

Table 2. Clinical characteristics of the study population: symptoms, medical history, and clinical course

Number of cases (% vs number of patients)	HUS-5 (n = 16)	HUS+5 (n = 58)	pF	All patients (n = 74)
Diarrhea	9 (56.3%)	47 (81.0%)	0.046	56 (75.7%)
Abdominal pain	12 (75.0%)	46 (79.3%)	0.474	58 (78.4%)
Nausea/vomiting	12 (75.0%)	44 (75.9%)	0.584	56 (75.7%)
Blood in stool	5 (31.3%)	24 (41.4%)	0.332	29(39.2%)
Fever/subfebrile	9 (56.3%)	25 (43.1%)	0.257	34 (46.0%)
Respiratory tract infection	8 (50.0%)	16 (27.6%)	0.084	24 (32.4%)
Neurological symptoms	5 (31.3%)	22 (37.8%)	0.428	27 (36.5%)
Jaundice	7 (43.8%)	25 (43.1%)	0.591	32 (43.2%)
Oligo/anuria	12 (75.0%)	39 (67.2%)	0.395	51 (68.9%)
RRT	11 (68.8%)	31 (53.5%)	0.210	42 (56.8%)
HT (during hospitalization)	10 (62.5%)	35 (60.3%)	0.557	45 (60.8%)
HT (at discharge)	8 (50.0%)	23 (39.7%)	0.322	31 (41.9%)
Variables (median, IQR)*	**Median (IQR)**	**Median (IQR)**	**pW**	**Median (IQR)**
Diarrhea [days] (only patients with diarrhea)	3.0	5.0 (4.0)	0.162	4.0 (4.0)
Diarrhea [days] (among the entire population)	1.5 (3.0)	4.0 (4.0)	0.023	3.0 (4.0)
Fever – max temp. [°C]	38.0 (0.0)	38.0 (0.8)	0.908	38.0 (0.7)
Fever [days]	3.0 (1.0)	3.0 (2.0)	0.759	3.0 (1.0)
Schistocytes [number/μL]	19.0 (1.0)	44.5 (56.0)	0.0003	32.0 (50.0)
RRT [days] (only patients with RRT)	9.0 (18.0)	12.0 (17.0)	0.375	12.0 (17.0)
Oligo/anuria [days] (only patients with oligo/anuria)	3.0 (13.5)	9.0 (12.0)	0.124	9.0 (14.0)
Circulatory failure [days] (only patients with CF)	0.0 (0.0)	7.0 (38.0)	0.470	7.0 (38.0)
Respiratory failure [days] (only patients with RF)	21.0 (29.0)	18.0 (24.0)	0.502	19.0 (24.0)
Oxygen therapy [days] (only patients with OT)	4.5 (1.0)	7.0 (12.0)	0.386	6.0 (12.0)
Intubation/SIMV [days] (only intubated patients)	16.0 (25.0)	14.0 (22.0)	0.861	15.0 (21.5)
Intubation [% days] (only intubated patients)	35.5 (50)	24.5 (50.9)	0.596	32.0 (68.5)

Data are presented as absolute numbers and percentages, with p-values from the one-sided Fisher's exact test (pF) *medians with interquartile ranges (IQR) and corresponding p-values from the Wilcoxon rank-sum test (pW). HUS – hemolytic uremic syndrome; RRT – renal replacement therapy; HT – hypertension; CF – circulatory failure; RF – respiratory failure; OT – oxygen therapy; SIMV – synchronized intermittent mandatory ventilation.

of which (5 out of 8; 62.5%) were severe. The overall incidence of strokes in the entire study population did not reach statistical significance, although it showed a trend toward significance (p = 0.067) (Table 3).

The most common neurological symptoms in the entire study group were reduced or absent responsiveness and confusion (39.4% of all symptoms), occurring with similar frequency in both groups. Seizures, stroke, and ophthalmic symptoms were relatively rare. In the HUS+5 group, the spectrum of neurological symptoms was 5 times higher than in the HUS-5 group (83.3% vs 16.7%, p = 0.001), while the type of symptoms did not differ significantly between the groups (Table 4). When considering the distinction between typical and atypical HUS, neurological symptoms were more frequent in the aHUS group than in the typical HUS group (51.9% vs 27.7%, p = 0.03).

In the HUS-5 group, no permanent neurological deficits were observed, while in the HUS+5 group, the most common symptoms at discharge were disturbances in muscle tone and strength, as well as psychomotor slowing (together accounting for 41.2% of all neurological symptoms). Additionally, cranial nerve disorders were observed in 5.2% of these patients, along with single cases of Babinski's sign, epilepsy, depression, or the need for ventriculoperitoneal shunt placement (Supplementary Table 1).

Full recovery occurred in 17.6% of patients, being slightly more frequent, although not statistically significant, in the HUS-5 group. Partial recovery with mild or moderate kidney damage (eGFR ≥ 45 mL/min) was significantly more common in the HUS+5 group (46.6% vs 18.8%, p = 0.04), while the more severe form (eGFR ≤44 mL/min) occurred with similar frequency in both groups. Nephrotic-range proteinuria and the final eGFR value (at discharge or death) were similar in both groups. No notable differences in mortality were observed between the HUS-5 and HUS+5 groups (6.3% and 6.9%, respectively). This may be due to the small sample size in the HUS-5 group (Table 5).

Neuroimaging was performed in 19 (25.7%) patients (HUS-5, n = 3; HUS+5, n = 16). Computed tomography (CT) was obtained in 10 patients (13.5%), magnetic resonance imaging (MRI) in 8 (10.8%), and USG in 1 (1.4%). In the outcome analysis, normal findings were present in all 3 HUS-5 patients and 4 (25%) HUS+5 patients (p = 0.036). Abnormal findings occurred in 12 of 16 HUS+5 patients

Table 3. Severity of neurological symptoms in the study population

Severity of neurological symptoms during hospitalization (% vs number of patients)	HUS-5 (n = 16)	HUS+5 (n = 58)	pF	All patients (n = 74)
Mild	2 (12.5%)	7 (12.0%)	0.626	9 (12.2%)
Moderate	1 (6.2%)	4 (6.9%)	0.706	5 (6.8%)
Severe	2 (12.5%)	11 (19.0%)	0.428	13 (17.6%)
All symptoms	5 (31.2%)	22 (37.9%)	0.428	27 (36.5%)
Type of stroke (% vs number of patients)	**HUS-5 (n = 16)**	**HUS+5 (n = 58)**	**pF**	**All patients (n = 74)**
Ischemic	0	4 (6.9%)	0.369	4 (5.4%)
Hemorrhagic	0	3 (5.2%)	0.476	3 (4.1%)
Total	0	7 (12%)	0.067	7 (9.5%)
Severity of neurological symptoms at discharge (% vs survivors)	**HUS-5 (n = 15)**	**HUS+5 (n = 54)**	**pF**	**All patients (n = 69)**
Moderate	0	3 (5.6%)	0.476	3 (4.3%)
Severe	0	5 (9.3%)	0.284	5 (7.2%)
Any neurological symptoms	0	8 (14.8%)	0.127	8 (11.6%)

Data are presented as absolute numbers and percentages, with p-values from the one-sided Fisher's exact test (pF); HUS – hemolytic uremic syndrome.

Table 4. Detailed characterization of the reported types of neurological symptoms in the study population during hospitalization

Neurological symptoms (% vs number of all symptoms 11/55/66)	HUS-5 (n = 11)	HUS+5 (n = 55)	pF	All symptoms (n = 66)
Reduced/lack of responsiveness, drowsiness, confusion	5 (45.4%)	21 (38.3%)	0.449	26 (39.4%)
Seizures	1 (9.1%)	6 (10.9%)	0.670	7 (10.6%)
Stroke	0	7 (12.7%)	0.260	7 (10.6%)
Ophthalmic symptoms (forced gaze deviation, sluggish pupillary response, anisocoria)	2 (18.2%)	5 (9.1%)	0.330	7 (10.6%)
Hypotonia, diminished deep tendon reflexes	0	6 (10.9%)	0.319	6 (9.1%)
Pyramidal tract involvement	0	4 (7.3%)	0.473	4 (6.1%)
Extrapyramidal symptoms	1 (9.1%)	2 (3.6%)	0.427	3 (4.5%)
Headache	1 (9.1%)	2 (3.6%)	0.427	3 (4.5%)
Bulbar symptoms	1 (9.1%)	1 (1.8%)	0.308	2 (3.1%)
Impaired balance	0	1 (1.8%)	0.833	1 (1.5%)
All symptoms (% vs 66)	11 (16.7%)	55 (83.3%)	0.001	66 (100%)

Data are presented as absolute numbers and percentages, with p-values from the one-sided Fisher's exact test (pF); HUS – hemolytic uremic syndrome.

Table 5. Overall outcome after the HUS episode in the survivor population

Outcome (% vs number of patients)	HUS-5 (n = 15)	HUS+5 (n = 54)	pF	All survivors (n = 69)
Complete recovery	4 (26.7%)	9 (16.7%)	0.296	13 (18.8%)
Superior partial recovery (eGFR ≥ 45 mL/min)	3 (20.0%)	27 (50%)	0.035	30 (43.5%)
Inferior partial recovery (eGFR ≤ 44 mL/min)	8 (53.3%)	18 (33.3%)	0.133	26 (37.7%)
Death	1 (6.3%)	4 (6.9%)	0.703	N/A
Nephrotic range proteinuria	7 (46.7%)	12 (22.2%)	0.065	19 (27.5%)
eGFR [mL/min] at endpoint*	102.5 (34.5)	85 (38.4)	0.177 (pW)	–

Data are presented as absolute numbers and percentages, with p-values from the one-sided Fisher's exact test (pF; comparison of surviving subpopulations). *Values are presented as medians with interquartile ranges (IQR); p-values were calculated using the Wilcoxon rank-sum test (pW); eGFR – estimated glomerular filtration rate; HUS – hemolytic uremic syndrome; N/A – not applicable.

(75%), all detected with CT, accounting for 63.2% of the total evaluated group.

Furthermore, no notable differences in complement components were observed between the studied groups. This may indicate a similar level of complement system activation in both analyzed time periods. On the other hand, the HUS-5 group was significantly smaller and therefore may not be representative (Supplementary Table 2).

Most biochemical parameters did not differ significantly between the analyzed groups at any stage of hospitalization.

Table 6. Evolution of renal USG findings based on semi-quantitative and point-based assessment

Evolution of USG imaging (% vs number of patients); semi-quantitative assessment	HUS-5 (n = 16)	HUS+5 (n = 58)	pF	All patients (n = 74)
Improvement	11 (68.75%)	15 (25.9%)	0.002	26 (35.1%)
Stable image	3 (18.75%)	37 (63.8%)	0.002	40 (54.1%)
Deterioration	2 (12.5%)	6 (10.3%)	0.554	8 (10.8%)
Evolution of USG imaging (% vs number of patients); point-based assessment	**HUS-5 (n = 16)**	**HUS+5 (n = 58)**	**pF**	**All patients (n = 74)**
Improvement	11 (68.75%)	23 (39.7%)	0.04	34 (46.0%)
Stable image	3 (18.75%)	29 (50.0%)	0.02	32 (43.2%)
Deterioration	2 (12.5%)	6 (10.3%)	0.554	8 (10.8%)

Data are presented as absolute numbers and percentages, with p-values from the one-sided Fisher's exact test (pF); HUS – hemolytic uremic syndrome.

The only significant difference was a clearly higher lactate dehydrogenase (LDH) activity in the HUS-5 group at admission, during hospitalization, and at discharge ($p = 0.003$, $p < 0.001$, $p = 0.006$, respectively) (Supplementary Table 3).

At admission, the USG findings were abnormal in both studied populations, but not statistically significant. Most patients showed minor kidney damage (56.25% in the HUS-5 and 72.4% in the HUS+5), while major kidney damage was observed in 37.5% of the HUS-5 and 19% of the HUS+5 patients. In both groups, improvement in USG findings was noted between the beginning and the end of hospitalization, although this was significantly more frequent in the HUS-5 (semi-quantitative assessment: 68.75% vs 25.9%, $p = 0.002$; point-based assessment: 68.75% vs 39.7%, $p = 0.04$). Stable USG findings were more frequently observed in the HUS+5 group. In the overall population, there were no significant differences in the percentage of normal semi-quantitative USG results at admission compared to the endpoint (discharge or death) (6 (8.1%) vs 14 (18.9%), respectively), nor in minor kidney damage (51 (68.9%) vs 52 (70.3%), respectively). However, there was a significant reduction in the percentage of patients with major kidney damage on USG (17 (23%) vs 8 (10.8%); $p = 0.04$, McNemar's test) (Table 6, Supplementary Table 4).

Discussion

In this study, we analyzed the clinical course and outcomes of pediatric patients with HUS 5 years before and 5 years after the outbreak of the COVID-19 pandemic. These findings suggest that the pandemic may have a relevant effect on the epidemiology and complications of HUS in children.

Hemolytic uremic syndrome is a rare disease, with an estimated global incidence of 6.3–14.2 cases per million age-related population per year.[13,14] In Poland, approx. 3.9 cases per million age-related population of typical HUS are detected, and an increase in the number of cases has been observed in recent years. In contrast, the incidence of aHUS in Poland has remained stable at around 1.8 cases per million age-related population.[25] In our center, the estimated incidence was 4.7 cases per million age-related population for typical HUS and 2.7 cases per million age-related population for aHUS, which appears consistent with national epidemiological data.

In our study, we also observed a significant increase in HUS cases in the 5-year period following the outbreak of the COVID-19 pandemic, with the incidence of typical HUS being 7 times higher than in the corresponding period before the pandemic (42 vs 6 cases). It is worth noting that, according to the European Centre for Disease Prevention and Control (ECDC), the overall notification rate of STEC infection in the European Union was 2.5 cases per 100,000 population, exceeding the pre-pandemic level and representing a 25% increase compared with that in 2021.[26]

COVID-19 increases the risk of thrombosis and disseminated intravascular coagulation (DIC).[12,27] Additionally, by stimulating the complement system, it may lead to the development of TMA.[28–30] Ziaee and Assari described the occurrence of syndromes similar to HUS, with a positive history of infection or contact with a person infected with COVID-19 within the preceding 1–2 weeks.[31] The literature describes the possibility of exacerbation of HUS symptoms or induction of HUS in genetically predisposed individuals through infection with SARS-CoV-2.[11,32,33] Within our patient population, 1/3 of patients hospitalized for HUS after the outbreak of the COVID-19 pandemic had a documented history of past COVID-19 contact.

Furthermore, the higher percentage of schistocytes observed in the present study in the HUS+5 group may reflect that SARS-CoV-2 acted as an exacerbating factor for TMA through endothelial injury and complement activation, although no significant differences in complement system activity were observed.

Both COVID-19 and HUS share similar pathological mechanisms, such as endothelial injury, cytokine storm, and complement activation, which may result in multiorgan failure.[12,20,31,34] Shiga toxin can directly activate the alternative complement pathway, which is particularly evident in severe cases of STEC-HUS.[35,36] Moreover,

some studies indicate that neurological symptoms more often arise as a result of other factors, such as electrolyte imbalances, dehydration, or HT.[37,38] SARS-CoV-2 can also reach the brain through hematogenous dissemination.[39] Additionally, a cytokine storm could also contribute to neurotoxicity, and the degree of complement component C3 consumption correlates with the severity of renal and neurological complications.[39,40]

Furthermore, SARS-CoV-2 uses the angiotensin-converting enzyme 2 (ACE2) receptor to enter cells; this receptor is present not only in respiratory epithelial cells,[29,31,41] but also in oligodendrocytes and cerebral vascular endothelium, which explains the possibility of neurological complications.[39,42] In addition, ACE2 is found on podocytes, renal tubular cells, and cardiac myocytes, which indicates the renal and cardiac tropism of SARS-CoV-2.[41,43,44] Excessive angiotensin production due to renin–angiotensin system activation, in both COVID-19 and STEC-HUS, may contribute to the development of TMA, influencing the clinical progression of the disease.[45,46] Thus, the observed increase in STEC-HUS cases after the COVID-19 pandemic may be explained by several pathophysiological mechanisms, including endothelial injury, coagulation abnormalities, and long-lasting immune dysregulation. Moreover, alterations in gut microbiota and increased exposure to STEC following the relaxation of lockdown restrictions may also have contributed to the higher incidence of STEC-HUS.

According to the literature, neurological complications affect 10–33% of patients with STEC-HUS[47,48] and 8–48% of those with aHUS.[49,50] Ylinen et al. reported that the most common severe neurological symptoms in STEC-HUS were seizures (28%) and disturbances of consciousness (17%).[48] Zagożdżon et al. observed that neurological complications, such as cerebral edema, seizures, or stroke, were the most common cause of death in the course of STEC-HUS in Poland.[25] In our analysis, neurological complications were observed in 36.5% of patients with HUS (including both STEC-HUS and aHUS), and this value did not differ significantly before and after the outbreak of the pandemic. The most common symptoms were impaired responsiveness, drowsiness, and confusion, accounting for almost 40% of all neurological symptoms. Strokes, on the other hand, occurred in 7 patients, only in the HUS+5 group. Four out of 7 had ischemic stroke (with 2 of these patients dying), which occurred only in STEC-HUS, while 3 out of 7 had hemorrhagic stroke, observed only in aHUS. A 5-fold increase in the occurrence of neurological symptoms was also observed after the outbreak of the pandemic. This may result from both direct and indirect effects of the pandemic, such as SARS-CoV-2 co- or post-infection, modification of the immune system by the virus, and changes in the functioning of the healthcare system at the beginning of the pandemic (initially delayed patients' presentation to hospital and their more severe condition at admission).

The literature describes the incidence of arterial HT at admission, which is a serious complication of HUS, as 34–48.5% in STEC-HUS and 60% in aHUS.[25,48] In our study, HT was observed in approx. 60% of the entire study population, similar in both the HUS-5 and HUS+5 groups. These discrepancies may result from differences in study populations (such as age, sex, and environmental factors), measurement methods, severity of HUS, sample size, or changing guidelines regarding the diagnostic criteria for HT in children over the years.

In our study, USG assessment at admission revealed that only 8.1% of patients presented with normal renal findings, while the vast majority demonstrated minor (68.9%) or major (23%) kidney damage, comparable between the studied populations. During the course of hospitalization, USG findings improved in 35.1% of our patients (based on semi-quantitative assessment), with a statistically significant improvement more frequently observed in the pre-pandemic group. At discharge, the proportion of patients with a normal renal USG increased to 18.9%, with a higher frequency observed in the HUS-5 group. Additionally, the proportion of patients with major damage decreased to 10.8%. These findings are consistent with previous studies, which also demonstrated enlarged kidney size, a notable increase in renal parenchymal echogenicity, and cortical thickening at disease onset in both STEC-HUS and aHUS. Moreover, the published data indicate that abnormalities on USG at disease onset tend to normalize as clinical improvement occurs.[51,52]

In the present study, after the acute phase of HUS, less than 1/5 of patients achieved complete recovery, and the mortality rate was 6.8%, with both outcomes being comparable between the 2 analyzed groups. However, the HUS-5 group was substantially smaller, which may have influenced the statistical analysis. It is also worth emphasizing that eculizumab has been available in Poland since 2018. According to the literature, in the pre-eculizumab era, patients were treated with fresh frozen plasma and plasma exchange, and the mortality at the first episode of aHUS was 6.7–15%, while 16–50% of patients developed end-stage chronic kidney disease (CKD stage 5, CKD5).[25,53] In a recent study from Poland, the total mortality rate was 2% for STEC-HUS and 3.7% for aHUS, with no deaths observed among those treated with eculizumab, and most fatalities linked to neurological complications,[25] whereas in the Finnish study by Ylinen et al., no deaths were reported during the acute phase of HUS.[48] Moreover, the literature shows that several years after an episode of HUS, complete recovery occurs in approx. 70–74% of patients. However, with longer follow-up, an increased risk of progression to CKD is observed in these patients.[25,48]

Limitations of the study

Our study is a retrospective analysis, which may result in missing data or patient information. Furthermore, it is a single-center study and therefore cannot be fully generalized to the entire population. The relatively small

study group in the HUS-5 group increases the risk of statistical error. It should also be noted that one of the possible reasons for the increased recognition of STEC-HUS after the COVID-19 pandemic is that PCR-based detection of intestinal pathogens was only implemented in our center in 2021. Prior to that, diagnostics relied on stool bacterial cultures and enzymatic assays for Shiga toxin detection, which may have produced false-negative results and consequently led to the misclassification of patients as atypical HUS. Nevertheless, the present study covers an extensive 10-year observation period and adopts an innovative approach aimed at a detailed comparison of pediatric HUS populations from the periods before and after the outbreak of the COVID-19 pandemic. To the best of the authors' knowledge, at the time of manuscript preparation, no such study has yet been published in the literature.

Conclusions

The COVID-19 pandemic significantly increased the number of HUS cases hospitalized in our center. It appears that the greatest impact was on STEC-HUS cases and neurological complications. Among these children, a severe neurological complication was stroke, which was not previously observed in patients with HUS. Additionally, prior to the pandemic, no neurological deficits were observed at discharge, whereas after the outbreak, such deficits (often severe) were noted. To better understand the impact of the COVID-19 pandemic, further multi-center studies involving a larger group of patients are needed.

Supplementary data

The supplementary materials are available at https://doi.org/10.5281/zenodo.17803156. The package contains the following files:

Supplementary Table 1. Detailed assessment of neurological status at discharge.

Supplementary Table 2. Complement system parameters in the study population at admission.

Supplementary Table 3. Biochemical parameters at hospital admission, minimum/maximum values during hospitalization, and at endpoint (discharge/death) in the study population.

Supplementary Table 4. Ultrasound findings in the study population at hospital admission and at discharge/death.

Supplementary Table 5. Results of the assessment of test assumptions (normality of distributions and homogeneity of variances).

Data Availability Statement

The datasets supporting the findings of the current study are openly available in Zenodo at https://doi.org/10.5281/zenodo.17798989.

Consent for publication of personal information

Not applicable.

Use of AI and AI-assisted technologies

Not applicable.

ORCID iDs

Ewelina Jarosz-Wójcik https://orcid.org/0009-0000-0094-6128
Mateusz A. Zajączkowski https://orcid.org/0009-0006-5308-9880
Dorota Drożdż https://orcid.org/0000-0002-1281-1164
Palina Warmachowska https://orcid.org/0000-0001-8784-3155
Mikołaj Brzeźniak https://orcid.org/0009-0004-5121-6562
Aleksandra M. Molek https://orcid.org/0009-0009-2226-0392
Oliwia Andrasz https://orcid.org/0009-0004-0876-4985
Olga Szczerbak https://orcid.org/0009-0007-3498-3198
Monika Miklaszewska https://orcid.org/0000-0003-0776-4946

References

1. Aigner C, Schmidt A, Gaggl M, Sunder-Plassmann G. An updated classification of thrombotic microangiopathies and treatment of complement gene variant-mediated thrombotic microangiopathy. *Clin Kidney J*. 2019;12(3):333–337. doi:10.1093/ckj/sfz040
2. Lopes Da Silva R. Viral-associated thrombotic microangiopathies. *Hematol Oncol Stem Cell Ther*. 2011;4(2):51–59. doi:10.5144/1658-3876.2011.51
3. Raina R, Krishnappa V, Blaha T, et al. Atypical hemolytic-uremic syndrome: An update on pathophysiology, diagnosis, and treatment. *Ther Apher Dial*. 2019;23(1):4–21. doi:10.1111/1744-9987.12763
4. Fakhouri F, Zuber J, Frémeaux-Bacchi V, Loirat C. Haemolytic uraemic syndrome. *Lancet*. 2017;390(10095):681–696. doi:10.1016/S0140-6736(17)30062-4
5. Loirat C, Frémeaux-Bacchi V. Atypical hemolytic uremic syndrome. *Orphanet J Rare Dis*. 2011;6(1):60. doi:10.1186/1750-1172-6-60
6. Scheiring J, Andreoli SP, Zimmerhackl LB. Treatment and outcome of Shiga-toxin-associated hemolytic uremic syndrome (HUS). *Pediatr Nephrol*. 2008;23(10):1749–1760. doi:10.1007/s00467-008-0935-6
7. Raina R, Vijayvargiya N, Khooblall A, et al. Pediatric atypical hemolytic uremic syndrome advances. *Cells*. 2021;10(12):3580. doi:10.3390/cells10123580
8. Smarz-Widelska I, Syroka-Główka M, Janowska-Jaremek J, Kozioł MM, Załuska W. Atypical hemolytic uremic syndrome after SARS-CoV-2 infection: Report of two cases. *Int J Environ Res Public Health*. 2022;19(18):11437. doi:10.3390/ijerph191811437
9. Khandelwal P, Krishnasamy S, Govindarajan S, et al. Anti-factor H antibody associated hemolytic uremic syndrome following SARS-CoV-2 infection. *Pediatr Nephrol*. 2022;37(9):2151–2156. doi:10.1007/s00467-021-05390-4
10. Kaufeld J, Reinhardt M, Schröder C, et al. Atypical hemolytic and uremic syndrome triggered by infection with SARS-CoV2. *Kidney Int Rep*. 2021;6(10):2709–2712. doi:10.1016/j.ekir.2021.07.004
11. Ville S, Le Bot S, Chapelet-Debout A, et al. Atypical HUS relapse triggered by COVID-19. *Kidney Int*. 2021;99(1):267–268. doi:10.1016/j.kint.2020.10.030
12. Tiwari NR, Phatak S, Sharma VR, Agarwal SK. COVID-19 and thrombotic microangiopathies. *Thromb Res*. 2021;202:191–198. doi:10.1016/j.thromres.2021.04.012
13. Ardissino G, Salardi S, Colombo E, et al. Epidemiology of haemolytic uremic syndrome in children: Data from the North Italian HUS network. *Eur J Pediatr*. 2016;175(4):465–473. doi:10.1007/s00431-015-2642-1
14. Ong KL, Apostal M, Comstock N, et al. Strategies for surveillance of pediatric hemolytic uremic syndrome: Foodborne Diseases Active Surveillance Network (FoodNet), 2000–2007. *Clin Infect Dis*. 2012;54(Suppl 5):S424–S431. doi:10.1093/cid/cis208
15. Alfandary H, Rinat C, Gurevich E, et al. Hemolytic uremic syndrome: A contemporary pediatric experience. *Nephron*. 2020;144(3):109–117. doi:10.1159/000505401

16. Mittal A, Nadig P, Singh K. Renal manifestations of COVID 19 in children. *J Family Med Prim Care*. 2022;11(6):2302–2310. doi:10.4103/jfmpc.jfmpc_1777_21
17. Gu Q, Zhang Y, He X. An umbrella analysis assessing the risk of acute kidney injury in COVID-19 patients. *Adv Clin Exp Med*. 2024;34(5):831–845. doi:10.17219/acem/187998
18. May RM, Cassol C, Hannoudi A, et al. A multi-center retrospective cohort study defines the spectrum of kidney pathology in coronavirus 2019 disease (COVID-19). *Kidney Int*. 2021;100(6):1303–1315. doi:10.1016/j.kint.2021.07.015
19. Dalkıran T, Kandur Y, Kara EM, Dağoğlu B, Taner S, Öncü D. Thrombotic microangiopathy in a severe pediatric case of COVID-19. *Clin Med Insights Pediatr*. 2021;15:11795565211049897. doi:10.1177/11795565211049897
20. Parolin M, Nosadini M, Meneghesso D, et al. Severe Shiga toxin producing *E. coli* hemolytic uremic syndrome in a child with COVID-19. *Arch Clin Med Case Rep*. 2022;6(4):577–581. doi:10.26502/acmcr.96550520
21. Lorestani P, Maleki Dana P, Tohidi MR. Atypical hemolytic uremic syndrome triggered by COVID-19 infection in a pediatric patient with CD46 mutation. *Clin Case Rep*. 2025;13(3):e70308. doi:10.1002/ccr3.70308
22. Qiagen. QIAstat-Dx Gastrointestinal Panel 2 For quick and accurate detection of gastrointestinal infections. Hilden, Germany: Qiagen; 2022. https://www.qiagen.com/us/applications/syndromic-testing/syndromic-testing-benefits/diagnosing-gastrointestinal-infections-with-qiastat-dx. Accessed December 9, 2025.
23. Lurbe E, Mancia G, Calpe J, et al. Joint statement for assessing and managing high blood pressure in children and adolescents. Chapter 1: How to correctly measure blood pressure in children and adolescents. *Front Pediatr*. 2023;11:1140357. doi:10.3389/fped.2023.1140357
24. Schwartz GJ, Muñoz A, Schneider MF, et al. New equations to estimate GFR in children with CKD. *J Am Soc Nephrol*. 2009;20(3):629–637. doi:10.1681/ASN.2008030287
25. Zagożdżon I, Szczepańska M, Leszczyńska B, et al. Changing epidemiology and outcomes of hemolytic uremic syndrome in children: A prospective national cohort study from the Polish Pediatric HUS Registry and the Polish Registry of Renal Replacement Therapy in Children. *J Clin Med*. 2024;13(21):6499. doi:10.3390/jcm13216499
26. European Centre for Disease Prevention and Control (ECDC). Annual epidemiological report for 2022. Stockholm, Sweden: European Centre for Disease Prevention and Control (ECDC); 2024. https://www.ecdc.europa.eu/sites/default/files/documents/STEC_AER_2022_Report.pdf. Accessed December 9, 2025.
27. Helms J, Tacquard C, Severac F, et al; CRICS TRIGGERSEP Group (Clinical Research in Intensive Care and Sepsis Trial Group for Global Evaluation and Research in Sepsis). High risk of thrombosis in patients with severe SARS-CoV-2 infection: A multicenter prospective cohort study. *Intensive Care Med*. 2020;46(6):1089–1098. doi:10.1007/s00134-020-06062-x
28. Magro C, Mulvey JJ, Berlin D, et al. Complement associated microvascular injury and thrombosis in the pathogenesis of severe COVID-19 infection: A report of five cases. *Transl Res*. 2020;220:1–13. doi:10.1016/j.trsl.2020.04.007
29. Matošević M, Kos I, Davidović M, et al. Hemolytic uremic syndrome in the setting of COVID-19 successfully treated with complement inhibition therapy: An instructive case report of a previously healthy toddler and review of literature. *Front Pediatr*. 2023;11:1092860. doi:10.3389/fped.2023.1092860
30. Moradiya P, Khandelwal P, Raina R, Mahajan RG. Systematic review of individual patient data COVID-19 infection and vaccination-associated thrombotic microangiopathy. *Kidney Int Rep*. 2024;9(11):3134–3144. doi:10.1016/j.ekir.2024.07.034
31. Ziaee V, Assari R. The post-COVID-19 complications in children: Hemolytic uremic syndrome, new-onset vasculitis, and acute hepatitis. *Iran J Pediatr*. 2022;32(4):e128727. doi:10.5812/ijp-128727
32. Mat O, Ghisdal L, Massart A, et al. Kidney thrombotic microangiopathy after COVID-19 associated with *C3* gene mutation. *Kidney Int Rep*. 2021;6(6):1732–1737. doi:10.1016/j.ekir.2021.03.897
33. Kurian CJ, French Z, Kukulich P, et al. Case series: Coronavirus disease 2019 infection as a precipitant of atypical hemolytic uremic syndrome. Two case reports. *J Med Case Rep*. 2021;15(1):587. doi:10.1186/s13256-021-03144-2
34. Balgradean M, Cinteza E, Aria LA, et al. Clinical and pathogenic correlations between SARS-CoV-2 infection and hemolytic uremic syndrome in children. *Maedica (Bucur)*. 2020;15(3):376–380. doi:10.26574/maedica.2020.15.3.376
35. Morigi M, Galbusera M, Gastoldi S, et al. Alternative pathway activation of complement by Shiga toxin promotes exuberant C3a formation that triggers microvascular thrombosis. *J Immunol*. 2011;187(1):172–180. doi:10.4049/jimmunol.1100491
36. Noris M, Mescia F, Remuzzi G. STEC-HUS, atypical HUS and TTP are all diseases of complement activation. *Nat Rev Nephrol*. 2012;8(11):622–633. doi:10.1038/nrneph.2012.195
37. Giordano P, Netti GS, Santangelo L, et al. A pediatric neurologic assessment score may drive the eculizumab-based treatment of *Escherichia coli*-related hemolytic uremic syndrome with neurological involvement. *Pediatr Nephrol*. 2019;34(3):517–527. doi:10.1007/s00467-018-4112-2
38. Trachtman H, Austin C, Lewinski M, Stahl RAK. Renal and neurological involvement in typical Shiga toxin-associated HUS. *Nat Rev Nephrol*. 2012;8(11):658–669. doi:10.1038/nrneph.2012.196
39. Aghagoli G, Gallo Marin B, Katchur NJ, Chaves-Sell F, Asaad WF, Murphy SA. Neurological involvement in COVID-19 and potential mechanisms: A review. *Neurocrit Care*. 2021;34(3):1062–1071. doi:10.1007/s12028-020-01049-4
40. Netti GS, Santangelo L, Paulucci L, et al. Low C3 serum levels predict severe forms of STEC-HUS with neurologic involvement. *Front Med (Lausanne)*. 2020;7:357. doi:10.3389/fmed.2020.00357
41. Cao W, Li T. COVID-19: Towards understanding of pathogenesis. *Cell Res*. 2020;30(5):367–369. doi:10.1038/s41422-020-0327-4
42. Hernández-Fernández F, Sandoval Valencia H, Barbella-Aponte RA, et al. Cerebrovascular disease in patients with COVID-19: Neuroimaging, histological and clinical description. *Brain*. 2020;143(10):3089–3103. doi:10.1093/brain/awaa239
43. Li W, Moore MJ, Vasilieva N, et al. Angiotensin-converting enzyme 2 is a functional receptor for the SARS coronavirus. *Nature*. 2003;426(6965):450–454. doi:10.1038/nature02145
44. Pan XW, Xu D, Zhang H, Zhou W, Wang LH, Cui XG. Identification of a potential mechanism of acute kidney injury during the COVID-19 outbreak: A study based on single-cell transcriptome analysis. *Intensive Care Med*. 2020;46(6):1114–1116. doi:10.1007/s00134-020-06026-1
45. Kuba K, Imai Y, Rao S, et al. A crucial role of angiotensin converting enzyme 2 (ACE2) in SARS coronavirus-induced lung injury. *Nat Med*. 2005;11(8):875–879. doi:10.1038/nm1267
46. Nestoridi E, Kushak RI, Tsukurov O, Grabowski EF, Ingelfinger JR. Role of the renin angiotensin system in TNF-α and Shiga-toxin-induced tissue factor expression. *Pediatr Nephrol*. 2008;23(2):221–231. doi:10.1007/s00467-007-0636-6
47. Brown CC, Garcia X, Bhakta RT, Sanders E, Prodhan P. Severe acute neurologic involvement in children with hemolytic-uremic syndrome. *Pediatrics*. 2021;147(3):e2020013631. doi:10.1542/peds.2020-013631
48. Ylinen E, Salmenlinna S, Halkilahti J, et al. Hemolytic uremic syndrome caused by Shiga toxin-producing *Escherichia coli* in children: Incidence, risk factors, and clinical outcome. *Pediatr Nephrol*. 2020;35(9):1749–1759. doi:10.1007/s00467-020-04560-0
49. Formeck C, Swiatecka-Urban A. Extra-renal manifestations of atypical hemolytic uremic syndrome. *Pediatr Nephrol*. 2019;34(8):1337–1348. doi:10.1007/s00467-018-4039-7
50. Fidan K, Göknar N, Gülhan B, et al. Extra-renal manifestations of atypical hemolytic uremic syndrome in children. *Pediatr Nephrol*. 2018;33(8):1395–1403. doi:10.1007/s00467-018-3933-3
51. Reising A, Hafer C, Hiss M, et al. Ultrasound findings in EHEC-associated hemolytic-uremic syndrome and their clinical relevance. *Int Urol Nephrol*. 2016;48(4):561–570. doi:10.1007/s11255-015-1194-7
52. Rink L, Finkelberg I, Kreuzer M, Schipper L, Pape L, Cetiner M. Ultrasound analysis of different forms of hemolytic uremic syndrome in children. *Front Pediatr*. 2024;12:1433812. doi:10.3389/fped.2024.1433812
53. Zagożdżon I, Szczepańska M, Rubik J, et al. Haemolytic uremic syndrome as a cause of chronic kidney disease stage 5 in children is in retreat: Results from the Polish Registry of Kidney Replacement Therapy in children (2000–2023). *Pediatr Nephrol*. 2025;40(4):1069–1079. doi:10.1007/s00467-024-06584-2

Antibiotic resistance and molecular characteristics of OXA-48-producing *Klebsiella pneumoniae* isolates from northeastern Poland

Dominika Giżycka[1,A–D,F], Paweł Sacha[2,A,C,E,F], Piotr Majewski[2,B,C], Karolina Maternia-Dudzik[1,B,C], Marta Musz-Kawecka[1,3,E,F], Anna Żaczek[1,E,F], Jan Kochanowicz[4,E,F], Elżbieta A. Tryniszewska[2,E,F]

[1] Department of Microbiology, Faculty of Medicine, University of Rzeszow, Poland
[2] Department of Microbiological Diagnostics and Infectious Immunology, Medical University of Bialystok, Poland
[3] Department of Microbiology, Medical Center of Łańcut, Poland
[4] Department of Neurology, Medical University of Bialystok, Poland

A – research concept and design; B – collection and/or assembly of data; C – data analysis and interpretation; D – writing the article; E – critical revision of the article; F – final approval of the article

Advances in Clinical and Experimental Medicine, ISSN 1899–5276 (print), ISSN 2451–2680 (online) *Adv Clin Exp Med*. 2026;35(7):1163–1168

Address for correspondence
Dominika Giżycka
E-mail: dgizycka@ur.edu.pl

Funding sources
The research supported by University of Rzeszow statutory sources and Medical University of Bialystok statutory sources (B.SUB.25.430).

Conflict of interest
None declared

Acknowledgements
We thank Steven J. Snodgrass for editorial assistance.

Received on June 17, 2025
Reviewed on September 8, 2025
Accepted on October 10, 2025

Published online on July 30, 2026

Cite as
Giżycka D, Sacha P, Majewski P, et al. Antibiotic resistance and molecular characteristics of OXA-48-producing *Klebsiella pneumoniae* isolates from northeastern Poland. *Adv Clin Exp Med*. 2026;35(7):1163–1168. doi:10.17219/acem/211911

DOI
10.17219/acem/211911

Copyright
Copyright by Author(s)
This is an article distributed under the terms of the Creative Commons Attribution 3.0 Unported (CC BY 3.0) (https://creativecommons.org/licenses/by/3.0/)

Abstract

Background. Resistance of *Klebsiella pneumoniae* to carbapenems is complex and involves the production of carbapenemases. Infections caused by carbapenemase-producing *K. pneumoniae* represent a significant public health concern due to the limited treatment options available.

Objectives. The aim of the study was to identify OXA-48-like-producing *K. pneumoniae* isolates, characterize their multidrug resistance phenotypically and genetically, and classify them into appropriate sequence types (STs).

Materials and methods. The study was conducted on 3 *K. pneumoniae* isolates producing OXA-48 carbapenemase obtained from patients hospitalized at the University Hospital of Bialystok, Poland. Identification and antimicrobial susceptibility testing were performed using the automated VITEK 2 system and the broth microdilution method for colistin. Screening for OXA-48 production was performed using a disc containing 30 µg of temocillin. Carbapenemase production was confirmed using the Carba NP test. The presence of the bla_{OXA-48} gene and genes encoding resistance to quinolones (*qnrA*, *qnrB*, *qnrD*, *qnrS*) and aminoglycosides (*aac(3)-Ia*, *aac(6')-Ib*, *ant(4')-IIa*, *ant(2'')-Ia*, and *aph(3'')-Ib*) was detected using polymerase chain reaction (PCR). The ST of the isolates was determined based on sequence analysis of conserved housekeeping genes (*rpoB*, *gapA*, *mdh*, *pgi*, *phoE*, *infB*, *tonB*).

Results. Analysis of antimicrobial susceptibility revealed that the tested strains were resistant to all tested β-lactam antibiotics and exhibited resistance to amikacin, gentamicin, ciprofloxacin, colistin, and trimethoprim–sulfamethoxazole. Polymerase chain reaction analysis revealed the presence of the *aac(6')-Ib* and *aph(3'')-Ib* genes encoding aminoglycoside-modifying enzymes in all OXA-48-positive strains. Among the genes encoding quinolone resistance, *qnrS* was detected in all tested isolates. Multilocus sequence typing (MLST) revealed that 2 OXA-48-positive strains belonged to *ST15*, whereas 1 isolate belonged to *ST2193*.

Conclusions. Two sequence types of *K. pneumoniae*, *ST15* and *ST2193*, producing OXA-48 carbapenemase and exhibiting resistance to aminoglycosides and fluoroquinolones associated with the *aac(6')-Ib*, *aph(3'')-Ib*, and *qnrS* genes, respectively, were identified.

Key words: *Klebsiella pneumoniae*, OXA-48 beta-lactamase, antimicrobial resistance, multilocus sequence typing, Poland

Highlights

- OXA-48-producing *Klebsiella pneumoniae* isolates exhibited extensive multidrug resistance, including resistance to β-lactams, aminoglycosides, fluoroquinolones, and colistin.
- Molecular analysis identified the bla_{OXA-48} carbapenemase gene alongside aminoglycoside resistance genes *aac(6')-Ib* and *aph(3")-Ib*, and the quinolone resistance gene *qnrS*.
- Multilocus sequence typing (MLST) revealed the circulation of high-risk *Klebsiella pneumoniae* clones belonging to sequence types ST15 and ST2193.
- The emergence of multidrug-resistant OXA-48-producing *Klebsiella pneumoniae* highlights the growing challenge of antimicrobial resistance and the need for enhanced surveillance strategies.

Background

Carbapenems are an important group of antibiotics widely used for the treatment of severe bacterial infections.[1] The prevalence of carbapenem resistance among Gram-negative rods is increasing and has become a serious problem worldwide.[2] Gram-negative bacteria of the species *Klebsiella pneumoniae* are among the most important producers of carbapenem resistance mechanisms.[3] Carbapenem-resistant *K. pneumoniae* very often exhibits multidrug resistance to antibiotics from different groups simultaneously.[4] It is well known that carbapenem-resistant *K. pneumoniae* usually carries resistance determinants for at least 3 groups of antibiotics: β-lactams, aminoglycosides, and fluoroquinolones. This considerably limits therapeutic options.[5] Inappropriate antimicrobial treatment is associated with higher patient mortality rates.[6] Infections caused by carbapenem-resistant *K. pneumoniae* represent a major public health challenge due to limitations in selecting appropriate treatment.[7]

Antibiotic resistance in *K. pneumoniae* strains is mediated by several mechanisms. The 1st mechanism involves the synthesis of enzymes that hydrolyze β-lactam antibiotics, known as β-lactamases, or aminoglycoside-modifying enzymes. The 2nd mechanism results from efflux pump overexpression. The 3rd mechanism, referred to as porin-mediated resistance, results from decreased cellular permeability due to the loss of outer membrane proteins (Omps). The last mechanism involves modification of the antimicrobial target site.[8]

The phenomenon of carbapenem resistance in *K. pneumoniae* is complex and may involve the production of extended-spectrum β-lactamases (ESBLs), overexpression of AmpC β-lactamase combined with the loss of porin channels, or the hydrolytic activity of carbapenemases.[9]

All β-lactamases constitute a large group of enzymes with considerable molecular and functional diversity. Molecular classification, based on amino acid structure, distinguishes 4 classes of these enzymes: A, B, C, and D. Carbapenemases are classified into 3 groups, including class A serine carbapenemases (*Klebsiella pneumoniae* carbapenemases (KPC)), class B metallo-β-lactamases (MBLs) (imipenemase (IMP), Verona integron-encoded metallo-β-lactamase (VIM), and New Delhi metallo-β-lactamase (NDM)), and class D β-lactamases (OXA-48).[10]

Carbapenem resistance mediated by carbapenemases in *K. pneumoniae* has been reported worldwide. Enzymes classified as KPC and NDM are the most frequently reported.[11] In Poland, the first case of KPC was identified in 2008 among *K. pneumoniae* isolates obtained from a patient with a urinary tract infection.[12] As of 2021, 741 cases of KPC-positive isolates had been reported, with *K. pneumoniae* being the major producer.[13] The first case of an NDM-positive isolate was reported in 2012 in a patient with a history of international travel.[14] In 2021, 3,036 cases of NDM-positive strains were detected in clinical samples obtained from different sites of infection.[13] The first reported NDM-positive isolate belonged to *Escherichia coli*; however, *K. pneumoniae* was the main producer of NDM enzymes.[13]

Enzymes from the OXA-48 oxacillinase family are less common in Poland compared to KPC and NDM. The number of strains producing OXA-48 enzymes in 2021 was 285.[13] The first OXA-48-family enzymes were isolated in 2012 from *Enterobacter cloacae*; however, their main producers were *K. pneumoniae* and *E. coli*.[15] The least common carbapenemases are MBLs from the VIM group, with 110 positive isolates reported in 2021, and *Enterobacter hormaechei*, *K. pneumoniae*, and *Klebsiella oxytoca* as the main producers.[13]

Here, we report and describe *K. pneumoniae* strains carrying a rare mechanism of carbapenem resistance mediated by the class D oxacillinase OXA-48.

Objectives

The main aim of this study was to identify the presence of the bla_{OXA-48} gene among *K. pneumoniae* isolates obtained from clinical samples. Moreover, we aimed to define the antibiotic resistance profiles of OXA-48-like-producing *K. pneumoniae* and determine the prevalence of genes encoding other carbapenemases (bla_{KPC}, bla_{IMP}, bla_{VIM}, bla_{NDM}), as well as plasmid-mediated quinolone resistance genes (*qnrA*, *qnrB*, *qnrD*, *qnrS*). Additionally,

we aimed to screen for aminoglycoside resistance genes, including *aac(3)-Ia*, *aac(6')-Ib*, *ant(4')-IIa*, *ant(2")-Ia*, and *aph(3")-Ib*. Finally, we aimed to determine the sequence type (ST) of the tested OXA-48-positive isolates.

Materials and methods

The study was conducted between January 1, 2015, and September 15, 2016. In 2015, 5 carbapenemase-producing *K. pneumoniae* isolates were identified, whereas in the first 9 months of 2016, 117 carbapenemase-producing *K. pneumoniae* isolates were detected. Among these isolates, only 3 were identified as OXA-48 producers.

The tested isolates were collected and processed at the Department of Microbiological Diagnostics and Infectious Immunology, Medical University of Bialystok (Białystok, Poland). The 1st strain (*K. pneumoniae* 1) was responsible for a bloodstream infection and was isolated from a blood sample obtained from a hematology patient in 2015. The remaining isolates were associated with gastrointestinal tract colonization. The 2nd strain was isolated from a stool sample obtained from a patient hospitalized in the hematology department in 2016, and the 3rd strain (*K. pneumoniae* 3) was isolated from a rectal swab collected from a patient in the intensive care unit (ICU), also in 2016. All patients were hospitalized at the University Hospital of Bialystok.

The VITEK 2 automated system (bioMérieux, Marcy-l'Étoile, France) was used for identification and antimicrobial susceptibility testing. Colistin minimum inhibitory concentration (MIC) determination was performed using Microlatest MIC Colistin tests (Erba Lachema, Brno, Czech Republic) according to the manufacturer's protocol. The results of antibiotic susceptibility testing were interpreted according to the criteria of the European Committee on Antimicrobial Susceptibility Testing (EUCAST, 2016).[16]

Screening tests for carbapenemase production were performed using ethylenediaminetetraacetic acid (EDTA) for MBL detection, boric acid for KPC detection, and a disc containing 30 µg of temocillin for OXA-48 detection according to EUCAST (Version 2.0, July 2017).[17] In addition, the biochemical Nordmann–Poirel carbapenemase (Carba NP) test was performed.[18]

Plasmid DNA was isolated from *K. pneumoniae* isolates after overnight cultivation at 37°C in Trypticase Soy Broth (TSB; Emapol, Warsaw, Poland) using a Plasmid Mini Kit according to the manufacturer's instructions (A&A Biotechnology, Gdynia, Poland). Detection of bla_{KPC}, bla_{IMP}, bla_{VIM}, bla_{NDM}, and bla_{OXA-48} genes was performed using polymerase chain reaction (PCR) with specific primers.[19] Moreover, to determine the mechanism of quinolone resistance, we amplified *qnrA*, *qnrB*, *qnrD*, and *qnrS* genes associated with plasmid-mediated quinolone resistance (PMQR).[20] Additionally, we screened for aminoglycoside resistance genes, including *aac(3)-Ia*, *aac(6')-Ib*, *ant(4')-IIa*, *ant(2")-Ia*, and *aph(3")-Ib*.[21] All PCR reactions, as well as visualization of the PCR products, were performed according to previously described protocols.[19,20]

Furthermore, multilocus sequence typing (MLST) was conducted to classify *K. pneumoniae* strains harboring OXA-48 carbapenemase genes (bla_{OXA-48}) based on analysis of housekeeping gene sequences (*rpoB*, *gapA*, *mdh*, *pgi*, *phoE*, *infB*, *tonB*) and typing profiles obtained from the MLST database.[22]

Results

Isolates *K. pneumoniae* 1 and 2 were negative in the double-disc synergy test (DDST) for extended-spectrum β-lactamases (ESBLs), whereas isolate *K. pneumoniae* 3 was positive in this test. All tested isolates were negative in the DDST for MBLs and in the disc-diffusion test with boronic acid for KPC detection. Moreover, all 3 tested strains were positive in phenotypic tests using a disc containing 30 µg of temocillin. Additionally, all tested strains were positive in the biochemical Carba NP test used for carbapenemase detection.

Analysis of antimicrobial susceptibility revealed that all tested strains were resistant to β-lactam antibiotics, including amoxicillin–clavulanic acid, cefepime, cefotaxime, ceftazidime, cefuroxime, and piperacillin–tazobactam. Two isolates (*K. pneumoniae* 1 and 2) were non-susceptible to imipenem and meropenem, with MICs > 16 µg/mL. One isolate (*K. pneumoniae* 3) was susceptible to imipenem and meropenem, with MICs of 2 µg/mL and 1 µg/mL, respectively. Additionally, all tested isolates were resistant to amikacin, gentamicin, ciprofloxacin, colistin, and trimethoprim–sulfamethoxazole (Table 1).

Polymerase chain reaction analysis revealed the presence of the bla_{OXA-48} gene in all tested *K. pneumoniae*

Table 1. Antibiotic susceptibility of OXA-48-like-producing *Klebsiella pneumoniae* isolates

Isolate	MIC [µg/mL]												
	AK	AMC	FEP	CTX	CAZ	CXM	CIP	COL	GM	IMP	MEM	TZP	SXT
K. pneumoniae 1	R ≥ 64	R ≥ 32	R ≥ 32	R ≥ 64	R ≥ 64	R ≥ 64	R ≥ 4	R ≥ 16	R ≥ 16	R ≥ 16	R ≥ 16	R ≥ 128	R ≥ 320
K. pneumoniae 2	R ≥ 64	R ≥ 32	R ≥ 32	R ≥ 64	R ≥ 64	R ≥ 64	R ≥ 4	R ≥ 16	R ≥ 16	R ≥ 16	R ≥ 16	R ≥ 128	R ≥ 320
K. pneumoniae 3	R ≥ 64	R ≥ 32	R ≥ 32	R ≥ 64	R ≥ 64	R ≥ 64	R ≥ 4	R ≥ 16	R ≥ 16	S = 2	S = 1	R ≥ 128	R ≥ 320

MIC – minimum inhibitory concentration; R – resistant; S – susceptible; AK – amikacin; AMC – amoxicillin-clavulanic acid; FEP – cefepime; CTX – cefotaxime; CAZ – ceftazidime; CXM – cefuroxime; CIP – ciprofloxacin; COL – colistin; GM – gentamicin; IMP – imipenem; MEM – meropenem; TZP – piperacillin-tazobactam; SXT – trimethoprim-sulfamethoxazole.

Table 2. Characteristics of OXA-48-like-producing *Klebsiella pneumoniae* isolates and identified resistance genes

Gene category	Gene	*K. pneumoniae* 1	*K. pneumoniae* 2	*K. pneumoniae* 3
Genes encoding carbapenemases	bla_{OXA-48}	+	+	+
	bla_{NDM}	–	–	–
	bla_{IMP}	–	–	–
	bla_{VIM}	–	–	–
	bla_{KPC}	–	–	–
Genes encoding aminoglycoside-modifying enzymes	*aac(3)-Ia*	–	–	–
	aac(6')-Ib	+	+	+
	ant(4')-IIa	–	–	–
	ant(2")-Ia	–	–	–
	aph(3")-Ib	+	+	+
Genes encoding Qnr-like proteins	*qnrB*	–	–	–
	qnrS	+	+	+
	qnrA	–	–	–
	qnrD	–	–	–

+ gene detected; – gene not detected.

strains. The *aac(6')-Ib* and *aph(3")-Ib* genes encoding aminoglycoside-modifying enzymes were also detected in all tested strains. Among the tested genes encoding Qnr-like proteins, only *qnrS* was detected in all tested *K. pneumoniae* strains. The identified antibiotic resistance genes of the tested *K. pneumoniae* strains are shown in Table 2.

MLST analysis revealed that 2 OXA-48-positive strains (*K. pneumoniae* 1 and *K. pneumoniae* 3) belonged to the pandemic clone ST15, whereas 1 strain (*K. pneumoniae* 2) belonged to ST2193.

Discussion

Carbapenem resistance in *K. pneumoniae* may result from several mechanisms, including β-lactamase activity combined with the loss of porin channels or the production of carbapenemases.[23] Class D is the most diverse group of β-lactamases and is referred to as oxacillinases due to their preferential hydrolysis of isoxazolyl penicillins. Among them, carbapenemases are defined as carbapenem-hydrolyzing class D β-lactamases (CHDLs).[24] CHDL enzymes have been detected mainly in bacteria of the genus *Acinetobacter*. Among the order Enterobacterales, the most important are oxacillinases of the OXA-48-like type. These enzymes have been identified in bacteria of various species, including *K. pneumoniae*, *E. coli*, and the *Enterobacter cloacae* complex.[25]

The first case of OXA-48-producing *K. pneumoniae* was detected and described in Turkey in 2001.[26] To date, strains producing OXA-48 have been detected in Europe (e.g., Poland, Germany, Denmark, and France), North Africa, and the Middle East.[27] We identified a rare mechanism of carbapenem resistance resulting from the production of OXA-48 oxacillinases among clinical *K. pneumoniae* isolates obtained from patients hospitalized at the University Hospital of Bialystok in northeastern Poland.

A positive result in the phenotypic test using a temocillin-containing disc for OXA-48 detection was genetically confirmed by demonstrating the presence of the corresponding bla_{OXA-48} gene. Additional analysis of the bla_{KPC}, bla_{IMP}, bla_{VIM}, and bla_{NDM} genes, which encode KPC, IMP, VIM, and NDM carbapenemases, respectively, did not reveal their presence.

The resistance profile of *K. pneumoniae* 1 and *K. pneumoniae* 2, as confirmed genetically with PCR, was consistent with their phenotypic resistance to imipenem and meropenem. In contrast, *K. pneumoniae* 3 showed a discrepancy, as it was phenotypically susceptible to imipenem and meropenem despite being positive for the bla_{OXA-48} gene. One explanation for this phenomenon may be the low carbapenem-hydrolyzing efficiency of OXA-48-type oxacillinases.[28] On the other hand, defects in porin channels or rearrangements of bla_{OXA-48} gene promoters may be responsible for increased resistance to carbapenems. All of these factors contribute to the substantial phenotypic diversity in carbapenem resistance observed among OXA-48-producing Enterobacterales.

The additional hydrolytic activity of OXA-48-type oxacillinases includes penicillins and first-generation cephalosporins.[29] Cases of strains resistant to penicillins and their combinations with β-lactamase inhibitors, while exhibiting only reduced susceptibility to carbapenems, have been reported. Susceptibility to carbapenems among Enterobacterales producing OXA-48 was also observed by Bonnin et al., who reported susceptibility rates of 75.5% for imipenem and 63.5% for meropenem.[30] Moreover, our study showed that the tested isolates were resistant to other β-lactam antibiotics, including amoxicillin–clavulanic acid, cefepime, cefotaxime, ceftazidime, cefuroxime, and piperacillin–tazobactam.

Moreover, in our study, we evaluated the antibiotic susceptibility of OXA-48-producing *K. pneumoniae* isolates to other groups of antibiotics, including aminoglycosides, fluoroquinolones, colistin, and trimethoprim–sulfamethoxazole. We observed resistance of the tested isolates to amikacin, gentamicin, ciprofloxacin, colistin, and trimethoprim–sulfamethoxazole. The demonstrated resistance of the tested strains to multiple groups of antibiotics allows us to conclude that OXA-48 producers are multidrug-resistant strains.

Multidrug resistance among OXA-48-producing Enterobacterales was also observed by Lee et al., who reported this phenomenon among isolates obtained from patients with both nosocomial and community-acquired infections.[31] *Klebsiella pneumoniae* isolates carrying it should be: bla_{OXA-48} genes and resistant to 3 or more classes of antibiotics were also reported by Kamel et al. According to their study, all isolates were resistant to amikacin and gentamicin.[32] Multidrug-resistant *K. pneumoniae* strains exhibiting resistance to both amikacin and ciprofloxacin were also described by Takei et al.[33]

The results of our antimicrobial susceptibility testing correlated with the findings of the molecular analyses of antimicrobial resistance genes. Our molecular studies revealed the presence of the *aac(6')-Ib*, *aph(3")-Ib*, and *qnrS* genes, which confer resistance to aminoglycosides and fluoroquinolones in the studied isolates. Resistance to aminoglycosides and fluoroquinolones in clinical *K. pneumoniae* strains was also reported by Swedan et al. According to their study, *ant(3")-I* and *aac(6')-Ib* were the most common genes encoding aminoglycoside-modifying enzymes. Moreover, *qnrS* was among the most prevalent plasmid-mediated quinolone resistance genes.[34]

Analyses of antimicrobial resistance genes in OXA-48-producing *K. pneumoniae* performed by Meng et al. revealed that *aph* genes (100%) were the predominant aminoglycoside resistance genes. Furthermore, *qnr* genes (53.4%), particularly *qnrB1* and *qnrS1*, were the major fluoroquinolone resistance genes.[35] Additionally, we classified *K. pneumoniae* strains harboring OXA-48 carbapenemase genes based on the results of allelic profile analysis, including the *rpoB*, *gapA*, *mdh*, *pgi*, *phoE*, *infB*, and *tonB* genes. MLST analysis revealed that 1 OXA-48-positive strain belonged to sequence type 2193 (ST2193) (*K. pneumoniae* 2), whereas 2 strains belonged to sequence type 15 (ST15) (*K. pneumoniae* 1 and *K. pneumoniae* 3).

Klebsiella pneumoniae ST2193 was reported in China by Yang et al. following a study of carbapenem-non-susceptible and hypervirulent isolates.[36] However, clone ST15 is more common and, according to Peirano et al., belongs to the high-risk multidrug-resistant clones of *K. pneumoniae*, together with clones ST14, ST147, and ST307.[37] According to Shankar et al., these clones play important roles in the global dissemination of OXA-48 enzymes.[38]

Limitations of the study

The main limitation of our study was the small number of isolates analyzed. Our work describes the outcomes of a preliminary study; therefore, the number of tested isolates was limited. Since carbapenem resistance caused by the production of OXA-48 enzymes is relatively rare among *K. pneumoniae* isolates, extending the study period could increase the number of isolates available for analysis. Moreover, this study focused only on the most frequently observed plasmid-mediated mechanisms of fluoroquinolone and aminoglycoside resistance. Further studies are needed to improve our understanding of these resistance mechanisms.

Conclusions

We present OXA-48-like-producing *K. pneumoniae* isolates belonging to ST15 and ST2193, exhibiting resistance to aminoglycosides and fluoroquinolones mediated by the *aac(6')-Ib*, *aph(3")-Ib*, and *qnrS* genes, respectively.

Data Availability Statement

Data sharing does not apply to this article, as all data are already included in the manuscript.

Consent for publication of personal information

Not applicable.

Use of AI and AI-assisted technologies

Not applicable.

ORCID iDs

Dominika Giżycka https://orcid.org/0000-0002-7790-0328
Paweł Sacha https://orcid.org/0000-0003-0578-7335
Piotr Majewski https://orcid.org/0000-0002-3097-4581
Karolina Maternia-Dudzik https://orcid.org/0000-0002-7436-4929
Marta Musz-Kawecka https://orcid.org/0000-0003-1387-7293
Anna Żaczek https://orcid.org/0000-0001-7443-9348
Jan Kochanowicz https://orcid.org/0000-0003-0382-6193
Elżbieta A. Tryniszewska https://orcid.org/0000-0002-8428-9088

References

1. Armstrong T, Fenn SJ, Hardie KR. JMM profile. Carbapenems: A broad-spectrum antibiotic. *J Med Microbiol*. 2021;70(12):001462. doi:10.1099/jmm.0.001462
2. Wise MG, Karlowsky JA, Mohamed N, et al. Global trends in carbapenem- and difficult-to-treat-resistance among World Health Organization priority bacterial pathogens: ATLAS surveillance program 2018–2022. *J Glob Antimicrob Resist*. 2024;37:168–175. doi:10.1016/j.jgar.2024.03.020
3. Paudel R, Shrestha E, Chapagain B, Tiwari BR. Carbapenemase producing Gram-negative bacteria: Review of resistance and detection methods. *Diagn Microbiol Infect Dis*. 2024;110(1):116370. doi:10.1016/j.diagmicrobio.2024.116370

4. Bandić Pavlović D, Pospišil M, Nađ M, et al. Multidrug-resistant bacteria in surgical intensive care units: Antibiotic susceptibility and β-lactamase characterization. *Pathogens*. 2024;13(5):411. doi:10.3390/pathogens13050411
5. Lee CR, Lee JH, Park KS, Kim YB, Jeong BC, Lee SH. Global dissemination of carbapenemase-producing *Klebsiella pneumoniae*: Epidemiology, genetic context, treatment options, and detection methods. *Front Microbiol*. 2016;7:895. doi:10.3389/fmicb.2016.00895
6. Allel K, Peters A, Furuya-Kanamori L, et al. Impact of inappropriate empirical antibiotic therapy on in-hospital mortality: A retrospective multicentre cohort study of patients with bloodstream infections in Chile, 2018–2022. *BMJ Public Health*. 2024;2(2):e001289. doi:10.1136/bmjph-2024-001289
7. Paul M, Carrara E, Retamar P, et al. European Society of Clinical Microbiology and Infectious Diseases (ESCMID) guidelines for the treatment of infections caused by multidrug-resistant Gram-negative bacilli (endorsed by European Society of Intensive Care Medicine). *Clin Microbiol Infect*. 2022;28(4):521–547. doi:10.1016/j.cmi.2021.11.025
8. Karampatakis T, Tsergouli K, Behzadi P. Carbapenem-resistant *Klebsiella pneumoniae*: Virulence factors, molecular epidemiology and latest updates in treatment options. *Antibiotics (Basel)*. 2023;12(2):234. doi:10.3390/antibiotics12020234
9. Haji SH, Aka STH, Ali FA. Prevalence and characterisation of carbapenemase encoding genes in multidrug-resistant Gram-negative bacilli. *PLoS One*. 2021;16(11):e0259005. doi:10.1371/journal.pone.0259005
10. Tooke CL, Hinchliffe P, Bragginton EC, et al. β-lactamases and β-lactamase inhibitors in the 21st century. *J Mol Biol*. 2019;431(18):3472–3500. doi:10.1016/j.jmb.2019.04.002
11. Logan LK, Weinstein RA. The epidemiology of carbapenem-resistant *Enterobacteriaceae*: The impact and evolution of a global menace. *J Infect Dis*. 2017;215(Suppl 1):S28–S36. doi:10.1093/infdis/jiw282
12. Baraniak A, Izdebski R, Fiett J, et al. KPC-like carbapenemase-producing *Enterobacteriaceae* colonizing patients in Europe and Israel. *Antimicrob Agents Chemother*. 2016;60(3):1912–1917. doi:10.1128/AAC.02756-15
13. Hryniewicz W, Kuch A, Wanke-Rytt M, Żukowska A. *Pałeczki Enterobacterales Wytwarzające Karbapenemazy (CPE) Epidemiologia, Diagnostyka, Leczenie i Profilaktyka Zakażeń*. Warsaw, Poland: National Medicines Institute https://korld.nil.gov.pl/wp-content/uploads/2023/03/Rekomendacje-Paleczki-Enterobacterales_2023.21.02-1.pdf.
14. Pitart C, Solé M, Roca I, et al. Molecular characterization of bla_{NDM-5} carried on an IncFII plasmid in an *Escherichia coli* isolate from a non-traveler patient in Spain. *Antimicrob Agents Chemother*. 2015;59(1):659–662. doi:10.1128/AAC.04040-14
15. Izdebski R, Baraniak A, Żabicka D, et al. Enterobacteriaceae producing OXA-48-like carbapenemases in Poland, 2013–January 2017. *J Antimicrob Chemother*. 2018;73(3):620–625. doi:10.1093/jac/dkx457
16. European Committee on Antimicrobial Susceptibility Testing (EUCAST). Breakpoint tables for interpretation of MICs and zone diameters. Version 6.0, valid from 2016-01-01. Växjö, Sweden: EUCAST Development Laboratory, Central Hospital; 2015. https://www.eucast.org/fileadmin/src/media/PDFs/EUCAST_files/Breakpoint_tables/v_6.0_Breakpoint_table.pdf.
17. European Committee on Antimicrobial Susceptibility Testing (EUCAST). EUCAST guidelines for detection of resistance mechanisms and specific resistances of clinical and/or epidemiological importance. Version 2.01 (July 2017). Växjö, Sweden: EUCAST Development Laboratory, Central Hospital; 2017. http://www.aurosan.de/images/mediathek/servicematerial/EUCAST_detection_of_resistance_mechanisms.pdf.
18. Dortet L, Agathine A, Naas T, Cuzon G, Poirel L, Nordmann P. Evaluation of the RAPIDEC® CARBA NP, the Rapid CARB Screen® and the Carba NP test for biochemical detection of carbapenemase-producing *Enterobacteriaceae*. *J Antimicrob Chemother*. 2015;70(11):3014–3022. doi:10.1093/jac/dkv213
19. Ojdana D, Sacha P, Olszańska D, et al. First report of *Klebsiella pneumoniae*–carbapenemase-3-producing *Escherichia coli* ST479 in Poland. *Biomed Res Int*. 2015;2015:256028. doi:10.1155/2015/256028
20. Boushra MR, Gad GFM, Hassuna NA, Waly NGF, Ibrahem RA. Phenotypic and genotypic assessment of fluoroquinolones and aminoglycosides resistances in *Pseudomonas aeruginosa* collected from Minia hospitals, Egypt during COVID-19 pandemic. *BMC Infect Dis*. 2024;24(1):763. doi:10.1186/s12879-024-09605-5
21. Ojdana D, Sieńko A, Sacha P, et al. Genetic basis of enzymatic resistance of *E. coli* to aminoglycosides. *Adv Med Sci*. 2018;63(1):9–13. doi:10.1016/j.advms.2017.05.004
22. Guo C, Yang X, Wu Y, et al. MLST-based inference of genetic diversity and population structure of clinical *Klebsiella pneumoniae*, China. *Sci Rep*. 2015;5(1):7612. doi:10.1038/srep07612
23. Iovleva A, Doi Y. Carbapenem-resistant *Enterobacteriaceae*. *Clin Lab Med*. 2017;37(2):303–315. doi:10.1016/j.cll.2017.01.005
24. Boyd SE, Holmes A, Peck R, Livermore DM, Hope W. OXA-48-like β-lactamases: Global epidemiology, treatment options, and development pipeline. *Antimicrob Agents Chemother*. 2022;66(8):e00216-22. doi:10.1128/aac.00216-22
25. Pitout JDD, Peirano G, Kock MM, Strydom KA, Matsumura Y. The global ascendency of OXA-48-type carbapenemases. *Clin Microbiol Rev*. 2019;33(1):e00102-19. doi:10.1128/CMR.00102-19
26. Lim FH, Modha DE, Collins E, Westmoreland D, Ashton C, Jenkins DR. An outbreak of two strains of OXA-48 producing *Klebsiella pneumoniae* in a teaching hospital. *Infect Prev Pract*. 2020;2(3):100033. doi:10.1016/j.infpip.2019.100033
27. Alvisi G, Curtoni A, Fonnesu R, et al. Epidemiology and genetic traits of carbapenemase-producing enterobacterales: A global threat to human health. *Antibiotics (Basel)*. 2025;14(2):141. doi:10.3390/antibiotics14020141
28. Hirvonen VHA, Spencer J, Van Der Kamp MW. Antimicrobial resistance conferred by OXA-48 β-lactamases: Towards a detailed mechanistic understanding. *Antimicrob Agents Chemother*. 2021;65(6):e00184-21. doi:10.1128/AAC.00184-21
29. Oueslati S, Nordmann P, Poirel L. Heterogeneous hydrolytic features for OXA-48-like β-lactamases. *J Antimicrob Chemother*. 2015;70(4):1059–1063. doi:10.1093/jac/dku524
30. Bonnin RA, Bernabeu S, Emeraud C, et al. Susceptibility of OXA-48-producing *Enterobacterales* to imipenem/relebactam, meropenem/vaborbactam and ceftazidime/avibactam. *Int J Antimicrob Agents*. 2022;60(4):106660. doi:10.1016/j.ijantimicag.2022.106660
31. Lee YL, Wang WY, Ko WC, Hsueh PR. Global epidemiology and antimicrobial resistance of *Enterobacterales* harbouring genes encoding OXA-48-like carbapenemases: Insights from the results of the Antimicrobial Testing Leadership and Surveillance (ATLAS) programme 2018–2021. *J Antimicrob Chemother*. 2024;79(7):1581–1589. doi:10.1093/jac/dkae140
32. Kamel NA, El-Tayeb WN, El-Ansary MR, Mansour MT, Aboshanab KM. XDR-*Klebsiella pneumoniae* isolates harboring bla_{OXA-48}: In vitro and in vivo evaluation using a murine thigh-infection model. *Exp Biol Med (Maywood)*. 2019;244(18):1658–1664. doi:10.1177/1535370219886826
33. Takei S, Tabe Y, Miida T, et al. Multidrug-resistant *Klebsiella pneumoniae* clinical isolates producing NDM- and OXA-type carbapenemase in Nepal. *J Glob Antimicrob Resist*. 2024;37:233–243. doi:10.1016/j.jgar.2024.04.008
34. Swedan S, Alabdallah EA, Ababneh Q. Resistance to aminoglycoside and quinolone drugs among *Klebsiella pneumoniae* clinical isolates from northern Jordan. *Heliyon*. 2024;10(1):e23368. doi:10.1016/j.heliyon.2023.e23368
35. Meng L, Liu Z, Liu C, Li C, Shen H, Cao X. The distribution characteristics of global bla_{OXA}-carrying *Klebsiella pneumoniae*. *BMC Infect Dis*. 2023;23(1):182. doi:10.1186/s12879-023-08156-5
36. Yang X, Sun Q, Li J, et al. Molecular epidemiology of carbapenem-resistant hypervirulent *Klebsiella pneumoniae* in China. *Emerg Microbes Infect*. 2022;11(1):841–849. doi:10.1080/22221751.2022.2049458
37. Peirano G, Pitout JDD. Rapidly spreading *Enterobacterales* with OXA-48-like carbapenemases. *J Clin Microbiol*. 2025;63(2):e01515-24. doi:10.1128/jcm.01515-24
38. Shankar C, Mathur P, Venkatesan M, et al. Rapidly disseminating $bla_{OXA-232}$ carrying *Klebsiella pneumoniae* belonging to ST231 in India: Multiple and varied mobile genetic elements. *BMC Microbiol*. 2019;19(1):137. doi:10.1186/s12866-019-1513-8

Single-cell RNA sequencing reveals immunological heterogeneity of the tumor microenvironment in acute myeloid leukemia

Junyi Li[1,2,E,F], Huoyan Zhu[1,A,B], Chaoqiong Ye[1,B,C], Shengnan Xu[1,C,D], Zhihua Wu[1,A,D], Yuping Deng[1,C,D]

[1] Department of Hematology, The Second Affiliated Hospital of Guangzhou Medical University, China
[2] Circular Agriculture Innovation Center, Guangdong Laboratory for Lingnan Modern Agriculture, Heyuan, China

A – research concept and design; B – collection and/or assembly of data; C – data analysis and interpretation; D – writing the article; E – critical revision of the article; F – final approval of the article

Advances in Clinical and Experimental Medicine, ISSN 1899–5276 (print), ISSN 2451–2680 (online) *Adv Clin Exp Med*. 2026;35(7):1169–1185

Address for correspondence
Junyi Li
E-mail: Leizeonngai1206@163.com

Funding sources
The authors received funding from the Postdoctoral Research Startup Fund of the Second Affiliated Hospital of Guangzhou Medical University (grant No. 31010406-094).

Conflict of interest
None declared

Received on April 30, 2025
Reviewed on August 23, 2025
Accepted on October 14, 2025

Published online on July 28, 2026

Abstract

Background. Acute myeloid leukemia (AML) is a malignancy characterized by abnormal myeloid proliferation. Despite therapeutic advances, relapse is frequent. Understanding the tumor microenvironment (TME), particularly the dysfunction and interactions of natural killer (NK) cells, is essential for improving immunotherapeutic strategies such as chimeric antigen receptor T-cell (CAR-T) and chimeric antigen receptor natural killer cell (CAR-NK) therapies.

Objectives. This study aimed to characterize the AML TME using single-cell RNA sequencing (scRNA-seq), focusing on NK cell dysfunction and their interactions with immunosuppressive cell populations.

Materials and methods. We investigated single-cell RNA sequencing data from 59 samples, comprising 40 AML and 19 healthy donor (HD) samples, obtained from public sources and processed using standard methods. After quality control and doublet removal, 284,687 high-quality cells were retained. Acute myeloid leukemia malignant cells were identified using cluster-specific occupancy scores and inferred copy number variations. Batch effects were corrected with Harmony, followed by clustering and cell-type annotation using SingleR and established markers. We performed pathway activity profiling with gene set variation analysis (GSVA), explored intercellular communication using CellChat, and inferred cellular trajectories with Monocle3. Functional characteristics of NK cell subsets were evaluated using curated gene sets, and transcriptional regulation was assessed with pySCENIC.

Results. Single-cell RNA sequencing of 40 AML and 19 HD samples identified 76 cell clusters, including patient-specific malignant cells with elevated copy number variations (CNVs). Acute myeloid leukemia samples showed altered immune composition, with increased plasma cells and hematopoietic stem cell (HSC)/progenitor populations. T-cell analysis revealed higher proportions of exhausted CD8+T_LAG3 and immunosuppressive CD4+T_FOXP3 cells in AML, while CD4+T_GZMK cells were more abundant in HD samples. Natural killer (NK) cells exhibited AML-specific subtypes, notably NK_CD56dim_DNAJB1, characterized by terminal exhaustion and high stress scores. Myeloid analysis showed elevated LAMP3$^+$ dendritic cells and macrophages in AML. Notably, enhanced interactions between NK_CD56dim_DNAJB1 and CD8$^+$ T cells via TGFB1-TGFBR signaling suggest key immunoregulatory mechanisms in AML progression.

Conclusions. This study highlights the cellular heterogeneity and complex immune interactions within the AML microenvironment, offering insights into immune evasion and informing future immunotherapeutic and targeted treatment strategies.

Key words: tumor microenvironment, NK cell, T cell, acute myeloid leukemia, scRNA-seq

Cite as
Li J, Zhu H, Ye C, Xu S, Wu Z, Deng Y. Single-cell RNA sequencing reveals immunological heterogeneity of the tumor microenvironment in acute myeloid leukemia. *Adv Clin Exp Med*. 2026;35(7):1169–1185. doi:10.17219/acem/212574

DOI
10.17219/acem/212574

Copyright
Copyright by Author(s)
This is an article distributed under the terms of the Creative Commons Attribution 3.0 Unported (CC BY 3.0) (https://creativecommons.org/licenses/by/3.0/)

Highlights

- Single-cell RNA sequencing reveals 76 distinct cell clusters in acute myeloid leukemia (AML) and healthy bone marrow samples.
- Natural killer (NK) cells in AML show subtype-specific dysfunction and terminal exhaustion under high cellular stress.
- T cell profiling identifies increased exhausted $CD8^+$ T cells and immunosuppressive $CD4^+$ T cells in AML.
- Enhanced TGFB1-TGFBR signaling suggests NK–T cell interactions contribute to immune evasion in AML.
- Findings offer potential targets for developing personalized immunotherapies in acute myeloid leukemia.

Background

Acute myeloid leukemia (AML) is a type of blood cancer caused by the unregulated growth of myeloid progenitor cells in the bone marrow.[1] Despite the high incidence and mortality rates associated with AML, advancements in chemotherapy, hematopoietic stem cell transplantation, and targeted therapy have significantly improved complete remission and disease-free survival (DFS) rates. However, the overall survival (OS) rate remains low due to the high risk of relapse.[2] Immunotherapy has emerged as a viable alternative for AML treatment. Among these therapies, CAR-NK therapy, which employs natural killer (NK) cells instead of T cells, has demonstrated impressive clinical outcomes.[3,4] These therapies leverage the concept of the tumor microenvironment (TME).[5] However, a limited understanding of the AML TME poses a significant challenge to the development of effective immunotherapies.

The AML TME is a complex network consisting of various components, including the vascular system, stromal cells, immune cells, extracellular matrix (ECM), and molecular signals.[6] Natural killer cells are key components of the innate immune system that play an important role in tumor immunotherapy.[7] These cells are categorized into 2 primary subgroups based on the expression of surface markers CD56 (NCAM1) and CD16 (FCGR3A): CD56bri and CD56dim. CD56bri NK cells predominantly produce antiviral pro-inflammatory cytokines such as interferon gamma (IFN-γ) and tumor necrosis factor alpha (TNF-α), whereas CD56dim NK cells exhibit potent cytotoxic capabilities due to higher levels of perforin and granzyme B.[8–10] Additionally, CD56dim NK cells express CD16, enabling them to perform antibody-dependent cell-mediated cytotoxicity (ADCC) to target and eliminate antibody-marked cells.[11]

Despite their crucial role, NK cell function is often impaired within the TME due to factors such as hypoxia-induced limitations on NK cell activity and mitochondrial fragmentation, as well as the immunosuppressive effects of soluble factors like transforming growth factor beta (TGF-β).[12–14] Various cell types in the TME, such as regulatory T cells (Tregs), myeloid-derived suppressor cells (MDSCs), and $LAMP3^+$ DCs, decrease NK-cell immune responses, demonstrating the intricate relationship between NK cells and the TME.[15,16] Tregs suppress NK-cell cytotoxicity by downregulating NKG2D through membrane-bound TGF-β and by secreting interleukin (IL)-10, IL-35, and TGF-β to induce functional exhaustion.[17,18] MDSCs, via high arginase 1 (*ARG1*), inducible nitric oxide synthase (iNOS), and reactive oxygen species (ROS), deplete L-arginine and generate oxidative stress.[19] The IL-6/TGF-β/programmed death-ligand 1 (PD-L1) axis they deploy further attenuates activating receptor expression and cytotoxic activity in NK cells,[20] while indoleamine 2,3-dioxygenase (IDO)-mediated tryptophan catabolism exacerbates NK dysfunction. Additionally, $LAMP3^+$ dendritic cells (DCs) secrete CCL17 and CCL22, recruiting $CCR4^+$ Tregs into the tumor niche.[21–23]

Recently, single-cell RNA sequencing (scRNA-seq) technology has emerged as a powerful tool for analyzing gene expression patterns at the single-cell level, greatly improving our understanding of the functional states of distinct cell types. This technology has made substantial progress in the study of various tumors, including glioma,[24] endometrial carcinomas,[25] and colon cancer.[26] In the context of AML, scRNA-seq has provided a comprehensive landscape by detecting a variety of malignant cell types using single-cell genotyping.[27] Furthermore, a study by Van et al., using paired scRNA-seq and T-cell receptor (TCR) repertoire profiling data, demonstrated that T-cell plasticity and genomic modifications are important in determining responses to programmed cell death protein 1 (PD-1) inhibition.[28]

Objectives

Our prior research focused on the microenvironment, emphasizing the dysfunctional status of T cells in AML.[29] However, little attention has been paid to NK-cell dysfunction and its interactions with other immunosuppressive cell types. To further understand the association between the TME and AML progression, this study used scRNA-seq expression data from the current literature to create a comprehensive tumor ecosystem. We then investigated

the dysfunction of tumor-infiltrating NK cells and their cell–cell interactions with other cell types. These findings offer valuable insights for the development of effective immunotherapies. This study aimed to construct a comprehensive map of the AML TME using single-cell RNA sequencing, with a particular focus on NK-cell dysfunction and interactions with immunosuppressive cell types. By doing so, we hoped to gain a better understanding of how the TME contributes to AML development and immune evasion, resulting in more effective immunotherapeutic strategies.

Materials and methods

Data collection

In this study, we collected expression matrices from a total of 59 samples for analysis. Nine samples were obtained from Petti et al.[30] using 10X Genomics technology, including 5 AML and 4 healthy donor (HD) samples. Additionally, we acquired expression matrices from GSE116256 for 20 samples, including 16 AML and 4 HD samples sequenced using Seq-Well (https://shaleklab.com/resources/seq-well). It is important to note that only the 16 AML samples collected at diagnosis were included in our analysis. Furthermore, we retrieved the original sequencing data from GSE185381, which included 19 AML and 11 HD samples. The raw sequencing reads were processed using the Cell Ranger Software Suite (10× Genomics, v. 7.2.0) (https://www.10xgenomics.com) and refdata-gex-GRCh38-2020-A as the reference, yielding unique molecular identifier (UMI) matrices.

Ambient RNA correction and doublet removal

Ambient RNA contamination was estimated and corrected using the SoupX package v. 1.6.2.[31] For each sample, a SoupChannel object was initialized, and the contamination fraction was estimated with the autoEstCont function. When automatic estimation was unsuccessful, a fixed contamination fraction of 0.2 was applied using the setContaminationFraction function, as recommended by the developers. Doublet detection was performed using the DoubletFinder package v. 2.0.4.[32] Parameter optimization was conducted via the paramSweep function and the summarizeSweep function, and the optimal pK value was selected using the find.pK function based on the BCmetric. The expected doublet rate was estimated as nCells × 8 × 10^{-6}, in line with platform-specific loading guidelines. To account for homotypic doublets, we applied the modelHomotypic function and adjusted the expected doublet number accordingly. Predicted doublets were excluded from all subsequent analyses.

Preprocessing, integration, and clustering of scRNA data

Filtered count matrices for each sample were imported into Seurat v. 5.0.2[33] for downstream analysis. Genes expressed in fewer than 10 cells were excluded using the CreateSeuratObject (min.cells = 10) function. Cells were filtered based on standard quality control criteria: those with fewer than 300 detected genes, fewer than 1,000 UMIs, or >20% mitochondrial UMI content were excluded as low-quality cells. Additionally, cells with more than 8,000 genes or 20,000 UMIs were removed to eliminate likely doublets. Standard Seurat preprocessing steps were applied, including NormalizeData, FindVariableFeatures, ScaleData, RunPCA, FindNeighbors, and FindClusters. Clustering was performed across multiple resolutions (0.2, 0.5, 0.8, 1.0, 1.2, and 1.5), and the results were assessed based on silhouette width and biological interpretability. A resolution of 0.8 was selected for final clustering, as it provided optimal granularity and biological coherence. To address batch effects arising from the use of different platforms (10× Genomics and Seq-Well), we implemented a 2-step integration strategy. First, Seurat objects were constructed separately for each platform, retaining only the intersecting gene set to ensure consistency. Batch correction was then performed using the Harmony (v. 1.2.0; https://github.com/immunogenomics/harmony)[34] algorithm via the RunHarmony function, specifying group.by.vars = c("Sample", "Plate") and theta = c(2, 2) to account for both sample- and plate-specific variation. Post-integration, the datasets demonstrated high concordance in joint low-dimensional embeddings, validating the effectiveness of batch correction and enabling unified downstream analyses. After stringent quality control and integration, a total of 284,687 high-quality cells were retained for further analysis, comprising 175,335 AML cells and 109,352 HD cells.

AML malignant cells identification

Given the scarcity of chromosome gains or losses in AML malignancies, as well as the lack of reliable and highly repetitive markers for identifying malignant cells in AML, 2 techniques were used in this investigation to distinguish malignant cells from healthy counterparts. Initially, 59 samples were combined without removing batch effects between them. Using a resolution of 0.8 in the "FindClusters" function, the cells were divided into 77 clusters. Each cluster's occupancy score was then determined. For each AML patient and cluster, we divided the patient's cell count by the total number of patient and control cells. If the occupancy score surpassed 0.75, we classified the cluster as AML patient-specific and likely malignant.[35] First, immune cell markers were used to annotate the clusters, identifying T/NK and B cell populations. Subsequently, T/NK and B cells from normal samples were extracted to serve as reference cells. The sliding window size was set to: window_length = 101, smooth_method = "pyramidal".

Furthermore, inferCNV was run on each cluster with normal cells as references. InferCNV was ran with the default options, which included setting de-noise to TRUE, HMM to TRUE, and analysis_mode to "subclusters". Through these approaches, only clusters demonstrating AML patient-specificity and distinct copy number variations (CNVs) were identified as AML malignancies.

Clustering and cell type annotation

After excluding malignant AML cells, the remaining non-malignant cells were re-clustered using the same analytical pipeline. Batch effects across samples were corrected using the Harmony algorithm (RunHarmony v. 1.0), ensuring improved alignment across datasets. Cluster-specific marker genes were identified using the FindAllMarkers (only.pos = FALSE, min.pct = 0.15, logfc.threshold = 0.2) function. To refine marker selection, only genes with higher expression in the target cluster (pct.1 > pct.2) were retained. Cell type annotation was performed using the SingleR tool v. 1.4.1 in combination with the CellMarker database (http://www.bio-bigdata.center) and curated marker sets from Zhang et al.[36]

Statistical analysis of cell-type proportions

To quantify and compare cell-type composition between AML and HD samples, we performed a sample-level proportion analysis. Each individual cell was annotated by cell type and grouped by sample identity and disease group. The relative proportion of each cell type per sample was calculated by normalizing the number of cells of that type to the total number of cells within the same sample. Differences in cell-type proportions between AML and HD groups were statistically assessed using 2-sided unpaired Student's t-tests, as implemented by the stat_compare_means function from the ggpubr R package v. 0.4.0 (https://cran.r-project.org/package=ggpubr). Group comparisons were performed independently for each cell type using a faceted boxplot representation. For each comparison, individual samples were treated as independent observations (n = number of samples per group), and each point on the plot corresponds to a single patient/sample. To control the false discovery rate arising from multiple testing across cell types, p-values were adjusted using the Benjamini–Hochberg (BH) method. Adjusted p-values (FDR) were reported in scientific format directly in the figures. Significance was determined at a threshold of adjusted $p < 0.05$.

Gene set variation analysis

To evaluate pathway activity at the single-cell level, we performed gene set variation analysis (GSVA) using the single-sample gene set enrichment analysis (ssGSEA) method, implemented via the GSVA R package v. 1.26.0 (https://bioconductor.org/packages/release/bioc/html/GSVA.html). The analysis was conducted on a log-normalized gene expression matrix, with genes as rows and individual cells as columns. The gsva function was used with the following parameters: method = "ssgsea" to specify the ssGSEA algorithm, kcdf = "Gaussian" to accommodate continuous log-transformed input data, and abs.ranking = TRUE to enable absolute gene ranking, which enhances the robustness of ssGSEA scoring.

Receptor-ligand interaction analysis

To better understand the interactions between NK cells and other immune cells, we used CellChat (https://github.com/sqjin/CellChat) to compute ligand–receptor communication networks. CellChat is a computational tool for statistically inferring and analyzing cell–cell communication networks using scRNA-seq data, allowing the prediction of important signaling relationships and their coordination in cellular activity. It accomplishes this by incorporating prior knowledge about signaling molecules, receptors, and their cofactors.

Monocle trajectory analysis

We used the Monocle3 tool (https://cole-trapnell-lab.github.io/monocle3) to determine the transition states between $CD8^+$ T-cell and CD56dim NK-cell subtypes. For $CD8^+$ T cells, we designated CD8T_CCR7, representing naive T cells, as the root. Similarly, for CD56dim NK cells, we set NK_CD56dim_CCL3 as the root.

Definition of cytotoxicity, inflammatory, and stress gene sets

To assess functional differences between NK-cell subsets, we compiled a comprehensive list of cytotoxicity-, inflammatory-, and stress-related gene sets, as well as activating and inhibitory receptors from prior studies. The gene sets described by Tang et al.[37] (Supplementary Table 1) were included. We calculated the scores for each gene set using Seurat's AddModuleScore function (https://www.rdocumentation.org/packages/Seurat/versions/2.3.4/topics/AddModuleScore).

Single-cell regulatory network analysis

A cis-regulatory analysis using pySCENIC v. 0.11.2 (https://github.com/aertslab/pySCENIC) was performed to identify important transcription factors (TFs) across different cell types. The analysis concentrated on 5 types of tumor-associated macrophages (TAMs). Transcription factors were identified using GENIE3 (https://github.com/aertslab/GENIE3), organized into modules known as regulons, and evaluated using RcisTarget (https://github.com/aertslab/RcisTarget) with default gene–motif rankings. The regulon activity of each cell in the dataset was then analyzed using AUCell (https://github.com/aertslab/AUCell).

Statistical analyses

Statistical analyses were performed using R v. 4.1.2 (R Foundation for Statistical Computing, Vienna, Austria). Data are presented as mean ± standard deviation (SD). Student's t-test was applied for statistical analyses of differences between 2 groups. In the receptor–ligand interaction analysis, the statistical significance of interaction pairs was determined using a one-sided Wilcoxon rank-sum test. Differences with $p < 0.05$ were considered statistically significant.

Results

Single-cell RNA landscape of AML and HD

To study the cellular components in AML, we performed scRNA-seq analysis on 40 AML and 19 HD samples collected from public datasets. Following standard processing and quality screening of the raw sequencing data, 284,687 cells were selected for analysis. Unsupervised clustering was then carried out, resulting in the identification of 76 cellular subpopulations (Fig. 1A). We grouped all cells and assigned an occupancy score to each cluster, which represents the proportion of cells from a particular patient within that cluster. Clusters with an occupancy value greater than 0.75 were classified as patient-specific clusters. These patient-specific clusters were then identified as malignant cells unique to a given patient with AML (Fig. 1B–D). We validated the malignant cells by inferring aneuploidy status using inferCNV (https://github.com/broadinstitute/infercnv), which estimates CNVs. Acute myeloid leukemia malignant cells had higher CNV levels than AML B cells, T cells, and erythroid cells (Supplementary Fig. 1).

After excluding the identified malignant cells, we performed unsupervised clustering of immune cells and annotated these clusters into the following main cell types: B cells, Early Erythroid, granulocyte-monocyte progenitors (GMPs), hematopoietic stem cell (HSC)/progenitors,

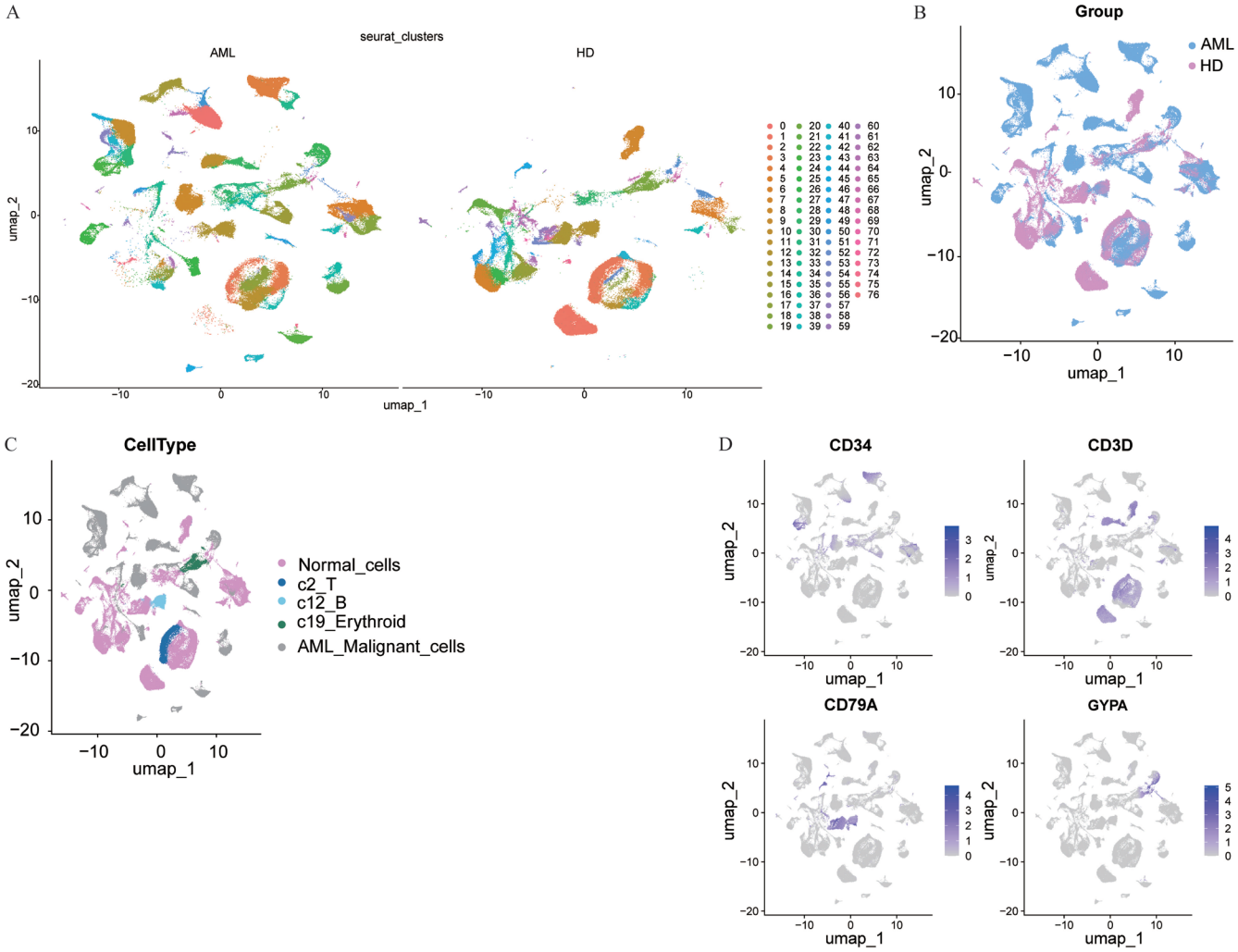

Fig. 1. scRNA-seq profiling of acute myeloid leukemia (AML) and healthy donors (HDs). A. Uniform Manifold Approximation and Projection (UMAP) showing cell clusters in AML and HD samples, with different colors representing different cell types according to their characteristic gene expression profiles; B. Distribution of 5 cell types in AML and HD; C. UMAP plot of annotated cell types in AML and HD; D. UMAP showing the expression of characteristic genes in different subsets

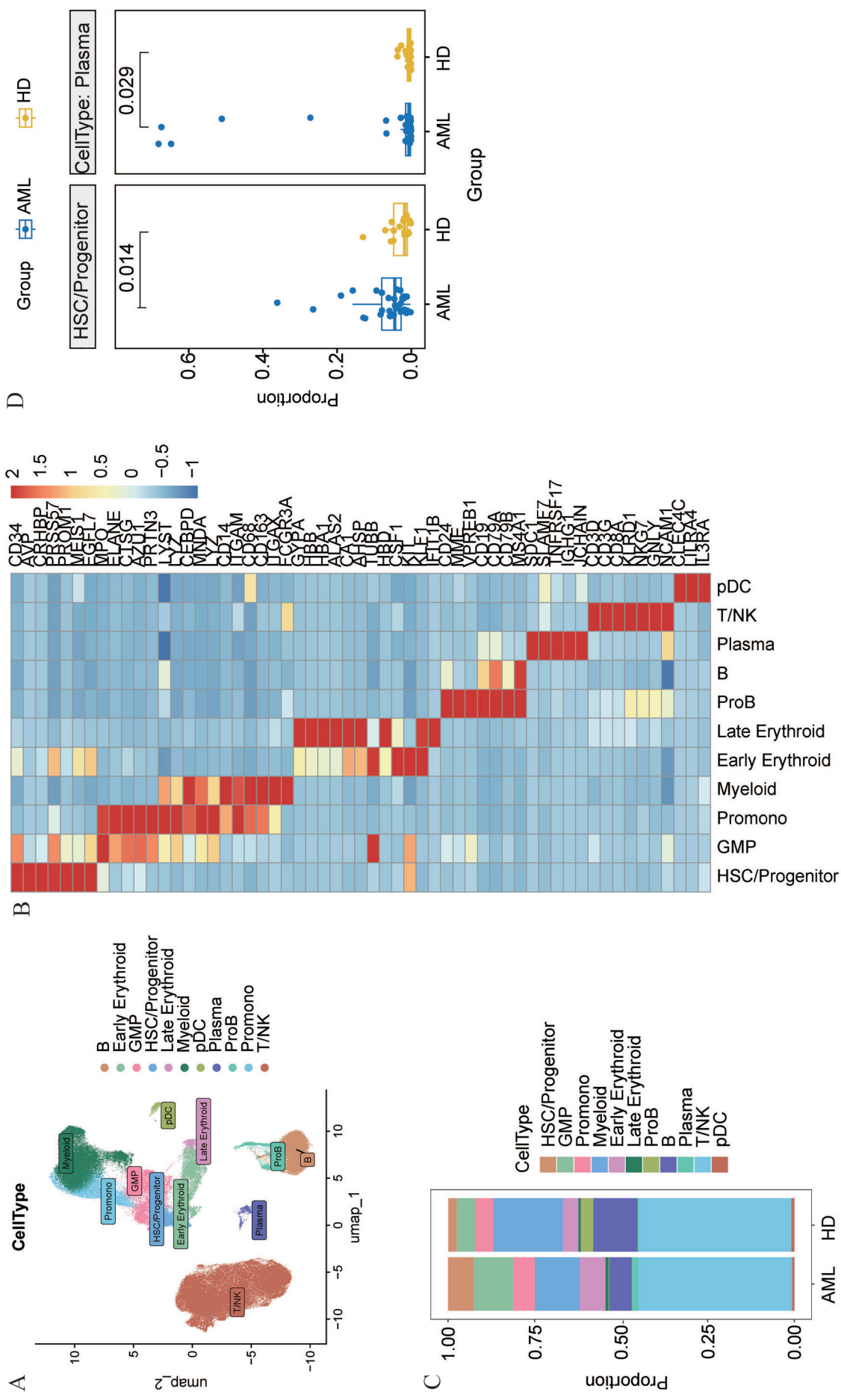

Fig. 2. Comparison of cell annotation and subset proportions between acute myeloid leukemia (AML) and healthy donors (HDs). A. Uniform Manifold Approximation and Projection (UMAP) showing the 11 cell clusters, with different colors representing different cell types according to their characteristic gene expression profiles; B. Heatmap showing significantly differentially expressed genes among the 11 cell subsets; C. Proportions of the 11 cell subsets in AML and HD; D. Proportional differences in Plasma and HSC/Progenitor cells between the AML (n = 40) and HD (n = 19) groups. Significant differences were determined using Student's t-test

NK – natural killer cells; pDC – plasmacytoid dendritic cells.

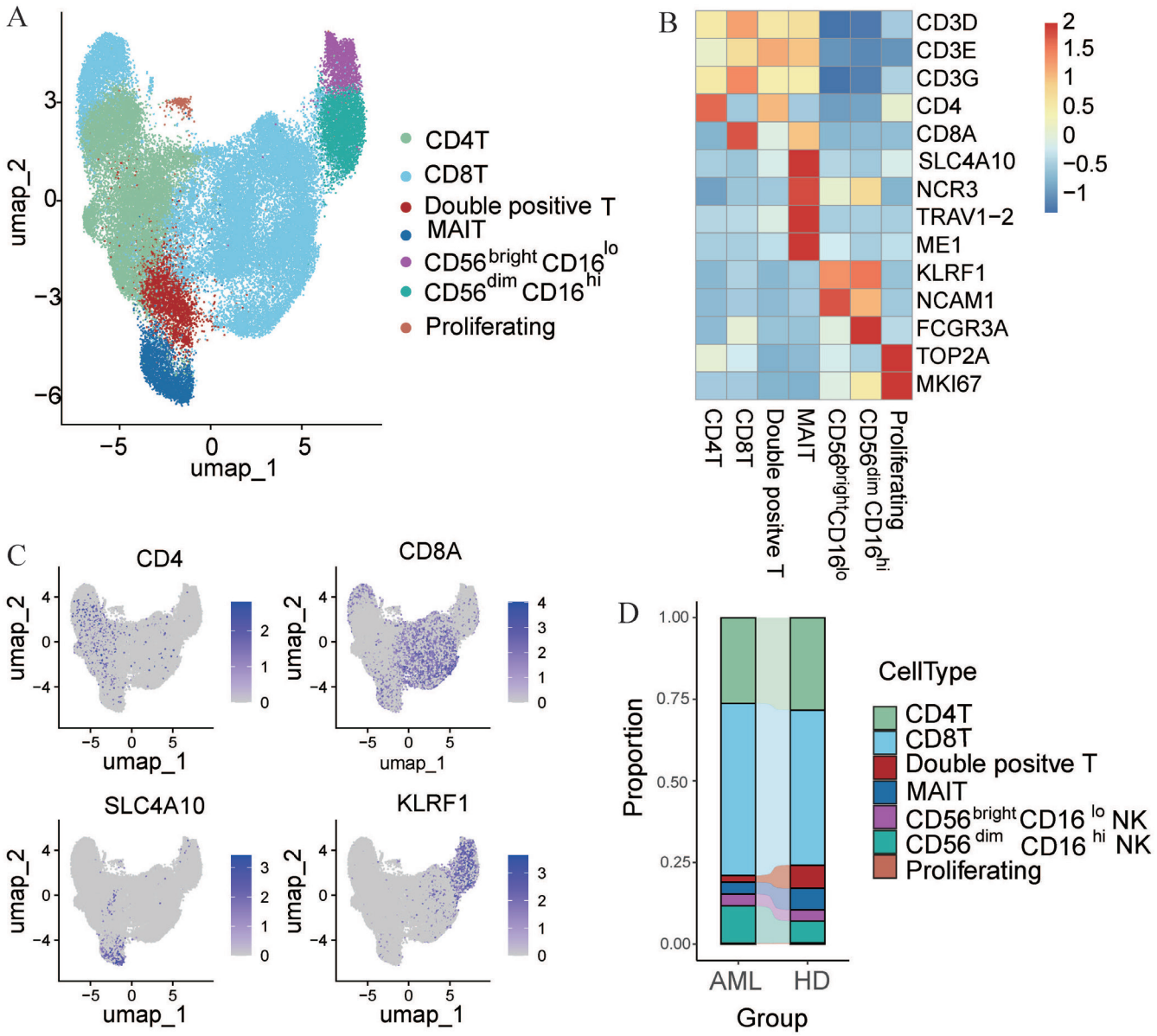

Fig. 3. Re-clustering of T cells and functional analysis. A. T cells were divided into 7 different subgroups; Uniform Manifold Approximation and Projection (UMAP) of T cells annotated by cell type; B. Heatmap showing significantly differentially expressed genes among T-cell subsets; C. UMAP showing the expression of marker genes specifically localized to T-cell subsets; D. Proportions of T-cell subsets in acute myeloid leukemia (AML) and healthy donors (HDs)

Late Erythroid, Myeloid, plasmacytoid dendritic cells (pDCs), Plasma, Pro-B cells (ProB), Promon, and T/NK cells (Fig. 2A,B). We next explored differences in cell-type proportions between AML and HD samples. The results showed that the distribution of cell subtypes differed between the 2 groups, with significantly enriched Plasma and HSC/Progenitor populations in AML compared with the HD group ($p < 0.05$) (Fig. 2C,D).

Re-clustering of T cells and functional analysis in AML

Because T cells play an important role in the evolution of AML, we performed unsupervised clustering of T cells and identified 7 cell subtypes using conventional markers. $CD4^+$ and $CD8^+$ T lymphocytes accounted for the majority of cell subtypes in these clusters (Fig. 3A–C). We compared the cell proportions in HD and AML samples, and the results showed that AML had a greater proportion of $CD8^+$ T cells, whereas HD had a higher proportion of $CD4^+$ T cells (Fig. 3D). We then performed a re-clustering analysis of $CD8^+$ T cells, and 6 cell subsets were identified based on marker genes (Fig. 4A,B). CD8+T_LAG3 cells had a substantially larger proportion in AML than in HD ($p < 0.05$) (Fig. 4C). This finding implies that $CD8^+$ T cells in AML are likely to become exhausted as the disease progresses. In addition, pseudotime analysis of $CD8^+$ T cells revealed that CD8+T_CCR7 represents an early stage and CD8+T_LAG3 corresponds to a later stage in the pseudotime sequence

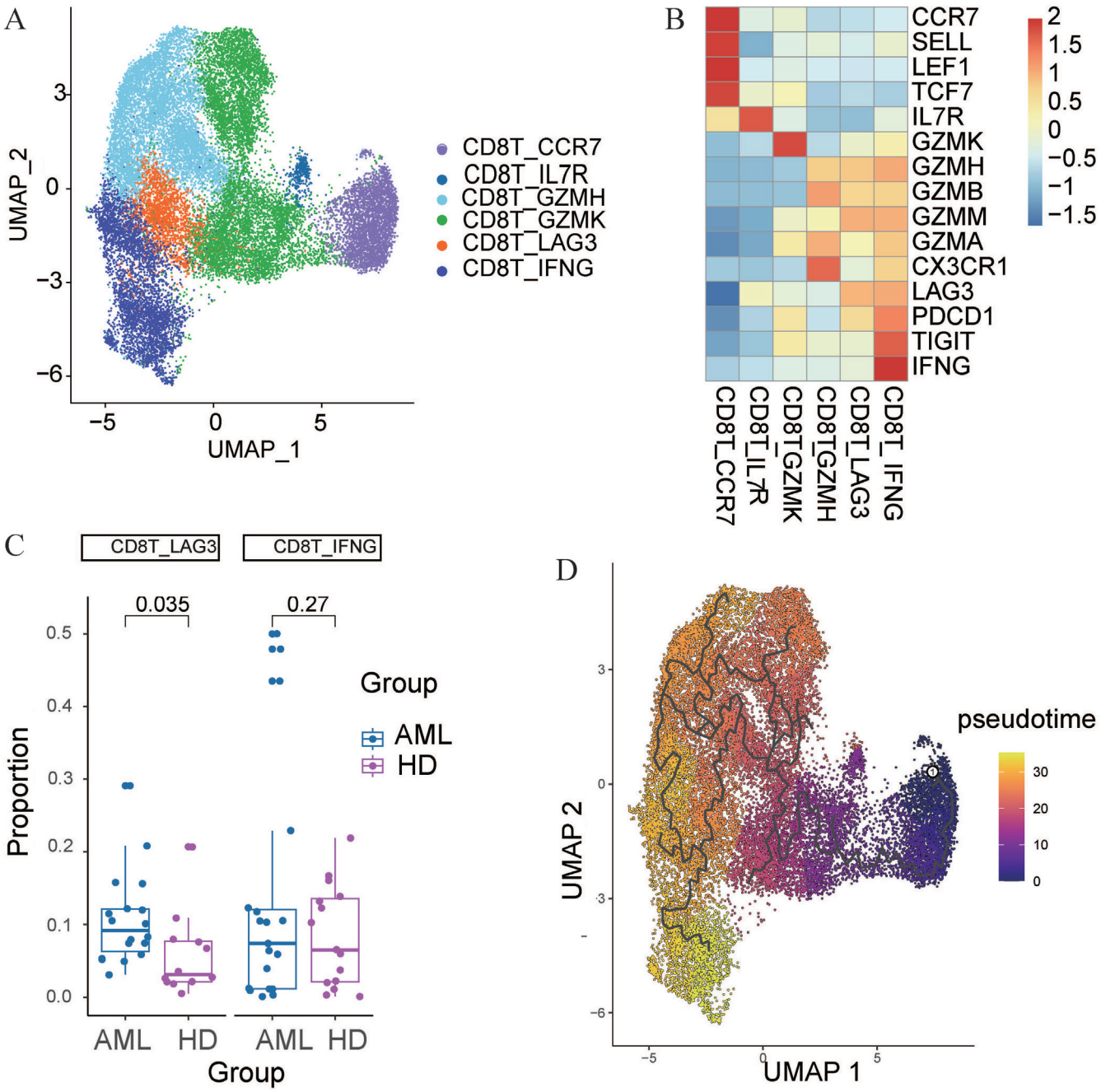

Fig. 4. Re-clustering of CD8⁺ T cells and functional analysis. A. CD8⁺ T cells were divided into 6 different subgroups; Uniform Manifold Approximation and Projection (UMAP) of CD8⁺ T cells annotated by marker genes; B. Heatmap showing significantly differentially expressed genes among CD8⁺ T-cell subsets; C. Proportional differences in CD8+T_LAG3 and CD8+T_IFNG between the acute myeloid leukemia (AML) (n = 40) and healthy donor (HD; n = 19) groups. Significant differences were determined using Student's t-test; D. Developmental trajectory of CD8⁺ T-cell subsets

(Fig. 4D).In addition, we performed a re-clustering analysis of CD4⁺ T cells and identified 5 subtypes based on canonical T-cell marker genes (Fig. 5A). Notably, the proportion of CD4+T_GZMK was significantly higher in HD than in AML (p = 0.035), while CD4+T_FOXP3 was prominently present in AML (p = 0.018) (Fig. 5B). GSVA revealed that CD4+T_ICOS is mainly associated with MYC_TARGETS, MYOGENESIS, and P53_PATHWAY, while CD4+T_CCR7 is predominantly enriched in NOTCH_SIGNALING. CD4+T_CCR6 is primarily involved in HALLMARK_SPERMATOGENESIS and TGF_BETA_SIGNALING. CD4+T_GZMK is enriched in HALLMARK_PANCREAS_BETA_CELL, ALLOGRAFT_REJECTION, and APOCAL_JUNCTION. CD4+T_FOXP3 is notably enriched in HALLMARK_HEME_METABOLISM (Supplementary Fig. 2).

We then performed GSVA on genes that were highly and lowly expressed in CD4⁺ T cells. The results revealed that highly expressed genes in CD4⁺ T cells were primarily enriched in HALLMARK_PROTEIN_SECRETION

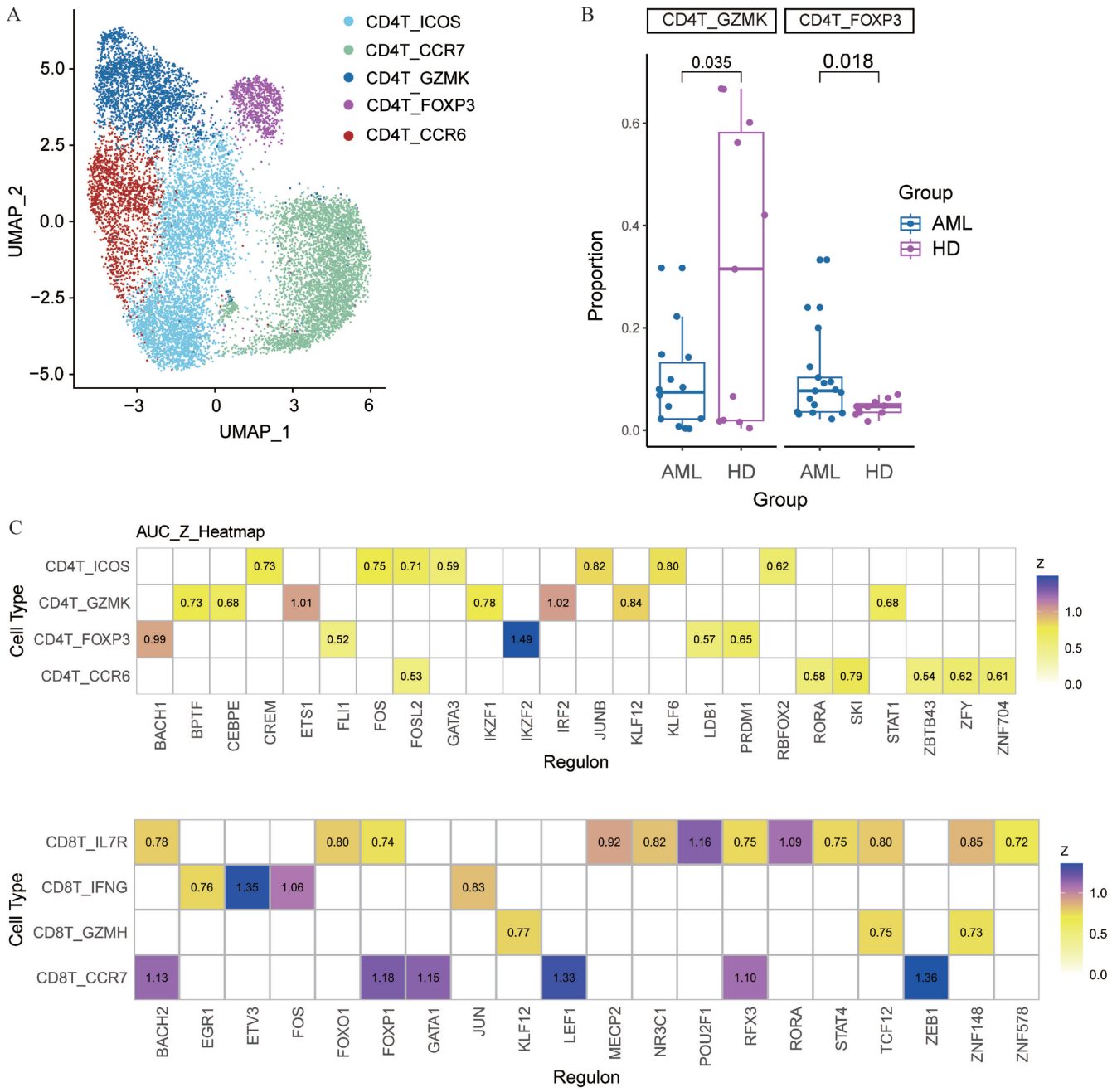

Fig. 5. Re-clustering of CD4⁺ T cells and functional analysis. A. CD4⁺ T cells were divided into 5 different subgroups; Uniform Manifold Approximation and Projection (UMAP) of CD4⁺ T cells annotated by marker genes; B. Proportional differences in CD4+T_GZMK and CD4+T_FOXP3 between the acute myeloid leukemia (AML) (n = 40) and healthy donor (HD; n = 19) groups. Significant differences were determined using Student's t-test; C. Heatmap showing differentially expressed TFs among CD4⁺ T-cell subsets

and HALLMARK_OXIDATIVE_PHOSPHORYLATION. Lowly expressed genes in CD4⁺ T cells were concentrated in HALLMARK_HEDGEHOG_SIGNALING, HALLMARK_MYOGENESIS, and HALLMARK_KRAS_SIGNALING_DN (Supplementary Fig. 2).

Additionally, the expression differences of TFs among CD4⁺ T and CD8⁺ T subtypes were analyzed. We found that IKZF2 and IRF2 were highly expressed in CD4+T_FOXP3 cells. ETV3 and FOS were highly expressed in CD8+T_IFNG cells, with ZEB1 also showing higher expression in CD8+T_IFNG (Fig. 5C and Supplementary Fig. 3).

Identification and analysis of NK-cell subtypes

Natural killer cells were further re-clustered. We identified 3 subtypes within NK_CD56bri, including NK_CD56bri_CREM, NK_CD56bri_CCL3, and NK_CD56bri_IL7R (Fig. 6A). NK_CD56dim cells were classified into 2 subtypes: NK_CD56dim_CCL3 and NK_CD56dim_DNAJB1 (Fig. 6B). We analyzed the proportions of the 2 NK_CD56dim subtypes between AML and HD, and the results indicated that NK_CD56dim_CCL3 was

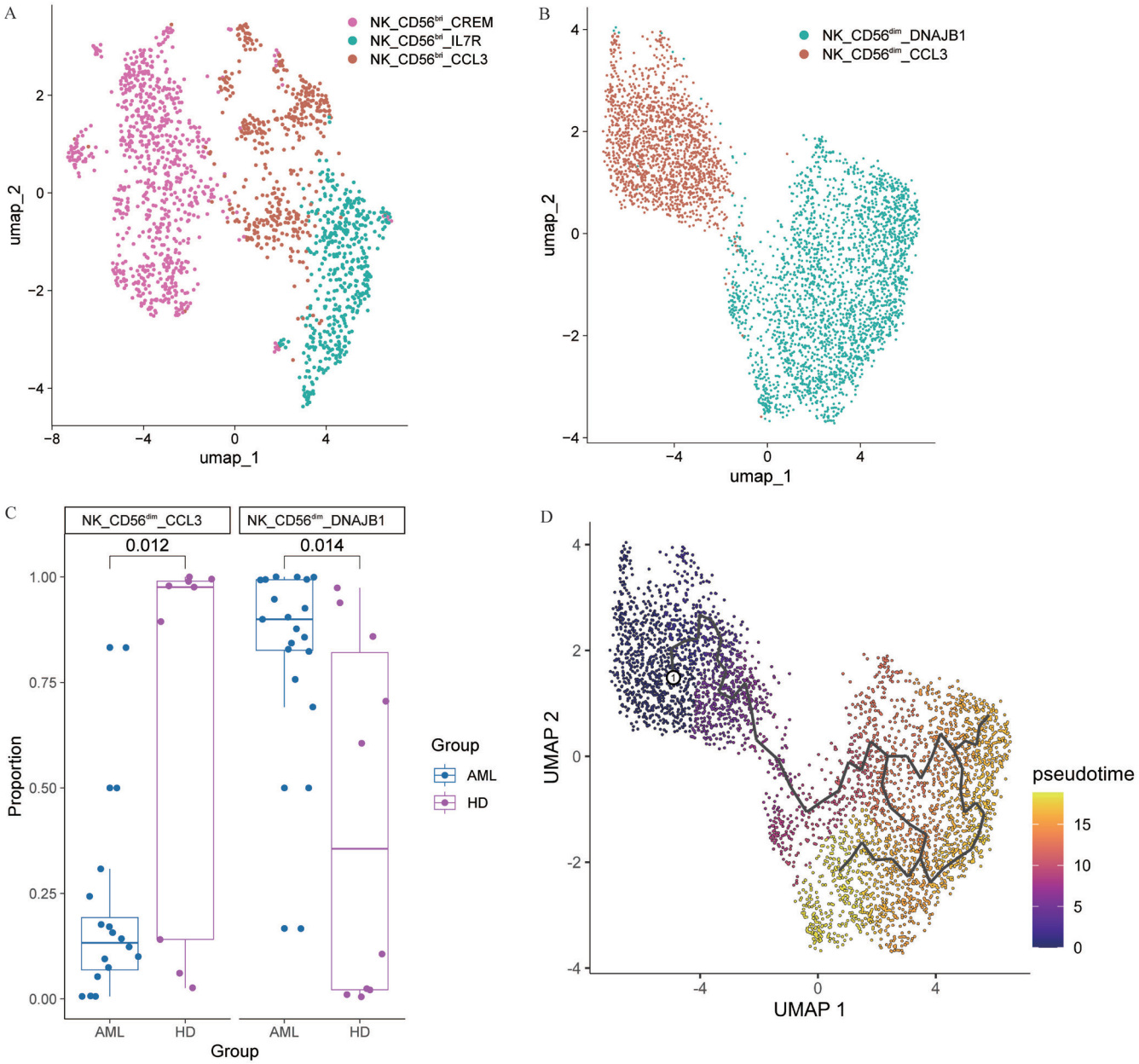

Fig. 6. Natural killer (NK) cell re-clustering and pseudotime trajectory analysis. NK cells were divided into 3 different NK_CD56bri subgroups (A) and 2 different NK_CD56dim subgroups (B); C. Proportional differences in NK_CD56dim_CCL3 and NK_CD56dim_DNAJB1 between the acute myeloid leukemia (AML) (n = 40) and healthy donor (HD; n = 19) groups; D. Developmental trajectory of NK_CD56dim subsets

significantly more highly represented in the HD group (p = 0.012), whereas NK_CD56dim_DNAJB1 was significantly more highly represented in AML (p = 0.014) (Fig. 6C).

Pseudotime analysis indicated that NK_CD56dim_CCL3 represents an earlier stage, while NK_CD56dim_DNAJB1 corresponds to the terminal stage of the pseudotime trajectory (Fig. 6D). GSVA analysis was applied to investigate pathway variation between AML and HD. The GSVA data showed that the KRAS_SIGNALING pathway was enriched in NK cells of the NK_CD56bri_CCL3 subtype. HALLMARK_COAGULATION was enriched in NK_CD56dim_CCL3, and HALLMARK_INTERFERON_ALPHA_RESPONSE was enriched in NK_CD56bri_IL7R (Supplementary Fig. 4A).

Differential gene enrichment analysis between the AML and HD groups indicated significant enrichment of HALLMARK_PROTEIN_SECRETION and OXIDATIVE_PHOSPHORYLATION in AML, while HYPOXIA and HALLMARK_TNFA_SIGNALING_VIA_NFKB were more active in HD (Fig. 7 and Supplementary Fig. 4B). Additionally, compared to NK_CD56^{dim}_DNAJB1 subtype, NK_CD56^{dim}_CCL3 exhibited higher scores for cytotoxicity, activating, and inhibitory receptors, whereas NK_CD56^{dim}_DNAJB1 had a higher stress score (Fig. 8A–C and Supplementary Fig. 5A).

We also analyzed differences in TF expression between AML and HD. The results revealed that *BCLAF1*, *NFKB1*, and *BACH2* were more highly expressed in AML than

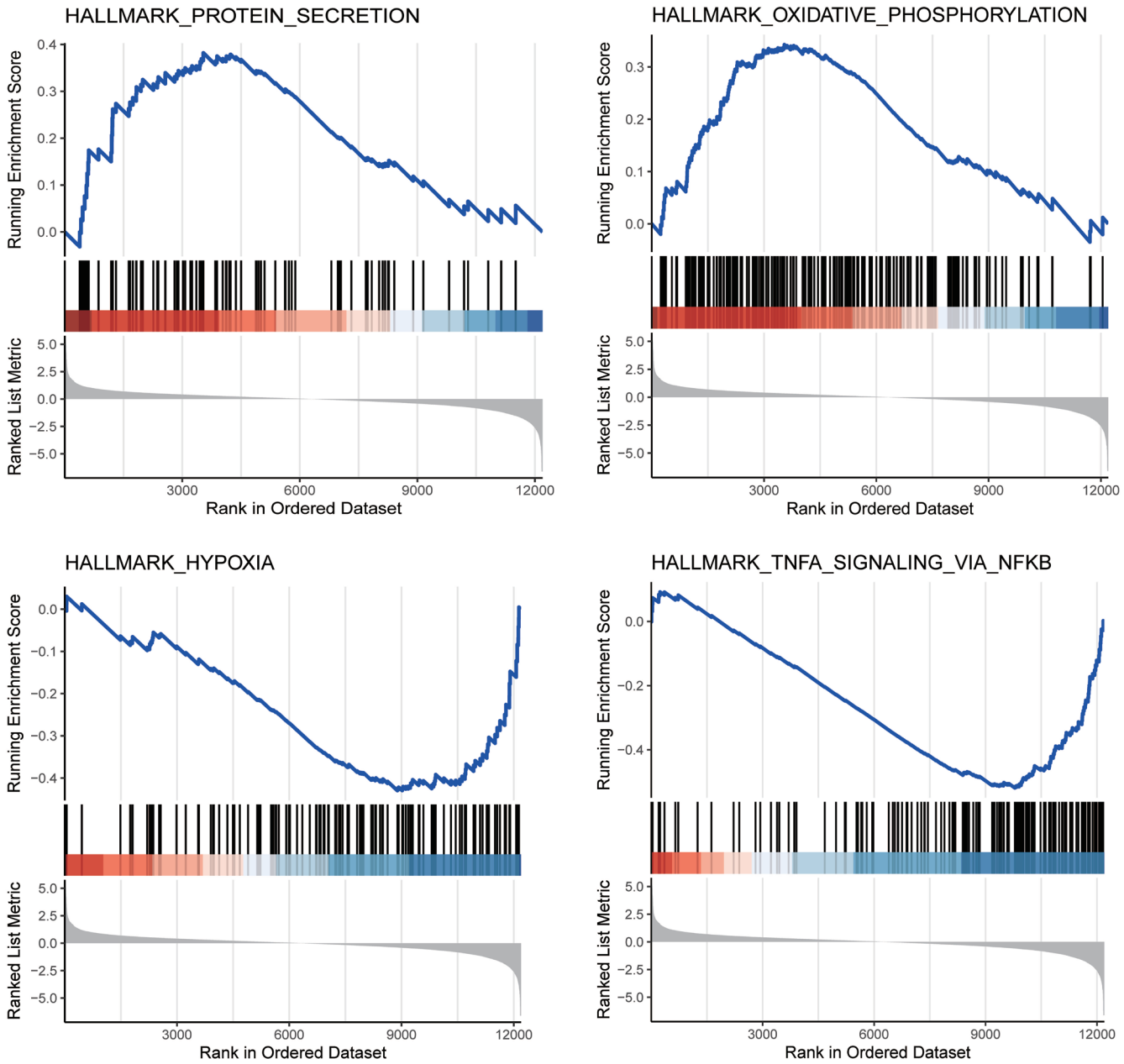

Fig. 7. Gene set enrichment analysis (GSEA) of differentially expressed genes between the acute myeloid leukemia (AML) and healthy donor (HD) groups

in HD, while *ZSCAN2*, *DRAP1*, *IRF2*, and *IKZF2* were more highly expressed in HD (Supplementary Fig. 5B). The results of TF expression analysis among NK_CD56dim subtypes showed that *BCLAF1* and *JUND* were more highly expressed in NK_CD56dim_DNAJB1, whereas STAT1 and KLF12 were more highly expressed in NK_CD56dim_CCL3 (Fig. 8D and Supplementary Fig. 5C).

Analysis of myeloid cell subtypes and intercellular interactions in AML

We next performed a re-clustering analysis of myeloid cells, resulting in their classification into 5 cell subtypes (Fig. 9A). Monocytes exhibited high levels of VCAN, S100A8, S100A9, and S100A12. Macrophages could be recognized by the expression of genes such as *FCGR3A*, *C1QA*, and *C1QC*. cDC1 cells exhibited significant expression of the hallmark genes *XCR1* and *CLEC9A*. *CLEC10A*, *FCER1A*, *CCR7*, and *LAMP3* were all substantially expressed in cDC2 and LAMP3_DC cells (Fig. 9B). Among these subtypes, the proportions of LAMP3_DC and Macrophages were significantly higher in AML compared with HD, with no significant differences observed in the other subtypes (Fig. 9C). To investigate cell–cell interactions in the TME, we examined interactions among T cells, NK cells, and myeloid cells in AML and HD. In the HD group, NK_CD56bri_CCL3 showed a higher interaction strength with cDC1, whereas in AML there was increased interaction strength between LAMP3_DC and NK_CD56dim_CCL3HI, as well as between LAMP3_DC and

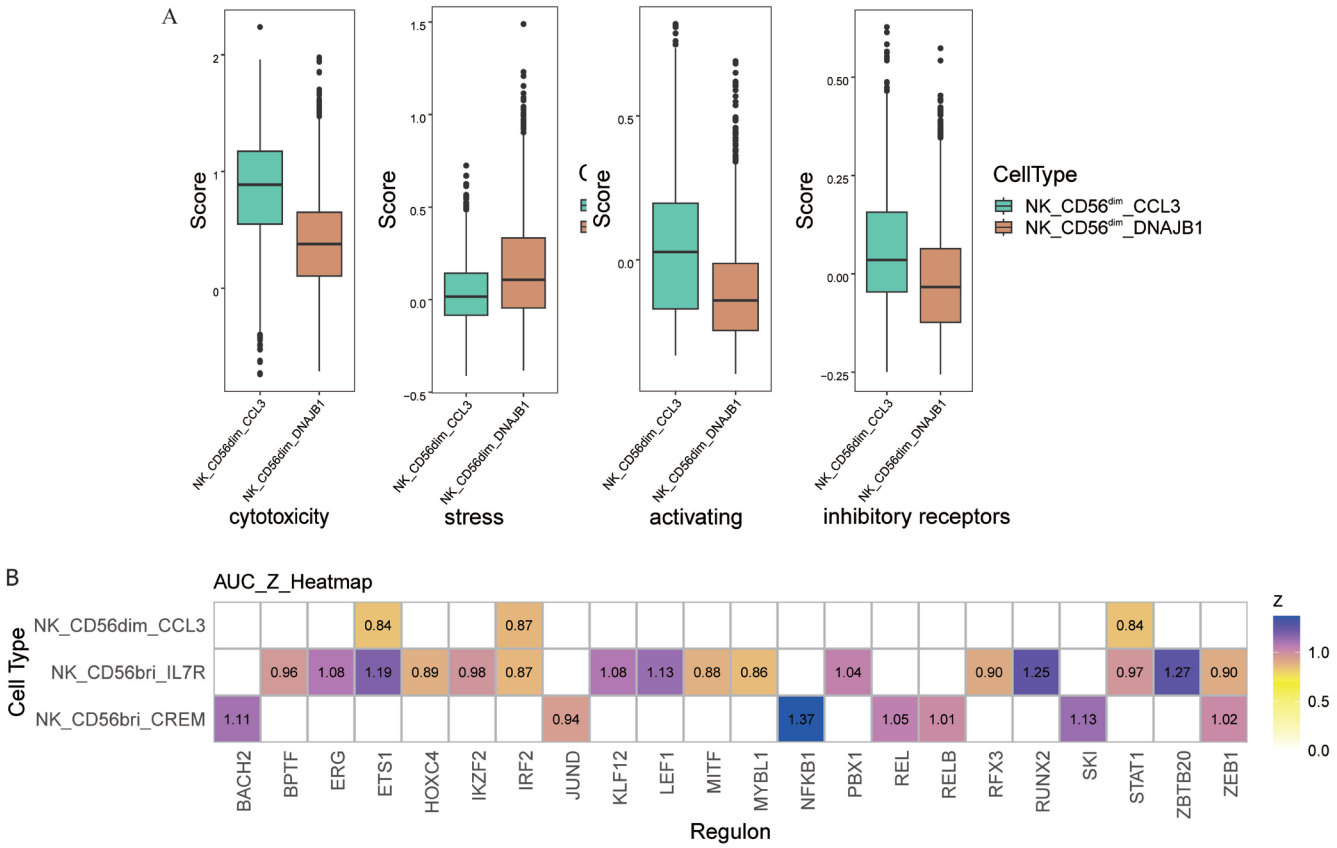

Fig. 8. Comparative analysis of natural killer (NK) cell subsets in acute myeloid leukemia (AML) and healthy donors (HDs); A. Differences in cytotoxicity, activating receptor, and inhibitory receptor scores between the AML and HD groups; B. Heatmap showing differentially expressed transcription factors (TFs) among NK_CD56dim cell subsets

AUC – area under the curve.

NK_CD56dim_DNAJB1 (Fig. 10A). Compared with the HD group, AML exhibited a greater number of ligand–receptor communication pairs and stronger intercellular communication intensity between cell clusters (Supplementary Fig. 6A). In addition, cell–cell interaction networks indicated enhanced communication between NK_CD56dim_DNAJB1 and CD8+T_GZMK, NK_CD56dim_DNAJB1 and CD8+T_GZMH, and NK_CD56dim_DNAJB1 and CD8+T_LAG3 (Fig. 10B and Supplementary Fig. 6B).

We analyzed the metabolic pathways between the AML and HD groups. We found that *TNF*, *IL6*, *XCR*, and *BTLA* were significantly upregulated in HD. *TGFβ*, *CALCR*, *BAG*, *GRN*, *FLT3*, *CCL*, and *PARs* showed significantly higher expression in AML (Fig. 10C). We also analyzed the signal strength of receptor–ligand interactions in AML with NK-cell subsets as the source cells (Supplementary Fig. 7). We found that NK_CD56dim_DNAJB1 and CD8+T_GZMH exhibited the highest interaction strength in AML through TGFB1-(TGFBR1+TGFBR2). Consistent with the above findings, the results of cell–cell interactions with NK cells as the target cells indicated that NK_CD56dim_DNAJB1 and CD8+T_GZMH had higher interaction strength in AML through TGFB1-(TGFBR1+TGFBR2) and PPIA-BSG. In addition, these results suggest that NK_CD56dim_DNAJB1 plays an important role in AML.

Discussion

Acute myeloid leukemia is a malignant hematologic disease characterized by the expansion of aberrant myeloid blast cells in the bone marrow, blood, and other tissues, resulting in impaired hematopoiesis.[38] It is the most frequent type of acute leukemia in adults, and its pathogenesis is characterized by a wide range of genetic and molecular abnormalities.[39] The TME of AML plays an important role in disease progression, therapeutic response, and drug resistance. The TME is a complex network comprising various cell types in AML, including tumor cells, immune cells, stromal cells, and others.[3] These cells interact through the secretion of diverse signaling molecules, collectively influencing AML development and treatment outcomes. We present a detailed characterization of the TME in AML, finding significant variations in cellular composition and intercellular interactions between AML and HD. Our findings not only improve our understanding of the complexity of AML but also reveal prospective targets for future therapeutic strategies.

This study discovered that plasma cells and HSC/progenitor cells were considerably more prevalent in AML than in the HD group, implying that these cell subtypes may play an important role in the course of AML. Notably, the marked enrichment of HSC/progenitor cells may

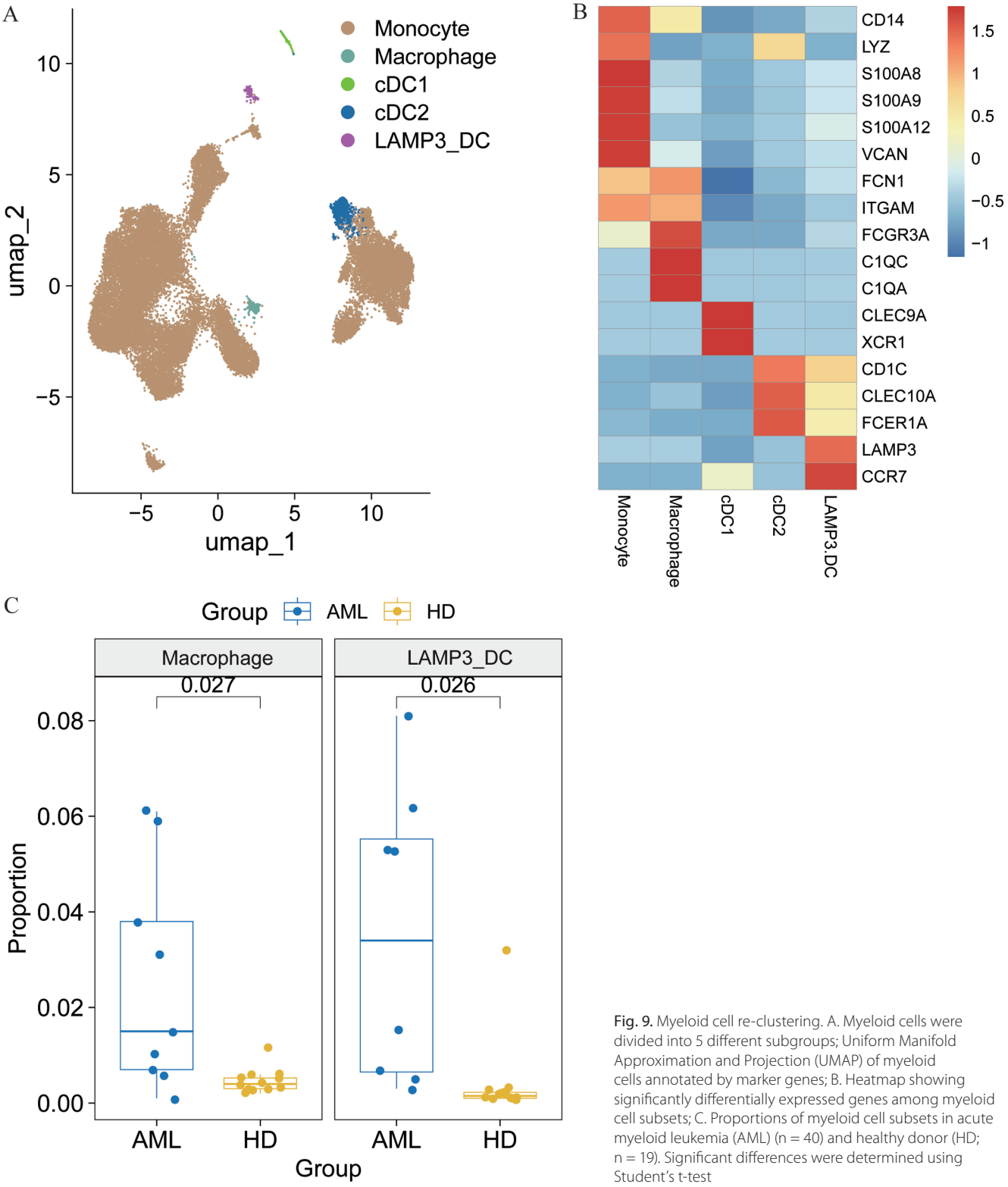

Fig. 9. Myeloid cell re-clustering. A. Myeloid cells were divided into 5 different subgroups; Uniform Manifold Approximation and Projection (UMAP) of myeloid cells annotated by marker genes; B. Heatmap showing significantly differentially expressed genes among myeloid cell subsets; C. Proportions of myeloid cell subsets in acute myeloid leukemia (AML) (n = 40) and healthy donor (HD; n = 19). Significant differences were determined using Student's t-test

be associated with the proliferation of AML cells and the maintenance of their stemness characteristics. Consistent with a previous study,[40] this research indicates that AML often originates from clonal abnormalities in HSC/progenitor cells, which acquire specific genetic or epigenetic alterations, leading to uncontrolled proliferation and the suppression of normal hematopoiesis.

Moreover, some researchers have confirmed a dysfunctional state of $CD8^+$ T cells in AML patients. However, some studies have reported no significant differences in T-cell populations between HD and AML patients.[41] In this study, $CD8^+$ T cells were identified as a major cell type in AML, but there were no significant differences between the AML and HD groups, indicating mechanisms

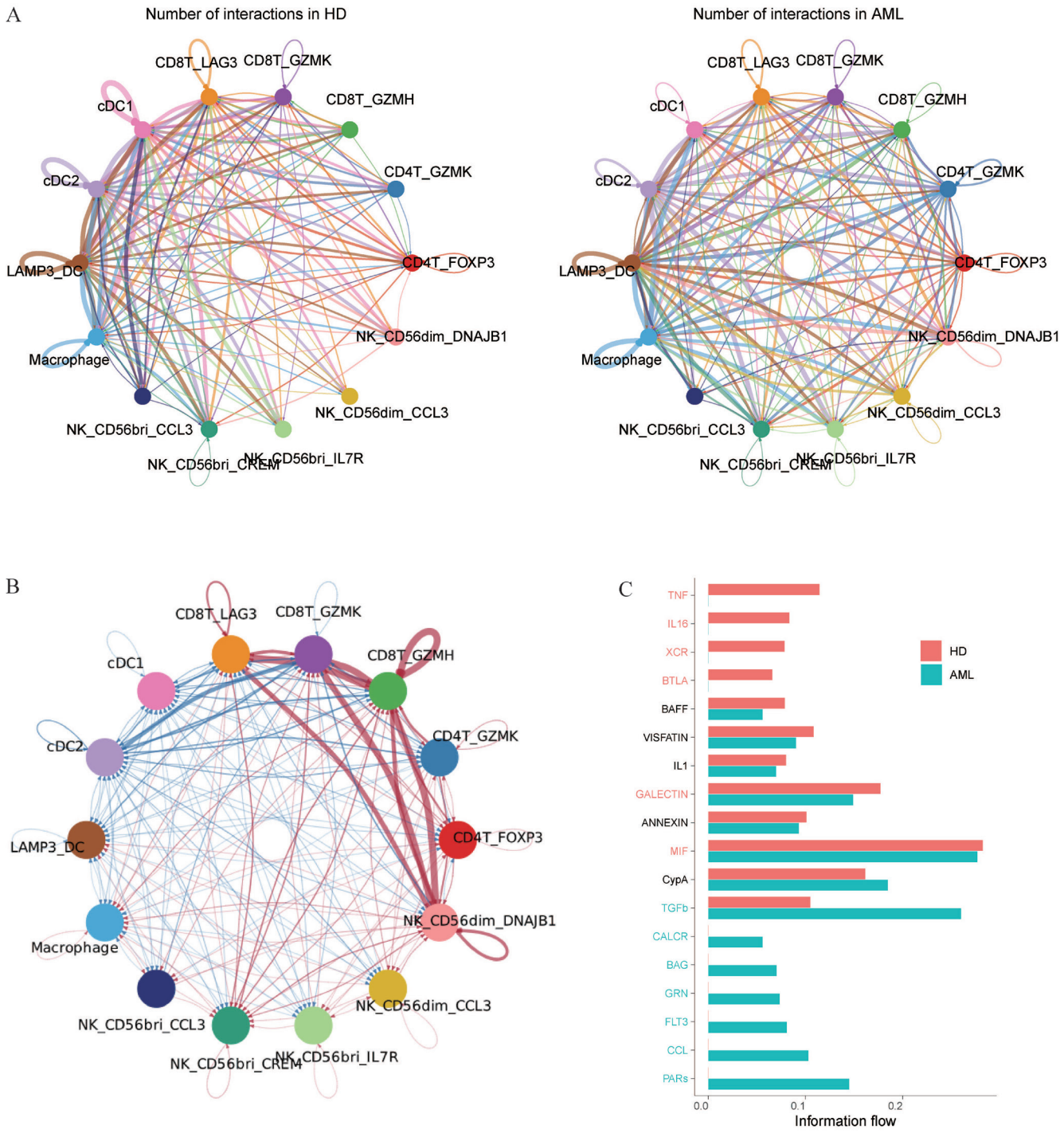

Fig. 10. Cell interaction networks in acute myeloid leukemia (AML) and healthy donors (HDs). A. Cell–cell interactions within the tumor microenvironment (TME) in AML and HD; B. Cell interaction networks in AML and HD; C. Metabolic pathways in the AML and HD groups

of exhaustion and dysfunction beyond typical immune checkpoint receptors. As a result, additional research on T-cell subsets is critical for understanding AML.

LAG3, an inhibitory receptor found on activated T cells, NK cells, and DCs, is frequently associated with T-cell exhaustion and impaired immune responses in AML.[42] Our findings revealed a considerable increase in the CD8+T_LAG3 cell subtype in AML compared with the HD group, indicating the potential for T-cell exhaustion in AML. Recent single-cell studies have likewise reported that ST2$^+$ Tregs in AML bone marrow highly express LAG3 and TIM3 and display an inverse correlation with CD8$^+$ T-cell abundance. In a Foxp3Cre-ST2 conditional knockout model, blockade of this pathway restored CD8$^+$ T-cell functionality and significantly prolonged survival.[43] These results are consistent with the pseudotime trajectory, which shows that CD8$^+$ T cells become exhausted in AML.

CD4+T_FOXP3 cells are an important T-lymphocyte subpopulation involved in negative immune regulation. They are necessary for self-tolerance and immune

homeostasis.[44] CD4+T_FOXP3 cells can interfere with immune system function, promoting tumor immune evasion and tumor growth.[45,46] Several studies have demonstrated a significant increase in CD4+T_FOXP3 cells in various types of cancer.[47,48] Similar to previous findings,[49] we discovered that the proportion of CD4+T_FOXP3 cells was considerably higher in AML patients than in HDs, implying that CD4+T_FOXP3 cells may contribute to AML progression. Consistent with these findings, a recent study monitoring peripheral blood lymphocyte subsets in AML patients found that Treg frequencies are significantly elevated at diagnosis and correlate with poor therapeutic response; multivariate analysis further identified an elevated Treg/Teff ratio as an independent risk factor for AML relapse.[50] Transcription factors are important in AML because they contribute to its development and progression. *IKZF2*, a member of the Ikaros TF family, is considerably overexpressed in AML relative to healthy HSCs.[51] In this study, our results confirmed that *IKZF2* is significantly overexpressed in CD4+T_FOXP3 cells, which may be related to the development and progression of AML.

Natural killer cells are typically divided into NK_CD56dim and NK_CD56bri subtypes. High expression of CD56 identifies NK cells as NK_CD56bri, whereas NK_CD56dim cells exhibit higher cytotoxicity. In the NK_CD56dim subtypes, we observed that NK_CD56dim_CCL3 is significantly overexpressed in HDs, while NK_CD56dim_DNAJB1 is significantly overexpressed in AML. This difference may indicate varying activation states and functions of NK cells in AML. GSVA revealed distinct biological pathways active in different NK-cell subtypes. The KRAS signaling pathway, which is crucial in AML and related to its occurrence and progression, was found to be active in the NK_CD56bri_CCL3 subtype, while the NK_CD56dim_CCL3 subtype was associated with the coagulation pathway. These findings indicate complex biological processes in which NK cells may participate within AML. *KLF12* (Krüppel-like factor 12), a member of the Krüppel-like factor family of TFs, is involved in multiple physiological and pathological processes, including the development of various cancers.[52] This study identified significant overexpression of *KLF12* in the NK_CD56dim_CCL3 cell subtype, suggesting that *KLF12* may play a role in immune regulation and disease progression in AML and other cancers, offering a potential molecular target for the development of novel therapeutic strategies.

Myeloid cells, particularly DCs and monocytes, are critical in immune regulation through cytokine secretion and surface molecule expression.[53] In AML, these cells may be influenced by the TME, thereby affecting immune cell activity and contributing to tumor immune escape.[54] This study observed a significant increase in LAMP3$^+$ DCs in AML, underscoring the important role of this cell subtype in the disease. The interactions between different immune cell subsets in the AML microenvironment are crucial for disease progression. Previous studies have shown that the interaction strength between LAMP3$^+$ DCs and NK-cell subtypes is high in AML, potentially impacting immune surveillance and tumor escape.[55] Consistent with these findings, this study found that the interaction strength between LAMP3$^+$ DCs and both NK_CD56dim_CCL3HI and NK_CD56dim_DNAJB1 was the highest, highlighting the significant role of NK-cell subtypes in AML. Furthermore, compared with HD, the AML tumor immune microenvironment exhibited a greater number of ligand–receptor communication pairs and stronger intercellular communication intensity. This suggests a more complex intercellular communication network in AML, which may facilitate immune escape and suppression by tumor cells.

Limitations of the study

While we observed changes in immune cell composition, particularly in plasma cells and HSC/progenitors, the functional roles of these subtypes require further validation. Although our findings highlight CD8$^+$ T-cell exhaustion and increased CD4+T_FOXP3 cells, some previous studies reported no significant differences in T-cell populations between AML and HD, pointing to potential heterogeneity among cohorts. Additionally, while we identified disease-specific NK-cell subtypes and their distinct signaling pathways, the complexity of NK-cell function in AML remains only partially understood. Lastly, the observed increase in intercellular communication in AML suggests immune evasion mechanisms, but the precise functional implications warrant further investigation. Moreover, inherent limitations of single-cell RNA sequencing, such as batch effects, platform variability, and detection sensitivity, can amplify or obscure true differences among cell subsets. Although Harmony was employed to correct batch effects, disparities in capture efficiency and gene dropout between the 10× Genomics and Seq-Well platforms may still influence the results. Prospective, multicenter cohort studies are warranted to validate our findings and further elucidate their functional and clinical significance.

Conclusions

We conducted an in-depth analysis of the TME in AML and HD by using recently published scRNA-seq data. The findings revealed the heterogeneity of cellular composition and the complexity of intercellular communication within the AML. These findings provide important insights into the processes of immune evasion in AML and lead to the development of new immunotherapeutic techniques, as well as the identification of prospective targets for future targeted treatments.

Supplementary data

The supplementary materials are available at https://doi.org/10.5281/zenodo.17591557. The package contains the following files:

Supplementary Table 1. Gene sets defining functional states of NK cells. This table lists the curated gene sets used to characterize different NK-cell functional states: naïve, exhausted, cytotoxic, inflammatory, effector, and regulatory.

Supplementary Fig. 1. Heatmap of CNA profiles inferred from the scRNA-seq data of malignant cells from AML patients. Red indicates genomic amplifications and blue indicates genomic deletions. The x-axis shows all chromosomes in numerical order. T cells, B cells, and erythroid cells were used as a reference.

Supplementary Fig. 2. A. GSVA pathway analysis of $CD4^+$ T-cell subtypes; B. GSVA pathway analysis of CD4+T_FOXP3.

Supplementary Fig. 3. UMAP showing the expression of TFs in $CD4^+$ T-cell subsets.

Supplementary Fig. 4. A. GSVA pathway analysis of NK_CD56dim subsets. Significant differences were determined using Student's t-test; B. GSEA analysis of differentially expressed genes between the AML and HD groups.

Supplementary Fig. 5. A. UMAP showing the expression of cytotoxicity-, activating-, and inhibitory-receptor genes in NK_CD56dim subsets; B. Heatmap visualizing the differential expression of TFs across distinct NK_CD56dim subsets; C. UMAP showing the expression of TFs in NK_CD56dim cell subsets.

Supplementary Fig. 6. A. Number and strength of cell–cell interactions between AML and HD; B. Heatmap showing the number of potential ligand–receptor pairs among cell subtypes in AML and HD. A deeper red color indicates stronger cell–cell communication.

Supplementary Fig. 7. Increased cell–cell communication signaling in AML with subsets as sources (A) and targets (B).

Data Availability Statement

All data generated or analyzed during this study are included in this published article. The expression profiles and clinical information of the patients analyzed in this study were downloaded from public databases (https://www.ncbi.nlm.nih.gov/geo).

Consent for publication of personal information

Not applicable.

Use of AI and AI-assisted technologies

Not applicable.

ORCID iDs

Junyi Li https://orcid.org/0009-0003-7954-7876
Huoyan Zhu https://orcid.org/0009-0005-1181-6608
Chaoqiong Ye https://orcid.org/0009-0007-3563-1725
Shengnan Xu https://orcid.org/0009-0005-9002-988X
Zhihua Wu https://orcid.org/0000-0003-3309-4042
Yuping Deng https://orcid.org/0009-0000-0986-898X

References

1. Stief SM, Hanneforth AL, Weser S, et al. Loss of KDM6A confers drug resistance in acute myeloid leukemia. *Leukemia*. 2020;34(1):50–62. doi:10.1038/s41375-019-0497-6
2. Döhner H, Weisdorf DJ, Bloomfield CD. Acute myeloid leukemia. *N Engl J Med*. 2015;373(12):1136–1152. doi:10.1056/NEJMra1406184
3. Menter T, Tzankov A. Tumor microenvironment in acute myeloid leukemia: Adjusting niches. *Front Immunol*. 2022;13:811144. doi:10.3389/fimmu.2022.811144
4. Zhang L, Meng Y, Feng X, Han Z. CAR-NK cells for cancer immunotherapy: From bench to bedside. *Biomark Res*. 2022;10(1):12. doi:10.1186/s40364-022-00364-6
5. Yao Y, Li F, Huang J, Jin J, Wang H. Leukemia stem cell–bone marrow microenvironment interplay in acute myeloid leukemia development. *Exp Hematol Oncol*. 2021;10(1):39. doi:10.1186/s40164-021-00233-2
6. Li Y, Hermanson DL, Moriarity BS, Kaufman DS. Human iPSC-derived natural killer cells engineered with chimeric antigen receptors enhance anti-tumor activity. *Cell Stem Cell*. 2018;23(2):181–192.e5. doi:10.1016/j.stem.2018.06.002
7. De Visser KE, Joyce JA. The evolving tumor microenvironment: From cancer initiation to metastatic outgrowth. *Cancer Cell*. 2023;41(3):374–403. doi:10.1016/j.ccell.2023.02.016
8. Méndez-Ferrer S, Bonnet D, Steensma DP, et al. Bone marrow niches in haematological malignancies. *Nat Rev Cancer*. 2020;20(5):285–298. doi:10.1038/s41568-020-0245-2
9. Witkowski MT, Kousteni S, Aifantis I. Mapping and targeting of the leukemic microenvironment. *J Exp Med*. 2020;217(2):e20190589. doi:10.1084/jem.20190589
10. Guilliams M, Ginhoux F, Jakubzick C, et al. Dendritic cells, monocytes and macrophages: A unified nomenclature based on ontogeny. *Nat Rev Immunol*. 2014;14(8):571–578. doi:10.1038/nri3712
11. Agrawal V, Gbolahan OB, Stahl M, et al. Vaccine and cell-based therapeutic approaches in acute myeloid leukemia. *Curr Cancer Drug Targets*. 2020;20(7):473–489. doi:10.2174/1568009620666200502011059
12. Ustun C, Miller JS, Munn DH, Weisdorf DJ, Blazar BR. Regulatory T cells in acute myelogenous leukemia: Is it time for immunomodulation? *Blood*. 2011;118(19):5084–5095. doi:10.1182/blood-2011-07-365817
13. Shao R, Li Z, Xin H, et al. Biomarkers as targets for CAR-T/NK cell therapy in AML. *Biomark Res*. 2023;11(1):65. doi:10.1186/s40364-023-00501-9
14. Pan W, Tao T, Qiu Y, Zhu X, Zhou X. Natural killer cells at the forefront of cancer immunotherapy with immune potency, genetic engineering, and nanotechnology. *Crit Rev Oncol Hematol*. 2024;193:104231. doi:10.1016/j.critrevonc.2023.104231
15. Cooper MA, Fehniger TA, Caligiuri MA. The biology of human natural killer-cell subsets. *Trends Immunol*. 2001;22(11):633–640. doi:10.1016/S1471-4906(01)02060-9
16. Poli A, Michel T, Thérésine M, Andrès E, Hentges F, Zimmer J. $CD56^{bright}$ natural killer (NK) cells: An important NK cell subset. *Immunology*. 2009;126(4):458–465. doi:10.1111/j.1365-2567.2008.03027.x
17. Chan A, Hong DL, Atzberger A, et al. CD56bright human NK cells differentiate into CD56dim cells: Role of contact with peripheral fibroblasts. *J Immunol*. 2007;179(1):89–94. doi:10.4049/jimmunol.179.1.89
18. Jacobs R, Hintzen G, Kemper A, et al. CD56bright cells differ in their KIR repertoire and cytotoxic features from CD56dim NK cells. *Eur J Immunol*. 10AD;31(10):3121α3126. doi:10.1002/1521-4141(2001010)31:10<3121::AID-IMMU3121>3.0.CO;2-4
19. Terrén I, Orrantia A, Vitallé J, Zenarruzabeitia O, Borrego F. NK cell metabolism and tumor microenvironment. *Front Immunol*. 2019;10:2278. doi:10.3389/fimmu.2019.02278
20. Close HJ, Stead LF, Nsengimana J, et al. Expression profiling of single cells and patient cohorts identifies multiple immunosuppressive pathways and an altered NK cell phenotype in glioblastoma. *Clin Exp Immunol*. 2020;200(1):33–44. doi:10.1111/cei.13403
21. Rouce RH, Shaim H, Sekine T, et al. The TGF-β/SMAD pathway is an important mechanism for NK cell immune evasion in childhood B-acute lymphoblastic leukemia. *Leukemia*. 2016;30(4):800–811. doi:10.1038/leu.2015.327
22. Ghiringhelli F, Ménard C, Terme M, et al. $CD4^+$ $CD25^+$ regulatory T cells inhibit natural killer cell functions in a transforming growth factor–β-dependent manner. *J Exp Med*. 2005;202(8):1075–1085. doi:10.1084/jem.20051511

23. Stiff A, Trikha P, Mundy-Bosse B, et al. Nitric oxide production by myeloid-derived suppressor cells plays a role in impairing Fc receptor-mediated natural killer cell function. *Clin Cancer Res*. 2018;24(8):1891–1904. doi:10.1158/1078-0432.CCR-17-0691
24. Zhang Q, He Y, Luo N, et al. Landscape and dynamics of single immune cells in hepatocellular carcinoma. *Cell*. 2019;179(4):829–845.e20. doi:10.1016/j.cell.2019.10.003
25. Pere H, Montier Y, Bayry J, et al. A CCR4 antagonist combined with vaccines induces antigen-specific $CD8^+$ T cells and tumor immunity against self antigens. *Blood*. 2011;118(18):4853–4862. doi:10.1182/blood-2011-01-329656
26. Berlato C, Khan MN, Schioppa T, et al. A CCR4 antagonist reverses the tumor-promoting microenvironment of renal cancer. *J Clin Invest*. 2017;127(3):801–813. doi:10.1172/JCI82976
27. Mathewson ND, Ashenberg O, Tirosh I, et al. Inhibitory CD161 receptor identified in glioma-infiltrating T cells by single-cell analysis. *Cell*. 2021;184(5):1281–1298.e26. doi:10.1016/j.cell.2021.01.022
28. Cassier PA, Navaridas R, Bellina M, et al. Netrin-1 blockade inhibits tumour growth and EMT features in endometrial cancer. *Nature*. 2023;620(7973):409–416. doi:10.1038/s41586-023-06367-z
29. McGinnis CS, Murrow LM, Gartner ZJ. DoubletFinder: Doublet detection in single-cell RNA sequencing data using artificial nearest neighbors. *Cell Syst*. 2019;8(4):329–337.e4. doi:10.1016/j.cels.2019.03.003
30. Petti AA, Williams SR, Miller CA, et al. A general approach for detecting expressed mutations in AML cells using single cell RNA-sequencing. *Nat Commun*. 2019;10(1):3660. doi:10.1038/s41467-019-11591-1.
31. Stuart T, Butler A, Hoffman P, et al. Comprehensive integration of single-cell data. *Cell*. 2019;177(7):1888–1902.e21. doi:10.1016/j.cell.2019.05.031
32. Van Galen P, Hovestadt V, Wadsworth Ii MH, et al. Single-cell RNA-seq reveals AML hierarchies relevant to disease progression and immunity. *Cell*. 2019;176(6):1265–1281.e24. doi:10.1016/j.cell.2019.01.031
33. Zhang Z, Deng C, Zhu P, et al. Single-cell RNA-seq reveals a microenvironment and an exhaustion state of T/NK cells in acute myeloid leukemia. *Cancer Sci*. 2023;114(10):3873–3883. doi:10.1111/cas.15932
34. Korsunsky I, Millard N, Fan J, et al. Fast, sensitive and accurate integration of single-cell data with Harmony. *Nat Methods*. 2019;16(12):1289–1296. doi:10.1038/s41592-019-0619-0
35. Aran D, Looney AP, Liu L, et al. Reference-based analysis of lung single-cell sequencing reveals a transitional profibrotic macrophage. *Nat Immunol*. 2019;20(2):163–172. doi:10.1038/s41590-018-0276-y
36. Zhang X, Lan Y, Xu J, et al. CellMarker: A manually curated resource of cell markers in human and mouse. *Nucl Acids Res*. 2019;47(D1):D721–D728. doi:10.1093/nar/gky900
37. Tang F, Li J, Qi L, et al. A pan-cancer single-cell panorama of human natural killer cells. *Cell*. 2023;186(19):4235–4251.e20. PMID:37607536.
38 Khwaja A, Bjorkholm M, Gale RE, et al. Acute myeloid leukaemia. *Nat Rev Dis Primers*. 2016;2(1):16010. doi:10.1038/nrdp.2016.10
39. Becker M, Farina KA, Mascarenhas J. Acute myeloid leukemia: Current understanding and management. *JAAPA*. 2024;37(1):34–39. doi:10.1097/01.JAA.0000995680.52352.b5
40. Long NA, Golla U, Sharma A, Claxton DF. Acute myeloid leukemia stem cells: Origin, characteristics, and clinical implications. *Stem Cell Rev Rep*. 2022;18(4):1211–1226. doi:10.1007/s12015-021-10308-6
41. Le Dieu R, Taussig DC, Ramsay AG, et al. Peripheral blood T cells in acute myeloid leukemia (AML) patients at diagnosis have abnormal phenotype and genotype and form defective immune synapses with AML blasts. *Blood*. 2009;114(18):3909–3916. doi:10.1182/blood-2009-02-206946
42. Guy C, Mitrea DM, Chou PC, et al. LAG3 associates with TCR–CD3 complexes and suppresses signaling by driving co-receptor–Lck dissociation. *Nat Immunol*. 2022;23(5):757–767. doi:10.1038/s41590-022-01176-4
43 Lu L, Barbi J, Pan F. The regulation of immune tolerance by FOXP3. *Nat Rev Immunol*. 2017;17(11):703–717. doi:10.1038/nri.2017.75
44. Bai Y, He T, Zhang L, et al. Prognostic value of $FOXP3^+$ regulatory T cells in patients with diffuse large B-cell lymphoma: A systematic review and meta-analysis. *BMJ Open*. 2022;12(9):e060659. doi:10.1136/bmjopen-2021-060659
45. Qiu Y, Ke S, Chen J, et al. $FOXP3^+$ regulatory T cells and the immune escape in solid tumours. *Front Immunol*. 2022;13:982986. doi:10.3389/fimmu.2022.982986
46. Arık D, Benli T, Telli E. Number of $FoxP3^+$ regulatory T-cells are associated with recurrence in vulvar squamous cell carcinoma. *J Gynecol Oncol*. 2023;34(2):e16. doi:10.3802/jgo.2023.34.e16
47. Norouzian M, Mehdipour F, Ashraf MJ, Khademi B, Ghaderi A. Regulatory and effector T cell subsets in tumor-draining lymph nodes of patients with squamous cell carcinoma of head and neck. *BMC Immunol*. 2022;23(1):56. doi:10.1186/s12865-022-00530-3
48 Wang M, Zhang C, Tian T, et al. Increased regulatory T cells in peripheral blood of acute myeloid leukemia patients rely on tumor necrosis factor (TNF)-α–TNF receptor-2 pathway. *Front Immunol*. 2018;9:1274. doi:10.3389/fimmu.2018.01274
49. Park SM, Cho H, Thornton AM, et al. IKZF2 drives leukemia stem cell self-renewal and inhibits myeloid differentiation. *Cell Stem Cell*. 2019;24(1):153–165.e7. doi:10.1016/j.stem.2018.10.016
50. Yuce K, Ozkan AI. The kruppel-like factor (KLF) family, diseases, and physiological events. *Gene*. 2024;895:148027. doi:10.1016/j.gene.2023.148027
51. Goswami S, Anandhan S, Raychaudhuri D, Sharma P. Myeloid cell-targeted therapies for solid tumours. *Nat Rev Immunol*. 2023;23(2):106–120. doi:10.1038/s41577-022-00737-w
52. Mumme H, Thomas BE, Bhasin SS, et al. Single-cell analysis reveals altered tumor microenvironments of relapse- and remission-associated pediatric acute myeloid leukemia. *Nat Commun*. 2023;14(1):6209. doi:10.1038/s41467-023-41994-0
53. Khaldoyanidi S, Nagorsen D, Stein A, Ossenkoppele G, Subklewe M. Immune biology of acute myeloid leukemia: Implications for immunotherapy. *J Clin Oncol*. 2021;39(5):419–432. doi:10.1200/JCO.20.00475
54. Luo Y, Luo J, Yang M, Zhao X. Mechanisms of T-cell metabolic reprogramming in the microenvironment of acute myeloid leukemia and its therapeutic potential (Review). *Oncol Lett*. 2025;30(4):455. doi:10.3892/ol.2025.15201
55. Rahmani S, Yazdanpanah N, Rezaei N. Natural killer cells and acute myeloid leukemia: Promises and challenges. *Cancer Immunol Immunother*. 2022;71(12):2849–2867. doi:10.1007/s00262-022-03217-1

Nanog promotes proliferation, migration, and invasion of gastric cancer cells via regulation of the KDM5B/H3K4me3 epigenetic axis

*Lili Ma[1,A,B], *Lin Lu[2,A,D], Xiaohui Liu[3,B], Lei Wang[4,B,C], Yan Liu[5,D], Yaqi Wang[6,B], Yankun Liu[2,B,C], Jinghua Zhang[7,E], Yufeng Li[8,E,F]

[1] Department of Gastroenterology, Tangshan People's Hospital, China
[2] Department of Medical Molecular Diagnosis, Tangshan People's Hospital, China
[3] Department of Thoracic Surgery, Tangshan People's Hospital, China
[4] Department of Pathology, Tangshan People's Hospital, China
[5] College of Life Sciences, North China University of Science and Technology, Tangshan, China
[6] Department of Breast Surgery, Tangshan People's Hospital, China
[7] School of Public Health, North China University of Science and Technology, Tangshan, China
[8] Hebei Key Laboratory of Molecular Oncology, Tangshan People's Hospital, China

A – research concept and design; B – collection and/or assembly of data; C – data analysis and interpretation;
D – writing the article; E – critical revision of the article; F – final approval of the article

Advances in Clinical and Experimental Medicine, ISSN 1899–5276 (print), ISSN 2451–2680 (online) *Adv Clin Exp Med*. 2026;35(7):1187–1197

Address for correspondence
Yufeng Li
E-mail: fengfly01@163.com

Funding sources
This work was supported by the Medical Science Research Project of Hebei (project No. 20221814) and the Medical Science Research Project of Hebei (project No. 20250228).

Conflict of interest
None declared

* Lili Ma and Lin Lu contributed equally to this work.

Received on March 5, 2025
Reviewed on June 22, 2025
Accepted on October 10, 2025

Published online on July 28, 2026

Cite as
Ma L, Lu L, Liu X, et al. Nanog contributes to proliferation, migration, and invasion of gastric cancer cell by regulating KDM5B/H3K4me axis. *Adv Clin Exp Med*. 2026;35(7):1187–1197. doi:10.17219/acem/211940

DOI
10.17219/acem/211940

Copyright
Copyright by Author(s)
This is an article distributed under the terms of the Creative Commons Attribution 3.0 Unported (CC BY 3.0) (https://creativecommons.org/licenses/by/3.0/)

Abstract

Background. Nanog, a transcription factor, is involved in cancer initiation and progression.

Objectives. To explore the potential regulatory mechanism of Nanog in gastric cancer.

Materials and methods. Immunohistochemistry (IHC) was used to examine E-cadherin, N-cadherin, Nanog, and KDM5B in gastric cancer (Ca), metastatic lymph node cancer (L), and adjacent normal tissues (N). MTT, migration, and invasion assays were used to evaluate cell viability, migration, and invasion of gastric cancer cells SGC-7901 induced by transforming growth factor (TGF)-β1, or with Nanog overexpression/knockdown. Western blot was used to examine the relative protein expression of E-cadherin, N-cadherin, Nanog, and lysine-specific demethylase 5B (KDM5B) in cells. KDM5B was silenced by siRNA in cells, and E-cadherin, N-cadherin, and H3K4me3 were examined with western blot, while the interaction between Nanog and KDM5B was examined using a co-immunoprecipitation (Co-IP) assay. Furthermore, H3K4me3 protein expression was validated in N, Ca, and L tissues using IHC.

Results. E-cadherin was hypoexpressed, while N-cadherin, Nanog, and KDM5B were hyperexpressed in the Ca and L groups compared with the N group. TGF-β1 and Nanog enhanced cell viability, migration, and invasion by promoting epithelial–mesenchymal transition (EMT). KDM5B was identified to bind to Nanog and was positively regulated by Nanog, and functioned as a negative regulator of histone H3 Lys4 trimethylation (H3K4me3) in SGC-7901 cells. KDM5B knockdown inhibited cell invasion and EMT. The Nanog/KDM5B/H3K4me3 pathway contributes to the proliferation, migration, and invasion of SGC-7901 cells by inhibiting E-cadherin and enhancing N-cadherin.

Conclusions. This study provides new insights into the regulatory role and mechanism of Nanog/KDM5B/H3K4me3 in gastric cancer, which might be potential biomarkers in the diagnosis and prognosis of gastric cancer.

Key words: Nanog, gastric cancer, KDM5B, H3K4me3, epithelial–mesenchymal transition

Highlights

- Nanog and KDM5B overexpression promote epithelial–mesenchymal transition (EMT), enhancing gastric cancer cell proliferation, migration, and invasion.
- Nanog directly binds and regulates KDM5B, modulating H3K4me3 demethylation to drive gastric cancer progression.
- Silencing KDM5B suppresses EMT and invasiveness in SGC-7901 gastric cancer cells, restoring E-cadherin expression.
- The Nanog/KDM5B/H3K4me3 signaling axis may serve as a novel biomarker and therapeutic target for gastric cancer diagnosis and prognosis.

Background

As one of the most common malignancies worldwide, gastric cancer ranks as the 5th most prevalent cancer and the 3rd leading cause of cancer-related deaths globally, and its development is often linked to various factors, including dietary habits, *Helicobacter pylori* infection, smoking, and genetic predispositions.[1,2] Surgical resection remains a major treatment despite advances in discoveries related to the pathogenesis and molecular biology of gastric cancer. The optimal extent of lymphadenectomy and the rapid development of screening-based interventional techniques have been the dominant themes.[3] Gastric cancer is a phenotypically highly heterogeneous disease. Numerous studies indicate that the development and progression of gastric cancer involve a number of genetic and epigenetic changes, such as c-myc and p21 downregulation[4] and epigenetic downregulation of mucin 17.[5] However, the molecular mechanisms underlying malignancy in gastric cancer cells are largely unknown.

Nanog is a critical transcription factor involved in the self-renewal and pluripotency of embryonic stem cells (ESCs).[6,7] Similar to ESCs, tumor-initiating cells (TICs) undergo molecular regulation, proliferation, self-renewal, and unlimited differentiation.[8] In addition, TICs tend to be more drug-resistant and metastatic than non-TICs.[9,10] Recent evidence has demonstrated that Nanog dysregulation contributes to cancer initiation and progression through TICs,[11] and it is enriched in various cancers, including hepatocellular carcinoma (HCC),[12] breast carcinoma[13] and colorectal carcinoma.[14] A recent study indicated that Nanog was overexpressed in gastric cancer tissues and positively associated with lymph node status and advanced clinical stage in patients.[15] High Nanog levels in cancer tissues were strongly correlated with 5-year overall survival (OS) in patients.[14] The functional and mechanistic roles of Nanog in gastric cancer remain largely unclear and require further exploration.

Epigenetic modulation plays an important role in tumorigenesis. Recent studies have indicated that inhibitors of DNA methyltransferases or histone deacetylases have been applied in clinical epigenetic therapy[16–18] or have been designed as new therapies for human diseases.[19] Histone lysine demethylases, on the other hand, are potential therapeutic targets for various diseases. A lysine-specific demethylase 5 (KDM5) inhibitor reduces demethylation of H3K4me3 at transcription start sites and decreases the growth of myeloma cells.[20] KDM5 consists of 4 family members: KDM5A, KDM5B, KDM5C, and KDM5D. These proteins can remove di- and trimethylation marks from activated H3K4 and are also involved in the differentiation of hematopoietic stem cells and tumorigenesis.[21,22] Recent studies have reported that KDM5B is highly expressed in cancers, including non-small cell lung cancer (NSCLC) and liver cancer, and that its expression is correlated with tumor size, advanced stage, and poor OS in patients with liver cancer and NSCLC.[23,24] KDM5B is a transcriptional target of Nanog, while Nanog occupies the KDM5B genomic locus and promotes self-renewal of embryonic stem cells.[25] However, the specific regulatory mechanism between KDM5B and Nanog in gastric cancer remains to be explored.

Objectives

We examined the effects of KDM5B and Nanog on cell viability and invasion in vitro to investigate the specific regulatory mechanisms of KDM5B and Nanog in gastric cancer.

Materials and methods

Human tissues and cell lines

Twenty pairs of gastric cancer and adjacent non-tumor tissues were obtained from gastric cancer patients undergoing gastrectomy without prior radiotherapy or chemotherapy. Written informed consent was obtained from each patient. This study was approved by the Ethics Committee of Tangshan People's Hospital (Tangshan, China) and conducted in accordance with the Declaration of Helsinki of 1964 and its subsequent revisions (approval No. RMYY-LLKS-2024026). SGC-7901 cells were purchased from the Chinese Academy of Medical Sciences and Peking Union Medical College (Beijing, China) and routinely

cultured in complete medium containing 90% RPMI-1640 and 10% fetal bovine serum (FBS; Gibco, Waltham, USA) at 37°C in 5% CO_2.

Plasmid construction and siRNA synthesis

The pEGFP-N1 vector was used to generate plasmids overexpressing Nanog and KDM5B. All plasmids were designed and constructed by Sangon Biotech (Shanghai, China). All siRNAs and primers were synthesized by GenePharma (Suzhou, China). The respective sequences are provided in Table 1.

RNA isolation and RT-qPCR

Total RNA was routinely extracted using the TRIzol method. Complementary DNA (cDNA) was synthesized using the PrimeScript RT Reagent Kit (Takara, Shiga, Japan), and the polymerase chain reaction (PCR) program was set at 94°C for 3 min, followed by 40 cycles of 94°C for 30 s, 60°C for 30 s, and 72°C for 30 s. *GAPDH* was used as the internal reference. The primers used in this experiment are listed in Table 1.

MTT assay

Cells were initially seeded in 96-well plates at a density of 7×10^3 cells per well in complete medium. After 24 h, 10 µL of 3-(4,5-dimethylthiazol-2-yl)-2,5-diphenyltetrazolium bromide (MTT) was added to each well. The cells were then incubated for an additional 4 h in a cell incubator. Following the protocol, absorbance was measured at 570 nm using a microplate reader (Bio-Tek, Winooski, USA).

Western blot

Western blotting was used to examine changes in relative protein expression in cells. Total protein was extracted using radioimmunoprecipitation assay (RIPA) buffer containing phenylmethylsulfonyl fluoride (PMSF). The extracted proteins were boiled for 15 min at 100°C, separated using the sodium dodecyl sulfate–polyacrylamide gel electrophoresis (SDS-PAGE) method, and transferred to polyvinylidene difluoride (PVDF) membranes. The membranes were blocked in 5% non-fat milk for 1 h at room temperature. Primary antibodies were diluted in Tris-buffered saline with Tween (TBST) and applied to the membranes for incubation at 4°C overnight. Anti-KDM5B (1:800, CSB-PA295068; Cusabio, Wuhan, China), anti-Nanog (1:2,000, bs-10414R; Bioss, Beijing, China), anti-E-cadherin (1:2000, bsm-60814R; Bioss), anti-N-cadherin (1:2,000, bsm-52389R; Bioss), and anti-H3K4me3 (1:1000, bs-4715R; Bioss) were used in the experiments. The membranes were washed 3 times with a sufficient volume of TBST and then incubated with secondary antibody (1:10,000, bs-0295G; Bioss) for 1 h at room temperature. Blots were visualized using the electrochemiluminescence (ECL; Bio-High, Hebei, China) method on a chemiluminescence imager (Peiqing, Shanghai, China) and quantified using ImageJ (National Institutes of Health (NIH), Bethesda, USA), with normalization to *GAPDH*.

Immunohistochemistry assay

Immunohistochemistry (IHC) assays were applied to examine the relative protein distribution and expression levels in gastric cancer tissues (Ca) and paired metastatic lymph node cancer tissues (L) compared with adjacent normal tissues (N). Formalin-fixed and paraffin-embedded (FFPE) tissues were cut into 5 µm sections for further IHC analysis. The sections were prepared as described in our previous study.[26] The slides were stained with secondary antibodies and diaminobenzidine tetrahydrochloride (ZSGB-BIO, Beijing, China) and then counterstained with hematoxylin.[26]

The primary antibodies used in this study included anti-E-cadherin (bs-1519R, 1:500; Bioss), anti-N-cadherin (bs-1172R, 1:500 dilution; Bioss), anti-Nanog, anti-KDM5B (bs-6139R, 1:500; Bioss), and anti-H3K4me3 (bs-4715, 1:500; Bioss). The IHC results were evaluated by 2 independent pathologists blinded to the sample groups.

Table 1. Primers and oligonucleotides used

Name	Sequences (5′-3′)
Nanog-homo-810 siRNA	CCAUGGAUUUAUUCCUAAATTUUUAGGAAUAAAUCCAUGGTT
KDM5B-homo siRNA	GGCUUCAACUGUUCAGAAATTUUUCUGAACAGUUGAAGCCTT
Negative control siRNA	UUCUCCGAACGUGUCACGUTTACGUGACACGUUCGGAGAATT
GAPDH positive control siRNA	UGACCUCAACUACAUGGUUTTAACCAUGUAGUUGAGGUCATT
H-KDM5B-FO-3	GGGACTATACCCTCCGTACTTTT
H-KDM5B-RE-3	TATTCCACTGTGACATCCTCCTC
H-NANOG HOMEOBOX-FO-4	CCTCCAGCAGATGCAAGAACTC
H-NANOG HOMEOBOX-RE-4	GTAAAGGCTGGGGTAGGTAGGTG
H-GAPDH-FO	CATGAGAAGTATGACAACAGCCT
H-GAPDH-RE	AGTCCTTCCACGATACCAAAGT

Hematoxylin and eosin staining

The tissue sections were stained with hematoxylin solution for 5 min and then stained with 0.3% eosin solution for 3 min after washing in distilled water. The stained sections were dehydrated using graded ethanol and xylene. The sections were observed under an Olympus IX71 microscope (Olympus Corp., Tokyo, Japan; magnification ×100 and ×600).

Wound healing assay

Sixty-millimeter dishes were used for the wound healing assay. In brief, cells were seeded in dishes containing complete medium and cultured for 12–18 h. Then, a 200-μL pipette tip was used to create a scratch in a straight line. The dishes were then washed twice. Images of the same field were captured after 24 h and 48 h under a microscope (Olympus IX71). ImageJ was used to analyze wound healing.

Invasion ability analysis

Cells (5×10^4/well) were inoculated into the upper chambers of Boyden chamber transwells (8-μm pore size; Corning Company, Corning, USA) containing serum-free medium and pre-coated with 40 μL of Matrigel (BD Biosciences, Franklin Lakes, USA). The lower chamber was filled with complete medium. After 24 h, the cells attached to the lower surface of the inserts were fixed with 4% paraformaldehyde (PFA), stained with 1% crystal violet, and counted.

Co-IP assay

This assay was performed to evaluate the impact of Nanog overexpression on KDM5B in cells. Cells were cultured in 250-mL cell culture flasks and transfected with 15.0 μg of Nanog overexpression plasmid or an empty vector control. Forty-eight hours later, the cells were washed with 1× phosphate-buffered saline (PBS) and then placed on a shaker at 4°C for 30 min with 2 mL of co-immunoprecipitation (Co-IP) buffer. The mixture was centrifuged at 4°C and 12,000 rpm for 10 min. The supernatant was then collected, and the proteins were purified according to the protocol. Next, 50 μL of protein A/G beads was centrifuged at 4,000 rpm for 3 min, the supernatant was discarded, and 500 μL of Co-IP buffer was added (MilliporeSigma, St. Louis, USA). The reactions were incubated for 25 min, followed by western blotting.

Statistical analyses

In the IHC analysis, we first performed the Shapiro–Wilk test and Brown–Forsythe test to examine the normality and variance of the data in each group. Thereafter, Welch's analysis of variance (ANOVA) with Dunnett's T3 multiple-comparisons test was conducted to evaluate differences in relative protein expression based on the IHC results. For cellular assays and western blot analyses, because of the small sample size and the limited reliability of distributional testing under these conditions, nonparametric tests were used without assuming normal data distribution. The statistical significance of differences was analyzed using the Kruskal–Wallis test with Dunn's post hoc test for multiple-group comparisons and the Mann–Whitney U test for comparisons between 2 groups using GraphPad Prism v. 10 (GraphPad, San Diego, USA). Significant associations between Nanog and KDM5B expression were assessed using Pearson's correlation analysis ($p < 0.05$).

Results

Nanog and KDM5B are abundantly expressed in gastric cancer tissues and metastatic lymph node tissues

Epithelial–mesenchymal transition (EMT) is one of the key steps in tumor metastasis. As shown in Fig. 1A,B, the epithelial marker E-cadherin was hypoexpressed, while the mesenchymal marker N-cadherin was hyperexpressed in gastric cancer tissues (Ca) and paired metastatic lymph node cancer tissues (L) compared with adjacent normal tissues (N). This finding confirmed that cancer cells underwent EMT in both in situ and metastatic foci. In addition, Nanog and KDM5B were upregulated in both Ca and L tissues compared with N tissues. Furthermore, Pearson's correlation analysis demonstrated that Nanog was positively correlated with KDM5B in the Ca and L groups (Fig. 1C,D). These findings suggest that Nanog and KDM5B may be involved in gastric cancer progression.

Nanog and KDM5B are overexpressed in TGF-β1-induced SGC-7901 cells

Evidence has indicated that activation of transforming growth factor (TGF)-β1 promotes an epithelial plasticity response that may induce EMT in carcinomas.[27] Thus, TGF-β1 was used to establish an EMT model in gastric cancer cells. SGC-7901 cells treated with TGF-β1 exhibited enhanced cell viability and stronger migration and invasion abilities (Fig. 2A–C) than non-induced cells. E-cadherin was overexpressed in non-induced cells, while N-cadherin was increased in TGF-β1-induced cells (Fig. 2D). These results confirmed that cells treated with TGF-β1 exhibited an EMT phenotype. Moreover, both Nanog and KDM5B were significantly increased in TGF-β1-induced cells (Fig. 2D). These results indicated that Nanog and KDM5B were involved in EMT progression in gastric cancer cells, which was in accordance with the results of gastric histology shown in Fig. 1.

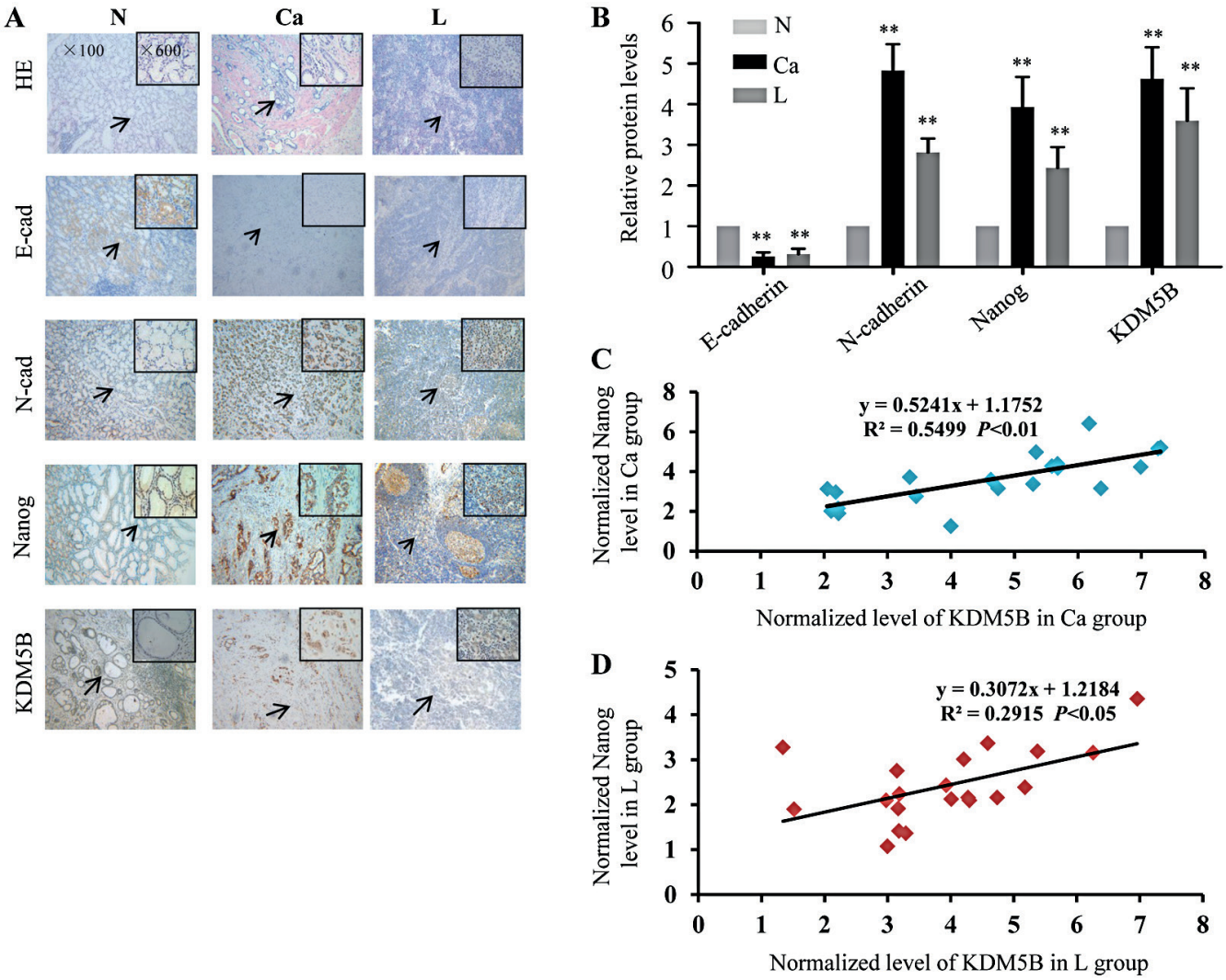

Fig. 1. Expression of Nanog, lysine-specific demethylase 5B (KDM5B), E-cadherin, and N-cadherin in adjacent normal gastric tissues (N), gastric cancer tissues (Ca), and corresponding lymph node metastatic tissues (L) from the same gastric cancer patient. A. Upper panel: Hematoxylin and eosin (H&E) staining (magnification ×100 and ×600). Lower panel: Representative images of immunohistochemistry (IHC) staining of E-cadherin (E-cad), N-cadherin (N-cad), Nanog, and KDM5B in N, Ca, and L tissues; B. Normalized protein levels of E-cadherin, N-cadherin, Nanog, and KDM5B in N, Ca, and L tissues. n = 20. Welch's analysis of variance (ANOVA) with Dunnett's T3 multiple-comparisons test was performed for multiple-group comparisons; C,D. Correlation between Nanog and KDM5B expression in the Ca (C) and L (D) groups, respectively. Pearson's correlation analysis was performed (**p < 0.05)

Nanog overexpression contributes to the proliferation, migration, invasion, EMT, and KDM5B expression of SGC-7901 cells

To further investigate the function of Nanog in gastric cancer cells, SGC-7901 cells were transfected with empty pEGFP-N1 plasmids (N1) and pEGFP-N1 plasmids containing the sequence encoding Nanog (N1-Nanog). The viability of SGC-7901 cells was enhanced in the Nanog overexpression group (Fig. 3A). The wound-healing and invasion assays showed that Nanog overexpression increased cell migration and invasion (Fig. 3B,C). At 24 h and 48 h post-transfection, the protein level of Nanog was enhanced 1.4-fold in the N1-Nanog group compared with that in the N1 group (Fig. 3D). Western blot results confirmed that E-cadherin was decreased, whereas N-cadherin was increased in Nanog-overexpressing cells (Fig. 3D). KDM5B protein expression was enhanced by Nanog overexpression (Fig. 3D). These results suggest that Nanog overexpression promotes proliferation, migration, invasion, and the EMT phenotype of SGC-7901 cells, as well as KDM5B expression.

Nanog knockdown inhibits proliferation, migration, invasion, EMT, and KDM5B expression of SGC-7901 cells

SGC-7901 cells were transfected with small interfering RNA targeting Nanog (si-Nanog) and a negative control (si-NC). The viability of SGC-7901 cells decreased following Nanog knockdown (Fig. 4A). The wound-healing assay and in vitro invasion assay indicated that Nanog knockdown reduced cell migration and invasion activities (Fig. 4B,C). The efficiency of Nanog knockdown was verified using

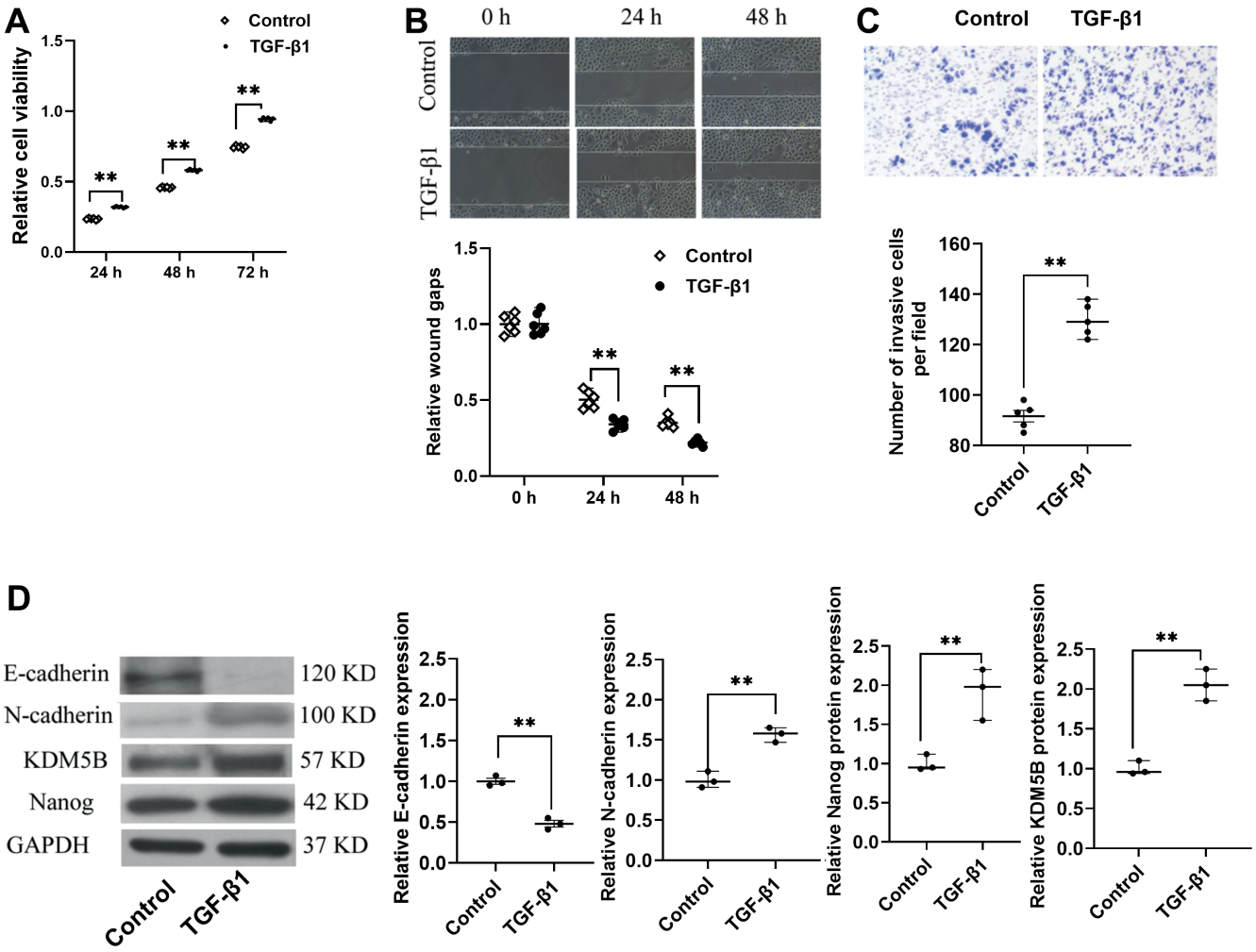

Fig. 2. Nanog and lysine-specific demethylase 5B (KDM5B) were overexpressed in transforming growth factor-β1 (TGF-β1)-induced SGC-7901 cells. A. Viability of SGC-7901 cells treated with TGF-β1 for 24, 48, and 72 h; B. Upper panel: Representative images (×100) and relative migration ability of SGC-7901 cells induced by TGF-β1 for 0, 24, and 48 h, as determined using a wound-healing assay; C. Relative invasion ability of SGC-7901 cells induced by TGF-β1 for 24 h (×200); D. Western blot analysis of E-cadherin, N-cadherin, Nanog, and KDM5B in SGC-7901 cells induced by TGF-β1 for 24 h. Mann–Whitney U test was performed to analyze differences between groups (**$p < 0.05$)

western blotting (Fig. 4D). Western blot assays also indicated that E-cadherin expression increased while N-cadherin expression decreased in the si-Nanog group (Fig. 4D), suggesting that Nanog knockdown blocked EMT progression. Moreover, KDM5B expression was markedly downregulated by Nanog knockdown (Fig. 4D). These data suggest that Nanog silencing suppresses the proliferation, migration, invasion, and EMT process of SGC-7901 cells, as well as KDM5B expression. Taken together, KDM5B is a downstream gene positively regulated by Nanog in SGC-7901 cells.

Silencing KDM5B inhibits the invasion and EMT of SGC-7901 cells by upregulation of H3K4me3 level

First, the silencing effects of si-KDM5B on KDM5B expression at the mRNA and protein levels were confirmed in SGC-7901 cells (Fig. 5A,C). In addition, KDM5B knockdown impaired the invasive capability of the cells, inducing E-cadherin expression and inhibiting N-cadherin expression (Fig. 5B–D). Given that KDM5B is recognized as an H3K4me3 demethylase, H3K4me3 levels in SGC-7901 cells following KDM5B knockdown were examined. Western blot results showed that the H3K4me3 level in the si-KDM5B group was significantly increased (Fig. 5C,D). Moreover, 5'-deoxy-5'-methylthioadenosine (MTA), an inhibitor of histone arginine and lysine methylation, counteracted the changes in E-cadherin and N-cadherin expression induced by KDM5B knockdown in SGC-7901 cells (Fig. 5E). The H3K4me3 levels in both Ca and L tissues were lower than those in N tissues, which was opposite to the KDM5B expression pattern shown in Fig. 1A,B (Fig. 6A). These data indicated that KDM5B regulates EMT markers by affecting H3K4me3 levels. Co-immunoprecipitation results further confirmed that KDM5B was bound to Nanog and was also upregulated by Nanog overexpression (Fig. 6B,C).

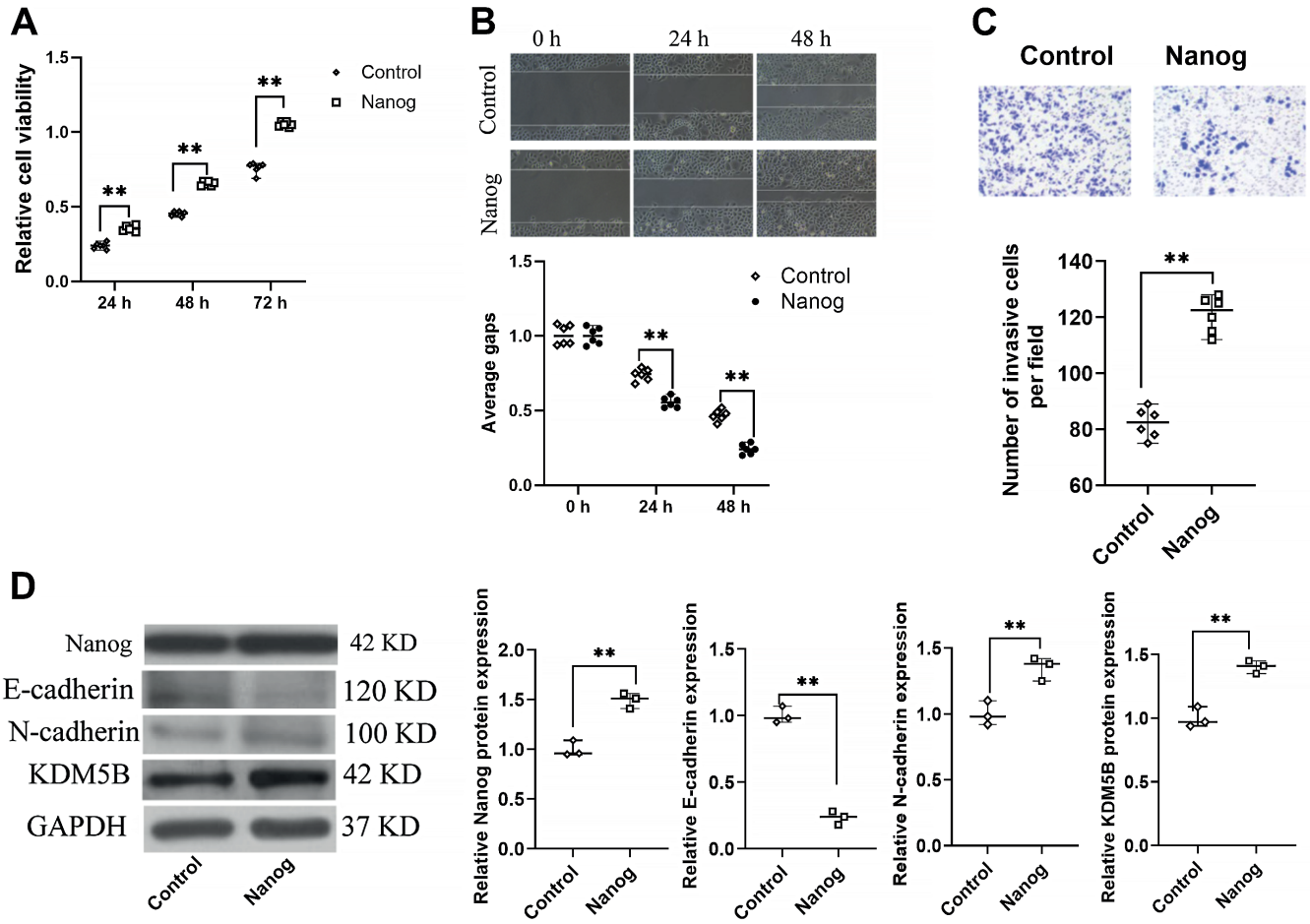

Fig. 3. Nanog overexpression promoted SGC-7901 cell migration and invasion. A. The viability of SGC-7901 cells in the control and Nanog overexpression groups was measured using the Cell Counting Kit-8 (CCK-8) assay; B. Invasion ability of SGC-7901 cells (×200); C. Migration activity of SGC-7901 cells; D. Western blot analysis of Nanog, E-cadherin, N-cadherin, and lysine-specific demethylase 5B (KDM5B) in SGC-7901 cells. Histograms of the protein levels of E-cadherin, N-cadherin, and KDM5B in SGC-7901 cells are shown. Mann–Whitney U test was performed to analyze differences between groups (**$p < 0.05$)

Discussion

In the current study, Nanog and KDM5B were both overexpressed in gastric cancer tissues, metastatic lymph node cancer tissues, and TGF-β1-induced gastric cancer cells, suggesting that Nanog/KDM5B might play a role in gastric cancer metastasis in vitro and in vivo. Nanog is recognized as a transcription factor and plays a critical role in maintaining self-renewal and pluripotency in normal embryonic stem cells (ESCs).[28,29] It was previously reported that higher expression levels of Nanog in gastric cancer tissues were significantly associated with tumor size, TNM stage, tumor grade, and shorter OS.[30] In this study, we verified in vitro that Nanog positively regulates the proliferation, migration, invasion, and EMT of gastric cancer cells. This study also demonstrated that Nanog could regulate its downstream target KDM5B, while silencing KDM5B inhibited invasion and EMT in gastric cancer cells by enhancing H3K4me3 levels. These results suggest that Nanog might play an important role in gastric cancer development through regulating the KDM5B/H3K4me3 pathway; clinically, targeting Nanog or KDM5B might serve as a promising strategy to suppress metastasis, particularly in patients with high Nanog/KDM5B expression, who may benefit from therapies disrupting this axis. Previously, the KDM5B degrader GT-653 was discovered to increase H3K4me3 levels and activate the type I interferon pathway, facilitating inhibition of immune escape.[31] In breast cancer, several KDM5B inhibitors have also displayed anticancer effects, representing promising therapeutic strategies.[32] Recently, it was discovered that targeting Nanog inhibited cell migration in gastric cancer, which is in accordance with the findings of this study. In other cancers, such as liver cancer, increased levels of Nanog are correlated with poor patient survival, and Nanog upregulation in cancer cells activates EMT, invasion, and drug resistance.[33] Taken together with the functions of Nanog in other cancers,[34] Nanog is not only a critical stem cell factor but also contributes to EMT and metastasis development in gastric cancer. Previous studies have shown that Nanog can interact with other canonical pathways,

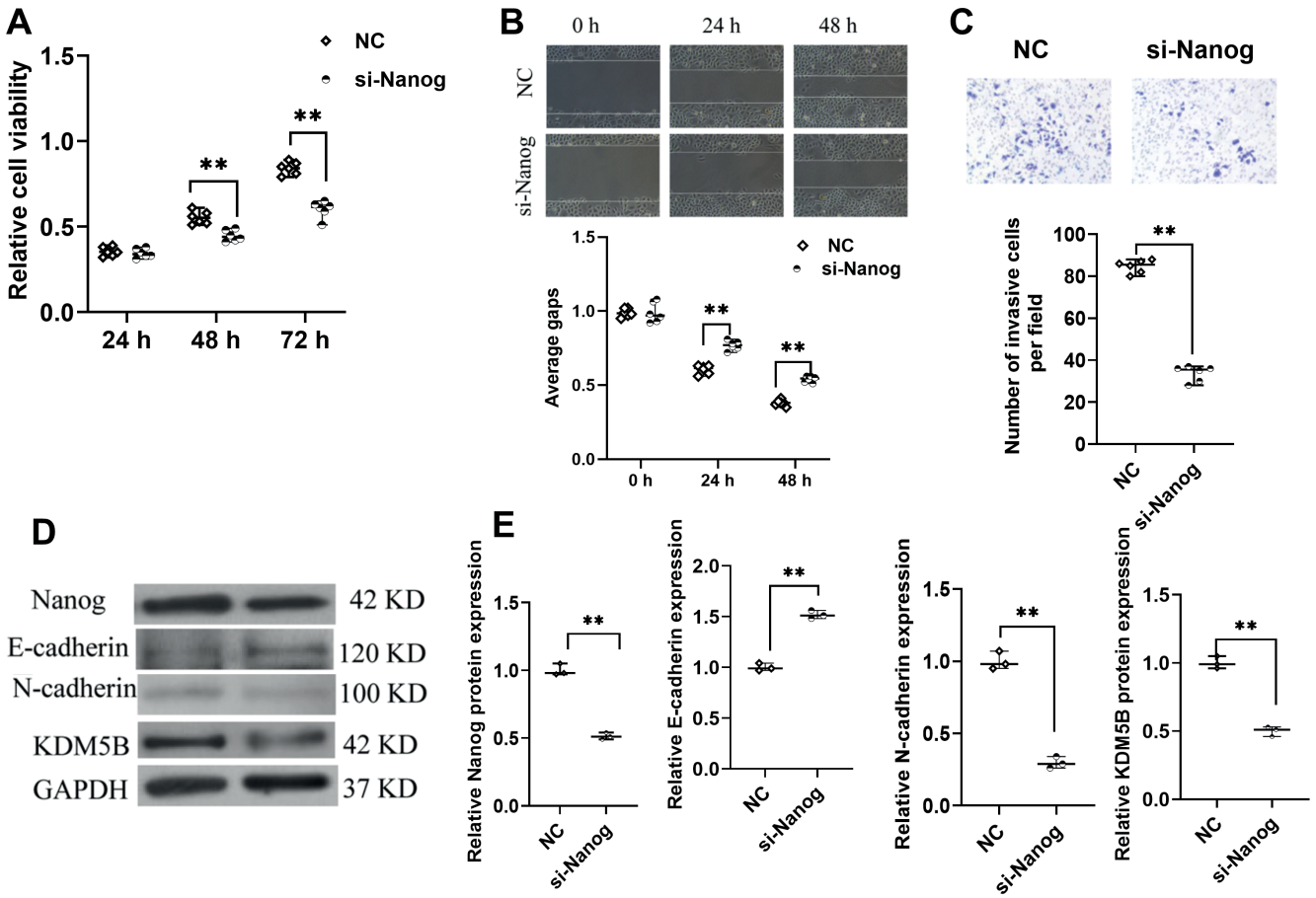

Fig. 4. Nanog knockdown inhibited SGC-7901 cell migration and invasion. A. The viability of SGC-7901 cells was measured using the Cell Counting Kit-8 (CCK-8) assay; B. Wound-healing assay of SGC-7901 cells in the si-NC (negative control) and si-Nanog groups at 0, 24, and 48 h; C. Invasion assay performed in SGC-7901 cells. Representative images are shown (×200); D. Western blot analysis of Nanog, E-cadherin, N-cadherin, and lysine-specific demethylase 5B (KDM5B) in SGC-7901 cells in the indicated groups. Mann–Whitney U test was performed to analyze differences between groups (**$p < 0.05$)

such as the Wnt/β-catenin pathway, JAK/STAT3 pathway, and Smad family proteins, to regulate EMT and cell self-renewal.[6,35,36] Therefore, future studies can explore the potential interactions between Nanog and other canonical pathways in gastric cancer.

KDM5B is upregulated in many cancers, including lung cancer,[24] head and neck squamous cell carcinoma,[37] breast cancer,[38] and gastric cancer.[39] KDM5B is a major target of Nanog in regulating ESC self-renewal in mice, as identified with ChIP-seq screening.[25] In this study, we confirmed that *KDM5B* was a downstream gene positively regulated by Nanog in gastric cancer cells, suggesting a possibly conserved regulatory pattern between Nanog and KDM5B in mammals. In addition, KDM5B was positively correlated with Nanog expression levels in gastric cancer tissues and metastatic lymph node cancer tissues. In HCC, Nanog was also highly expressed in KDM5B-high cases.[40] In basal-like breast cancer, the phosphorylated KDM5B level at Ser1456 inhibited KDM5B occupancy on the promoter regions of the *Nanog* gene, leading to suppression of Nanog due to decreased H3K4me3 levels.[41] Therefore, the function of KDM5B in different cancers and molecular subtypes needs to be specifically analyzed. For the first time, this study unveiled an interaction between Nanog and KDM5B at the protein level in gastric cancer. These data suggest that not only the expression but also the post-transcriptional modification and protein interaction of KDM5B in gastric cancer should be investigated in the future.

Specific histone methylation is involved in gene reprogramming during EMT and the associated malignant features in primary prostate cells.[42] In general, methylation of H3K4 around the transcription start site (TSS) is associated with active transcription. KDM5B specifically demethylates H3K4, thereby repressing gene transcription, and in the pluripotency of ESCs, KDM5B promotes H3K4 methylation at gene promoters and enhancers.[43] In our study, KDM5B was verified to promote invasion and EMT of gastric cancer cells by decreasing H3K4me3 levels. We also found that H3K4me3 levels were lower in gastric cancer and metastatic lymph node cancer tissues than in normal gastric tissues. Enkhbaatar et al.[44] reported that KDM5B overexpression could decrease H3K4me3 levels at the TSS of microRNA-200 (miR-200) and facilitate miR-200 transcription, which downregulates the transcription factors ZEB1 and ZEB2 and results

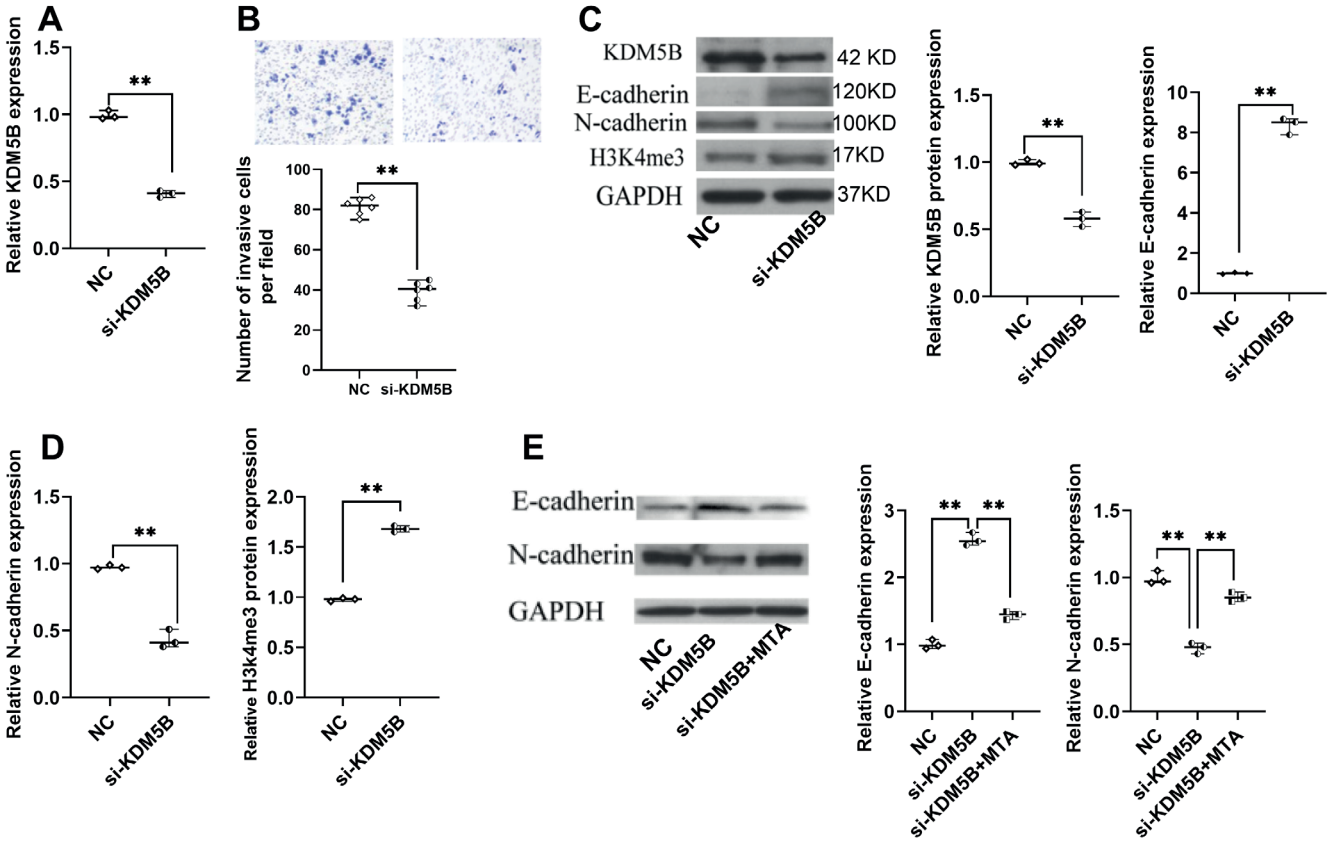

Fig. 5. H3K4me3 is involved in epithelial–mesenchymal transition (EMT) in SGC-7901 cells induced by lysine-specific demethylase 5B (KDM5B) knockdown. A. The mRNA expression of KDM5B in SGC-7901 cells with KDM5B overexpression and knockdown; B. The invasion ability of SGC-7901 cells with KDM5B knockdown; C,D. Western blotting was performed to detect E-cadherin, H3K4me3, and N-cadherin expression in SGC-7901 cells in the indicated groups. Mann–Whitney U test was performed to analyze differences between groups (**p < 0.05); E. Western blot assays were performed to evaluate E-cadherin and N-cadherin expression levels in SGC-7901 cells with KDM5B knockdown and MTA (5′-deoxy-5′-methylthioadenosine) treatment. Kruskal–Wallis test with Dunn's post hoc test was performed to analyze differences in multiple comparisons (**p < 0.05)

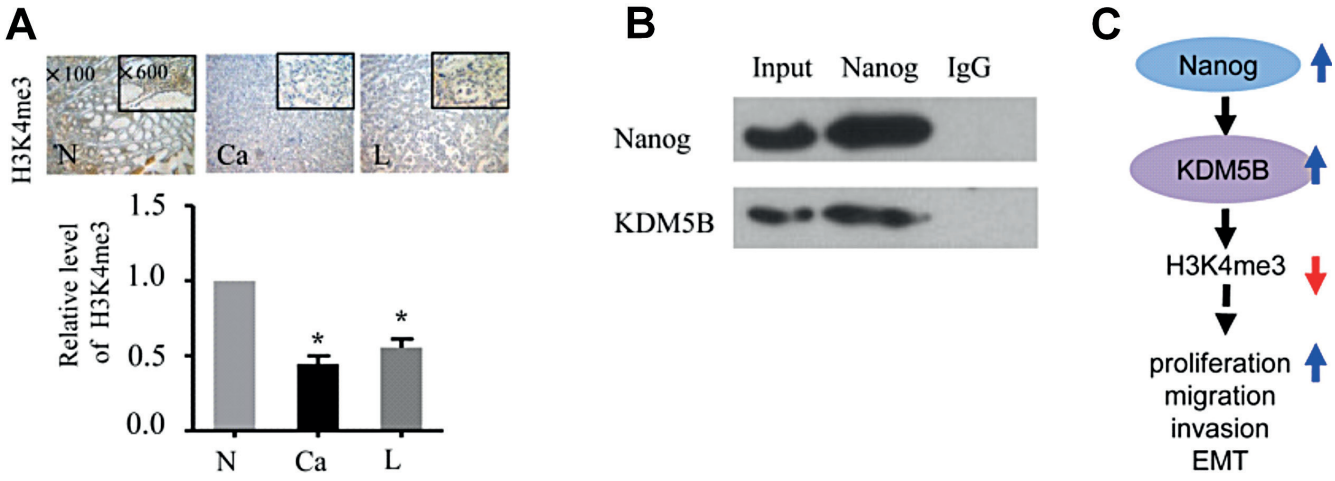

Fig. 6. Lysine-specific demethylase 5B (KDM5B) was bound to Nanog and upregulated by Nanog. A. Hematoxylin and eosin (H&E) and immunohistochemistry (IHC) staining. Above: Representative images (×100 and ×600). Below: Relative expression levels of H3K4me3 in N, Ca, and L tissues. Welch's analysis of variance (ANOVA) with Dunnett's T3 multiple-comparisons test was performed to examine differences in multiple comparisons; B. Co-immunoprecipitation (Co-IP) assay was performed to detect the interaction between Nanog and KDM5B; C. Schematic diagram of the study (**p < 0.05)

in hypoexpression of E-cadherin in lung and colon cancer cells. Wang et al.[39] reported that KDM5B expression is abnormally high in gastric cancer tissues and is entailed for the proliferation and metastasis of gastric cancer cells via regulation of the Akt pathway. It can be speculated that demethylation of H3K4me3 mediated by KDM5B in gastric cancer probably promotes EMT by affecting microRNAs, at least partially.

Limitations of the study

While our findings identify the Nanog/KDM5B/H3K4me3 pathway as a promising therapeutic target, 2 limitations should be noted. First, the restricted clinical sample size may limit the statistical power of subgroup analyses, although consistent trends were observed in the functional assays. Second, potential intratumoral heterogeneity could lead to sampling bias in the IHC results despite evaluation by 2 independent pathologists.

Conclusions

In the current study, we identified that Nanog and KDM5B were enriched in gastric cancer tissues (including metastatic lymph node cancer tissues) and TGF-β1-induced gastric cancer cells. The expression levels of Nanog in gastric cancer tissues and the corresponding metastatic lymph node cancer tissues were both positively associated with the levels of KDM5B. Loss- and gain-of-function experiments demonstrated that Nanog facilitated the progression of SGC- 7901 cells. KDM5B was a downstream gene positively regulated by Nanog. Silencing KDM5B inhibited invasion and EMT of SGC-7901 cells mediated by changes in histone H3 Lys4 trimethylation (H3K4me3) levels. Together, these findings reveal that Nanog plays a regulatory role in cell mobility by upregulating KDM5B in gastric cancer cells, which might provide new strategies for gastric cancer therapy. These data suggest that not only the expression but also the post-transcriptional modification and protein interactions of KDM5B in gastric cancer should be investigated in the future.

Supplementary data

The supplementary materials are available at: https://doi.org/10.5281/zenodo.15068902. The package contains the following files:

Supplementary Table 1. Normality assessment (Shapiro–Wilk test) for Fig. 1B and Fig. 6A.

Supplementary Table 2. Variance assessment (Brown–Forsythe test) for Fig. 1B and Fig. 6A.

Supplementary Table 3. Welch's ANOVA with Dunnett's T3 multiple-comparisons test.

Supplementary Table 4. Mann–Whitney statistical analysis.

Supplementary Table 5. Kruskal–Wallis test with Dunn's multiple-comparisons test.

Supplementary Table 6. Two-way repeated measures (RM) ANOVA with Geisser–Greenhouse correction and Šídák's post hoc test.

Data Availability Statement

The datasets supporting the findings of the current study are openly available in Zenodo at https://doi.org/10.5281/zenodo.17398533.

Consent for publication of personal information

Not applicable.

Use of AI and AI-assisted technologies

Not applicable.

ORCID iDs

Lili Ma https://orcid.org/0009-0009-4622-6404
Lin Lu https://orcid.org/0009-0003-7175-4053
Xiaohui Liu https://orcid.org/0009-0007-1761-231X
Lei Wang https://orcid.org/0009-0002-9745-8810
Yan Liu https://orcid.org/0009-0009-2814-0682
Yaqi Wang https://orcid.org/0009-0009-9201-9545
Yankun Liu https://orcid.org/0009-0001-9405-3570
Jinghua Zhang https://orcid.org/0009-0007-7122-6188
Yufeng Li https://orcid.org/0000-0002-7715-5903

References

1. Panda SK, Sahoo PK, Agarwala SK, et al. Evolution of treatment in gastric cancer: A systematic review. *J Egypt Natl Canc Inst*. 2022;34(1):12. doi:10.1186/s43046-022-00114-7
2. Ma C, Gao L, Song K, et al. Exploring the therapeutic potential of diterpenes in gastric cancer: Mechanisms, efficacy, and clinical prospects. *Biomol Biomed*. 2024;25(1):1–15. doi:10.17305/bb.2024.10887
3. Smyth EC, Nilsson M, Grabsch HI, Van Grieken NC, Lordick F. Gastric cancer. *Lancet*. 2020;396(10251):635–648. doi:10.1016/S0140-6736(20)31288-5
4. Gurung SK, Dana S, Mandal K, Mukhopadhyay P, Mondal N. Downregulation of c-Myc and p21 expression and induction of S phase arrest by naphthalene diimide derivative in gastric adenocarcinoma cells. *Chem Biol Interact*. 2019;304:106–123. doi:10.1016/j.cbi.2019.02.010
5. Lin S, Zhang Y, Hu Y, et al. Epigenetic downregulation of MUC17 by *H. pylori* infection facilitates NF-κB-mediated expression of CEACAM1-3S in human gastric cancer. *Gastric Cancer*. 2019;22(5):941–954. doi:10.1007/s10120-019-00932-0
6. Vasefifar P, Motafakkerazad R, Maleki LA, et al. Nanog as a key cancer stem cell marker in tumor progression. *Gene*. 2022;827:146448. doi:10.1016/j.gene.2022.146448
7. Grubelnik G, Boštjančič E, Pavlič A, Kos M, Zidar N. NANOG expression in human development and cancerogenesis. *Exp Biol Med (Maywood)*. 2020;245(5):456–464. doi:10.1177/1535370220905560
8. Yin W, Wang J, Jiang L, James Kang Y. Cancer and stem cells. *Exp Biol Med (Maywood)*. 2021;246(16):1791–1801. doi:10.1177/15353702211005390
9. Gupta PB, Onder TT, Jiang G, et al. Identification of selective inhibitors of cancer stem cells by high-throughput screening. *Cell*. 2009;138(4):645–659. doi:10.1016/j.cell.2009.06.034
10. Ganesh K, Massagué J. Targeting metastatic cancer. *Nat Med*. 2021;27(1):34–44. doi:10.1038/s41591-020-01195-4
11. Iv Santaliz-Ruiz LE, Xie X, Old M, Teknos TN, Pan Q. Emerging role of Nanog in tumorigenesis and cancer stem cells. *Int J Cancer*. 2014;135(12):2741–2748. doi:10.1002/ijc.28690
12. Shan J, Shen J, Liu L, et al. Nanog regulates self-renewal of cancer stem cells through the insulin-like growth factor pathway in human hepatocellular carcinoma. *Hepatology*. 2012;56(3):1004–1014. doi:10.1002/hep.25745
13. Nagata T, Shimada Y, Sekine S, et al. Prognostic significance of NANOG and KLF4 for breast cancer. *Breast Cancer*. 2014;21(1):96–101. doi:10.1007/s12282-012-0357-y

14. Meng HM, Zheng P, Wang XY, et al. Over-expression of Nanog predicts tumor progression and poor prognosis in colorectal cancer. *Cancer Biol Ther*. 2010;9(4):295–302. doi:10.4161/cbt.9.4.10666
15. Lin T, Ding YQ, Li JM. Overexpression of Nanog protein is associated with poor prognosis in gastric adenocarcinoma. *Med Oncol*. 2012;29(2):878–885. doi:10.1007/s12032-011-9860-9
16. Chu X, Di C, Chang P, et al. Lactylated histone H3K18 as a potential biomarker for the diagnosis and predicting the severity of septic shock. *Front Immunol*. 2022;12:786666. doi:10.3389/fimmu.2021.786666
17. Arrowsmith CH, Bountra C, Fish PV, Lee K, Schapira M. Epigenetic protein families: A new frontier for drug discovery. *Nat Rev Drug Discov*. 2012;11(5):384–400. doi:10.1038/nrd3674
18. Bertino EM, Otterson GA. Romidepsin: A novel histone deacetylase inhibitor for cancer. *Exp Opin Investig Dugs*. 2011;20(8):1151–1158. doi:10.1517/13543784.2011.594437
19. Cheng F, Zheng B, Wang J, et al. Histone deacetylase 10, a potential epigenetic target for therapy. *Biosci Rep*. 2021;41(6):BSR20210462. doi:10.1042/BSR20210462
20. Tumber A, Nuzzi A, Hookway ES, et al. Potent and selective KDM5 inhibitor stops cellular demethylation of H3K4me3 at transcription start sites and proliferation of MM1S myeloma cells. *Cell Chem Biol*. 2017;24(3):371–380. doi:10.1016/j.chembiol.2017.02.006
21. Horton JR, Engstrom A, Zoeller EL, et al. Characterization of a linked Jumonji domain of the KDM5/JARID1 family of histone H3 lysine 4 demethylases. *J Biol Chem*. 2016;291(6):2631–2646. doi:10.1074/jbc.M115.698449
22. Harrington J, Wheway G, Willaime-Morawek S, Gibson J, Walters ZS. Pathogenic KDM5B variants in the context of developmental disorders. *Biochim Biophys Acta Gene Regul Mech*. 2022;1865(5):194848. doi:10.1016/j.bbagrm.2022.194848
23. Du X, Zhou P, Zhang H, et al. Downregulated liver-elevated long intergenic noncoding RNA (LINC02428) is a tumor suppressor that blocks KDM5B/IGF2BP1 positive feedback loop in hepatocellular carcinoma. *Cell Death Dis*. 2023;14(5):301. doi:10.1038/s41419-023-05831-y
24. Hao F. Systemic profiling of KDM5 subfamily signature in non-small-cell lung cancer. *Int J Gen Med*. 2021;14:7259–7275. doi:10.2147/IJGM.S329733
25. Xie L, Pelz C, Wang W, et al. KDM5B regulates embryonic stem cell self-renewal and represses cryptic intragenic transcription: KDM5B regulates ESC self-renewal. *EMBO J*. 2011;30(8):1473–1484. doi:10.1038/emboj.2011.91
26. Liu Y, Zhang Y, Wu H, et al. miR-10a suppresses colorectal cancer metastasis by modulating the epithelial-to-mesenchymal transition and anoikis. *Cell Death Dis*. 2017;8(4):e2739–e2739. doi:10.1038/cddis.2017.61
27. Katsuno Y, Lamouille S, Derynck R. TGF-β signaling and epithelial–mesenchymal transition in cancer progression. *Curr Opin Oncol*. 2013;25(1):76–84. doi:10.1097/CCO.0b013e32835b6371
28. Boiani M, Schöler HR. Regulatory networks in embryo-derived pluripotent stem cells. *Nat Rev Mol Cell Biol*. 2005;6(11):872–881. doi:10.1038/nrm1744
29. Nichols J, Zevnik B, Anastassiadis K, et al. Formation of pluripotent stem cells in the mammalian embryo depends on the POU transcription factor Oct4. *Cell*. 1998;95(3):379–391. doi:10.1016/S0092-8674(00)81769-9
30. Basati G, Mohammadpour H, Emami Razavi A. Association of high expression levels of SOX2, NANOG, and OCT4 in gastric cancer tumor tissues with progression and poor prognosis. *J Gastrointest Cancer*. 2020;51(1):41–47. doi:10.1007/s12029-018-00200-x
31. Guan T, Zhang Y, Li S, et al. Discovery of an efficacious KDM5B PROTAC degrader GT-653 upregulating *IFN* response genes in prostate cancer. *Eur J Med Chem*. 2024;272:116494. doi:10.1016/j.ejmech.2024.116494
32. Li CY, Wang W, Leung CH, Yang GJ, Chen J. KDM5 family as therapeutic targets in breast cancer: Pathogenesis and therapeutic opportunities and challenges. *Mol Cancer*. 2024;23(1):109. doi:10.1186/s12943-024-02011-0
33. Sun C, Sun L, Jiang K, et al. NANOG promotes liver cancer cell invasion by inducing epithelial–mesenchymal transition through NODAL/SMAD3 signaling pathway. *Int J Biochem Cell Biol*. 2013;45(6):1099–1108. doi:10.1016/j.biocel.2013.02.017
34. Najafzadeh B, Asadzadeh Z, Motafakker Azad R, et al. The oncogenic potential of NANOG: An important cancer induction mediator. *J Cell Physiol*. 2021;236(4):2443–2458. doi:10.1002/jcp.30063
35. Suzuki A, Raya Á, Kawakami Y, et al. Nanog binds to Smad1 and blocks bone morphogenetic protein-induced differentiation of embryonic stem cells. *Proc Natl Acad Sci U S A*. 2006;103(27):10294–10299. doi:10.1073/pnas.0506945103
36. Xu RH, Sampsell-Barron TL, Gu F, et al. NANOG is a direct target of TGFβ/activin-mediated SMAD signaling in human ESCs. *Cell Stem Cell*. 2008;3(2):196–206. doi:10.1016/j.stem.2008.07.001
37. Huang D, Qiu Y, Li G, et al. KDM5B overexpression predicts a poor prognosis in patients with squamous cell carcinoma of the head and neck. *J Cancer*. 2018;9(1):198–204. doi:10.7150/jca.22145
38. Jose A, Kulkarni P, Kumar NA, et al. Abacavir enhances the efficacy of doxorubicin via inhibition of histone demethylase KDM5B in breast cancer. *Sci Rep*. 2025;15(1):28531. doi:10.1038/s41598-025-13845-z
39. Wang Z, Tang F, Qi G, et al. KDM5B is overexpressed in gastric cancer and is required for gastric cancer cell proliferation and metastasis. *Am J Cancer Res*. 2015;5(1):87–100. PMID:25628922. PMCID:PMC4300698.
40. Wang X, Oishi N, Shimakami T, et al. Hepatitis B virus X protein induces hepatic stem cell-like features in hepatocellular carcinoma by activating KDM5B. *World J Gastroenterol*. 2017;23(18):3252. doi:10.3748/wjg.v23.i18.3252
41. Yeh IJ, Esakov E, Lathia JD, Miyagi M, Reizes O, Montano MM. Phosphorylation of the histone demethylase KDM5B and regulation of the phenotype of triple negative breast cancer. *Sci Rep*. 2019;9(1):17663. doi:10.1038/s41598-019-54184-0
42. Ke XS, Qu Y, Cheng Y, et al. Global profiling of histone and DNA methylation reveals epigenetic-based regulation of gene expression during epithelial to mesenchymal transition in prostate cells. *BMC Genomics*. 2010;11(1):669. doi:10.1186/1471-2164-11-669
43. Kidder BL, Hu G, Zhao K. KDM5B focuses H3K4 methylation near promoters and enhancers during embryonic stem cell self-renewal and differentiation. *Genome Biol*. 2014;15(2):R32. doi:10.1186/gb-2014-15-2-r32
44. Enkhbaatar Z, Terashima M, Oktyabri D, et al. KDM5B histone demethylase controls epithelial–mesenchymal transition of cancer cells by regulating the expression of the microRNA-200 family. *Cell Cycle*. 2013;12(13):2100–2112. doi:10.4161/cc.25142

Let-7e-5p promotes cardiac hypertrophy by targeting *LBH* and regulating the IGF–PI3K–AKT signaling pathway

Shushu Yu[1,A–D,F], Mingliang Wang[2,B,C,E,F], Yun Xie[2,B,C,E,F], Bo Wang[1,3,B,C,E,F], Yawei Xu[3,1,A,B,E,F]

[1] School of Medicine, Tongji University, Shanghai, China
[2] Department of Cardiology, Putuo District People's Hospital, Shanghai, China
[3] Department of Cardiology, Shanghai Tenth People's Hospital, Shanghai, China

A – research concept and design; B – collection and/or assembly of data; C – data analysis and interpretation; D – writing the article; E – critical revision of the article; F – final approval of the article

Advances in Clinical and Experimental Medicine, ISSN 1899–5276 (print), ISSN 2451–2680 (online) *Adv Clin Exp Med*. 2026;35(7):1199–1213

Address for correspondence
Yawei Xu
E-mail: xuyawei@tongji.edu.cn

Funding sources
None declared

Conflict of interest
None declared

Received on July 11, 2025
Reviewed on September 11, 2025
Accepted on September 26, 2025

Published online on July 30, 2026

Abstract

Background. Cardiac hypertrophy refers to the compensatory response of the heart to various physiological or pathological stimuli in order to maintain its function. Let-7e-5p has been reported to be upregulated in patients with cardiac hypertrophy.

Objectives. This study aimed to investigate the role of let-7e-5p in the progression of cardiac hypertrophy using animal and cell models.

Materials and methods. Peripheral blood was collected from patients with cardiac hypertrophy and healthy controls to detect let-7e-5p expression via reverse transcription quantitative polymerase chain reaction (RT-qPCR). An aortic banding (AB)-induced cardiac hypertrophy rat model was established to explore let-7e-5p expression in vivo. Antagomir let-7e-5p was used to investigate the effects of let-7e-5p silencing on cardiac hypertrophy progression in an AB-induced rat model. Angiotensin II (Ang II) was used to induce hypertrophy in H9c2 rat cardiomyocytes in vitro. The downstream regulatory mechanism of let-7e-5p was investigated in H9c2 cells.

Results. We first examined and verified that let-7e-5p was upregulated in blood samples from patients with hypertrophic cardiomyopathy (HCM) compared to healthy controls and showed good diagnostic performance according to receiver operating characteristic (ROC) analysis. In vivo, let-7e-5p was overexpressed in the heart tissues of AB-induced cardiac hypertrophy rats. Let-7e-5p deficiency alleviated AB surgery-induced cardiac hypertrophy in rat models. In vitro, let-7e-5p expression was higher in Ang II-induced H9c2 rat cardiomyocytes. Let-7e-5p inhibition reversed the Ang II-induced increase in cardiomyocyte size and the upregulation of ANP, BNP, and β-MHC expression, whereas let-7e-5p overexpression showed the opposite effects. Mechanistically, limb-bud and heart (*LBH*) was identified as a target of let-7e-5p, and *LBH* overexpression reversed the promotive effects of let-7e-5p on hypertrophy in Ang II-treated H9c2 cells. IGF–PI3K–AKT signaling was activated in Ang II-treated H9c2 cells, and let-7e-5p silencing suppressed its activation by targeting *LBH*. The IGF1R inhibitor PQ401 reversed the enhancement of H9c2 hypertrophy induced by let-7e-5p upregulation or *LBH* silencing.

Conclusions. Let-7e-5p promotes cardiac hypertrophy by targeting *LBH* and regulating the IGF–PI3K–AKT signaling pathway, which may provide novel insights into targeted therapy.

Key words: Let-7e-5p, cardiac hypertrophy, LBH protein, IGF–PI3K–AKT signaling pathway, microRNA regulation

Cite as
Yu S, Wang M, Xie Y, Wang B, Xu Y. Let-7e-5p promotes cardiac hypertrophy by targeting *LBH* and regulating the IGF–PI3K–AKT signaling pathway. *Adv Clin Exp Med*. 2026;35(7):1199–1213. doi:10.17219/acem/211410

DOI
10.17219/acem/211410

Copyright
Copyright by Author(s)
This is an article distributed under the terms of the Creative Commons Attribution 3.0 Unported (CC BY 3.0) (https://creativecommons.org/licenses/by/3.0/)

Highlights

- Let-7e-5p aggravates aortic banding-caused cardiac hypertrophy in rats.
- Let-7e-5p promotes Ang II-stimulated cardiomyocyte hypertrophy.
- LBH is targeted by Let-7e-5p in H9c2 cardiomyocytes.
- Let-7e-5p enhances Ang II-stimulated cardiomyocyte hypertrophy by targeting LBH.
- Let-7e-5p facilitates the activation of the IGF-PI3K-Akt pathway via LBH.

Background

Cardiac hypertrophy refers to the compensatory response of the heart to various physiological or pathological stimuli in order to maintain its function. This process is accompanied by an increase in cardiomyocyte size, changes in cardiomyocyte morphology, modifications in gene expression, and cytoskeletal remodeling.[1] Pathological cardiac hypertrophy can be induced by various factors, such as hypertension, pressure or volume overload, drug toxicity, and others, leading to the development of heart failure and affecting the clinical outcomes and quality of life of patients.[2,3] Currently, classical drugs, including β-adrenergic receptor blockers and renin–angiotensin–aldosterone system inhibitors, are commonly used for the treatment of hypertrophic cardiomyopathy (HCM). However, their therapeutic effects remain limited due to the high incidence of heart failure.[4,5] Thus, the exploration of novel therapeutic targets is needed to develop effective treatment strategies.

MicroRNAs (miRNAs) are endogenous small non-coding RNAs (~22 nucleotides) that regulate the expression of protein-coding genes at the post-transcriptional level.[6] MiRNAs also serve as important regulators of biological processes such as cell proliferation, differentiation, and survival. Substantial evidence has revealed that dysregulated miRNAs may affect the development of diverse cardiovascular diseases, including pathological cardiac hypertrophy.[7] For example, miR-30d has been reported to be downregulated in cardiac hypertrophy both in vivo and in vitro, and its overexpression attenuates pathological cardiomyocyte hypertrophy in vitro and in vivo.[8] MiR-27b-3p is highly expressed during the process of cardiac hypertrophy, and its depletion significantly ameliorates cardiac fibrosis, inflammation, and hypertrophy in TAC-induced mice by targeting *FGF1*.[9] MiR-214 is highly expressed in the myocardial tissue of Ang II-stimulated mice. Its overexpression has been shown to downregulate *SIRT3*, thereby inducing mitochondrial dysfunction and contributing to cardiac hypertrophy.[10] Let-7e-5p has previously been reported to be highly expressed in the blood of patients with congestive heart failure, suggesting its role in heart disease.[11] Bioinformatics analyses have also revealed that let-7e-5p is a biologically meaningful miRNA involved in the regulation of molecular mechanisms underlying cardiac hypertrophy.[12] Additionally, a previous study demonstrated that let-7e-5p is upregulated in isoproterenol (ISO)-induced cardiac hypertrophy in rats. However, the function and precise mechanisms of let-7e-5p in cardiac hypertrophy remain unclear.

Limb-bud and heart (*LBH*) is a protein-coding gene involved in embryonic growth and heart development.[13] Aberrant expression of *LBH* is closely linked to the progression of a variety of cardiovascular diseases. For example, *LBH* is upregulated in response to transforming growth factor (TGF)-β1 stimulation in cardiac fibroblasts, and ectopic expression of *LBH* promotes the activation of cardiac fibroblasts under hypoxic conditions, suggesting its potential as a target for cardiac repair and antifibrotic therapy.[14,15] Additionally, *LBH* has also been suggested to protect against myocardial ischemia/reperfusion (I/R) injury by reducing cardiomyocyte apoptosis and ferroptosis. Bioinformatics analysis suggests that *LBH* is a potential target of let-7e-5p, and *LBH* has been shown to be downregulated in the heart tissue of patients with HCM based on the GSE89714 dataset from the Gene Expression Omnibus (GEO) database (https://www.ncbi.nlm.nih.gov/geo/query/acc.cgi?acc=GSE89714). The regulatory mechanism between let-7e-5p and *LBH* still requires further investigation.

Objectives

The current study aimed to validate the expression of let-7e-5p in blood samples from human patients and to explore the potential function and downstream mechanisms of let-7e-5p in cardiac hypertrophy using aortic banding (AB)-induced rat models in vivo and angiotensin II (Ang II)-induced rat cardiomyocytes (H9c2) in vitro. We hypothesized that let-7e-5p exerts detrimental effects on cardiac hypertrophy by targeting *LBH*.

Material and methods

Animals

Sprague Dawley rats (200 g; Vital River, Beijing, China) were housed at 22 ±3°C under a 12 h/12 h light/dark cycle.

Aortic banding surgery was performed to induce cardiac hypertrophy in rats as previously described.[16] Briefly, rats were anesthetized with pentobarbital sodium (50 mg/kg; MilliporeSigma, St. Louis, USA) via intraperitoneal injection. Next, the aorta was exposed by opening the left thoracic intercostal space between the 2nd and 3rd ribs and then ligated with a 7-0 silk suture and a 26- or 27-gauge needle. After gently withdrawing the needle, the aorta was constricted. Rats in the sham group underwent the same surgical procedure, but no aortic ligation was performed. To explore the effects of let-7e-5p on cardiac hypertrophy in vivo, chemically modified antisense oligonucleotides (antagomirs) targeting let-7e-5p and the negative control (NC) were synthesized by GenePharma (Shanghai, China). Rats in the model group were injected daily with antagomir let-7e-5p or antagomir NC via the tail vein for 3 days beginning 24 h after surgery. The body weight of the rats was measured throughout the experiment. At the end of the experiment, rats were euthanized by inhalation of 5% isoflurane, and their hearts and tibias were collected and measured. The ratios of heart weight to body weight (HW/BW) and heart weight to tibia length (HW/TL) were calculated. Ventricular tissue was harvested and either frozen at –80°C or embedded in paraffin.

All procedures were approved by the Ethics Committee of Shanghai Tenth People's Hospital, Tongji University (Shanghai, China; approval No. 2023-0721L issued on July 21, 2023) and were conducted in strict accordance with the recommendations of the National Institutes of Health (NIH) Guide for the Care and Use of Laboratory Animals. The study is reported in accordance with the ARRIVE (Animal Research: Reporting of In Vivo Experiments) guidelines.[17]

Echocardiography and histological analyses

Echocardiography was performed in rats as previously described.[18] After light general anesthesia, left ventricular (LV) functional parameters were monitored and recorded. Fractional shortening (FS%) and ejection fraction (EF%) were subsequently calculated.

Paraffin-embedded heart tissues from each group of rats were subjected to hematoxylin and eosin (H&E) staining using a Hematoxylin and Eosin Staining Kit (Beyotime, Shanghai, China) according to the manufacturer's instructions. Image-Pro Plus software (Media Cybernetics, Bethesda, USA) was used to analyze cardiomyocyte size.

Immunohistochemistry

Paraffin-embedded rat heart tissues were sectioned, dewaxed in xylene, and rehydrated through graded alcohol solutions. After antigen retrieval, the sections were rinsed with phosphate-buffered saline (PBS), treated with 3% H_2O_2 solution, and then incubated with primary antibodies against atrial natriuretic peptide (ANP; PA5-29559, 1:200, Thermo Fisher Scientific, Waltham, USA), B-type natriuretic peptide (BNP; PA5-96084, 1:200; Thermo Fisher Scientific), and beta-myosin heavy chain (β-MHC; PA5-100023, 1:200, Thermo Fisher Scientific) at 37°C for 2 h. The sections were then rinsed 3 times with PBS and incubated with secondary antibodies for 60 min at room temperature. After staining with diaminobenzidine (DAB) and hematoxylin, the sections were observed and imaged under a BX51 light microscope (Olympus Corp., Tokyo, Japan).

Clinical samples collection

A total of 30 patients with HCM and 30 healthy controls matched for age and sex were enrolled in this study. The inclusion criteria were as follows: 1) age between 18 and 75 years; 2) diagnosis confirmed by echocardiography, electrocardiography, and magnetic resonance imaging (MRI) by 2 cardiologists, with left ventricular maximal wall thickness (LVMWT) >15 mm; and 3) provision of written informed consent and willingness to participate in the study. The exclusion criteria were as follows: 1) diabetes mellitus, hyperlipidemia, infectious diseases, cancer, or other severe medical conditions; 2) pregnancy; and 3) a history of transplantation. Venous blood was collected at enrollment and centrifuged at 2,000 × g for 10 min to obtain serum.

All participants signed written informed consent before enrollment. The study was conducted in full accordance with the principles outlined in the Declaration of Helsinki (2013 revision).

Cell culture and treatment

Rat cardiomyocytes (H9c2) were obtained from Procell (Wuhan, China). Cells were cultured in Dulbecco's modified Eagle's medium (DMEM) containing 10% fetal bovine serum (FBS; Gibco, Waltham, USA) and 1% penicillin/streptomycin (P/S; MilliporeSigma) at 37°C in a humidified atmosphere containing 5% CO_2. To induce cardiomyocyte hypertrophy in vitro, H9c2 cells were exposed to 1 μM Ang II (MilliporeSigma) for 48 h.

Cell transfection

The let-7e-5p inhibitor and mimics, NC inhibitor, and NC mimics were synthesized by RiboBio Co. (Guangzhou, China). For *LBH* overexpression or knockdown, pcDNA3.1/*LBH* (oe-*LBH*), sh-*LBH*, and the corresponding empty control vectors (oe-NC and sh-NC) were provided by GenePharma. H9c2 cells were transfected with these vectors using Lipofectamine 3000 reagent (Invitrogen, Waltham, USA) for 48 h.

Reverse transcription quantitative PCR

Total RNA was isolated from human blood samples and rat heart tissues using TRIzol Reagent (Thermo Fisher Scientific). RNA was then reverse-transcribed using the TaqMan miRNA Reverse Transcription Kit for miRNAs and

an appropriate cDNA synthesis kit for mRNAs. Reverse transcription quantitative polymerase chain reaction (RT-qPCR) was performed using a SYBR Green I Master Mix kit (Invitrogen) on a 7500 Real-Time PCR System (Applied Biosystems, Waltham, USA). Relative gene expression levels were calculated using the $2^{-\Delta\Delta Ct}$ method, with *U6* serving as the internal control for miRNAs and *GAPDH* serving as the internal control for mRNAs.

Western blot

Total protein was extracted from H9c2 cardiomyocytes and rat cardiac tissues using radioimmunoprecipitation assay (RIPA) buffer (Epizyme, Shanghai, China), followed by determination of protein concentration using a bicinchoninic acid (BCA) assay kit. Sodium dodecyl sulfate–polyacrylamide gel electrophoresis (SDS-PAGE) was then used for protein separation, and the proteins were subsequently transferred onto polyvinylidene difluoride (PVDF) membranes (MilliporeSigma). After incubation with primary antibodies (Thermo Fisher Scientific) overnight at 4°C, the membranes were incubated with a secondary antibody (31460; 1:10,000; Thermo Fisher Scientific) at room temperature for 60 min. Enhanced chemiluminescence (ECL) was then used for protein band visualization, and ImageJ software v. 6.1.0 (National Institutes of Health (NIH), Bethesda, USA) was used for data analysis.

Immunofluorescence

Immunofluorescence staining was used to evaluate the size of H9c2 cardiomyocytes. Briefly, H9c2 cells were collected 48 h after the indicated transfection and then stimulated with Ang II. After fixation with formaldehyde and permeabilization with Triton X-100 (0.1%; Beyotime), the cells were incubated with anti-α-actinin antibody (ab137346; 1:1,000; Abcam, Cambridge, UK) at 4°C overnight and then incubated with the secondary antibody (ab150077; 1:1,000; Abcam) the following day. Cell nuclei were stained with 4′,6-diamidino-2-phenylindole (DAPI). Images were captured using a fluorescence microscope (Olympus IX73; Olympus Corp.). The cell surface area was quantified using ImageJ software (NIH).

Luciferase reporter assays

The wild-type (WT) or mutant (MUT) *LBH* 3′UTR sequences containing the let-7e-5p binding site were cloned into the pmirGLO reporter vector, generating pmirGLO-*LBH*-WT and pmirGLO-*LBH*-MUT constructs. H9c2 cardiomyocytes were co-transfected with the NC inhibitor or let-7e-5p inhibitor together with pmirGLO-*LBH*-WT or pmirGLO-*LBH*-MUT using Lipofectamine 3000 (Invitrogen). After 48 h, luciferase activity was measured using a dual-luciferase reporter assay system (Promega, Madison, USA) according to the manufacturer's protocol.

RNA pulldown assay

Biotinylated let-7e-5p provided by RiboBio was incubated with cardiomyocytes for 48 h. Afterward, H9c2 cardiomyocytes were harvested and lysed, followed by incubation with beads (MilliporeSigma). After washing, the bound RNA was purified, and RT-qPCR was performed to analyze the enrichment of candidate mRNAs.

Statistical analyses

Results were analyzed using SPSS v. 17.0 (SPSS Inc., Chicago, USA) and are presented as mean ± standard deviation (SD). Each experiment was independently performed at least 3 times, with at least 3 biological samples included in each assay. Normality was evaluated using the Shapiro–Wilk test, with $p > 0.05$ indicating a normal distribution. Homogeneity of variance was assessed using the F test for comparisons between 2 groups and the Brown–Forsythe test or Levene's test for comparisons among 3 or more groups.

If the data conformed to a normal distribution and exhibited homogeneous variance, comparisons between 2 groups or among multiple groups were performed using a two-tailed unpaired Student's t-test or one-way analysis of variance (ANOVA) followed by Tukey's post hoc test. Two-way ANOVA followed by Bonferroni's post hoc test was used for comparisons involving 2 independent variables. If the data did not conform to a normal distribution or exhibited heterogeneous variance, the Mann–Whitney U test or Welch's t-test was applied for comparisons between 2 groups, and the Kruskal–Wallis test followed by Dunn's post hoc test was applied for comparisons among 3 or more groups. Receiver operating characteristic (ROC) curves were used to assess the diagnostic performance of let-7e-5p in cardiac hypertrophy. A $p < 0.05$ was considered statistically significant.

Results

Let-7e-5p aggravates aortic banding-induced cardiac hypertrophy in rats

The let-7e-5p level in patients with HCM (n = 30) and healthy control individuals (n = 30) was detected using RT-qPCR. It was found to be dramatically upregulated in cardiac hypertrophy (Fig. 1A). As shown by the ROC curve, let-7e-5p may serve as a robust biomarker for the diagnosis of cardiac hypertrophy, with an area under the curve (AUC) of 0.875 ($p < 0.001$; 95% confidence interval (95% CI): 0.791–0.959) (Fig. 1B). Overall, let-7e-5p is aberrantly overexpressed in cardiac hypertrophy and may have high predictive value for the diagnosis of cardiac hypertrophy.

Aortic banding surgery was performed in rats to induce cardiac hypertrophy. We found that let-7e-5p was upregulated in the model group and was successfully silenced

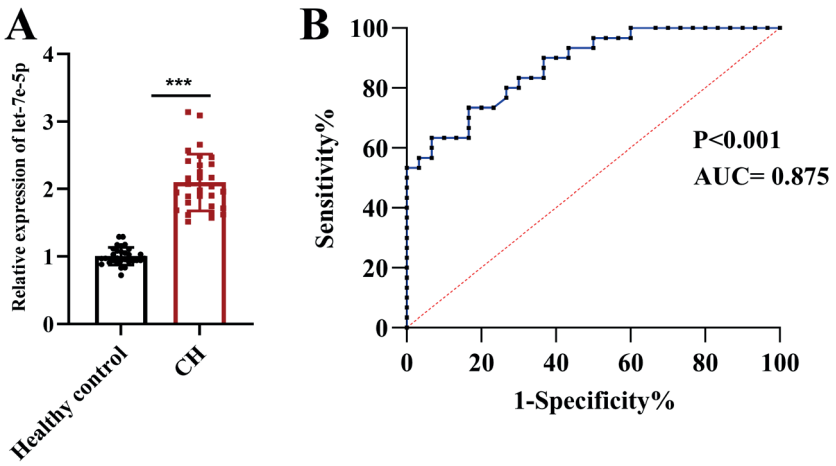

Fig. 1. Let-7e-5p is highly expressed in patients with cardiac hypertrophy. A. Reverse transcription quantitative polymerase chain reaction (RT-qPCR) was performed to detect let-7e-5p levels in the serum of patients with cardiac hypertrophy (n = 30) and healthy controls (n = 30 per group; ***p < 0.001, Welch's t-test); B. Receiver operating characteristic (ROC) curve analysis was used to evaluate the predictive value of let-7e-5p for the diagnosis of cardiac hypertrophy (p < 0.001; 95% confidence interval (95% CI): 0.791–0.959)

by the administration of antagomir let-7e-5p (Supplementary Fig. 1A). Next, we measured heart weight (HW), body weight (BW), and tibial length (TL) in each group of rats. We found that the hypertrophy indices HW/BW and HW/TL were both elevated in the model group and were reversed by antagomir let-7e-5p treatment, indicating that its deficiency significantly attenuated pathological cardiac enlargement in rats (Fig. 2A,B).

Hematoxylin and eosin staining showed a significant increase in heart size in the model group, accompanied

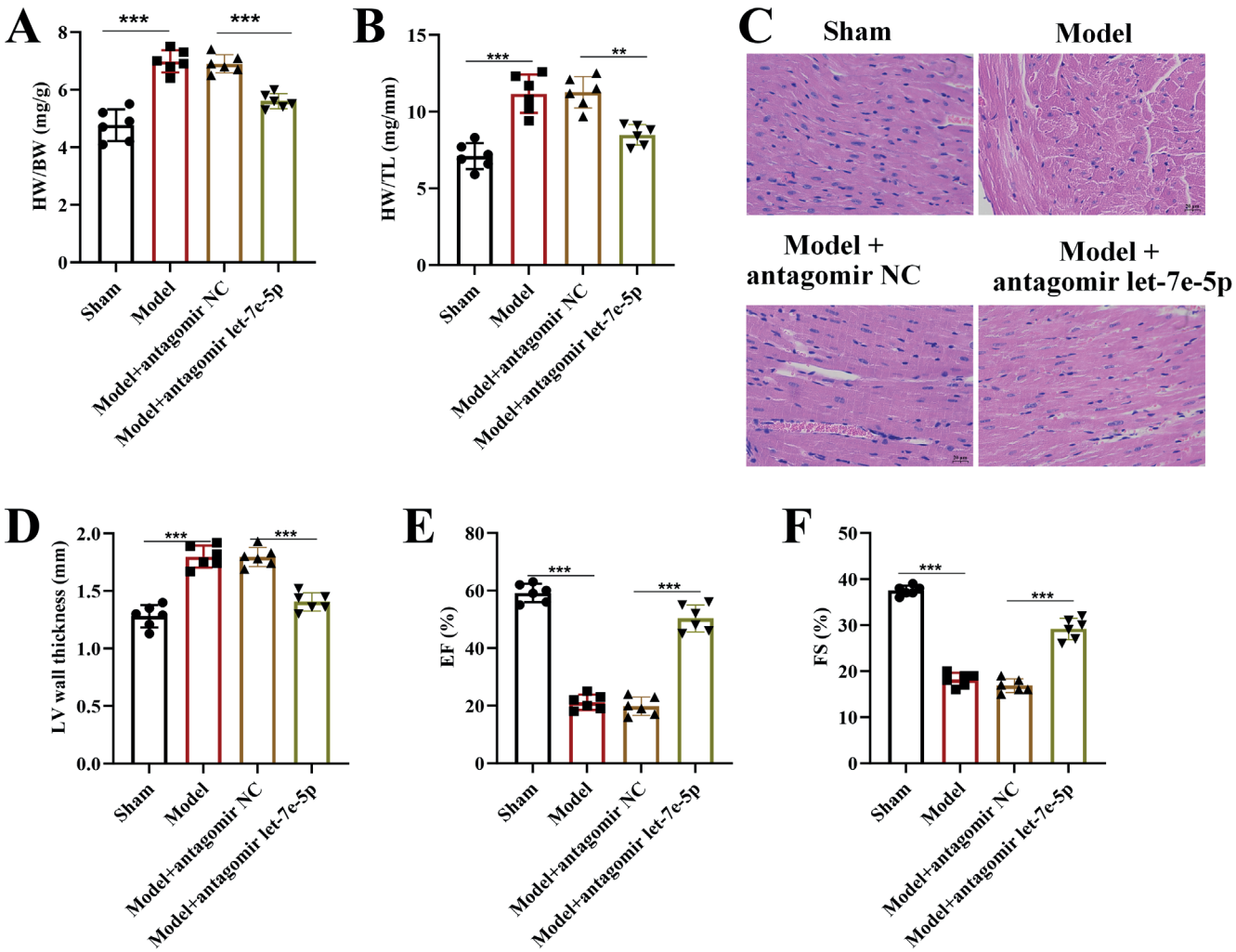

Fig. 2. Let-7e-5p deficiency alleviates aortic banding (AB)-induced cardiac dysfunction in rats. A. HW/BW; B. HW/TL. Hematoxylin and eosin (H&E) staining was performed to analyze histological changes in rat hearts (C), and left ventricular (LV) wall thickness was quantified (D). Echocardiography was performed to evaluate cardiac function in rats. Ejection fraction (EF%) (E) and fractional shortening (FS%) (F) were measured in each group (***p < 0.001)

HW – heart weight; BW – body weight; TL – tibial length; NC – negative control.

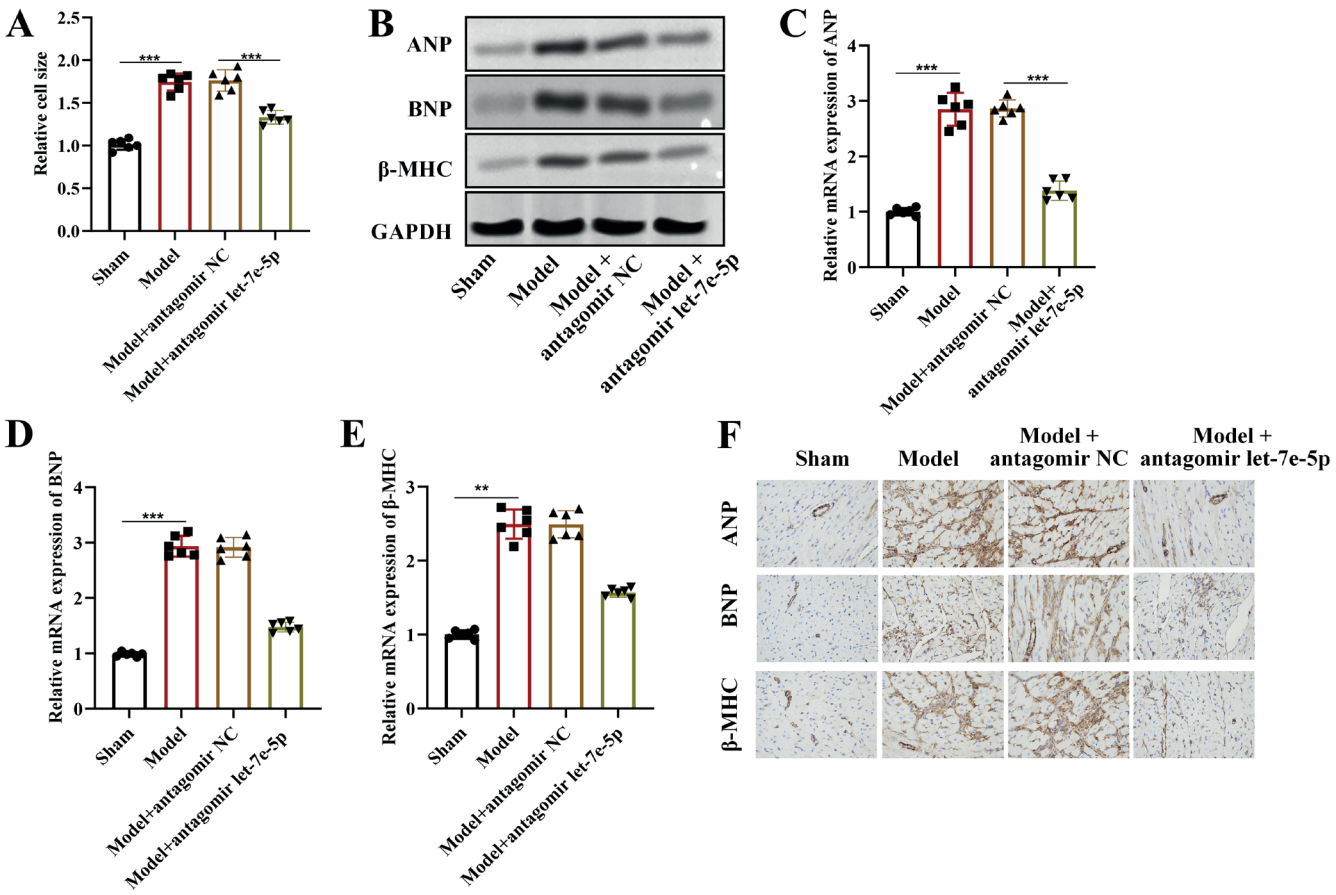

Fig. 3. Let-7e-5p promotes aortic banding (AB)-induced cardiomyocyte hypertrophy in rats. A. Quantification of cardiomyocyte size in rat heart tissues from each group; B. Western blot analysis of the protein levels of cardiac hypertrophy markers (ANP, BNP, and β-MHC) in rat hearts. Reverse transcription quantitative polymerase chain reaction (RT-qPCR) was used to detect ANP (C), BNP (D), and β-MHC (E) mRNA expression in each group; F. Immunohistochemical analysis was used to detect the expression levels of cardiac hypertrophy markers (ANP, BNP, and β-MHC) in rat hearts from each group (**p < 0.01, ***p < 0.001)

NC – negative control.

by histological changes such as tissue damage and fibrosis, whereas antagomir let-7e-5p treatment reduced heart size, LV wall thickness, and the pathological changes induced by AB surgery (Fig. 2C,D). Echocardiographic analysis showed that the EF% and FS% of rats in the model group were both decreased relative to the sham group, whereas administration of antagomir let-7e-5p significantly restored EF% and FS% levels (Fig. 2E,F).

Similarly, we observed an increase in cardiomyocyte size in response to AB surgery, and antagomir let-7e-5p significantly inhibited cardiomyocyte enlargement in the model group (Fig. 3A). Furthermore, we detected the expression levels of cardiac hypertrophy markers in rat hearts. According to western blot analysis, the elevated expression of ANP, BNP, and β-MHC proteins observed in the model group was markedly reduced by antagomir let-7e-5p treatment (Fig. 3B). RT-qPCR results also indicated that the increased mRNA levels of ANP, BNP, and β-MHC induced by AB surgery were restored by administration of antagomir let-7e-5p in rat hearts (Fig. 3C–E). Consistently, immunohistochemical analysis showed enhanced staining intensity of ANP, BNP, and β-MHC in rat hearts from the model group, which was reduced by antagomir let-7e-5p treatment (Fig. 3F).

Let-7e-5p promotes Ang II-stimulated cardiomyocyte hypertrophy

Rat cardiomyocytes (H9c2) were treated with Ang II to induce hypertrophy in vitro. The transfection efficiency of the let-7e-5p inhibitor or mimics was confirmed using RT-qPCR (Fig. 4A). The let-7e-5p level was increased in Ang II-treated H9c2 cells and was restored by transfection with the let-7e-5p inhibitor (Fig. 4B). According to the immunofluorescence staining results, the increase in cardiomyocyte size induced by Ang II treatment was significantly reversed by let-7e-5p inhibition (Fig. 4C,D). Meanwhile, we demonstrated that the protein levels of ANP, BNP, and β-MHC, which were upregulated by Ang II treatment, were reversed by let-7e-5p silencing in H9c2 cells (Fig. 4E).

Moreover, we explored the effects of let-7e-5p overexpression on Ang II-stimulated cardiomyocytes to further confirm the role of let-7e-5p. The transfection efficiency of let-7e-5p mimics was verified with RT-qPCR

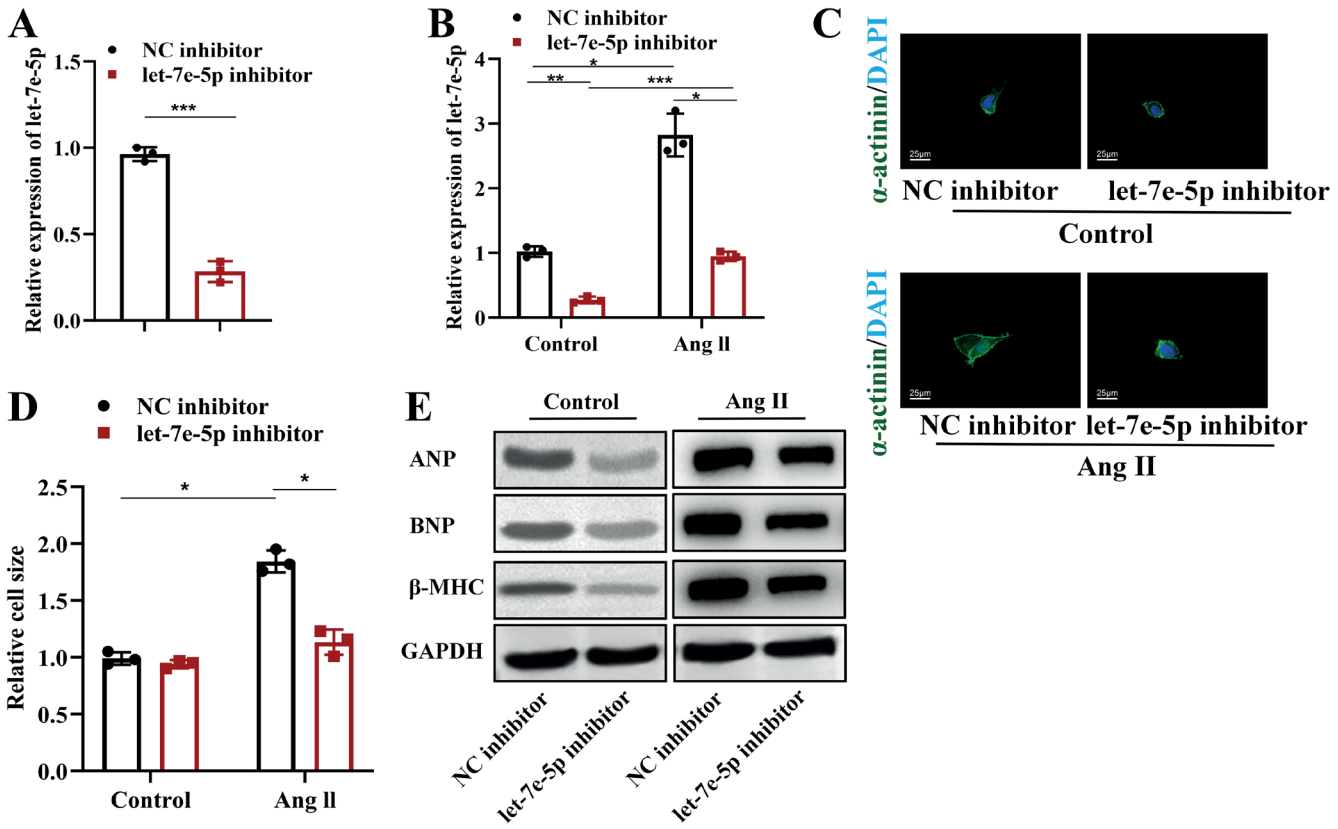

Fig. 4. Let-7e-5p inhibition represses angiotensin II (Ang II)-stimulated cardiomyocyte hypertrophy. A. Reverse transcription quantitative polymerase chain reaction (RT-qPCR) was performed to measure let-7e-5p expression after transfection with let-7e-5p inhibitor or negative control (NC) inhibitor; B. RT-qPCR was used to detect let-7e-5p expression in H9c2 cells treated with or without Ang II and transfected with NC inhibitor or let-7e-5p inhibitor; C. The effects of let-7e-5p inhibition on the size of H9c2 cells treated with or without Ang II were evaluated using immunofluorescence staining for α-actinin and DAPI; D. Quantification of H9c2 cell size; E. Western blot analysis of the effects of let-7e-5p inhibition on the protein levels of ANP, BNP, and β-MHC in H9c2 cells treated with or without Ang II (*$p < 0.05$, **$p < 0.01$, ***$p < 0.001$)

(Fig. 5A). We found that transfection with let-7e-5p mimics significantly increased let-7e-5p levels in H9c2 cells in the presence or absence of Ang II exposure (Fig. 5B). Immunofluorescence staining revealed that the increase in cardiomyocyte size induced by Ang II treatment was further enhanced by let-7e-5p upregulation (Fig. 5C,D). Consistently, the protein levels of ANP, BNP, and β-MHC, which were upregulated by Ang II, were further enhanced by let-7e-5p overexpression (Fig. 5E). Overall, let-7e-5p enhances Ang II-stimulated cardiomyocyte hypertrophy.

LBH is targeted by Let-7e-5p in H9c2 cardiomyocytes

The downstream targets of rno-let-7e-5p were explored using the TargetScan database (https://www.targetscan.org/vert_80). A total of 2,022 genes were predicted to contain potential binding sites for let-7e-5p. We then explored dysregulated genes in cardiac hypertrophy based on analysis of the GSE89714 dataset from the GEO database, and 311 downregulated genes were identified. Next, we intersected the downregulated genes identified in cardiac hypertrophy with the predicted target genes of let-7e-5p, yielding 21 genes for further analysis (Supplementary Fig. 2A), including *RBFOX1*, *LBH*, *ATP2A2*, *FRK*, *CCDC141*, *ADRB1*, *NCEH1*, *MEIS1*, *VSNL1*, *SCUBE3*, *TMEM178B*, *GRIN3A*, *NFXL1*, *HOOK1*, *SCD*, *SYT2*, *HAS2*, *B3GNT7*, *CADM2*, *GRIK2*, and *VASH2*. We then examined the expression of the candidate mRNAs in H9c2 cells following let-7e-5p inhibition, and *LBH*, *ADRB1*, and *HOOK1* were found to be upregulated in H9c2 cells after let-7e-5p silencing (Supplementary Fig. 2B). Next, we evaluated the expression of these 3 candidate genes in cardiac tissues from rats in the sham and model groups. *LBH* was found to be downregulated in AB-induced rats, whereas *ADRB1* and *HOOK1* were both upregulated, and the expression of all 3 genes was significantly increased by antagomir let-7e-5p treatment (Supplementary Fig. 2C–E). The results for *ADRB1* and *HOOK1* were not consistent with the database analysis. Additionally, previous studies have identified *ADRB1* and *HOOK1* as potential biomarkers of cardiac hypertension.[19,20] Therefore, *LBH* was selected as a potential target of let-7e-5p in the regulation of cardiac hypertrophy. The expression pattern of *LBH* in the GSE89714 dataset is shown in Fig. 6A, demonstrating that *LBH* was expressed at low levels in the heart tissue of patients with HCM. We then detected *LBH* expression in rat cardiac tissues from each group using immunohistochemistry (IHC) and

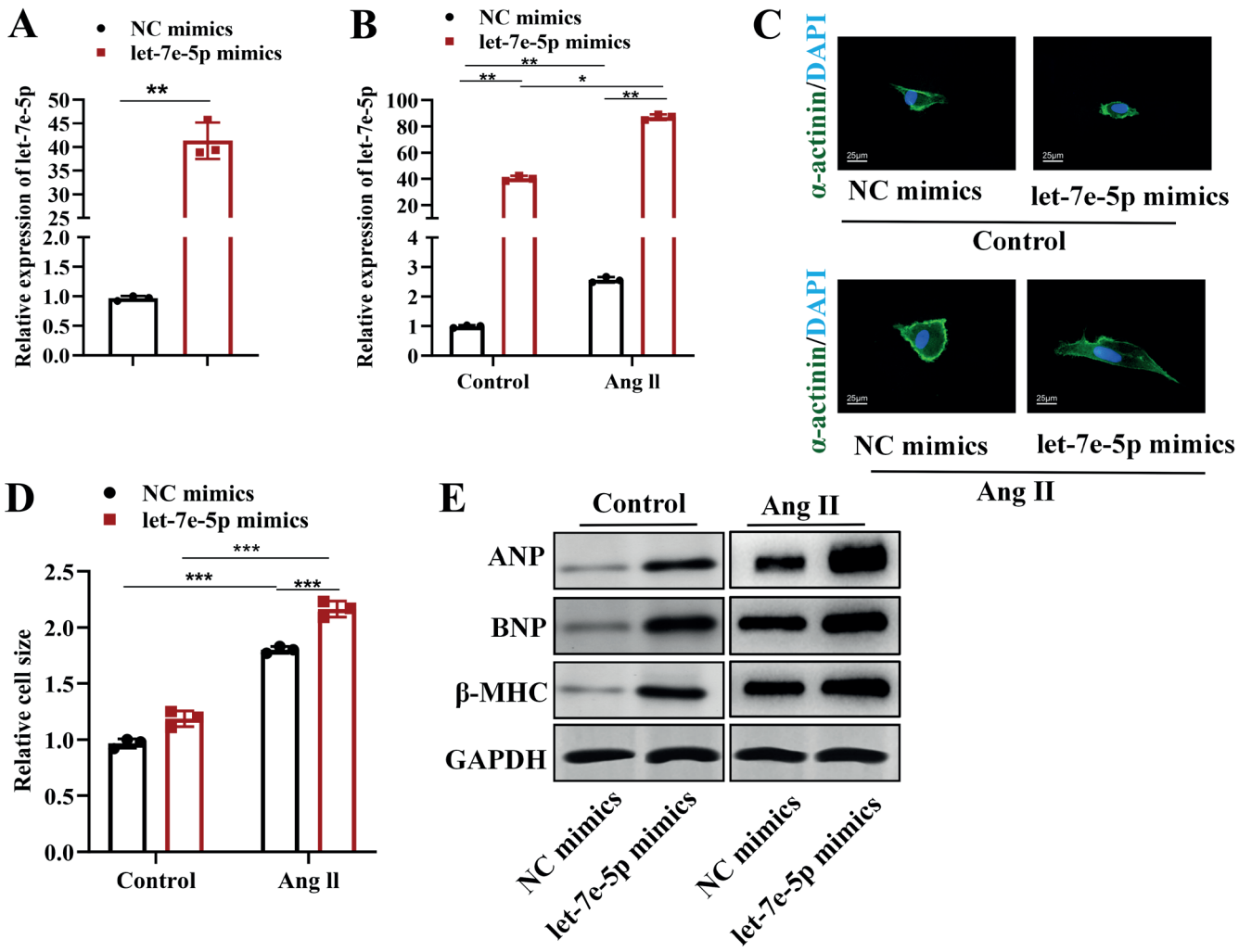

Fig. 5. Let-7e-5p overexpression enhances angiotensin II (Ang II)-stimulated cardiomyocyte hypertrophy. A. Reverse transcription quantitative polymerase chain reaction (RT-qPCR) was performed to measure let-7e-5p expression after transfection with let-7e-5p mimics or negative control (NC) mimics in H9c2 cells; B. RT-qPCR was used to detect let-7e-5p expression in H9c2 cells treated with or without Ang II and transfected with NC mimics or let-7e-5p mimics; C. The effects of let-7e-5p overexpression on the size of H9c2 cells treated with or without Ang II were evaluated using immunofluorescence staining for α-actinin and DAPI; D. Quantification of H9c2 cell size; E. Western blot analysis of the effects of let-7e-5p overexpression on the protein levels of ANP, BNP, and β-MHC in H9c2 cells treated with or without Ang II (*p < 0.05, **p < 0.01, ***p < 0.001)

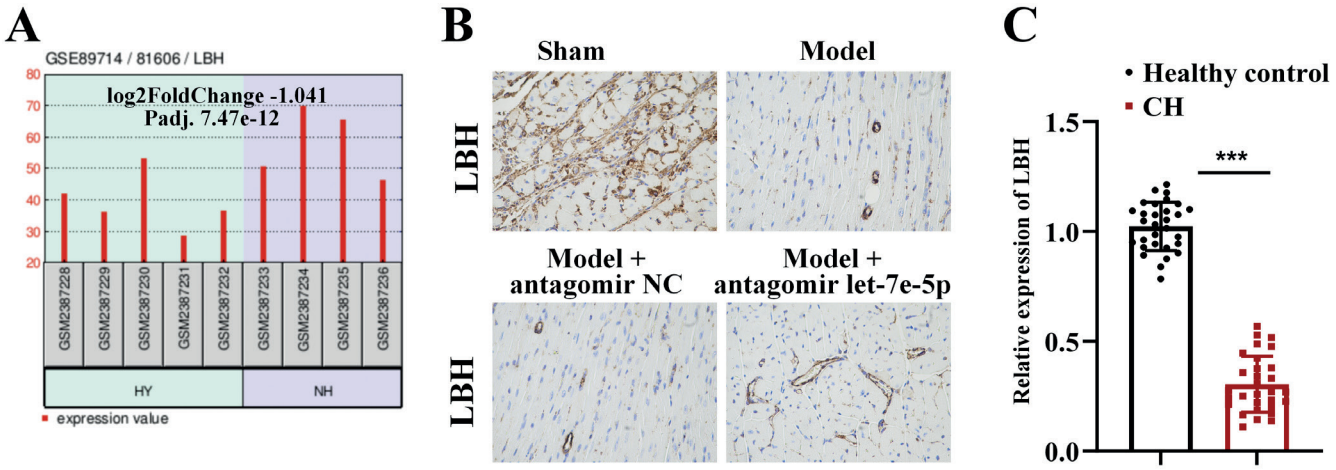

Fig. 6. Expression pattern of limb-bud and heart (*LBH*) in hypertrophic cardiomyopathy(HCM). A. Expression profile of *LBH* in heart tissues from patients with HCM and normal donor left ventricles in the GSE89714 dataset; B. Immunohistochemical analysis of *LBH* protein expression in rat heart tissues from each group; C. Reverse transcription quantitative polymerase chain reaction (RT-qPCR) analysis of *LBH* expression in the serum of patients with hypertrophic cardiomyopathy (n = 30) and healthy donors (n = 30) (***p < 0.001)

found that antagomir let-7e-5p treatment significantly restored *LBH* expression in the model group of rats (Fig. 6B). We also measured serum *LBH* expression in patients with HCM and healthy controls, and *LBH* was likewise found to be downregulated in HCM (Fig. 6C). Furthermore, we examined *LBH* expression in Ang II-exposed H9c2 cells. *LBH* expression was shown to be decreased following Ang II stimulation and increased by transfection with the let-7e-5p inhibitor (Fig. 7A,B).

The binding site between let-7e-5p and *LBH* was predicted using the TargetScan database (Fig. 7C,D). Luciferase reporter assays showed that the luciferase activity of WT *LBH* was elevated after let-7e-5p silencing, whereas that of mutant *LBH* was not significantly altered, confirming the interaction between *LBH* and let-7e-5p (Fig. 7E). We then explored the effects of Ang II treatment on the interaction between *LBH* and let-7e-5p in H9c2 cells using RNA pull-down assays. The results showed that the enrichment of *LBH* in the RNA complex pulled down by let-7e-5p probes was significantly increased in the Ang II group relative to the control group, indicating that Ang II treatment enhanced the interaction between let-7e-5p and *LBH* (Fig. 7F). Overall, these results indicate that let-7e-5p targets *LBH* and negatively regulates its expression, which may be related to the progression of cardiac hypertrophy.

Let-7e-5p enhances Ang II-stimulated cardiomyocyte hypertrophy by targeting *LBH*

Rescue assays were performed to explore whether let-7e-5p regulates cardiac hypertrophy by modulating *LBH* in Ang II-exposed H9c2 cardiomyocytes. As shown in Fig. 8A,B, let-7e-5p was downregulated after transfection with the let-7e-5p inhibitor, whereas no significant alteration was observed after *LBH* knockdown. In contrast, *LBH* was found to be upregulated in response to let-7e-5p inhibition in H9c2 cells and was significantly reduced after transfection with sh-*LBH*. According to the immunofluorescence results, the size of Ang II-stimulated H9c2 cardiomyocytes was reduced by let-7e-5p silencing and was significantly increased after co-transfection with sh-*LBH* relative to the let-7e-5p inhibitor group (Fig. 8C,D). Similarly, we found that the reduced protein expression levels of ANP, BNP, and β-MHC induced by let-7e-5p inhibition were significantly restored after *LBH* silencing (Fig. 8E).

Furthermore, let-7e-5p was overexpressed using let-7e-5p mimics, and *LBH* was overexpressed using the pcDNA/*LBH* vector (oe-*LBH*) to verify the role of the let-7e-5p/*LBH* axis in cardiac hypertrophy. RT-qPCR results confirmed that let-7e-5p was upregulated by let-7e-5p mimics and was not significantly altered by oe-*LBH*, whereas *LBH* was downregulated by let-7e-5p overexpression, which was significantly reversed by oe-*LBH* transfection in H9c2 cells (Fig. 9A,B). Moreover, we demonstrated that the increase in the size of Ang II-exposed H9c2 cells induced by let-7e-5p overexpression was partially reversed by *LBH* upregulation (Fig. 9C,D). Similarly, the upregulation of ANP, BNP, and β-MHC proteins induced by transfection with let-7e-5p mimics was reversed by *LBH* overexpression (Fig. 9E). Overall, let-7e-5p targets *LBH* to promote the development of cardiac hypertrophy.

Let-7e-5p facilitates the activation of the IGF–PI3K–Akt pathway via *LBH*

Previous studies have reported that the IGF–PI3K–Akt signaling pathway plays a crucial role in the development of cardiac hypertrophy and that let-7e-5p may activate the PI3K–Akt pathway in the heart.[21,22] Therefore, we investigated the impact of the let-7e-5p/*LBH* axis on IGF–PI3K–Akt signaling in Ang II-induced H9c2 cells. As shown in Fig. 10A, Ang II treatment was found to upregulate the levels of IGF1R, p-PI3K/PI3K, and p-Akt/Akt in H9c2 cells, whereas let-7e-5p silencing exerted the opposite effects. Moreover, the reduced expression of IGF1R, p-PI3K/PI3K, and p-Akt/Akt induced by let-7e-5p silencing was significantly reversed after *LBH* knockdown in Ang II-treated H9c2 cells, suggesting that let-7e-5p targets *LBH* to activate the IGF–PI3K–Akt pathway (Fig. 10B).

Additionally, the IGF1R inhibitor PQ401 was used in rescue assays. Immunofluorescence results showed that H9c2 cell size was increased after let-7e-5p overexpression, whereas a marked reduction was observed in the let-7e-5p mimics + PQ401 group, indicating that inhibition of the IGF–PI3K–Akt pathway partially reversed the promotive effect of let-7e-5p on cardiomyocyte hypertrophy (Fig. 10C,D). Meanwhile, we also found that the increase in H9c2 cardiomyocyte size induced by *LBH* knockdown was significantly reversed by PQ401 treatment (Fig. 10E,F). These results indicate that let-7e-5p promotes cardiomyocyte hypertrophy by targeting *LBH* and activating IGF–PI3K–Akt signaling.

Discussion

Currently, effective treatment options for cardiac hypertrophy remain limited, and it is imperative to develop therapeutic strategies to improve cardiac function and prevent progression to heart failure. Understanding the potential mechanisms involved in cardiac hypertrophy is essential for discovering diagnostic biomarkers and therapeutic targets. In this study, we found that let-7e-5p was aberrantly upregulated in patients with cardiac hypertrophy. Further analyses demonstrated that let-7e-5p plays a detrimental role and facilitates cardiac hypertrophy both in vitro and in vivo, which may provide novel insights into the diagnosis and treatment of this condition in clinical practice.

MicroRNAs are critical regulatory RNAs involved in the progression of a variety of heart diseases. Growing evidence has indicated that circulating miRNAs are promising noninvasive and accessible biomarkers for HCM diagnosis.[23]

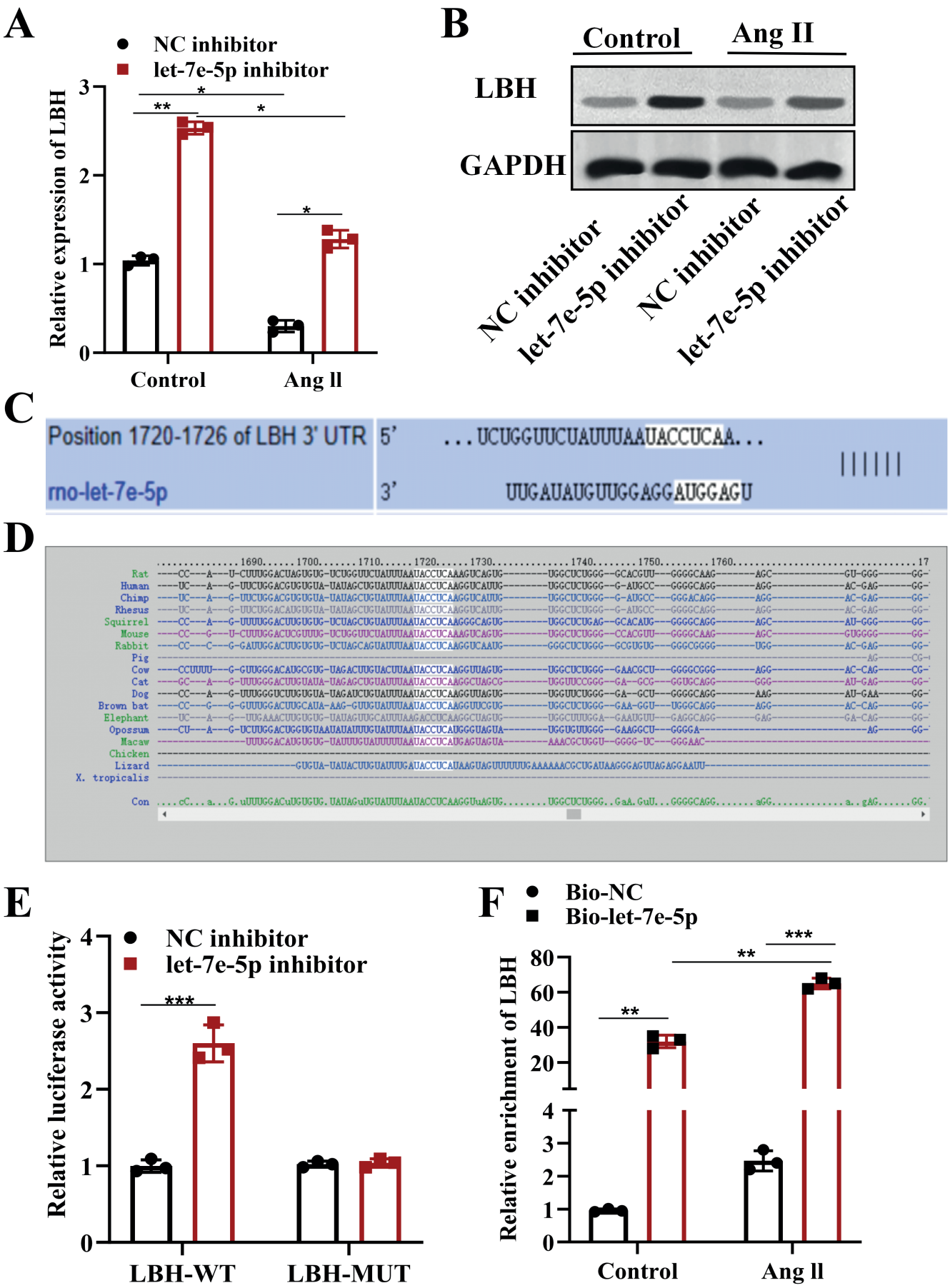

Fig. 7. Let-7e-5p targets limp-bud and heart (*LBH*) in H9c2 cells. Reverse transcription quantitative polymerase chain reaction (RT-qPCR) (A) and western blot analysis (B) were performed to measure LBH mRNA and protein expression in H9c2 cells treated with or without Angiotensin II (Ang II) and transfected with negative control (NC) inhibitor or let-7e-5p inhibitor; C,D. Potential binding sequences between let-7e-5p and *LBH* in rats and other species were predicted using the TargetScan database; E. Luciferase reporter assay was used to detect the interaction between let-7e-5p and *LBH* in H9c2 cells; F. RNA pull-down assays were used to explore the effects of Ang II treatment on the interaction between let-7e-5p and *LBH* in H9c2 cells (*p < 0.05, **p < 0.01, ***p < 0.001)

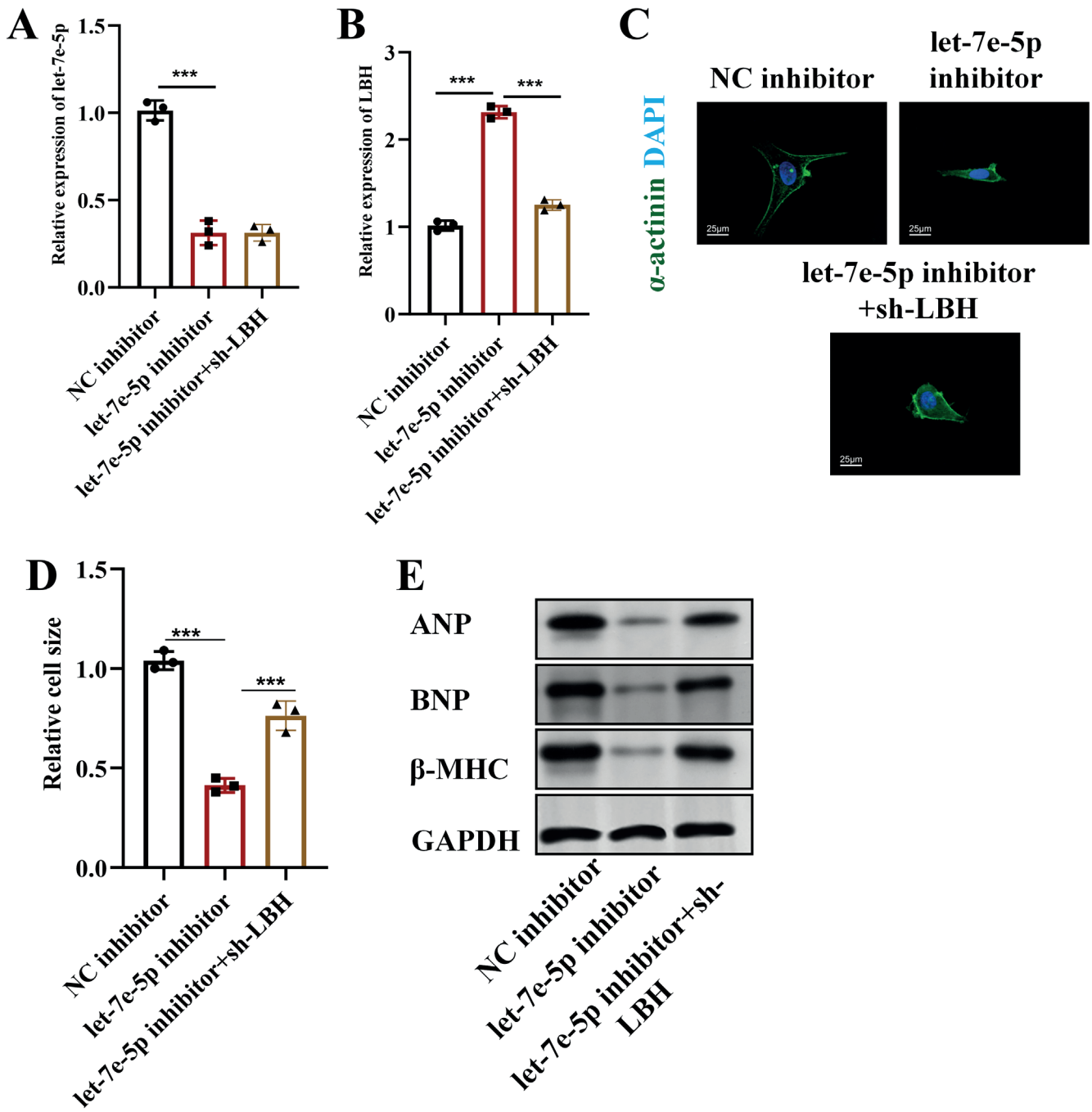

Fig. 8. Limp-bud and heart (*LBH*) silencing rescues the suppressive effects of let-7e-5p inhibition on cardiomyocyte hypertrophy. A. Reverse transcription quantitative polymerase chain reaction (RT-qPCR) analysis of let-7e-5p expression; B. RT-qPCR analysis of *LBH* expression in H9c2 cells transfected with negative control (NC) inhibitor, let-7e-5p inhibitor, or let-7e-5p inhibitor + sh-*LBH*; C. Immunofluorescence analysis of the size of Angiotensin II (Ang II)-stimulated H9c2 cardiomyocytes in each transfection group; D. Quantification of H9c2 cardiomyocyte size; E. Western blot analysis of ANP, BNP, and β-MHC protein levels in Ang II-stimulated H9c2 cells after the indicated transfection (***$p < 0.001$)

In our study, ROC curve analysis revealed that let-7e-5p expression showed good diagnostic performance for cardiac hypertrophy, suggesting its potential utility in HCM diagnosis. The function of miRNAs can be modulated through systemic or local delivery of miRNA mimics or inhibitors to block the interaction between miRNAs and their target genes.[24] Preclinical studies have been conducted to explore their efficacy against cardiac pathology. For example, miR-218 has been reported to be downregulated in cardiac hypertrophy, and its upregulation significantly suppresses isoprenaline-induced cardiomyocyte hypertrophy by targeting *REST*.[25] MiR-27a-3p levels have been shown to be increased in Ang II-treated cardiomyocytes, and transfection with a miR-27a-3p inhibitor significantly reduced myocardial hypertrophy and electrical remodeling through regulation of *Hoxa10*.[26]

Let-7e-5p dysregulation has been identified in many diseases, including multiple cancers.[27,28] Let-7e-5p is also

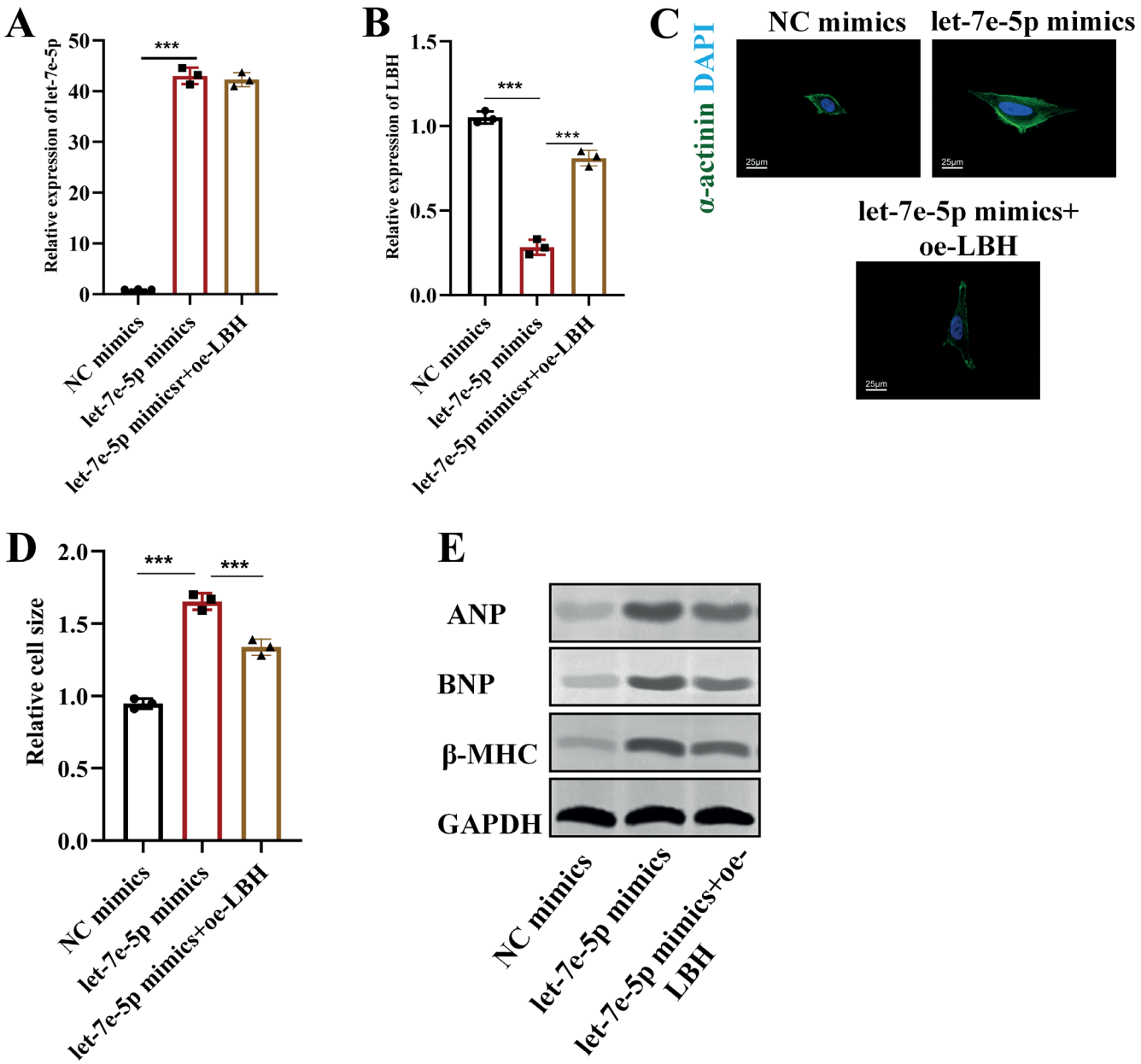

Fig. 9. Limp-bud and heart (*LBH*) overexpression reverses let-7e-5p overexpression-enhanced cardiomyocyte hypertrophy. A,B. Reverse transcription quantitative polymerase chain reaction (RT-qPCR) analysis of let-7e-5p and *LBH* expression in H9c2 cells transfected with negative control (NC) mimics, let-7e-5p mimics, or let-7e-5p mimics + oe-*LBH*; C. Immunofluorescence analysis of the size of Angiotensin II (Ang II)-treated H9c2 cells after the indicated transfection; D. Quantification of H9c2 cardiomyocyte size; E. Western blot analysis of ANP, BNP, and β-MHC protein expression in Ang II-treated H9c2 cells after the indicated transfection (***$p < 0.001$)

aberrantly expressed after myocardial infarction and may be involved in the pathophysiology of cardiovascular diseases.[29,30] In our study, we demonstrated the upregulation of let-7e-5p in the heart tissues of AB-induced rats. Administration of antagomir let-7e-5p effectively alleviated cardiac hypertrophy in rats subjected to AB surgery. Additionally, let-7e-5p was shown to be upregulated by Ang II in H9c2 cardiomyocytes. Let-7e-5p inhibition exerted suppressive effects on Ang II-induced cardiomyocyte hypertrophy, whereas let-7e-5p overexpression significantly enhanced the cardiomyocyte hypertrophy induced by Ang II treatment. These results indicate a critical role of let-7e-5p in cardiac hypertrophy.

LBH was identified as a target gene of let-7e-5p. *LBH* is recognized as being crucial for embryonic and cardiac development.[13] Accumulating evidence has revealed that *LBH* is aberrantly expressed and implicated in the progression of diverse diseases, including cancers, liver diseases, rheumatoid arthritis, and others.[15,31,32] Additionally, *LBH* has been shown to mediate the activation of cardiac fibroblasts and has been suggested as a valuable therapeutic target for myocardial I/R injury.[14,15,33]

In this study, we demonstrated that *LBH* was downregulated in the serum of patients with HCM, and bioinformatics analysis of the GSE89714 dataset similarly showed that *LBH* was expressed at low levels in heart tissues from these patients.

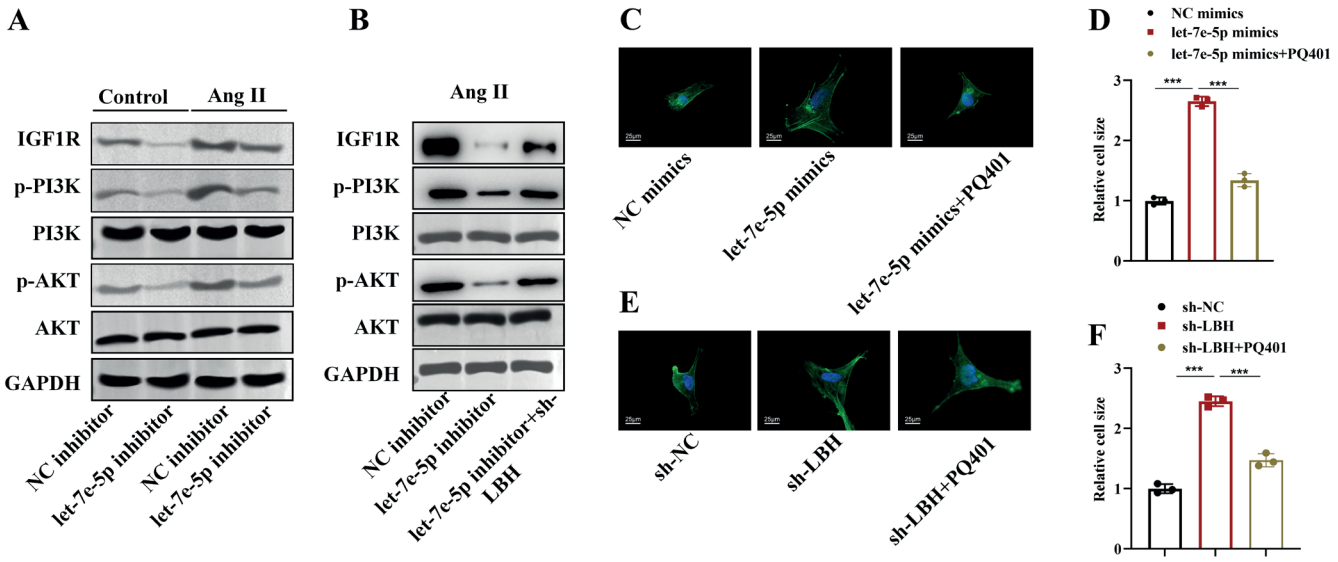

Fig. 10. Let-7e-5p promotes activation of IGF–PI3K–Akt signaling through limp-bud and heart (*LBH*). A. Western blot analysis of IGF1R, p-PI3K, PI3K, p-Akt, and Akt protein levels in H9c2 cells treated with or without Angiotensin II (Ang II) and subjected to the indicated transfection; B. Western blot analysis of IGF1R, p-PI3K, PI3K, p-Akt, and Akt protein levels in Ang II-treated H9c2 cells after the indicated transfection; C. Immunofluorescence analysis of the size of Ang II-treated H9c2 cells in the negative control (NC) mimics, let-7e-5p mimics, and let-7e-5p mimics + PQ401 groups; D. Quantification of H9c2 cardiomyocyte size in each group; E. Immunofluorescence analysis of the size of Ang II-treated H9c2 cells in the sh-NC, sh-*LBH*, and sh-*LBH* + PQ401 groups; F. Quantification of H9c2 cardiomyocyte size in the indicated groups (***p < 0.001)

Moreover, we found downregulation of *LBH* in the heart tissues of rats subjected to AB surgery and in H9c2 cells treated with Ang II. The interaction between let-7e-5p and *LBH* was confirmed, and let-7e-5p was shown to negatively regulate *LBH* expression in both rat heart tissues and H9c2 cells.

Furthermore, we demonstrated that *LBH* is essential for let-7e-5p-mediated cardiac hypertrophy, as evidenced by rescue assays. *LBH* silencing reversed the suppressive effects of let-7e-5p silencing on Ang II-treated H9c2 cells, whereas *LBH* overexpression reversed the promotive effects of let-7e-5p overexpression on H9c2 hypertrophy.

The IGF–PI3K–Akt pathway has previously been reported to be associated with endothelial dysfunction in the heart. Insulin-like growth factor (IGF) is a peptide hormone with a structure similar to that of insulin and is associated with cardiac function. It binds to its receptor, IGF1R, followed by the phosphorylation of PI3K and Akt.[34] Multiple studies have revealed that activation of the IGF–PI3K–Akt pathway can exert protective effects against cardiac injury by suppressing cardiomyocyte apoptosis.[35,36] Furthermore, a study has demonstrated the promotive effect of activation of this pathway on cardiomyocyte hypertrophy.[37] Consistently, our study demonstrated that let-7e-5p promotes activation of this pathway by targeting *LBH*, and inhibition of the pathway using the IGF1R inhibitor PQ401 reversed the effects of let-7e-5p mimics or the sh-*LBH* vector on H9c2 hypertrophy.

Limitations of the study

First, although AB mimics pressure overload-induced hypertrophy, this model cannot fully replicate the complex pathogenesis of cardiac hypertrophy in humans, and the role and mechanisms of let-7e-5p should be further validated in other models of cardiac hypertrophy. Second, the upstream regulatory mechanisms responsible for let-7e-5p upregulation in cardiac hypertrophy remain unclear and warrant further investigation in future studies.

Conclusions

Let-7e-5p is highly expressed in cardiac hypertrophy and aggravates the development of cardiac hypertrophy by targeting *LBH* and activating the IGF–PI3K–Akt pathway. The results of our study may provide new insights into targeted therapy for cardiac hypertrophy.

Supplementary data

The supplementary materials are available at https://doi.org/10.5281/zenodo.17733961. The package contains the following files:

Supplementary Table 1. Results of the Shapiro–Wilk normality test.

Supplementary Table 2. Results of the homogeneity of variance test.

Supplementary Table 3. Results of the statistical analyses.

Supplementary Fig. 1. Expression of let-7e-5p in rat heart tissues in vivo. RT-qPCR was used to detect let-7e-5p expression in the heart tissues of rats in the sham, model, model + antagomir NC, and model + antagomir let-7e-5p groups (***p < 0.001).

Supplementary Fig. 2. Identification of candidate mRNA targets of let-7e-5p. A. Venn diagram showing the overlap between downregulated genes in the heart tissue of patients with HCM from the GSE89714 dataset and predicted targets of let-7e-5p in the TargetScan database. A total of 21 candidate mRNAs were identified. B. RT-qPCR analysis of the expression of 21 candidate mRNAs in H9c2 cells transfected with NC inhibitor or let-7e-5p inhibitor. C. RT-qPCR analysis of the expression levels of 3 candidate mRNAs in rat heart tissues from each group (**$p < 0.01$, ***$p < 0.001$).

Data Availability Statement

The datasets supporting the findings of the current study are openly available in the Figshare repository at https://doi.org/10.6084/m9.figshare.30453719.

Consent for publication of personal information

Not applicable.

Use of AI and AI-assisted technology

Not applicable.

ORCID iDs

Shushu Yu https://orcid.org/0009-0006-2378-7733
Mingliang Wang https://orcid.org/0000-0002-6781-7993
Yun Xie https://orcid.org/0000-0002-3739-7078
Bo Wang https://orcid.org/0000-0002-6616-3473
Yawei Xu https://orcid.org/0000-0002-2175-6988

References

1. Oka T, Akazawa H, Naito AT, Komuro I. Angiogenesis and cardiac hypertrophy: Maintenance of cardiac function and causative roles in heart failure. *Circ Res*. 2014;114(3):565–571. doi:10.1161/CIRCRESAHA.114.300507
2. Nakamura M, Sadoshima J. Mechanisms of physiological and pathological cardiac hypertrophy. *Nat Rev Cardiol*. 2018;15(7):387–407. doi:10.1038/s41569-018-0007-y
3. Teekakirikul P, Zhu W, Huang HC, Fung E. Hypertrophic cardiomyopathy: An overview of genetics and management. *Biomolecules*. 2019;9(12):878. doi:10.3390/biom9120878
4. Palandri C, Santini L, Argirò A, et al. Pharmacological management of hypertrophic cardiomyopathy: From bench to bedside. *Drugs*. 2022;82(8):889–912. doi:10.1007/s40265-022-01728-w
5. Sebastian SA, Panthangi V, Singh K, et al. Hypertrophic cardiomyopathy: Current treatment and future options. *Curr Probl Cardiol*. 2023;48(4):101552. doi:10.1016/j.cpcardiol.2022.101552
6. Rani V, Sengar RS. Biogenesis and mechanisms of microRNA-mediated gene regulation. *Biotech Bioeng*. 2022;119(3):685–692. doi:10.1002/bit.28029
7. Wehbe N, Nasser S, Pintus G, Badran A, Eid A, Baydoun E. MicroRNAs in cardiac hypertrophy. *Int J Mol Sci*. 2019;20(19):4714. doi:10.3390/ijms20194714
8. Li J, Sha Z, Zhu X, et al. Targeting miR-30d reverses pathological cardiac hypertrophy. *eBioMedicine*. 2022;81:104108. doi:10.1016/j.ebiom.2022.104108
9. Li G, Shao Y, Guo HC, et al. MicroRNA-27b-3p down-regulates *FGF1* and aggravates pathological cardiac remodelling. *Cardiovasc Res*. 2022;118(9):2139–2151. doi:10.1093/cvr/cvab248
10. Ding YQ, Zhang YH, Lu J, et al. MicroRNA-214 contributes to Ang II-induced cardiac hypertrophy by targeting SIRT3 to provoke mitochondrial malfunction. *Acta Pharmacol Sin*. 2021;42(9):1422–1436. doi:10.1038/s41401-020-00563-7
11. Marques FZ, Vizi D, Khammy O, Mariani JA, Kaye DM. The transcardiac gradient of cardio-microRNAs in the failing heart. *Eur J Heart Fail*. 2016;18(8):1000–1008. doi:10.1002/ejhf.517
12. Recamonde-Mendoza M, Werhli AV, Biolo A. Systems biology approach identifies key regulators and the interplay between miRNAs and transcription factors for pathological cardiac hypertrophy. *Gene*. 2019;698:157–169. doi:10.1016/j.gene.2019.02.056
13. Briegel KJ, Joyner AL. Identification and characterization of Lbh, a novel conserved nuclear protein expressed during early limb and heart development. *Dev Biol*. 2001;233(2):291–304. doi:10.1006/dbio.2001.0225
14. Wu A, Zhang L, Chen J, et al. Limb-bud and heart (*LBH*) mediates proliferation, fibroblast-to-myofibroblast transition and EMT-like processes in cardiac fibroblasts. *Mol Cell Biochem*. 2021;476(7):2685–2701. doi:10.1007/s11010-021-04111-7
15. Xu Y, Wu A, Chen J, Song X, Chen M, Liu Q. Limb-bud and heart (*LBH*) upregulation in cardiomyocytes under hypoxia promotes the activation of cardiac fibroblasts via exosome secretion. *Mediators Inflamm*. 2022;2022:8939449. doi:10.1155/2022/8939449
16. Yuan Y, Yan L, Wu QQ, et al. Mnk1 (mitogen-activated protein kinase-interacting kinase 1) deficiency aggravates cardiac remodeling in mice. *Hypertension*. 2016;68(6):1393–1399. doi:10.1161/HYPERTENSIONAHA.116.07906
17. Percie Du Sert N, Ahluwalia A, Alam S, et al. Reporting animal research: Explanation and elaboration for the ARRIVE guidelines 2.0. *PLoS Biol*. 2020;18(7):e3000411. doi:10.1371/journal.pbio.3000411
18. Cingolani OH, Yang XP, Cavasin MA, Carretero OA. Increased systolic performance with diastolic dysfunction in adult spontaneously hypertensive rats. *Hypertension*. 2003;41(2):249–254. doi:10.1161/01.HYP.0000052832.96564.0B
19. Sun X, Zhou M, Wen G, et al. Paroxetine attenuates cardiac hypertrophy via blocking GRK2 and ADRB1 interaction in hypertension. *J Am Heart Assoc*. 2021;10(1):e016364. doi:10.1161/JAHA.120.016364
20. Lim TB, Aliwarga E, Luu TDA, et al. Targeting the highly abundant circular RNA circSlc8a1 in cardiomyocytes attenuates pressure overload induced hypertrophy. *Cardiovasc Res*. 2019;115(14):1998–2007. doi:10.1093/cvr/cvz130
21. Bhullar SK, Dhalla NS. Angiotensin II-induced signal transduction mechanisms for cardiac hypertrophy. *Cells*. 2022;11(21):3336. doi:10.3390/cells11213336
22. Xu Y, Li X, Kong M, et al. Cardiac-targeting magnetic lipoplex delivery of SH-IGF1R plasmid attenuate norepinephrine-induced cardiac hypertrophy in murine heart. *Biosci Rep*. 2014;34(5):e00140. doi:10.1042/BSR20130107
23. Cheng X, Jian D, Xing J, et al. Circulating cardiac MicroRNAs safeguard against dilated cardiomyopathy. *Clin Transl Med*. 2023;13(5):e1258. doi:10.1002/ctm2.1258
24. Tham YK, Bernardo BC, Ooi JYY, Weeks KL, McMullen JR. Pathophysiology of cardiac hypertrophy and heart failure: Signaling pathways and novel therapeutic targets. *Arch Toxicol*. 2015;89(9):1401–1438. doi:10.1007/s00204-015-1477-x
25. Liu JJ, Zhao CM, Li ZG, et al. miR-218 involvement in cardiomyocyte hypertrophy is likely through targeting REST. *Int J Mol Sci*. 2016;17(6):848. doi:10.3390/ijms17060848
26. Cao X, Zhang Z, Wang Y, et al. MiR-27a-3p/Hoxa10 axis regulates angiotensin II-induced cardiomyocyte hypertrophy by targeting Kv4.3 expression. *Front Pharmacol*. 2021;12:680349. doi:10.3389/fphar.2021.680349
27. Wang S, Jin S, Liu MD, et al. Hsa-let-7e-5p inhibits the proliferation and metastasis of head and neck squamous cell carcinoma cells by targeting chemokine receptor 7. *J Cancer*. 2019;10(8):1941–1948. doi:10.7150/jca.29536
28. Silva CMS, Barros-Filho MC, Wong DVT, et al. Circulating let-7e-5p, miR-106a-5p, miR-28-3p, and miR-542-5p as a promising microRNA signature for the detection of colorectal cancer. *Cancers (Basel)*. 2021;13(7):1493. doi:10.3390/cancers13071493
29. Mompeón A, Pérez-Cremades D, Paes AB, et al. Circulating miRNA fingerprint and endothelial function in myocardial infarction: Comparison at acute event and one-year follow-up. *Cells*. 2022;11(11):1823. doi:10.3390/cells11111823

30. Chouvarine P, Legchenko E, Geldner J, Riehle C, Hansmann G. Hypoxia drives cardiac miRNAs and inflammation in the right and left ventricle. *J Mol Med*. 2019;97(10):1427–1438. doi:10.1007/s00109-019-01817-6
31. Wu A, Luo N, Xu Y, Du N, Li L, Liu Q. Exosomal *LBH* inhibits epithelial-mesenchymal transition and angiogenesis in nasopharyngeal carcinoma via downregulating VEGFA signaling. *Int J Biol Sci*. 2022;18(1):242–260. doi:10.7150/ijbs.66506
32. Matsuda S, Hammaker D, Topolewski K, et al. Regulation of the cell cycle and inflammatory arthritis by the transcription cofactor *LBH* gene. *J Immunol*. 2017;199(7):2316–2322. doi:10.4049/jimmunol.1700719
33. Wu A, Zhong C, Song X, et al. The activation of LBH-CRYAB signaling promotes cardiac protection against I/R injury by inhibiting apoptosis and ferroptosis. *iScience*. 2024;27(5):109510. doi:10.1016/j.isci.2024.109510
34. Ge P, Cui Y, Liu F, Luan J, Zhou X, Han J. L-carnitine affects osteoblast differentiation in NIH3T3 fibroblasts by the IGF-1/PI3K/Akt signalling pathway. *Biosci Trends*. 2015;9(1):42–48. doi:10.5582/bst.2015.01000
35. Chen YP, Sivalingam K, Shibu MA, et al. Protective effect of Fisetin against angiotensin II-induced apoptosis by activation of IGF-IR-PI3K-Akt signaling in H9c2 cells and spontaneous hypertension rats. *Phytomedicine*. 2019;57:1–8. doi:10.1016/j.phymed.2018.09.179
36. Zeng B, Liao X, Liu L, Zhang C, Ruan H, Yang B. Thyroid hormone mediates cardioprotection against postinfarction remodeling and dysfunction through the IGF-1/PI3K/AKT signaling pathway. *Life Sci*. 2021;267:118977. doi:10.1016/j.lfs.2020.118977
37. Wahyuni T, Kobayashi A, Tanaka S, et al. Maresin-1 induces cardiomyocyte hypertrophy through IGF-1 paracrine pathway. *Am J Physiol Cell Physiol*. 2021;321(1):C82–C93. doi:10.1152/ajpcell.00568.2020

Identification and validation of novel diagnostic biomarkers across multiple tissues in osteoarthritis

Guihao Zheng[1,2,A,D], Yulong Ouyang[1,A], Shuilin Chen[1,B], Bei Hu[1,2,C], Shuai Xu[1,2,B], Guicai Sun[1,E,F]

[1] Department of Sports Medicine, Orthopedic Hospital, The First Affiliated Hospital, Jiangxi Medical College, Nanchang University, China
[2] Graduate School of Jiangxi Medical College, Nanchang University, China

A – research concept and design; B – collection and/or assembly of data; C – data analysis and interpretation;
D – writing the article; E – critical revision of the article; F – final approval of the article

Advances in Clinical and Experimental Medicine, ISSN 1899–5276 (print), ISSN 2451–2680 (online) *Adv Clin Exp Med*. 2026;35(7):1215–1233

Address for correspondence
Guicai Sun
E-mail: ndsfy0740@ncu.edu.cn

Funding sources
None declared

Conflict of interest
None declared

Received on June 4, 2025
Reviewed on September 1, 2025
Accepted on September 26, 2025

Published online on July 3, 2026

Abstract

Background. Osteoarthritis (OA) is a degenerative joint disease characterized by synovial inflammation, cartilage degradation, and subchondral bone remodeling. Currently, no universally accepted or clinically validated biomarkers exist for OA diagnosis and treatment, highlighting the need to identify potential genetic biomarkers to support early detection and therapeutic research.

Objectives. This study aimed to identify and preliminarily validate potential diagnostic biomarkers for OA using integrated bioinformatics and machine learning (ML) approaches to provide molecular insights supporting early diagnosis and therapeutic strategies.

Materials and methods. Gene expression data from OA patients and normal controls were obtained from the Gene Expression Omnibus (GEO) database. Differentially expressed genes (DEGs) were identified using R. Protein–protein interaction (PPI) network analysis and functional module analysis were performed to screen for hub genes. Gene Ontology and Kyoto Encyclopedia of Genes and Genomes (KEGG) enrichment analyses were conducted to determine the biological roles and pathways of DEGs, along with transcription factor prediction. Three ML models (least absolute shrinkage and selection operator (LASSO), support vector machine recursive feature elimination (SVM-RFE), and Random Forest) were used to identify OA-specific characteristic genes. Key diagnostic genes were identified from the intersection of the ML results and validated using external datasets of cartilage, synovium, and blood. IRS2 expression was further validated via in vivo (animal model) and in vitro (cell culture) experiments.

Results. Fifteen OA-related characteristic genes were identified, including *IRS2*, *ADM*, *SIK1*, *PTN*, *CX3CR1*, *WNT5A*, *IL21R*, *APOD*, *CRLF1*, *FKBP5*, *PNMAL1*, *NPR3*, *RARRES1*, *ASPN*, and *POSTN*. Functional enrichment analysis suggested involvement in extracellular matrix (ECM) organization, interleukin-17 (IL-17) and relaxin signaling, and the AGE-RAGE pathway in diabetic complications. Three genes showed strong diagnostic potential. IRS2 was downregulated, while WNT5A and PTN were upregulated in OA samples. Immunohistochemistry (IHC), real-time quantitative polymerase chain reaction (qPCR), and western blotting (WB) confirmed the downregulation of IRS2 in OA samples, consistent with bioinformatics predictions, in both chondrocytes and mouse joint tissues.

Conclusions. *IRS2*, *WNT5A*, and *PTN* may serve as potential diagnostic biomarkers for osteoarthritis, supporting early or tissue-specific diagnosis and offering insights for future clinical and therapeutic applications.

Key words: machine learning, osteoarthritis, biomarkers, bioinformatics, tissue-specific expressed genes

Cite as
Zheng G, Ouyang Y, Chen S, Hu B, Xu S, Sun G. Identification and validation of novel diagnostic biomarkers across multiple tissues in osteoarthritis. *Adv Clin Exp Med*. 2026;35(7):1215–1233. doi:10.17219/acem/211377

DOI
10.17219/acem/211377

Copyright
Copyright by Author(s)
This is an article distributed under the terms of the Creative Commons Attribution 3.0 Unported (CC BY 3.0) (https://creativecommons.org/licenses/by/3.0/)

Highlights

- Integrated bioinformatics and machine learning identified IRS2, WNT5A, and PTN as key diagnostic biomarkers for osteoarthritis (OA).
- IRS2 was significantly downregulated in OA cartilage, synovium, and blood, confirmed through qPCR, immunohistochemistry, and western blot analyses.
- Functional enrichment linked OA pathogenesis to IL-17, relaxin, and AGE-RAGE signaling pathways, emphasizing inflammation and extracellular matrix remodeling.
- Machine learning algorithms (LASSO, SVM-RFE, Random Forest) demonstrated strong diagnostic accuracy, offering promising tools for early OA detection and personalized therapy.

Background

Osteoarthritis (OA) remains a global health challenge,[1] affecting an estimated 600 million people worldwide, or 7.6% of the world's population,[2] with a higher prevalence among women.[3] The incidence and disability rates of OA have been rising since 1990,[4] and its prevalence is expected to nearly double in the next decade.[5] Additionally, similar to rheumatoid arthritis, OA imposes a substantial socioeconomic burden, with costs estimated to have reached 80 billion USD in 2016 and growing at 5.7% per year.[4,6] In the elderly, OA is a leading cause of mobility impairment and disability.[7,8]

Osteoarthritis is clinically characterized by chronic joint pain, stiffness, swelling, reduced range of motion, and progressive loss of function, which can significantly impair quality of life.[9] Pathologically, it involves extracellular matrix (ECM) degradation, altered type II collagen (COL2A1) synthesis, elevated matrix metalloproteinase 13 (MMP13) expression, and cyclooxygenase-2 (COX2)-mediated inflammation triggered by pro-inflammatory cytokines.[10] These factors act on cartilage, synovium, and subchondral bone, which interact and contribute to disease progression.[11–13] The etiology of OA is multifactorial, involving age, obesity, joint injury, genetics, and mechanical stress.[7,8] However, the exact mechanisms remain unclear, and effective early diagnostic tools are still lacking.

With the rapid development of high-throughput sequencing technology, an increasing number of OA-related datasets have been generated and utilized.[14–18] Although some studies have focused on OA biomarkers, most have been based on single tissues or individual datasets.[19] The occurrence and development of OA are closely related to interactions among cartilage, subchondral bone, and synovitis. Despite some controversy regarding the order of pathological events, it is undeniable that these components are all involved in disease progression,[20,21] which may contribute to the limited reliability of current research findings.[22–25] The application of machine learning (ML) in OA biomarker development has garnered growing research interest. For instance, Chen et al.[25] applied synovial tissue microarray datasets and identified *ZBTB16*, *TNFSF11*, *SCRG1*, and *KDELR3* as diagnostic biomarkers for OA. A study by Han et al.[23] also reported that *TLR7*, *CSF1R*, *APOE*, *C1QA*, and *CCL5* are key genes with high diagnostic value for OA after applying weighted gene co-expression network analysis (WGCNA) and the cytoHubba algorithm. Although these findings may contribute to a better understanding of OA and provide new insights into its diagnosis and treatment, the limited sample sizes and the small number of algorithms used may undermine the reliability and robustness of these studies to some extent.

Objectives

This study aimed to identify and validate reliable diagnostic biomarkers for OA using integrated bioinformatics and ML approaches to improve early diagnosis and inform therapeutic strategies

Materials and methods

Data collection

The datasets GSE51588, GSE12021, GSE55457, GSE56409, GSE114007, GSE168505, GSE169077, GSE55235, GSE129147, and GSE48556 were obtained from the Gene Expression Omnibus (GEO) database (https://www.ncbi.nlm.nih.gov/geo). GSE51588 is a whole-genome expression profile of subchondral bone. GSE12021, GSE55457, GSE56409, and GSE55235 contain data obtained from synovial samples of OA patients and normal controls. GSE114007, GSE168505, GSE169077, and GSE129147 are RNA sequencing datasets derived from joint cartilage tissues collected from both OA patients and healthy individuals, while GSE48556 consists of mononuclear cells isolated from the blood of OA patients and normal controls. All these datasets were derived from human samples.

Identification of differentially expressed genes (DEGs)

Identification of DEGs using the Robust Rank Aggregation method

The 7 raw datasets were processed using the limma package in Bioconductor, including normalization and log transformation. Subsequently, DEGs were analyzed using the limma package (https://bioconductor.org/packages/release/bioc/html/limma.html), and ranked lists of upregulated and downregulated DEGs were generated for each dataset based on fold-change values. Finally, we integrated the results of these 7 datasets using the R package "RobustRankAggreg" based on the Robust Rank Aggregation (RRA) method to identify the most significant DEGs. In the RRA analysis, genes with a log fold change (logFC) >1 and an adjusted p-value <0.05 were selected as significant DEGs.

Identification of DEGs using the Surrogate Variable Analysi) method

Before merging the 7 microarray datasets, we used the ComBat function in the Surrogate Variable Analysis (SVA) package to correct for batch effects, aiming to minimize experimental variance before subsequent analyses. Box plots, principal component analysis (PCA), and other methods were used to assess the data before and after correction (Supplementary Fig. 1). The final merged dataset consisted of 167 samples, including 66 normal control samples and 101 OA samples. In the SVA analysis, genes with a log fold change (logFC) >1 and an adjusted p-value <0.05 were selected as significant DEGs. Finally, the genes identified by both the RRA and SVA methods were considered key genes for OA.

Identification of gene clusters and construction of protein–protein interaction networks

Gene Ontology (GO) functional annotation, Kyoto Encyclopedia of Genes and Genomes (KEGG) analysis, and Disease Ontology (DO) enrichment analysis were performed using R packages (clusterProfiler: https://bioconductor.org/packages/release/bioc/html/clusterProfiler.html; DOSE: https://bioconductor.org/packages/release/bioc/html/DOSE.html; org.Hs.eg.db: https://bioconductor.org/packages/release/data/annotation/html/org.Hs.eg.db.html; enrichplot: https://bioconductor.org/packages/release/bioc/html/enrichplot.html).

An adjusted p-value <0.05 was considered statistically significant for enrichment.

The STRING database (https://string-db.org) was used to construct the protein–protein interaction (PPI) network, which was then imported into Cytoscape v. 3.9.1 software (https://cytoscape.org/index.html), to visualize the key nodes in the molecular interaction network. The cytoHubba algorithms were employed to analyze the PPI network. Only genes identified as hub genes by all cytoHubba algorithms ("MCC", "DMNC", "MNC", "Degree", "EPC", "BottleNeck", "EcCentricity", "Closeness", "Radiality", "Betweenness", "Stress", and "ClusteringCoefficient") were included in the final selection. The interacting genes and functions of these hub genes were predicted, and relevant PPI networks were generated using the GeneMANIA database (https://genemania.org). Enrichment analysis of the hub genes was further conducted using GO functional terms and KEGG pathway analysis, with $p < 0.05$ considered statistically significant.

Machine learning

We used the `train` function from the caret package to identify the best-performing model using various ML methods, including least absolute shrinkage and selection operator (LASSO), Support Vector Machine (SVM), Decision Tree (DT), Random Forest (RF), eXtreme Gradient Boosting (XGBoost), and Generalized Linear Model (GLM). LASSO regression is a linear regression technique that incorporates L1 regularization to constrain model complexity, thereby achieving feature selection and preventing overfitting.[26] Support Vector Machine is a powerful supervised learning model that can be used for classification and regression tasks. It has shown wide applicability and superior performance in high-dimensional data, complex data structures, and small-sample learning.[27] Decision Tree is a supervised learning algorithm that splits nodes by selecting the features that best partition the data.[28] Random Forest is an ensemble learning method that improves model performance and stability by voting (classification) or averaging (regression) the results of multiple decision trees. It is particularly effective in identifying subtle patterns in complex datasets.[29] XGBoost is a gradient boosting framework that uses tree-based models to provide efficient and flexible ML algorithms. It is widely recognized for its excellent performance and efficiency and is extensively used in ML competitions and real-world applications.[30] Generalized Linear Model is an extension of linear models that can be applied to a wide range of data types, offering strong interpretability and broad applicability.

Through training and testing these models, we selected the 3 best-performing models to analyze the differentially expressed genes and identify the optimal feature genes. The resulting genes were intersected with the hub genes and used as diagnostic genes for the disease.

Validation of feature genes with receiver operating characteristic curve and construction of clinical diagnostic model

To validate the diagnostic importance of the candidate genes, we used the "rms" R package (https://hbiostat.org/R/rms) to construct a nomogram and to predict and

interpret the resulting model. Box plots and violin plots were used to visualize differential gene expression between the control and OA groups. We further evaluated the diagnostic value of the candidate genes through receiver operating characteristic (ROC) analysis, obtaining the area under the ROC curve (AUC) and the corresponding 95% confidence interval (95% CI). An AUC > 0.7 was considered indicative of good diagnostic performance.

Validation of feature genes using western blot and qPCR

Human SW1353 chondrocytes, commonly used for OA modeling,[10,31] were cultured in an incubator under standard conditions (37°C, 5% CO_2) using specialized SW1353 culture medium (Dulbecco's modified Eagle's medium (DMEM); Pricella, Wuhan, China), with the medium changed every 2–3 days. When SW1353 cells reached 50% confluence, they were stimulated with 10 ng/mL interleukin (IL)-1β (PeproTech, Rocky Hill, USA) for 24 h to model OA.[32–34]

For IRS2 overexpression, the IRS2-overexpressing plasmid was obtained from HanHeng Biotechnology (Shanghai, China). Transfection was performed in 6-well plates using the plasmid and Lipofectamine 3000 (Thermo Fisher Scientific, Waltham, USA), following the manufacturer's instructions. SW1353 cells were transfected at 70–90% confluence, incubated for 48 h, and then treated with 10 ng/mL IL-1β for an additional 24 h. Successful overexpression of IRS2 was confirmed before proceeding with subsequent experiments.

The treated chondrocytes were lysed in radioimmunoprecipitation assay (RIPA) buffer (Solarbio, Beijing, China) containing 1% protease and phosphatase inhibitors (GlpBio, Montclair, USA) for 30 min. The lysates were collected by thoroughly scraping the adherent cells and then incubated on a shaker at 4°C for 1 h before centrifugation to collect the supernatant for subsequent experiments. The protein concentration in the supernatant was measured using a bicinchoninic acid (BCA) assay kit (Solarbio) on a microplate reader (Thermo Fisher Scientific) at a wavelength of 562 nm.

Subsequently, equal amounts of sample protein and protein markers were separated by 10% sodium dodecyl sulfate–polyacrylamide gel electrophoresis (SDS-PAGE) and transferred to polyvinylidene difluoride (PVDF) membranes (MilliporeSigma, St. Louis, USA). After blocking with 5% bovine serum albumin (BSA; Servicebio, Wuhan, China) for 1 h, the membranes were incubated with primary antibodies overnight at 4°C. After washing 3 times with Tris-buffered saline with Tween (TBST), the membranes were incubated with secondary antibodies at room temperature for 2 h. Details of the primary and secondary antibodies are listed in Table 1. Protein bands were visualized using an enhanced chemiluminescence reagent (Yeasen, Shanghai, China) and imaged with a Bio-Rad scanner (Bio-Rad, Hercules, USA). *GAPDH* was used as the housekeeping gene. Band analysis was performed using ImageJ v. 1.8.0 (National Institutes of Health (NIH), Bethesda, USA).

Table 1. Antibody information

Name	Type	Species	Source
Collagen II	primary antibody	rabbit	Proteintech
IRS2	primary antibody	mouse	Proteintech
MMP13	primary antibody	rabbit	Proteintech
SOX9	primary antibody	rabbit	Zenbio
COX2	primary antibody	rabbit	Zenbio
GAPDH	primary antibody	mouse	Proteintech
Goat anti-Rabbit IgG	secondary antibody	–	Proteintech
Goat anti-Mouse IgG	secondary antibodies	–	Proteintech

IgG – immunoglobulin G; MMP – matrix metalloproteinase.

Table 2. Primer information (all primers were designed for human genes)

Primer name	Primer sequence (5′-3′)
Collagen II	forward: TGGACGATCAGGCGAAACC
	reverse: GCTGCGGATGCTCTCAATCT
IRS2	forward: CGGTGAGTTCTACGGGTACAT
	reverse: TCAGGGTGTATTCATCCAGCG
MMP13	forward: ACTGAGAGGCTCCGAGAAATG
	reverse: GAACCCCGCATCTTGGCTT
SOX9	forward: AGCGAACGCACATCAAGAC
	reverse: CTGTAGGCGATCTGTTGGGG
COX2	forward: GCACCCCGACATAGAGAGC
	reverse: CTGCGGAGTGCAGTGTTCT
GAPDH	forward: TGTGGGCATCAATGGATTTGG
	reverse: ACACCATGTATTCCGGGTCAAT

Similarly, total RNA was extracted from the treated chondrocytes using TRIzol reagent (Takara, Shiga, Japan) and purified with an RNA extraction kit (TransGen, Beijing, China). The total RNA concentration of the samples was measured using a micro-UV spectrophotometer (Thermo Fisher Scientific). The RNA samples were then reverse transcribed into cDNA using a reverse transcription kit (TransGen). Finally, the target mRNA was amplified on a real-time quantitative polymerase chain reaction (qPCR) instrument (Bio-Rad). The final quantitative results were normalized to *GAPDH* and calculated using the $2^{-\Delta\Delta Ct}$ method. The primer sequences for the target genes are shown in Table 2.

Animal experiments

All animal procedures were approved by the Institutional Animal Care and Use Committee (IACUC) of The First Affiliated Hospital of Nanchang University, China (approval No. CDYFY-IACUC-202505GR093). All experiments involving animals were conducted in strict accordance with the guidelines set forth by the IACUC and the Guide for the Care and Use of Laboratory Animals. Mice were maintained under

specific pathogen-free (SPF) conditions in a 12 h light/dark cycle, with ad libitum access to food and water.

To investigate the differential expression of IRS2 in OA, a total of 12 ten-week-old male C57BL/6 mice were subjected to destabilization of the medial meniscus (DMM) surgery on the right knee.[35] Briefly, 12 mice were used, with 6 mice per group (sham and OA). The OA model was established by performing DMM surgery on the right knee. Briefly, mice were anesthetized with sodium pentobarbital, and the DMM procedure involved transecting the medial meniscotibial ligament (MMTL) to destabilize the meniscus. Sham-operated mice underwent identical surgical exposure without MMTL transection. The DMM model is a validated and widely used method for inducing OA in mice. Mice were euthanized 8 weeks after surgery, and whole knee joints were harvested from both groups for subsequent histological and molecular analyses.

Immunohistochemistry

Bone tissues were fixed in formalin and decalcified in ethylenediaminetetraacetic acid (EDTA) solution for 1 month, with the solution refreshed every 3–7 days. After decalcification, tissues were dehydrated, embedded in paraffin, and sectioned at a thickness of 5 µm. Sections were deparaffinized in xylene, rehydrated through graded ethanol, and subjected to antigen retrieval by boiling in 0.01% sodium citrate buffer. Endogenous peroxidase activity was blocked using hydrogen peroxide, followed by blocking with 5% BSA for 1 h at room temperature.

Primary antibodies diluted in 5% BSA were incubated overnight at 4°C, including anti-IRS2, anti-COX2, and anti-type II collagen (all from Sanying, Wuhan, China; dilution 1:50). The next day, sections were incubated with a horseradish peroxidase (HRP)-conjugated goat anti-mouse/rabbit IgG secondary antibody (Golden Bridge Biotechnology, Beijing, China; 1:50 dilution), followed by 3,3′-diaminobenzidine (DAB) staining and hematoxylin counterstaining to visualize nuclei. Finally, slides were mounted with neutral resin and coverslipped. Images of the stained sections were captured using a digital imaging system (Shunyu Instruments, Zhejiang, China).

Statistical analyses

Data were analyzed using R 4.3.0 (R Foundation for Statistical Computing, Vienna, Austria), Cytoscape 3.9.1, Perl 5.32.1 (https://www.perl.org), and GraphPad Prism 9.7 (GraphPad Software, San Diego, USA). Continuous data were expressed as mean ± standard deviation (SD). For comparisons between 2 groups, if the continuous data followed a normal distribution and had equal variances, Student's t-test was used. If the data did not follow a normal distribution, a nonparametric test (Mann–Whitney U test) was employed. All experiments were independently repeated 3 times, and $p < 0.05$ was considered statistically significant.

Results

Identification of DEGs

Table 3 summarizes the characteristics of the included datasets. Using the RRA method, we identified 202 upregulated and 49 downregulated DEGs (Fig. 1A). A heatmap showing the top 50 upregulated and top 10 downregulated genes is presented in Supplementary Fig. 2A. Figure 1B shows the differential gene expression profile in the merged dataset, revealing 64 upregulated and 30 downregulated genes. By intersecting the RRA and SVA results, we identified 83 key DEGs associated with OA (Fig. 1C).

Functional enrichment and pathway analysis of key genes

We performed GO, KEGG, and DO enrichment analyses to explore the biological roles of the key genes. The GO results showed that these genes are mainly involved in ECM

Table 3. Characteristics of the included datasets

GEO dataset	Platform	Tissue	Total samples	Normal	OA	Group
GSE51588	GPL13497	subchondral bone	50	10	40	training
GSE12021	GPL96	synovium	19	9	10	training
GSE55457	GPL96	synovium	20	10	10	training
GSE56409	GPL570	synovium	22	11	11	training
GSE114007	GPL11154/GPL18573	cartilage	38	18	20	training
GSE168505	GPL16791	cartilage	7	3	4	training
GSE169077	GPL96	cartilage	11	5	6	training
GSE55235	GPL96	synovium	20	10	10	test
GSE129147	GPL6947	cartilage	40	7	33	test
GSE48556	GPL6947	blood	139	33	106	test

GEO – Gene Expression Omnibus; OA – osteoarthritis.

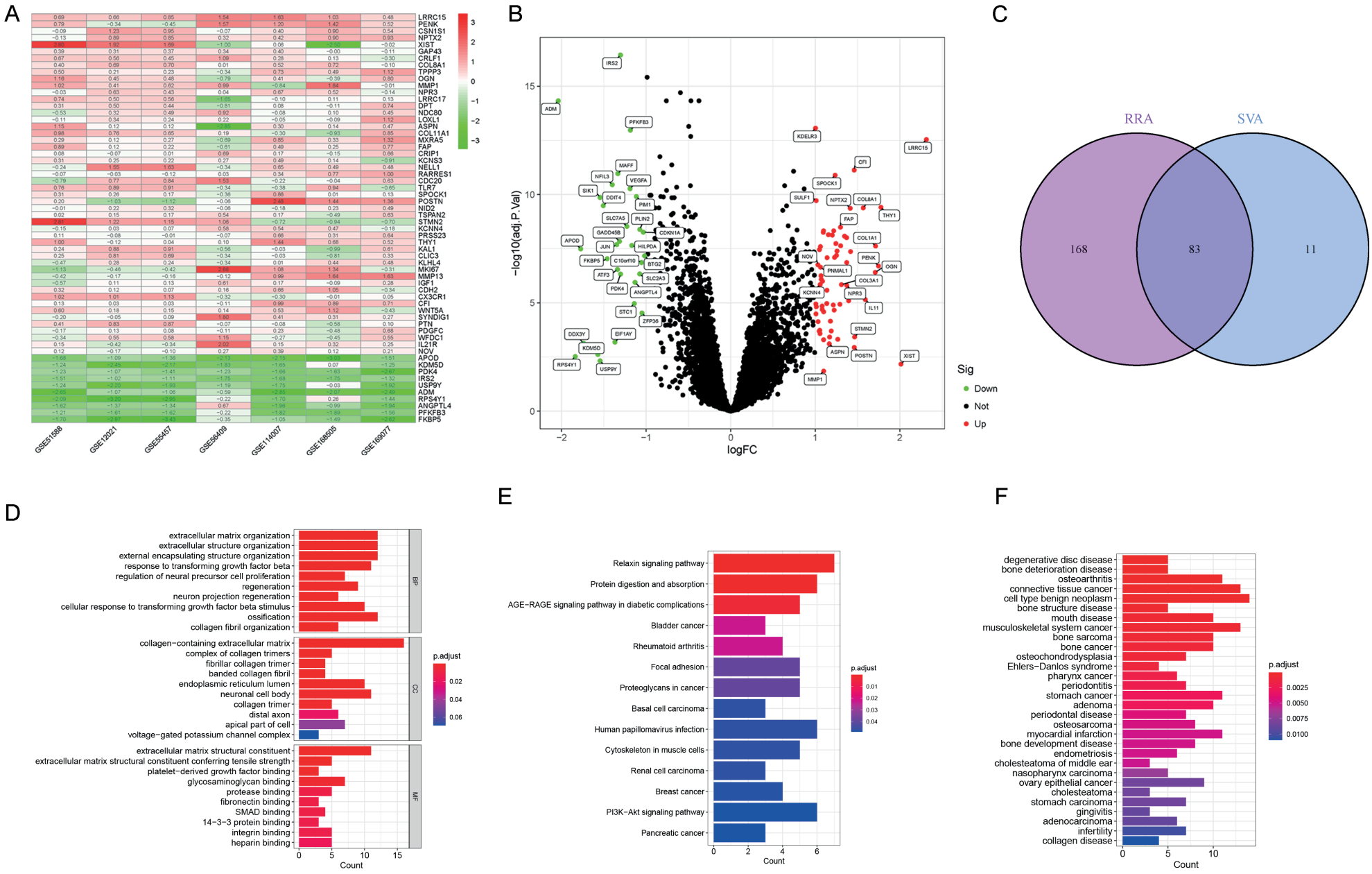

Fig. 1. Identification and enrichment analysis of differentially expressed genes (DEGs) in osteoarthritis (OA). A. Robust Rank Aggregation (RRA) heatmap of the top 50 upregulated and top 10 downregulated genes across 7 datasets (red: upregulated; green: downregulated); B. Volcano plot of DEGs; C. Venn diagram showing the overlap of DEGs identified by RRA and Surrogate Variable Analysis (SVA); D. Gene Ontology (GO) enrichment bar plots; E. Kyoto Encyclopedia of Genes and Genomes (KEGG) enrichment bar plots; F. Disease Ontology (DO) enrichment bar plots

and structural organization (BP), are localized to collagen-containing extracellular components (CC), and function as structural constituents of the ECM (MF) (Fig. 1D, Supplementary Fig. 2B). KEGG analysis revealed enrichment in pathways such as relaxin signaling, protein digestion and absorption, advanced glycation end products–receptor for advanced glycation end products (AGE-RAGE) signaling in diabetic complications, and rheumatoid arthritis (Fig. 1E, Supplementary Fig. 2C). DO analysis indicated associations with diseases including OA, degenerative disc disease, connective tissue cancer, and musculoskeletal system tumors (Fig. 1F, Supplementary Fig. 2D).

Construction of PPI network for key genes

We used the key genes to construct a PPI network in STRING (minimum interaction score = 0.4, $p < 0.001$) to explore potential protein interactions. The resulting network was visualized using Cytoscape (Fig. 2A). To identify hub genes, we applied all algorithms within the cytoHubba plugin, and only genes identified by all methods were retained, resulting in 25 hub genes (Fig. 2B), including *COL1A2*, *COL3A1*, *POSTN*, *WNT5A*, and *IRS2*, among others. We also generated volcano plots and heatmaps of hub gene expression (Fig. 3A,B).

Further enrichment analysis showed that the hub genes participate in biological processes such as ECM organization, structural organization, axon development, and regeneration. They are localized to collagen-containing ECM components, including the fibrillar collagen trimer and endoplasmic reticulum (ER) lumen. Molecular functions included ECM structural constituent activity, integrin binding, and growth factor binding (Fig. 3C). KEGG analysis revealed enrichment in the relaxin, IL-17, AGE-RAGE, and PI3K-Akt signaling pathways, as well as protein digestion and absorption (Fig. 3D).

Identifying diagnostic biomarkers through machine learning

To identify key diagnostic biomarkers for OA, we conducted a thorough feature selection process. Initially, we employed the `train` function from the caret package to identify the optimal ML algorithms. The dataset was divided into training and validation sets, with training set proportions of either 0.7 or 0.8. Among the 6 ML methods evaluated, XGBoost, SVM, and LASSO regression consistently ranked highly in terms of residuals and root mean square error (Supplementary Fig. 3A,B), with AUCs exceeding 0.9 (Supplementary Fig. 3C,D), indicating superior diagnostic performance and learning capability. Consequently, we selected XGBoost, SVM, and LASSO regression to screen for key diagnostic biomarkers for OA.

Using the XGBoost algorithm, we identified 23 candidate genes (Fig. 4A). The SVM algorithm identified 23 key genes (Fig. 4B,C), and LASSO regression selected 26 candidate genes (Fig. 4D,E). By intersecting the feature genes identified by these 3 ML methods, we identified 15 candidate genes: *IRS2*, *ADM*, *SIK1*, *PTN*, *CX3CR1*, *WNT5A*, *IL21R*, *APOD*, *CRLF1*, *FKBP5*, *PNMAL1*, *NPR3*, *RARRES1*, ASPN, and *POSTN*. Further intersecting these candidate genes with the hub genes, we identified *IRS2*, *PTN*, *POSTN*, and *WNT5A* as diagnostic biomarkers for OA (Fig. 4F).

The functional annotations, interaction partners, and network features of the final diagnostic biomarkers (*IRS2*, *PTN*, *POSTN*, and *WNT5A*) are summarized in Supplementary Table 1.

Next, we constructed box plots for these candidate genes, which demonstrated differential expression within the dataset. We used ROC curves to evaluate the specificity and sensitivity of these 4 features for distinguishing OA from normal tissues in the test set. The diagnostic values of the 4 genes were as follows: *IRS2* (AUC = 0.879, 95% CI: 0.826–0.927), *PTN* (AUC = 0.784, 95% CI: 0.707–0.852), *POSTN* (AUC = 0.668, 95% CI: 0.583–0.748), and *WNT5A* (AUC = 0.783, 95% CI: 0.706–0.857) (Fig. 5A). Since the AUC of POSTN in the test dataset was 0.668, which is below 0.7, we ultimately selected IRS2, PTN, and WNT5A as diagnostic biomarkers for OA. We then constructed a diagnostic nomogram based on the training dataset to develop a clinically applicable diagnostic model for OA (Fig. 5B). The calibration curve (Fig. 5C) and decision curve (Fig. 5D) clearly demonstrated the model's high predictive ability for OA (AUC = 0.913, 95% CI: 0.866–0.953; Fig. 5E).

Validation of relevant screening genes

To better validate the clinical diagnostic capability of the candidate genes, we used the cartilage tissue dataset GSE129147, the synovial tissue dataset GSE55235, and the blood sample dataset GSE48556 from OA patients for validation, with sample sizes of 40, 20, and 139, respectively. We constructed violin plots for the candidate genes, which demonstrated differential expression across the datasets (Fig. 6A–C). Additionally, we plotted ROC curves to evaluate the diagnostic value of each gene in different tissue samples (Fig. 6D–F).

Among these genes, *WNT5A* had lower diagnostic efficiency in cartilage and blood samples, *PTN* had poor diagnostic efficiency in blood samples, and only *IRS2* exhibited high differential expression ($p < 0.01$) in all sample types, together with good diagnostic performance, indicating high clinical value.

Experimental validation of *IRS2* gene

To validate the reliability and potential role of the candidate gene *IRS2* in OA, we established a DMM-induced OA model in C57BL/6 mice. Successful model

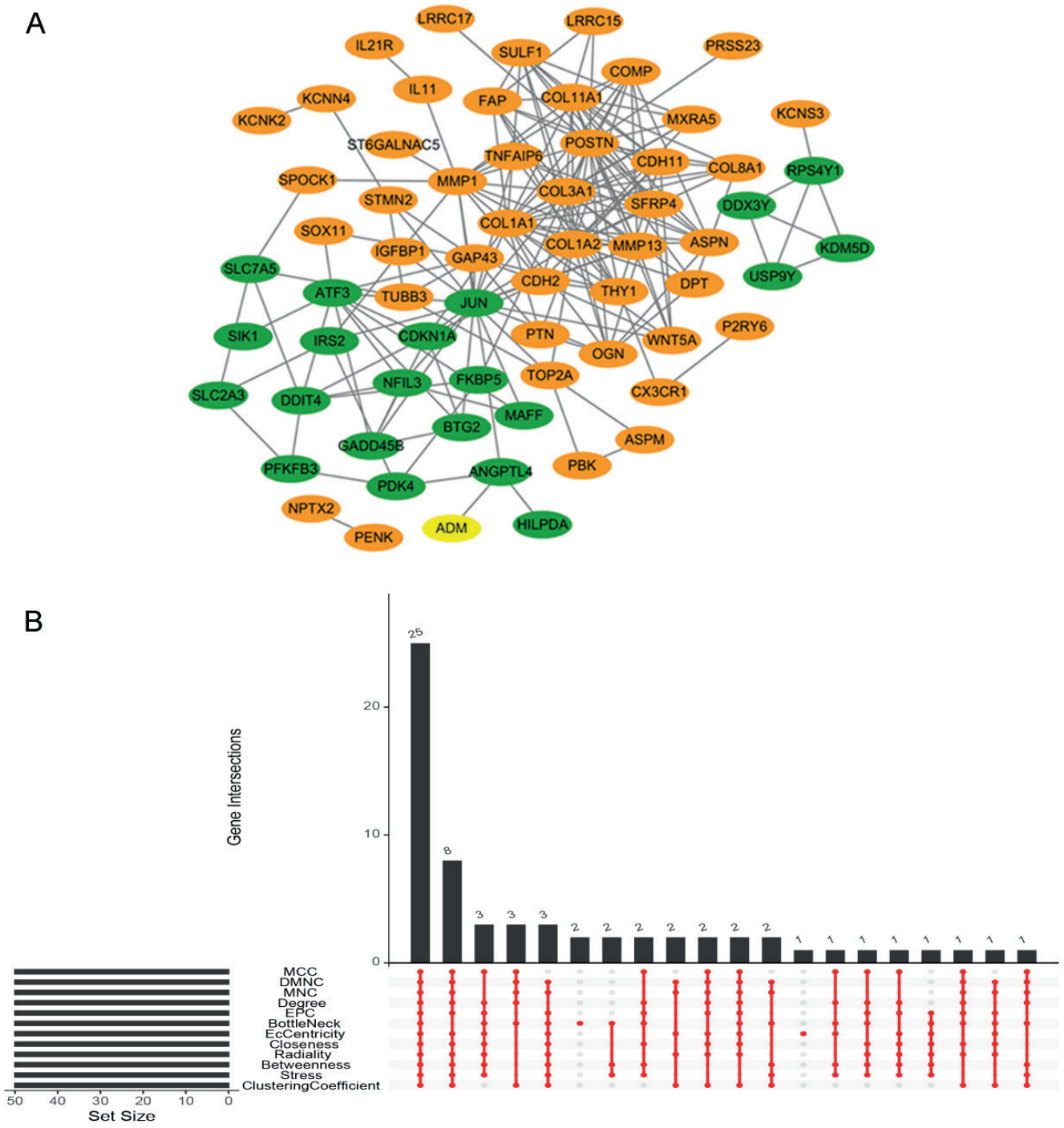

Fig. 2. Protein–protein interaction (PPI) network and hub gene identification. A. PPI network of hub genes (orange: upregulated; green: downregulated); B. Twenty-five hub genes identified using cytoHubba, with scores based on algorithm overlap

establishment was confirmed through Safranin O–Fast Green and hematoxylin and eosin (H&E) staining, as well as by assessing the expression levels of the OA-related markers COX2 and type II collagen. Immunohistochemical staining for *IRS2* (Fig. 7A,B) revealed a significant downregulation of *IRS2* in OA tissues, consistent with our initial hypothesis.

In vitro, we mimicked the OA pathological environment by stimulating the human chondrocyte cell line SW1353 with IL-1β and examined the protein and mRNA expression levels of IRS2 using western blotting (WB) and qPCR. Additionally, to ensure the fidelity of OA modeling, we assessed key phenotypic markers associated with OA. The results showed that, compared to the control group, COL2A1 and SOX9 levels were significantly decreased, whereas MMP13 and COX2 levels were markedly increased in the OA model group, consistent with the typical characteristics of OA. Importantly, IRS2 expression at both

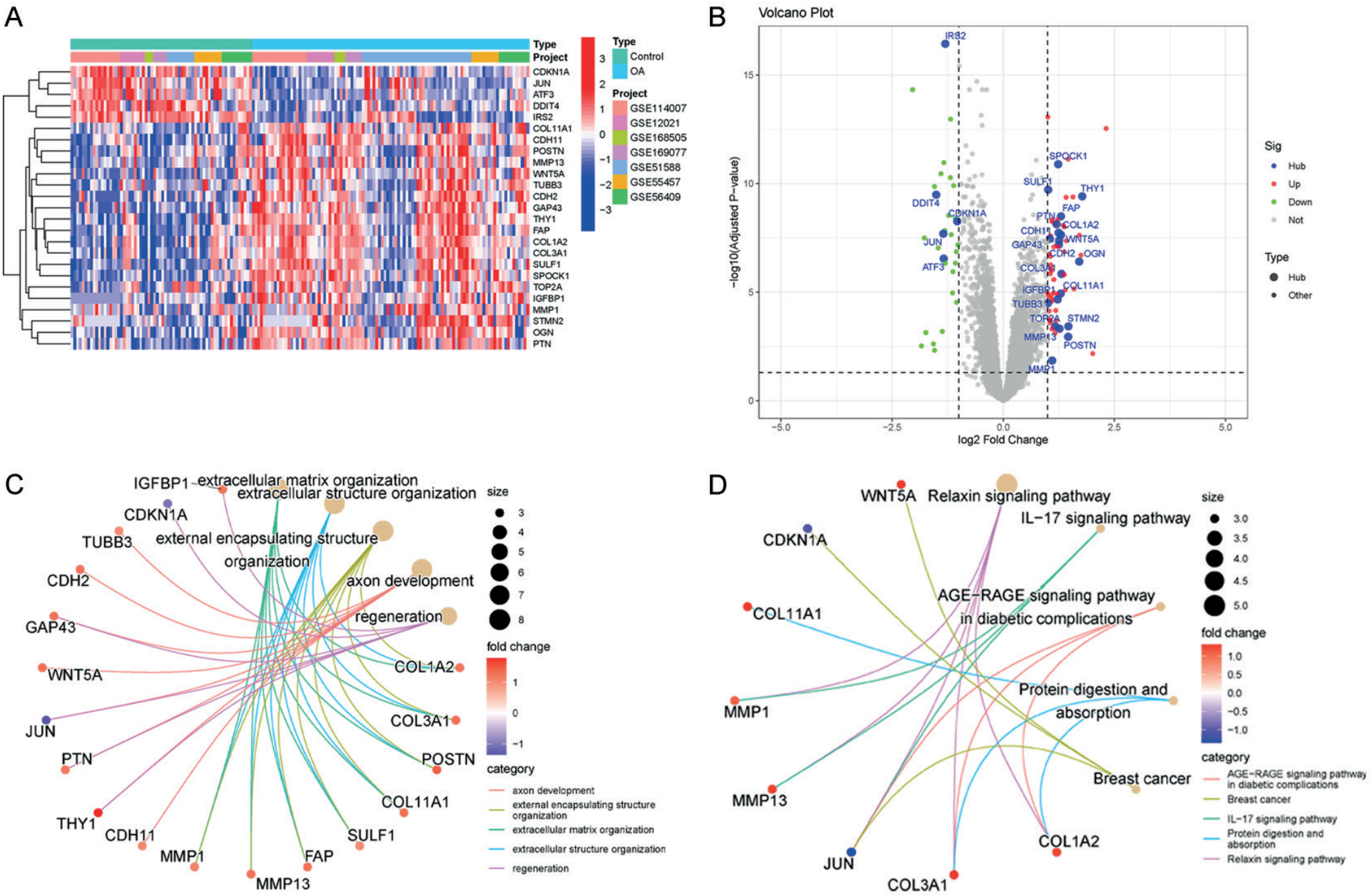

Fig. 3. Expression and functional enrichment analysis of hub genes. A. Heatmap of hub gene expression; B. Volcano plot of hub genes; C. Gene Ontology (GO) network plot; D. Kyoto Encyclopedia of Genes and Genomes (KEGG) network plot. In the network plots, term node size represents gene count; gene color indicates regulation (red: upregulated; purple: downregulated); node size reflects term involvement

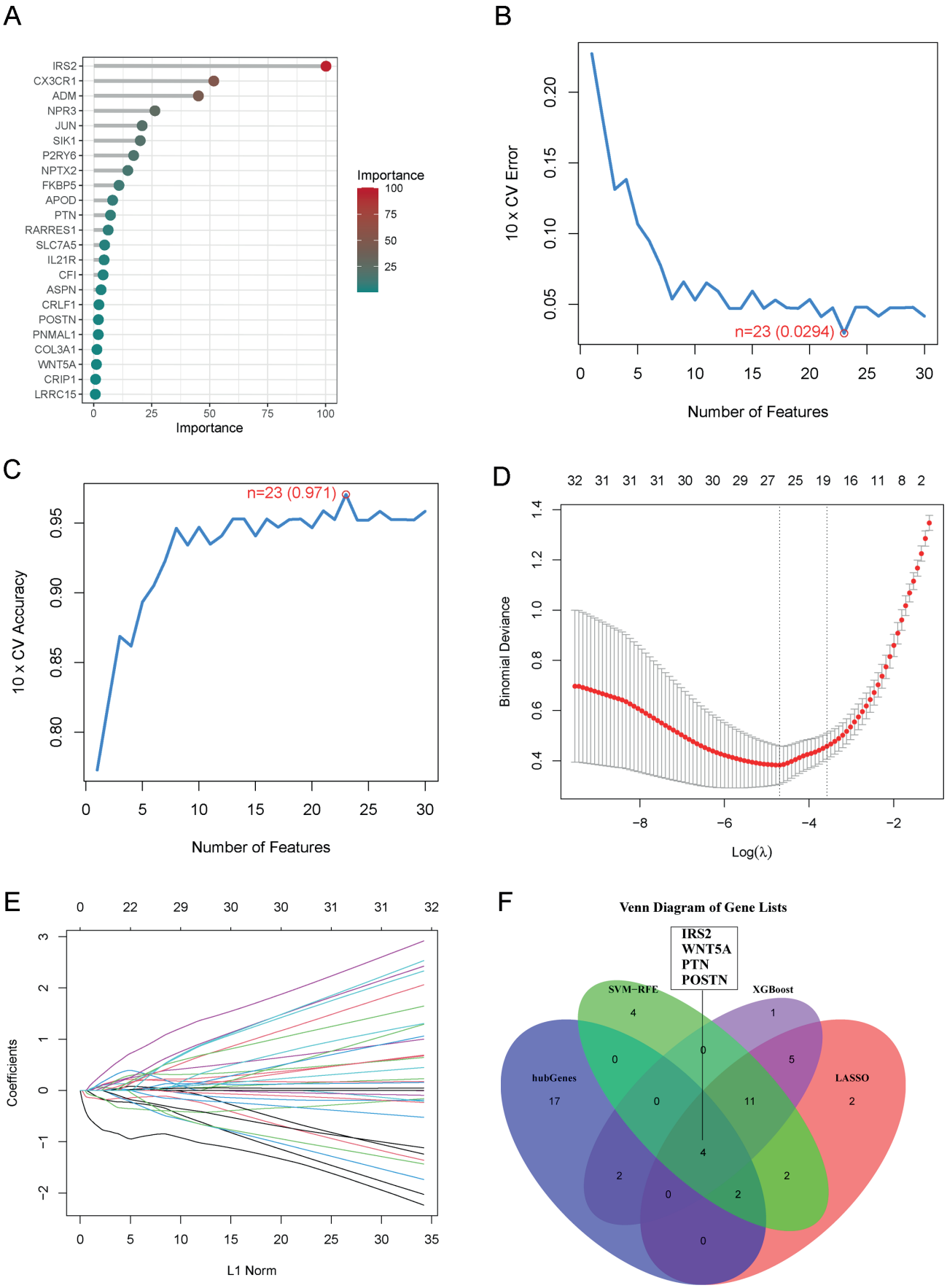

Fig. 4. Machine learning-based screening of osteoarthritis (OA) feature genes. A. Gene importance ranking by XGBoost; B,C. Support vector machine recursive feature elimination (SVM-RFE) accuracy and error plots; D. Least absolute shrinkage and selection operator (LASSO) coefficient analysis with the optimal lambda value; E. LASSO cross-validation curves; F. Venn diagram of feature genes identified by XGBoost, LASSO, and SVM-RFE

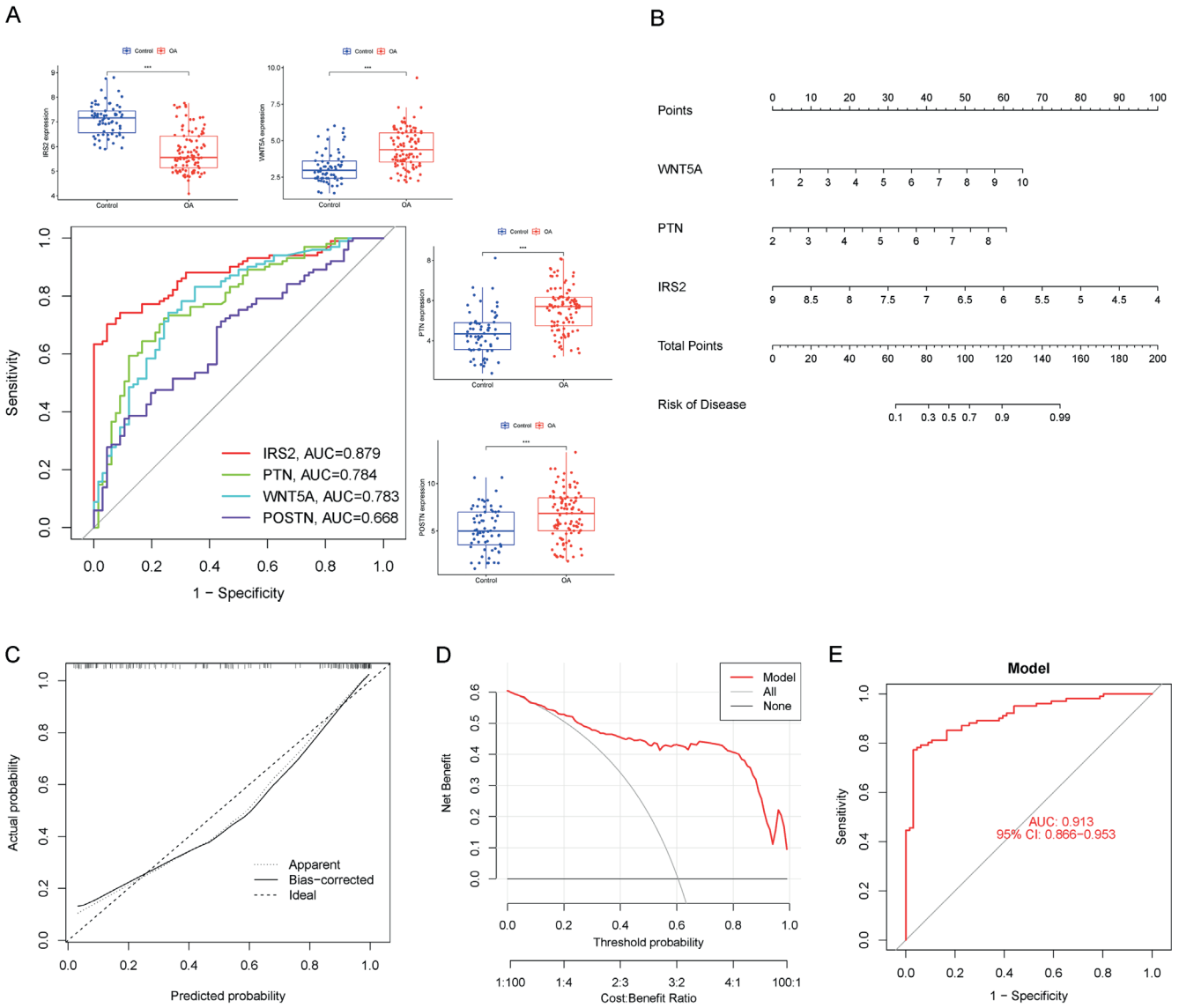

Fig. 5. Risk prediction model based on feature genes. A. Receiver operating characteristic (ROC) curves and expression boxplots of feature genes; B. Nomogram for osteoarthritis (OA) diagnosis; C. Calibration curve (closer to the dashed line = higher accuracy); D. Decision curve analysis (greater distance from the gray line = higher clinical utility); E. ROC curve of the prediction model (*p < 0.05; **p < 0.01; ***p < 0.001)

the protein and mRNA levels was significantly reduced in the OA group (Fig. 8).

To further elucidate the role of *IRS2* in OA, we constructed a plasmid-based *IRS2* overexpression system in SW1353 cells and again measured *IRS2* expression at both the protein and mRNA levels using WB and qPCR. Osteoarthritis-related phenotypic markers were reassessed to confirm the functional impact of *IRS2* overexpression. The data demonstrated that *IRS2* overexpression significantly restored the expression of COL2A1 and SOX9 while suppressing the upregulation of MMP13 and COX2. Compared to the OA group, the *IRS2* overexpression group exhibited significantly increased protein and mRNA levels of *IRS2*, along with a marked recovery of OA-related phenotypes, with statistically significant differences (Fig. 9).

Discussion

Based on the above integrative analysis, we further interpreted the biological significance and potential mechanisms underlying OA. In this study, we explored and validated OA-related biomarkers across multiple tissues using bioinformatics and ML algorithms, aiming to provide new insights into the mechanisms of OA from multiple perspectives. First, we identified 83 DEGs from multiple tissue datasets using the RRA and SVA methods. Functional enrichment, pathway analysis, and DO enrichment analysis of these DEGs revealed their involvement in ECM organization, extracellular structure organization, the relaxin signaling pathway, the PI3K-Akt signaling pathway, and diseases such as connective tissue cancer and musculoskeletal system cancer.

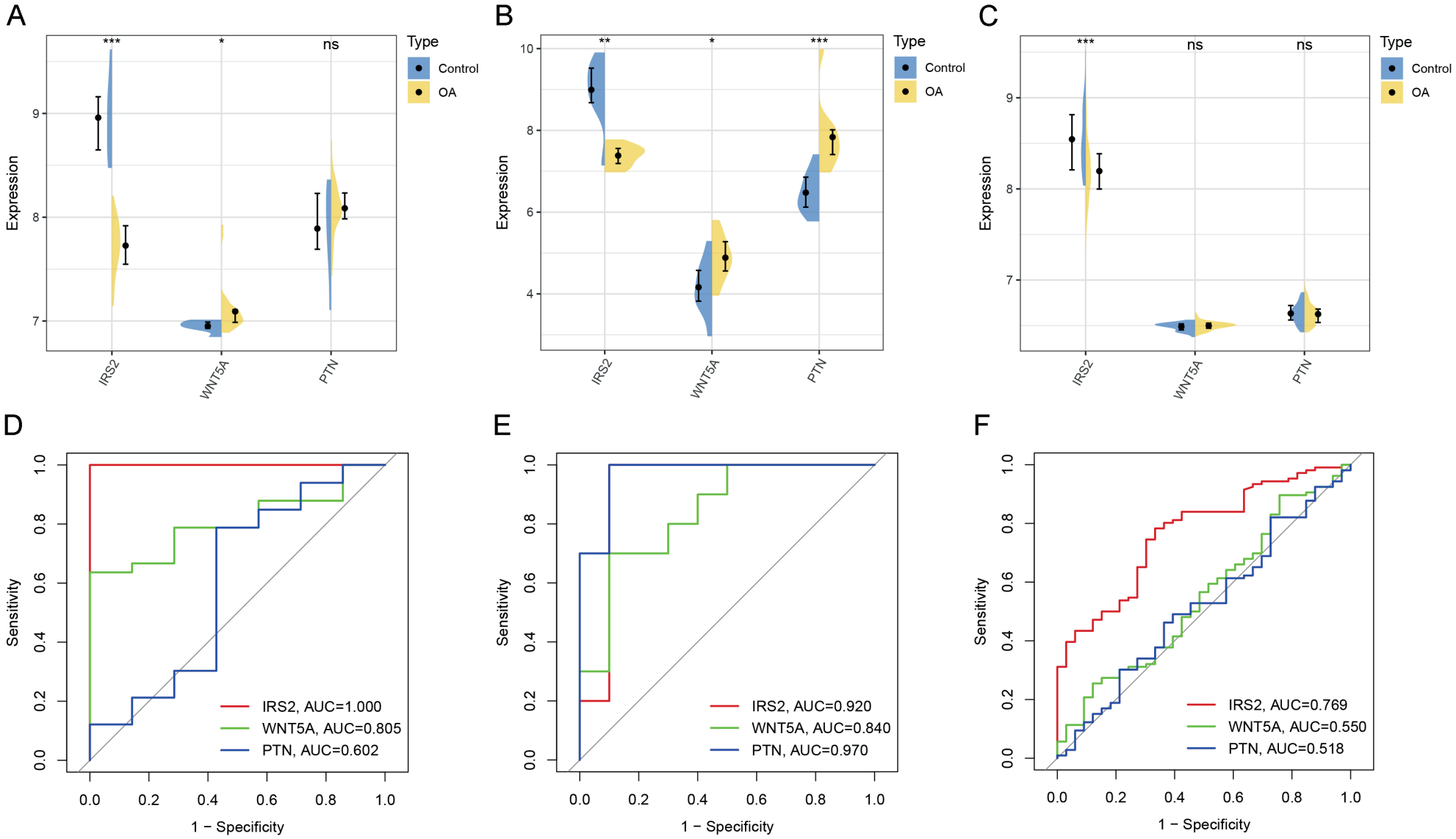

Fig. 6. Validation of feature genes in external datasets. A–C. Violin plots of gene expression in cartilage, synovial, and blood samples (*p < 0.05; **p < 0.01; ***p < 0.001); D–F. Receiver operating characteristic (ROC) curves in the corresponding sample types

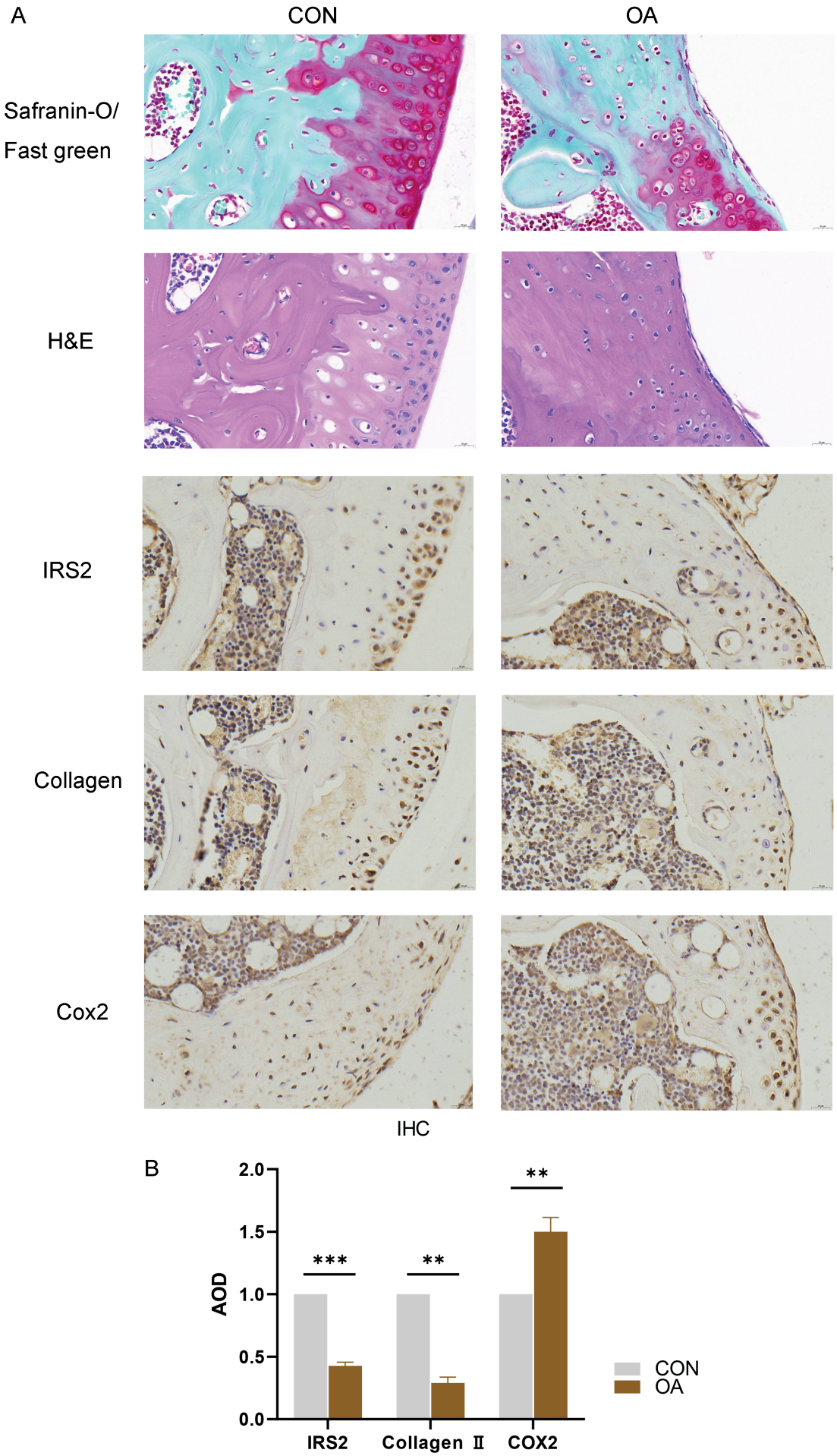

Fig. 7. Histological analysis of IRS2 expression in osteoarthritis (OA). A. Hematoxylin and eosin (H&E), Safranin O–Fast Green staining, and immunohistochemistry (IHC) for collagen II, COX2, and IRS2; B. Quantification of IHC (**p < 0.01; ***p < 0.001; n = 6)

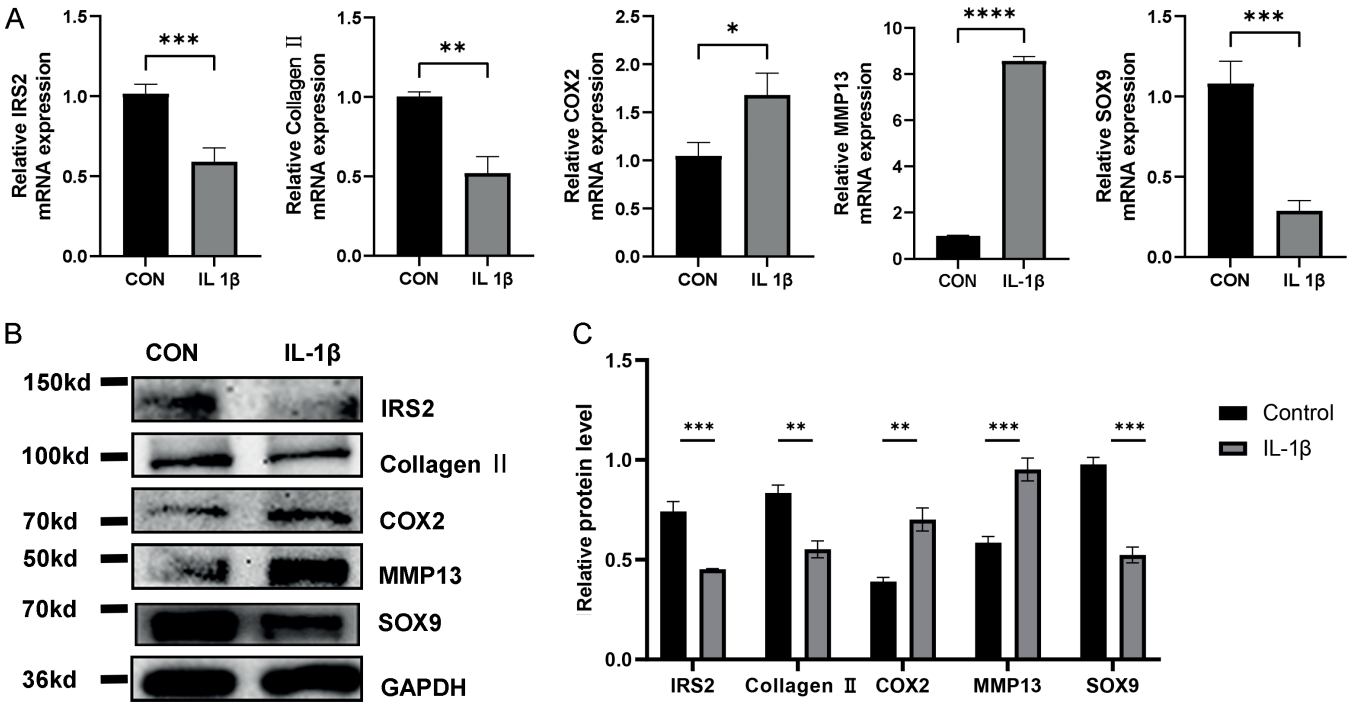

Fig. 8. IRS2 downregulation in osteoarthritis (OA). A. Real-time quantitative polymerase chain reaction (qPCR) analysis of collagen II, SOX9, COX2, and MMP13 in control and OA groups; B. Western blot analysis of the same markers; C. Quantified protein levels (mean ± standard deviation (SD); *p < 0.05; **p < 0.01; ***p < 0.001; n = 3)

Next, we constructed a PPI network and identified hub genes from the DEGs. Our methods identified 25 hub genes associated with OA. Functional enrichment and pathway analysis of these hub genes revealed their involvement in ECM organization, extracellular structure organization, the relaxin signaling pathway, the IL-17 signaling pathway, the AGE-RAGE signaling pathway in diabetic complications, and the PI3K-Akt signaling pathway. These pathways and functions were highly consistent with those identified for the DEGs, demonstrating the representative value of the identified hub genes. Additionally, these pathways and enrichment results are consistent with previous studies.[22,36–38]

To better identify OA-specific biomarkers, we employed ML algorithms for screening. Initially, we divided the dataset into training and test sets and evaluated the performance of 6 commonly used ML methods. We found that, regardless of the proportion of the training set, XGBoost, SVM, and LASSO regression demonstrated superior performance in identifying OA biomarkers and exhibited higher diagnostic accuracy, significantly outperforming the other ML methods. Consequently, we selected these 3 algorithms for screening OA-specific biomarkers and identified 15 candidates: *IRS2*, *ADM*, *SIK1*, *PTN*, *CX3CR1*, *WNT5A*, *IL21R*, *APOD*, *CRLF1*, *FKBP5*, *PNMAL1*, *NPR3*, *RARRES1*, *ASPN*, and *POSTN*. By intersecting these genes with the identified hub genes, we identified *IRS2*, *WNT5A*, *PTN*, and *POSTN* as diagnostic biomarkers for OA.

Although POSTN showed statistically significant differences in OA ($p < 0.01$), its ROC curve yielded an AUC below 0.7, indicating poor diagnostic performance. Thus, we constructed an OA risk prediction model based on the remaining 3 genes. The constructed and validated risk score nomogram was able to distinguish OA from normal tissues, with an AUC of 0.913, indicating high diagnostic accuracy. We validated these diagnostic genes using external datasets of OA cartilage, synovial, and blood samples. In the cartilage dataset, PTN did not show significant expression differences and had an AUC below 0.7. In the synovial tissue dataset, POSTN did not exhibit differential expression compared to the control group. However, in OA blood samples, IRS2 showed statistically significant expression differences and exhibited differential expression across all 3 tissue types ($p < 0.01$). Its AUC was consistently above 0.7, demonstrating good diagnostic performance. Thus, we have reason to believe that IRS2 may be involved in multiple aspects of OA progression, highlighting its potential as a promising diagnostic biomarker for OA.

Periostin (POSTN) is a 90 kDa matricellular protein discovered in 1993,39 involved in the pathogenesis of various diseases, including tumors, pulmonary fibrosis, and allergic diseases, with expression levels increasing as disease progresses in most cases.[39–41] POSTN interacts with ECM proteins to regulate cell–matrix organization, leading to remodeling and fibrosis. The unique characteristics of POSTN can be attributed to highly complex signaling pathways that lead to increased POSTN production.[39] In recent years, its association with orthopedic diseases has also become apparent.[42] Numerous studies have confirmed elevated POSTN expression in OA cartilage,[43–46] although its expression in OA synovial tissue and peripheral blood

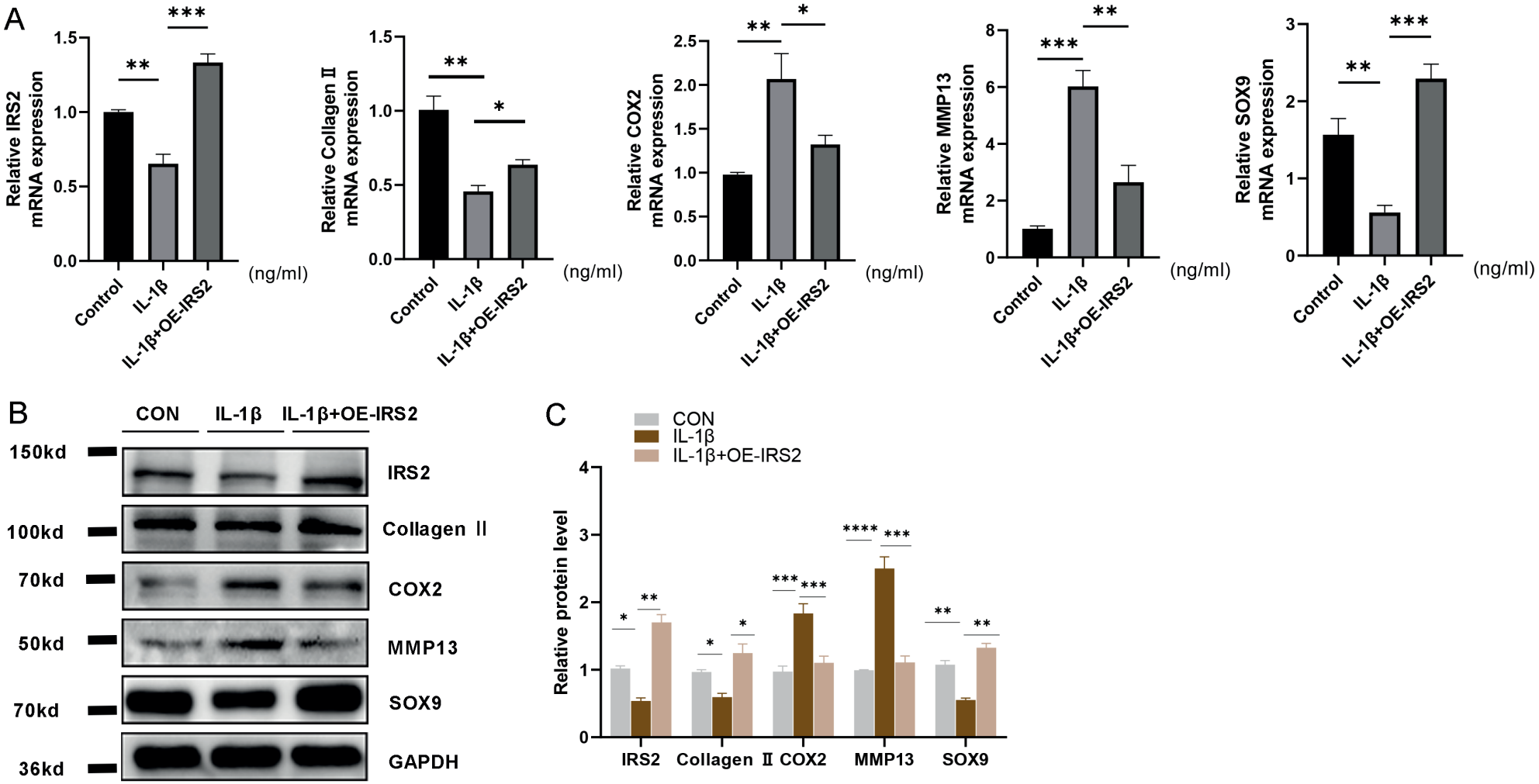

Fig. 9. IRS2 overexpression mitigates the effects of interleukin-1 beta (IL-1β) in chondrocytes. A. Real-time quantitative polymerase chain reaction (qPCR) analysis of markers after IRS2 overexpression and IL-1β treatment; B. Western blot analysis of the same markers; C. Representative blots (mean ± standard deviation (SD); *p < 0.05; **p < 0.01; ***p < 0.001; ****p < 0.0001; n = 3)

remains controversial. For example, Tajika et al.[47] reported high POSTN expression in OA synovial cells, while Attur et al.[48] observed no significant difference in expression between OA and control samples. Similarly, Rousseau et al[49] found serum POSTN to be associated with OA progression in women, but Sittisak Honsawek et al.[50] and Tan et al.[51] suggested that serum POSTN levels lack diagnostic value for OA. In our study, POSTN was consistently upregulated in OA cartilage samples but showed no significant changes in synovial or blood tissues. Although it was not ultimately selected as a diagnostic biomarker due to suboptimal performance (AUC < 0.7), its tissue-specific expression pattern may still reflect pathological remodeling in OA cartilage. These findings suggest that POSTN may play a role in disease progression, particularly in cartilage, and warrant further investigation in larger, well-characterized cohorts.

Pleiotrophin is a member of the midkine family,[52] a secreted heparin-binding peptide expressed during development in mesodermal and neuroectodermal cells but rarely in adult tissues.[53] Pufe et al.[54] found that PTN is almost undetectable in normal cartilage and synovial cells but is highly expressed in OA, with significant expression in the early and middle stages of OA but not in the late stage. Furthermore, Pufe et al.[55] suggested that PTN might participate in the early onset and development of OA by stimulating the activation of the activator protein-1 (AP-1) transcription factor and altering gene expression. In blood, studies by Fadda et al.[56] showed no significant difference in average PTN levels between OA patients and healthy controls, suggesting that while PTN may play an important role in OA, its potential as a disease biomarker requires larger-scale investigation and further research.

In our study, as shown in Fig. 6, PTN did not show statistically significant differences in the external cartilage tissue dataset, possibly because our cartilage tissue dataset represented late-stage OA. However, its high expression in the OA synovial tissue dataset is consistent with previous findings. Taken together, these results suggest that PTN may play a role in the diagnosis of early synovitis in OA.

WNT5A is a member of the Wnt protein family, which comprises a group of highly conserved signaling proteins that play crucial roles in embryonic development and various cellular processes, such as cell migration, polarity, and differentiation. WNT5A operates in the non-canonical Wnt signaling pathway, particularly influencing cell movement and polarity rather than directly affecting cell proliferation.[57] The high expression of WNT5A in OA cartilage has been confirmed in numerous studies, and its mechanisms of action in OA have been widely explored.[58–62] However, the role of WNT5A in OA synovium is less well understood. Lambert et al.[63] found high expression of WNT5A in OA synovium, regulated via the Wnt signaling pathway. This finding aligns with our conclusions. However, the expression of WNT5A in OA blood remains unstudied, necessitating further investigation.

Insulin receptor substrate 2 (IRS2) is a crucial member of the insulin receptor substrate family, playing a key role in insulin signaling and metabolic regulation. It primarily mediates signaling downstream of insulin and other growth factor receptors.[64] IRS2 is expressed in various cell types, including those in the liver, muscle, and adipose tissue, and is involved in multiple physiological processes.[65] The absence of IRS2 can lead to insulin resistance, which in turn promotes the development of type 2 diabetes.[66] Numerous studies have focused on the role of IRS2 in type 2 diabetes, obesity, and non-alcoholic fatty liver disease, exploring its molecular mechanisms.[65,66] Research has shown that the absence of IRS2 can have detrimental effects in various cell types and disease conditions.[67] However, the role of IRS2 in OA remains underexplored. In our study, we used external datasets from cartilage, synovial tissue, and OA blood samples for validation and observed consistently low expression of IRS2 across these tissues and sample types. Given the lack of in vivo and in vitro studies investigating IRS2 in OA, we conducted further validation through in vitro experiments. Western blotting and qPCR analyses revealed a significant reduction in IRS2 expression in OA chondrocytes, consistent with the findings from the datasets and statistically significant ($p < 0.001$). This suggests that IRS2 may play a role in the pathogenesis of OA.

Currently, the precise pathways through which IRS2 contributes to the progression of OA remain unclear. However, existing research suggests that IRS2 may influence disease progression by regulating inflammatory and apoptotic pathways. For instance, a study by Mayumi et al.[67] found that, under hypoxic conditions, high expression of IRS2 in macrophages contributes to anti-inflammatory effects in pulmonary vascular remodeling. Similarly, Baquedano et al.[68] observed increased oxidative stress and apoptosis in the hypothalamus of diabetic male mice with *IRS2* gene knockout. These studies indicate that *IRS2* might affect the progression of OA by modulating inflammation and apoptosis. Additionally, research by Kaede et al.[69] demonstrated that vitamin C enhances insulin-induced chondrocyte differentiation in ATDC5 cells by upregulating the expression of *IRS2* and other insulin signaling molecules. This further supports the potential role of *IRS2* in OA.

Future research should focus on elucidating the specific functions and regulatory mechanisms of IRS2 in OA and exploring its feasibility as a potential therapeutic target. Through further mechanistic studies and clinical validation, it is hoped that the role of *IRS2* in the pathological process of OA will be elucidated, offering new insights and approaches for the diagnosis and treatment of OA.

Limitations of the study

This study has several limitations. First, it relies on publicly available GEO datasets, which, despite offering rich biological information, may vary in quality, consistency, and

sequencing platforms – potentially affecting the reliability of the results despite batch effect correction (e.g., SVA). Second, although 3 diagnostic genes (*IRS2*, *WNT5A*, *PTN*) were identified and showed good performance in ROC analysis, their clinical utility requires further validation. Third, while multiple ML methods (XGBoost, LASSO, SVM) were applied, other models like deep learning were not explored, and model performance on external datasets needs further verification. Lastly, *IRS2* expression was only validated in chondrocytes; its role in other OA-relevant tissues (e.g., synovium, subchondral bone, blood) remains to be clarified. Future studies should include broader datasets and deeper functional validation to strengthen the findings.

Conclusions

This study integrates bioinformatics analysis and ML algorithms to identify and validate 3 diagnostic biomarkers for OA: *IRS2*, *WNT5A*, and *PTN*. IRS2 demonstrated high and consistent diagnostic performance across multiple tissue types and external datasets, highlighting its potential as a robust biomarker. WNT5A exhibited good discriminatory ability, particularly in cartilage and synovial tissues. Although PTN showed moderate diagnostic performance overall, its expression patterns suggest potential relevance for early OA diagnosis and warrant further investigation.

Supplementary data

The supplementary materials are available at https://doi.org/10.5281/zenodo.17409505. The package contains the following files:

Supplementary Table 1. Final diagnostic biomarkers for OA and their functional annotations, interacting genes, and network characteristics.

Supplementary Fig. 1. Comprehensive visualization of batch-effect correction and sample grouping.

Supplementary Fig. 2. Identification and enrichment analysis of DEGs in osteoarthritis.

Supplementary Fig. 3. Machine-learning screening of OA feature genes.

Data Availability Statement

The data from the GEO dataset can be downloaded here: https://www.ncbi.nlm.nih.gov/geo

Consent for publication of personal information

Not applicable

Use of AI and AI-assisted technologies

Not applicable.

Preprint disclosure

This paper was previously made available as a preprint on Research Square at https://www.researchsquare.com/article/rs-4706641/v1.

ORCID iDs

Guihao Zheng https://orcid.org/0000-0002-0850-1569
Yulong Ouyang https://orcid.org/0000-0002-0690-053
Shuilin Chen https://orcid.org/0009-0007-7533-0329
Bei Hu https://orcid.org/0009-0002-4900-3766
Shuai Xu https://orcid.org/0000-0007-1722-451X
Guicai Sun https://orcid.org/0000-0002-1306-7592

References

1. Vos T, Flaxman AD, Naghavi M, et al. Years lived with disability (YLDs) for 1160 sequelae of 289 diseases and injuries 1990–2010: A systematic analysis for the Global Burden of Disease Study 2010. *Lancet*. 2012;380(9859):2163–2196. doi:10.1016/S0140-6736(12)61729-2
2. Steinmetz JD, Culbreth GT, Haile LM, et al. Global, regional, and national burden of osteoarthritis, 1990–2020 and projections to 2050: A systematic analysis for the Global Burden of Disease Study 2021. *Lancet Rheumatol*. 2023;5(9):e508–e522. doi:10.1016/S2665-9913(23)00163-7
3. Puig-Junoy J, Ruiz Zamora A. Socio-economic costs of osteoarthritis: A systematic review of cost-of-illness studies. *Semin Arthritis Rheum*. 2015;44(5):531–541. doi:10.1016/j.semarthrit.2014.10.012
4. Peat G, Thomas MJ. Osteoarthritis year in review 2020: Epidemiology & therapy. *Osteoarthritis Cartilage*. 2021;29(2):180–189. doi:10.1016/j.joca.2020.10.007
5. Holt HL, Katz JN, Reichmann WM, et al. Forecasting the burden of advanced knee osteoarthritis over a 10-year period in a cohort of 60–64 year-old US adults. *Osteoarthritis Cartilage*. 2011;19(1):44–50. doi:10.1016/j.joca.2010.10.009
6. Cao M, Li C, Li M, et al. Prevalence and incidence of rheumatoid arthritis in urban China: A national population-based study. *Int J Rheum Dis*. 2025;28(5):e70184. doi:10.1111/1756-185X.70184
7. Guccione AA, Felson DT, Anderson JJ, et al. The effects of specific medical conditions on the functional limitations of elders in the Framingham Study. *Am J Public Health*. 1994;84(3):351–358. doi:10.2105/AJPH.84.3.351
8. Chen D, Shen J, Zhao W, et al. Osteoarthritis: Toward a comprehensive understanding of pathological mechanism. *Bone Res*. 2017;5(1):16044. doi:10.1038/boneres.2016.44
9. Katz JN, Arant KR, Loeser RF. Diagnosis and treatment of hip and knee osteoarthritis: A review. *JAMA*. 2021;325(6):568. doi:10.1001/jama.2020.22171
10. Xiong H, Huang TY, Chang YL, Su WT. Achyranthes bidentate extracts protect the IL-1β-induced osteoarthritis of SW1353 chondrocytes. *J Biosci Bioeng*. 2023;136(6):462–470. doi:10.1016/j.jbiosc.2023.09.008
11. Li X, Chen W, Liu D, et al. Pathological progression of osteoarthritis: A perspective on subchondral bone. *Front Med (Lausanne)*. 2024;18(2):237–257. doi:10.1007/s11684-024-1061-y
12. Yang D, Xu K, Xu X, Xu P. Revisiting prostaglandin E2: A promising therapeutic target for osteoarthritis. *Clin Immunol*. 2024;260:109904. doi:10.1016/j.clim.2024.109904
13. Wen Z, Sun Q, Shan Y, et al. Endoplasmic reticulum stress in osteoarthritis: A novel perspective on the pathogenesis and treatment. *Aging Dis*. 2022;14(2):283–286. doi:10.14336/AD.2022.0725
14. Wang Q, Rozelle AL, Lepus CM, et al. Identification of a central role for complement in osteoarthritis. *Nat Med*. 2011;17(12):1674–1679. doi:10.1038/nm.2543
15. Woetzel D, Huber R, Kupfer P, et al. Identification of rheumatoid arthritis and osteoarthritis patients by transcriptome-based rule set generation. *Arthritis Res Ther*. 2014;16(2):R84. doi:10.1186/ar4526
16. Filer A, Antczak P, Parsonage GN, et al. Stromal transcriptional profiles reveal hierarchies of anatomical site, serum response and disease and identify disease specific pathways. *PLoS One*. 2015;10(3):e0120917. doi:10.1371/journal.pone.0120917

17. Fisch KM, Gamini R, Alvarez-Garcia O, et al. Identification of transcription factors responsible for dysregulated networks in human osteoarthritis cartilage by global gene expression analysis. *Osteoarthritis Cartilage*. 2018;26(11):1531–1538. doi:10.1016/j.joca.2018.07.012
18. Xu S, Ye J, Cai X. Identification of energy metabolism-related subtypes and diagnostic biomarkers for osteoarthritis by integrating bioinformatics and machine learning. *J Multidiscip Healthc*. 2025;18: 1353–1369. doi:10.2147/JMDH.S510308
19. Dong S, Xia T, Wang L, Zhao Q, Tian J. Investigation of candidate genes for osteoarthritis based on gene expression profiles. *Acta Orthop Traumatol Turc*. 2016;50(6):686–690. doi:10.1016/j.aott.2016.04.002
20. Coppola C, Greco M, Munir A, et al. Osteoarthritis: Insights into diagnosis, pathophysiology, therapeutic avenues, and the potential of natural extracts. *Curr Issues Mol Biol*. 2024;46(5):4063–4105. doi:10.3390/cimb46050251
21. Luo H, Li L, Han S, Liu T. The role of monocyte/macrophage chemokines in pathogenesis of osteoarthritis: A review. *Int J Immunogenet*. 2024;51(3):130–142. doi:10.1111/iji.12664
22. Zhou J, Huang J, Li Z, et al. Identification of aging-related biomarkers and immune infiltration characteristics in osteoarthritis based on bioinformatics analysis and machine learning. *Front Immunol*. 2023;14:1168780. doi:10.3389/fimmu.2023.1168780
23. Han Y, Wu J, Gong Z, et al. Identification and development of a novel 5-gene diagnostic model based on immune infiltration analysis of osteoarthritis. *J Transl Med*. 2021;19(1):522. doi:10.1186/s12967-021-03183-9
24. Yin W, Lei Y, Yang X, Zou J. A two-gene random forest model to diagnose osteoarthritis based on RNA-binding protein-related genes in knee cartilage tissue. *Aging*. 2023;15(1):193–212. doi:10.18632/aging.204469
25. Chen Z, Wang W, Zhang Y, Xue X, Hua Y. Identification of four-gene signature to diagnose osteoarthritis through bioinformatics and machine learning methods. *Cytokine*. 2023;169:156300. doi:10.1016/j.cyto.2023.156300
26. Friedman J, Hastie T, Tibshirani R. Regularization paths for generalized linear models via coordinate descent. *J Stat Softw*. 2010;33(1):1–22. PMID:20808728. PMCID:PMC2929880.
27. Luts J, Ojeda F, Van De Plas R, De Moor B, Van Huffel S, Suykens JAK. A tutorial on support vector machine-based methods for classification problems in chemometrics. *Anal Chim Acta*. 2010;665(2):129–145. doi:10.1016/j.aca.2010.03.030
28. Decup F, Léger S, Lefèvre S, Doméjean S, Grosgogeat B. Risk factors or indicators for dental caries and tooth wear and their relative importance in adults according to age. *J Dent*. 2024;147:105092. doi:10.1016/j.jdent.2024.105092
29. Hart CR, Wilson DK, Pettit CL, Nykaza ET. Machine-learning of long-range sound propagation through simulated atmospheric turbulence. *J Acoust Soc Am*. 2021;149(6):4384–4395. doi:10.1121/10.0005280
30. Islam SMS, Talukder A, Awal MdA, et al. Machine learning approaches for predicting hypertension and its associated factors using population-level data from three South Asian countries. *Front Cardiovasc Med*. 2022;9:839379. doi:10.3389/fcvm.2022.839379
31. Xiao J, Luo C, Li A, et al. Icariin inhibits chondrocyte ferroptosis and alleviates osteoarthritis by enhancing the SLC7A11/GPX4 signaling. *Int Immunopharmacol*. 2024;133:112010. doi:10.1016/j.intimp.2024.112010
32. Chen Y, Pan X, Zhao J, et al. Icariin alleviates osteoarthritis through PI3K/Akt/mTOR/ULK1 signaling pathway. *Eur J Med Res*. 2022;27(1):204. doi:10.1186/s40001-022-00820-x
33. Mu Y, Wang L, Fu L, Li Q. Knockdown of LMX1B suppressed cell apoptosis and inflammatory response in IL-1β-induced human osteoarthritis chondrocytes through NF-κB and NLRP3 signal pathway. *Mediators Inflamm*. 2022;2022:1870579. doi:10.1155/2022/1870579
34. Xu H, Chen S, Meng C, He Y, Huang XJ, You HB. Inhibition of CC chemokine receptor 1 ameliorates osteoarthritis in mouse by activating PPAR-γ. *Mol Med*. 2024;30(1):74. doi:10.1186/s10020-024-00823-w
35. Glasson SS, Blanchet TJ, Morris EA. The surgical destabilization of the medial meniscus (DMM) model of osteoarthritis in the 129/SvEv mouse. *Osteoarthritis Cartilage*. 2007;15(9):1061–1069. doi:10.1016/j.joca.2007.03.006
36. Sun K, Luo J, Guo J, Yao X, Jing X, Guo F. The PI3K/AKT/mTOR signaling pathway in osteoarthritis: A narrative review. *Osteoarthritis Cartilage*. 2020;28(4):400–409. doi:10.1016/j.joca.2020.02.027
37. Xiao J, Zhang P, Cai FL, et al. IL-17 in osteoarthritis: A narrative review. *Open Life Sci*. 2023;18(1):20220747. doi:10.1515/biol-2022-0747
38. Wang K, Li Y, Lin J. Identification of diagnostic biomarkers for osteoarthritis through bioinformatics and machine learning. *Heliyon*. 2024; 10(6):e27506. doi:10.1016/j.heliyon.2024.e27506
39. Ono J, Takai M, Kamei A, Azuma Y, Izuhara K. Pathological roles and clinical usefulness of periostin in type 2 inflammation and pulmonary fibrosis. *Biomolecules*. 2021;11(8):1084. doi:10.3390/biom11081084
40. Yu Y, Tan CM, Jia YY. Research status and the prospect of POSTN in various tumors. *Neoplasma*. 2021;68(4):673–682. doi:10.4149/neo_2021_210223N239
41. Sonnenberg-Riethmacher E, Miehe M, Riethmacher D. Periostin in allergy and inflammation. *Front Immunol*. 2021;12:722170. doi:10.3389/fimmu.2021.722170
42. Yoshihara T, Morimoto T, Hirata H, et al. Mechanisms of tissue degeneration mediated by periostin in spinal degenerative diseases and their implications for pathology and diagnosis: A review. *Front Med (Lausanne)*. 2023;10:1276900. doi:10.3389/fmed.2023.1276900
43. Han T, Mignatti P, Abramson SB, Attur M. Periostin interaction with discoidin domain receptor-1 (DDR1) promotes cartilage degeneration. *PLoS One*. 2020;15(4):e0231501. doi:10.1371/journal.pone.0231501
44. Chijimatsu R, Kunugiza Y, Taniyama Y, Nakamura N, Tomita T, Yoshikawa H. Expression and pathological effects of periostin in human osteoarthritis cartilage. *BMC Musculoskelet Disord*. 2015;16(1):215. doi:10.1186/s12891-015-0682-3
45. Duan X, Cai L, Pham CTN, et al. Amelioration of posttraumatic osteoarthritis in mice using intraarticular silencing of periostin via nanoparticle-based small interfering RNA. *Arthritis Rheum*. 2021;73(12): 2249–2260. doi:10.1002/art.41794
46. Attur M, Yang Q, Shimada K, et al. Elevated expression of periostin in human osteoarthritic cartilage and its potential role in matrix degradation via matrix metalloproteinase-13. *FASEB J*. 2015;29(10): 4107–4121. doi:10.1096/fj.15-272427
47. Tajika Y, Moue T, Ishikawa S, et al. Influence of periostin on synoviocytes in knee osteoarthritis. *In Vivo*. 2017;31(1):69–78. doi:10.21873/invivo.11027
48. Attur M, Duan X, Cai L, et al. Periostin loss-of-function protects mice from post-traumatic and age-related osteoarthritis. *Arthritis Res Ther*. 2021;23(1):104. doi:10.1186/s13075-021-02477-z
49. Rousseau JC, Sornay-Rendu E, Bertholon C, Garnero P, Chapurlat R. Serum periostin is associated with prevalent knee osteoarthritis and disease incidence/progression in women: The OFELY study. *Osteoarthritis Cartilage*. 2015;23(10):1736–1742. doi:10.1016/j.joca.2015.05.015
50. Honsawek S, Wilairatana V, Udomsinprasert W, Sinlapavilawan P, Jirathanathornnukul N. Association of plasma and synovial fluid periostin with radiographic knee osteoarthritis: Cross-sectional study. *Joint Bone Spine*. 2015;82(5):352–355. doi:10.1016/j.jbspin.2015.01.023
51. Tan Q, Yang Z, Xin X, et al. Serum periostin level is not sufficient to serve as a clinically applicable biomarker of osteoarthritis. *BMC Musculoskelet Disord*. 2022;23(1):1039. doi:10.1186/s12891-022-06017-x
52. Yazihan N. Midkine in inflammatory and toxic conditions. *Curr Drug Deliv*. 2013;10(1):54–57. doi:10.2174/1567201811310010009
53. Mentlein R. Targeting pleiotropin to treat osteoarthritis. *Exp Opin Ther Targets*. 2007;11(7):861–867. doi:10.1517/14728222.11.7.861
54. Pufe T, Bartscher M, Petersen W, Tillmann B, Mentlein R. Pleiotrophin, an embryonic differentiation and growth factor, is expressed in osteoarthritis. *Osteoarthritis Cartilage*. 2003;11(4):260–264. doi:10.1016/S1063-4584(02)00385-0
55. Pufe T, Groth G, Goldring MB, Tillmann B, Mentlein R. Effects of pleiotrophin, a heparin-binding growth factor, on human primary and immortalized chondrocytes. *Osteoarthritis Cartilage*. 2007;15(2): 155–162. doi:10.1016/j.joca.2006.07.005
56. Fadda SMH, Bassyouni IH, Khalifa RH, Elsaid NY. Pleiotrophin, the angiogenic and mitogenic growth factor: Levels in serum and synovial fluid in rheumatoid arthritis and osteoarthritis, and correlation with clinical, laboratory and radiological indices. *Z Rheumatol*. 2018;77(4):322–329. doi:10.1007/s00393-016-0234-8
57. Suthon S, Perkins RS, Bryja V, Miranda-Carboni GA, Krum SA. WNT5B in physiology and disease. *Front Cell Dev Biol*. 2021;9:667581. doi:10.3389/fcell.2021.667581

58. Shao L, Gou Y, Fang J, et al. The protective effects of parathyroid hormone (1-34) on cartilage and subchondral bone through down-regulating JAK2/STAT3 and WNT5A/ROR2 in a collagenase-induced osteoarthritis mouse model. *Orthop Surg*. 2021;13(5):1662–1672. doi:10.1111/os.13019
59. Martineau X, Abed É, Martel-Pelletier J, Pelletier JP, Lajeunesse D. Alteration of Wnt5a expression and of the non-canonical Wnt/PCP and Wnt/PKC-Ca_2^+ pathways in human osteoarthritis osteoblasts. *PLoS One*. 2017;12(8):e0180711. doi:10.1371/journal.pone.0180711
60. Li Y, Xiao W, Sun M, et al. The expression of osteopontin and Wnt5a in articular cartilage of patients with knee osteoarthritis and its correlation with disease severity. *Biomed Res Int*. 2016;2016:9561058. doi:10.1155/2016/9561058
61. Qi Y, Tang R, Shi Z, Feng G, Zhang W. Wnt5a/Platelet-rich plasma synergistically inhibits IL-1β-induced inflammatory activity through NF-κB signaling pathway and prevents cartilage damage and promotes meniscus regeneration. *J Tissue Eng Regen Med*. 2021;15(7):612–624. doi:10.1002/term.3198
62. Ding D, Wang L, Yan J, et al. Zoledronic acid generates a spatiotemporal effect to attenuate osteoarthritis by inhibiting potential Wnt5a-associated abnormal subchondral bone resorption. *PLoS One*. 2022;17(7):e0271485. doi:10.1371/journal.pone.0271485
63. Lambert C, Dubuc J, Montell E, et al. Gene expression pattern of cells from inflamed and normal areas of osteoarthritis synovial membrane. *Arthritis Rheum*. 2014;66(4):960–968. doi:10.1002/art.38315
64. Lee YH, White MF. Insulin receptor substrate proteins and diabetes. *Arch Pharm Res*. 2004;27(4):361–370. doi:10.1007/BF02980074
65. Eckstein SS, Weigert C, Lehmann R. Divergent roles of IRS (insulin receptor substrate) 1 and 2 in liver and skeletal muscle. *Curr Med Chem*. 2017;24(17):1827–1852. doi:10.2174/0929867324666170426142826
66. White MF. IRS2 integrates insulin/GF1 signalling with metabolism, neurodegeneration and longevity. *Diabetes Obes Metab*. 2014;16(Suppl 1):4–15. doi:10.1111/dom.12347
67. Nakahara M, Ito H, Skinner JT, et al. The inflammatory role of dysregulated IRS2 in pulmonary vascular remodeling under hypoxic conditions. *Am J Physiol Lung Cell Mol Physiol*. 2021;321(2):L416–L428. doi:10.1152/ajplung.00068.2020
68. Baquedano E, Burgos-Ramos E, Canelles S, et al. Increased oxidative stress and apoptosis in the hypothalamus of diabetic male mice in the insulin receptor substrate-2 knockout model. *Dis Model Mech*. 2016;9(5):573–583. doi:10.1242/dmm.023515
69. Okita K, Hikiji H, Koga A, et al. Ascorbic acid enhances chondrocyte differentiation of ATDC5 by accelerating insulin receptor signaling. *Cell Biol Int*. 2023;47(10):1737–1748. doi:10.1002/cbin.12067

Family and dietary risk factors associated with childhood sleep disorders: Evidence from a cross-sectional study in China

Lifeng Zhang[1,2,A,B], Xiangjing Chen[2,B,C], Xin Zhang[2,C,D], Ya Yan[1,A,D], Renzhong Wang[2,E,F]

[1] The First College for Clinical Medicine, Shandong University of Traditional Chinese Medicine, Jinan, China
[2] Department of Otolaryngology, Shandong University of Traditional Chinese Medicine Affiliated Hospital, Jinan, China

A – research concept and design; B – collection and/or assembly of data; C – data analysis and interpretation; D – writing the article; E – critical revision of the article; F – final approval of the article

Advances in Clinical and Experimental Medicine, ISSN 1899–5276 (print), ISSN 2451–2680 (online) *Adv Clin Exp Med*. 2026;35(7):1235–1245

Address for correspondence
Renzhong Wang
E-mail: renz1022@163.com

Funding sources
This work was funded by Shandong Provincial Natural Science Foundation (grant No. ZR2023LZY013).

Conflict of interest
None declared

Received on June 18, 2025
Reviewed on July 19, 2025
Accepted on October 14, 2025

Published online on July 30, 2026

Abstract

Background. Childhood sleep disorders are common and are associated with family- and diet-related factors, such as parental snoring and unhealthy eating habits. However, culturally relevant studies remain limited, and existing research often overlooks weak correlations in large populations.

Objectives. This study aimed to identify family- and diet-related risk factors for childhood sleep disorders in a Chinese population and to provide insights for prevention.

Materials and methods. A cross-sectional study was conducted in Jinan, China, between January 2022 and December 2023, enrolling 845 children aged 1–7 years through convenience sampling. Sleep disorders were defined based on parent-reported symptoms (mouth breathing, habitual snoring, apnea, or gasping) using a validated questionnaire. Demographic, family, and dietary factors were collected. Associations were analyzed using multivariable logistic regression with stepwise selection based on the Akaike information criterion (AIC), adjusted for age, with subgroup analyses according to age (1–3, 4–5, and 6–7 years). Statistical significance was set at $p < 0.05$.

Results. Among the 845 children (mean age: 5.2 years), 192 (22.7%) had sleep disorders. Multivariable analysis showed that parental snoring (father: odds ratio (OR) = 2.20, 95% confidence interval (95% CI): 1.44–3.41; mother: OR = 1.76, 95% CI: 1.15–2.66), maternal education at the associate degree level (OR = 2.58, 95% CI: 1.27–5.66) or bachelor's degree level (OR = 2.44, 95% CI: 1.21–5.29), and children's preferences for fried foods (OR = 6.49, 95% CI: 2.51–17.40), meat (OR = 2.19, 95% CI: 1.43–3.35), and sweets (OR = 2.15, 95% CI: 1.31–3.51) were significant risk factors. Moderate sweet consumption (1–2 times/week: OR = 0.53, 95% CI: 0.29–0.95; 3–5 times/week: OR = 0.51, 95% CI: 0.27–0.94) was associated with a protective effect compared with daily consumption.

Conclusions. Childhood sleep disorders were significantly associated with parental snoring, higher maternal educational attainment, and children's preferences for fried foods, meat, and sweets, whereas moderate sweet consumption appeared to have a protective effect.

Key words: risk factors, dietary habits, childhood sleep disorders, parental snoring, maternal education

Cite as
Zhang L, Chen X, Zhang X, Yan Y, Wang R. Family and dietary risk factors associated with childhood sleep disorders: Evidence from a cross-sectional study in China. *Adv Clin Exp Med*. 2026;35(7):1235–1245. doi:10.17219/acem/212573

DOI
10.17219/acem/212573

Copyright
Copyright by Author(s)
This is an article distributed under the terms of the Creative Commons Attribution 3.0 Unported (CC BY 3.0) (https://creativecommons.org/licenses/by/3.0/)

Highlights

- Parental snoring significantly increases the risk of sleep disorders in young children.
- Children who prefer fried foods, meat, and sweets are more likely to experience sleep-related symptoms.
- Higher maternal education level is unexpectedly linked to increased childhood sleep disorder risk.
- Moderate sweet consumption (1–5 times per week) may help protect children from sleep disturbances.

Background

Childhood sleep disorders are a common and significant health concern, affecting 20–30% of children globally, with even higher rates observed in preschool-aged populations.[1] Characterized by symptoms such as snoring, mouth breathing, and difficulty initiating or maintaining sleep, these disorders compromise not only sleep quality but also cognitive, emotional, and behavioral development.[2] Sleep disturbances are also associated with physical health risks, including impaired growth, weakened immune function, obesity, and cardiovascular problems.[3,4]

Although a growing body of literature highlights the multifactorial nature of childhood sleep disorders, many studies inadequately address modifiable risk factors, particularly within culturally specific contexts. Family environment and dietary habits have emerged as influential determinants. Parental snoring, educational attainment, and psychological health have been consistently associated with childhood sleep outcomes.[5,6] For instance, several large-scale studies have confirmed the association between parental snoring and children's sleep-disordered breathing (SDB). Kaditis et al.[7] identified parental snoring and passive smoking as significant risk factors for SDB in a Greek pediatric population. Similarly, Li et al.[8] and Katila et al.[9] reported associations between parental snoring and habitual snoring in children across different age groups. Socioeconomic factors, including parental education and household income, have also been implicated in children's sleep health.[10]

Dietary behavior plays a similarly important role. High consumption of sweets and fried foods, as well as irregular eating habits, has been shown to negatively affect sleep, whereas healthier dietary patterns rich in vegetables and protein may improve sleep quality.[11–13] However, existing studies are often fragmented, lack a systematic framework, or yield inconsistent findings across different populations.

Moreover, while large sample sizes improve statistical power, they may also increase the likelihood of detecting weak associations with limited clinical relevance. This highlights the need for cautious interpretation of findings derived from large-scale studies.

To address these limitations, the present study draws upon Bronfenbrenner's Bioecological Model, which emphasizes the interplay between individual biological characteristics and microsystem-level influences, such as family behaviors and daily routines. Within this framework, parental snoring, educational attainment, and dietary practices are considered proximal factors that may influence children's sleep through both direct and indirect mechanisms.

Objectives

This study aimed to conduct a systematic analysis of family- and diet-related risk factors for childhood sleep disorders among children aged 1–7 years. We hypothesized that parental snoring, parental educational attainment, and children's dietary preferences (including preferences for meat, sweets, and fried foods) would be associated with an increased risk of sleep disorders. These variables were selected based on existing evidence suggesting their influence on sleep health. By identifying potentially modifiable risk factors, this study sought to provide targeted and culturally relevant insights for early prevention.

Materials and methods

Study design and setting

This cross-sectional observational study was conducted between January 2022 and December 2023 in Jinan, China. Participants were recruited through convenience sampling from the Department of Otolaryngology at the Affiliated Hospital of Shandong University of Traditional Chinese Medicine, a large tertiary-care hospital, and its affiliated community health service center. This region was selected because of its diverse urban population and accessibility to pediatric outpatient services. A cross-sectional design was chosen to examine associations between sleep-related symptoms and family- and diet-related factors at a single point in time.

The study protocol was approved by the Ethics Committee of the Affiliated Hospital of Shandong University of Traditional Chinese Medicine (approval No. AF/SC-08/02.0). Written informed consent was obtained from the parents or legal guardians of all participating children prior to data collection. All procedures were conducted in accordance with the Declaration of Helsinki.

Sample size and sampling method

Convenience sampling was used to enroll children aged 1–7 years who attended outpatient clinics for routine consultations or health check-ups during the study period. The sample size of 845 participants was determined based on the expected patient flow and logistical feasibility. No formal sample size or statistical power calculation was performed due to the exploratory nature of the study. Participants were recruited consecutively to minimize sampling bias. No stratification or matching procedures were applied.

However, the use of convenience sampling introduces the potential for selection bias, as participants were limited to children seeking medical care or attending health check-ups at specific facilities and may therefore not be representative of the general pediatric population. Families with greater health awareness or particular socioeconomic characteristics may have been overrepresented, potentially influencing dietary and sleep-related findings. Furthermore, because recruitment was conducted in a single city, regional cultural and dietary patterns may limit the generalizability of the findings to other areas of China.

Participants

Children were eligible for inclusion if they were aged 1–7 years and were accompanied by a parent or legal guardian who provided informed consent for participation. Exclusion criteria included congenital malformations, neurological or developmental disorders (e.g., epilepsy or autism spectrum disorder (ASD)), chronic respiratory diseases, and any medical conditions that could affect growth or sleep. Eligibility was assessed by trained pediatric clinicians before questionnaire administration.

Children were classified as having sleep disorders if they exhibited 1 or more parent-reported symptoms, including mouth breathing during sleep, habitual snoring, apnea, or gasping for breath. Children without these symptoms were classified as not having sleep disorders. Classification was based on caregiver reports referring to the previous month and was consistent with established pediatric sleep disorder screening protocols.

Data sources and measurement

Data were collected using a structured parent-reported questionnaire developed on the basis of previously validated instruments used in pediatric sleep research. The 34-item questionnaire assessed: 1) demographic characteristics; 2) family environment (e.g., parental snoring and educational attainment); 3) dietary behaviors (e.g., food preferences and consumption frequency); and 4) sleep-related symptoms.

The questionnaire was developed with reference to Chinese dietary recall surveys and pediatric sleep screening tools. A pilot study involving 50 participants yielded a Cronbach's alpha coefficient of 0.83, indicating good internal consistency. Content validity was assessed and confirmed by 2 pediatric sleep specialists. The questionnaires were completed on-site under the supervision of trained staff to ensure completeness, and any ambiguous responses were clarified in real time.

Statistical analyses

Descriptive statistics were used to summarize all variables. Quantitative data were expressed as mean ± standard deviation (SD) for normally distributed variables and as median (interquartile range (IQR)) for non-normally distributed variables. Qualitative data were summarized as frequencies and percentages.

The normality of continuous variables was assessed using the Kolmogorov–Smirnov test with Lilliefors correction, supplemented by visual inspection of histograms and normal quantile-quantile (Q-Q) plots, in accordance with the journal's statistical guidelines. Skewness values were also calculated to provide additional confirmation. The results of the normality tests for each variable and subgroup are presented in Supplementary Table 1. For correlation analyses, Pearson's correlation coefficient (r) was used for continuous variables, whereas Kendall's tau-b correlation coefficient was applied to ordinal dietary frequency variables (e.g., fruit, vegetable, seafood, fried food, sweet, and beverage consumption frequencies).

Baseline characteristics were reported for the overall study population and further stratified according to sleep disorder status (sleep disorder group vs non-sleep disorder group). Group comparisons were performed using independent-samples t-tests for normally distributed continuous variables and Mann–Whitney U tests for non-normally distributed continuous variables. Categorical variables were compared using the χ^2 test or Fisher's exact test, as appropriate.

To identify independent risk factors for childhood sleep disorders, multivariable logistic regression analysis was performed. All candidate predictors were initially entered into the model, and variable selection was conducted using a stepwise procedure based on the Akaike information criterion (AIC), retaining variables that minimized the AIC to achieve an optimal balance between model fit and parsimony. No predefined AIC threshold was applied. The selection procedure was terminated when neither the addition nor removal of any variable resulted in a further reduction in the AIC. Univariate analyses were conducted for descriptive purposes only (Supplementary Table 2) and were not used for inferential analyses. Given the wide age range of the participants (1–7 years), 2 complementary approaches were applied:

1. Age was included as a continuous covariate in the main multivariable model (Supplementary Table 3), allowing the assessment of independent effects while adjusting for other predictors.

2. Subgroup analyses stratified by age group (1–3, 4–5, and 6–7 years) were conducted as a sensitivity analysis to examine age-specific effects (Supplementary Table 4).

Model assumptions and diagnostics were evaluated as follows:

– Multicollinearity was assessed using the variance inflation factor (VIF), with VIF values >5 considered indicative of collinearity.

– The goodness-of-fit of the final model was assessed using the Hosmer–Lemeshow test, Nagelkerke R^2, and Cox and Snell R^2. Model discrimination was evaluated using the concordance index (C-index).

Potential confounders, such as screen time, family stress, and housing conditions, were not measured, which represents a limitation of this study. All statistical analyses were conducted using IBM SPSS Statistics v. 24.0 (IBM Corp., Armonk, USA) and R v. 4.2.0 (R Foundation for Statistical Computing, Vienna, Austria), with RStudio 2025.05.1+513 used as the integrated development environment. SPSS was primarily used for descriptive statistics and group comparisons, whereas R was employed for multivariable logistic regression modeling, variable selection using the AIC, and diagnostic testing. Statistical significance was defined as a 2-tailed $p < 0.05$.

Results

Basic characteristics of the sample

Table 1 presents the basic characteristics of the study sample, including age, height, weight, body mass index (BMI [kg/m^2]), sex, and sleep disorder status among the 845 participating children. The mean age was 5.24 ±1.13 years, mean height was 111.75 ±9.53 cm, mean weight was 19.99 ±4.78 kg, and mean BMI was 15.89 ±2.39 kg/m^2. The sample comprised 476 boys (56.33%) and 369 girls (43.67%).

Table 1. Basic characteristics of the study sample

Characteristic		Mean ±SD/n (%)
Age [years]		5.24 ±1.13
Height [cm]		111.75 ±9.53
Weight [kg]		19.99 ±4.78
BMI [kg/m^2]		15.89 ±2.39
Sex, n (%)	male	476 (56.33)
	female	369 (43.67)
Sleep disorder status, n (%)	no	653 (77.28)
	yes	192 (22.72)

BMI – body mass index; SD – standard deviation. Continuous variables are presented as mean ±SD and categorical variables as n (%).

Regarding sleep disorder status, 192 children (22.72%) were classified as having sleep disorders, whereas 653 (77.28%) were classified as not having sleep disorders. These findings indicate that a substantial proportion of children experienced sleep-related symptoms. No significant demographic differences were observed between the groups.

Group comparisons between children with and without sleep disorders

A total of 845 children were included in the analysis, of whom 192 (22.7%) were classified as having sleep disorders. Associations between family- and diet-related factors and childhood sleep disorders are summarized in Table 2.

Table 2. Association of family and dietary factors with childhood sleep disorders (n = 845)

Factor	No sleep disorder (n = 653)	Sleep disorder (n = 192)	t/χ^2	p-value	Association measure
Continuous variables					
Age [years]	5.26 ±1.11	5.18 ±1.20	1.007	0.314	r = –0.035
Height [cm]	111.73 ±9.43	111.82 ±9.91	–0.112	0.911	r = 0.004
Weight [kg]	19.84 ±4.38	20.49 ±5.94	–1.421	0.157	r = 0.058
BMI [kg/m^2]	15.81 ±2.31	16.14 ±2.64	–1.687	0.092	r = 0.058
Categorical variables					
Gender (male)	358 (54.8)	118 (61.5)	2.655	0.103	0.79 (0.56–1.11)
COVID-19 infection (yes)	510 (78.1)	160 (83.3)	2.474	0.116	0.64 (0.41–0.99)
Father snores (yes)	420 (64.3)	157 (81.8)	20.867	<0.001	0.43 (0.28–0.65)
Mother snores (yes)	98 (15.0)	51 (26.6)	13.640	<0.001	0.60 (0.40–0.89)
Father obese (yes)	206 (31.5)	71 (37.0)	1.987	0.159	0.63 (0.44–0.90)
Mother obese (yes)	110 (16.8)	44 (22.9)	3.670	0.055	0.88 (0.57–1.35)
Smoking by cohabitants (yes)	245 (37.5)	69 (35.9)	0.159	0.690	0.87 (0.62–1.23)
Mother's education level	middle: 68 (10.4)	middle: 11 (5.7)	10.122	0.038	r = 0.080
	high: 117 (17.9)	high: 22 (11.5)			
	assoc: 171 (26.2)	assoc: 61 (31.8)			
	bach: 230 (35.2)	bach: 78 (40.6)			
	grad: 67 (10.3)	grad: 20 (10.4)			

Table 2. Association of family and dietary factors with childhood sleep disorders (n = 845) – cont.

Factor	No sleep disorder (n = 653)	Sleep disorder (n = 192)	t/χ^2	p-value	Association measure
Father's education level	middle: 71 (10.9)	middle: 10 (5.2)	10.552	0.032	r = 0.092
	high: 131 (20.1)	high: 28 (14.6)			
	assoc: 179 (27.4)	assoc: 59 (30.7)			
	bach: 208 (31.9)	bach: 76 (39.6)			
	grad: 64 (9.8)	grad: 19 (9.9)			
Birth method (cesarean)	331 (50.7)	100 (52.1)	0.115	0.734	1.09 (0.78–1.53)
Gestational age at birth (preterm)	34 (5.2)	10 (5.2)	0.001	0.999	1.01 (0.49–2.11)
Infant feeding method	breast: 418 (64.0)	breast: 122 (63.5)	1.060	0.589	r = 0.017
	mixed: 197 (30.2)	mixed: 55 (28.6)			
	formula: 38 (5.8)	formula: 15 (7.8)			
Duration of breastfeeding (≤6 months)	145 (22.2)	36 (18.7)	1.052	0.305	r = –0.035
Dietary preferences	none: 407 (62.3)	none: 79 (41.2)	36.882	<0.001	r = 0.132
	meat: 123 (18.8)	meat: 55 (28.6)			
	sweets: 91 (13.9)	sweets: 42 (21.9)			
	fried: 9 (1.4)	fried: 12 (6.3)			
	carbonated drinks: 12 (1.8)	carbonated drinks: 2 (1.0)			
	vegetables: 11 (1.7)	vegetables: 2 (1.0)			
Frequency of fruit intake	daily: 481 (73.7)	daily: 122 (63.5)	15.343	0.004	τb = –0.100
	1–2/wk: 41 (6.3)	1–2/wk: 28 (14.6)			
	3–5/wk: 112 (17.2)	3–5/wk: 35 (18.2)			
	1–3/mo: 13 (2.0)	1–3/mo: 4 (2.1)			
	rare: 6 (0.9)	rare: 3 (1.6)			
Frequency of seafood, beef, lamb intake	daily: 43 (6.6)	daily: 12 (6.3)	18.797	0.001	τb = –0.094
	1–2/wk: 273 (41.8)	1–2/wk: 53 (27.6)			
	3–5/wk: 101 (15.5)	3–5/wk: 26 (13.5)			
	1–3/mo: 169 (25.9)	1–3/mo: 76 (39.6)			
	rare: 67 (10.3)	rare: 25 (13.0)			
Frequency of vegetable intake	daily: 472 (72.3)	daily: 115 (59.9)	15.135	0.004	τb = –0.109
	1–2/wk: 45 (6.9)	1–2/wk: 28 (14.6)			
	3–5/wk: 95 (14.5)	3–5/wk: 35 (18.2)			
	1–3/mo: 17 (2.6)	1–3/mo: 5 (2.6)			
	rare: 24 (3.7)	rare: 9 (4.7)			
Frequency of fried food intake	daily: 7 (1.1)	daily: 2 (1.0)	4.348	0.361	τb = 0.064
	1–2/wk: 214 (32.8)	1–2/wk: 74 (38.5)			
	3–5/wk: 25 (3.8)	3–5/wk: 9 (4.7)			
	1–3/mo: 266 (40.7)	1–3/mo: 77 (40.1)			
	rare: 141 (21.6)	rare: 30 (15.6)			
Frequency of sweets intake	daily: 55 (8.4)	daily: 30 (15.6)	13.145	0.011	τb = 0.010
	1–2/wk: 266 (40.7)	1–2/wk: 59 (30.7)			
	3–5/wk: 132 (20.2)	3–5/wk: 35 (18.2)			
	1–3/mo: 153 (23.4)	1–3/mo: 50 (26.0)			
	rare: 47 (7.2)	rare: 18 (9.4)			
Frequency of carbonated drinks intake	daily: 2 (0.3)	daily: 1 (0.5)	1.738	0.784	τb = 0.030
	1–2/wk: 63 (9.6)	1–2/wk: 24 (12.5)			
	3–5/wk: 17 (2.6)	3–5/wk: 4 (2.1)			
	1–3/mo: 128 (19.6)	1–3/mo: 39 (20.3)			
	rare: 443 (67.8)	rare: 124 (64.6)			

wk – weeks; mo – months; BMI – body mass index.

Continuous variables

No significant differences were observed in age, height, weight, or BMI between children with and without sleep disorders (all $p > 0.05$). Correlation analyses likewise revealed only weak associations, with all correlation coefficients close to zero ($|r| < 0.06$).

For categorical variables, most associations were also weak, with the largest effect observed for dietary preferences ($r = 0.132$). Similarly, for dietary frequency variables, Kendall's tau-b correlation coefficients indicated only weak associations ($|\tau b| \leq 0.11$).

Family factors

Among the categorical family variables, child sex was not significantly associated with sleep disorders (odds ratio (OR) = 0.79, 95% confidence interval (95% CI): 0.56–1.11, $p = 0.103$). A history of COVID-19 infection was also not significantly associated with sleep disorders (OR = 0.64, 95% CI: 0.41–0.99, $p = 0.116$). Parental obesity showed no consistent association with childhood sleep disorders: paternal obesity was not significant (OR = 0.63, 95% CI: 0.44–0.90, $p = 0.159$), whereas maternal obesity demonstrated a borderline association (OR = 0.88, 95% CI: 0.57–1.35, $p = 0.055$). Cohabitant smoking and mode of delivery were likewise unrelated to childhood sleep disorders. Similarly, preterm birth was not significantly associated with sleep disorders (OR = 1.01, 95% CI: 0.49–2.11, $p = 0.999$).

In contrast, parental snoring emerged as a significant predictor. Paternal snoring was associated with lower odds of childhood sleep disorders (OR = 0.43, 95% CI: 0.28–0.65, $p < 0.001$), and a similar inverse association was observed for maternal snoring (OR = 0.60, 95% CI: 0.40–0.89, $p < 0.001$). Moreover, both maternal and paternal educational attainment were positively correlated with childhood sleep disorders ($r = 0.080$ and $r = 0.092$, respectively; $p < 0.05$), suggesting that higher parental education may be associated with an increased likelihood of reporting or identifying sleep disorders in children.

Infant feeding and early nutrition

Feeding method (breastfeeding, mixed feeding, or formula feeding) was not significantly associated with childhood sleep disorders ($p = 0.589$). Likewise, breastfeeding duration (≤6 months vs >6 months) was not significantly associated with sleep disorders ($p = 0.305$, $r = -0.035$).

Dietary preferences and intake frequency

Dietary patterns showed marked differences between children with and without sleep disorders. Children with sleep disorders were more likely to report preferences for meat (28.6% vs 18.8%) and sweets (21.9% vs 13.9%) than children without sleep disorders ($p < 0.001$, $r = 0.132$). The frequencies of fruit consumption ($p = 0.004$, $\tau b = -0.100$), seafood/beef/lamb consumption ($p = 0.001$, $\tau b = -0.094$), and vegetable consumption ($p = 0.004$, $\tau b = -0.109$) were significantly associated with sleep disorders, suggesting that lower consumption of these food groups was associated with a higher prevalence of sleep disturbances. In contrast, the frequencies of fried food, sweet, and carbonated drink consumption did not show robust associations with sleep disorders (all $p > 0.05$, $|\tau b| \leq 0.064$). However, children with sleep disorders tended to consume sweets more frequently ($p = 0.011$, $\tau b = 0.010$).

Multivariate logistic regression analysis

Candidate variables identified in the univariate analyses (Supplementary Table 2) were entered into a multivariable logistic regression model. Variable selection was performed using the AIC. The final model (Table 3, Fig. 1) explained 16.7% of the variance in childhood sleep disorders (Nagelkerke $R^2 = 0.167$; Cox and Snell $R^2 = 0.110$).

Parental snoring was independently associated with an increased risk of childhood sleep disorders. Children whose fathers snored had more than twice the odds of developing sleep disorders compared with those whose fathers did not snore (OR = 2.20, 95% CI: 1.44–3.41, $p < 0.001$). Maternal snoring was also identified as a significant predictor (OR = 1.76, 95% CI: 1.15–2.66, $p = 0.008$).

Higher maternal educational attainment was associated with an increased risk of childhood sleep disorders. Compared with mothers who had completed only middle school education, a high school education was not significantly associated with sleep disorders (OR = 1.28, 95% CI: 0.57–3.03, $p = 0.561$). In contrast, children of mothers with an associate degree (OR = 2.58, 95% CI: 1.27–5.66, $p = 0.012$) or a bachelor's degree (OR = 2.44, 95% CI: 1.21–5.29, $p = 0.017$) had more than twice the odds of sleep disorders. A similar trend was observed for graduate-level education (OR = 2.24, 95% CI: 0.95–5.49, $p = 0.069$), although this association did not reach statistical significance.

Children's dietary preferences also showed strong associations with sleep disorders. Preferences for meat (OR = 2.19, 95% CI: 1.43–3.35, $p < 0.001$), sweets (OR = 2.15, 95% CI: 1.31–3.51, $p = 0.002$), and especially fried foods (OR = 6.49, 95% CI: 2.51–17.40, $p < 0.001$) were associated with a markedly increased risk of sleep disorders. Preferences for carbonated drinks and vegetables were not significantly associated with sleep disorders (both $p > 0.05$).

No consistent associations were observed between sleep disorders and the frequency of seafood, beef, and lamb consumption. Although children who consumed these foods 1–3 times per month showed a borderline increased risk of sleep disorders (OR = 1.94, 95% CI: 0.94–4.25,

Table 3. Multivariable logistic regression analysis of risk factors for childhood sleep disorders (stepwise Akaike information criterion (AIC) method)

Variables		B	Standardized β	OR (Exp(B))	95% CI	p-value
Intercept		−2.94	−2.94	0.05	0.02–0.16	<0.001
Father snores (n = 845)	no (n = 268)	–	–	–	–	–
	yes (n = 577)	0.79	0.79	2.20	1.44–3.41	<0.001
Mother snores (n = 845)	no (n = 696)	–	–	–	–	–
	yes (n = 149)	0.56	0.56	1.76	1.15–2.66	0.008
Mother's education level (n = 845)	middle school (n = 79)	–	–	–	–	–
	high school (including vocational school) (n = 139)	0.25	0.25	1.28	0.57–3.03	0.561
	associate degree (n = 232)	0.95	0.95	2.58	1.27–5.66	0.012
	bachelor's degree (n = 308)	0.89	0.89	2.44	1.21–5.29	0.017
	graduate degree (n = 87)	0.81	0.81	2.24	0.95–5.49	0.069
Dietary preference (n = 845)	no specific preference (n = 486)	–	–	–	–	–
	meat (n = 178)	0.79	0.79	2.19	1.43–3.35	<0.001
	sweets (n = 133)	0.77	0.77	2.15	1.31–3.51	0.002
	fried food (n = 21)	1.87	1.87	6.49	2.51–17.40	<0.001
	carbonated drinks (n = 14)	−0.33	−0.33	0.72	0.11–2.83	0.677
	vegetables (n = 13)	−0.26	−0.26	0.77	0.12–3.09	0.746
Frequency of seafood, beef, and lamb intake (n = 845)	daily (n = 55)	–	–	–	–	–
	1–2 times/week (n = 326)	−0.06	−0.06	0.94	0.46–2.06	0.880
	3–5 times/week (n = 127)	0.31	0.31	1.36	0.61–3.16	0.466
	1–3 times/month (n = 245)	0.66	0.66	1.94	0.94–4.25	0.082
	rarely (n = 92)	0.37	0.37	1.45	0.63–3.46	0.392
Frequency of sweets intake (n = 845)	daily (n = 85)	–	–	–	–	–
	1–2 times/week (n = 325)	−0.64	−0.64	0.53	0.29–0.95	0.032
	3–5 times/week (n = 167)	−0.68	−0.68	0.51	0.27–0.94	0.031
	1–3 times/month (n = 203)	−0.13	−0.13	0.87	0.47–1.64	0.672
	rarely (n = 65)	0.12	0.12	1.13	0.51–2.48	0.766

OR – odds ratio; 95% CI – 95% confidence interval. Reference category indicated by "–". B – regression coefficient; standardized β – standardized regression coefficient.

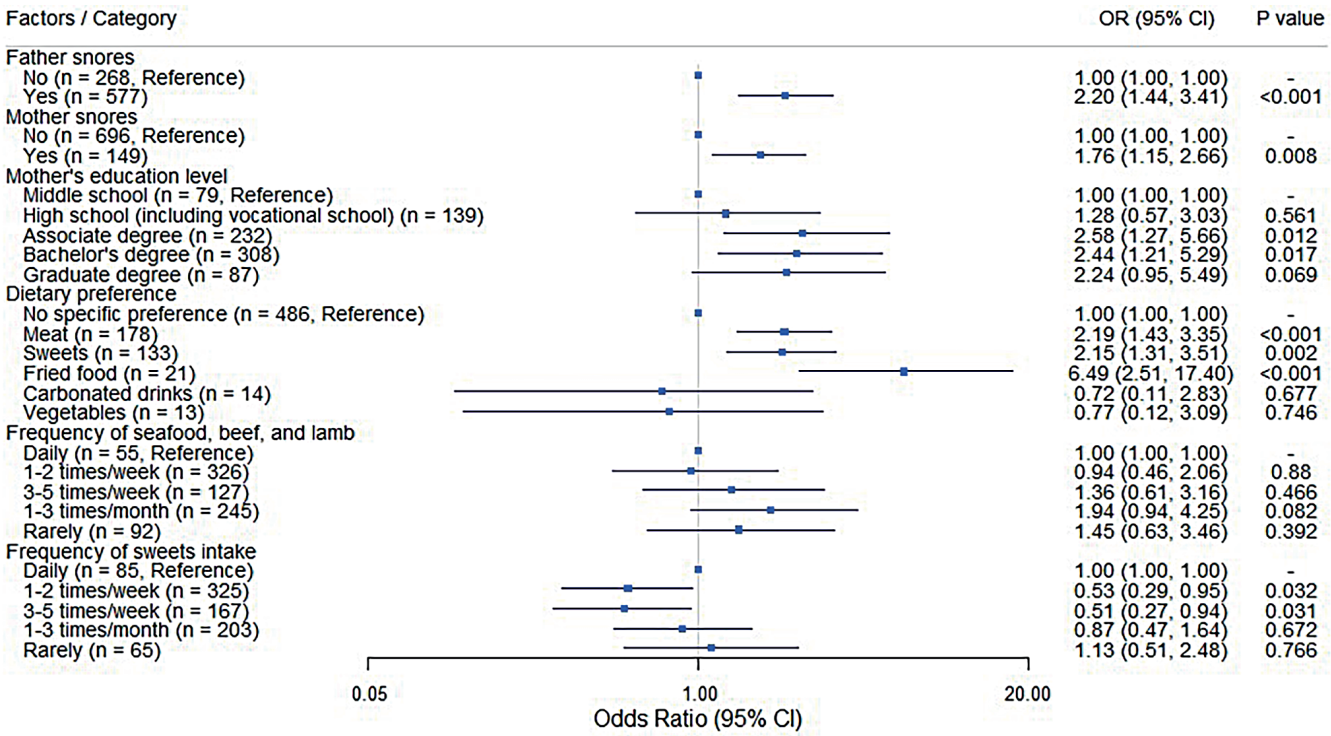

Fig. 1. Multivariate logistic regression analysis

p = 0.082), the overall pattern did not reach statistical significance.

However, moderate sweet consumption appeared to have a protective effect. Compared with daily consumption, children who consumed sweets 1–2 times per week (OR = 0.53, 95% CI: 0.29–0.95, p = 0.032) or 3–5 times per week (OR = 0.51, 95% CI: 0.27–0.94, p = 0.031) had significantly lower odds of sleep disorders. Consumption 1–3 times per month (OR = 0.87, 95% CI: 0.47–1.64, p = 0.672) and rare consumption (OR = 1.13, 95% CI: 0.51–2.48, p = 0.766) were not significantly associated with sleep disorders. These findings indicate that parental snoring and children's dietary preferences, particularly preferences for fried foods, are independent risk factors for childhood sleep disorders, whereas moderate sweet consumption may exert a protective effect.

Age, sex, and BMI were included as covariates in the multivariable model (Supplementary Table 3). Age (OR = 0.94, 95% CI: 0.82–1.09, p = 0.437) and sex (OR = 0.79, 95% CI: 0.56–1.11, p = 0.167) were not significantly associated with sleep disorders. Body mass index showed a significant association only in the 6–7-year age group (OR = 1.12, 95% CI: 1.01–1.24, p = 0.039) in the age-stratified analysis (Supplementary Table 4).

Subgroup analyses stratified by age group (1–3, 4–5, and 6–7 years) were conducted (Supplementary Table 4). These analyses demonstrated patterns generally consistent with those observed in the main model. Parental snoring and children's dietary preferences, particularly preferences for fried foods, remained important risk factors across age groups, although effect sizes varied slightly. For example, paternal snoring was significantly associated with sleep disorders among children aged 4–5 years (OR = 0.53, 95% CI: 0.30–0.91, p = 0.021) and 6–7 years (OR = 0.30, 95% CI: 0.15–0.60, p = 0.001), whereas maternal snoring was significant only in the 6–7-year age group (OR = 0.48, 95% CI: 0.26–0.89, p = 0.020). These findings suggest that the identified risk factors were robust and were not solely driven by the age distribution of the study sample.

Model diagnostics

Variance inflation factors for all predictors ranged from 1.06 to 1.33 (all <5), indicating the absence of multicollinearity (Supplementary Table 5). The Hosmer–Lemeshow goodness-of-fit test confirmed an adequate model fit (χ^2 = 5.939, degrees of freedom (df) = 8, p = 0.654). The Nagelkerke R^2 and Cox and Snell R^2 values were 0.167 and 0.110, respectively, suggesting that the model explained a moderate proportion of the variance in childhood sleep disorders. Model discrimination was acceptable, with a C-index, equivalent to the area under the receiver operating characteristic curve (AUC), of 0.728. Collectively, these results support the adequacy, reliability, and discriminative performance of the multivariable logistic regression model (Supplementary Table 6).

Discussion

This study identified significant associations between childhood sleep disorders and several family- and diet-related factors, including parental snoring, maternal educational attainment, and children's preferences for meat, sweets, and fried foods. These findings provide practical insights into how family behaviors and dietary habits may be associated with pediatric sleep outcomes.

The association between parental snoring and childhood sleep disorders suggests that shared familial sleep behaviors may influence children's sleep quality. Parental snoring may contribute to nighttime disturbances and may also reflect underlying conditions such as obesity or sleep apnea, which could affect the child's sleep.[14–16] Our findings are consistent with previous research indicating that children often adopt parental sleep habits, reinforcing the importance of family-based sleep hygiene interventions.[17,18]

Maternal educational attainment was also independently associated with childhood sleep disorders. Although higher maternal education is generally associated with improved health literacy, our findings suggest that certain educational levels (associate and bachelor's degrees) were associated with an increased risk of childhood sleep disorders. This association may reflect indirect factors, such as increased professional responsibilities, highly structured family routines, or academic expectations, rather than a direct causal relationship.[19–21] Therefore, psychosocial factors and parenting practices may mediate the relationship between maternal education and children's sleep.

Dietary preferences, particularly preferences for meat, sweets, and fried foods, showed strong associations with childhood sleep disorders. These foods are known to influence glucose metabolism and may disrupt circadian rhythms, thereby contributing to poorer sleep quality.[22–25] Our findings support previous studies linking energy-dense, nutrient-poor dietary patterns with shorter sleep duration and more frequent nighttime awakenings.[26]

Interestingly, moderate sweet consumption (1–5 times per week) was associated with a lower risk of sleep disorders compared with daily consumption. This nonlinear relationship may reflect behavioral or metabolic regulatory mechanisms; however, the wide CIs and the possibility of residual confounding warrant cautious interpretation.[27–30] Similar dose-dependent associations have been reported in previous studies, but further validation using objective measures of dietary intake and sleep is needed.

In the multivariable analysis, parental snoring and children's dietary preferences for meat, sweets, and fried foods remained independent predictors of childhood sleep disorders. In contrast, associations with maternal educational attainment and fruit consumption were attenuated, suggesting that some associations observed in the univariate analyses may have been confounded by other variables.

Subgroup analyses stratified by age group (1–3, 4–5, and 6–7 years) further supported these findings (Supplementary Table 4). Parental snoring and dietary preferences, particularly preferences for fried foods, remained significant risk factors across all age groups, although effect sizes varied slightly. Specifically, paternal snoring significantly increased the odds of childhood sleep disorders among children aged 4–5 years (OR = 1.89, 95% CI: 1.10–3.33, p = 0.021) and 6–7 years (OR = 3.33, 95% CI: 1.67–6.67, p = 0.001), whereas maternal snoring significantly increased the risk among children aged 6–7 years (OR = 2.08, 95% CI: 1.16–3.85, p = 0.020). These findings indicate that the identified risk factors were robust across age strata and support the predictive value of parental sleep behaviors in relation to childhood sleep disorders.

These findings highlight the importance of adjusting for potential confounding variables and interpreting correlation coefficients with caution. Consistent with this, our correlation analyses revealed only weak Pearson correlations for continuous variables and weak-to-moderate Kendall's tau-b correlations for dietary frequency variables, suggesting that statistical significance may, in some cases, reflect the large sample size rather than strong practical effects.

Our findings are consistent with Bronfenbrenner's Bioecological Model, which emphasizes the influence of immediate family environments on child development. Within this framework, parental behaviors, educational attainment, and household dietary practices function as microsystem-level factors that may shape sleep hygiene and daily routines.

This study adds to the limited literature from non-Western populations, particularly China, where pediatric sleep research remains relatively underdeveloped.[7–9] The prevalence of sleep disorders in our sample (22.72%) falls within the range reported globally, highlighting the growing need for culturally adapted, family-based interventions in Asian populations.

Although organizations such as the World Health Organization (WHO) and the American Academy of Sleep Medicine (AASM) provide recommendations regarding pediatric sleep, their implementation remains inconsistent. Our findings support the integration of sleep education into family health promotion strategies, with particular emphasis on dietary guidance and parental role modeling.

The strengths of this study include its relatively large sample size, a multidimensional approach encompassing both family- and diet-related factors, and the use of validated instruments.

Limitations of the study

This study has several limitations. First, its cross-sectional design precludes any inference of causality. Second, all data were based on parent-reported information and are therefore subject to recall and social desirability biases; objective measures of sleep and dietary behavior were not available. Third, although several covariates were included in the analyses, unmeasured confounders, such as genetic predisposition, household stress, and screen time exposure, may still have influenced the observed associations. In addition, the imbalance in group sizes between children with and without sleep disorders may have affected the stability of the regression estimates, despite the use of multivariable and age-stratified analyses. Finally, the sample was drawn from a single urban region in China, which may limit the generalizability of the findings to other cultural or socioeconomic settings.[31,32]

Conclusions

This study highlights several potentially modifiable factors associated with childhood sleep disorders in a Chinese population. Parental snoring and unhealthy dietary preferences emerged as independent factors associated with an increased risk of sleep disorders. Although maternal educational attainment was also associated with childhood sleep disorders, its role is likely complex and may be mediated by other psychosocial and environmental factors. These findings may contribute to the development of family-centered strategies aimed at promoting healthy sleep habits among children, particularly through improvements in parental health behaviors and dietary practices.

This study identified statistically significant associations between childhood sleep disorders and several factors, including parental snoring, maternal educational attainment, and children's dietary preferences. Children whose fathers or mothers snored had significantly higher odds of sleep disorders, with ORs ranging from 1.76 to 2.20 in the overall sample, and these associations remained significant in age-stratified analyses. Children of mothers with an associate or bachelor's degree had more than twice the odds of sleep disorders, whereas graduate-level education demonstrated a borderline association. Preferences for meat, sweets, and fried foods were also significantly associated with an increased risk of sleep disorders, while moderate sweet consumption (1–5 times per week) appeared to have a protective effect.

However, the overall effect sizes were small. Pearson's correlation coefficients did not exceed 0.132 for categorical variables, and Kendall's tau-b coefficients did not exceed 0.11 for dietary frequency variables. Age and sex were not significantly associated with sleep disorders, and BMI showed a significant association only among children aged 6–7 years. These findings suggest that, although statistically significant, the observed associations may have limited practical significance and may partially reflect the influence of the large sample size.

Therefore, the results should be interpreted with caution and regarded as preliminary evidence of association rather than evidence of causality. They may help generate hypotheses for future research and identify potential family- and diet-related factors associated with childhood

sleep disorders; however, they do not support strong clinical or public health recommendations at the present stage of evidence.

Supplementary data

The supplementary materials are available in at https://doi.org/10.5281/zenodo.17173852. The package contains the following files:

Supplementary Table 1. Descriptive statistics and skewness for continuous and converted frequency variables (total sample and subgroups).

Supplementary Table 2. Univariate logistic regression analysis of potential risk factors.

Supplementary Table 3. Multivariate logistic regression of childhood sleep disorder risk factors with age as a continuous variable.

Supplementary Table 4. Multivariate logistic regression of childhood sleep disorder risk factors by age group (1–3, 4–5, 6–7 years).

Supplementary Table 5. Multicollinearity assessment (VIF).

Supplementary Table 6. Overall model fit statistics.

Data Availability Statement

The raw data generated and analyzed during the current study are openly available in Zenodo at https://doi.org/10.5281/zenodo.14970151.

Consent for publication of personal information

Not applicable.

Use of AI and AI-assisted technologies

Not applicable.

ORCID iDs

Lifeng Zhang https://orcid.org/0009-0001-7714-0162
Xiangjing Chen https://orcid.org/0000-0002-7310-1721
Xin Zhang https://orcid.org/0009-0008-5714-3834
Ya Yan https://orcid.org/0009-0003-6527-634X
Renzhong Wang https://orcid.org/0000-0002-6364-5039

References

1. Garbarino S. Sleep disorders across the lifespan: A different perspective. *Int J Environ Res Public Health*. 2020;17(23):9025. doi:10.3390/ijerph17239025
2. Ogundele MO, Yemula C. Management of sleep disorders among children and adolescents with neurodevelopmental disorders: A practical guide for clinicians. *World J Clin Pediatr*. 2022;11(3):239–252. doi:10.5409/wjcp.v11.i3.239
3. Wei R, Duan X, Guo L. Effects of sleep deprivation on coronary heart disease. *Korean J Physiol Pharmacol*. 2022;26(5):297–305. doi:10.4196/kjpp.2022.26.5.297
4. Worley SL. The extraordinary importance of sleep: The detrimental effects of inadequate sleep on health and public safety drive an explosion of sleep research. *P T*. 2018;43(12):758–763. PMID:30559589. PMCID:PMC6281147.
5. Fadzil A. Factors affecting the quality of sleep in children. *Children (Basel)*. 2021;8(2):122. doi:10.3390/children8020122
6. Covington LB, Patterson F, Hale LE, et al. The contributory role of the family context in early childhood sleep health: A systematic review. *Sleep Health*. 2021;7(2):254–265. doi:10.1016/j.sleh.2020.11.010
7. Kaditis AG, Finder J, Alexopoulos EI, et al. Sleep-disordered breathing in 3,680 Greek children. *Pediatr Pulmonol*. 2004;37(6):499–509. doi:10.1002/ppul.20002
8. Li AM, Au CT, So HK, Lau J, Ng PC, Wing YK. Prevalence and risk factors of habitual snoring in primary school children. *Chest*. 2010;138(3):519–527. doi:10.1378/chest.09-1926
9. Katila M, Saarenpää-Heikkilä O, Saha M, Vuorela N, Paavonen EJ. Parental reports showed that snoring in infants at three and eight months associated with snoring parents and smoking mothers. *Acta Paediatr*. 2019;108(9):1686–1694. doi:10.1111/apa.14758
10. Chang RY, Chen TL, Yeh CC, et al. Risk of obesity among children aged 2–6 years who had prolonged screen time in Taiwan: A nationwide cross-sectional study. *Clin Epidemiol*. 2023;15:165–176. doi:10.2147/CLEP.S382956
11. Holmes JF, St. Laurent CW, Spencer RMC. Unhealthy diet is associated with poor sleep in preschool-aged children. *J Genet Psychol*. 2021;182(5):289–303. doi:10.1080/00221325.2021.1905598
12. Ward AL, Jospe M, Morrison S, et al. Bidirectional associations between sleep quality or quantity, and dietary intakes or eating behaviors in children 6–12 years old: A systematic review with evidence mapping. *Nutr Rev*. 2021;79(10):1079–1099. doi:10.1093/nutrit/nuaa125
13. Calcaterra V, Rossi V, Tagi VM, et al. Food intake and sleep disorders in children and adolescents with obesity. *Nutrients*. 2023;15(22):4736. doi:10.3390/nu15224736
14. Bilgin N, Ozdogan S, Kaya A, Yildirmak Y. Sleep-related breathing disorders in children with asthma: Impact on asthma control. *J Coll Physicians Surg Pak*. 2022;32(4):473–477. doi:10.29271/jcpsp.2022.04.473
15. Chehri A, Taheri P, Khazaie H, Jalali A, Ahmadi A, Mohammadi R. The relationship between parents' sleep quality and sleep hygiene and preschool children' sleep habits. *Sleep Sci*. 2022;15(3):272–278. doi:10.5935/1984-0063.20220051
16. Katila M, Saarenpää-Heikkilä O, Saha MT, et al. Prevalence and evolution of snoring and the associated factors in two-year-old children. *Sleep Med*. 2021;84:275–282. doi:10.1016/j.sleep.2021.06.004
17. Gunn HE, Eberhardt KR. Family dynamics in sleep health and hypertension. *Curr Hypertens Rep*. 2019;21(5):39. doi:10.1007/s11906-019-0944-9
18. Matsuoka M, Matsuishi T, Nagamitsu S, et al. Sleep disturbance has the largest impact on children's behavior and emotions. *Front Pediatr*. 2022;10:1034057. doi:10.3389/fped.2022.1034057
19. Gilbertson M, Richardson C, Eastwood P, et al. Determinants of sleep problems in children with intellectual disability. *J Sleep Res*. 2021;30(5):e13361. doi:10.1111/jsr.13361
20. Jeon M, Dimitriou D, Halstead EJ. A systematic review on cross-cultural comparative studies of sleep in young populations: The roles of cultural factors. *Int J Environ Res Public Health*. 2021;18(4):2005. doi:10.3390/ijerph18042005
21. Abuhammad S, Bani Younis A, Ahmed AH. Impact of a structured sleep education program on mothers' knowledge and attitudes toward infant sleeping. *Heliyon*. 2024;10(9):e29885. doi:10.1016/j.heliyon.2024.e29885
22. Zarpellon RSM, Vilela DRM, Louzada FM, Radominski DRB, Crippa DACDS. Association of food intake with sleep disorders in children and adolescents with obesity. *Sleep Med*. 2022;4:100053. doi:10.1016/j.sleepx.2022.100053
23. Wang S, Fan C, Zhu Y, Tang X, Ling L. The obesity-related dietary pattern is associated with higher risk of sleep disorders: A cross-sectional study from NHANES. *Nutrients*. 2022;14(19):3987. doi:10.3390/nu14193987

24. Afonso A, Jacinto G, Infante P, Engana T. Primary school children's sleep habits: Association with socioeconomic factors and physical activity habits. *Children (Basel)*. 2022;9(7):965. doi:10.3390/children9070965
25. Hermes FN, Nunes EEM, Melo CMD. Sleep, nutritional status and eating behavior in children: A review study. *Rev Paul Pediatr.* 2022;40: e2020479. doi:10.1590/1984-0462/2022/40/2020479in
26. Jansen EC, Zhao W, Jones AD, et al. Early childhood diet in relation to toddler nighttime sleep duration trajectories. *Nutrients*. 2022; 14(15):3059. doi:10.3390/nu14153059
27. Vlahoyiannis A, Giannaki CD, Sakkas GK, Aphamis G, Andreou E. A systematic review, meta-analysis and meta-regression on the effects of carbohydrates on sleep. *Nutrients*. 2021;13(4):1283. doi:10.3390/nu13041283
28. Benton D, Bloxham A, Gaylor C, Brennan A, Young HA. Carbohydrate and sleep: An evaluation of putative mechanisms. *Front Nutr.* 2022;9:933898. doi:10.3389/fnut.2022.933898
29. Rusu A, Ciobanu DM, Inceu G, et al. Variability in sleep timing and dietary intake: A scoping review of the literature. *Nutrients*. 2022; 14(24):5248. doi:10.3390/nu14245248
30. Theorell-Haglöw J, Lemming EW, Michaëlsson K, Elmståhl S, Lind L, Lindberg E. Sleep duration is associated with healthy diet scores and meal patterns: Results from the population-based EpiHealth study. *J Clin Sleep Med*. 2020;16(1):9–18. doi:10.5664/jcsm.8112
31. Grady CL, Rieck JR, Nichol D, Rodrigue KM, Kennedy KM. Influence of sample size and analytic approach on stability and interpretation of brain-behavior correlations in task-related <fMRI data. *Hum Brain Mapp*. 2021;42(1):204–219. doi:10.1002/hbm.25217
32. Matheson GJ. We need to talk about reliability: Making better use of test-retest studies for study design and interpretation. *PeerJ*. 2019; 7:e6918. doi:10.7717/peerj.6918

Effect of low-level laser therapy on healing after sinus floor augmentation using allograft and xenograft bone materials

Sebastian Dominiak[1,A,B,D], Aleksandra Kowalczyk[2,C,D], Paweł Kubasiewicz-Ross[1,D,F], Marzena Dominiak[1,E], Alicja Baranowska[3,B], Cyprian Olchowy[4,B,C], Michał Ciszyński[1,A,B,D]

[1] Department of Oral Surgery, Wroclaw Medical University, Poland
[2] private practice, Wrocław, Poland
[3] Student's Scientific Organization, Department of Oral Surgery, Wroclaw Medical University, Poland
[4] Clinical Department of Cardiovascular Diseases, Collegium Medicum, Jan Dlugosz University in Czestochowa, Poland

A – research concept and design; B – collection and/or assembly of data; C – data analysis and interpretation; D – writing the article; E – critical revision of the article; F – final approval of the article

Advances in Clinical and Experimental Medicine, ISSN 1899–5276 (print), ISSN 2451–2680 (online) *Adv Clin Exp Med*. 2026;35(7):1247–1257

Address for correspondence
Paweł Kubasiewicz-Ross
E-mail: pawelkubasiewicz@wp.pl

Funding sources
Doctoral subsidy from Wroclaw Medical University (No. SUBK. 040.23.051).

Conflict of interest
None declared

Received on May 18, 2025
Reviewed on August 4, 2025
Accepted on September 25, 2025

Published online on July 3, 2026

Abstract

Background. In cases of alveolar bone atrophy prior to implant treatment, sinus floor elevation remains the treatment of choice. During a sinus lift procedure, a stabilizing grafting material is required. Among the many available options, xenografts and allografts are widely used. Owing to their different properties, they can be applied in various clinical settings. Low-level laser therapy (LLLT) is an increasingly popular adjunctive tool in regenerative dentistry. Its beneficial effects on the healing process are well established. However, its ability to influence bone healing following sinus floor elevation remains insufficiently investigated.

Objectives. The primary objective was to compare 2 bone grafts of different origins (allograft and xenograft) used in sinus lift procedures. The secondary objective was to evaluate the influence of LLLT on postoperative recovery in terms of pain, trismus, and soft tissue response.

Materials and methods. Twenty patients were randomly allocated to 2 groups. A xenograft was used in half of the patients, whereas an allograft was used in the remaining patients. In each group, 5 patients were randomly selected to receive adjunctive LLLT using a diode laser with a wavelength of 635 nm and an energy density of 6 J/cm^2. All patients underwent clinical and radiological examinations before surgery. Subsequently, a standard lateral sinus lift procedure was performed. Follow-up visits were conducted on postoperative days 3 and 7, during which pain, trismus, and swelling were assessed. After 135 days, cone-beam computed tomography (CBCT) and clinical examinations were performed to evaluate bone gain, density, and homogeneity.

Results. Low-level laser therapy significantly reduced trismus. Trismus was also less pronounced in male patients. Low-level laser therapy was associated with increased facial swelling. Pain levels were low, with no significant differences between the study groups. After 135 days, allografts demonstrated greater homogeneity, whereas xenografts exhibited higher radiographic density.

Conclusions. Low-level laser therapy may improve recovery following sinus lift surgery by reducing postoperative trismus. No significant differences were observed between the grafting materials in terms of bone gain. However, differences in radiodensity suggest distinct resorption patterns, with xenografts exhibiting higher density values after 135 days.

Key words: laser, xenograft, allograft, sinus-lift, biomodulation

Cite as
Dominiak S, Kowalczyk A, Kubasiewicz-Ross P, et al. Effect of low-level laser therapy on healing after sinus floor augmentation using allograft and xenograft bone materials. *Adv Clin Exp Med*. 2026;35(7):1247–1257. doi:10.17219/acem/211363

DOI
10.17219/acem/211363

Copyright
Copyright by Author(s)
This is an article distributed under the terms of the Creative Commons Attribution 3.0 Unported (CC BY 3.0) (https://creativecommons.org/licenses/by/3.0/)

Highlights

- Low-level laser therapy (LLLT) may improve postoperative jaw opening after sinus-lift surgery.
- LLLT did not significantly reduce postoperative pain or midfacial swelling.
- Xenograft and allograft materials resulted in comparable vertical bone gain after 135 days.
- Xenografts showed higher radiological bone density than allografts on CBCT assessment.
- Allografts appeared more homogeneous than xenografts during early graft remodeling.

Background

Despite the rapid pace at which dentistry has developed over recent years, tooth loss remains a significant challenge that requires restoration of the missing dentition. Among the available treatment options, dental implant therapy is considered the most desirable due to the high level of comfort it provides to patients. It also demonstrates a very high success rate and does not require the involvement of adjacent teeth in the treatment, which is a major drawback of conventional prosthetic crowns and bridges. Despite its obvious benefits, implant-prosthetic rehabilitation of missing dentition also has limitations, mainly associated with gradual bone loss following tooth extraction, resulting from remodeling of the alveolar process of the maxilla and pneumatization of the maxillary sinuses.[1–3]

Bone volume, if insufficient for implant treatment, can be restored through augmentation procedures, which commonly involve the use of bone grafting materials of autogenous, allogenous, or xenogenous origin. Autogenous grafts are considered the gold standard due to their osteogenic, osteoinductive, and osteoconductive properties. Nonetheless, their availability is often limited, and their use requires an additional surgical procedure at the donor site, which may increase morbidity.[4] Therefore, bone substitute biomaterials have been introduced into regenerative medicine. They are characterized by chemical and biological biocompatibility, osteoconductivity, and, in some cases, even osteoinductivity.[5] Xenogenous bone grafts are commercially available; however, they possess only osteoconductive properties. These biomaterials are derived from other species, most commonly bovine, porcine, or equine, and exhibit favorable biomechanical properties.[6] As allografts, in addition to being osteoconductive, may also possess osteoinductive potential, they are often preferred, and their use is becoming increasingly common.[7–9] The osteoconductive potential of xeno- and allografts may be enhanced through the additional application of growth factors. One of the possible options in this regard, particularly preferred in oral surgery, is platelet concentrates. Human platelets are a source of numerous growth factors, including platelet-derived growth factor (PDGF), vascular endothelial growth factor (VEGF), and transforming growth factor beta (TGF-β), which play a role in the initial stages of bone defect healing. They also act as attractants for immune cells, which may serve as a source of additional growth factors during later stages of healing.[10] When it comes to surgical techniques, in cases of severe atrophy of the lateral aspects of the maxillary alveolar ridge, sinus lift surgery is considered the treatment of choice. Initially introduced by Tatum in 1975, it involves surgically creating an opening in the lateral wall of the maxillary sinus and carefully elevating the Schneiderian membrane to create a space for the bone grafting material. A cavity prepared in this manner exhibits highly osteoconductive properties because it is surrounded predominantly by osseous and well-vascularized tissues. Although highly predictable in terms of long-term outcomes, this method may lead to several early complications, including pain, trismus, and swelling caused by hematoma formation, which can significantly reduce patient satisfaction.[11]

Among the available methods for reducing these symptoms, the use of lasers has recently gained considerable attention. So-called low-level laser therapy (LLLT) is known to modulate the inflammatory proceess, reduce pain intensity and swelling, and promote tissue healing without causing adverse effects.[12,13] It has been evaluated in many oral surgery procedures, particularly surgical tooth extractions. Most authors report its positive influence on soft tissue healing.[14,15] Although its effectiveness has been well documented in numerous dental procedures, there is still a lack of evidence regarding the effects of LLLT in sinus lift surgery.

Objectives

The main objective of this study was to evaluate the influence of adjunctive LLLT following sinus lift surgery on patient recovery in cases involving 2 grafting materials of different origins, as assessed by trismus, pain scores, and midfacial swelling. An additional objective was to compare 2 different grafting materials used in sinus floor elevation procedures with regard to new bone height, density, and homogeneity based on cone-beam computed tomography (CBCT) examinations.

Materials and methods

This prospective study was conducted at the Department of Oral Surgery, Wroclaw Medical University (Poland), between 2023 and 2024. It included 20 patients requiring a lateral sinus lift procedure prior to implant-prosthetic treatment. The assignment of the medical intervention was not at the discretion of the investigators but was determined by the need for implant-based restoration in cases of reduced maxillary alveolar bone height. The study was approved by the Local Bioethics Committee of Wroclaw Medical University (approval No. KB 10/2023N). All participants provided 2 forms of written informed consent: the 1st for the lateral sinus lift procedure and the 2nd for participation in the study. The study was conducted in full compliance with the Declaration of Helsinki and adhered to personal data protection regulations under the General Data Protection Regulation (GDPR). The study followed the CONsolidated Standards Of Reporting Trials (CONSORT) guidelines, and the flow diagram presents patient enrollment (Fig. 1).[16]

Inclusion and exclusion criteria

Patient recruitment was performed by an investigator who was not involved in the surgical procedures (A.B.). The inclusion criteria were as follows: 1) adults capable of providing informed consent for the surgical procedure; 2) single or multiple missing teeth in the posterior region of the maxillary dental arch; 3) alveolar ridge height of less than 5 mm and width greater than 7 mm; and 4) at least 2 mm of keratinized tissue height (HKT) in the region of interest.

The exclusion criteria were as follows: 1) poor oral hygiene (Plaque Index (PI) >20%); 2) pregnancy; 3) breastfeeding; and 4) general or local contraindications to surgical procedures, including active sinus infection, large sinus cysts, previous radiation therapy to the head and neck region, and severe systemic conditions such as uncontrolled diabetes, immunocompromised states, and severe cardiovascular disease (CVD). The study group consisted of 20 adult Caucasian patients (Fig. 1). Subsequently, each participant was randomly assigned to 1 of the study groups

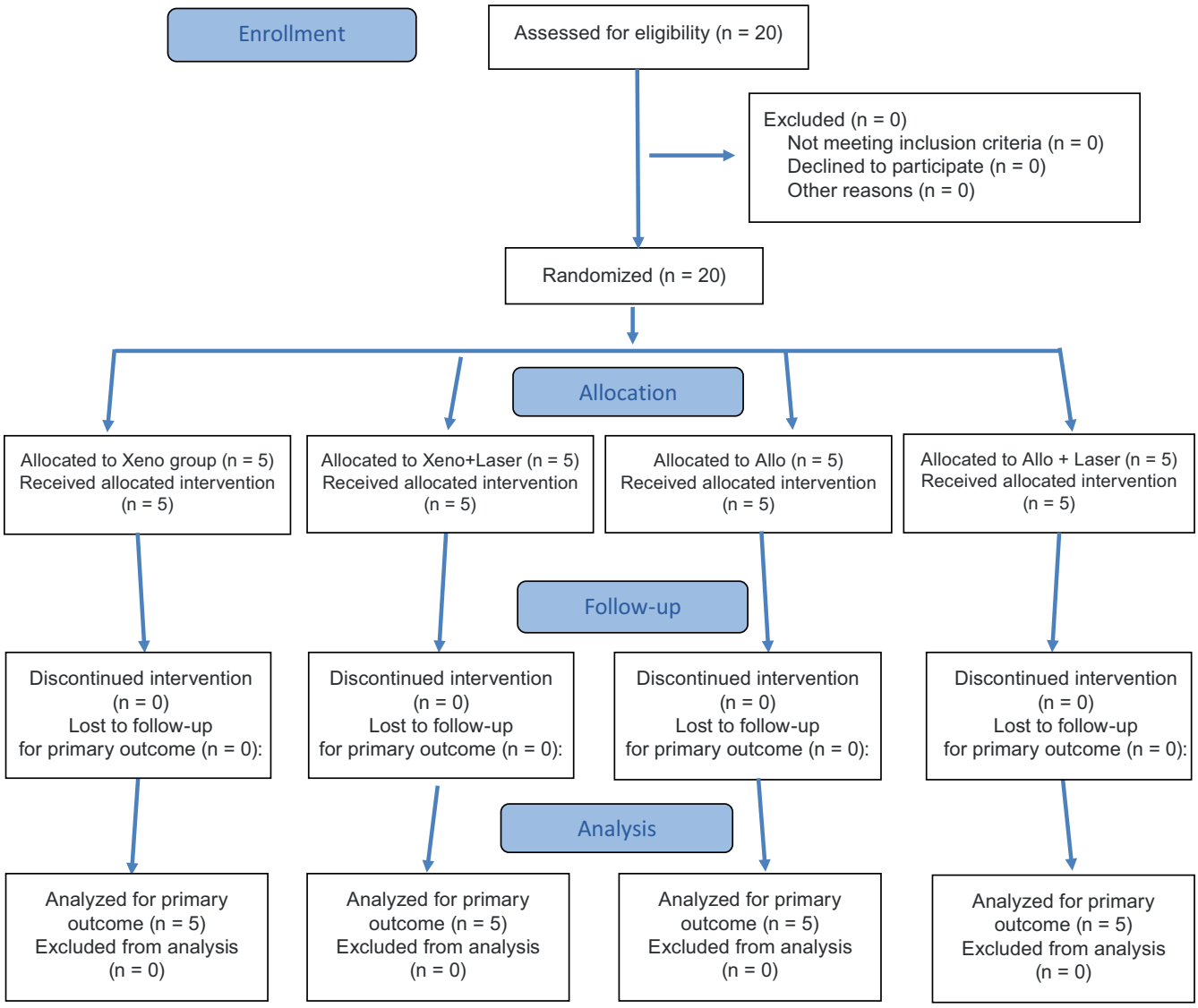

Fig. 1. Flow diagram of patient enrollment

and underwent the procedure according to the protocol of the allocated group.

Study group design

Patients were randomly divided into 2 equal groups, each consisting of 10 patients. The division was based on the type of bone grafting material used during the sinus lift procedure. In half of the patients, an allogenic bone graft in the form of cortico-cancellous bone granules "S" (granulometry: 0.5 mm; Biobank, Lieusaint, France) was used. In the remaining patients, a xenogenic grafting material in the form of cancellous bone granules (granulometry: 0.25–1.0 mm; Geistlich, Wolhusen, Switzerland) was used. From each group, 5 patients were randomly selected to receive LLLT during the postoperative period. As a result, 4 equal groups, each consisting of 5 patients, were created. The groups were as follows: 1) xenograft; 2) xenograft + LLLT; 3) allograft; and 4) allograft + LLLT.

Protocol of the experiment

Presurgical examination (T1)

Every patient included in the study underwent a clinical examination. Measurements were performed by one of the researchers who was not involved in the subsequent clinical procedures (A.B.). Particular emphasis was placed on the evaluation of the future surgical site; therefore, the following parameters were recorded: height (HKT) and width (WKT) of the keratinized gingiva, alveolar ridge dimensions, and the PI according to Silness and Löe. Additionally, maximum jaw opening was measured as the distance between the upper and lower central incisors. Facial swelling was also assessed by measuring 3 reference lines. This method was a modification of the technique originally introduced by Laskin. As the surgical field in the present study involved the midface rather than the lower face, as assessed by Laskin, the measurement lines were modified accordingly.[17] The lines used in this study were as follows:

– Line A – a straight line extending from the lateral canthus of the eye to the angle of the mandible;

– Line B – a straight line extending from the midpoint of the tragus of the ear to the base of the nasal ala (Camper's plane);

– Line C – a straight line extending from the midpoint of the tragus of the ear to the corner of the mouth (Fig. 2).

Following the clinical examination, every patient was referred for radiological assessment. Cone-beam computed tomography scans were acquired using the Planmeca Viso® G7 system (Planmeca®, Helsinki, Finland). A field of view (FOV) centered on the maxilla, measuring 300 mm in width and 200 mm in height, was used. The scans were analyzed using Romexis® software (Planmeca®), and the foll day owing parameters were measured and assessed:

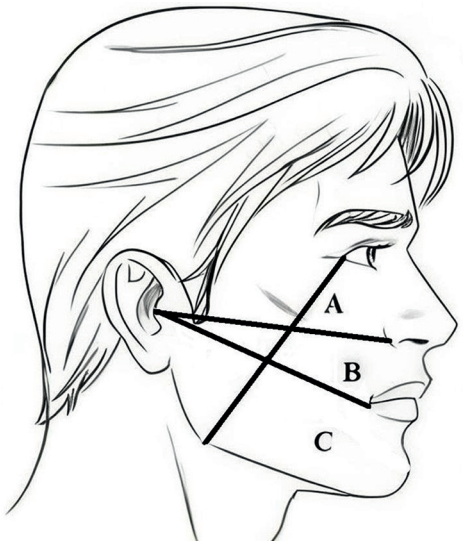

Fig. 2. Facial reference lines used for the assessment of facial swelling

residual bone height (RBH); sinus condition, including Schneiderian membrane thickening; the presence of sinus polyps, cysts, or septa; and periapical inflammatory lesions associated with adjacent teeth. All measurements were performed by a researcher who was not involved in the surgical procedures (C.O.).

Surgical procedure for the lateral sinus-lift

Regardless of study group allocation, all patients were treated according to the same surgical protocol. Under local anesthesia with 4% articaine and epinephrine 1:200,000 (Septanest® 1:200,000; Septodont, Saint-Maur-des-Fossés, France), an envelope-type full-thickness mucoperiosteal flap with a distal releasing incision was elevated to expose the lateral wall of the maxillary sinus. Subsequently, a standardized osteotomy and elevation of the Schneiderian membrane were performed using the DASK® kit (Dentium® Co., Ltd, Suwon, South Korea). First, a bony window was created using identical 8-mm diamond burs under constant saline irrigation and minimal pressure. Next, DASK® elevators were used to prepare an appropriate recipient site for the bone grafting material. The augmented area was covered with a collagen membrane (Bio-Gide®) to prevent epithelial ingrowth into the regenerated region. The flap was repositioned and sutured without tension in the primary position using non-resorbable 5-0 nylon monofilament sutures (Atramat®, Mexico City, Mexico).

Follow-up procedures

Low-level laser therapy

In the appropriate groups (+LLLT), diode laser therapy was applied using a laser device (Lasotronix®, Piaseczno, Poland) with a wavelength of 635 nm, a beam diameter of 0.5 cm^2, and

an energy density of 6 J/cm^2 for 1 min in continuous-wave mode. Low-level laser therapy was performed intraorally, with the laser tip positioned directly over the osteotomy site and the overlying soft tissues immediately after the sinus lift procedure, as well as 3 and 7 days postoperatively.

Postoperative treatment

Every patient, regardless of group allocation, was prescribed Eludril Classic® mouthwash for 2 weeks (twice daily) and an antibiotic (2.0 g/day; Duomox®; Astellas Pharma, Tokyo, Japan). The sutures were removed after 7 days. The 1st follow-up visit was scheduled for postoperative day 3 (T2), and the 2nd for postoperative day 7 (T3). On both occasions, a clinical examination was performed in the same manner as before surgery. On postoperative day 135, a follow-up examination was performed (T4). Clinical and radiological evaluations were repeated in the same manner, with the inclusion of the following additional parameters:

– Bone gain (BG) measured within the region of interest (ROI) as the difference between the postoperative radiographic height of the alveolar process and the RBH.

– Homogeneity of the augmented area, assessed according to the following features:

- initial union observed at the junctional area;
- appearance of mottled radiographic shadows throughout the grafted area;
- differentiation of newly formed bone into a trabecular pattern;
- absence of highly radiopaque particles of non-resorbed graft material.

The presence of at least 3 of the abovementioned features was considered indicative of high graft homogeneity, whereas the presence of fewer than 3 features was considered indicative of low graft homogeneity.

– Bone density, expressed in Hounsfield units (HU), was assessed as follows: First, the imaging plane was positioned at the graft site and aligned parallel to the panoramic curve to visualize the area in which the greatest bone gain had been recorded. Next, an oval region of measurement was carefully selected to include as much of the grafted area as possible. The mean HU value generated by the software was then recorded for subsequent analysis.

Statistical analyses

Due to the relatively small sample size, nonparametric tests were conducted using the nparLD package (https://CRAN.R-project.org/package=nparLD) in R (R Foundation for Statistical Computing, Vienna, Austria). Fisher's exact test is a nonparametric test of statistical significance used, among other purposes, to examine hypotheses concerning the association between 2 nominal-scale variables, often dichotomous in nature. Its advantages lie in its applicability to small sample sizes. An extension of this test is the Fisher–Freeman–Halton test, which is designed for larger contingency tables and, unlike Fisher's exact test, allows for analyses involving more extensive data sets. Friedman's rank test is a nonparametric statistical test based on rank ordering, used to assess differences among at least 3 dependent (i.e., correlated) groups. The rank corresponds to the sequential number assigned to a statistical observation within a sample after ordering the observations according to the value of a given variable. On the other hand, the Kruskal–Wallis test is a rank-based statistical test employed to compare the distributions of a variable across populations. Particularly suitable for small sample sizes, this test does not assume normality of distributions and is regarded as a nonparametric alternative to one-way analysis of variance (ANOVA) for comparisons across groups.

Table 1 presents the results of comparisons for parameters measured once, whereas Table 2 contains the results for parameters measured at 4 time points. In addition, to assess the potential impact of interactions between independent variables on dependent variables, nonparametric statistical analyses for longitudinal data in mixed designs were performed. The results are presented in Table 3.

Table 1. Descriptive statistics of the analyzed parameters according to graft material and laser application

Parameter	Group				Test result – p-value
	Xeno	Xeno+LLLT	Allo	Allo+LLLT	
Women, n (%)	2 (40)	3 (60)	1 (20)	3 (60)	**0.77**[a]
Age [years], Me (min–max)	47 (33–59)	44 (33–52)	54 (43–60)	56 (49–76)	0.09[b]
Bone density [HU], Me (min–max)	466 (312–710)	498 (197–660)	296 (204–420)	267 (198–321)	0.04[b]
Procedure duration [min], Me (min–max)	40 (30–45)	65 (33–91)	50 (30–65)	50 (40–60)	0.08[b]
Graft quantity [g], Me (min–max)	2 (0.5–2)	0.6 (0.5–2)	2 (2–2)	2 (0.4–5)	0.16[b]
Interdental gap, n (%)	3 (60)	4 (80)	2 (40)	1 (20)	**0.46**[a]
RBH [mm], Me (min–max)	**1 (0.4-4)**	2.5 (1–5.5)	3 (1–4.5)	**2 (2-4.5)**	0.74[b]
HKT [mm], Me (min–max)	4 (3–7)	4 (2–7)	4 (2–7)	3 (2–10)	0.71[b]
WKT [mm], Me (min–max)	4.5 (2–5)	4 (2–9)	4 (4–15)	6 (2–11)	0.46[b]

LLLT – low-level laser therapy; Me – median; HU – Hounsfield units; HKT – height of keratinized gingiva; WKT – width of keratinized gingiva; RBH – residual bone height; [a] Fisher–Freeman–Halton test; [b] Kruskal–Wallis test. Values in bold are statistically significant.

Table 2. Descriptive statistics (median and range) of the analyzed parameters according to graft material, laser application, and measurement time, with results of significance tests

Parameter	Group				Test result (p-value)
	Xeno	Xeno + LLLT	Allo	Allo + LLLT	
Jaw openinig [mm]					
T1	49 [41–56]	48 [37–56]	46 [40–55]	50 [41–59]	0.91[a]
T2	47 [41–55]	44 [40–51]	45 [40–54]	47 [40–59]	0.89[a]
T3	48 [41–56]	46 [43–56]	52 [40–52]	51 [44–59]	0.87[a]
T4	47 [40–56]	47 [37–55]	47 [41–57]	48 [46–59]	0.80[a]
p-value	0.64[b]	0.25[b]	0.72[b]	0.44[b]	×
Line A [mm]					
T1	105 [81–110]	100 [90–120]	106 [95–125]	100 [85–105]	0.56
T2	105 [84–114]	100 [100–120]	106 [100–125]	103 [90–110]	0.71
T3	100 [82–115]	100 [95–120]	107 [98–123]	100 [93–105]	0.62
T4	105 [86–111]	100 [95–114]	110 [97–120]	98 [95–105]	0.48
p-value	0.44[b]	0.12[b]	0.85[b]	0.62[b]	×
Line B [mm]					
T1	123 [114–136]	122 [112–135]	122 [118–132]	127 [112–131]	0.99
T2	123 [120–134]	122 [112–135]	125 [121–134]	130 [115–134]	0.94
T3	121 [117–135]	118 [110–135]	122 [119–136]	125 [109–135]	0.81
T4	121 [120–135]	116 [111–135]	128 [120–140]	127 [109–130]	0.77
p-value	0.92[b]	0.66[b]	**0.02**[b]	0.28[b]	×
Line C [mm]					
T1	110 [108–127]	105 [101–123]	115 [112–127]	120 [110–123]	0.53
T2	115 [110–127]	117 [110–130]	121 [117–133]	127 [110–135]	0.71
T3	115 [109–123]	115 [101–125]	119 [115–132]	115 [99–132]	0.78
T4	112 [110–132]	108 [104–123]	120 [115–130]	119 [105–120]	0.38
p-value	0.39[b]	**0.03**[b]	**0.03**[b]	0.07[b]	×
VAS score					
T1	1 [0–2]	0 [0–1]	0 [0–2]	0 [0–1]	0.54
T2	1 [0–1]	1 [0–3]	1 [0–4]	1 [0–2]	0.59
T3	0 [0–0]	0 [0–2]	0 [0–0]	0 [0–1]	0.23
T4	0 [0–0]	0 [0–0]	0 [0–0]	0 [0–0]	1.00
p-value	0.05[b]	0.06[b]	**0.04**[b]	**0.04**[b]	×
PI score					
T1	0 [0–1]	0 [0–1]	1 [0–1]	1 [0–1]	0.55
T2	0 [0–3]	0 [0–2]	1 [0–1]	1 [0–2]	0.96
T3	1 [0–1]	1 [0–1]	1 [0–2]	0 [0–1]	0.48
T4	1 [0–1]	1 [0–1]	1 [0–2]	0 [0–1]	0.70
p-value	0.88[b]	0.82[b]	0.84[b]	0.39[b]	×

[a] Kruskal–Wallis test, [b] Friedman's test; VAS – visual analogue scale; LLLT – low-level laser therapy; PI – Plaque Index. Values in bold are statistically significant.

To evaluate the effects of the between-subject factors (graft and laser) and the within-subject factor (time) on quantitative dependent variables (Jaw Opening, Line A, Line B, Line C, visual analogue scale (VAS), and PI), nonparametric statistical analyses for longitudinal data in mixed designs were carried out. The nparLD package in R was used for this purpose. The results are summarized in Table 3. To evaluate the statistical significance and effect size of 3 independent factors on the dependent variables, repeated-measures ANOVA was performed. The sample size (n = 20) was determined using the G*Power software (https://www.psychologie.hhu.de/arbeitsgruppen/allgemeine-psychologie-und-arbeitspsychologie/gpower), assuming a significance level of $\alpha = 0.05$, statistical power of at least $1 - \beta = 0.80$, 8 groups ($2 \times 2 \times 2$ design), 4 repeated measurements, an inter-measurement correlation of $r = 0.7$, and a nonsphericity correction factor of $\varepsilon = 0.7$ (Fig. 3).

Table 3. Results of the nonparametric repeated-measures analysis of variance

Variable	Effect	Statistic	df	p-value
Jaw opening [mm]	Graft	0.182	1	0.670
	LLLT	0.055	1	0.814
	Time	8.515	3	**0.036**
	Graft : LLLT	0.233	1	0.630
	Graft : Time	0.764	3	0.858
	LLLT : Time	1.435	3	0.697
	Graft : LLLT : Time	1.074	3	0.783
Line A [mm]	Graft	0.001	1	0.984
	LLLT	1.011	1	0.315
	Time	9.669	3	**0.022**
	Graft : LLLT	1.062	1	0.303
	Graft : Time	0.702	3	0.873
	LLLT : Time	1.344	3	0.719
	Graft : LLLT : Time	0.358	3	0.949
Line B [mm]	Graft	0.210	1	0.647
	LLLT	0.227	1	0.634
	Time	13.25	3	**0.004**
	Graft : LLLT	0.007	1	0.934
	Graft : Time	1.499	3	0.683
	LLLT: Time	2.519	3	0.472
	Graft : LLLT : Time	0.297	3	0.961
Line C [mm]	Graft	1.256	1	0.262
	LLLT	0.287	1	0.592
	Time	23.39	3	**<0.001**
	Graft : LLLT	0.070	1	0.791
	Graft : Time	3.253	3	0.354
	LLLT : Time	15.10	3	**0.002**
	Graft : LLLT : Time	6.720	3	0.081
VAS (score)	Graft	0.390	1	0.532
	LLLT	0.126	1	0.723
	Time	41.94	3	**<0.001**
	Graft : LLLT	0.309	1	0.578
	Graft : Time	2.028	3	0.567
	LLLT : Time	9.601	3	**0.022**
	Graft : LLLT : Time	2.583	3	0.460
PI (score)	Graft	0.190	1	0.663
	LLLT	0.211	1	0.646
	Time	0.410	3	0.938
	Graft : LLLT	0.190	1	0.663
	Graft : Time	1.450	3	0.694
	LLLT : Time	1.058	3	0.787
	Graft : LLLT : Time	1.099	3	0.777

LLLT – low-level laser therapy; VAS – visual analogue scale; PI – plaque index. Values in bold are statistically significant.

Results

The mean age of the participants was 50.7 years. The study groups were homogeneous with respect to sex distribution, as 9 of the 20 included patients (45%) were women. Detailed data on patient age and sex distribution among the subgroups are presented in Table 1. After completion of the follow-up period for all included patients, a statistical analysis of the collected data was performed. On the day of surgery, patients in all 4 groups were homogeneous with respect to the analyzed clinical parameters (Table 1). The analysis of jaw opening indicated that the measured values depended on whether laser photobiomodulation had been applied after surgery. Jaw opening values were higher in both patient groups that received photobiomodulation compared with those that did not. Although LLLT appeared to increase jaw opening after surgery, the observed association did not reach statistical significance (Tables 2,3). The analysis of the lengths of Lines A, B, and C showed higher values in male patients than in female patients and in patients who received allografts (Tables 2,3; Fig. 4). Pain scores were not associated with either graft type or sex. Photobiomodulation increased VAS scores on postoperative day 3 but did not influence pain levels at later stages of healing. The main finding for this variable was that pain intensity was time-dependent in patients from both groups. Patients reported significantly higher pain scores on day 3 than on days 7 and 135 after surgery ($p < 0.05$; Table 3). The analysis of radiological parameters based on CBCT examinations revealed no statistically significant differences between the groups in bone gain after 135 days. However, the analysis of HU in the regenerated bone clearly demonstrated higher values in the xenograft group than in the allograft group, and the standard deviation (SD) was also significantly higher in the xenograft group (Fig. 5). We also observed that the allograft was more homogeneous after 135 days compared with the xenograft. This finding is likely related to the longer resorption time characteristic of xenografts compared with allografts.

Discussion

The positive effect of photobiomodulation on postoperative healing has been reported previously in oral surgery procedures. Landucci et al., in a study involving third-molar surgery, demonstrated that laser therapy is effective in reducing postoperative pain, trismus, and swelling.[18] In contrast, Momeni et al. and Alan et al. found that LLLT had no significant effect on edema or trismus; however, it was associated with reduced postoperative pain levels.[19,20]

In the present study, a positive effect of LLLT on trismus was observed, whereas no statistically significant effects on pain levels or swelling following sinus lift surgery were found. This may be explained by differences in the surgical site (i.e., the distal region of the mandibular alveolar

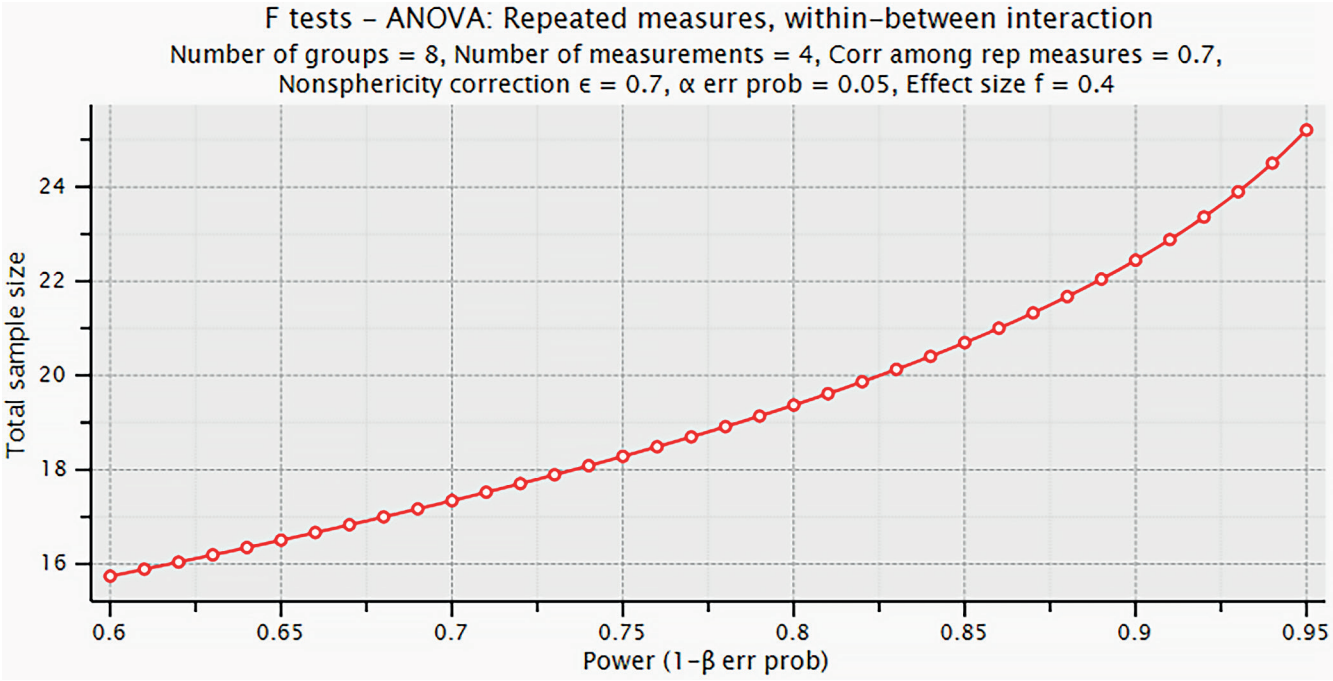

Fig. 3. Relationship between required sample size and statistical power

ANOVA – analysis of variance.

process vs the lateral wall of the maxilla). Previous studies evaluated surgical sites within the oral cavity characterized by strong muscle attachments adjacent to the elevated flap,[18–20] making trismus more likely to occur. Another important consideration is that the VAS scores recorded immediately after surgery in our study were already remarkably low. Therefore, the additional application of LLLT may not have provided a clinically meaningful benefit in terms of pain reduction for our patients.

Despite numerous reports on the influence of LLLT in oral surgery procedures, as mentioned above, its role in recovery following sinus lift surgery remains poorly described in the literature. In a study investigating this procedure, Ozturan et al. reported a positive effect of LLLT on swelling and quality of life. However, it is worth noting that, similarly to our findings, no effect of LLLT on postoperative pain intensity was observed.[21] Trismus is a common symptom during postsurgical recovery. Although it is recognized as part of the physiological healing process, its severity may indicate the influence of additional factors on recovery. More severe trismus may be associated with inflammation, extensive surgical trauma, or prolonged operative time; however, anatomical factors may also contribute. In our study, we observed that male patients exhibited greater jaw opening ranges regardless of the use of LLLT or the grafting material applied. Most studies related to this topic have been conducted in the context of third molar extraction; nevertheless, certain similarities can be identified. In a study by Vranckx et al., the influence of sex on postsurgical healing was evaluated among other factors. Consistent with our findings, the authors reported that women exhibited more pronounced trismus than men.[22] However, reduced jaw opening following surgical procedures is not always associated with patient sex. In contrast, Kiencało et al. found no correlation between sex and trismus after evaluating 339 wisdom tooth extractions.[23]

The aim of every bone grafting procedure is to achieve new bone formation. This is particularly important in procedures followed by implant placement, as direct contact between the implant surface and bone tissue fulfills the definition of osseointegration. New bone formation can be confirmed with certainty only through histological examination; however, this requires a trephine biopsy and may significantly increase the risk to the patient. Therefore, most studies have employed less invasive radiographic methods, particularly CBCT, to assess bone graft remodeling and turnover.[24–26]

It is also a routine method for assessing the outcomes of sinus lift procedures in everyday dental practice. It is generally accepted that the presence of a trabecular pattern and the absence of voids within the grafted area on CBCT images are indicative of bone maturation, whereas increases in radiodensity following bone grafting should be considered a normal stage of healing, as more mature bone typically exhibits a denser appearance.[24–26]

In studies with a follow-up period similar to ours, the origin of the bone graft usually does not influence the degree of bone gain, which is consistent with our findings. A similar conclusion was reached by Al-Moraissi et al., whose large meta-analysis of 52 studies found no differences in new bone height among different grafting materials.[27] The density and homogeneity of the augmented bone, however, are closely related to graft origin. Autologous and allogenic bone grafts are more likely to mimic the properties of the recipient site's residual bone at an earlier stage.

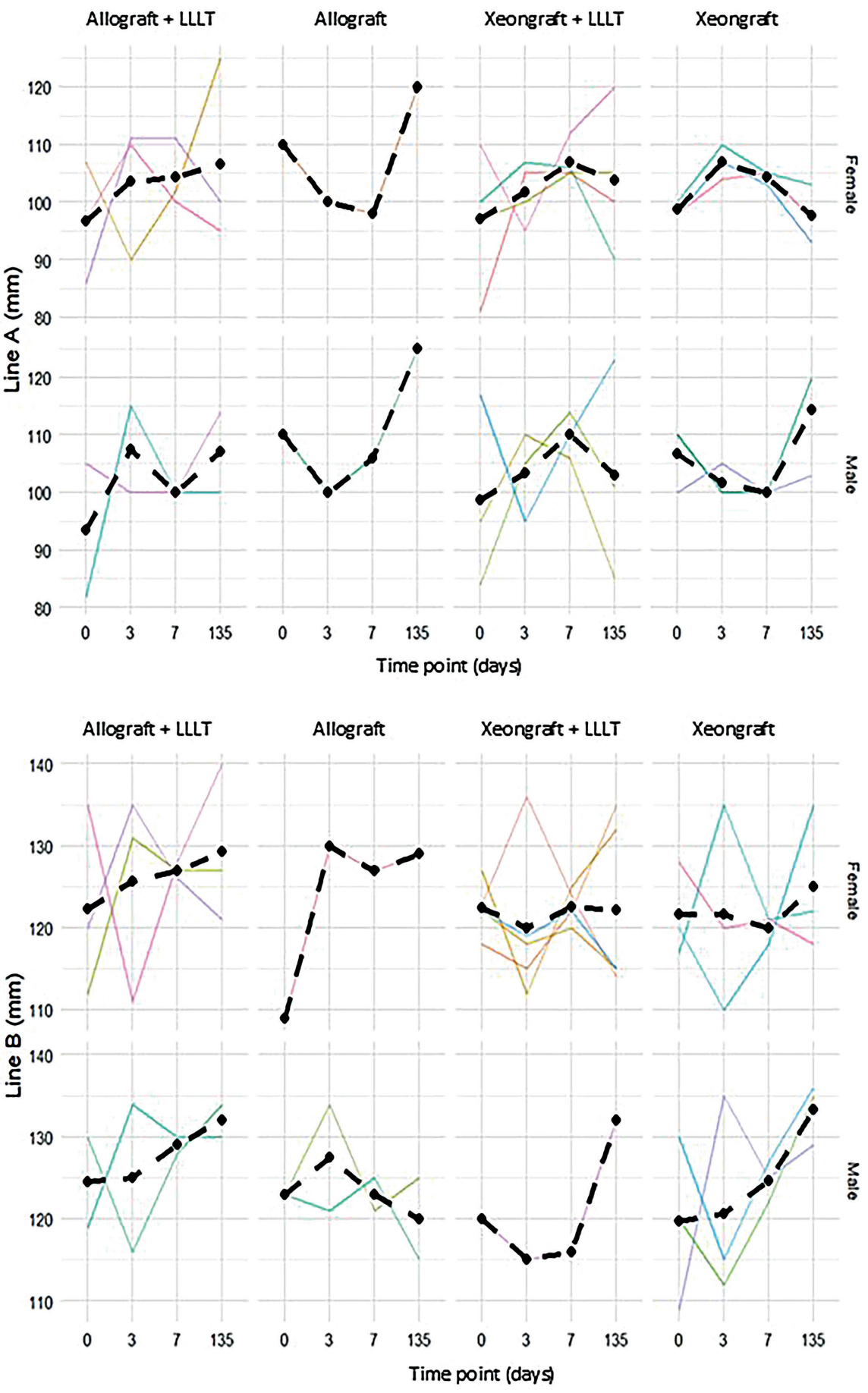

Fig. 4. Effects of gender, low-level laser therapy (LLLT), and graft type on facial swelling

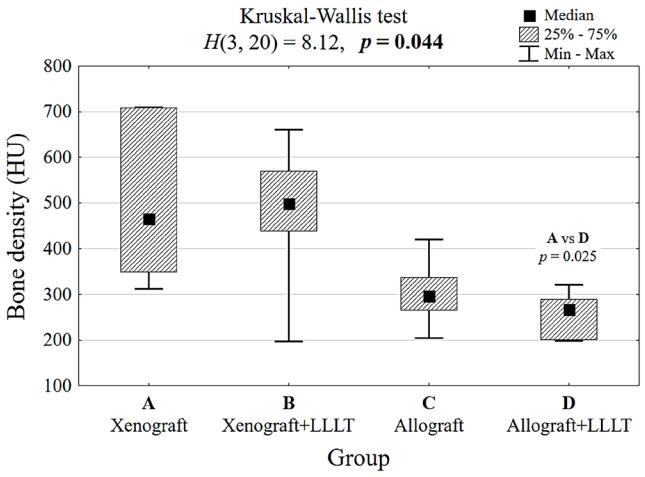

Fig. 5. Hounsfield unit (HU) values according to graft type and laser application, with results of the statistical analysis

LLLT – low-level laser therapy.

Xenografts and alloplastic materials, on the other hand, exhibit prolonged remodeling times, which may explain the differences in homogeneity and density of the newly formed bone. In our study, after 135 days, allogenic bone grafts tended to be more homogeneous, whereas xenografts achieved higher values on the Hounsfield scale. Tabrizi et al. reported similar findings, as xenografts in their study demonstrated significantly higher CBCT density values compared with allogenic material 9 months after maxillary sinus augmentation.[28]

Limitations of the study

The main limitation of this study is the small sample size, which resulted from funding constraints associated with the Doctoral Subsidy program, limiting enrollment to a maximum of 20 patients and the observation period to no more than 12 months. Additional limitations include the fact that new bone formation can be confirmed with absolute certainty only through histological examination, which was not performed in the present study. Furthermore, 2 grafting materials of different origins were used, and these materials exhibit distinct characteristics in radiological evaluation, which may have influenced the interpretation of the radiographic findings.

Conclusions

Low-level laser therapy may improve patient recovery following sinus lift surgery by reducing postoperative limitations in jaw opening. The observation period used in this study corresponds to the average waiting time before implant placement after maxillary sinus floor elevation. The data obtained from this study suggest that different types of bone substitutes do not influence the amount of newly formed bone. However, differences in radiodensity between allografts and xenografts suggest distinct resorption patterns of the 2 materials.

Data Availability Statement

The datasets supporting the findings of the current study are openly available in Zenodo at https://doi.org/10.5281/zenodo.15447878.

Consent for publication of personal information

Not applicable.

Use of AI and AI-assisted technologies

Not applicable.

ORCID iDs

Sebastian Dominiak https://orcid.org/0000-0001-7623-7811
Paweł Kubasiewicz-Ross https://orcid.org/0000-0001-7305-7161
Marzena Dominiak https://orcid.org/0000-0001-8943-0549
Alicja Baranowska https://orcid.org/0009-0008-2508-8295
Cyprian Olchowy https://orcid.org/0000-0002-6559-3973
Michał Ciszyński https://orcid.org/0000-0002-3515-8479

References

1. Dominiak S, Karuga-Kuźniewska E, Popecki P, Kubasiewicz-Ross P. PRF versus xenograft in sinus augmentation in case of HA-coating implant placement: A 36-months retrospective study. *Adv Clin Exp Med*. 2021;30(6):633–640. doi:10.17219/acem/134202
2. Targonska S, Dominiak S, Wiglusz RJ, Dominiak M. Investigation of different types of micro- and nanostructured materials for bone grafting application. *Nanomaterials*. 2022;12(21):3752. doi:10.3390/nano12213752
3. Lim HC, Kim S, Kim DH, Herr Y, Chung JH, Shin SI. Factors affecting maxillary sinus pneumatization following posterior maxillary tooth extraction. *J Periodont Implant Sci*. 2021;51(4):285. doi:10.5051/jpis.2007220361
4. Sakkas A, Wilde F, Heufelder M, Winter K, Schramm A. Autogenous bone grafts in oral implantology: Is it still a "gold standard"? A consecutive review of 279 patients with 456 clinical procedures. *Int J Implant Dent*. 2017;3(1):23. doi:10.1186/s40729-017-0084-4
5. Bianchi S, Bernardi S, Simeone D, Torge D, Macchiarelli G, Marchetti E. Proliferation and morphological assessment of human periodontal ligament fibroblast towards bovine pericardium membranes: An in vitro study. *Materials (Basel)*. 2022;15(23):8284. doi:10.3390/ma15238284
6. Bianchi S, Bernardi S, Mattei A, et al. Morphological and biological evaluations of human periodontal ligament fibroblasts in contact with different bovine bone grafts treated with low-temperature deproteinisation protocol. *Int J Mol Sci*. 2022;23(9):5273. doi:10.3390/ijms23095273
7. Hnitecka S, Dominiak M, Olchowy C, Gedrange T. An innovative method for three-dimensional bone reconstruction of the anterior mandible with preserved dentition using an allogeneic bone block: A 6-month follow-up. *Adv Clin Exp Med*. 2024;34(5):763–775. doi:10.17219/acem/189840
8. Ciszyński M, Dominiak S, Dominiak M, Gedrange T, Hadzik J. Allogenic bone graft in dentistry: A review of current trends and developments. *Int J Mol Sci*. 2023;24(23):16598. doi:10.3390/ijms242316598
9. Zhao R, Yang R, Cooper PR, Khurshid Z, Shavandi A, Ratnayake J. Bone grafts and substitutes in dentistry: A review of current trends and developments. *Molecules*. 2021;26(10):3007. doi:10.3390/molecules26103007

10. Bianchi S, Torge D, Rinaldi F, Piattelli M, Bernardi S, Varvara G. Platelets' role in dentistry: From oral pathology to regenerative potential. *Biomedicines*. 2022;10(2):218. doi:10.3390/biomedicines10020218
11. Alshamrani AM, Mubarki M, Alsager AS, Alsharif HK, AlHumaidan SA, Al-Omar A. Maxillary sinus lift procedures: An overview of current techniques, presurgical evaluation, and complications. *Cureus*. 2023;15(11):e49553. doi:10.7759/cureus.49553
12. Carroll JD, Milward MR, Cooper PR, Hadis M, Palin WM. Developments in low level light therapy (LLLT) for dentistry. *Dent Mater*. 2014; 30(5):465–475. doi:10.1016/j.dental.2014.02.006
13. Gopal L, Palwankar P, Dhalla N. The efficacy of low-level laser therapy on the healing of oral wounds: A systematic review. *Cureus*. 2024; 16(10):e70832. doi:10.7759/cureus.70832
14. Metin R, Tatli U, Evlice B. Effects of low-level laser therapy on soft and hard tissue healing after endodontic surgery. *Lasers Med Sci*. 2018;33(8):1699–1706. doi:10.1007/s10103-018-2523-8
15. Zou Q, Zhang S, Jiang C, Xiao S, Wang Y, Wen B. Low-level laser therapy on soft tissue healing after implantation: A randomized controlled trial. *BMC Oral Health*. 2024;24(1):1477. doi:10.1186/s12903-024-05258-7
16. Hopewell S, Chan AW, Collins GS, et al. CONSORT 2025 statement: Updated guideline for reporting randomised trials. *BMJ*. 2025;389: e081123. doi:10.1136/bmj-2024-081123
17. Laskin DM. *Cirugía bucal y maxilofacial*. Buenos Aires, Argentina: Médica Panamericana; 1987. ISBN:978-950-06-1337-8.
18. Landucci A, Wosny AC, Uetanabaro LC, Moro A, Araujo MR. Efficacy of a single dose of low-level laser therapy in reducing pain, swelling, and trismus following third molar extraction surgery. *Int J Oral Maxillofac Surg*. 2016;45(3):392–398. doi:10.1016/j.ijom.2015.10.023
19. Momeni E, Kazemi F, Sanaei-rad P. Extraoral low-level laser therapy can decrease pain but not edema and trismus after surgical extraction of impacted mandibular third molars: A randomized, placebo-controlled clinical trial. *BMC Oral Health*. 2022;22(1):417. doi:10.1186/s12903-022-02461-2
20. Alan H, Yolcu Ü, Koparal M, Özgür C, Öztürk SA, Malkoç S. Evaluation of the effects of the low-level laser therapy on swelling, pain, and trismus after removal of impacted lower third molar. *Head Face Med*. 2016;12(1):25. doi:10.1186/s13005-016-0121-1
21. Ozturan S, Sirali A, Sur H. Effects of Nd:YAG laser irradiation for minimizing edema and pain after sinus lift surgery: Randomized controlled clinical trial. *Photomed Laser Surg*. 2015;33(4):193–199. doi:10.1089/pho.2014.3823
22. Vranckx M, Fieuws S, Jacobs R, Politis C. Surgical experience and patient morbidity after third molar removal. *J Stomatol Oral Maxillofac Surg*. 2022;123(3):297–302. doi:10.1016/j.jormas.2021.07.004
23. Kiencało A, Jamka-Kasprzyk M, Panaś M, Wyszyńska-Pawelec G. Analysis of complications after the removal of 339 third molars. *Dent Med Probl*. 2021;58(1):75–80. doi:10.17219/dmp/127028
24. Bayat N, Ghavimi MA, Rahimipour K, Razi S, Esmaeili F. Radiographic texture analysis of the hard tissue changes following socket preservation with allograft and xenograft materials for dental implantation: A randomized clinical trial. *Oral Maxillofac Surg*. 2023;28(2):705–713. doi:10.1007/s10006-023-01193-z
25. Aghaloo TL, Moy PK. Which hard tissue augmentation techniques are the most successful in furnishing bony support for implant placement? *Int J Oral Maxillofac Implants*. 2007;22(Suppl):49–70. PMID:18437791.
26. Draenert F, Gebhart F, Berthold M, Gosau M, Wagner W. Evaluation of demineralized bone and bone transplants in vitro and in vivo with cone beam computed tomography imaging. *Dentomaxillofac Radiol*. 2010;39(5):264–269. doi:10.1259/dmfr/147454468
27. Al-Moraissi EA, Alkhutari AS, Abotaleb B, Altairi NH, Del Fabbro M. Do osteoconductive bone substitutes result in similar bone regeneration for maxillary sinus augmentation when compared to osteogenic and osteoinductive bone grafts? A systematic review and frequentist network meta-analysis. *Int J Oral Maxillofac Surg*. 2020;49(1): 107–120. doi:10.1016/j.ijom.2019.05.004
28. Tabrizi R, Sadeghi H, Mohammadi M, Barouj M, Kheyrkhahi M. Evaluation of bone density in sinus elevation by using allograft and xenograft: A CBCT study. *Int J Oral Maxillofac Implants*. 2022;37(1):114–119. doi:10.11607/jomi.9116

Correlation between dental, bone, and chronological age in children with growth hormone deficiency

Natalia Torlińska-Walkowiak[1,A–F], Katarzyna Anna Majewska[2,C,E,F], Anna Sowińska[3,C,E,F], Andrzej Kędzia[2,C,E,F], Justyna Opydo-Szymaczek[1,C–F]

[1] Department of Pediatric Dentistry, Poznan University of Medical Sciences, Poland
[2] Department of Pediatric Diabetes, Auxology and Obesity, Poznan University of Medical Sciences, Poland
[3] Department of Computer Science and Statistics, Poznan University of Medical Sciences, Poland

A – research concept and design; B – collection and/or assembly of data; C – data analysis and interpretation; D – writing the article; E – critical revision of the article; F – final approval of the article

Advances in Clinical and Experimental Medicine, ISSN 1899–5276 (print), ISSN 2451–2680 (online) *Adv Clin Exp Med*. 2026;35(7):1259–1267

Address for correspondence
Natalia Torlińska-Walkowiak
E-mail: ntw@umed.poznan.pl

Funding sources
The research was supported by Poznan University of Medical Sciences statutory funds (grant No. 502--20--22073190).

Conflict of interest
None declared

Received on April 10, 2025
Reviewed on June 22, 2025
Accepted on September 30, 2025

Published online on July 28, 2026

Abstract

Background. The correlation between dental age, bone age, and chronological age is crucial for understanding the growth and development of children. This relationship is particularly important in the diagnosis and management of growth disorders. In children with isolated growth hormone deficiency (GHD), these correlations may provide insights into the extent and consistency of developmental delay and the effectiveness of therapeutic interventions.

Objectives. The aim of this study was to assess how dental and skeletal maturation correspond to chronological age.

Materials and methods. Among the 93 patients recruited, 48 with GHD (30 males and 18 females), aged 10.57 ± 2.24 years, met the inclusion criteria. The control group consisted of 48 healthy children. Clinical and biochemical assessments were performed. Dental age was assessed through clinical examination, whereas skeletal maturation was evaluated using hand-wrist radiographs. Analyses were conducted for the entire GHD group and for subgroups during and after treatment.

Results. The correlations between dental, skeletal, and chronological age were strong and statistically significant ($p < 0.05$). No significant correlation was found between the extent of dental age delay and bone age delay. Dental age delay was significantly greater in patients with GHD before treatment than in healthy children (−0.31 vs 0.41, $p = 0.024$). Bone age delay in children with GHD was more pronounced than dental age delay; it was 1.99 years before treatment and 1.32 years during treatment.

Conclusions. Our results revealed significant differences between bone age and chronological age, as well as between bone age and dental age, in children with GHD, and these differences were reduced during treatment. Significant correlations between bone, dental, and chronological ages indicate that as chronological age increases, dental age and bone age also increase in a predictable manner. Dental and skeletal age delays in patients with GHD are not synchronized, and clinicians should therefore be aware of these discrepancies, particularly when planning dental interventions.

Key words: growth hormone deficiency, bone age, dental age, chronological age, child development

Cite as
Torlińska-Walkowiak N, Majewska KA, Sowińska A, Kędzia A, Opydo-Szymaczek J. Comparative analysis of dental, bone, and chronological age in children with growth hormone deficiency. *Adv Clin Exp Med*. 2026;35(7):1259–1267. doi:10.17219/acem/211566

DOI
10.17219/acem/211566

Copyright
Copyright by Author(s)
This is an article distributed under the terms of the Creative Commons Attribution 3.0 Unported (CC BY 3.0) (https://creativecommons.org/licenses/by/3.0/)

Highlights

- Strong correlations between dental, bone, and chronological age were observed in children with growth hormone deficiency (GHD), providing valuable insights into developmental assessment.
- Bone age delay was greater than dental age delay, especially before treatment, highlighting the differential impact of growth hormone deficiency on skeletal and dental maturation.
- Dental and skeletal age delays in children with GHD are not synchronized, underscoring the importance of individualized timing of dental and orthopedic interventions in pediatric patients.

Background

The growth of children is multifactorial and influenced by a combination of disease, nutrition, and environmental conditions.[1] Reliable growth indicators that can be easily compared are essential for guiding therapeutic interventions. Bone age and dental age serve as key metrics used to assess the biological maturity and developmental stage of a child. Factors such as malnutrition,[2] chronic diseases, and genetic syndromes can adversely affect biological age, particularly dental and skeletal maturation, thereby altering growth velocity and the development of the stomatognathic system.[3,4]

Dental development, from tooth bud formation to eruption, can be influenced by endocrine disorders and may vary across different regions of the world.[5] Interestingly, although systemic diseases may delay physiological growth, dental maturation is generally less delayed than skeletal maturation.[3,6] The relationships among chronological age, bone age, and dental age are crucial for understanding the determinants of growth and development in children.

Studies have shown inconsistent correlations among growth indicators in both healthy children and children with chronic diseases. Some research indicates a positive correlation among skeletal, dental, and chronological age in children.[7–11] Conversely, some authors have reported little correlation among biological age markers in children.[12–14] Certain congenital diseases, such as cleidocranial dysplasia, Silver–Russell syndrome, and Williams syndrome, can disrupt typical patterns of growth and development, and the correlation among biological age indicators may decrease due to variability in how these diseases affect different individuals.[15–17]

Among young patients diagnosed with isolated growth hormone deficiency (GHD), evaluating discrepancies among dental, skeletal, and chronological ages, as well as correlations among these growth indicators, can provide valuable insights into the extent of developmental delays across various organs and the effectiveness of therapeutic interventions. Understanding these relationships helps in tailoring treatments to address specific developmental issues associated with GHD.[3]

Clinical studies involving children with GHD rarely include, in addition to general medical aspects, an evaluation of potential abnormalities in the stomatognathic system.[3,18–21] Although the clinical manifestations of certain conditions associated with growth disorders have been described in detail in recent years, there is still insufficient information in the medical literature regarding patients with isolated GHD.[11,22] The results of such studies could contribute to providing more comprehensive care for these patients.

Objectives

This study aimed to assess how dental and skeletal age correspond to chronological age in children with GHD. We hypothesized that, in children with isolated GHD, delayed dental age would be positively correlated with delayed bone age, suggesting that both developmental processes are similarly influenced by GHD.

Materials and methods

Research design and studied population

This cross-sectional observational study was conducted in children with GHD aged 6–14 years. Patients were recruited and diagnosed at a tertiary referral endocrine center (Department of Pediatric Diabetes, Auxology and Obesity, Poznan University of Medical Sciences, Poland) between October 2015 and May 2024. The correlation among dental age, skeletal age, and chronological age was the primary objective of the clinical investigation. Based on previous literature and biological rationale, a strong positive correlation ($r = 0.60$) was anticipated. Therefore, a one-tailed test was considered appropriate. Using an alpha level of 0.05 and a power of 0.80, the minimum required sample size to detect a statistically significant correlation was calculated to be 15 participants. To enhance the generalizability of the findings, we recruited a larger sample, including all eligible participants available during the study period.

Inclusion and exclusion criteria

The inclusion criteria comprised: age between 6 and 14 years; short stature (height ≤ –2 standard deviation

scores (SDS) for age and sex); diagnosis of GHD; and the presence of more than 1 erupted permanent tooth or up to 3 erupted permanent second molars. To limit the influence of factors other than pituitary disorders on tooth development, strict exclusion criteria were applied. Patients with any systemic, metabolic, or syndromic diseases, as well as those with malnutrition, were excluded.

For the control group, male and female children were selected from among patients treated at the pediatric dental clinic. Every 3rd generally healthy patient, with a height between the 10th and 90th percentiles according to local Polish growth charts appropriate for age and sex and with no history of any systemic or metabolic disease affecting normal growth, was invited to participate in the study. Patients were matched for sex and age relative to the study group.

Socioeconomic status was not analyzed in detail in our study. However, all included children came from the same geographical region, attended public schools, and had equal access to public healthcare. Therefore, their socioeconomic status can be considered similar.

Medical and dental outcomes

Growth hormone (GH) deficiency diagnosis was based on 2 stimulation tests: glucagon (0.03 mg/kg body weight), insulin (0.1 units/kg body weight), or clonidine (100 mcg/m^2). According to the currently applicable Polish national therapeutic program, the GH cutoff was set at 10 ng/mL; therefore, GHD was diagnosed in children whose peak serum GH level did not exceed 10 ng/mL.

Thyroid status was assessed based on thyroid-stimulating hormone (TSH) and free thyroid hormone (free thyroxine – fT4) levels. To assess bone age, hand-wrist radiographs were evaluated using the Greulich and Pyle method. These examinations were performed only in children with GHD during hospital-based diagnostic evaluation.

In both the study and control groups, height measurements (in cm) were performed using a stadiometer (SECA, Hamburg, Germany), with an accuracy of 1 mm. For all children included in the study, the hSDS was calculated in accordance with the guidelines.[23]

The oral cavity was examined by a pediatric dentist (N.T.-W.) who had previously been calibrated using children not included in the study. A high level of agreement was observed for repeated measurements (kappa value >0.80).

To evaluate dental age, the Matiegka and Lukasova method was selected. Clinical age estimation was necessary due to the lack of panoramic radiographs for all patients.[24] For ethical reasons, performing orthopantomograms solely for research purposes was not possible. In the present study, calculation of dental age was based on tooth eruption status – a tooth was considered present if any part of its crown was visible in the oral cavity.[25,26] The eruption status was then converted into dental age using sex-specific conversion tables.

Dental age delay and bone age delay were defined as the differences between dental or bone age and chronological age. For data analysis, the GHD group was divided into 2 subgroups (before and during rhGH (recombinant human growth hormone) therapy) due to the suspected influence of GH treatment on dental and bone age.

The legal guardians of the patients provided written informed consent for participation in the study. The clinical investigation was conducted in accordance with the Declaration of Helsinki, and the protocol was approved by the Bioethical Committee of Poznan University of Medical Sciences, Poland (approvals No. 785/15 and No. 777/23).

Statistical analyses

The groups were matched using propensity score matching, comparing the GHD group with the control group. Propensity scores were calculated as the probability of group membership conditional on age and sex. Using a nearest-neighbor matching algorithm without replacement and with a caliper of 0.01, the most appropriately matched pairs were selected.

The normality of the distribution was tested using the Shapiro–Wilk test, and equality of variances was assessed using Levene's test (see shared data). Descriptive statistics are presented as percentages for categorical variables, means with standard deviations (SDs) for normally distributed continuous variables, and medians with minimum and maximum values for non-normally distributed continuous variables. Differences between 2 groups were assessed using the paired-samples Student's t-test or the Wilcoxon signed-rank test. For comparisons involving more than 2 groups, we applied the Friedman's test with Dunn's post hoc test or a two-way analysis of variance (two-way ANOVA) with a post hoc least significant difference (LSD) test. This analysis was used to assess the main and interaction effects of group (study vs control) and time point (before vs after hormone administration). Correlations among chronological age, dental age, and bone age in short-statured children and the control group were evaluated using Spearman's rank correlation coefficient (rho) or Pearson's correlation coefficient (r). All results were considered statistically significant at $p < 0.05$. Statistical analyses were conducted using Statistica v. 13.0 (StatSoft Inc., Round Rock, USA), PQStat Software (2024), v. 1.8.6.120 (Poznań, Poland), or MedCalc® Statistical Software v. 22.014 (MedCalc Software Ltd., Ostend, Belgium).

Results

Out of a total of 93 examined patients with short stature, 48 (18 females and 30 males) fulfilled the inclusion criteria. Thus, the present study included 48 patients with GHD,

either before or during treatment, and 48 healthy controls. Table 1 presents the clinical data, including means and SDs (or medians and ranges, where appropriate), for all groups. There were more male than female patients. Most patients presented with mixed dentition.

Table 2 presents the results of the two-way ANOVA, LSD post hoc test, and Student's t-test among the examined groups. Chronological age and dental age did not differ significantly between the control and GHD groups ($p = 0.715$ and $p = 0.784$, respectively).

The difference in dental age delay between the study and control groups was statistically significant ($p = 0.045$). The post hoc LSD test revealed significant differences between the GHD during-treatment group and the control group (–0.48 vs 0.41 years, $p = 0.014$) and between the GHD before-treatment group and the control group (–0.31 vs 0.41 years, $p = 0.024$).

For children with GHD before treatment, the dental age delay was –0.31 ±1.25 years, whereas the bone age delay was significantly greater at –1.99 ±0.97 years ($p < 0.001$). During treatment, the dental age delay was –0.48 ± 0.98 years, and the bone age delay was –1.32 ±1.28 years, with a significant difference between them ($p = 0.042$).

Table 3 presents a comparison of dental age, chronological age, and bone age in children with GHD and matched controls. For children with GHD before treatment, the median dental age was 10 years (range: 6.50–14.00 years), the chronological age was 10.45 ±2.21 years, and the bone age was 8.47 ±2.52 years. There was a highly significant difference between chronological age and bone age ($p < 0.001$) and between bone age and dental age ($p < 0.001$). For children with GHD during treatment, the dental age was 10.27 ±2.31 years, the chronological age was 10.75 ±2.32 years, and the bone age was 9.43 ±2.93 years. There was a significant difference between chronological age and bone age ($p = 0.022$). For the matched control children, the median dental age was 10.29 years (range: 6.08–14.00 years), and the chronological age was 10.44 ±2.33 years. There was no significant difference between chronological age and dental age ($p = 0.167$) (Table 3).

Table 4 shows the correlation coefficients between skeletal age, dental age, and chronological age according to sex and treatment status (before treatment vs during therapy). Skeletal age, chronological age, and dental age were significantly correlated in all patients and subgroups. Spearman's and Pearson's correlation coefficients were greater than 0.69 in both groups and in both sexes, indicating a strong correlation. Dental age delay and bone age delay were not correlated (Table 4).

Table 1. Clinical characteristics of children with growth hormone deficiency (GHD) and the control group

Variable	GHD during treatment	GHD before treatment	Total GHD	Control group
Number of patients	19	29	48	48
Age [years]	10.75 ±2.32	10.45 ±2.21	10.57 ±2.24	10.44 ±2.33
TSH [μIU/mL]	1.93 ±0.78	2.25 ±0.85	N/A	N/A
fT4 [ng/dL]	1.01 (0.87–1.24)	1.08 ±0.16	N/A	N/A
Sex (male/female)	14/5	16/13	30/18	29/19
Mixed dentition, n (%)	14 (74)	22 (76)	36 (75)	34 (71)
Permanent dentition, n (%)	5 (26)	7 (24)	12 (25)	14 (29)
hSDS	–1.51 ±0.92	–2.48 ±0.40	N/A	0.13 ±0.87

hSDS – height standard deviation score; TSH – thyroid-stimulating hormone; fT4 – free thyroid hormone (free thyroxine).

Table 2. Dental age, chronological age, dental age delay, and bone age delay in the examined patients

Statistical test		Mean ±SD	Mean ±SD	p-value	Statistical significance
Two-way ANOVA with 2 factors: group (study vs control) and treatment status	dental age delay	–	–	0.045	*
	dental age	–	–	0.715	NS
	chronological age	–	–	0.784	NS
Post hoc LSD test for dental age delay	GHD during treatment (n = 19) vs control (n = 29)	–0.48 ±0.98	0.41 ±1.22	0.014	*
	GHD before treatment (n = 29) vs control (n = 29)	–0.31 ±1.25	0.41 ±1.22	0.024	*
Paired-samples Student's t-test	bone age delay vs dental age delay – during treatment	–1.32 ±1.28	–0.48 ±0.98	0.042	*
	bone age delay vs dental age delay – before treatment	–1.99 ±0.97	–0.31 ±1.25	0.001	*

SD – standard deviation; ANOVA – analysis of variance; LSD – least significant difference; NS – not significant.

Table 3. Comparison of dental age, chronological age, and bone age in children with growth hormone deficiency (GHD) and matched control children

Group of patients	Dental age [years] (median, min–max range)	Chronological age [years] (mean ±SD)	Bone age [years] (mean ±SD)	p-value
Children with GHD before treatment	10 (6.50–14.00)	10.45 ±2.21	8.47 ±2.52	<0.001[a] CA vs BA, p < 0 .001 CA vs DA, p = 0.793 BA vs DA, p < 0.001
Children with GHD during treatment	10.27 ±2.31	10.75 ±2.32	9.43 ±2.93	0.022[a] CA vs BA, p = 0.022 CA vs DA, p = 0.155 BA vs DA, p = 1.000
Matched control children	10.29 (6.08–14.00)	10.44 ±2.33	–	CA vs DA 0.167[b]

[a]Friedman test (post hoc Dunn's test), [b]Wilcoxon test; SD – standard deviation; CA – chronological age; BA – bone age; DA – dental age.

Table 4. Correlation coefficients between skeletal age, dental age, and chronological age according to sex and treatment status (before treatment vs during therapy)

Pearson's or Spearman's correlation coefficients			Study group		Control group	
			r (rho)	p-value	r (rho)	p-value
Dental age and chronological age	males	before treatment	0.81	<0.001[b]	0.85	<0.001[a]
		during treatment	0.80	<0.001[b]	–	–
	females	before treatment	0.85	<0.001[b]	0.80	<0.001[a]
		during treatment	0.95	0.006[b]	–	–
	total	before treatment	0.89	<0.001[a]	–	–
		during treatment	0.94	<0.001[a]	–	–
Dental age and bone age	males	before treatment	0.75	<0.001[b]	–	–
		during treatment	0.69	<0.001[b]	–	–
	females	before treatment	0.85	<0.001[b]	–	–
		during treatment	0.80	0.039[b]	–	–
	total	before treatment	0.86	<0.001[a]	–	–
		during treatment	0.85	<0.001[a]	–	–
Bone age and chronological age	males	before treatment	0.86	<0.001[b]	–	–
		during treatment	0.87	<0.001[b]	–	–
	females	before treatment	0.85	<0.001[b]	–	–
		during treatment	0.81	0.036[b]	–	–
	total	before treatment	0.92	<0.001[b]	–	–
		during treatment	0.91	<0.001[b]	–	–
Dental age delay and bone age delay	males	before treatment	0.03	0.506[b]	–	–
		during treatment	0.01	0.781[b]	–	–
	females	before treatment	0.09	0.328[b]	–	–
		during treatment	0.001	0.949[b]	–	–
	total	before treatment	0.24	0.210[b]	–	–
		during treatment	–0.09	0.713[b]	–	–

[a] Spearman's rank correlation coefficient (rho); [b] Pearson's correlation coefficient (r).

Discussion

This manuscript emphasizes the strong correlation among dental, bone, and chronological age in patients with isolated GHD. Interestingly, our results did not confirm the initial hypothesis. Although dental age was significantly delayed in children with GHD compared to healthy peers, we found no significant correlation between the extent of dental age delay and bone age delay. This indicates that, despite both being affected by GHD, the degree of delay in dental and skeletal development may not progress in a synchronized manner in individual patients. This finding suggests that dental and skeletal maturation may be regulated by partially independent biological mechanisms and that dental development is less sensitive to GH levels than bone development. From a clinical perspective, these results emphasize the need to independently assess both dental and skeletal maturity when managing patients with

GHD, rather than assuming that one parameter reliably reflects the other.

Interestingly, the clinical implications of discrepancies between dental and bone age remain relatively underexplored. However, recent studies[27,28] have reported delayed tooth eruption in children with GHD, which may be associated with a mismatch between tooth and bone size. Furthermore, the consequences of such discrepancies appear to be supported by a previous study by Torlińska et al., in which greater dental crowding was observed in children with delayed bone age in both idiopathic short stature (ISS) and GHD cohorts.[3] It is also worth noting that a relationship exists among skeletal maturation, dental development, and the formation of the permanent dentition.[21,29] Nevertheless, further research is needed to fully elucidate the mechanisms underlying these interrelated processes.

Data on the extent of dental age delay in short-stature patients and the impact of GH replacement therapy on dental development are scarce and frequently conflicting. The incomplete and inconsistent information on this topic prompted us to explore the relationships among maturation indicators in children with GHD.

In the study by Torlińska et al., dental age delay, bone age delay, and occlusal traits were assessed in a cohort of short-stature children with GHD and ISS. The findings indicated significant dental age delay in children with GHD before treatment compared to healthy peers, as well as a more pronounced bone age delay.[3] To expand on these findings, we decided to recruit a larger sample of participants with isolated GHD and analyze correlations within specific subgroups to gain deeper insights into the developmental delays associated with GHD. Dental age assessment is essential in the daily practice of dentists and orthodontists. Planning conservative treatment and potential tooth extractions as part of an orthodontic treatment plan must be based not only on a dental examination but also on comprehensive knowledge of the patient's general health and growth patterns associated with the underlying condition.

Skeletal maturation occurs in consistent and defined stages across different ethnic groups, although the timing may vary due to genetic, environmental, regional, and climatic factors.[30] For this reason, all participants in our study were from the same geographical region and ethnic group. Skeletal maturation is commonly assessed based on the stages of skeletal development observed in hand-wrist radiographs.[30] Compared with skeletal maturation, tooth mineralization and eruption are less affected by endocrine, environmental, and nutritional factors. This makes them very useful for age estimation,[31] which can be based on the stage of development of dental germs and the progressive sequence of their eruption in the oral cavity.[2,32] Nevertheless, it should be noted that dental development and eruption can vary due to factors such as climate, nutrition, race, and genetic inheritance.[5,32] The advantage of methods based on tooth mineralization is that they can be applied at any stage of dental development. In contrast, clinical dental age cannot be determined once all permanent teeth have erupted. In this study, because panoramic radiographs were not available, we based our analysis on clinical examination, which allows for a quick and non-invasive assessment.

Only a few researchers have evaluated the biological age of individuals with hypopituitarism or impaired growth velocity. Valejo-Bolaños et al. investigated the relationships among dental, bone, and chronological age in children with isolated GHD. They reported a significant difference of 1.52 years between chronological age and bone age and 0.92 years between chronological age and dental age. The study concluded that both dental and bone age were significantly delayed compared to chronological age after 2.5 years of GH therapy.[33]

Our current results confirm the presence of significant differences between skeletal age and chronological age in young patients with GHD. The delay in bone age in the study group was as much as 1.99 years, but this delay was reduced during treatment. In contrast, we did not observe similarly large differences between the dental and chronological ages of the patients studied. A statistically significant difference indicating a slight delay in dental age in patients with GHD was observed when they were compared with an age- and sex-matched control group.

In the previous study by Torlińska et al., dental, skeletal, and chronological age in children with GHD and ISS was examined. The clinical investigation was carried out in 46 children (aged 5–14 years): 15 with ISS, 17 with GHD before GH replacement therapy, and 14 with GHD during therapy. The study confirmed dental age delay in children with GHD before GH therapy. Both children with ISS and untreated GHD showed marked bone age delay.[3] In the present study, which focused solely on patients with GHD, these findings were confirmed in a larger cohort.

More extensive analyses have been conducted in syndromic patients with short stature. Pinchi et al. carried out research to understand the influence of genetic syndromes (Down syndrome and Williams syndrome) on dental maturation. The study sample included 159 children with chromosomal abnormalities and a control group of 157 healthy children aged 4.49–19.8 years. The results revealed no statistically significant differences in dental age estimates between syndromic and healthy individuals or between sexes and age cohorts.[1]

Diz et al. examined 155 patients with cerebral palsy, intellectual disability, and Down syndrome. The control group comprised 688 children. No significant differences between dental age and chronological age were found in boys with the studied disorders. However, dental age was significantly delayed compared to chronological age in girls with cerebral palsy or Down syndrome.[6]

This finding was confirmed by de Moraes et al., who observed that the mean dental age was slightly lower than the chronological age in children with Down syndrome, with a significant difference observed only in females.[32]

Another study by Pozsonyi et al. found delayed bone development up to the age of 8 years in children with Down syndrome compared with healthy controls.[34] De Moraes et al. reported that the skeletal age of subjects with Down syndrome aged 6–16 years was significantly delayed compared to their chronological age, particularly at the age of 7 years.[35]

The delay in dental age among patients with Williams syndrome is not uniform, reflecting the syndrome's broad range of dental manifestations. Some individuals exhibit eruption delays of approx. 1–2 years,[36] whereas others may have more typical eruption timelines.[16,36] Regarding cleidocranial dysplasia, patients present with a range of dental abnormalities, such as delayed exfoliation of primary teeth, delayed eruption of permanent teeth by up to several years, and often the presence of supernumerary teeth. Not all patients experience the same degree of dental age delay. This variability can be attributed to genetic differences, phenotypic expression, the presence and number of supernumerary teeth, and differences in skeletal development.[15]

Children with Silver–Russell syndrome may exhibit delayed dental age. However, some may have relatively minor delays, whereas others exhibit more significant delays. This variability can be influenced by the extent of growth restriction and the presence of other craniofacial abnormalities. Bergman et al. reported that the dental maturity of children with Silver–Russell syndrome was within normal limits, whereas the timing of tooth eruption was delayed by approx. 1 year.[16] Ioannidou-Marathiotou et al. reported an atypical pattern of tooth eruption in a girl with Silver–Russell syndrome who, at the age of 10 years, was in the early mixed dentition stage, with normal eruption of permanent upper and lower incisors only.[37] These findings highlight the considerable research attention given to syndromic forms of short stature. In contrast, studies involving children with isolated GHD remain limited. The present study aims to address this gap in the literature.

Notably, even if dental development occurs later than usual, there can still be a high correlation between dental age and chronological age if the delay is consistent across the population. This means that although dental age or skeletal age might be lower than expected for a given chronological age, the relationship between the 2 ages can remain strong and predictable. For orthodontists and pediatric dentists, understanding the mismatch among dental, skeletal, and chronological age is crucial for treatment planning. Treatments may need to be adjusted based on dental and skeletal maturity rather than the patient's chronological age.

Some research has been conducted on the correlation among indicators of biological age in children from different geographical regions. In a study by Bala et al.,[2] 160 healthy North Indian children aged 8–14 years, equally divided by sex, were examined. The study revealed that skeletal age and dental age were not strongly correlated with chronological age across all age groups. However, there was a significant correlation between skeletal age and dental age in children aged 12–14 years of both sexes. Conversely, another Indian study reported a very strong correlation among chronological, skeletal, and dental age.[7]

Poulsen et al.[5] reported significant correlations between dental and skeletal maturation in healthy children with a mean age of 11.48 years. In the Swedish population, a study revealed strong correlations between wisdom tooth development and chronological age, skeletal age, and dental age.[10] Similarly, significant correlations were found between mandibular third molar mineralization and chronological age in Croatian subjects.[9]

A study of Yugoslavian children with cerebral palsy revealed varying degrees of delay in dental and skeletal age compared with chronological age, highlighting poor correlation in some cases due to the diverse impact of the condition on development.[38]

In the study by de Moraes et al.,[32] Pearson's correlation coefficient for dental age compared to skeletal age was greater than 0.9 in both the Down syndrome group and the healthy control group, regardless of sex. In the present study, strong correlations of 0.69 or greater were found among dental age, chronological age, and bone age in Caucasian children with GHD. This means that as chronological age increases, dental age and bone age also increase in a predictable manner.

Limitations of the study

Our study has several limitations. First, the method used for dental age estimation is clinically acceptable but not widely adopted, making it unclear to what extent the results are applicable to other populations, as tooth eruption patterns may vary among ethnic groups. Future studies should include dental age assessment based on radiographic images in this patient population. Second, the sample size, particularly for patients with GHD during treatment, was relatively small. Third, we did not account for variables such as socioeconomic background or physical activity, which could influence both dental and skeletal development. Despite these limitations, this study contributes to understanding the developmental patterns of children with GHD. By highlighting discrepancies among different indicators of biological age, it provides valuable insights into how GHD affects physical development. These findings may help clinicians better monitor and manage the growth and development of children with GHD, particularly with regard to treatment planning.

Conclusions

This study underscores the importance of considering multiple indicators of biological age in the management of children with GHD. Our results confirm the presence of significant differences between bone age and chronological age, as well as between bone age and dental age, in children with GHD. These differences were reduced during treatment. Significant

correlations among bone age, dental age, and chronological age indicate that, as chronological age increases, dental age and bone age also increase in a predictable manner. Although delays in both dental age and bone age are observed in children with isolated GHD, the expected correlation between these delays was not confirmed. This suggests that dental and skeletal development may not always progress in parallel in patients with GHD. Therefore, when assessing growth and planning orthodontic or medical interventions, clinicians should consider that dental age and bone age may provide complementary but independent information.

Data Availability Statement

The datasets supporting the current study are openly available in Zenodo at https://doi.org/10.5281/zenodo.15065743.

Consent for publication of personal information

Not applicable

Use of AI and AI-assisted technology

Not applicable

ORCID iDs

Natalia Torlińska-Walkowiak https://orcid.org/0000-0002-4761-737X
Katarzyna Anna Majewska https://orcid.org/0000-0002-3573-2274
Anna Sowińska https://orcid.org/0000-0001-5319-5057
Andrzej Kędzia https://orcid.org/0000-0001-8206-6094
Justyna Opydo-Szymaczek https://orcid.org/0000-0001-5091-3316

References

1. Pinchi V, Vitale G, Pradella F, Farese L, Focardi M. Dental age estimation in children with chromosomal syndromes. *J Forensic Odontostomatol*. 2018;36(1):44–52. PMID:29864029. PMCID:PMC6195943.
2. Bala M, Pathak A, Jain R. Assessment of skeletal age using MP_3 and hand-wrist radiographs and its correlation with dental and chronological ages in children. *J Indian Soc Pedod Prev Dent*. 2010;28(2):95. doi:10.4103/0970-4388.66746
3. Torlińska-Walkowiak N, Majewska KA, Sowińska A, Kędzia A, Opydo-Szymaczek J. Skeletal and dental age discrepancy and occlusal traits in children with growth hormone deficiency and idiopathic short stature. *Clin Oral Invest*. 2022;26(10):6165–6175. doi:10.1007/s00784-022-04566-y
4. Klupś D, Kaźmierczak J, Torlińska-Walkowiak N. Tooth agenesis: Genes and syndromic diseases. Literature review. *J Pre Clin Clin Res*. 2022;16(4):149–152. doi:10.26444/jpccr/157097
5. Poulsen AR, Sonnesen L. Association between dental and skeletal maturation in Scandinavian children born between 2005 and 2010. *Acta Odontol Scand*. 2023;81(6):464–472. doi:10.1080/00016357.2023.2176920
6. Diz P, Limeres J, Salgado AFP, et al. Correlation between dental maturation and chronological age in patients with cerebral palsy, mental retardation, and Down syndrome. *Res Dev Disabil*. 2011;32(2):808–817. doi:10.1016/j.ridd.2010.10.019
7. Behera CK, Rath R, Das SN, Sahu G, Sharma G, Bhatta A. Correlation of skeletal age by Greulich–Pyle atlas, physiological age by body development index, and dental age by London Atlas and modified Demirjian's technique in children and adolescents of an Eastern Indian population. *Egypt J Forensic Sci*. 2023;13(1):40. doi:10.1186/s41935-023-00359-w
8. Palanisamy V, Rao A, Shenoy R, Baranya S. Correlation of dental age, skeletal age, and chronological age among children aged 9–14 years: A retrospective study. *J Indian Soc Pedod Prev Dent*. 2016;34(4):310. doi:10.4103/0970-4388.191408
9. Legović M, Sasso A, Legović I, et al. The reliability of chronological age determination by means of mandibular third molar development in subjects in Croatia. *J Forensic Sci*. 2010;55(1):14–18. doi:10.1111/j.1556-4029.2009.01238.x
10. Engström C, Engström H, Sagne S. Lower third molar development in relation to skeletal maturity and chronological age. *Angle Orthod*. 1983;53(2):97–106. PMID:6576657.
11. Moraes MELD, Bastos MS, Santos LRDAD, Castilho JCDM, Moraes LCD, Medici Filho E. Dental age in patients with Down syndrome. *Braz Oral Res*. 2007;21(3):259–264. doi:10.1590/S1806-83242007000300012
12. Demirjian A, Buschang PH, Tanguay R, Patterson DK. Interrelationships among measures of somatic, skeletal, dental, and sexual maturity. *Am J Orthod*. 1985;88(5):433–438. doi:10.1016/0002-9416(85)90070-3
13. Arciniega Ramos NA, Ballesteros Lozano M, Meléndez Ocampo A. Comparative analysis between dental, skeletal and chronological age. *Rev Mex Ortod*. 2013;1(1):e33–e37. doi:10.1016/S2395-9215(16)30118-0
14. Uysal T, Sari Z, Ramoglu SI, Basciftci FA. Relationships between dental and skeletal maturity in Turkish subjects. *Angle Orthod*. 2004;74(5):657–664. doi:10.1043/0003-3219(2004)074<0657:RBDASM>2.0.CO;2
15. Satish V, Parvez M. Cleidocranial dysplasia: Case report of three siblings. *Int J Clin Pediatr Dent*. 2009;2(2):32–39. doi:10.5005/jp-journals-10005-1027
16. Bergman A, Kjellberg H, Dahlgren J. Craniofacial morphology and dental age in children with Silver–Russell syndrome. *Orthod Craniofac Res*. 2003;6(1):54–62. doi:10.1046/j.1439-0280.2003.2c209.x
17. Vavetsi K, Panagopoulou O, Koromantzos P, et al. Oral manifestations of nine individuals with Williams syndrome: A case series. *Spec Care Dent*. 2024;44(2):438–449. doi:10.1111/scd.12881
18. Torlińska-Walkowiak N, Majewska KA, Kędzia A, Opydo-Szymaczek J. Clinical implications of growth hormone deficiency for oral health in children: A systematic review. *J Clin Med*. 2021;10(16):3733. doi:10.3390/jcm10163733
19. Torlińska-Walkowiak N, Majewska KA, Sowińska A, Kędzia A, Opydo-Szymaczek J. Developmental enamel defects and dental anomalies of number and size in children with growth hormone deficiency. *Sci Rep*. 2023;13(1):14707. doi:10.1038/s41598-023-41892-x
20. Litsas G. Growth hormone and craniofacial tissues: An update. *Open Dent J*. 2015;9(1):1–8. doi:10.2174/1874210601509010001
21. Davidopoulou S, Chatzigianni A. Craniofacial morphology and dental maturity in children with reduced somatic growth of different aetiology and the effect of growth hormone treatment. *Prog Orthod*. 2017;18(1):10. doi:10.1186/s40510-017-0164-2
22. Tallón-Walton V, Sánchez-Molins M, Hu W, Martínez-Abadías N, Casado A, Manzanares-Céspedes MC. Comprehensive oral diagnosis and management for women with Turner syndrome. *Diagnostics (Basel)*. 2024;14(7):769. doi:10.3390/diagnostics14070769
23. Kułaga Z, Litwin M, Tkaczyk M, et al. Polish 2010 growth references for school-aged children and adolescents. *Eur J Pediatr*. 2011;170(5):599–609. doi:10.1007/s00431-010-1329-x
24. Janiszewska-Olszowska J, Doniec-Zawidzka I, Karłowska I, et al., eds. *Zarys współczesnej ortodoncji: podręcznik dla studentów i lekarzy dentystów*. wyd. IV uaktualnione. Warsaw, Poland: Wydawnictwo Lekarskie PZWL; 2016. ISBN:978-83-200-5221-3.
25. Cecere S, Leroy R, Groenen PJF, Lesaffre E, Declerck D. Estimating emergence sequences of permanent teeth in Flemish schoolchildren using interval-censored biplots: A graphical display of tooth emergence sequences. *Commun Dent Oral Epidemiol*. 2012;40(Suppl 1):49–55. doi:10.1111/j.1600-0528.2011.00666.x
26. Diamanti J, Townsend G. New standards for permanent tooth emergence in Australian children. *Aust Dent J*. 2003;48(1):39–42. doi:10.1111/j.1834-7819.2003.tb00007.x
27. Cantu G, Buschang PH, Gonzalez JL. Differential growth and maturation in idiopathic growth-hormone-deficient children. *Eur J Orthod*. 1997;19(2):131–139. doi:10.1093/ejo/19.2.131
28. Kjellberg H, Beiring M, Wikland KA. Craniofacial morphology, dental occlusion, tooth eruption, and dental maturity in boys of short stature with or without growth hormone deficiency. *Eur J Oral Sci*. 2000;108(5):359–367. doi:10.1034/j.1600-0722.2000.108005359.x

29. Flores-Mir C, Mauricio FR, Orellana MF, Major PW. Association between growth stunting with dental development and skeletal maturation stage. *Angle Orthod*. 2005;75(6):935–940. doi:10.1043/0003-3219(2005)75[935:ABGSWD]2.0.CO;2
30. Mohammed RB, Reddy MAL, Jain M, Singh JR, Sanghvi P, Thetay AAR. Digital radiographic evaluation of hand-wrist bone maturation and prediction of age in South Indian adolescents. *Hand (N Y)*. 2014;9(3):375–383. doi:10.1007/s11552-013-9598-2
31. Pereira CP, Russell LM, De Pádua Fernandes M, Alves Da Silva RH, Vargas De Sousa Santos RF. Dental age estimation based on Development Dental Atlas Assessment in a child/adolescent population with systemic diseases. *Acta Stomatol Croat*. 2019;53(4):307–317. doi:10.15644/asc53/4/1
32. De Moraes MEL, De Moraes LC, Cardoso M, Ursi W, De Castro Lopes SLP. Age assessment based on dental calcification in individuals with Down syndrome. *Res Dev Disabil*. 2013;34(11):4274–4279. doi:10.1016/j.ridd.2013.09.005
33. Vallejo-Bolaños E, España-López AJ, Muñoz-Hoyos A, Fernandez-Garcia JM. The relationship between bone age, chronological age and dental age in children with isolated growth hormone deficiency. *Int J Paediatr Dent*. 1999;9(3):201–206. doi:10.1046/j.1365-263x.1999.00129.x
34. Pozsonyi J, Gibson D, Zarfas DE. Skeletal maturation in mongolism (Down's syndrome). *J Pediatr*. 1964;64(1):75–78. doi:10.1016/S0022-3476(64)80319-X
35. De Moraes MEL, Tanaka JLO, De Moraes LC, Filho EM, De Melo Castilho JC. Skeletal age of individuals with Down syndrome. *Spec Care Dent*. 2008;28(3):101–106. doi:10.1111/j.1754-4505.2008.00020.x
36. Joseph C, Landru MM, Bdeoui F, Gogly B, Dridi SM. Periodontal conditions in Williams–Beuren syndrome: A series of 8 cases. *Eur Arch Paediatr Dent*. 2008;9(3):142–147. doi:10.1007/BF03262626
37. Ioannidou-Marathiotou I, Sluzker A, Athanasiou AE. Orthodontic management of Silver–Russell syndrome: A case report. *Open Dent J*. 2012;6(1):131–136. doi:10.2174/1874210601206010131
38. Ozerovic B. Correlation of dental and skeletal age in children with cerebral palsy. *Eur J Orthod*. 1980;2(3):193–195. doi:10.1093/ejo/2.3.193

Optical coherence tomography and biometric ultrasound for gingival phenotype and epithelial thickness assessment: A cross-sectional pilot study

Nanxi Tao[1,A,B,D–F], Renata Samulak[1,A–F], Łukasz Wilczyński[1,B–D], Maciej Mularczyk[2,C,D], Mariusz Suwała[1,B,D], Joanna Hetmańska-Kołacz[1,B,D], Monika Machoy-Rakoczy[1,A–F]

[1] Department of Periodontology, Pomeranian Medical University, Szczecin, Poland
[2] Department of Gross Anatomy, Pomeranian Medical University, Szczecin, Poland

A – research concept and design; B – collection and/or assembly of data; C – data analysis and interpretation; D – writing the article; E – critical revision of the article; F – final approval of the article

Advances in Clinical and Experimental Medicine, ISSN 1899–5276 (print), ISSN 2451–2680 (online) *Adv Clin Exp Med*. 2026;35(7):1269–1279

Address for correspondence
Monika Machoy-Rakoczy
E-mail: monika.machoy@pum.edu.pl

Funding sources
None declared

Conflict of interest
None declared

Received on January 29, 2025
Reviewed on April 18, 2025
Accepted on September 11, 2025

Published online on July 30, 2026

Abstract

Background. Digital medical imaging is the basis for effective medical diagnostics and is currently part of a dynamically developing field of science. Optical coherence tomography (OCT) allows for in situ imaging of tissues in real time, without the need to perform biopsies, histological procedures, or X-rays. Pirop® Echo-son device measures the tissue ultrasonographically.

Objectives. The aim of this cross-sectional pilot study was to propose a new method of gingival tissue analysis by evaluating the possibility of using OCT and echo-son jointly in periodontal diagnostics and clinical practice for assessing the horizontal mucosal thickness of healthy gingiva in adult patients.

Materials and methods. Thirteen patients were examined using a biometric ultrasound scanner and 3D–OCT camera. The obtained results were compared and analyzed. Comparisons between age groups or sex were made with Kruskal–Wallis analysis of variance (ANOVA) and Mann–Whitney U tests, respectively. A correlation analysis was performed between Pirop® and OCT parameters, also divided into age groups and sex.

Results. The mean gingival thickness (GT) was 1.31 mm and the mean epithelial thickness was 0.33 mm. There was no statistically significant correlation between epithelial thickness and total GT. The thickness of the gingiva and epithelium did not depend on age or sex. Due to the limited sample size, this pilot study provides exploratory, descriptive findings that warrant confirmation in a larger, adequately powered study. No comparison reached statistical significance (all $p > 0.05$); effect sizes varied in magnitude and were imprecise.

Conclusions. Optical coherence tomography imaging may complement ultrasonographic measurement of total GT by providing information on epithelial thickness. The combined approach warrants validation as a potential aid for donor-site assessment and periodontal surgery planning.

Key words: gingiva, ultrasonography, optical coherence tomography, periodontics, gingival phenotype

Cite as
Tao N, Samulak R, Wilczyński Ł, et al. Optical coherence tomography and biometric ultrasound for gingival phenotype and epithelial thickness assessment: A cross-sectional pilot study. *Adv Clin Exp Med*. 2026;35(7):1269–1279. doi:10.17219/acem/210586

DOI
10.17219/acem/210586

Copyright
Copyright by Author(s)
This is an article distributed under the terms of the Creative Commons Attribution 3.0 Unported (CC BY 3.0) (https://creativecommons.org/licenses/by/3.0/)

Highlights

- Optical coherence tomography (OCT) and ultrasound (Pirop® Echo-son) jointly enable noninvasive measurement of gingival and epithelial thickness in periodontal diagnostics.
- This pilot study showed a mean gingival thickness of 1.31 mm and a mean epithelial thickness of 0.33 mm, with no significant differences according to age or sex.
- OCT provides detailed epithelial imaging, complementing ultrasound, which measures total gingival thickness without histological differentiation.
- Combining OCT with ultrasound warrants further validation as a potential aid for donor-site assessment and periodontal surgery planning.

Background

Periodontal phenotype comprises 2 terms: bone morphotype – buccal bone plate thickness, and the overlying gingival phenotype – keratinized tissue width (KTW) and gingival thickness (GT).[1,2] The gingiva extends from the gingival margin to the mucogingival border. It consists of connective tissue and a covering epithelium, which is a keratinized stratified squamous epithelium on the oral cavity side.[3] Gingival thickness ranges from 0.7 mm to 1.5 mm,[4] whereas its width is more variable, ranging from 1 mm to as much as 9 mm.[5] The position of the tooth in the alveolar bone affects GT; therefore, thinner gingiva is often associated with a buccal tooth position, and vice versa.[6] The 2017 World Workshop on the Classification of Periodontal and Peri-Implant Diseases and Conditions classified periodontal biotype into 3 categories: thin scalloped, thick flat, and thick scalloped.[2,6,7] Patients with a thick gingival phenotype are less likely to experience gingival recession. Gingival thickness at a given tooth surface may influence the recession process. Thin gingiva may be more prone to recession caused by trauma or inflammation.[8] In clinical practice, proper assessment of the periodontal biotype, particularly GT, is important when planning treatment in the esthetic zone. The presence of keratinized tissue facilitates implantological, prosthetic, and orthodontic treatment. It also helps patients perform oral hygiene procedures at home.

Gingival thickness can be assessed using many methods, both invasive and noninvasive. Visual assessment is the simplest method and relies on knowledge of features typical of various periodontal biotypes. A periodontal probe inserted into the gingival sulcus centrally on the labial surface of the tooth may also be used. However, relying solely on visual or probe-based assessment may lead to underestimation or overestimation of GT, as these methods do not consistently account for subtle variations in soft-tissue density and underlying bone morphology. According to current recommendations of the American Academy of Periodontology and the European Federation of Periodontology, periodontal phenotypes are divided into thin ≤1 mm (visible probe) and thick >1 mm.[7,9] These methods, although simple and minimally invasive, do not allow for actual assessment of GT.[10,11] Measurements of gingival and oral mucosal thickness are most often performed under local anesthesia, which may cause local volume increase.[6] This technique uses a periodontal probe or a more precise puncture method using an endodontic instrument or an injection needle with a silicone stop (transgingival probing (TGP) and bone sounding (BS)).[12] Cone beam computed tomography (CBCT) can also be used to measure both gingival and labial bone plate thickness.[11,13] Ultrasonic GT measurement (UGTM) is a safe and painless method, but it requires the use of an appropriate device. A device useful in clinical practice for measuring GT is the Pirop® ultrasonic biometer (Echo-son, Puławy, Poland).[14] It has been suggested in the literature that combining ultrasonic measurements with advanced imaging (e.g., CBCT or optical coherence tomography (OCT)) improves the accuracy and reliability of soft-tissue assessment, especially in regions adjacent to thin buccal bone plates. A similar diagnostic benefit from multimodal imaging has recently been demonstrated in ophthalmology, where OCT, optical coherence tomography angiography (OCT-A), and fundus autofluorescence were correlated for optic disc drusen assessment.[15] None of the above-mentioned methods for measuring GT allow selective assessment of epithelial thickness in relation to other gingival layers. A promising device in this context may be OCT.

Objectives

The aim of this pilot study was to evaluate a novel and clinically applicable method for measuring gingival tissue. The primary objective was to assess the correlation between epithelial thickness and total GT using 2 noninvasive methods: OCT and ultrasonographic assessment. The hypothesis regarding the correlation between epithelial thickness and gingival phenotype was reframed as exploratory because of the limited sample size. The goal was to generate preliminary data and provide methodological insights for future investigations. An important

assumption of the study was that the research and analysis of the obtained images would be performed exclusively by clinicians, without the involvement of an IT specialist, in order to develop a method that could be practically applied by dentists rather than merely present a theoretical technique. Additionally, measurements were independently performed by multiple clinicians to reduce single-operator dependence.

Materials and methods

Thirteen patients were invited to participate in the study – 7 women and 6 men, aged 30–65 years, with no systemic diseases or medications that could affect periodontal health. The patients provided informed consent for the diagnostics performed at the dental chair during a routine dental check-up, and they voluntarily attended a private ophthalmology clinic to undergo OCT. The study was conducted in accordance with the Declaration of Helsinki and approved by the Ethics Committee of the Pomeranian Medical University in Szczecin (approval No. KB-006/61/2024). All participants were periodontally healthy, with no signs of inflammation, no implants, and no history of periodontal surgery in the examined region. These parameters were verified clinically to ensure homogeneity of tissue conditions and eliminate confounding variables. The sample was selected using purposive sampling, focusing on accessibility and compliance with the inclusion criteria. Given the pilot nature of the study, no formal a priori sample size calculation was performed. This phase aimed to evaluate feasibility and inform the design of a future adequately powered study. Patients were examined using the Pirop® Echo-son device and the Topcon 3D OCT-2000® system (Topcon Corporation, Tokyo, Japan).

The examined area was the gingival region on the vestibular surface of the maxilla above the right central incisor (tooth 11). To verify calibration of the Pirop® device and measurement accuracy, one researcher assessed the gingival phenotype of another researcher, who also served as the first participant, by measuring tissue thickness using the depth of insertion of an endodontic instrument with a silicone stop (TGP). Penetration depth was read on an endodontic ruler in millimeters (Fig. 1). This single-participant comparison served as an initial descriptive agreement check and was not a formal calibration or accuracy validation. The initial comparison using the TGP method in the first participant served as a confirmatory calibration step aimed at verifying the basic accuracy of the Pirop® device. The measurement using the endodontic instrument is shown in Fig. 2. The area selected for examination included the attached gingiva centrally above the right central incisor and was defined by a 6 × 6 mm frame (Fig. 3). The shape and size of the frame are visible in Fig. 4. The tissue thickness obtained from the TGP measurement was compared with Pirop® measurements performed by another physician. Based on this comparison, agreement between the TGP and Pirop® measurements was assessed descriptively in this participant. The Pirop® device and the measurement method are presented in Fig. 5 and Fig. 6. Pirop® measurements were conducted by 2 operators, whereas OCT imaging and analysis were independently performed by 3 blinded evaluators. To ensure consistency, measurement sets with an standard deviation

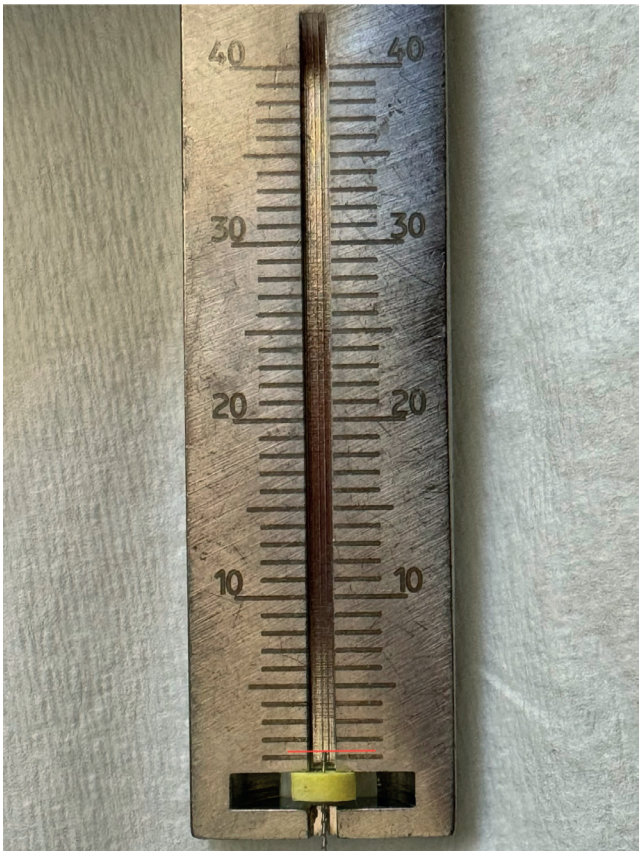

Fig. 1. Measurement of penetration depth of the endodontic spreader using an endodontic ruler (in millimeters)

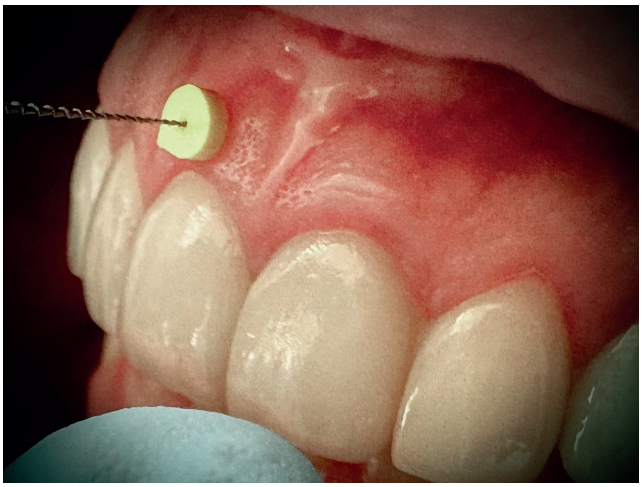

Fig. 2. Measurement of gingival thickness using a No. 15 endodontic spreader

Fig. 3. Acquisition of a horizontal section of the gingiva of the maxillary incisor

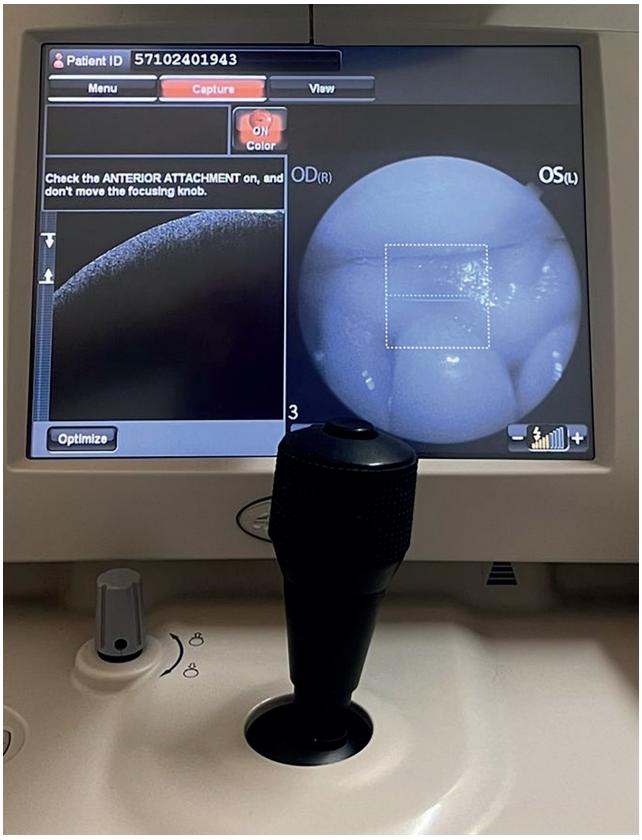

Fig. 4. View of the optical coherence tomography (OCT) image displayed on the screen

Fig. 5. Pirop® Echo-son device. Ten repeated A-scan readings obtained at 1 measurement point

Fig. 6. Measurement of gingival thickness using the echo-son device

(SD) > 0.05 mm were repeated. Final values were averaged to improve reliability and minimize operator bias.

The Pirop® device operates at a frequency of 20 MHz, sending a wave at a speed of 1,540 m/s. The wave reflected from the bone or tooth surface returns, and the return path length makes it possible to determine the metric value of GT. The device sends 10 pulses to measure 1 point and calculates the mean value. The device can operate in A-scan mode, which allows measurement of GT

at a given point, and in TM mode, which allows recording of GT while moving the probe head. The round probe head, with a diameter of 1.7 mm, enables measurement of GT at several points. The measurement range is from 0.25 to 6.0 mm, with an axial resolution of 0.01 mm (Fig. 6).

In the present study, the Pirop® device was used in A-scan mode. The probe head, covered with chlorhexidine gel, was placed on the gingival surface without pressure in a plane perpendicular to the tooth or bone surface. Measurements were performed 3 times above the bone level (subcrestal gingival thickness (SGT)) and on the surface of the bone covering the tooth (crestal gingival thickness (CGT)). At each of these points, the device performed 10 measurements and calculated the mean value. If the SD exceeded 0.05 mm, the measurement was repeated once. The data obtained using the Echo-son device were compared with those obtained using TGP measurements. If the values were similar to the 2nd decimal place, they were considered identical.

Another clinician used an OCT device to image a specific gingival area. The OCT device operated at a wavelength of 840 nm. The acquired OCT images (B-scans) had a resolution of M × N = 884 × 512 pixels (where M denotes the number of rows and N denotes the number of columns), with each pixel covering an area of 5 × 11.7 µm at a color resolution of 8 bits/pixel. For each patient, 128 B-scans (every 47 µm) were obtained, allowing full 3D reconstruction of the gingival image. All data were acquired using the Topcon 3D OCT-2000® system and analyzed in the source formats *.fda and *.fds. Due to technical limitations, raw data could only be accessed and visualized using the proprietary Topcon IMAGEnet software. Therefore, data export in the form of screen-captured images was used to document the results, which accurately represented the acquired scans. The data were anonymized, and the analysis was performed in accordance with the Declaration of Helsinki.

Measurement of epithelial thickness was performed within the measurement area (frame) described above. Within the frame, 2 lines were marked on each scan – upper and lower – along which a minimum of 10 points were selected for epithelial measurements using the Caliper function of the tomography software. The inner surface of the epithelium was considered the boundary between the tissue image and noise, where light did not penetrate deeper and therefore did not produce an image. Examples of the performed measurements are shown in Fig. 7. All measurements were averaged, and on this basis the thickness of the gingival epithelium was determined for each patient. Three clinicians independently performed OCT scan measurements to reduce single-examiner dependence. The method of obtaining images with the OCT camera is shown in Fig. 4. Three independent examiners, each blinded to the others' measurements, used the Caliper function of the tomography software to determine epithelial thickness. This approach was implemented to reduce potential inter-operator bias.

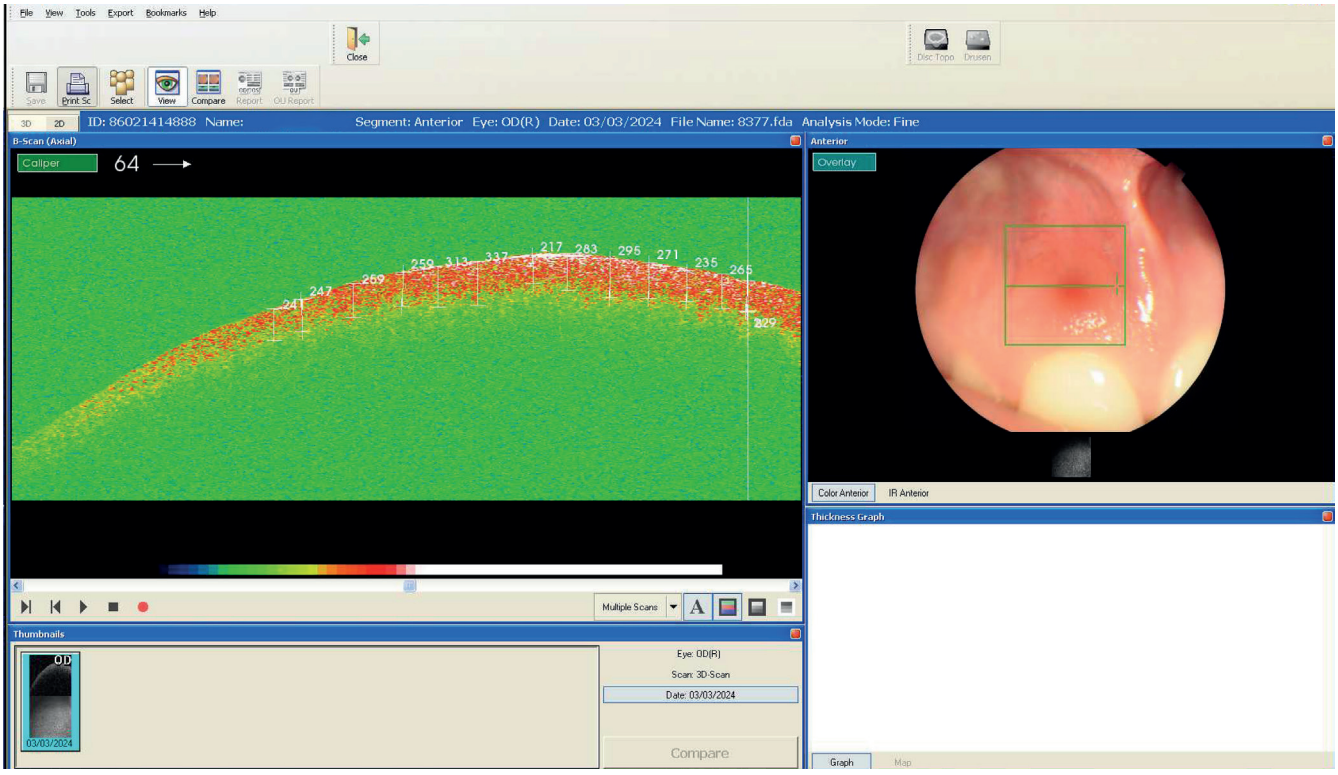

Fig. 7. Epithelial thickness measurements (in micrometers) performed directly on a computer using the Caliper function

Statistical analyses

All analyses were performed using R v. 4.4.0 (R Foundation for Statistical Computing, Vienna, Austria). The statistical strategy followed the Strengthening the Reporting of Observational Studies in Epidemiology (STROBE) recommendations for cross-sectional studies.

Results

Exploratory data screening

Normality of continuous variables (Pirop® thickness and OCT epithelial thickness) was assessed using the Shapiro–Wilk test and confirmed through visual inspection of kernel-density and Q–Q plots. As both variables deviated from normality ($p < 0.05$) and the sample size was small ($n = 13$), nonparametric statistical methods were applied throughout.

Descriptive statistics

Continuous outcomes are summarized as medians and interquartile ranges (IQRs) and, where helpful for clinical interpretation, also as means ±SD. Categorical variables are reported as absolute counts and percentages.

Group comparisons

Kruskal–Wallis one-way analysis of variance (ANOVA) by ranks was used to compare Pirop® and OCT thickness across 3 age strata (30–40, 41–50, and 61–70 years). Mann–Whitney U tests were used to assess differences between male and female patients. Effect sizes were reported as η^2KW (Kruskal–Wallis) and rank-biserial correlation (rrb; Mann–Whitney), with 95% confidence intervals (95% CIs) estimated through bootstrapping (10,000 resamples).

Correlation analysis

Spearman's rank correlation coefficient (ρ) was used to examine associations between Pirop® and OCT measures (Fig. 8) and their relationship with age (ordinal) and sex (binary coded: M = 0, F = 1). The assumption of monotonicity was verified using locally estimated scatterplot smoothing (LOESS)-fitted scatter plots and inspection of partial residuals. In cases where visual assessment suggested deviation from monotonicity, the correlation results were interpreted cautiously and flagged in the Discussion section. Confidence intervals for ρ were derived using Fisher's z-transformation.

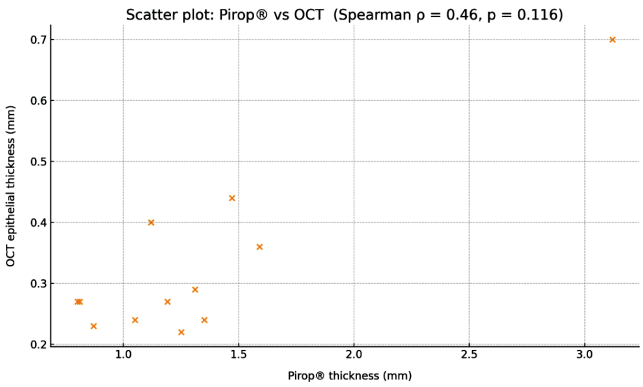

Fig. 8. Scatter plot showing the relationship between total gingival thickness (Pirop®) and epithelial thickness measured using optical coherence tomography (OCT). A locally estimated scatterplot smoothing (LOESS) line is shown. Spearman's ρ = 0.458; p = 0.116. The association was not statistically significant

Statistical significance

Two-sided p-values below 0.05 were considered statistically significant. Given the pilot and exploratory nature of this study, p-values were interpreted in conjunction with effect sizes and CIs.

Sample-size and power considerations

No formal a priori sample-size calculation was conducted because this was a pilot feasibility study. Estimates and CIs should therefore be interpreted as exploratory and imprecise. The thickness of the gingiva and epithelium did not differ significantly by age group or sex (Tables 2–5). Fig. 9 shows the overall distribution, whereas Tables 2–5 show age- and sex-based comparisons. Detailed statistical analysis results, including test statistics, p-values, effect sizes, and CIs, are presented in Tables 1–8.

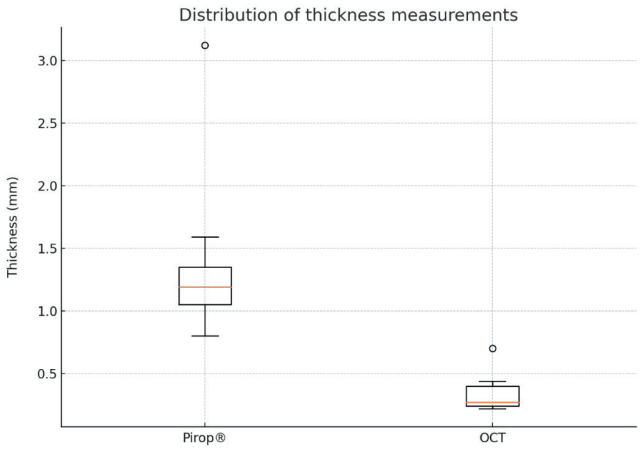

Fig. 9. Box-and-whisker plots showing the distribution of Pirop® and optical coherence tomography (OCT) measurements across all participants. Median, interquartile range (IQR), and outliers are indicated. This visualization serves as a general descriptive summary

Table 1. Descriptive statistics of Pirop® and OCT parameters: mean ±SD, median, IQR, minimum, and maximum values for all patients (n = 13). No statistical tests were applied

Parameter	n	Mean	SD	Min	Max	Median	Q1	Q3
Pirop®	13	1.31	0.59	0.80	3.12	1.19	1.05	1.35
OCT	13	0.33	0.13	0.22	0.70	0.27	0.24	0.40

OCT – optical coherence tomography; IQR – interquartile range; SD – standard deviation.

Table 2. Descriptive statistics of Pirop® thickness by age group (30–40, 41–50, and 61–70 years). Kruskal–Wallis test: H(2) = 5.2, p = 0.074; η^2KW = 0.46 (95% CI: 0.00–0.77)

Age [years]	n	Mean	SD	Min	Max	Median	Q1	Q3	p-value
30–40	6	1.01	0.20	0.80	1.25	1.00	0.81	1.19	0.074
41–50	4	1.77	0.91	1.12	3.12	1.41	1.24	2.30	
61–70	3	1.32	0.27	1.05	1.59	1.31	1.05	1.59	

SD – standard deviation; 95% CI – 95% confidence interval.

Table 3. Descriptive statistics of Pirop® thickness by sex. Mann–Whitney U test: U = 22.0, p = 0.999; rank-biserial correlation (rrb) = 0.01 (95% CI: −0.71 to 0.72)

Sex	n	Mean	SD	Min	Max	Median	Q1	Q3	p-value
Female	7	1.41	0.82	0.80	3.12	1.19	0.81	1.59	0.999
Male	6	1.20	0.12	1.05	1.35	1.19	1.12	1.31	

SD – standard deviation; 95% CI – 95% confidence interval.

Table 4. Descriptive statistics of OCT epithelial thickness by age group. Kruskal–Wallis test: H(2) = 3.3, p = 0.195; η^2KW = 0.29 (95% CI: 0.00–0.66)

Age [years]	n	Mean	SD	Min	Max	Median	Q1	Q3	p-value
30–40	6	0.28	0.06	0.22	0.40	0.27	0.23	0.27	0.195
41–50	4	0.45	0.19	0.24	0.70	0.42	0.32	0.57	
61–70	3	0.30	0.06	0.24	0.36	0.29	0.24	0.36	

SD – standard deviation; 95% CI – 95% confidence interval; OCT – optical coherence tomography.

Table 5. Descriptive statistics of OCT epithelial thickness by sex. Mann–Whitney U test: U = 15.0, p = 0.521; rank-biserial correlation (rrb) = 0.28 (95% CI: −0.46 to 0.79)

Sex	n	Mean	SD	Min	Max	Median	Q1	Q3	p-value
Female	7	0.36	0.16	0.23	0.70	0.27	0.27	0.44	0.521
Male	6	0.30	0.08	0.22	0.40	0.27	0.24	0.40	

SD – standard deviation; 95% CI – 95% confidence interval; OCT – optical coherence tomography.

Table 6. Spearman's rank correlation between Pirop® and OCT: ρ = 0.458, 95% CI: −0.125 to 0.806, p = 0.116, n = 13 (df = 11).

Variable	OCT	p-value
Pirop®	0.458	0.116

95% CI – 95% confidence interval; OCT – optical coherence tomography; df – degrees of freedom.

Discussion

Given the pilot design and small sample, the results should be interpreted as exploratory and hypothesis-generating rather than confirmatory. The morphometric parameters of the gingiva show significant individual variability. Even within the same patient, they may differ between the maxilla and mandible depending on the tooth type. Previous studies have demonstrated considerable site-related variability in GT. Müller et al. reported that the thickness of the masticatory mucosa varied according to periodontal phenotype, gender, and anatomical location.[16] Vandana and Savitha found that facial gingiva in the mandibular anterior region was thinner than that in the corresponding maxillary region.[17] Such discrepancies may stem from variations in measurement techniques, the specific sites sampled (anterior vs posterior regions), and ethnic or genetic diversity across populations. Our findings, which did not demonstrate a statistically significant association between epithelial thickness and total GT, could reflect the multifactorial nature of GT determination, encompassing not only epithelial tissue but also connective tissue composition, alveolar bone height, and overall phenotype.

Table 7. Individual Pirop® and OCT thickness values and the percentage of epithelial thickness within total gingival thickness for each patient. Descriptive comparison only; no statistical test applied

Patient No.	Average Pirop®	Average OCT	Epithelial thickness/total gingival thickness [%]
1	1.31	0.29	22.14
2	1.19	0.27	22.69
3	1.12	0.40	35.71
4	3.12	0.70	22.44
5	1.35	0.24	17.78
6	1.47	0.44	29.93
7	0.81	0.27	33.33
8	1.12	0.40	35.71
9	0.87	0.23	26.44
10	1.59	0.36	22.64
11	1.05	0.24	22.86
12	1.25	0.22	17.6
13	0.80	0.27	33.75

OCT – optical coherence tomography.

Table 8. Frequency distribution of thin and thick gingival phenotypes across age groups and sex. Categorical count data only; no statistical tests were applied

Age [years]	n	Sex	n	Gingival phenotype	n
30–40	6	female	4	thin	3
				thick	1
		male	2	thin	0
				thick	2
41–50	4	female	2	thin	0
				thick	2
		male	2	thin	0
				thick	2
61–70	3	female	1	thin	0
				thick	1
		male	2	thin	0
				thick	2

One potential limitation of this study is the small sample size, which reduces the power to detect subtle correlations. In addition, minor differences in operator technique – despite efforts to standardize measurements – could introduce measurement variability. The lack of histological confirmation of epithelial thickness is another limitation. Although OCT has high resolution, its correlation with true histological thickness can be influenced by factors such as signal penetration and scatter.

According to some authors, the thick gingival phenotype is found in approx. 85% of the population, whereas the thin phenotype occurs in 15%.[18] Others, however, have demonstrated that a thin phenotype may be present in as many as 30% of individuals.[19] Similar results (77% thick and 23% thin) were obtained in our study. It is believed that variability in this respect may be influenced by race, genetic predisposition, age (the younger the individual, the thicker the gingiva), and sex.[17] Rasool et al. demonstrated that the thin periodontal biotype is 4.2 times more common in women than in men, and thin gingiva is 5 times more common in the mandibular incisor region.[20]

In our study, we did not detect statistically significant differences in periodontal phenotype by age group or sex. To date, the correlation between gingival and epithelial thickness has not been investigated; therefore, this issue was addressed in the present study. The above tests were designed to assess the thickness of horizontal gingival tissue around the maxillary incisors and to develop a method enabling precise measurement of gingival epithelial thickness and its percentage relative to the entire tissue. The estimated association between epithelial thickness and total GT was positive but imprecise (Spearman's $\rho = 0.458$, 95% CI: −0.125 to 0.806; $p = 0.116$). Because the CI was wide and included zero, the study cannot establish either independence or a definite association. It can be concluded that within the thin and thick phenotypes, there may be subtypes with greater or smaller epithelial thickness. These preliminary findings suggest that "proportion of epithelial thickness within total GT may vary within both thin and thick phenotypes. We hypothesize that within each phenotype, there may exist subtypes with differing epithelial thickness, a concept that warrants further investigation in larger, histologically validated studies. Histological studies may enable identification of these subtypes. It is known that the thicker the epithelial layer, the greater the tissue resistance to mechanical damage or water loss. This could explain why some patients with a thin phenotype (and similar hygiene habits) experience recessions, whereas others do not. This issue is certainly worth exploring. Given the small sample size, the results should be interpreted as preliminary and descriptive rather than confirmatory. The study was not powered to detect small or moderate effects, which increases the risk of type II error. Additionally, heterogeneity in age and phenotype may further limit the generalizability of the findings to broader populations.

Importantly, OCT provides images of tissue sections in a non-contact and noninvasive manner. The device measures the time delay and intensity of light scattered or reflected from biological tissues, resulting in tomographic imaging of their internal structure. This is achieved by scanning tissues at resolutions ranging from 1 to 15 µm. Therefore, real-time in situ tissue imaging is possible without the need for biopsies, histological procedures, or X-rays, allowing OCT to be used in many fields of medicine. In dentistry, studies using OCT focus primarily on the early diagnosis of caries,[21] assessment of dental fillings,[22] analysis of enamel thickness,[23] and, increasingly, assessment of periodontal tissues.[24] The possibility of using OCT in the diagnosis of oral mucosa and

epithelium has been described in several studies.[25–29] So far, only imaging capabilities, i.e., lesion screening, have been described. However, correct assessment of the scan requires knowledge of the ultrastructural images of the tissue.[30] In normal tissue, the epithelial layer is always hyporeflective (except for the keratinized layer). The lamina propria is always hyperreflective, with various internal non-reflective areas. The difference between these 2 degrees of reflectance allows estimation of the position of the basal membrane.

The authors of the study aimed to assess the feasibility of performing measurements of the examined tissue and to analyze the reliability of the obtained measurements by comparing the results with those obtained using another device. For the authors, it was important to present an innovative approach to oral mucosa diagnostics and measurements. So far, no device has been available that can noninvasively and independently measure epithelial thickness as well as the thickness of the subepithelial connective tissue. To overcome this limitation, fusion of 2 noninvasive methods was proposed. The thickness of the subepithelial tissue is crucial when selecting a donor site during connective tissue transplantation procedures at the recipient site around the tooth, and it varies from person to person. So far, the Pirop® device has been used for noninvasive measurements, and its reliability, demonstrated in the article by Gánti et al.,[14] formed the basis of the authors' methodology. Currently, the main limitation of OCT imaging is the lack of reliable studies analyzing the capabilities of OCT devices, which have limited imaging depth.[31] Another limitation is that OCT requires considerable skill and experience from both the operator and the individual analyzing the scans and performing the measurements.

Knowledge of gingival epithelial thickness may be important in diagnostics before mucogingival surgery, particularly in assessing the quality of harvested gingival grafts. Various types of grafts have been described for the surgical treatment of gingival recession, including free gingival grafts (FGG), connective tissue grafts (CTG), and deepithelialized free gingival grafts (DFGG). In a 1-year randomized clinical trial (RCT), Ripoll et al. assessed late complications following the use of CTGs and DFGGs combined with coronally advanced flap procedures (CTG + CAF and DFGG + CAF). The authors identified re-epithelialization of the graft, epithelial bands, cul-de-sac formation, epithelial cysts, and bone exostoses as major late complications associated exclusively with the use of DFGGs. Minor late complications included gingival color changes and superficial revascularization, which were significantly more frequent with the DFGG + CAF method compared with CTG+CAF.[32] The use of DFGGs allows for greater width of keratinized gingiva because the connective tissue from the deeper palatal layers used in CTGs does not possess the full potential to induce epithelial cell keratinization.[33]

The thickness of the gingival epithelium at the recipient site may potentially influence postoperative complications following gingival recession coverage procedures. The possibility of assessing gingival epithelial thickness before surgery using DFGGs may influence appropriate graft preparation immediately after harvesting, including the depth of de-epithelialization and selection of the recipient site. Further research in this area is necessary, and the OCT method may prove helpful. Although the method shows potential, further validation in larger, standardized cohorts is required before clinical applicability can be established. Current findings are preliminary and should be confirmed in adequately powered prospective studies.

Limitations of the study

Study limitations include the small sample size, which yielded imprecise estimates and limited generalizability. However, the small sample size may limit the generalizability of our findings and reduce the power to detect moderate associations or subgroup differences. Another limitation is the use of OCT without a dental head, which would make it possible to examine other gingival areas. In addition, minor differences in operator technique – despite efforts to standardize measurements – could introduce measurement variability. The lack of histological confirmation of epithelial thickness is another limitation. Although OCT has high resolution, its correlation with true histological thickness can be influenced by factors such as signal penetration and scatter. Additionally, the lack of a formal training protocol for interpreting OCT images – despite efforts to standardize measurements – could introduce interobserver variability, which could influence the accuracy and reproducibility of the measurements. Further studies are needed to address these issues. Moreover, the presence of subclinical inflammation might have affected local tissue thickness. Even though patients did not exhibit any clinical signs of periodontal disease, subclinical edema cannot be entirely ruled out and may slightly alter thickness measurements. Future studies with a larger patient cohort, possibly including multiple tooth regions (anterior vs posterior, maxilla vs mandible), and employing histological validation in cases where tissue samples are available, would help clarify the interplay between epithelial thickness and overall GT.

Although visual inspection using LOESS curves was performed, the possibility of non-monotonic relationships cannot be ruled out because of the small sample size. This may affect the reliability of correlation results and warrants cautious interpretation.

Conclusions

Our pilot study demonstrated the feasibility of obtaining total gingival and epithelial thickness measurements using ultrasound and OCT, respectively. The association

estimate was imprecise and does not establish the absence of a relationship between epithelial thickness and total GT. The concept of multimodal imaging has already been clinically validated in other specialties,[15] and the combined use of noninvasive ultrasound and OCT in periodontology could be refined and applied on a larger scale to enhance diagnostic accuracy and clinical treatment planning for various periodontal and implantology procedures. Although the combined use of OCT and ultrasound may improve diagnostic insight, its clinical value remains theoretical at this stage. Larger studies are needed before the method can be reliably incorporated into clinical decision-making. The present results serve as a foundation for further investigation.

There was no statistically significant correlation between total GT and epithelial thickness. These findings suggest that future classifications of gingival phenotypes might benefit from considering epithelial and connective tissue components separately, rather than relying solely on overall thickness measurements. Optical coherence tomography imaging of the epithelium may serve as a diagnostic tool complementing the data obtained from the Echo-son device, which measures horizontal tissue thickness over the bone without differentiation into histological structures.

By correlating the results obtained using OCT with those obtained using the Echo-son device, it may be possible to estimate epithelial thickness as a proportion of total GT (ET/GT) and estimate subepithelial thickness as GT–ET, subject to spatial co-registration and validation. This approach may enhance pre-surgical planning by providing a more nuanced understanding of tissue composition, especially when selecting graft donors or evaluating the likelihood of recession relapse.

Combining both imaging methods and using an OCT dental head would make it possible to assess connective tissue on the palate, perform its overall measurement, and, after subtracting the measured epithelial thickness, determine the thickness of the graft that can be harvested from a given donor site. Application of this method, or rather the combination of these 2 diagnostic methods, may improve the predictability of periodontal surgery and assessment of the donor site, which is often a weak point during the procedure.

Further research is important in the context of the development and availability of dental OCT devices that could be implemented in clinical practice. In periodontal surgery, precise data on epithelial thickness would enable the selection or development of new surgical tools appropriately adjusted in terms of blade thickness to epithelial thickness.

Data Availability Statement

We would like to clarify that the OCT data were recorded and processed using the manufacturer's dedicated software (Topcon IMAGEnet), which generates and stores images in device-specific formats. Unfortunately, export of raw data in this format prevents reading or analysis outside this software and is limited by the technical specifications of the system. During our study, OCT image analysis was performed directly in Topcon's dedicated software. Screenshots were used as a form of data export to document the results. The images faithfully represent the obtained results and were not edited other than removal of patient-identifying information (first and last names) for anonymization in accordance with the Declaration of Helsinki. The Pirop® device is a manual diagnostic tool designed to measure soft-tissue thickness in dental procedures. Its design does not allow data recording, storage, or digital transmission. Due to the lack of an electronic data-storage function, all measurements must be manually recorded by the operator. As a result, it is not possible to generate or provide measurement records directly from the device. We have included all of this information in the manuscript to improve clarity and provide transparency regarding the limitations of the devices.

Consent for publication of personal information

Not applicable.

Use of AI and AI-assisted technologies

Not applicable.

ORCID iDs

Nanxi Tao https://orcid.org/0009-0003-7270-1084
Renata Samulak https://orcid.org/0000-0003-0145-9131
Łukasz Wilczyński https://orcid.org/0000-0003-0131-379X
Maciej Mularczyk https://orcid.org/0000-0001-9885-6939
Mariusz Suwała https://orcid.org/0000-0002-5192-3353
Joanna Hetmańska-Kołacz https://orcid.org/0009-0008-7922-5144
Monika Machoy-Rakoczy https://orcid.org/0000-0001-5787-222X

References

1. Barootchi S, Tavelli L, Zucchelli G, Giannobile WV, Wang H. Gingival phenotype modification therapies on natural teeth: A network meta-analysis. *J Periodontol*. 2020;91(11):1386–1399. doi:10.1002/JPER.19-0715
2. Malpartida-Carrillo V, Tinedo-Lopez PL, Guerrero ME, Amaya-Pajares SP, Özcan M, Rösing CK. Periodontal phenotype: A review of historical and current classifications evaluating different methods and characteristics. *J Esthet Restor Dent*. 2021;33(3):432–445. doi:10.1111/jerd.12661
3. Groeger S, Meyle J. Oral mucosal epithelial cells. *Front Immunol*. 2019;10:208. doi:10.3389/fimmu.2019.00208
4. Albughaylil AS, Sayed AJ, Alsoli MA, et al. Gingival biotypes and its relation to biologic width, alveolar bone thickness, dehiscence and fenestration in mandibular anterior region: A CBCT analysis study. *J Pharm Bioallied Sci*. 2023;15(Suppl 1):S367–S371. doi:10.4103/jpbs.jpbs_598_22
5. Bowers GM. A study of the width of attached gingiva. *J Periodontol*. 1963;34(3):201–209. doi:10.1902/jop.1963.34.3.201
6. Cortellini P, Bissada NF. Mucogingival conditions in the natural dentition: Narrative review, case definitions, and diagnostic considerations. *J Periodontol*. 2018;89(Suppl 1):S204–S213. doi:10.1002/JPER.16-0671

7. Jepsen S, Caton JG, Albandar JM, et al. Periodontal manifestations of systemic diseases and developmental and acquired conditions: Consensus report of workgroup 3 of the 2017 World Workshop on the Classification of Periodontal and Peri-Implant Diseases and Conditions. *J Periodontol*. 2018;89(Suppl 1):S237–S248. doi:10.1002/JPER.17-0733
8. Bhattacharya HS, Gummaluri SS, Rani A, Verma S, Bhattacharya P, Rayashettypura Gurushanth SM. Additional benefits of titanium platelet-rich fibrin (T-PRF) with a coronally advanced flap (CAF) for recession coverage: A case series. *Dent Med Probl*. 2023;60(2):279–285. doi:10.17219/dmp/141919
9. Zhao H, Zhang L, Li H, Hieawy A, Shen Y, Liu H. Gingival phenotype determination: Cutoff values, relationship between gingival and alveolar crest bone thickness at different landmarks. *J Dent Sci*. 2023;18(4):1544–1552. doi:10.1016/j.jds.2023.03.003
10. Zhong C, Yingzi X, Zhiqiang L, et al. Analysis of crown morphology and gingival shape in the maxillary anterior dentition. *Int J Periodontics Restorative Dent*. 2020;40(6):925–931. doi:10.11607/prd.4696
11. Amid R, Mirakhori M, Safi Y, Kadkhodazadeh M, Namdari M. Assessment of gingival biotype and facial hard/soft tissue dimensions in the maxillary anterior teeth region using cone beam computed tomography. *Arch Oral Biol*. 2017;79:1–6. doi:10.1016/j.archoralbio.2017.02.021
12. Schwarz L, Andrukhov O, Rausch MA, Rausch-Fan X, Jonke E. Difference in buccal gingival thickness between the mandible and maxilla in the aesthetic zone: A systematic review and meta-analysis. *J Clin Med*. 2024;13(6):1789. doi:10.3390/jcm13061789
13. El Khalifa M, Abu El Sadat S, Gaweesh Y, Gaweesh Y. Assessment of gingival thickness using CBCT compared to transgingival probing and its correlation with labial bone defects: A cross-sectional study. *Int J Oral Maxillofac Implants*. 2022;37(3):464–472. doi:10.11607/jomi.9234
14. Gánti B, Bednarz W, Kőműves K, Vág J. Reproducibility of the PIROP ultrasonic biometer for gingival thickness measurements. *J Esthet Restor Dent*. 2019;31(3):263–267. doi:10.1111/jerd.12446
15. Szabelska P, Brydak-Godowska J, Krajewski P, Różycki R, Gołębiewska J. Correlations between OCT, OCT angiography and fundus autofluorescence in adults with superficial optic disc drusen: The importance of multimodal imaging. *Adv Clin Exp Med*. 2025;34(11):1959–1968. doi:10.17219/acem/202319
16. Müller HP, Heinecke A, Schaller N, Eger T. Masticatory mucosa in subjects with different periodontal phenotypes. *J Clin Periodontol*. 2000;27(9):621–626. doi:10.1034/j.1600-051x.2000.027009621.x
17. Vandana KL, Savitha B. Thickness of gingiva in association with age, gender and dental arch location. *J Clin Periodontol*. 2005;32(7):828–830. doi:10.1111/j.1600-051X.2005.00757.x
18. Olsson M, Lindhe J. Periodontal characteristics in individuals with varying form of the upper central incisors. *J Clin Periodontol*. 1991;18(1):78–82. doi:10.1111/j.1600-051X.1991.tb01124.x
19. Müller HP, Könönen E. Variance components of gingival thickness. *J Periodontal Res*. 2005;40(3):239–244. doi:10.1111/j.1600-0765.2005.00798.x
20. Rasool G, Iqbal N, Tasneem A, Hussain U. Influence of incisor inclination and position on the gingival biotype of orthodontic patients. *Pak Orthod J*. 2014;6(2):60–64. https://mail.poj.org.pk/index.php/poj/article/view/100.
21. Wang TA, Trung NH, Lee HC, Lee CK, Tsai MT, Wang YL. Quantitative evaluation of caries and calculus with ultrahigh-resolution optical coherence tomography. *Bioengineering*. 2023;10(11):1317. doi:10.3390/bioengineering10111317
22. Naguib GH, Bakhsh T, Mazhar J, et al. Noninvasive assessment of novel nanohybrid resin cement adaptation using cross-polarization optical coherence tomography. *Dent Mater*. 2024;40(4):643–652. doi:10.1016/j.dental.2024.02.004
23. Machoy ME, Koprowski R, Szyszka-Sommerfeld L, Safranow K, Gedrange T, Woźniak K. Optical coherence tomography as a noninvasive method of enamel thickness diagnosis after orthodontic treatment by 3 different types of brackets. *Adv Clin Exp Med*. 2019;28(2):211–218. doi:10.17219/acem/79974
24. Wang G, Le NM, Hu X, et al. Semi-automated registration and segmentation for gingival tissue volume measurement on 3D OCT images. *Biomed Opt Express*. 2020;11(8):4536–4547. doi:10.1364/BOE.396599
25. Gambino A, Martina E, Panzarella V, et al. Potential use of optical coherence tomography in oral potentially malignant disorders: In vivo case series study. *BMC Oral Health*. 2023;23(1):540. doi:10.1186/s12903-023-03263-w
26. Albrecht M, Schnabel C, Mueller J, Golde J, Koch E, Walther J. In vivo endoscopic optical coherence tomography of the healthy human oral mucosa: Qualitative and quantitative image analysis. *Diagnostics (Basel)*. 2020;10(10):827. doi:10.3390/diagnostics10100827
27. Chen X, Zhou G, Zhang J. Optical coherence tomography: Promising imaging technique for the diagnosis of oral mucosal diseases. *Oral Dis*. 2024;30(6):3638–3651. doi:10.1111/odi.14851
28. Prestin S, Rothschild SI, Betz CS, Kraft M. Measurement of epithelial thickness within the oral cavity using optical coherence tomography. *Head Neck*. 2012;34(12):1777–1781. doi:10.1002/hed.22007
29. Di Stasio D, Lauritano D, Iquebal H, Romano A, Gentile E, Lucchese A. Measurement of oral epithelial thickness by optical coherence tomography. *Diagnostics (Basel)*. 2019;9(3):90. doi:10.3390/diagnostics9030090
30. Yang L, Chen Y, Ling S, et al. Research progress on the application of optical coherence tomography in the field of oncology. *Front Oncol*. 2022;12:953934. doi:10.3389/fonc.2022.953934
31. Monroy GL, Won J, Spillman DR, Dsouza R, Boppart SA. Clinical translation of handheld optical coherence tomography: Practical considerations and recent advancements. *J Biomed Opt*. 2017;22(12):121715. doi:10.1117/1.JBO.22.12.121715
32. Ripoll S, Fernández De Velasco-Tarilonte Á, Bullón B, Ríos-Carrasco B, Fernández-Palacín A. Complications in the use of deepithelialized free gingival graft vs. connective tissue graft: A one-year randomized clinical trial. *Int J Environ Res Public Health*. 2021;18(9):4504. doi:10.3390/ijerph18094504
33. Naziker Y, Ertugrul AS. Aesthetic evaluation of free gingival graft applied by partial de-epithelialization and free gingival graft applied by conventional method: A randomized controlled clinical study. *Clin Oral Investig*. 2023;27(7):4029–4038. doi:10.1007/s00784-023-05029-8

Oxaliplatin-induced peripheral neuropathy in cancer treatment: Mechanisms, risk factors, and management strategies

Justyna A. Pigońska[1,A–F], Marta Banach[2,A–F], Paweł S. Walkowiak[3,B,D,F], Aneta Zygulska[4,A–F]

[1] Department of Clinical Physiology, Medical University of Lodz, Poland
[2] Department of Neurology, Jagiellonian University Medical College, Cracow, Poland
[3] Department of Neurology with Stroke Subdivision, John Paul II Regional Hospital, Bełchatów, Poland
[4] Department of Oncology, Jagiellonian University Medical College, Cracow, Poland

A – research concept and design; B – collection and/or assembly of data; C – data analysis and interpretation;
D – writing the article; E – critical revision of the article; F – final approval of the article

Advances in Clinical and Experimental Medicine, ISSN 1899–5276 (print), ISSN 2451–2680 (online) *Adv Clin Exp Med*. 2026;35(7):1281–1295

Address for correspondence
Justyna A. Pigońska
E-mail: justyna.pigonska@umed.lodz.pl

Funding sources
None declared

Conflict of interest
None declared

Received on May 15, 2025
Reviewed on October 10, 2025
Accepted on October 16, 2025

Published online on April 2, 2026

Abstract

Oxaliplatin (OXI) is a platinum-based chemotherapeutic agent commonly used in the systemic treatment of colorectal, gastric, pancreatic, and esophageal cancers. Like other cytotoxic agents, OXI is associated with various adverse effects; however, OXI-induced peripheral neuropathy (OIPN) represents a particularly challenging clinical problem for both oncologic patients and their clinicians. The severity of neuropathic symptoms may necessitate dose reduction or premature discontinuation of therapy, which can ultimately shorten recurrence-free survival. This paper discusses the symptoms, mechanisms of onset, risk factors, preventive strategies, treatment options, and grading scales associated with OIPN. Both the prevention and treatment of OIPN require further innovative and effective research. It is hoped that the outcomes of ongoing trials will address both chronic and acute OIPN in the near future, as this condition remains a persistent clinical concern for patients with gastrointestinal cancers.

Key words: oxaliplatin, peripheral nervous system diseases, neurophysiology, oxaliplatin-induced peripheral neuropathy, high-resolution ultrasonography

Cite as
Pigońska JA, Banach M, Walkowiak PS, Zygulska A. Oxaliplatin-induced peripheral neuropathy in cancer treatment: Mechanisms, risk factors, and management strategies. *Adv Clin Exp Med*. 2026;35(7):1281–1295. doi:10.17219/acem/213218

DOI
10.17219/acem/213218

Copyright
Copyright by Author(s)
This is an article distributed under the terms of the Creative Commons Attribution 3.0 Unported (CC BY 3.0) (https://creativecommons.org/licenses/by/3.0/)

Highlights

- Oxaliplatin-induced peripheral neuropathy is a major dose-limiting toxicity in gastrointestinal cancer treatment.
- Clinical features, pathophysiological mechanisms, and risk factors underlying oxaliplatin-related neurotoxicity are comprehensively reviewed in this paper.
- Current prevention and management strategies, including grading scales, remain limited and inconsistently effective.
- Novel therapeutic approaches and ongoing clinical trials are essential to reduce neurotoxicity and improve recurrence-free survival.

Introduction

Oxaliplatin (OXI)-induced neuropathy is a common and challenging adverse effect of this platinum-based anticancer agent. This neuropathy can be classified into acute neuropathy (affecting 85–96% of treated patients) and chronic peripheral neuropathy (affecting 40–93% of treated patients), with sensory symptoms such as tingling and numbness of the limbs being more prevalent than motor symptoms.[1] Cold-induced peripheral paresthesia, cold-induced pharyngolaryngeal dysesthesia, muscle cramps, dysphagia, jaw stiffness, laryngospasm, and voice and ocular changes (such as blurred vision, visual loss, color perception abnormalities, eye pain, ptosis, and excessive lacrimation) are typical features of acute OXI-induced neuropathy. According to Grothey, 15% of patients receiving a cumulative OXI dose of 780–850 mg/m^2 develop sensory ataxia as a chronic manifestation of neuropathy.[2] Nine of the 14 analyzed studies reported acute neuropathic symptoms in 4–98% of patients during the 1st treatment cycle (within 14 days of initiating OXI therapy). Symmetrical paresthesia of the limbs, mouth, pharynx, and larynx occurs or worsens in response to low-temperature exposure in acute neuropathy and typically resolves within a few days.[3,4] Acute OXI-induced neuropathy leads to dose reduction in 15–43% of patients, prolongation of infusion times in 12–22%, and premature treatment discontinuation in 6–21% of cases. These adjustments may, to some extent, mitigate the negative effects of neuropathy.[5–10]

Persistent numbness, paresthesia, allodynia, and burning pain in the hands and feet are reported in approx. 40% of patients with chronic peripheral neuropathy.[11] Chronic symptoms, particularly pain, lead to difficulties with tasks such as writing, buttoning, and walking. These impairments significantly affect quality of life, sleep, and daily functioning. Moreover, they represent a primary reason for treatment discontinuation, which consequently shortens recurrence-free survival.[3,12–14] As mentioned above, oncologists must learn to distinguish painful from non-painful peripheral neuropathy, as the painful form significantly worsens quality of life.[15] Results from the population-based PROFILES registry in the Netherlands indicate that a more advanced stage of colorectal cancer, osteoarthritis, and higher levels of anxiety symptoms are associated with an increased risk of non-painful peripheral neuropathy. In contrast, a longer time since oncological diagnosis was positively correlated with a decreased risk of painful peripheral neuropathy. Additionally, painful peripheral neuropathy had a detrimental effect on quality of life and social functioning.[15]

It is noteworthy that OXI-induced neuropathy can worsen even several months after treatment has been discontinued. This phenomenon is referred to as "coasting." Approximately 30% of patients experienced symptoms of peripheral neuropathy 6 months or more after chemotherapy cessation, while about 2/3 of patients reported symptoms 1 month following the completion of chemotherapy.[16] According to an analysis of 27 trials, chemotherapy-induced peripheral neuropathy (CIPN) diminished by 26% per year after the completion of systemic treatment.[17]

There are various definitions of acute and chronic neuropathy. One definition suggests that chronic neuropathy occurs 12 ±2 months after the completion of OXI administration.[18,19] Baek et al. defined chronic neuropathy as grade 2 neuropathy lasting seven days or longer, or grade 3 neuropathy of any duration.[20] In contrast, Alejandro et al. categorized this adverse effect into acute neuropathy, lasting a maximum of 13 days, and chronic neuropathy, which persists for 14 days or longer.[21]

Objectives

This systematic review aimed to analyze the issues surrounding oxaliplatin-induced peripheral neuropathy (OIPN) in cancer patients. The mechanisms of onset, risk factors, clinical signs and symptoms, as well as treatment and prevention strategies, were examined.

Material and methods

The research was conducted using the PubMed database. The review included preclinical studies, clinical trials, and meta-analyses published between 1997 and 2024, with particular emphasis on studies from the past decade. Studies not published in English were excluded.

Pathomechanism of oxaliplatin-induced peripheral neuropathy

Chemotherapy-induced peripheral neuropathy is a common adverse effect of chemotherapy, with a variable, time-dependent incidence.[22,23] According to available data, approx. 50% of patients with peripheral neuropathy reported resolution of symptoms 6 months after completion of therapy.[16] Treatment with OXI may cause myelotoxicity, fever, liver function abnormalities, as well as central and peripheral neurotoxicity, including OIPN.

Central neuropathy involves brain tissue influencing peripheral nerves; e.g., damage to the central nociceptive system can induce mechanical hyperalgesia, which patients report as pain during the course of acute OIPN. Platinum analogues are standard treatments for various gastrointestinal cancers, including advanced colorectal, esophageal, gastric, liver, and pancreatic tumors, with neuropathic symptoms persisting for up to 6 months after completion of the treatment cycle.[23] The antitumor activity and toxicity of OXI are associated with ultrafiltrate platinum which is irreversibly bound to plasma proteins and red blood cells, transforming into a non-active pharmacological structure. Interestingly, the peak concentration of OXI is observed 2 h after administration.[24,25] An exceptional feature of OXI is its fast, nonenzymatic transformation into reactive platinum complexes and oxalate-free cytotoxic analogue. Both of these products induce peripheral sensory neuropathy, but it is the oxalate that primarily has an impact on the early and later decrease in mechanical threshold as well as acute cold-induced neuropathy, the most characteristic OIPN symptom.[23] Total platinum content is taken out from the blood vessels by binding to plasma and/or blood constant components, tissue uptake, and urine elimination, which can explain the mechanisms underlying acute OIPN.[24]

Given the pharmacokinetics of OXI, OIPN manifests as 2 distinct temporal types of neuropathies: 1) the characteristic acute peripheral sensorimotor polyneuropathy, which typically occurs during or within hours after drug infusion and is usually reversible; and 2) sensory neuropathy, which is associated with cumulative drug dose.[24]

Oxaliplatin-induced peripheral neuropathy is characterized by complex, multifocal pathomechanisms involving several structures of the central and peripheral nervous systems (Fig. 1,2).[25–27] These mechanisms are associated with the aggregation of platinum products in dorsal root ganglion (DRG) and trigeminal ganglion (TG) neurons, with consequential functional impairment of the myelin sheath, neuronal cell body, and glial structures. The exact mechanism of OIPN remains ambiguous; however, it is believed that some aspects of ion channels abnormalities, disruption of normal axonal membrane potential, and typical antitumor mechanisms contribute to the toxic effect on neurons and glial cells.[23,28] The mechanisms of chemotherapy involve binding of the drug to tumor cell nuclear DNA followed by inhibition of DNA replication and RNA transcription, along with inhibition of mitochondrial DNA replication and transcription. This leads to altered mitochondrial function, disruption of the respiratory chain, and overproduction of reactive oxygen species (ROS). Additionally, chemotherapy activates the immune system, resulting in the production of pro-inflammatory cytokines and protein kinases. Ultimately, all of these processes contribute to apoptosis.

In acute OIPN, the pathomechanisms are connected with a dysfunction of voltage-gated ion channels (e.g., sodium, potassium, and calcium channels), transient receptor potential channels, organic cation transporters 1 and 2, the Mate-1 transporter, and glial cells. The chronic form of OIPN is primarily characterized by DNA and mitochondrial damage, ROS production, and inflammation, which are associated with immune activation of nervous system cells.[29] The exact pathomechanisms of OIPN remain unclear and it is believed that several inducers with different mechanisms of action may affect the same targets.[30]

The onset of OIPN, occurring independently of chemotherapy agent mechanisms, is associated with microtubule disruption in neurons.[23] The DRG (regions lacking the blood–brain barrier (BBB)), sensory neurons, satellite cells, Schwann cells, as well as neuronal and glial cells in the spinal cord are the most sensitive sites where the neurotoxicity-induced chemotherapy begins.[28,31] Alterations in channel activity leading to ectopic nociceptors activation, myelin sheath damage, and electrophysiological abnormalities are also observed as a result of OIPN.[28]

Studies conducted during OXI treatment have revealed the development of an acute sodium (Na^+) channelopathy in sensory and motor axons. Slowing of sodium channel inactivation induces reversible cold allodynia. Motor nerve hyperexcitability may serve as a marker for the potential of more severe neurotoxicity.[32,33] Several studies have shown that although sensory symptoms predominate in the patients studied, the activity of voltage-gated sodium channels in motor axons are closely related to cold allodynia and exhibit a reversible nature.[33–35]

Membrane hyperexcitability may also be connected with chelation of intracellular calcium during activation of voltage-gated sodium channels.[5] Gene ablation of Nav1.6 prevented the action potential burst upon electrical stimulation after OXI treatment at low temperatures, demonstrating that the induction of cold allodynia by OXI is linked to Nav1.6.[36] Observations also suggest a role in the regulation of MAP kinase, which is transcriptionally regulated by the MAPK-ERK-CREB signaling pathway encoded by *Scn8A*.[37] Transient axonal hyperexcitability, resulting from an imbalance in voltage-gated Na^+ channels, leads to sustained depolarization and activation of the Na^+/Ca_2^+ exchanger 2 (*NCX2*) reverse sodium-calcium channel, with subsequent increase in calcium cations concentration and axonal damage. In both in vitro and in vivo studies, the inhibition of *NCX* was observed to reduce axonal damage.[31]

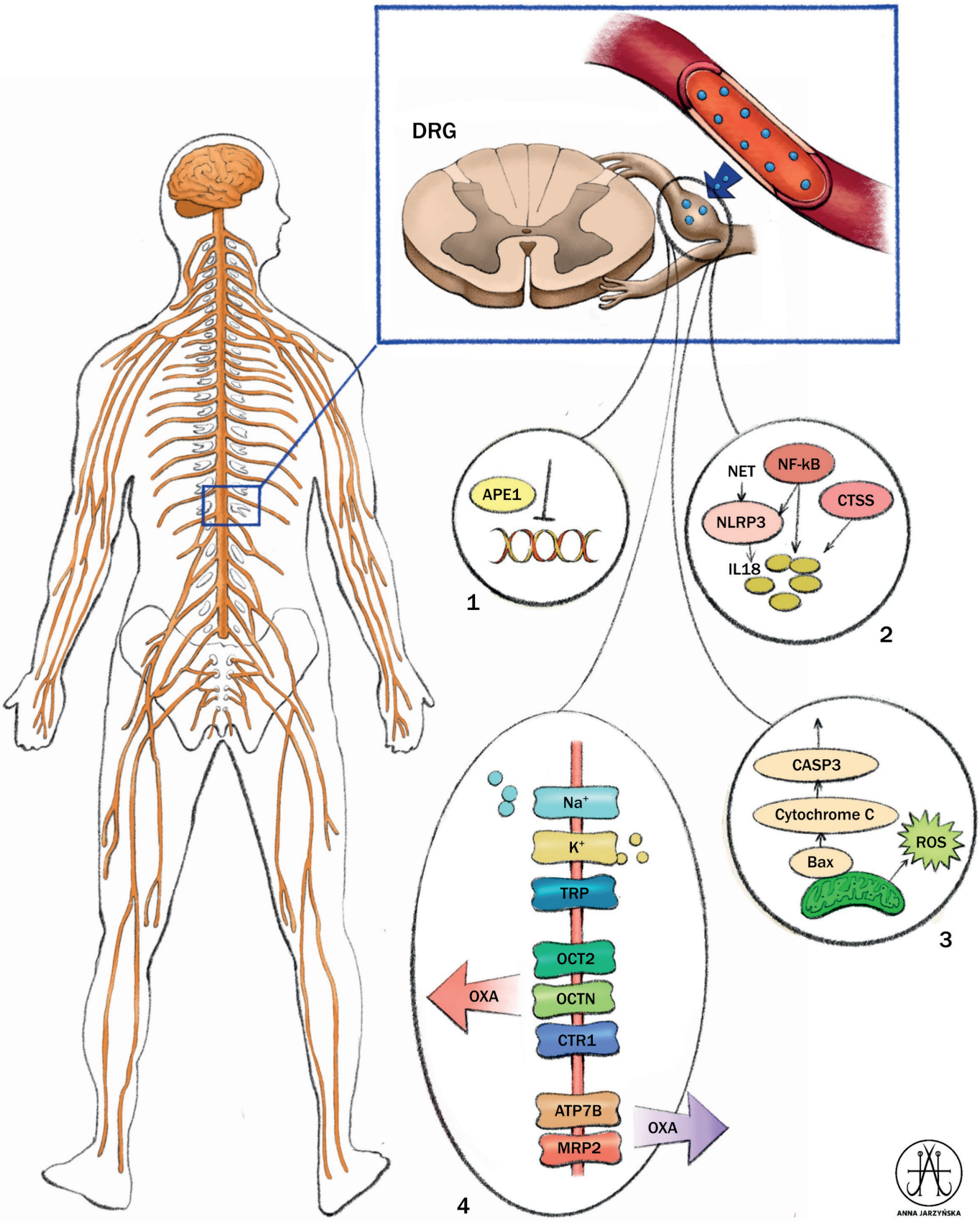

Fig. 1. The scheme of the different inflammatory pathways in the onset of the oxaliplatin (OXI)-induced peripheral neuropathy (OIPN). 1) DNA damage; 2) neuroinflammation; 3) mitochondrial dysfunction and oxidative stress; 4) dysfunction of voltage-gated ion channels and uptake and efflux transporters[24,25]

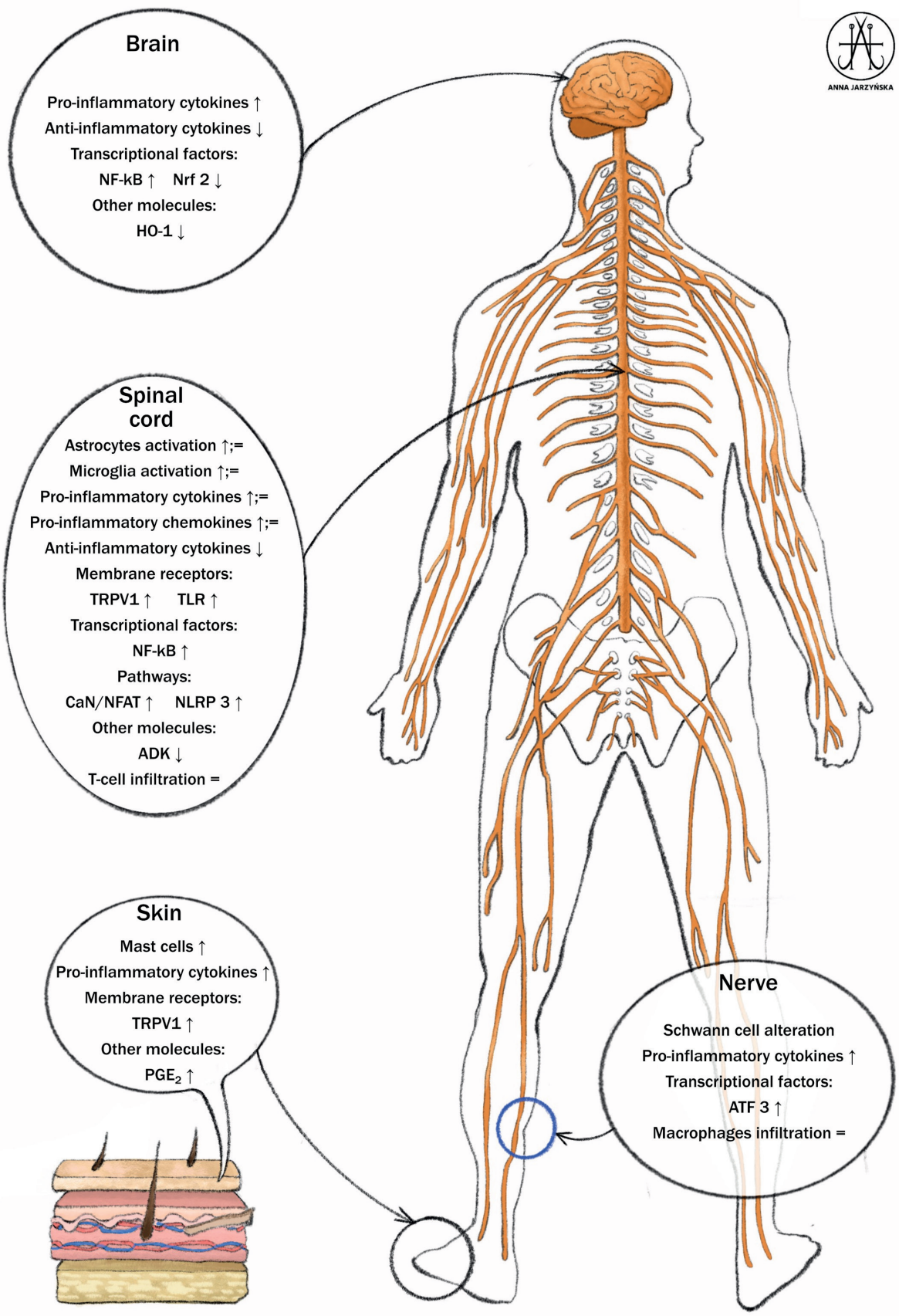

Fig. 2. The scheme of the different places in the pathomechanism of the oxaliplatin (OXI)-induced peripheral neuropathy (OIPN)[26]

Abnormalities in DRG

Most well-known mechanisms include processes in the DRG which are influenced by the specific structure of the first sensory pathway cell. Dorsal root ganglion is not protected by the BBB, making it more susceptible to the accumulation of OXI and other platinum derivatives. Abnormalities in DRG are associated with several dysfunctions including those related to the organic cation transporter 2 (OCT2), as well as potassium, chloride, and calcium voltage-gate channels which are also involved in pain-induced pathways.

Due to a local expression of OCT2, DRG is predisposed to the absorption of OXI especially in the early phase of treatment. In experimental models, the absence of OCT2 diminishes hypersensitivity to cold or allodynia during the acute phase of OXI treatment.[38] Additionally, several transport enzymes including organic cation transporters, high affinity copper uptake protein 1 (CTR1), copper transporter ATPase alpha (*ATP7A*), and multidrug and toxin extrusion protein 1 (MATE1), can be responsible for OIPN.[25]

Research has shown that DRGs from OXI-treated mice exhibited a significant downregulation of mRNA expression of potassium voltage-gated channel Kv1.1, as well as K2P-TREK1 and TRAAK, which are thermosensitive and mechanosensitive 2-pore-domain potassium channels. Additionally, OXI-induced mechanical and cold allodynia was observed following co-ablation of TREK1 and TRAAK in mice.[36]

Elevated expression of the calcium channel subunit *α2δ1* has also been detected in rat DRG neurons and spinal cord following paclitaxel or OXI treatment. Calcium channels are known to be crucial mediators of peripheral sensitization and are also the target of gabapentin, a recognized treatment for neuropathic pain.[36,39]

The upregulation of gene and protein expression of voltage-gated Nav1.6 in rat DRGs is responsible for the generation of action potential peripheral nerve fibers, as well as repetitive action potential discharges in myelinated axons.[36,40]

Although there are different expressions of NKCC1 and KCC2 in the cell bodies of DRG neurons and dorsal horn of the spinal cord, evidence supports the notion that the dysregulation of chloride balance activates disinhibition not only in DRG but also in the spinal cord. This, in turn, increases neuronal excitability, leading to hyperalgesia and allodynia. A new question has arisen regarding the role of other chloride channels in the pathogenesis of OIPN.[36]

The OXI treatment also induces an increase in intracellular hydrogen ion concentrations in the DRG during the acute phase by affecting the activity of the plasma membrane protein isoform 1 NHE1. This protein is responsible for Na^+/H^+ transport and is located on nociceptors, where it plays an important role in maintaining intracellular pH homeostasis.[41] In preclinical rat models, the inhibition of FABP5, localized in DRG, attenuates pain in OIPN. *FABP3*, *FABP5*, and *FABP7* are intracellular chaperones of endocannabinoids (eCB), which are expressed throughout the nervous system and activated in various pain models.[29]

Research using the cannabinoid receptor agonist CB2-β-caryophyllene (BCP) in animal models has shown that OXI therapy results in dysregulation of neuroinflammatory pathways, including an increased content of interleukin (IL)-1β, IL-6, and tumor necrosis factor alpha (TNF-α), along with reduced levels of IL-10 protein in the spinal cord. The use of BCP reduces the frequency and severity of nociceptive effects in these models. Additionally, studies on its beneficial effects have demonstrated that BCP restores TNF and IL-10 concentrations, as well as decreases ROS products and lipid peroxidation in the spinal cord.[42]

Wallerian degeneration of intraepidermal nerve fibers (IENFs), including unmyelinated C-fibers and, to a lesser extent, thinly myelinated axonal A-fibers responsible for transmitting touch, pain and thermal sensations, is also implicated in the mechanism of OIPN. Observations have shown ectopic firing – abnormal electrical activity in the distal ends of the IENFs. This leads to a phenomenon known as central sensitization, which refers to enhanced activation of pain pathways in the central nervous system, particularly in the spinal cord and brain. Central sensitization reinforces and perpetuates the activation of pain pathways thereby contributing to the persistence of chronic pain.[36]

Glial cells, including satellite and Schwann cells, might take part in the neuroinflammatory process in DRG and axons. Neuroinflammatory components have also been shown in the spinal cord, where microglia and astrocytes play a prominent role in OIPN development.[43] Neuroinflammation, as indicated by the activation of glial cells and proinflammatory cytokines (e.g., NF-B), is detected not only at the peripheral nerve system structure but also in the spinal cord, contributing to the central sensitization. Oxaliplatin may also affect the activity of mast cells through the activation of proteinase-activated receptor 2 (PAR2), leading to intraepidermal nerve fibers degeneration and resulting in mechanical allodynia.[36]

The chemotherapy-related central effect of OXI administration have been explained by Branca et al.[43] The administration of OXI induces modifications of the tight junction (TJs) proteins, including zonula occludens-1 (ZO-1) and of F-actin, which activate BBB disruption in the central nervous system. Additionally, intracellular OXI activates ROS and induces endoplasmic reticulum stress, as evidenced by increased expression levels of glucose-regulated protein 78 (GRP78). The induction of caspase-3 leads to extracellular ATP release.[43,44]

Grading peripheral sensory neuropathy

It is well-established that the presence of peripheral neuropathy leads to a deterioration in a patient's quality of life, which, in turn, negatively affects social functioning and

work performance. Four grading systems, based on the patient's self-reporting of symptoms, have been developed in order to standardize the assessment of peripheral sensory neuropathy. There is no significant difference between the Eastern Clinical Oncology Group (ECOG) and the National Cancer Information Center Common Toxicity Criteria (NCIC-CTC) scales. The grading for these systems is as follows:

– Grade 0: 'none or no change';
– Grade 1: 'loss of deep tendon reflexes, mild paresthesias';
– Grade 2: 'mild or moderate objective sensory loss; moderate paresthesias';
– Grade 3: 'mild or moderate objective sensory loss; moderate paresthesias'[45];

According to World Health Organization (WHO):

– Grade 0 indicates 'no symptoms';
– Grade 1 denotes 'presence of paresthesias and/or decreased deep tendon reflexes';
– Grade 2 is characterized by 'severe paresthesias and/or light muscle weakness';
– Grade 3 refers to 'intolerable paresthesias and/or marked weakness'; and
– Grade 4 denotes 'paralysis'.[46]

The National Cancer Institute (NCI) Common Terminology has introduced grade 5 which signifies 'death' and has modified the definition of grade 4 to indicate 'life-threatening consequences: urgent intervention indicated.'[47]

Another valuable tool for assessing the grade of neuropathy is the questionnaires that evaluate the functional consequences of CIPN in cancer patients. One such tool is the Functional Assessment of Cancer Therapy/Gynecologic Oncology Group Neurotoxicity (FACT/GOG-Ntx-13), where a higher score correlates with a better quality of life. This validated 13-item questionnaire rates items on a 5-point Likert scale, ranging from "not at all" to "very much", with a total possible score of 52.[48]

The Chemotherapy-Induced Peripheral Neuropathy Assessment Tool (CIPNAT), European Organization for Research & Treatment in Cancer Quality of Life QuestCIPN 20 (EORTC QLQ-CIPN 20), Modified Total Neuropathy Score (mTNS), and Total Neuropathy Score clinical version (TNSc) and Total Neuropathy Score-reduced (TNSr) are all valuable patient-reported outcome measures used to evaluate the impact of neuropathy on patients' lives.[49] Oncologists using these scales should be aware that factors such as subjective misjudgment, poor anti-interference, and low sensitivity represent limitations of these questionnaires. A reduced version of the European Organization for Research and Treatment of Cancer (EORTC) Quality of Life Questionnaire Chemotherapy-Induced Peripheral Neuropathy scale (QLQ-CIPN20), called CIPIN15, has been shown to be a reliable and significant self-reporting tool for assessing CIPN.[50]

In a population of Chinese patients, a 20-item CIPN assessment tool, known as the Chemotherapy-Induced Peripheral Neuropathy Integrated Assessment–Oxaliplatin Subscale (CIPNIA-OS), was evaluated. The results were encouraging as the CIPNIA-OS questionnaire demonstrated higher sensitivity than QLQ-CIPN20 in the evaluation of OIPN. However, the small sample size remains the major limitation of this study.[51]

In an Australian study, patients receiving OXI completed a questionnaire containing standardized CIPN patient-reported outcome assessments (EORTC CIPN-20, PRO-CTCAE) using a tablet device. Patient-reported outcome assessment scores were correlated with the NCI-CTCAE grade and analyzed with consideration of cumulative dose of OXI. It is surprising that CIPN patient-reported outcomes provide additional information beyond the nurse-assessed NCI-CTCAE grade, particularly during the earlier stages of chemotherapy.[52]

Risk factors

A meta-analysis including nearly 11,000 participants from 20 studies identified factors associated with OIPN. Older age (above 60 years), female sex, a higher body mass index (BMI) (>25 km/m^2), a larger body surface area (BSA) (≥2.0 m^2), and those with low physical activity levels were associated with an increased risk of OIPN [53–58]

An analysis of 1,401 patients from 23 studies found that in patients aged 65 years and older at the time of cancer diagnosis age was an independent predictor of the development of CIPN. This finding was confirmed in a subsequent study of more than 3,500 patients aged ≥70 years.[59–62] In contrast, some investigators have reported that age is not associated with OIPN.[8–20,63,64] One study recorded that female sex was associated with the incidence and severity of OIPN.[65] Contrastingly, however, many published studies (including studies with multivariate analysis) reported no difference in the peripheral neuropathy rates between the sexes.[18,20,64–67]

The latest study by Lee et al. noted that reduced physical activity increased the severity of peripheral neuropathy, as assessed using the CTCAE and the Functional Assessment of Cancer Therapy/Gynecologic Oncology Group-Neurotoxicity-13 (FACT/GOG-NTX-13). The FACT/GOG-NTX-13 subscale evaluates the degree and impact of sensory and motor neurotoxicity symptoms in the preceding 7 days.[59]

Comorbidities such as diabetes mellitus, alcoholism, anemia, and hypomagnesemia are also significantly associated with a higher risk of this kind of neuropathy.[53,58,60,61] Furthermore, lower hemoglobin before starting therapy with OXI correlated with more severe symptoms of persistent peripheral neuropathy after chemotherapy.[56,61] Additionally, peripheral neuropathy occurred twice as often in patients with autoimmune diseases.[60]

On the other hand, some reports did not show correlation between well-known risk factors such as sex, BMI,

diabetes mellitus, alcohol consumption, and preexisting peripheral neuropathy.[20,56,61,66,68,69]

The probability of OIPN increases after 6 cycles of OXI based chemotherapy.[53] High BSA (>2.0 m^2) and acute neuropathy after 3 cycles of OXI were identified as predictive factors for persistent neuropathy.[20]

There are discrepancies regarding the cumulative dose of OXI and peripheral neuropathy. In a meta-analysis by Wang et al., a cumulative OXI dose above 500 mg/m^2 was associated with OIPN.[53] In 2 studies, median cumulative doses of OXI were 810 mg/m^2 and 766 mg/m^2, respectively, and these doses were correlated with acute neuropathy. Moreover, persistent symptoms of neuropathy were described in 24% and 16% of patients, respectively.[70,71] A cumulative dose of OXI of 675 mg/m^2 or higher, or treatment beyond the 8th cycle was correlated with grade 3 neuropathy and was an independent factor of persistent peripheral neuropathy.[20] In Asians with colorectal cancer, OIPN of grade 2 or higher occurred with a total dose of 680 mg or more while grade 3 or higher neuropathy was observed with a total dose of 1,040 mg or more.[72] According to Storey et al., a higher median cumulative OXI dose of 834 mg/m^2 (range: 447–1040 mg/m^2) compared to 702 mg/m^2 (range: 130–1040 mg/m^2) was associated with a statistically higher probability of chronic peripheral neuropathy, observed 12 months after completion of chemotherapy.[10] In turn, a median cumulative dose >780 mg/m^2 was identified as the main predictor of OIPN.[73] Storey et al. confirmed that cumulative OXI dose is the only factor that induces chronic peripheral neuropathy, while other factors – including age, sex, grade ≥2 acute peripheral neuropathy, 'legs like jelly', or pseudolaryngospasm during OXI treatment – were not significant.[10] On the other hand, Brouwers et al. showed that the dose of OXI is not related to OIPN.[74]

According to the aforementioned meta-analysis, smoking history and chemotherapy regimen (XELOX vs FOLFOX) did not result in an increased risk of OIPN.[53] In contrast to the meta-analysis by Wang et al., the SCOT randomized controlled trial, which compared 3 months to 6 months of OXI-containing adjuvant chemotherapy in colorectal cancer patients, revealed that patients receiving the CAPOX regimen (OXI + capecitabine) had lower OIPN scores than those receiving the FOLFOX (OXI + 5-fluorouracil) regimen. Moreover, both acute and chronic neuropathy occurring after 3 months of chemotherapy were milder or moderate compared to those occurring after 6 months of therapy. The presence of neuropathy prior to the initiation of the OXI-based chemotherapy was identified as the 2nd factor associated with increased severity of peripheral neuropathy.[75]

Furthermore, based on the study by Tanishima et al., hyperacute peripheral neuropathy was identified as a predictor of persisent OIPN.[76]

Additionally, some reports have noted that serum levels of albumin, magnesium, vitamin D, and gamma-glutamyl transferase (GGT) play a role in the onset and severity of neuropathy symptoms.[56,61,66]

The histopathologic type, such as mucinous carcinoma of colorectal cancer, was found to be significantly correlated with grade 2 to grade 3 OIPN; however, this result requires confirmation in large studies.[61]

Housley et al. presented evidence that chronic sensory neuropathy depends on nonlinear interactions between chemotherapy and the cancer itself. The pathomechanism mentioned above involved the DRG, neuronal excitability, and inflammatory processes, and is additionally connected with inappropriate sensory encoding potassium ion channel Kv3.3.[77]

Environmental factors, such as lower temperatures during winter, did not contribute to an increased risk of acute neuropathy in California.[20] In contrast, a study conducted in Denmark found the highest probability of dose modification and completion of OXI occurred during the period from December to February (mean temperature: 0.1–1.8°C).[78] A prospective clinical trial showed that vitamin B6 and celecoxib intake did not influence the occurrence or intensification/exacerbation of OIPN.[59]

Genes such as *CSHL1*, *GH1* (chorionic somatomammotropin hormone-like 1, growth hormone 1), *KCMF1* (potassium channel modulatory factor 1, also known as FIGC (bFGF-induced in gastric cancer)), *IL36G*, *EFCAB8* (EF-Hand Calcium Binding Domain 8), *CSRP2* (also known as *CRP2*, codes for cysteine and glycine-rich protein 2), *IQGAP1* (or p195, IQ motif containing the GTPase activating protein 1), *GNRH2, SMIM1* (small Integral Membrane Protein 1), and *C5orf17* are significantly up- or downregulated as a result of chemotherapy and are associated with the onset of OIPN.[79] Understanding their expression in peripheral white blood cells could be useful in predicting the occurrence of neurotoxicity.

Another study revealed that single-nucleotide polymorphisms (SNPs) in the *FARS2*, *ACYP2*, and *TAC1* genes contribute to a higher risk of OIPN. These outcomes should be explored further in cohort studies.[80]

The animal models have demonstrated a dependency between gut microbiota and the pathological condition of pain. Serum metabolomics correlated well with the impaired lipid metabolism, molecular transport, and augmented inflammatory responses. There are suggestions that changes in gut microbiota (dysbiosis) contributed to the development of OIPN.[34]

Neurophysiological examination

Oxaliplatin treatment induces 2 primary types of peripheral neuropathy: acute neurotoxicity and chronic neuropathy.[20] Acute neurotoxicity is characterized by temporary sensations, such as tingling, typically triggered by cold, as well as muscle spasms, especially in the limbs and jaw. These symptoms typically appear during the infusion and

resolve within several days, although they can intensify with repeated treatments. Nearly all patients experience these transient symptoms.[5,13,19] Chronic neuropathy occurs with cumulative doses and is marked by sensory loss and tingling in a glove-and-stocking distribution, potentially progressing to sensory ataxia.[20,81] Conventional nerve conduction studies (NCS) are insufficient for early detection of nerve dysfunction, as they only reveal abnormalities once significant axonal or myelin damage has occurred. In some patients treated with OXI, features of axonal polyneuropathy were observed: sensory polyneuropathy, manifested by a reduction in the amplitude of the response from sensory fibers (SNAP), or, less frequently, sensorimotor polyneuropathy, where the amplitude of the response was reduced to stimulation of both sensory (SNAP) and motor fibers (CMAP). No conduction velocity slowing or conduction block was observed in these patients. Polyneuropathy was also observed in subsequent studies, 2 years after treatment completion.[22] Nerve excitability testing offers additional insights by assessing ion channel function, energy-dependent pumps, and ion exchanges involved in nerve impulse conduction.[7] Excitability assessment, in addition to the classic neurophysiological methods presented by Park et al., is a useful and rapid technique for axonal excitability assessment. It is recognized as a biomarker assessing potential predisposition to more severe axonopathy during OXI treatment.[6]

The precise mechanisms underlying acute OIPN remain unclear; however, studies suggest that abnormal functioning in axonal sodium channels in both motor and sensory axons may contribute to the acute phase of the condition following treatment.[3,6,82,83]

High resolution ultrasound assessment of oxaliplatin-induced polyneuropathy

The high-resolution ultrasound (HRUS) examination is nowadays a widely accessible tool for assessing peripheral nervous system (PNS) lesions.[84] It also complements electrophysiological tests and the combination of these diagnostic methods significantly enhances the sensitivity and specificity of the PNS assessment.[84–89] High-resolution ultrasound employs probes with frequencies greater than >15 MHz allowing for the accurate visualization of various elements of the PNS, including the smallest sensory nerves.

Multiple studies have demonstrated the utility and significance of HRUS in the diagnosis of inflammatory polyneuropathies (PNP).[84–89] The use of HRUS in PNP is primarily based on the observation of swelling and thickening of peripheral nerves associated with demyelinating damage. Reports also suggest potential deviations from the normal ultrasound (US) image of nerves in cases of axonal damage.[85,88] A decreased cross-section area (CSA) of the nerves is thought to occur in certain axonal neuropathies.[85,87,88]

Chemotherapy-induced peripheral neuropathy constitutes a distinct subgroup of polyneuropathies. To date, there have been only single studies on US imaging of the PNS in OIPN, primarily focusing on the effect of OXI on PNS. Briani et al. examined 15 patients before and after the administration of OXI in an attempt to demonstrate US and neurophysiological correlations in peripheral nerve imaging and function.[90] Despite the presence of axonal lesions of the tested nerves, no decrease in the CSA of the nerves was observed. However, increased CSA at typical entrapment sites, such as median (wrist) and ulnar (elbow) nerves, was detected in 60% of the patients.[90] These findings suggest that OXI may increase the susceptibility of peripheral nerves to compression damage.

Data on ultrasonographic imaging of peripheral nerves in OIPN ar still lacking. However, previous studies on HRUS and PNS evaluation reveal further horizons regarding aspects of structural assessment of nerves in multiple neuropathies. In the case of OIPN, the clinical evaluation should particularly emphasize US assessment of sensory nerves, with specific attention to prior reports of structural damage to PNS in small-fiber neuropathy (SFN).

Prevention and treatment

To date, no pharmacological agents have been recommended for the prevention of CIPN. Numerous preclinical rodent studies have evaluated the efficacy of various agents aimed at inhibiting OIPN, but without significant success.[91] It is well established that oxidative stress plays a central role in the development of OIPN. Consequently, antioxidants, including vitamin C, vitamin E, acetyl-L-carnitine, alpha-lipoic acid, and glutathione, have been investigated for their potential protective effects against neuropathy.[92–95] Preclinical studies have confirmed the efficacy of these antioxidants. Additionally, several widely used and clinically approved drugs, including carvedilol, donepezil, dimethyl fumarate, and rosiglitazone, have demonstrated effectiveness in reducing OIPN in preclinical models.[96–99] However, some studies have reported inconsistent results, such as vitamin E failing to attenuate early symptoms of peripheral neuropathy.[100,101]

Nonsteroidal anti-inflammatory drugs (NSAIDs), when administered concomitantly with OXI-based chemotherapy, were found to reduce the risk of peripheral neuropathy, although further studies are required to confirm these findings.[72]

Interleukin-1β, IL-6, and TNF-α are pro-inflammatory cytokines whose levels are elevated in the DRG spinal cord of animals treated with OXI.[102,103] Certain agents, including minocycline, and rapamycin, have been shown to attenuate the neurological side effects of oxaliplatin.[104,105] Oxaliplatin also modulates voltage-gated sodium (Na^+)

and potassium (K^+) channels in neurons. Consequently, Na^+ channel inhibitors such as lidocaine, mexiletine, and lamotrigine, as well as K^+ channel inhibitors – including the glucosinolate glucoraphanin and isothiocyanates such as sulforaphane, allyl isothiocyanate, phenyl isothiocyanate, and carboxyphenyl isothiocyanate – have been reported to inhibit the development of peripheral neuropathy.[106,107]

Gabapentin and pregabalin, which act on the *α2δ* subunit of voltage-gated calcium channels, have been shown to prevent OIPN.[108–111] Downregulation of transient receptor potential (TRP) channels – temperature-sensitive cation channels – may attenuate OIPN. Agents such as topiramate, acetazolamide, shakuyakukanzoto, goshajinkigan, eel calcitonin, nifedipine, diltiazem, and mexiletine exert their effects through modulation of these channels.[112–115] Modulators of the monoaminergic nervous system, including duloxetine, fluoxetine, vortioxetine, tandospirone, venlafaxine, xaliproden, clomipramine, and clonidine, have demonstrated analgesic effects in animal models of painful OIPN.[116–129] A clinical study was conducted to evaluate the efficacy and safety of duloxetine at a dose of 60 mg for the prevention of OIPN. One study arm received duloxetine, while the 2nd arm received a placebo. Duloxetine (or placebo) was administered during the first 14 days of each chemotherapy cycle. Patients receiving duloxetine experienced a lower incidence of distal paresthesia and throat discomfort compared with those receiving placebo.[130]

In a separate clinical study, patients with chemotherapy-induced pain following treatment with paclitaxel, another taxane, or OXI were treated with 30 mg of duloxetine or placebo for the 1st week, followed by 60 mg of duloxetine or placebo daily for the subsequent 4 weeks. Patients who received duloxetine reported a significantly greater reduction in pain compared with the placebo group, with 59% of duloxetine-treated patients reporting pain relief, compared with 38% in the placebo group.[131] Currently, the European Society of Medical Oncology (ESMO) recommends duloxetine 30 mg daily for 1 week, followed by 60 mg daily, as a therapeutic intervention for CIPN.[132] The American Society of Clinical Oncology (ASCO) currently endorses duloxetine as the only recommended agent for the treatment of CIPN.[133]

Recently published preclinical studies have shown disappointing results regarding the use of a duloxetine–prazosin (α-blocker) combination to prevent the development of allodynia and hyperalgesia during OXI therapy. This combination demonstrated no superiority over duloxetine alone, showing comparable efficacy in preventing OIPN.[134] Other drug classes, such as riluzole, mirtazapine, ifenprodil, amitriptyline, trifluoperazine, and dimiracetam, act as modulators of the glutamatergic nervous system and reduce symptoms of OIPN.[135–142]

It should be noted that early studies suggested potential benefits of administering intravenous calcium and magnesium before and after OXI treatment to prevent OIPN.[143–145] However, subsequent larger studies failed to demonstrate a reduction in OIPN, indicating that calcium and magnesium are ineffective for the prevention of sensory neuropathy.[146–148]

An intriguing therapeutic approach involves the use of topical agents applied to the hands and feet to reduce or prevent symptoms of peripheral neuropathy. Wearing frozen gloves during chemotherapy to prevent CIPN in 180 patients with colorectal or breast cancer has been shown to alleviate certain neuropathic symptoms, such as reduced pain and muscle cramps in the hands and fingers, potentially leading to a modest improvement in quality of life.[149]

Additionally, a study by Arslan et al. demonstrated that applying henna to the palms, fingers, and soles of female patients after the 2nd, 3rd, and 4th cycles of OXI resulted in a reduction in symptoms of sensory neuropathy.[150]

The ongoing Danish OxaNeuro trial is a multicenter, double-blind, randomized study including 120 colorectal cancer patients receiving adjuvant OXI. Patients receive daily either fish oil capsules containing long-chain n-3 polyunsaturated fatty acids (n-3 LCPUFAs) or corn oil for a duration of 8 months. The results of this study are not yet available, as patient recruitment continued until the end of 2024.[151]

Mitochondrial therapy (mitotherapy) is a treatment strategy that relies on the transfer of functional exogenous mitochondria into mitochondria-defective cells to promote cellular recovery. This approach represents a novel therapeutic strategy for diseases caused by mitochondrial dysfunction, such as OIPN. In a preclinical study, mitotherapy was shown to prevent OIPN through anti-neuroinflammatory effects. Therefore, mitotherapy may offer potential as an analgesic adjunct during OXI-based chemotherapy.[152]

In the search for effective strategies to prevent and/or treat OIPN, the gold standard has been sought among traditional medicinal compounds used in various countries. Huangqi Guizhi Wuwu decoction (HGWD) is a traditional Chinese medicine (TCM) formula that has been investigated for its preventive potential against OIPN. Based on available study results, the preventive effects of HGWD are thought to arise from regulation of intestinal flora homeostasis and a reduction in serum lipopolysaccharide levels, including within the DRG.[24]

Similarly, Gosha-jinki-gan (GJG), a Japanese herbal medicine, with the expression of the transient receptor potential melastatin 8 (TRPM8) and transient receptor potential ankyrin 1 (TRPA1) channels is well-known for its effectiveness in minimizing symptoms of peripheral neuropathy by suppressing the overexpression of TRPM8 and TRPA1 mRNA.[153,154] Furthermore, a preclinical study demonstrated that 50% hydroalcoholic extract of *Astragali radix* exhibited analgesic effects and prevented neurological side effects induced by OXI.[102]

The positive effect of cannabis in oncologic patients treated with OXI was confirmed by Waissengrin et al. The effectiveness was significantly greater in patients who received cannabis prior to treatment with OXI compared with those who received it after the initiation of OXI therapy.[155] In another study, daily administration of 300 mg of cannabidiol oil for 8 days, beginning 1 day before the initiation of chemotherapy with either OXI or paclitaxel, reduced the early symptoms of peripheral neuropathy.[156] These findings, however, require confirmation in large randomized clinical trials.

Limitations of the study

The problem of neuropathy during OXI treatment remains under investigation and requires continued observation as well as further research into the pathophysiological mechanisms, diagnostic approaches, and therapeutic options. This paper discusses the relevant issues; however, one limitation should be acknowledged. As this is a narrative (literature) review rather than a systematic review, the systematic organization of the presented publications is limited.

Conclusions

Both the prevention and treatment of OIPN require further innovative and effective research. It is hoped that the outcomes of ongoing trials will address the issue of acute and OIPN in the near future, as this remains a persistent clinical concern for patients with gastrointestinal cancer.

Use of AI and AI-assisted technologies

Not applicable.

ORCID iDs

Justyna Anna Pigońska https://orcid.org/0009-0002-9280-7903
Marta Banach https://orcid.org/0000-0002-4656-3656
Paweł Stanisław Walkowiak https://orcid.org/0009-0008-2101-1485
Aneta Zygulska https://orcid.org/0000-0002-6748-042X

References

1. Brozou V, Vadalouca A, Zis P. Pain in platin-induced neuropathies: A systematic review and meta-analysis. *Pain Ther*. 2018;7(1):105–119. doi:10.1007/s40122-017-0092-3
2. Grothey A. Clinical management of oxaliplatin-associated neurotoxicity. *Clin Colorect Cancer*. 2005;5(Suppl 1):S38–S46. doi:10.3816/CCC.2005.s.006
3. Egashira N. Pathological mechanisms and preventive strategies of oxaliplatin-induced peripheral neuropathy. *Front Pain Res (Lausanne)*. 2021;2:804260. doi:10.3389/fpain.2021.804260
4. Park SB, Goldstein D, Krishnan AV, et al. Chemotherapy-induced peripheral neurotoxicity: A critical analysis. *CA Cancer J Clin*. 2013;63(6):419–437. doi:10.3322/caac.21204
5. Gebremedhn EG, Shortland PJ, Mahns DA. The incidence of acute oxaliplatin-induced neuropathy and its impact on treatment in the first cycle: A systematic review. *BMC Cancer*. 2018;18(1):410. doi:10.1186/s12885-018-4185-0
6. Park SB, Lin CSY, Krishnan AV, Goldstein D, Friedlander ML, Kiernan MC. Long-term neuropathy after oxaliplatin treatment: Challenging the dictum of reversibility. *Oncologist*. 2011;16(5):708–716. doi:10.1634/theoncologist.2010-0248
7. Lehky TJ, Leonard GD, Wilson RH, Grem JL, Floeter MK. Oxaliplatin-induced neurotoxicity: Acute hyperexcitability and chronic neuropathy. *Muscle Nerve*. 2004;29(3):387–392. doi:10.1002/mus.10559
8. Land SR, Kopec JA, Cecchini RS, et al. Neurotoxicity from oxaliplatin combined with weekly bolus fluorouracil and leucovorin as surgical adjuvant chemotherapy for stage II and III colon cancer: NSABP C-07. *J Clin Oncol*. 2007;25(16):2205–2211. doi:10.1200/JCO.2006.08.6652
9. De Gramont A, Figer A, Seymour M, et al. Leucovorin and fluorouracil with or without oxaliplatin as first-line treatment in advanced colorectal cancer. *J Clin Oncol*. 2000;18(16):2938–2947. doi:10.1200/JCO.2000.18.16.2938
10. Storey DJ, Sakala M, McLean CM, et al. Capecitabine combined with oxaliplatin (CapOx) in clinical practice: How significant is peripheral neuropathy? *Ann Oncol*. 2010;21(8):1657–1661. doi:10.1093/annonc/mdp594
11. Bennett MI, Rayment C, Hjermstad M, Aass N, Caraceni A, Kaasa S. Prevalence and aetiology of neuropathic pain in cancer patients: A systematic review. *Pain*. 2012;153(2):359–365. doi:10.1016/j.pain.2011.10.028
12. Oh SY, Shin SW, Koh SJ, et al. Multicenter, cross-sectional observational study of the impact of neuropathic pain on quality of life in cancer patients. *Support Care Cancer*. 2017;25(12):3759–3767. doi:10.1007/s00520-017-3806-5
13. Van Haren FGAM, Steegers MAH, Thijssen M, Van Der Wal SEI, Vissers KCP, Engels Y. Qualitative evaluation of the influence of acute oxaliplatin-induced peripheral neuropathy on quality of life and activities of daily life. *Pain Pract*. 2021;21(5):513–522. doi:10.1111/papr.12981
14. Prutianu I, Alexa-Stratulat T, Cristea EO, et al. Oxaliplatin-induced neuropathy and colo-rectal cancer patient's quality of life: Practical lessons from a prospective cross-sectional, real-world study. *World J Clin Cases*. 2022;10(10):3101–3112. doi:10.12998/wjcc.v10.i10.3101
15. Bonhof CS, Trompetter HR, Vreugdenhil G, Van De Poll-Franse LV, Mols F. Painful and non-painful chemotherapy-induced peripheral neuropathy and quality of life in colorectal cancer survivors: Results from the population-based PROFILES registry. *Support Care Cancer*. 2020;28(12):5933–5941. doi:10.1007/s00520-020-05438-5
16. Seretny M, Currie GL, Sena ES, et al. Incidence, prevalence, and predictors of chemotherapy-induced peripheral neuropathy: A systematic review and meta-analysis. *Pain*. 2014;155(12):2461–2470. doi:10.1016/j.pain.2014.09.020
17. Teng C, Cohen J, Egger S, Blinman PL, Vardy JL. Systematic review of long-term chemotherapy-induced peripheral neuropathy (CIPN) following adjuvant oxaliplatin for colorectal cancer. *Support Care Cancer*. 2022;30(1):33–47. doi:10.1007/s00520-021-06502-4
18. Attal N, Bouhassira D, Gautron M, et al. Thermal hyperalgesia as a marker of oxaliplatin neurotoxicity: A prospective quantified sensory assessment study. *Pain*. 2009;144(3):245–252. doi:10.1016/j.pain.2009.03.024
19. Argyriou AA, Cavaletti G, Briani C, et al. Clinical pattern and associations of oxaliplatin acute neurotoxicity: A prospective study in 170 patients with colorectal cancer. *Cancer*. 2013;119(2):438–444. doi:10.1002/cncr.27732
20. Baek KK, Lee J, Park SH, et al. Oxaliplatin-induced chronic peripheral neurotoxicity: A prospective analysis in patients with colorectal cancer. *Cancer Res Treat*. 2010;42(4):185. doi:10.4143/crt.2010.42.4.185
21. Alejandro LM, Behrendt CE, Chen K, Openshaw H, Shibata S. Predicting acute and persistent neuropathy associated with oxaliplatin. *Am J Clin Oncol*. 2013;36(4):331–337. doi:10.1097/COC.0b013e318246b50d
22. Banach M, Zygulska AL, Krzemieniecki K. Oxaliplatin treatment and peripheral nerve damage in cancer patients: A Polish cohort study. *J Cancer Res Ther*. 2018;14(5):1010–1013. doi:10.4103/jcrt.JCRT_971_16
23. Zajączkowska R, Kocot-Kępska M, Leppert W, Wrzosek A, Mika J, Wordliczek J. Mechanisms of chemotherapy-induced peripheral neuropathy. *Int J Mol Sci*. 2019;20(6):1451. doi:10.3390/ijms20061451
24. Cheng F, Zhang R, Sun C, et al. Oxaliplatin-induced peripheral neurotoxicity in colorectal cancer patients: Mechanisms, pharmacokinetics and strategies. *Front Pharmacol*. 2023;14:1231401. doi:10.3389/fphar.2023.1231401

25. Wei G, Gu Z, Gu J, et al. Platinum accumulation in oxaliplatin-induced peripheral neuropathy. *J Peripher Nerv Syst*. 2021;26(1):35–42. doi:10.1111/jns.12432
26. Fumagalli G, Monza L, Cavaletti G, Rigolio R, Meregalli C. Neuroinflammatory process involved in different preclinical models of chemotherapy-induced peripheral neuropathy. *Front Immunol*. 2021; 11:626687. doi:10.3389/fimmu.2020.626687
27. Gamelin E, Bouil AL, Boisdron-Celle M, et al. Cumulative pharmacokinetic study of oxaliplatin, administered every three weeks, combined with 5-fluorouracil in colorectal cancer patients. *Clin Cancer Res*. 1997;3(6):891–899. PMID:9815764.
28. Zygulska AL, Banach M, Krzemieniecki K. Electroneurography in the evaluation of oxaliplatin-induced neuropathy in colorectal cancer patients. *Neoplasma*. 2016;63(4):617–622. doi:10.4149/neo_2016_416
29. Warren G, Osborn M, Tsantoulas C, et al. Discovery and preclinical evaluation of a novel inhibitor of FABP5, ART26.12, effective in oxaliplatin-induced peripheral neuropathy. *J Pain*. 2024;25(7):104470. doi:10.1016/j.jpain.2024.01.335
30. Pozzi E, Fumagalli G, Chiorazzi A, et al. The relevance of multimodal assessment in experimental oxaliplatin-induced peripheral neurotoxicity. *Exp Neurol*. 2020;334:113458. doi:10.1016/j.expneurol.2020.113458
31. Ballarini E, Malacrida A, Rodriguez-Menendez V, et al. Sodium-calcium exchanger 2: A pivotal role in oxaliplatin induced peripheral neurotoxicity and axonal damage? *Int J Mol Sci*. 2022;23(17):10063. doi:10.3390/ijms231710063
32. Park SB, Lin CSY, Kiernan MC. Nerve excitability assessment in chemotherapy-induced neurotoxicity. *J Vis Exp*. 2012;(62):3439. doi:10.3791/3439
33. Heide R, Bostock H, Ventzel L, et al. Axonal excitability changes and acute symptoms of oxaliplatin treatment: In vivo evidence for slowed sodium channel inactivation. *Clin Neurophysiol*. 2018;129(3):694–706. doi:10.1016/j.clinph.2017.11.015
34. Makker PGS, White D, Lees JG, et al. Acute changes in nerve excitability following oxaliplatin treatment in mice. *J Neurophysiol*. 2020; 124(1):232–244. doi:10.1152/jn.00260.2020
35. Kokotis P, Papantoniou M, Carr RW, et al. Oxaliplatin-induced acute neurotoxicity recovers between repeat infusion cycles: An axonal excitability repeated multiple measurements study. *Cancer Diagn Progn*. 2024;4(3):320–325. doi:10.21873/cdp.10327
36. Chen X, Gan Y, Au NPB, Ma CHE. Current understanding of the molecular mechanisms of chemotherapy-induced peripheral neuropathy. *Front Mol Neurosci*. 2024;17:1345811. doi:10.3389/fnmol.2024.1345811
37. Shao J, Yu W, Wei W, et al. MAPK-ERK-CREB signaling pathway upregulates Nav1.6 in oxaliplatin-induced neuropathic pain in the rat. *Toxicol Lett*. 2023;384:149–160. doi:10.1016/j.toxlet.2023.07.010
38. Sprowl JA, Ciarimboli G, Lancaster CS, et al. Oxaliplatin-induced neurotoxicity is dependent on the organic cation transporter OCT2. *Proc Natl Acad Sci U S A*. 2013;110(27):11199–11204. doi:10.1073/pnas.1305321110
39. Cui W, Wu H, Yu X, Song T, Xu X, Xu F. The calcium channel α2δ1 subunit: Interactional targets in primary sensory neurons and role in neuropathic pain. *Front Cell Neurosci*. 2021;15:699731. doi:10.3389/fncel.2021.699731
40. Li Y, Yuan T, Huang B, et al. Structure of human NaV1.6 channel reveals Na^+ selectivity and pore blockade by 4,9-anhydro-tetrodotoxin. *Nat Commun*. 2023;14(1):1030. doi:10.1038/s41467-023-36766-9
41. Dionisi M, Riva B, Delconti M, et al. Inhibition of NHE1 transport activity and gene transcription in DRG neurons in oxaliplatin-induced painful peripheral neurotoxicity. *Sci Rep*. 2023;13(1):3991. doi:10.1038/s41598-023-31095-9
42. Agnes JP, Dos Santos B, Das Neves RN, et al. β-caryophyllene inhibits oxaliplatin-induced peripheral neuropathy in mice: Role of cannabinoid type 2 receptors, oxidative stress and neuroinflammation. *Antioxidants (Basel)*. 2023;12(10):1893. doi:10.3390/antiox12101893
43. Branca JJV, Maresca M, Morucci G, et al. Oxaliplatin-induced blood–brain barrier loosening: A new point of view on chemotherapy-induced neurotoxicity. *Oncotarget*. 2018;9(34):23426–23438. doi:10.18632/oncotarget.25193
44. Musch MW, Walsh-Reitz MM, Chang EB. Roles of ZO-1, occludin, and actin in oxidant-induced barrier disruption. *Am J Physiol Gastrointest Liver Physiol*. 2006;290(2):G222–G231. doi:10.1152/ajpgi.00301.2005
45. Eastern Cooperative Oncology Group (ECOG). ECOG Common Toxicity Criteria. Eastern Cooperative Oncology Group (ECOG); 2016. www.ecog.org/general/ctc.pdf.
46. World Health Organization (WHO). WHO Toxicity Scale. Geneva, Switzerland: World Health Organization (WHO); 2010. www.oncoprof.net/Generale2000/g09_Chimiotherapie/Complements/g09-gb_comp01.htm.
47. Abrahm JL. Assessment and management of patients with chemotherapy-induced peripheral neuropathy. *Hematologist*. 2014;11(3). doi:10.1182/hem.V11.3.2728
48. Cheng HL, Lopez V, Lam SC, et al. Psychometric testing of the Functional Assessment of Cancer Therapy/Gynecologic Oncology Group–Neurotoxicity (FACT/GOG-Ntx) subscale in a longitudinal study of cancer patients treated with chemotherapy. *Health Qual Life Outcomes*. 2020;18(1):246. doi:10.1186/s12955-020-01493-y
49. Kaplow R, Iyere K. Grading chemotherapy-induced peripheral neuropathy in adults. *Nursing*. 2017;47(2):67–68. doi:10.1097/01.NURSE.0000511823.41645.a1
50. Smith EML, Zanville N, Kanzawa-Lee G, et al. Rasch model-based testing of the European Organisation for Research and Treatment of Cancer (EORTC) Quality of Life Questionnaire–Chemotherapy-Induced Peripheral Neuropathy (QLQ-CIPN20) using Alliance for Clinical Trials in Oncology (Alliance) A151408 study data. *Support Care Cancer*. 2019; 27(7):2599–2608. doi:10.1007/s00520-018-4553-y
51. Gu Z, Chen C, Gu J, et al. Development and validation of the chemotherapy-induced peripheral neuropathy integrated assessment–oxaliplatin subscale: A prospective cohort study. *BMC Cancer*. 2023;23(1):1109. doi:10.1186/s12885-023-11541-7
52. Tan AC, McCrary JM, Park SB, Trinh T, Goldstein D. Chemotherapy-induced peripheral neuropathy: Patient-reported outcomes compared with NCI-CTCAE grade. *Support Care Cancer*. 2019;27(12):4771–4777. doi:10.1007/s00520-019-04781-6
53. Wang RY, Lin XL, Xiang ST, Sun QH, Ding XH. Risk factors for oxaliplatin-induced peripheral neuropathy: A systematic review and meta-analysis. *Eur Rev Med Pharmacol Sci*. 2022;26(11):4028–4043. doi:10.26355/eurrev_202206_28973
54. Timmins HC, Mizrahi D, Li T, Kiernan MC, Goldstein D, Park SB. Metabolic and lifestyle risk factors for chemotherapy-induced peripheral neuropathy in taxane and platinum-treated patients: A systematic review. *J Cancer Surviv*. 2023;17(1):222–236. doi:10.1007/s11764-021-00988-x
55. Timmins HC, Li T, Goldstein D, et al. The impact of obesity on neuropathy outcomes for paclitaxel- and oxaliplatin-treated cancer survivors. *J Cancer Surviv*. 2022;16(2):223–232. doi:10.1007/s11764-021-01012-y
56. Mizrahi D, Park SB, Li T, et al. Hemoglobin, body mass index, and age as risk factors for paclitaxel- and oxaliplatin-induced peripheral neuropathy. *JAMA Netw Open*. 2021;4(2):e2036695. doi:10.1001/jamanetworkopen.2020.36695
57. Griffith KA, Zhu S, Johantgen M, et al. Oxaliplatin-induced peripheral neuropathy and identification of unique severity groups in colorectal cancer. *J Pain Symptom Manage*. 2017;54(5):701–706.e1. doi:10.1016/j.jpainsymman.2017.07.033
58. Ben Mahmoud IT, Ben Said A, Berguiga S, et al. Incidence and risk factors associated with development of oxalipatin-induced acute peripheral neuropathy in colorectal cancer patients. *J Oncol Pharm Pract*. 2023;29(2):311–318. doi:10.1177/10781552211068138
59. Lee S, Ma C, Shi Q, et al. Potential mediators of oxaliplatin-induced peripheral neuropathy from adjuvant therapy in stage III colon cancer: Findings from CALGB (Alliance)/SWOG 80702. *J Clin Oncol*. 2023; 41(5):1079–1091. doi:10.1200/JCO.22.01637
60. Hershman DL, Till C, Wright JD, et al. Comorbidities and risk of chemotherapy-induced peripheral neuropathy among participants 65 years or older in Southwest Oncology Group Clinical Trials. *J Clin Oncol*. 2016;34(25):3014–3022. doi:10.1200/JCO.2015.66.2346
61. Yildirim N, Cengiz M. Predictive clinical factors of chronic peripheral neuropathy induced by oxaliplatin. *Support Care Cancer*. 2020; 28(10):4781–4788. doi:10.1007/s00520-020-05319-x
62. Raphael MJ, Fischer HD, Fung K, et al. Neurotoxicity outcomes in a population-based cohort of elderly patients treated with adjuvant oxaliplatin for colorectal cancer. *Clin Colorectal Cancer*. 2017; 16(4):397–404.e1. doi:10.1016/j.clcc.2017.03.013
63. Argyriou AA, Briani C, Cavaletti G, et al. Advanced age and liability to oxaliplatin-induced peripheral neuropathy: Post hoc analysis of a prospective study. *Eur J Neurol*. 2013;20(5):788–794. doi:10.1111/ene.12061

64. Sugihara K, Ohtsu A, Shimada Y, et al. Analysis of neurosensory adverse events induced by FOLFOX 4 treatment in colorectal cancer patients: A comparison between two Asian studies and four Western studies. *Cancer Med*. 2012;1(2):198–206. doi:10.1002/cam4.25
65. Wiela-Hojeńska A, Kowalska T, Filipczyk-Cisarż E, Łapiński Ł, Nartowski K. Evaluation of the toxicity of anticancer chemotherapy in patients with colon cancer. *Adv Clin Exp Med*. 2015;24(1):103–111. doi:10.17219/acem/38154
66. Vincenzi B, Frezza AM, Schiavon G, et al. Identification of clinical predictive factors of oxaliplatin-induced chronic peripheral neuropathy in colorectal cancer patients treated with adjuvant Folfox IV. *Support Care Cancer*. 2013;21(5):1313–1319. doi:10.1007/s00520-012-1667-5
67. Kim J, Ji E, Jung K, et al. Gender differences in patients with metastatic pancreatic cancer who received FOLFIRINOX. *J Pers Med*. 2021;11(2):83. doi:10.3390/jpm11020083
68. Zribi A, Nasr SB, Hamdi S, et al. Oxaliplatin-induced peripheral neuropathy risk factors and management in Tunisian population. *Pan Afr Med J*. 2020;35:83. doi:10.11604/pamj.2020.35.83.18357
69. Dijksterhuis WPM, Pruijt MJ, Van Der Woude SO, et al. Association between body composition, survival, and toxicity in advanced esophagogastric cancer patients receiving palliative chemotherapy. *J Cachexia Sarcopenia Muscle*. 2019;10(1):199–206. doi:10.1002/jcsm.12371
70. André T, Boni C, Mounedji-Boudiaf L, et al. Oxaliplatin, fluorouracil, and leucovorin as adjuvant treatment for colon cancer. *N Engl J Med*. 2004;350(23):2343–2351. doi:10.1056/NEJMoa032709
71. Park SB, Lin CSY, Krishnan AV, Goldstein D, Friedlander ML, Kiernan MC. Oxaliplatin-induced neurotoxicity: Changes in axonal excitability precede development of neuropathy. *Brain*. 2009;132(10):2712–2723. doi:10.1093/brain/awp219
72. Kanbayashi Y, Ishikawa T, Kuriu Y, Otsuji E, Takayama K. Predictors for development of oxaliplatin-induced peripheral neuropathy in cancer patients as determined by ordered logistic regression analysis. *PLoS One*. 2022;17(9):e0275481. doi:10.1371/journal.pone.0275481
73. Palugulla S, Dkhar SA, Kayal S, Narayan S. Oxaliplatin-induced peripheral neuropathy in South Indian cancer patients: A prospective study in digestive tract cancer patients. *Ind J Med Paediatr Oncol*. 2017;38(4):502–507. doi:10.4103/ijmpo.ijmpo_143_17
74. Brouwers EEM, Huitema ADR, Boogerd W, Beijnen JH, Schellens JHM. Persistent neuropathy after treatment with cisplatin and oxaliplatin. *Acta Oncol*. 2009;48(6):832–841. doi:10.1080/02841860902806609
75. Lemanska A, Harkin A, Iveson T, Kelly C, Saunders M, Faithfull S. The association of clinical and patient factors with chemotherapy-induced peripheral neuropathy (CIPN) in colorectal cancer: Secondary analysis of the SCOT trial. *ESMO Open*. 2023;8(6):102063. doi:10.1016/j.esmoop.2023.102063
76. Tanishima H, Tominaga T, Kimura M, Maeda T, Shirai Y, Horiuchi T. Hyperacute peripheral neuropathy is a predictor of oxaliplatin-induced persistent peripheral neuropathy. *Support Care Cancer*. 2017;25(5):1383–1389. doi:10.1007/s00520-016-3514-6
77. Housley SN, Nardelli P, Carrasco DI, et al. Cancer exacerbates chemotherapy-induced sensory neuropathy. *Cancer Res*. 2020;80(13):2940–2955. doi:10.1158/0008-5472.CAN-19-2331
78. Altaf R, Lund Brixen A, Kristensen B, Nielsen SE. Incidence of cold-induced peripheral neuropathy and dose modification of adjuvant oxaliplatin-based chemotherapy for patients with colorectal cancer. *Oncology*. 2014;87(3):167–172. doi:10.1159/000362668
79. Morales M, Ávila J, González-Fernández R, Boronat L, Soriano M, Martín-Vasallo P. Differential transcriptome profile of peripheral white cells to identify biomarkers involved in oxaliplatin induced neuropathy. *J Pers Med*. 2014;4(2):282–296. doi:10.3390/jpm4020282
80. Cliff J, Jorgensen AL, Lord R, et al. The molecular genetics of chemotherapy-induced peripheral neuropathy: A systematic review and meta-analysis. *Crit Rev Oncol Hematol*. 2017;120:127–140. doi:10.1016/j.critrevonc.2017.09.009
81. Briani C, Argyriou AA, Izquierdo C, et al. Long-term course of oxaliplatin-induced polyneuropathy: A prospective 2-year follow-up study. *J Peripher Nerv Syst*. 2014;19(4):299–306. doi:10.1111/jns.12097
82. Bennedsgaard K, Ventzel L, Andersen NT, et al. Oxaliplatin- and docetaxel-induced polyneuropathy: Clinical and neurophysiological characteristics. *J Peripher Nerv Syst*. 2020;25(4):377–387. doi:10.1111/jns.12413
83. Kokotis P, Schmelz M, Kostouros E, Karandreas N, Dimopoulos MA. Oxaliplatin-induced neuropathy: A long-term clinical and neurophysiologic follow-up study. *Clin Colorectal Cancer*. 2016;15(3):e133–140. doi:10.1016/j.clcc.2016.02.009
84. Preston DC, Shapiro BE. *Electromyography and Neuromuscular Disorders: Clinical-Electrophysiologic-Ultrasound Correlations*. 4th ed. Philadelphia, USA: Elsevier; 2021. ISBN:978-0-323-66180-5.
85. Goedee HS, Herraets IJT, Visser LH, et al. Nerve ultrasound can identify treatment-responsive chronic neuropathies without electrodiagnostic features of demyelination. *Muscle Nerve*. 2019;60(4):415–419. doi:10.1002/mus.26629
86. Herraets IJT, Goedee HS, Telleman JA, et al. Nerve ultrasound improves detection of treatment-responsive chronic inflammatory neuropathies. *Neurology*. 2020;94(14):e1470–e1479. doi:10.1212/WNL.0000000000008978
87. Grimm A, Oertl H, Auffenberg E, et al. Differentiation between Guillain–Barré syndrome and acute-onset chronic inflammatory demyelinating polyradiculoneuritis: A prospective follow-up study using ultrasound and neurophysiological measurements. *Neurotherapeutics*. 2019;16(3):838–847. doi:10.1007/s13311-019-00716-5
88. Kramer M, Grimm A, Winter N, et al. Nerve ultrasound as helpful tool in polyneuropathies. *Diagnostics (Basel)*. 2021;11(2):211. doi:10.3390/diagnostics11020211
89. Pigońska J, Paweł W, Banach M. Neurophysiological and ultrasound correlations in Guillain–Barré syndrome and CIDP: Case series. *J Pers Med*. 2024;14(6):603. doi:10.3390/jpm14060603
90. Briani C, Campagnolo M, Lucchetta M, et al. Ultrasound assessment of oxaliplatin-induced neuropathy and correlations with neurophysiologic findings. *Eur J Neurol*. 2013;20(1):188–192. doi:10.1111/j.1468-1331.2012.03852.x
91. Kawashiri T, Mine K, Kobayashi D, et al. Therapeutic agents for oxaliplatin-induced peripheral neuropathy: Experimental and clinical evidence. *Int J Mol Sci*. 2021;22(3):1393. doi:10.3390/ijms22031393
92. Ghirardi O, Lo Giudice P, Pisano C, et al. Acetyl-L-carnitine prevents and reverts experimental chronic neurotoxicity induced by oxaliplatin, without altering its antitumor properties. *Anticancer Res*. 2005;25(4):2681–2687. PMID:16080512.
93. Joseph EK, Chen X, Bogen O, Levine JD. Oxaliplatin acts on IB4-positive nociceptors to induce an oxidative stress-dependent acute painful peripheral neuropathy. *J Pain*. 2008;9(5):463–472. doi:10.1016/j.jpain.2008.01.335
94. Zheng H, Xiao WH, Bennett GJ. Functional deficits in peripheral nerve mitochondria in rats with paclitaxel- and oxaliplatin-evoked painful peripheral neuropathy. *Exp Neurol*. 2011;232(2):154–161. doi:10.1016/j.expneurol.2011.08.016
95. Lee M, Cho S, Roh K, et al. Glutathione alleviated peripheral neuropathy in oxaliplatin-treated mice by removing aluminum from dorsal root ganglia. *Am J Transl Res*. 2017;9(3):926–939. PMID:28386322. PMCID:PMC5375987.
96. Areti A, Komirishetty P, Kumar A. Carvedilol prevents functional deficits in peripheral nerve mitochondria of rats with oxaliplatin-evoked painful peripheral neuropathy. *Toxicol Appl Pharmacol*. 2017;322:97–103. doi:10.1016/j.taap.2017.03.009
97. Miyagi A, Kawashiri T, Shimizu S, Shigematsu N, Kobayashi D, Shimazoe T. Dimethyl fumarate attenuates oxaliplatin-induced peripheral neuropathy without affecting the anti-tumor activity of oxaliplatin in rodents. *Biol Pharm Bull*. 2019;42(4):638–644. doi:10.1248/bpb.b18-00855
98. Kawashiri T, Shimizu S, Shigematsu N, Kobayashi D, Shimazoe T. Donepezil ameliorates oxaliplatin-induced peripheral neuropathy via a neuroprotective effect. *J Pharmacol Sci*. 2019;140(3):291–294. doi:10.1016/j.jphs.2019.05.009
99. Zanardelli M, Micheli L, Cinci L, Failli P, Ghelardini C, Di Cesare Mannelli L. Oxaliplatin neurotoxicity involves peroxisome alterations: PPARγ agonism as preventive pharmacological approach. *PLoS One*. 2014;9(7):e102758. doi:10.1371/journal.pone.0102758
100. Afonseca SOD, Cruz FM, Cubero DDIG, et al. Vitamin E for prevention of oxaliplatin-induced peripheral neuropathy: A pilot randomized clinical trial. *Sao Paulo Med J*. 2013;131(1):35–38. doi:10.1590/S1516-31802013000100006
101. Salehi Z, Roayaei M. Effect of vitamin E on oxaliplatin-induced peripheral neuropathy prevention: A randomized controlled trial. *Int J Prev Med*. 2015;6(1):104. doi:10.4103/2008-7802.169021

102. Cheng X, Huo J, Wang D, et al. Herbal medicine AC591 prevents oxaliplatin-induced peripheral neuropathy in animal model and cancer patients. *Front Pharmacol*. 2017;8:344. doi:10.3389/fphar.2017.00344
103. Wan CF, Zheng LL, Liu Y, Yu X. Houttuynia cordata Thunb reverses oxaliplatin-induced neuropathic pain in rat by regulating Th17/Treg balance. *Am J Transl Res*. 2016;8(3):1609–1614. PMID:27186286. PMCID:PMC4859645.
104. Robinson CR, Zhang H, Dougherty PM. Astrocytes, but not microglia, are activated in oxaliplatin and bortezomib-induced peripheral neuropathy in the rat. *Neuroscience*. 2014;274:308–317. doi:10.1016/j.neuroscience.2014.05.051
105. Duan Z, Su Z, Wang H, Pang X. Involvement of pro-inflammation signal pathway in inhibitory effects of rapamycin on oxaliplatin-induced neuropathic pain. *Mol Pain*. 2018;14:1744806918769426. doi:10.1177/1744806918769426
106. Di Cesare Mannelli L, Lucarini E, Micheli L, et al. Effects of natural and synthetic isothiocyanate-based H 2 S-releasers against chemotherapy-induced neuropathic pain: Role of Kv7 potassium channels. *Neuropharmacology*. 2017;121:49–59. doi:10.1016/j.neuropharm.2017.04.029
107. Poupon L, Lamoine S, Pereira V, et al. Targeting the TREK-1 potassium channel via riluzole to eliminate the neuropathic and depressive-like effects of oxaliplatin. *Neuropharmacology*. 2018;140:43–61. doi:10.1016/j.neuropharm.2018.07.026
108. Zhao M, Nakamura S, Miyake T, et al. Pharmacological characterization of standard analgesics on oxaliplatin-induced acute cold hypersensitivity in mice. *J Pharmacol Sci*. 2014;124(4):514–517. doi:10.1254/jphs.13249SC
109. Deuis JR, Lim YL, Rodrigues de Sousa S, et al. Analgesic effects of clinically used compounds in novel mouse models of polyneuropathy induced by oxaliplatin and cisplatin. *Neuro Oncol*. 2014;16(10):1324–1332. doi:10.1093/neuonc/nou048
110. Ohsawa M, Otake S, Murakami T, Yamamoto S, Makino T, Ono H. Gabapentin prevents oxaliplatin-induced mechanical hyperalgesia in mice. *J Pharmacol Sci*. 2014;125(3):292–299. doi:10.1254/jphs.14058FP
111. Aoki M, Kurauchi Y, Mori A, Nakahara T, Sakamoto K, Ishii K. Comparison of the effects of single doses of elcatonin and pregabalin on oxaliplatin-induced cold and mechanical allodynia in rats. *Biol Pharm Bull*. 2014;37(2):322–326. doi:10.1248/bpb.b13-00735
112. Gauchan P, Andoh T, Kato A, Kuraishi Y. Involvement of increased expression of transient receptor potential melastatin 8 in oxaliplatin-induced cold allodynia in mice. *Neurosci Lett*. 2009;458(2):93–95. doi:10.1016/j.neulet.2009.04.029
113. Ta LE, Bieber AJ, Carlton SM, Loprinzi CL, Low PA, Windebank AJ. Transient receptor potential vanilloid 1 is essential for cisplatin-induced heat hyperalgesia in mice. *Mol Pain*. 2010;6:1744-8069-6-15. doi:10.1186/1744-8069-6-15
114. Descoeur J, Pereira V, Pizzoccaro A, et al. Oxaliplatin-induced cold hypersensitivity is due to remodelling of ion channel expression in nociceptors. *EMBO Mol Med*. 2011;3(5):266–278. doi:10.1002/emmm.201100134
115. Alberti P, Canta A, Chiorazzi A, et al. Topiramate prevents oxaliplatin-related axonal hyperexcitability and oxaliplatin induced peripheral neurotoxicity. *Neuropharmacology*. 2020;164:107905. doi:10.1016/j.neuropharm.2019.107905
116. Shidahara Y, Ogawa S, Nakamura M, et al. Pharmacological comparison of a nonhuman primate and a rat model of oxaliplatin-induced neuropathic cold hypersensitivity. *Pharmacology Res Perspect*. 2016;4(1):e00216. doi:10.1002/prp2.216
117. Furgała A, Sałat R, Sałat K. Acute cold allodynia induced by oxaliplatin is attenuated by amitriptyline. *Acta Neurobiol Exp (Wars)*. 2018;78(4):315–321. PMID:30624430.
118. Yeo JH, Yoon SY, Kwon SK, et al. Repetitive acupuncture point treatment with diluted bee venom relieves mechanical allodynia and restores intraepidermal nerve fiber loss in oxaliplatin-induced neuropathic mice. *J Pain*. 2016;17(3):298–309. doi:10.1016/j.jpain.2015.10.018
119. Kim W, Kim M, Go D, Min BI, Na H, Kim S. Combined effects of bee venom acupuncture and morphine on oxaliplatin-induced neuropathic pain in mice. *Toxins (Basel)*. 2016;8(2):33. doi:10.3390/toxins8020033
120. Lim BS, Moon HJ, Li DX, et al. Effect of bee venom acupuncture on oxaliplatin-induced cold allodynia in rats. *Evid Based Complement Alternat Med*. 2013;2013:369324. doi:10.1155/2013/369324
121. Li D, Lee Y, Kim W, Lee K, Bae H, Kim S. Analgesic effects of bee venom derived phospholipase A2 in a mouse model of oxaliplatin-induced neuropathic pain. *Toxins (Basel)*. 2015;7(7):2422–2434. doi:10.3390/toxins7072422
122. Kim W, Chung Y, Choi S, Min BI, Kim SK. Duloxetine protects against oxaliplatin-induced neuropathic pain and spinal neuron hyperexcitability in rodents. *Int J Mol Sci*. 2017;18(12):2626. doi:10.3390/ijms18122626
123. Balayssac D, Ling B, Ferrier J, Pereira B, Eschalier A, Authier N. Assessment of thermal sensitivity in rats using the thermal place preference test: Description and application in the study of oxaliplatin-induced acute thermal hypersensitivity and inflammatory pain models. *Behav Pharmacol*. 2014;25(2):99–111. doi:10.1097/FBP.0000000000000026
124. Baptista-de-Souza D, Di Cesare Mannelli L, Zanardelli M, et al. Serotonergic modulation in neuropathy induced by oxaliplatin: Effect on the 5HT2C receptor. *Eur J Pharmacol*. 2014;735:141–149. doi:10.1016/j.ejphar.2014.04.028
125. Choi S, Chae HK, Heo H, Hahm DH, Kim W, Kim SK. Analgesic effect of melittin on oxaliplatin-induced peripheral neuropathy in rats. *Toxins (Basel)*. 2019;11(7):396. doi:10.3390/toxins11070396
126. Sałat K, Kołaczkowski M, Furgała A, et al. Antinociceptive, antiallodynic and antihyperalgesic effects of the 5-HT1A receptor selective agonist, NLX-112 in mouse models of pain. *Neuropharmacology*. 2017;125:181–188. doi:10.1016/j.neuropharm.2017.07.022
127. Yoon SY, Lee JY, Roh DH, Oh SB. Pharmacopuncture with *Scolopendra subspinipes* suppresses mechanical allodynia in oxaliplatin-induced neuropathic mice and potentiates clonidine-induced anti-allodynia without hypotension or motor impairment. *J Pain*. 2018;19(10):1157–1168. doi:10.1016/j.jpain.2018.04.015
128. Andoh T, Sakamoto A, Kuraishi Y. 5-HT1A receptor agonists, xaliproden and tandospirone, inhibit the increase in the number of cutaneous mast cells involved in the exacerbation of mechanical allodynia in oxaliplatin-treated mice. *J Pharmacol Sci*. 2016;131(4):284–287. doi:10.1016/j.jphs.2016.07.008
129. Micov AM, Tomić MA, Todorović MB, et al. Vortioxetine reduces pain hypersensitivity and associated depression-like behavior in mice with oxaliplatin-induced neuropathy. *Prog Neuropsychopharmacol Biol Psychiatry*. 2020;103:109975. doi:10.1016/j.pnpbp.2020.109975
130. Aghili M, Darzikolaee NM, Babaei M, et al. Duloxetine for the prevention of oxaliplatin induced peripheral neuropathy: A randomized, placebo-controlled, double-blind clinical trial. *J Gastrointest Cancer*. 2023;54(2):467–474. doi:10.1007/s12029-022-00824-0
131. Smith EML, Pang H, Cirrincione C, et al. Effect of duloxetine on pain, function, and quality of life among patients with chemotherapy-induced painful peripheral neuropathy: A randomized clinical trial. *JAMA*. 2013;309(13):1359. doi:10.1001/jama.2013.2813
132. Jordan B, Margulies A, Cardoso F, et al. Systemic anticancer therapy-induced peripheral and central neurotoxicity: ESMO–EONS–EANO Clinical Practice Guidelines for diagnosis, prevention, treatment and follow-up. *Ann Oncol*. 2020;31(10):1306–1319. doi:10.1016/j.annonc.2020.07.003
133. Yang Y, Zhao B, Gao X, et al. Targeting strategies for oxaliplatin-induced peripheral neuropathy: Clinical syndrome, molecular basis, and drug development. *J Exp Clin Cancer Res*. 2021;40(1):331. doi:10.1186/s13046-021-02141-z
134. Wagner MA, Smith EML, Ayyash N, Holden JE. Prazosin as an adjuvant to increase effectiveness of duloxetine in a rat model of oxaliplatin-induced peripheral neuropathy. *Semin Oncol Nurs*. 2024;40(5):151686. doi:10.1016/j.soncn.2024.151686
135. Yamamoto S, Ushio S, Egashira N, et al. Excessive spinal glutamate transmission is involved in oxaliplatin-induced mechanical allodynia: A possibility for riluzole as a prophylactic drug. *Sci Rep*. 2017;7(1):9661. doi:10.1038/s41598-017-08891-1
136. Fariello RG, Ghelardini C, Di Cesare Mannelli L, et al. Broad spectrum and prolonged efficacy of dimiracetam in models of neuropathic pain. *Neuropharmacology*. 2014;81:85–94. doi:10.1016/j.neuropharm.2014.01.029
137. Wozniak KM, Wu Y, Vornov JJ, et al. The orally active glutamate carboxypeptidase II inhibitor E2072 exhibits sustained nerve exposure and attenuates peripheral neuropathy. *J Pharmacol Exp Ther*. 2012;343(3):746–754. doi:10.1124/jpet.112.197665

138. Zhou HH, Zhang L, Zhang HX, et al. Tat-HA-NR2B9c attenuate oxaliplatin-induced neuropathic pain. *Exp Neurol*. 2019;311:80–87. doi:10.1016/j.expneurol.2018.09.014
139. Liu X, Zhang G, Dong L, et al. Repeated administration of mirtazapine attenuates oxaliplatin-induced mechanical allodynia and spinal NR2B upregulation in rats. *Neurochem Res*. 2013;38(9):1973–1979. doi:10.1007/s11064-013-1103-3
140. Mihara Y, Egashira N, Sada H, et al. Involvement of spinal NR2B-containing NMDA receptors in oxaliplatin-induced mechanical allodynia in rats. *Mol Pain*. 2011;7:1744-8069-7-8. doi:10.1186/1744-8069-7-8
141. Sada H, Egashira N, Ushio S, Kawashiri T, Shirahama M, Oishi R. Repeated administration of amitriptyline reduces oxaliplatin-induced mechanical allodynia in rats. *J Pharmacol Sci*. 2012;118(4):547–551. doi:10.1254/jphs.12006SC
142. Shirahama M, Ushio S, Egashira N, et al. Inhibition of Ca^2/calmodulin-dependent protein kinase II reverses oxaliplatin-induced mechanical allodynia in rats. *Mol Pain*. 2012;8:1744-8069-8-26. doi:10.1186/1744-8069-8-26
143. Gamelin L, Boisdron-Celle M, Delva R, et al. Prevention of oxaliplatin-related neurotoxicity by calcium and magnesium infusions. *Clin Cancer Res*. 2004;10(12):4055–4061. doi:10.1158/1078-0432.CCR-03-0666
144. Knijn N, Tol J, Koopman M, et al. The effect of prophylactic calcium and magnesium infusions on the incidence of neurotoxicity and clinical outcome of oxaliplatin-based systemic treatment in advanced colorectal cancer patients. *Eur J Cancer*. 2011;47(3):369–374. doi:10.1016/j.ejca.2010.10.006
145. Xu XT, Dai ZH, Xu Q, et al. Safety and efficacy of calcium and magnesium infusions in the chemoprevention of oxaliplatin-induced sensory neuropathy in gastrointestinal cancers. *J Digest Dis*. 2013;14(6):288–298. doi:10.1111/1751-2980.12050
146. Loprinzi CL, Qin R, Dakhil SR, et al. Phase III randomized, placebo-controlled, double-blind study of intravenous calcium and magnesium to prevent oxaliplatin-induced sensory neurotoxicity (N08CB/Alliance). *J Clin Oncol*. 2014;32(10):997–1005. doi:10.1200/JCO.2013.52.0536
147. Pachman DR, Ruddy K, Sangaralingham LR, et al. Calcium and magnesium use for oxaliplatin-induced neuropathy: A case study to assess how quickly evidence translates into practice. *J Natl Compr Canc Netw*. 2015;13(9):1097–1101. doi:10.6004/jnccn.2015.0134
148. Jordan B, Jahn F, Beckmann J, Unverzagt S, Müller-Tidow C, Jordan K. Calcium and magnesium infusions for the prevention of oxaliplatin-induced peripheral neurotoxicity: A systematic review. *Oncology*. 2016;90(6):299–306. doi:10.1159/000445977
149. Beijers AJM, Bonhof CS, Mols F, et al. Multicenter randomized controlled trial to evaluate the efficacy and tolerability of frozen gloves for the prevention of chemotherapy-induced peripheral neuropathy. *Ann Oncol*. 2020;31(1):131–136. doi:10.1016/j.annonc.2019.09.006
150. Arslan S, Zorba Bahceli P, İlik Y, Artaç M. The preliminary effects of henna on chemotherapy-induced peripheral neuropathy in women receiving oxaliplatin-based treatment: A parallel-group, randomized, controlled pilot trial. *Eur J Oncol Nurs*. 2020;48:101827. doi:10.1016/j.ejon.2020.101827
151. Gehr NL, Karlsson P, Timm S, et al. Study protocol: Fish oil supplement in prevention of oxaliplatin-induced peripheral neuropathy in adjuvant colorectal cancer patients. A randomized controlled trial (OxaNeuro). *BMC Cancer*. 2024;24(1):168. doi:10.1186/s12885-024-11856-z
152. Maia JRLCB, Machado LKA, Fernandes GG, et al. Mitotherapy prevents peripheral neuropathy induced by oxaliplatin in mice. *Neuropharmacology*. 2024;245:109828. doi:10.1016/j.neuropharm.2023.109828
153. Kato Y, Tateai Y, Ohkubo M, et al. Gosha-jinki-gan reduced oxaliplatin-induced hypersensitivity to cold sensation and its effect would be related to suppression of the expression of TRPM8 and TRPA1 in rats. *Anticancer Drugs*. 2014;25(1):39–43. doi:10.1097/CAD.0000000000000022
154. Mizuno K, Kono T, Suzuki Y, et al. Goshajinkigan, a traditional Japanese medicine, prevents oxaliplatin-induced acute peripheral neuropathy by suppressing functional alteration of TRP channels in rat. *J Pharmacol Sci*. 2014;125(1):91–98. doi:10.1254/jphs.13244FP
154. Waissengrin B, Mirelman D, Pelles S, et al. Effect of cannabis on oxaliplatin-induced peripheral neuropathy among oncology patients: A retrospective analysis. *Ther Adv Med Oncol*. 2021;13:1758835921990203. doi:10.1177/1758835921990203
156. Nielsen SW, Hasselsteen SD, Dominiak HSH, et al. Oral cannabidiol for prevention of acute and transient chemotherapy-induced peripheral neuropathy. *Support Care Cancer*. 2022;30(11):9441–9451. doi:10.1007/s00520-022-07312-y

Diagnostic challenges in progressive familial intrahepatic cholestasis type 3 (PFIC3) misdiagnosed as Wilson's disease: A systematic review

Eyad Gadour[1,2,A–F], Bogdan Miutescu[3,4,A,E,F], Mohammed Saad AlQahtani[1,5,A,B,E,F], Deiana Vuletici[3,4,B–D], Ghassan Elsayed[6,B,D–F], Ielmina Domilescu[7,B–E], Antonio Facciorusso[8,A–F]

[1] Multiorgan Transplant Centre of Excellence, Liver Transplantation Unit, King Fahad Specialist Hospital, Dammam, Saudi Arabia
[2] Department of Medicine, Zamzam University College, School of Medicine, Khartoum, Sudan
[3] Department of Gastroenterology and Hepatology, University of Medicine and Pharmacy Victor Babes, Timișoara, Romania
[4] Advanced Regional Research Centre, University of Medicine and Pharmacy Victor Babes, Timișoara, Romania
[5] Department of Surgery, Imam Abdulrahman Bin Faisal University, Dammam, Saudi Arabia
[6] Department of Gastroenterology, Mediclinic Middle East Hospital, Abu Dhabi, UAE
[7] Doctoral School, Department of Gastroenterology and Hepatology, Faculty of Medicine, Victor Babes, Timișoara, Romania
[8] Department of Surgical and Medical Sciences, Section of Gastroenterology, University of Foggia, Italy

A – research concept and design; B – collection and/or assembly of data; C – data analysis and interpretation; D – writing the article; E – critical revision of the article; F – final approval of the article

Advances in Clinical and Experimental Medicine, ISSN 1899–5276 (print), ISSN 2451–2680 (online) *Adv Clin Exp Med*. 2026;35(7):1297–1305

Address for correspondence
Eyad Gadour
E-mail: eyadgadour@doctors.org.uk

Funding sources
None declared

Conflict of interest
None declared

Received on May 31, 2025
Reviewed on September 1, 2025
Accepted on October 1, 2025

Published online on January 21, 2026

Abstract

Progressive familial intrahepatic cholestasis type 3 (PFIC3) is a rare liver disorder caused by biallelic mutations in the *ABCB4* gene, leading to multidrug resistance protein 3 (MDR3) deficiency. PFIC3 often presents with clinical and biochemical features that overlap with Wilson's disease (WD), including hepatic copper accumulation and elevated urinary copper excretion. These similarities contribute to frequent misdiagnosis, resulting in inappropriate chelation therapy and delayed appropriate management. This systematic review examines reported cases of PFIC3 initially misdiagnosed as WD to highlight diagnostic challenges and assess patient outcomes. A comprehensive search across PubMed, ScienceDirect and Google Scholar identified 11 eligible studies involving 16 patients. Most cases were first treated as WD, receiving chelation therapy without clinical improvement. Diagnosis was later revised to PFIC3 following negative ATP7B mutation testing and identification of ABCB4 variants, often via whole-genome sequencing. Upon switching to ursodeoxycholic acid (UDCA), most patients experienced clinical stabilization. The findings underscore the need for heightened awareness of PFIC3 as a differential diagnosis in atypical WD cases, especially when ceruloplasmin is normal and Kayser–Fleischer (KF) rings are absent. Early genetic testing is essential to avoid mismanagement. Further observational studies are warranted to estimate misdiagnosis frequency and guide diagnostic protocols.

Key words: progressive familial intrahepatic cholestasis type 3, Wilson disease, misdiagnosis, genetic testing, *ABCB4* gene

Cite as
Gadour E, Miutescu B, AlQahtani MS, et al. Diagnostic challenges in progressive familial intrahepatic cholestasis type 3 (PFIC3) misdiagnosed as Wilson's disease: A systematic review. *Adv Clin Exp Med*. 2026;35(7):1297–1305. doi:10.17219/acem/211596

DOI
10.17219/acem/211596

Copyright
Copyright by Author(s)
This is an article distributed under the terms of the Creative Commons Attribution 3.0 Unported (CC BY 3.0) (https://creativecommons.org/licenses/by/3.0/)

Highlights

- Progressive familial intrahepatic cholestasis type 3 caused by ABCB4 mutations is frequently misdiagnosed as Wilson's disease due to overlapping abnormalities in copper metabolism.
- A systematic review of 16 misdiagnosed cases showed that chelation therapy was ineffective, resulting in delayed initiation of appropriate treatment.
- Genetic testing for *ABCB4* mutations should be considered in atypical Wilson's disease presentations, particularly in patients with normal ceruloplasmin levels and absence of Kayser–Fleischer rings.
- Switching to ursodeoxycholic acid therapy led to clinical stabilization, highlighting the importance of early and accurate diagnosis.

Introduction

Progressive familial intrahepatic cholestasis type 3 (PFIC3) represents the most severe phenotype associated with multidrug resistance protein 3 (MDR3) deficiency.[1,2] This condition arises due to biallelic pathogenic variations in the ATP-binding cassette subfamily B member 4 (*ABCB4*) gene.[3] Patients typically exhibit symptoms such as hepatosplenomegaly, jaundice, discolored stools, and a history of pruritus.[4] In the majority of cases, the disease advances to portal hypertension, cirrhosis and liver failure within the first 2 decades of life.[5] The management of PFIC3 primarily involves the administration of ursodeoxycholic acid (UDCA), which is the current first-line treatment. Ursodeoxycholic acid therapy has demonstrated efficacy in ameliorating symptoms in PFIC3 patients and improving liver function.[6] This diagnostic overlap has substantial clinical implications, as inappropriate chelation therapy not only fails to halt disease progression but can also contribute to unnecessary treatment-related adverse effects and delayed liver transplantation.

A notable characteristic of PFIC3 is the disruption of copper metabolism secondary to intrahepatic cholestasis, as indicated by elevated hepatic and urinary copper levels. The elevated copper levels in PFIC3 lead to the mimicry of other diseases of impaired copper metabolism, such as Wilson's disease (WD). Wilson's disease is a rare autosomal recessive copper metabolism disorder caused by pathogenic mutations in the copper transporter gene *ATP7B*. According to the Leipzig diagnostic criteria for WD presented in Supplementary Table 2, patients are diagnosed with WD if they have a score ≥2. However, most PFIC3 patients also meet these requirements for WD, leading to some being misdiagnosed with WD.[7] This misdiagnosis results in the administration of chelation therapy, to which PFIC3 patients do not respond, ultimately leading to disease progression and deterioration of liver function over time.[7] Therefore, we conducted a systematic review to examine current reports of PFIC3 cases mimicking WD, identify diagnostic challenges and assess patient outcomes.

Objectives

The primary objectives of this systematic review are: 1) to examine current reports of PFIC3 cases mimicking WD; 2) to identify diagnostic challenges in differentiating PFIC3 from WD; and 3) to assess patient outcomes in cases of PFIC3 initially misdiagnosed as WD.

Materials and methods

Protocol and registration

The methodology employed in this review conformed to the PRISMA 2020 guidelines (Preferred Reporting Items for Systematic Reviews and Meta-Analyses).[8] This study has been registered in PROSPERO with registration No. CRD420251065032.

Literature search

Two independent authors conducted an extensive literature review for pertinent articles up to May 2025. The initial strategy employed a specified search criterion across 3 databases: PubMed, ScienceDirect and Google Scholar. Boolean expressions were utilized to combine keywords for the electronic search (progressive familial intrahepatic cholestasis OR PFIC3 OR ABCB4 disease OR MDR3 deficiency) AND (mimicking OR misdiagnosed). Following the completion of the database search, the reviewers manually examined the references of the identified studies to locate additional relevant studies.

Eligibility criteria

Following the retrieval of studies from the databases, each study was evaluated against a predetermined set of eligibility criteria prior to inclusion in the review. A study was incorporated into the review upon satisfying the following inclusion criteria: studies involving patients with PFIC3 presenting as WD, and studies designed as case reports, case series or observational studies.

The exclusion criteria for the review were applied to omit studies that did not meet the following conditions: 1) studies published in languages other than English; 2) studies that did not include patients with PFIC3; 3) studies that did not involve patients with a misdiagnosis or potential misdiagnosis of PFIC3 as WD; and 4) secondary studies such as narrative reviews, meta-analyses and systematic reviews.

Data extraction

Two reviewers independently performed the data extraction for this review. In instances where consensus was not initially achieved during the data extraction process, the reviewers engaged in discussions to resolve any discrepancies until agreement was reached. In accordance with the PRISMA guidelines, the authors examined all references obtained through various phases prior to data extraction. The initial phases involved screening abstracts to assess the relevance of the articles, leading to the elimination of irrelevant articles. Subsequently, the remaining articles were retrieved and evaluated to determine their eligibility. All studies meeting the eligibility criteria were included in the review, and their data were extracted. The information obtained from each article encompassed the authors, participants' age and sex, initial presentation, initial laboratory investigations, first diagnosis and management regimen, response to the initial regimen, point of diagnosis change, alteration in management therapy, and patient outcomes.

Quality assessment

We employed the Joanna Briggs Institute (JBI) critical appraisal checklists for case series and case reports to evaluate their methodological quality.[9,10] Subsequently, the results of the methodological quality assessment were presented in tabular form. Although formal metrics for inter-rater reliability were not computed, any differences were addressed through discussion until agreement was reached, adhering to the standards of qualitative synthesis.

Results

Search results

A comprehensive search across the databases yielded 967 references. After identifying and removing 757 duplicates, 210 references remained for relevance assessment. Of these, 147 abstracts were excluded due to irrelevance to the study. Subsequently, 63 articles were retrieved and evaluated against the eligibility criteria for inclusion in the review. Ultimately, 11 studies were included, having met the inclusion criteria. The remaining articles were excluded based on the following criteria: 12 were not published in English, 23 did not involve patients with PFIC3 and 17 did not address a misdiagnosis of PFIC3 as WD. Figure 1 presents the PRISMA diagram, which summarizes the search strategy.

Characteristics of the included studies

This review encompasses 11 studies, of which 9 are case reports[11–19] and 2 are case series.[20,21] These studies present evidence from 16 patients diagnosed with PFIC3, who initially presented as WD and were predominantly diagnosed and treated as such. The cohort consisted of 8 males, 5 females and 1 individual whose sex was not reported. The age of the participants across the studies was normally distributed (Shapiro–Wilk test, $W = 0.918$, $p = 0.206$), and is presented as mean ± standard deviation (SD) (19 ±12 years). A summary of the characteristics of all patients is provided in Table 1.[11–21]

Methodological quality

Most of the included case reports demonstrated high methodological quality and comprehensively reported all relevant information regarding the treatment and diagnosis of PFIC3 in the included patients. However, a few studies did not adequately document the patients' medical histories, while others failed to report the interventions administered following the diagnosis of PFIC3. A complete summary of the methodological quality is provided in Supplementary Table 1.

Discussion

This systematic review synthesizes case reports concerning the diagnostic challenges associated with PFIC3. The studies included in this review highlight that both the failure to diagnose PFIC3 and its misdiagnosis as WD result in significant long-term consequences, as chelation therapy proves ineffective, leading to a progressive deterioration of liver function in patients.[20,21] Consequently, it is imperative to identify common diagnostic pitfalls to facilitate the differentiation between these 2 conditions. We also present a summary of the differences identified in the features of PFIC3 and WD, which can aid in differential diagnosis (Supplementary Table 3).

Presentation of PFIC3 patients

The typical age of symptom onset in these patients is within the first 2 decades of life.[18] The earliest reported presentation occurs at 2 years of age, with the latest initial presentation occurring during the teenage years.[18] Common symptoms among these patients include elevated liver indices, hepatosplenomegaly, ascites, increased liver copper levels, elevated urinary copper excretion, and evidence of cirrhosis upon liver biopsy.[16,17] Unlike in WD,

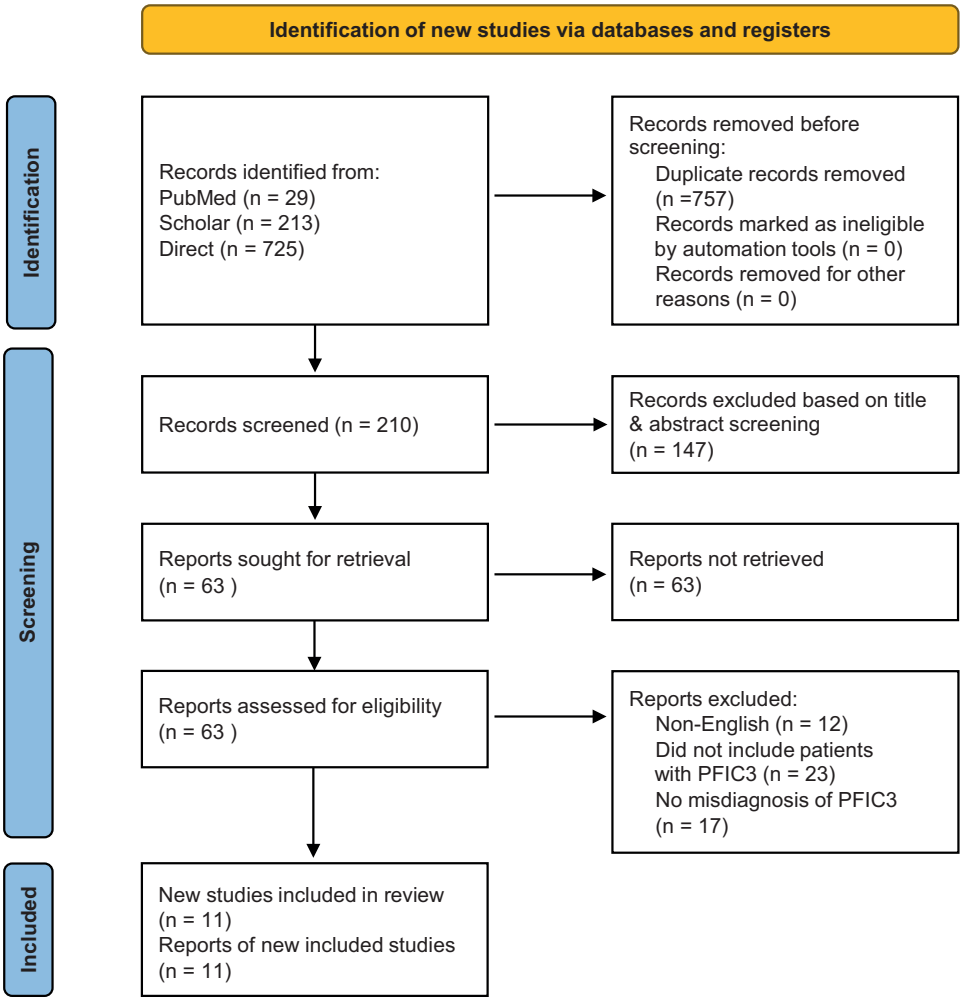

Fig. 1. Preferred Reporting Items for Systematic Reviews and Meta-Analyses (PRISMA) flow diagram

these patients do not exhibit Kayser–Fleischer (KF) rings upon ophthalmic examination.[17,18,22] Additionally, their ceruloplasmin levels are typically normal.[16,22] The presentation of impaired copper metabolism and accumulation often leads to the consideration of WD as the likely etiology of the observed liver disease in these patients.[23] Patients with PFIC3 also do not typically present with neurologic symptoms, unlike WD patients. Pathognomonic signs, especially in the putamen and globus pallidus, are common findings on brain magnetic resonance imaging (MRI) in WD patients.[24]

A distinguishing feature in the presentation of these patients is the absence of mutations in the *ATP7B* gene upon complete genome sequencing.[18,21] In most cases, ruling out WD due to the absence of this mutation prompts consideration of PFIC3 as a differential diagnosis, thereby reducing the likelihood of misdiagnosis.[16,20] Furthermore, the lack of *ATP7B* mutations often leads to further sequencing of the *ABCB4* gene, revealing mutations that confirm the diagnosis of PFIC3.[20] It is important to note that testing for MDR3 deficiency in biopsy specimens or explant samples may not yield conclusive results.[17] For example, Bansal and Rastogi reported negative findings for MDR3 deficiency in tissue samples, only to identify the mutation through whole-genome sequencing.[17] Therefore, whole-genome sequencing is recommended in cases of suspected PFIC3. Another distinguishing feature of these 2 conditions is the etiology of copper accumulation. In WD, copper accumulation is primarily due to impairment in copper transport, while in PFIC3, the cause of copper accumulation is cholestasis in most cases. Radiocopper testing, which typically relies on liver metabolism and transport of copper, is therefore a good diagnostic test for differentiating these 2 diseases. However, its use in the WD and PFIC3 diagnostic pitfalls is yet to be demonstrated.[25]

Management of PFIC3 in the context of misdiagnosis

In all included studies, the initial diagnosis of WD resulted in patients being placed on chelation therapy with either penicillamine, trientine or zinc.[16,19,20] However, evidence suggests that these patients do not benefit from chelation therapy, and liver function continues to deteriorate during the treatment period.[16,20] In some instances, this deterioration necessitates liver transplantation.[11,12,17] However, once PFIC3 is diagnosed and management is adjusted to UDCA at an initial dose

Table 1. Characteristics of the included studies

Reference	Sex (age [years])	Presentation, initial diagnostic findings	Initial diagnosis and therapy	Response to initial therapy	Point of change in diagnosis	Change in management	Outcome after final diagnosis
Sticova et al., 2020[11]	male (11)	Growth retardation, marked hepato-splenomegaly, right upper quadrant pain, intermittent pruritus, hepatomegaly, hirsutism, short stature, craniofacial dysmorphia, elevated liver enzymes, increased copper, fibrosis, no ATP7B mutations.	Wilson's disease was treated with conservative therapy.	Disease progression with further deterioration in laboratory indices necessitated split liver transplantation (LT).	After LT, immune-histological examination of the liver explant revealed the absence of the hepato-canalicular *ABCB4/MDR3* expression. PFIC3 was then confirmed through targeted resequencing of *ABCB4*.	No change since LT had already been done.	Doing well after LT.
Bardak et al., 2025[12]	male (33)	Fatigue, pruritus, jaundice, elevated liver enzymes, bilirubin; liver biopsy shows hepatitis, inflammation, fibrosis, copper accumulation; gallstones detected; increased urinary copper excretion, especially after penicillamine challenge.	WD (penicillamine) was changed to zinc and trientine after 3 years due to tremors.	The liver enzymes, conjugated bilirubin (0.21–2.17 mg/dL), remained elevated. Overall, there was an inadequate response to chelation therapy.	Repeat tests showed similar lab abnormalities; no Kayser–Fleischer rings on slit lamp; MRI revealed atypical basal ganglia changes; no ATP7B mutation; heterozygous ABCB4 mutations confirmed PFIC3.	Awaiting liver transplantation.	–
Panda et al., 2024[13]	male (12)	Progressive abdominal distention, flank fullness, edema, jaundice; hepatosplenomegaly; stunted growth; elevated liver enzymes, bilirubin; low albumin, pancytopenia; ascites; esophageal varices; no Kayser–Fleischer rings.	WD, which was managed by chelation therapy with D-penicillamine, increased to 20 mg/kg/day.	Liver function worsened, serum albumin decreased, transaminases increased, and an increase in INR.	Genetic analysis of *ATP7B* mutations came back negative. Further analysis found the *ABCB4* gene mutation, confirming the PFIC3 diagnosis.	Chelation therapy stopped. Ursodeoxycholic acid was started, and supportive management included fat-soluble vitamin supplementation and nutritional support.	Still deteriorating and awaiting liver transplant.
Flanagan et al., 2021[14]	female (6)	Epistaxis, abdominal pain, facial edema, pallor, fever; clubbing, icterus, splenomegaly; severe anemia, thrombocytopenia; elevated liver enzymes, bile acids; low ceruloplasmin; high urinary and hepatic copper; cirrhosis; no KF rings.	WD. Managed by chelation therapy before genetic testing.	Not reported	The cholestatic gene panel indicated the *ABCB4* gene variant, resulting in PFIC3 diagnosis.	Chelation therapy stopped. UDCA commenced after trientine was stopped.	Clinically stable, awaiting liver transplant.
Sondhi et al., 2025[15]	female (33)	Fatigue, elevated liver enzymes (2–3 years), painless progressive jaundice; high bilirubin; urinary copper 185 mcg; liver biopsy shows prominent cholestasis.	WD based on a history of jaundice in siblings. WD was managed by chelation therapy with oral D-penicillamine.	No improvement in the symptoms.	After failure of symptom improvement, whole-genome sequencing found the *ABCB4* mutation but did not find the *ATB7B* mutation, suggesting PFIC3 and ruling out WD.	Not reported.	Not reported.

Table 1. Characteristics of the included studies – cont.

Reference	Sex (age [years])	Presentation, initial diagnostic findings	Initial diagnosis and therapy	Response to initial therapy	Point of change in diagnosis	Change in management	Outcome after final diagnosis
Boga et al., 2015[16]	not reported (15)	Fatigue, esophageal varices, elevated urinary copper (342 µg), normal ceruloplasmin, absent Kayser–Fleischer rings, no ATP7B mutations; liver biopsy shows bridging fibrosis and high hepatic copper (1471 µg/g).	The original diagnosis of WD was managed with zinc, which was later switched to trientine due to the GI side effects of zinc. Nadolol was initiated as a prophylaxis against variceal bleeding.	No improvement after 12 months of trientine therapy. All the liver transaminases were elevated; urine copper excretion was elevated.	Due to poor response and lack of symptoms suggestive of WD (absent KF rings and lack of *ATB7B* mutation), other differential diagnoses were sought. Sequencing for the *ABCB4* gene was performed, and heterozygosity was found in the *ABCB4* gene mutations.	Patients were placed on the trial of UDCA, and after PFIC3 confirmatory diagnosis, the therapy was continued.	UDCA therapy reduced transaminases but not to normal; biopsy confirmed cirrhosis from initial presentation; mild persistent liver enzyme elevation; stable synthetic function; esophageal varices treated with banding.
Bansal and Rastogi 2017[17]	male (21)	Weakness, jaundice, ascites, abdominal pain, melena; grade III esophageal varices treated; anemia; high bilirubin; normal renal function; elevated urinary copper (1732.8 µg/24 h); hepatosplenomegaly; no Kayser–Fleischer rings.	Initial diagnosis of acute liver failure with a living donor transplant. WD was given as the etiology of cirrhosis observed on microscopic examination of the liver explant.	The patient was stable after LT, but liver enzymes became deranged after 4 months.	Explant tissues and biopsy slides were tested for the *MDR3* gene, all of which came back negative. A gene analysis was not possible, and thus, PFIC3 was diagnosed based on immunohistochemical findings.	Patients were placed on UDCA therapy.	All patients responded well to treatment.
Shneider et al., 2011[18]	female (2)	Abdominal distention, failure to thrive; elevated liver enzymes and copper; normal albumin, mild thrombocytopenia; high serum bile acids; liver biopsy shows bridging fibrosis; MRCP excludes sclerosing cholangitis.	–	–	–	Patient placed on UDCA.	Responded well to UDCA and is doing well with improvement in both liver and growth parameters.
Anheim et al., 2010[19]	male (35)	Bilateral keratoconus surgery; splenomegaly, cholelithiasis; elevated ALT, GGT (10x ULN); high bilirubin; thrombocytopenia; normal ceruloplasmin, serum, and urine copper; liver fibrosis with elevated copper; no ATP7B mutations.	A diagnosis of WD was evoked, and zinc was initiated.	Mild response	The patient presented with an epileptic seizure with delirium. Further evaluation led to a diagnosis of acanthocytosis. Liver function further worsened, and liver transplantation was performed, and a diagnosis of PFIC3 was made and confirmed by mutations found in the *ABCB4* genes.	UDCA was commenced alongside the acanthocytosis management regimen.	The patient is responding well to treatment.

Table 1. Characteristics of the included studies – cont.

Reference	Sex (age [years])	Presentation, initial diagnostic findings	Initial diagnosis and therapy	Response to initial therapy	Point of change in diagnosis	Change in management	Outcome after final diagnosis
Ramraj et al., 2012[20]	female (11) male (6)	Abdominal distention, hepatosplenomegaly, moderate ascites; liver biopsy shows elevated copper (860 µg/g); increased urinary copper; normal ceruloplasmin. Scleral icterus, hepatosplenomegaly; elevated AST, ALT, ALP, GGT; conjugated bilirubin 0.6 mg/dL; urine copper 66 µg/d; ceruloplasmin 44.6 mg/dL; liver biopsy shows bridging fibrosis, inflammation, and high copper (863 µg/g).	WD, which was treated with trientine as chelation therapy. Provisional diagnosis of WD, and the patient started on chelation therapy.	There was initial mild improvement in liver diseases. Not reported since the patient has not been on chelation therapy for long.	Patient referred for liver transplantation 2 years later. On evaluation, liver indices were elevated, and copper was also elevated. A liver biopsy showed inflammation and cirrhosis. *ATP7B* gene mutations were negative, so other etiologies were sought. After full gene sequencing, *ABCB4* gene mutations were discovered, and thus, PFIC3 was diagnosed. Whole gene sequencing found no *ATB7B* mutations but found an *ABCB4* gene mutation, and thus, PFIC3 was given as the final diagnosis.	Chelation therapy with trientine was discontinued, and UDCA was initiated at 20 mg/kg/d. Chelation therapy was discontinued, and UDCA was commenced at 20 mg/kg/d.	During a follow-up of 4 years, liver indices remained normal. The liver indices were stable during the follow-up of 18 months.
Nagral et al., 2024[21]	female (23)	6-year-old with jaundice, ascites; urinary copper 162 mcg/day; liver copper 1,692 mcg/g; positive penicillamine challenge; Leipzig score 4.	–	–	–	–	–
	male (27)	15-year-old with anger, poor school performance; ceruloplasmin 13.9 mg/dl; urinary copper 367.5 mcg/day; liver copper 90.4 mcg/g; Leipzig score 5.	Wilson's disease was managed with penicillamine.	No improvement was observed.	After reviewing the family history, whole gene sequencing was performed, and *ABCB4* mutations were found.	Not reported	Not reported.
	male (31)	24-year-old with abnormal LFTs; absent Kayser–Fleischer rings; urinary copper 192 mcg/day; liver biopsy shows elevated copper (166 mcg/g).	Wilson's disease was managed.	Presented after 7 years with worsening LFTs accompanied by itchiness.	The diagnosis was reviewed, whole-exome sequencing was performed, *ABCB4* gene mutations were found, and PFIC3 was diagnosed.	Not reported	Not reported.

ALT – alanine aminotransferase; AST – aspartate aminotransferase; CB – conjugated bilirubin; GGT – gamma-glutamyl transferase; INR – International Normalized Ratio; KF – Kayser–Fleischer; LT – liver transplantation; PFIC3 – progressive familial intrahepatic cholestasis type 3; TB – total bilirubin; UDCA – ursodeoxycholic acid; USG – ultrasonography; MRI – magnetic resonance imaging; ALP – alkaline phosphatase; Hb – hemoglobin; WBC – white blood cell count; GI – gastrointestinal; SAP – serum alkaline phosphatase; LFT – liver function test; MRCP – magnetic resonance cholangiopancreatography.

of 20 mg/kg/day, most patients experience stable liver function, and the liver disease does not progress.[19,20] While liver transplantation remains the definitive treatment for PFIC3, failure to diagnose PFIC3 can still lead to worsening liver function, as reported by Bansal and Rastogi, where a patient's liver indices became deranged 4 months post-liver transplantation. However, following the management change to UDCA, the patient responded well to treatment.[17]

Limitations of the study

This systematic review employed a comprehensive search strategy to examine all studies reporting PFIC3 presenting as WD. Nevertheless, the study encountered certain limitations. Primarily, we included only case reports, which suggests that these occurrences are rare. Consequently, while the findings may enhance awareness regarding the potential misdiagnosis of PFIC3, they cannot be generalized to the broader population. Furthermore, the exclusive reliance on case reports resulted in a minimal sample size from which our data were derived. The total sample size of 16 patients across 11 studies is quite small. Additionally, there is limited information provided on how data extraction and quality assessment were conducted – e.g., no formal metrics for inter-rater reliability are reported. The methodological quality assessment using JBI checklists is mentioned but details are lacking on how this was applied. There is also no formal synthesis or meta-analysis of data across studies due to the nature of the included reports. Finally, potential publication bias is not addressed, as case reports of successful diagnoses may be more likely to be published than misdiagnoses that were not eventually corrected.

Conclusions

Evidence synthesized from the included studies indicates that PFIC3 can manifest with symptoms resembling those of WD, potentially leading to misdiagnosis. It is important for clinicians to recognize that patients with PFIC3 do not exhibit KF rings upon slit lamp examination and typically present with normal ceruloplasmin levels. Consequently, whole-genome sequencing (WGS) of the *ATP7B* and *ABCB4* genes should be conducted to distinguish between WD and PFIC3. Furthermore, additional retrospective observational studies are warranted to ascertain the frequency with which PFIC3 is misdiagnosed as WD. This will facilitate the identification of diagnostic challenges and contribute to the development of diagnostic guidelines and protocols. Moreover, prospective studies should be undertaken to evaluate whether dual genetic testing for *ATP7B* and *ABCB4* gene mutations yields beneficial outcomes in the management of patients with either WD or PFIC3.

Supplementary data

The supplementary materials are available at https://doi.org/10.5281/zenodo.17242238. The package contains the following files:

Supplementary Table 1. A JBI checklist summarizing the methodological quality of the included case reports.

Supplementary Table 2. Leipzig criteria for WD diagnosis.

Supplementary Table 3. Differences in the presentation of WD and PFIC3.

Use of AI and AI-assisted technologies

Not applicable.

ORCID iDs

Eyad Gadour https://orcid.org/0000-0001-5087-1611
Bogdan Miutescu https://orcid.org/0000-0002-5336-5789
Deiana Vuletici https://orcid.org/0009-0005-6629-5280
Ghassan Elsayed https://orcid.org/0009-0007-2950-2118
Antonio Facciorusso https://orcid.org/0000-0002-2107-2156

References

1. Srivastava A. Progressive familial intrahepatic cholestasis. *J Clin Exp Hepatol*. 2014;4(1):25–36. doi:10.1016/j.jceh.2013.10.005
2. Agarwal S, Lal BB, Rawat D, Rastogi A, Bharathy KGS, Alam S. Progressive familial intrahepatic cholestasis (PFIC) in Indian children: Clinical spectrum and outcome. *J Clin Exp Hepatol*. 2016;6(3):203–208. doi:10.1016/j.jceh.2016.05.003
3. Gonzales E, Gardin A, Almes M, et al. Outcomes of 38 patients with PFIC3: Impact of genotype and of response to ursodeoxycholic acid therapy. *JHEP Rep*. 2023;5(10):100844. doi:10.1016/j.jhepr.2023.100844
4. Rosmorduc O, Poupon R, Hermelin B. *MDR3* gene defect in adults with symptomatic intrahepatic and gallbladder cholesterol cholelithiasis. *Gastroenterology*. 2001;120(6):1459–1467. doi:10.1053/gast.2001.23947
5. Jacquemin E, Bernard O, Hadchouel M, et al. The wide spectrum of multidrug resistance 3 deficiency: From neonatal cholestasis to cirrhosis of adulthood. *Gastroenterology*. 2001;120(6):1448–1458. doi:10.1053/gast.2001.23984
6. Chen R, Yang FX, Tan YF, et al. Clinical and genetic characterization of pediatric patients with progressive familial intrahepatic cholestasis type 3 (PFIC3): Identification of 14 novel *ABCB4* variants and review of the literatures. *Orphanet J Rare Dis*. 2022;17(1):445. doi:10.1186/s13023-022-02597-y
7. European Association for the Study of the Liver. EASL Clinical Practice Guidelines: Wilson's disease. *J Hepatol*. 2012;56(3):671–685. doi:10.1016/j.jhep.2011.11.007
8. Page MJ, McKenzie JE, Bossuyt PM, et al. The PRISMA 2020 statement: An updated guideline for reporting systematic reviews. *BMJ*. 2021;372:n71. doi:10.1136/bmj.n71
9. Barker TH, Stone JC, Sears K, et al. Revising the JBI quantitative critical appraisal tools to improve their applicability: An overview of methods and the development process. *JBI Evid Synth*. 2023;21(3):478–493. doi:10.11124/JBIES-22-00125
10. Gadour E. Lesson learnt from 60 years of liver transplantation: Advancements, challenges, and future directions. *World J Transplant*. 2025:18;15(1):93253. doi:10.5500/wjt.v15.i1.93253
11. Sticova E, Neroldova M, Kotalova R, Subhanova I, Jirsa M. ABCB4 disease mimicking morbus Wilson: A potential diagnostic pitfall. *Biomed Pap Med Fac Univ Palacky Olomouc Czech Repub*. 2020;164(1):121–125. doi:10.5507/bp.2019.054
12. Bardak AE, Kalaycı T, Çavuş B, Çifçibaşı Örmeci A, Demir K. From chelation to transplantation: Lessons from a progressive familial intrahepatic cholestasis type 3 case initially managed as Wilson's disease. *Gastroenterol Rep (Oxf)*. 2025;13:goaf017. doi:10.1093/gastro/goaf017

13. Panda K, Pradhan S, Dash M, Pati GK. Progressive familial intrahepatic cholestasis 3 camouflaging as Wilson disease in a 12-year-old: A diagnostic odyssey. *Gastroenterol Hepatol Bed Bench*. 2024;17(3):320–324. doi:10.22037/ghfbb.v17i3.2999
14. Flanagan M, Little R, Siddiqui I, Jones N, Ng V. A215 MDR3 deficiency mimicking Wilson disease. *J Can Assoc Gastroenterol*. 2021; 4(Suppl 1):247–248. doi:10.1093/jcag/gwab002.213
15. Sondhi P, Singh J, Kaur R, Kathait A, Brar AS. The neurological and hepatic nexus: Analyzing PFIC3 presentation as Wilson disease. Molecular genetic diagnosis and treatment response (P8-5.022). *Neurology*. 2025;104(7 Suppl 1):3239. doi:10.1212/WNL.0000000000210882
16. Boga S, Jain D, Schilsky ML. Presentation of progressive familial intrahepatic cholestasis type 3 mimicking Wilson disease: Molecular genetic diagnosis and response to treatment. *Pediatr Gastroenterol Hepatol Nutr*. 2015;18(3):202. doi:10.5223/pghn.2015.18.3.202
17. Bansal N, Rastogi M. An itchy experience: PFIC 3 masquerading as Wilson's disease. Learning from mistakes. *Oncol Gastroenterol Hepatol Rep*. 2017;6(2):67–71. https://pdfs.semanticscholar.org/dab0/307f092b889864a2ab1bb71f8440a789abc7.pdf.
18. Shneider BL. ABCB4 disease presenting with cirrhosis and copper overload-potential confusion with Wilson disease. *J Clin Exp Hepatol*. 2011;1(2):115–117. doi:10.1016/S0973-6883(11)60131-X
19. Anheim M, Chamouard P, Rudolf G, et al. Unexpected combination of inherited chorea-acanthocytosis with MDR3 (ABCB4) defect mimicking Wilson's disease. *Clin Genet*. 2010;78(3):294–295. doi:10.1111/j.1399-0004.2010.01386.x
20. Ramraj R, Finegold MJ, Karpen SJ. Progressive familial intrahepatic cholestasis type 3: Overlapping presentation with Wilson disease. *Clin Pediatr (Phila)*. 2012;51(7):689–691. doi:10.1177/0009922812451076
21. Nagral N, Poyekar S, Shah R, Wadia P, Nagral A. PFIC-3 mimicking Wilson disease: A case series. *J Clin Exp Hepatol*. 2024;14:102033. doi:10.1016/j.jceh.2024.102033
22. Schilsky ML, Roberts EA, Bronstein JM, et al. A multidisciplinary approach to the diagnosis and management of Wilson disease: Executive summary of the 2022 Practice Guidance on Wilson disease from the American Association for the Study of Liver Diseases. *Hepatology*. 2023;77(4):1428–1455. doi:10.1002/hep.32805
23. Wungjiranirun M, Sharzehi K. Wilson's disease. *Semin Neurol*. 2023; 43(4):626–633. doi:10.1055/s-0043-1771465
24. Singh P, Ahluwalia A, Saggar K, Grewal C. Wilson's disease: MRI features. *J Pediatr Neurosci*. 2011;6(1):27. doi:10.4103/1817-1745.84402
25. Członkowska A, Rodo M, Wierzchowska-Ciok A, Smolinski L, Litwin T. Accuracy of the radioactive copper incorporation test in the diagnosis of Wilson disease. *Liver Int*. 2018;38(10):1860–1866. doi:10.1111/liv.13715

Complex mosaic form of trisomy chromosome 18 and monosomy chromosome X in a girl with esophageal atresia and mild developmental delay: Diagnostic and therapeutic challenge and a review of literature

Joanna Chrzanowska[1,A–D], Aleksandra Oparska[2,B–D], Agata Wróblewska[2,B–D], Krzysztof Ciucias[2,B–D], Maria Luboińska-Cebula[1,B,C], Robert S. Śmigiel[1,A,E,F], Beata Wikiera[1,A,D–F]

[1] Department of Pediatrics, Endocrinology, Diabetology and Metabolic Diseases, Wroclaw Medical University, Poland
[2] Student Scientific Society at the Department and Clinic of Diabetology and Developmental Endocrinology within the Department and Clinic of Pediatrics, Endocrinology, Diabetology and Metabolic Diseases, Wroclaw Medical University, Poland

A – research concept and design; B – collection and/or assembly of data; C – data analysis and interpretation; D – writing the article; E – critical revision of the article; F – final approval of the article

Advances in Clinical and Experimental Medicine, ISSN 1899–5276 (print), ISSN 2451–2680 (online) *Adv Clin Exp Med*. 2026;35(7):1307–1312

Address for correspondence
Joanna Chrzanowska
E-mail: joanna.chrzanowska@umw.edu.pl

Funding sources
None declared

Conflict of interest
None declared

Received on February 12, 2026
Reviewed on April 27, 2026
Accepted on May 7, 2026

Published online on June 10, 2026

Abstract

The coexistence of mosaic trisomy 18 and Turner syndrome represents an extremely rare genetic constellation, with only a few cases reported in the literature to date. We present the case of a 7-year-old girl with esophageal atresia, full trisomy 18 in lymphocytes, and mosaic copy number changes involving trisomy 18 with coexisting monosomy X in fibroblasts, suggesting the presence of additional cell populations lacking trisomy 18. In addition, we provide a review of the relevant literature. This case is of particular clinical significance, as it describes long-term survival in a child with Edwards syndrome and illustrates the diagnostic challenges associated with tissue-limited mosaicism. Furthermore, it underscores that an established diagnosis of one genetic disorder does not preclude the coexistence of another, particularly when the clinical phenotype deviates from the classical presentation of the primary syndrome. Adequate analysis of a sufficient number of metaphases in karyotyping is essential to reliably detect or exclude mosaicism in Edwards syndrome, as the distinction between full and mosaic trisomy 18 carries important prognostic implications.

Key words: trisomy 18 syndrome, Turner syndrome, mosaicism, esophageal atresia, chromosomal aberrations

Cite as
Chrzanowska J, Oparska A, Wróblewska A, et al. Complex mosaic form of trisomy chromosome 18 and monosomy chromosome X in a girl with esophageal atresia and mild developmental delay: Diagnostic and therapeutic challenge and a review of literature. *Adv Clin Exp Med*. 2026;35(7):1307–1312. doi:10.17219/acem/221563

DOI
10.17219/acem/221563

Copyright
Copyright by Author(s)
This is an article distributed under the terms of the Creative Commons Attribution 3.0 Unported (CC BY 3.0) (https://creativecommons.org/licenses/by/3.0/)

Highlights

- Mosaic trisomy 18 with coexisting Turner syndrome is an exceptionally rare chromosomal disorder combination, with very few pediatric cases reported worldwide.
- Long-term survival in a child with Edwards syndrome highlights the clinical importance of identifying tissue-limited mosaicism and atypical genetic presentations.
- Combined trisomy 18 and monosomy X mosaicism demonstrates that multiple genetic syndromes may coexist when the clinical phenotype differs from the classic presentation.
- Comprehensive karyotype analysis with sufficient metaphase evaluation is essential for the accurate detection of mosaic Edwards syndrome due to its major prognostic implications.

Introduction

Mosaicism is a phenomenon in which distinct cell lineages carrying different genomes coexist within a single organism. Germline mosaicism is restricted to germ cells and is associated with heritability, whereas somatic mosaicism involves the remaining somatic cells and may contribute to the manifestation of a specific phenotype in an individual patient. Depending on the developmental stage at which a somatic mutation arises, the affected cells may be distributed throughout the entire organism or confined to particular tissues or organs, which can directly influence the severity of symptoms associated with the given genotype. In addition to situations in which a cell line carrying a chromosomal aberration coexists with a normal cell line, double mosaicism may also occur, in which both cell lines exhibit different types of chromosomal aberrations. This may result in the overlap of 2 distinct abnormal phenotypes, significantly complicating the patient's clinical presentation.[1]

Edwards syndrome is a severe chromosomal disorder caused by the presence of an extra chromosome 18. The condition occurs in approx. 1 in 6,000 live births. Of all trisomy 18 cases, 94% represent full trisomy (simple or translocation-associated), while 5% involve mosaicism, in which both normal and trisomy 18 cell lines are present. Suspicion of Edwards syndrome is typically raised prenatally or during the neonatal period based on characteristic dysmorphic features and prenatal-onset growth restriction, whereas survival is determined mainly by the severity of organ malformations, particularly congenital heart defects, as well as respiratory and feeding difficulties. The most common congenital malformations involve the cardiovascular and genitourinary systems. Gastrointestinal anomalies, such as esophageal atresia with tracheoesophageal fistula, are not a typical feature of trisomy 18 but occur with increased frequency compared with the general population. Severe psychomotor and cognitive developmental delay is typically present. However, the clinical presentation of mosaic trisomy 18 is highly variable, ranging from the complete trisomy 18 phenotype to the absence of dysmorphic features and preserved cognitive function. Approximately 50% of infants with trisomy 18 survive longer than 1 week, and 5–10% survive beyond the 1st year of life. Mortality is primarily associated with congenital heart defects, apnea, and recurrent respiratory infections. Survival is also strongly influenced by gestational age at delivery.[2,3]

Turner syndrome is a genetic disorder caused by the complete or partial loss of one X chromosome, leading to characteristic phenotypic features such as short stature, gonadal dysgenesis, and cardiovascular and renal abnormalities. The condition occurs in approx. 1 in 2,500 live-born females. Among all Turner syndrome cases, approx. 40–50% involve monosomy X (45,X), while mosaic forms account for about 28–40%, and structural X chromosome abnormalities represent approx. 15% of cases.[4] The simultaneous occurrence of both Turner syndrome and Edwards syndrome in mosaic form is an extremely rare phenomenon, with only a handful of cases documented in the medical literature. These rare reports suggest that the clinical presentation of such mosaic cases is highly variable, depending on the proportion of different cell lines and the extent of tissue involvement.

Below, we present the case of a 7-year-old girl with esophageal atresia, full trisomy 18 in lymphocytes, and mosaic copy number changes involving trisomy 18 with coexisting monosomy X in fibroblasts, suggesting the presence of additional cell populations lacking trisomy 18. This case is of particular clinical significance, as it describes a child with Edwards syndrome who demonstrated long-term survival and in whom an initial finding of trisomy 18 was later clarified through analysis of a 2nd tissue sample, revealing mosaicism.

A literature search was performed in PubMed using combinations of the terms "45,X" and "47,XX,+18". A total of 8 relevant case reports describing mosaicism involving both 45,X and 47,XX,+18 cell lines were identified and included in the analysis.[5–12]

Ethical considerations

Written informed consent was obtained from the patient's parents for publication of this paper. The patient's parents also provided informed consent for genetic testing, publication of this work, and presentation of their

child's image. The study was conducted in accordance with the principles of the Declaration of Helsinki and was approved by the Ethics Committee of Wroclaw Medical University, Wrocław, Poland (approval No. KB 430/2018).

Clinical presentation

The patient was born as the 3rd child to non-consanguineous parents (mother aged 36 years, father aged 37 years) following an uncomplicated vaginal delivery at 39 weeks of gestation. Birth weight was 2,390 g (standard deviation score (SDS) = –3.03 for gestational age), length 51 cm (SDS = 0.67 for gestational age), and head circumference 30 cm (SDS = –3.3), consistent with microcephaly. The Apgar score was 10. The pregnancy was complicated by polyhydramnios, a cardiac septal defect, and intrauterine growth restriction detected on prenatal ultrasonography.

On the 1st day of life, the girl underwent surgery for esophageal atresia with tracheoesophageal fistula. Postoperatively, she required intensive care due to sepsis and cardiorespiratory failure. Because of the cardiac septal defect, esophageal atresia, growth restriction, and dysmorphic features, cytogenetic analysis of peripheral blood lymphocytes was performed. Karyotype analysis, based on the evaluation of 15 metaphases, revealed 47,XX,+18 (the abnormality was present in cells from 2 independently established peripheral blood lymphocyte cultures). Following the genetic diagnosis, a care plan addressing the potential futility of further life-sustaining treatment was developed. The patient was extubated on day 10 and remained respiratory stable thereafter. In the following years, psychomotor developmental delay was observed, with sitting, walking, and speech milestones achieved at 10, 23, and 36 months of age, respectively. Between the 2nd and 3rd years of life, the patient experienced 3 episodes of lower gastrointestinal bleeding, which required hospitalization on 2 occasions. Infectious causes were clinically excluded. Technetium-99m pertechnetate scintigraphy was performed due to suspected Meckel's diverticulum, but the study revealed no focal tracer uptake suggestive of ectopic gastric mucosa. Additionally, abdominal ultrasonography revealed a focal hepatic lesion, which has remained under observation. The patient remained under regular follow-up in multiple specialist clinics. Cardiology follow-up revealed a hemodynamically insignificant ventricular septal defect; the atrial septal defect present at birth closed spontaneously. Orthopedic assessment identified right hip dysplasia and scoliosis associated with a congenital L3 hemivertebra. Ophthalmologic evaluation confirmed strabismus. Otolaryngologic follow-up documented a history of otitis media associated with hearing impairment. Renal ultrasonography findings were normal. At the age of 4 years, she underwent surgical excision of an epidermal cyst located in the suprasternal region. Due to the patient's prolonged survival, genetic testing was repeated using fibroblasts obtained during the surgical procedure. Array comparative genomic hybridization (array-CGH) revealed mosaic copy number changes involving trisomy 18 and monosomy X: arr(X)x1[0.35],(18)x3[0.65], suggesting the possible presence of a cell population with a normal copy number of chromosome 18.

At the age of 6.5 years, the girl was referred to the Department of Pediatric Endocrinology with a diagnosis of mosaic Edwards syndrome and mosaic Turner syndrome. From early childhood, growth retardation and breast enlargement had been observed. Ultrasonography performed at 2 years of age confirmed the presence of glandular breast tissue. The patient was diagnosed with mild intellectual disability and is currently enrolled in an early developmental support program. On admission, physical examination revealed short stature, gait with adduction of the right forefoot, scoliosis, asymmetry of the palpebral fissures (with the right fissure being narrower), and strabismus. Pubertal status was assessed as Tanner stage B3/P1. Auxological examination revealed a height of 105 cm (<3rd percentile; height SDS = –2.85), weight of 19.2 kg, and body mass index (BMI) of 17.4 kg/m^2 (75–90th percentile; SDS = 0.5). The patient's general appearance is shown in Fig. 1. Bone age was assessed

Fig. 1. The patient with complex mosaic form of trisomy 18 and monosomy X. Visible subtle dysmorphic features: low-set ears, small jaw, trunk-limb disproportion

as 6 years at a chronological age of 6.5 years. Hormonal parameters, including estradiol, follicle-stimulating hormone (FSH), and luteinizing hormone (LH), were within normal limits (estradiol <20.0 pg/mL; FSH 2.01 mIU/mL, reference range 0.5–3.2; LH <0.1 mIU/mL, reference range <0.3 mIU/mL). Pelvic ultrasonography revealed a uterine structure with dimensions at the upper limit of normal for age. The ovaries were not visualized.

Discussion

One of the most striking features in our patient is the relatively favorable clinical course and long-term survival, which are highly atypical for classic trisomy 18, in which survival beyond the 1st year is rare. An earlier study published in 1994 suggested that prolonged survival in children with full trisomy 18 may reflect natural variability in disease severity rather than undetected mosaicism. However, more recent studies consistently demonstrate that mosaic trisomy 18 is associated with a milder clinical presentation and improved survival. For example, an analysis based on parent questionnaires and medical records from 98 families showed that children with mosaic trisomy 18 exhibit a distinctly milder phenotype compared with those with full trisomy 18.[13] A subsequent study analyzing 326 live births with trisomy 18 (309 full trisomy and 17 mosaic cases) demonstrated that early survival is substantially higher in mosaic cases: approx. 70% survive the 1st year, and 41% survive at least 5 years, compared with 8% and 1%, respectively, in full trisomy 18.[14]

Another study published in 2025 reported that, in a cohort of 503 patients, 8.5% survived to the age of 10 years. After distinguishing between mosaic/partial trisomy 18 (considered jointly) and full trisomy 18, approx. 44% of individuals in the former group reached 10 years of age, whereas only 6.7% in the latter group did. It remains unclear whether these results were based solely on peripheral blood lymphocyte analysis or whether mosaicism may have been absent in blood but present in other tissues.[15]

Based on the review of the 8 analyzed articles, it was found that in 2 cases, the initial karyotype analysis of peripheral blood lymphocytes (evaluating 16 and 50 metaphases, respectively) suggested full trisomy 18. In both cases, however, the clinical presentation was atypical for Edwards syndrome, prompting further diagnostic evaluation. Subsequent extended investigations, including fibroblast analysis and fluorescence in situ hybridization (FISH), revealed mosaicism with a lower proportion of trisomy 18 cells; in 1 case, an additional ring chromosome 18 was identified.[10,12] In our case, the situation was somewhat different. The patient presented with phenotypic features consistent with Edwards syndrome; however, prolonged survival and a relatively milder clinical course were atypical for full trisomy 18.

Mosaic trisomy 18 is associated with longer survival and a milder phenotype; therefore, analysis of a sufficient number of metaphases to detect or exclude mosaicism is essential, as distinguishing mosaic from full trisomy 18 carries important prognostic significance. Our patient was initially diagnosed with full trisomy 18 based on karyotype analysis of peripheral blood lymphocytes. Mosaicism was subsequently demonstrated by array-GCH analysis of skin fibroblasts. The estimated 65% trisomic signal indicates that approx. 35% of the cell population does not harbor trisomy 18. In addition, the array profile suggests that approx. 35% of the cell population lacks 1 X chromosome.

The diagnosis of 1 genetic disorder does not exclude the presence of another, and this possibility should be considered, especially when the patient's clinical phenotype deviates from the typical spectrum of the primary syndrome.[16,17] According to current diagnostic guidelines, the diagnosis of Turner syndrome requires the presence of X chromosome abnormalities together with characteristic phenotypic features.[4]

The coexistence of mosaic Turner syndrome and trisomy 18 in a single patient represents an extremely rare genetic constellation, with very few cases documented in the literature to date.[5–12] The phenotype of these patients is highly variable, ranging from severe presentations with predominant features of trisomy 18 to relatively mild manifestations, and depends on the proportions and tissue distribution of the different cell lineages. However, the distribution of trisomic cells in critical organs cannot be predicted based on peripheral blood findings.[18]

The clinical presentation is not simply a composite of trisomy 18 and Turner syndrome but rather reflects the dominant karyotypic lineage in key tissues. In a case reported by Schluth-Bolard et al., cytogenetic analysis was performed for reasons unrelated to clinical suspicion of trisomy 18 or Turner syndrome, and the diagnosis was established only after genetic testing, followed by retrospective phenotypic evaluation. Cytogenetic and FISH studies revealed 45,X/47,XX,+18 mosaicism with clear tissue dependence, characterized by a predominance of monosomy X in skin fibroblasts and trisomy 18 in peripheral blood cells. This finding represented a rare example of tissue-specific mosaicism associated with distinctive facial features, bicuspid aortic valve, and ovarian agenesis.[10] Previous reports indicate that in 45,X/47,XX,+18 mosaicism, trisomy 18 tends to predominate in peripheral blood, whereas monosomy X is more prevalent in other tissues, consistent with the genetic findings observed in our patient.

This exceptional rarity presents significant diagnostic and therapeutic challenges. From the perspective of phenotype–genotype correlation, dual mosaicism may sometimes help explain the mixed clinical picture: several findings align with trisomy 18, whereas others may reflect the influence of Turner syndrome. Difficulties arise when a particular feature (e.g., short stature in our case) is observed in both syndromes. Impaired growth in Turner syndrome is caused by haploinsufficiency of the *SHOX* (short stature homeobox) gene located on the X chromosome and

requires treatment with recombinant growth hormone at supraphysiological doses. Growth retardation in Edwards syndrome is common and multifactorial, resulting from intrauterine growth restriction, severe congenital anomalies, feeding difficulties, and chronic cardiorespiratory failure. Its exact pathogenesis has not been fully elucidated. From a clinical perspective, management of Edwards syndrome is primarily determined by the severity of congenital defects and the high mortality in early life rather than by growth impairment itself. In the presence of full trisomy 18 in peripheral blood and mosaic copy number changes involving trisomy 18 with coexisting monosomy X in fibroblasts, with a phenotype clearly dominated by Edwards syndrome rather than Turner-related features, and in the context of concurrent scoliosis, there are no justified indications for initiating growth hormone therapy.

Cardiac defects suggestive of Turner syndrome typically involve left-sided cardiac structures, whereas a ventricular septal defect (VSD) is less characteristic. A VSD may be considered part of the Turner syndrome phenotype if accompanied by other typical features,[4] but it is more commonly associated with Edwards syndrome. Our patient presented with thelarche praecox, an atypical finding in Turner syndrome, in which spontaneous breast development is usually absent during puberty, whereas in mosaic Turner syndrome it may occur at the expected pubertal age. Isolated premature thelarche is defined as the development of breast tissue in the absence of other signs of pubertal development, such as accelerated growth velocity, rapid breast progression, or advanced skeletal maturation.[19] In pediatric patients, non-visualization of the ovaries on ultrasonography may reflect technical limitations or small gonadal size rather than true ovarian agenesis. Accordingly, thelarche in our patient may be consistent with isolated premature thelarche, a condition that can occur in otherwise healthy girls; in this case, it may be related to mosaic gonadal cell lines with preserved ovarian function.

In patients with mosaicism, genetic testing limited to a single cell type, such as peripheral blood lymphocytes, may be insufficient for detecting a pathogenic variant. The distribution and proportion of mutant cells across different tissues depend on several biological and technical factors.

First, the embryological origin of different tissues plays a crucial role. During early development, cells differentiate into distinct germ layers (ectoderm, mesoderm, and endoderm) which give rise to separate tissue lineages. Since blood cells originate primarily from the mesoderm, whereas tissues such as skin or oral epithelium derive from other germ layers, a postzygotic mutation may be confined to a single lineage, resulting in lineage-specific mosaicism detectable only in certain tissues.[20]

Second, cellular selection may influence the detectability of mosaicism. Cells carrying chromosomal or genomic aberrations may have reduced viability or proliferative potential in particular tissues, such as peripheral blood, leading to their gradual elimination. Consequently, the abnormal clone may persist in other tissues (e.g., gonadal or cutaneous cells) while being absent from blood-derived DNA, resulting in a false-negative lymphocyte-based result.

Third, technical limitations of genetic testing may contribute to underdetection. Conventional karyotype analysis typically examines a limited number of metaphase cells, resulting in relatively low sensitivity for detecting low-level mosaicism (<10%).

Finally, the timing of the postzygotic mutation affects the extent of its distribution. Mutations occurring later in embryogenesis tend to affect a smaller proportion of tissues, potentially sparing hematopoietic cells altogether.[21,22]

For these reasons, when the clinical presentation strongly suggests a genetic disorder but testing of a single cell type (e.g., lymphocytes) yields negative or inconclusive results, it is advisable to repeat the analysis using DNA from an alternative tissue source, such as fibroblasts, buccal epithelial cells, or urinary epithelial cells. This strategy increases the likelihood of detecting tissue-specific or low-level mosaic abnormalities and facilitates a more accurate molecular diagnosis.

Limitations of the study

This report is limited by evaluating mosaicism solely in peripheral tissues and lacking a classical fibroblast karyotype. Although expanding the phenotypic spectrum of trisomy 18 mosaicism, clinical findings must guide prognosis rather than peripheral cytogenetic percentages.

Conclusions

Analysis of a sufficient number of metaphases is essential to reliably detect or exclude mosaicism in Edwards syndrome, as the distinction between full and mosaic trisomy 18 carries important prognostic implications. When the clinical presentation is atypical, repeat analysis using biological material derived from an alternative tissue source should be considered. The diagnosis of one genetic disorder does not exclude the presence of another, and this possibility should be considered, particularly when the patient's clinical phenotype deviates from the typical spectrum of the primary syndrome.

Use of AI and AI-assisted technologies

ChatGPT 5 were used for language editing, stylistic refinement, and improvement of clarity.

ORCID iDs

Joanna Chrzanowska https://orcid.org/0000-0002-3210-6681
Aleksandra Oparska https://orcid.org/0009-0004-8284-5660
Agata Wróblewska https://orcid.org/0009-0009-8570-8326
Krzysztof Ciucias https://orcid.org/0009-0000-2445-8057
Maria Luboińska-Cebula https://orcid.org/0009-0001-6147-9890
Robert Stanisław Śmigiel https://orcid.org/0000-0003-2930-9549
Beata Wikiera https://orcid.org/0000-0001-8797-6636

References

1. Thorpe J, Osei-Owusu IA, Avigdor BE, Tupler R, Pevsner J. Mosaicism in human health and disease. *Annu Rev Genet*. 2020;54(1):487–510. doi:10.1146/annurev-genet-041720-093403
2. Cereda A, Carey JC. The trisomy 18 syndrome. *Orphanet J Rare Dis*. 2012;7(1):81. doi:10.1186/1750-1172-7-81
3. Śmigiel R, Patkowski D, Pyrek B, et al. Difficult therapeutic decision making in treatment of children with oesophageal atresia and trisomy of chromosome 18: Comments by geneticist, surgeon, neonatologist, paediatrician and anaesthesiologist [in Polish]. *Med Wieku Rozwoj*. 2011;15(1):7–15. PMID:21786507.
4. Gravholt CH, Andersen NH, Christin-Maitre S, et al. Clinical practice guidelines for the care of girls and women with Turner syndrome. *Eur J Endocrinol*. 2024;190(6):G53–G151. doi:10.1093/ejendo/lvae050
5. Franceschini P, Guala A, Camerano P, Franceschini D, Vardeu MP, Signorile F. Ullrich–Turner phenotype with unusual manifestation in a patient with mosaicism 45,X/47,XX,+18. *Am J Med Genet*. 1996; 62(1):26–28. doi:10.1002/(SICI)1096-8628(19960301)62:1%3C26::AID-AJMG6%3E3.0.CO;2-U
6. Genuardi M, Pomponi MG, Torrisi L, Neri G, Stagni ML, Tozzi C. 45,X/47,XX, + 18 constitutional mosaicism: Clinical presentation and evidence for a somatic origin of the aneuploid cell lines. *J Med Genet*. 1999;36(6):496–498. PMID:10874643. PMCID:PMC1734376.
7. Schubert R, Eggermann T, Hofstaetter C, Von Netzer B, Knöpfle G, Schwanitz G. Clinical, cytogenetic, and molecular findings in 45,X/47, XX,+18 mosaicism: Clinical report and review of the literature. *Am J Med Genet*. 2002;110(3):278–282. doi:10.1002/ajmg.10442
8. Lorda-Sanchez I, Trujillo MJ, Gomez-Garre P, et al. Turner phenotype in a girl with a 45,X/46,XX/47,XX,+18 mosaicism. *Am J Med Genet A*. 2003;121A(1):20–24. doi:10.1002/ajmg.a.10197
9. Picone O, Hirt R, Brisset S, Frydman R, Senat M, Tachdjian G. Double aneuploid mosaicism 45,X/46,XX/47,XX,+18 in a fetus with cerebral malformations. *Prenat Diagn*. 2006;26(8):755–757. doi:10.1002/pd.1489
10. Schluth-Bolard C, Sanlaville D, Labalme A, et al. Unexpected diagnosis of 45,X/47,XX,+18 mosaicism in a girl with mild phenotype. *Am J Med Genet A*. 2009;149A(11):2584–2587. doi:10.1002/ajmg.a.32772
11. Tyler CT, Rice GM, Grady M, Raca G. Mild clinical presentation in a child with prenatally diagnosed 45,X/47,XX,+18 mosaicism. *Am J Med Genet A*. 2009;149A(11):2588–2592. doi:10.1002/ajmg.a.33084
12. McGoey RR, Jackson K, Marble M. 45,X/47,XX,+18 and ring (18) mosaicism with mild phenotypic features including normal stature: Clinical report and review of the literature. *Clin Dysmorphol*. 2009;18(1): 59–61. doi:10.1097/MCD.0b013e3283186923
13. Baty BJ, Blackburn BL, Carey JC. Natural history of trisomy 18 and trisomy 13: I. Growth, physical assessment, medical histories, survival, and recurrence risk. *Am J Med Genet*. 1994;49(2):175–188. doi:10.1002/ajmg.1320490204
14. Wu J, Springett A, Morris JK. Survival of trisomy 18 (Edwards syndrome) and trisomy 13 (Patau syndrome) in England and Wales: 2004–2011. *Am J Med Genet A*. 2013;161(10):2512–2518. doi:10.1002/ajmg.a.36127
15. Ludorf KL, Benjamin RH, Shumate CJ, Canfield MA, Nguyen J, Agopian AJ. Long-term survival among children with trisomy 13 and trisomy 18 by cytogenetic status. *JAMA Netw Open*. 2025;8(9):e2529885. doi:10.1001/jamanetworkopen.2025.29885
16. Wikiera B, Nocoń-Bohusz J, Noczyńska A. Silver-Russell syndrome and Turner syndrome in a girl with short stature treated with growth hormone: Case report. *Pediatr Endocrinol Diabetes Metab*. 2022;28(4): 301–304. doi:10.5114/pedm.2022.121463
17. Jones KL, McNamara EA, Longoni M, et al. Dual diagnoses in 152 patients with Turner syndrome: Knowledge of the second condition may lead to modification of treatment and/or surveillance. *Am J Med Genet A*. 2018;176(11):2435–2445. doi:10.1002/ajmg.a.40470
18. Tucker ME, Garringer HJ, Weaver DD. Phenotypic spectrum of mosaic trisomy 18: Two new patients, a literature review, and counseling issues. *Am J Med Genet A*. 2007;143A(5):505–517. doi:10.1002/ajmg.a.31535
19. Cheuiche AV, Da Silveira LG, De Paula LCP, Lucena IRS, Silveiro SP. Diagnosis and management of precocious sexual maturation: An updated review. *Eur J Pediatr*. 2021;180(10):3073–3087. doi:10.1007/s00431-021-04022-1
20. Muyas F, Zapata L, Guigó R, Ossowski S. The rate and spectrum of mosaic mutations during embryogenesis revealed by RNA sequencing of 49 tissues. *Genome Med*. 2020;12(1):49. doi:10.1186/s13073-020-00746-1
21. Waldvogel SM, Posey JE, Goodell MA. Human embryonic genetic mosaicism and its effects on development and disease. *Nat Rev Genet*. 2024;25(10):698–714. doi:10.1038/s41576-024-00715-z
22. Choo S, Teo S, Tan M, Yong M, Ho L. Tissue-limited mosaicism in Pallister–Killian syndrome: A case in point. *J Perinatol*. 2002;22(5):420–423. doi:10.1038/sj.jp.7210712